

C19

A P O L L O

Mid-Term

ERROR ANALYSIS - TRANSEARTH GUIDANCE SYSTEM

Technical Memorandum No. TM-2

THE MARTIN COMPANY

Baltimore 3, Maryland

March 13, 1961

APOLLO MID-TERM PROGRESS REPORT (Martin Co.)  
422 p

N75-71340  
THRU  
N75-71352  
Unclas  
31300

00/98

REPRODUCED  
NATIONAL TECHNICAL  
INFORMATION SERVICE  
U.S. DEPARTMENT OF COMMERCE  
SPRINGFIELD, VA. 22161

## NOTICE

THIS DOCUMENT HAS BEEN REPRODUCED FROM THE BEST COPY FURNISHED US BY THE SPONSORING AGENCY. ALTHOUGH IT IS RECOGNIZED THAT CERTAIN PORTIONS ARE ILLEGIBLE, IT IS BEING RELEASED IN THE INTEREST OF MAKING AVAILABLE AS MUCH INFORMATION AS POSSIBLE.

The transearth portion of the total flight trajectory represents one of the most critical guidance areas due to the stringency of requirements for delivering the vehicle to a narrow re-entry corridor and the establishment of accurate initial conditions of velocity, position and local vertical orientation, the latter required to achieve the landing point accuracy.

For the purposes of this analysis, it has been assumed that all guidance is performed solely with vehicle borne equipment. It is further assumed that the actual vehicle trajectory will be determined by explicit techniques. There are many methods by which the vehicle trajectory can be obtained. For the self-contained system, these will be limited to data which can be directly obtained or computed from angle measurements between stars and features of the earth and moon, an accurate measurement of time and lunar ephemeris and star data. The general methods are as follows:

- 1) From a knowledge of range from the vehicle to the geocenter, the direction cosines between the local geocentric vertical and an inertial reference and time, these values being taken at a number of points along the trajectory, the trajectory can be computed. Thus, the trajectory can be determined by measurement of range, direction cosines and time at two points, range and the direction cosines at these points and the direction cosines and time at four points.
- 2) The trajectory can be computed from observation of the time of lunar occultation of six known stars or from the observation of the time of lunar occultation of three known stars and the identification of the point on the moon where occultation occurred.

- 3) More generally, the trajectory can be obtained from the measurements of six independent pieces of information. Thus, if the angle between a known pair of stars and an accurately known landmark such as a lunar crater and time are taken at six points along the trajectory, and the trajectory can be computed. For the trajectory to be computed, these six pieces of information can be diverse types (i.e., angles, range, etc., at each measurement).

The first method treats the parameters range and local vertical as if they were obtained at a discrete point along the trajectory. In actual practice the information required to determine these parameters represent readings taken at three or more discrete times and positions, this distributed data being updated in the digital computer to obtain the parameters range and local vertical at a specific future time. For the other two general methods considered, this problem does not arise as each reading is considered to be an independent piece of information which will be factored into the computational technique. This situation arises due to tracker configurations which appear to be the most favorable at this time:

- 1) For the automatic mode, a narrow angle optical tracker located on the inner gimbal of the inertial platform will serve the dual function of star and earth or moon tracking. The platform will be aligned to an inertial reference coordinate system using the tracker in the star tracking mode. The tracker will then be employed to sight on the edge of the earth disc or landmarks, the angle readout between the tracker and the inertial platform yielding the direction cosines of the tracker line sight with respect to the



inertial coordinate system. To obtain local vertical or range, three such readings are required.

- 2) For the manual mode of operation, the simplest and most reliable system will utilize a sextant for manually superimposing the image of a star on a landmark. Local vertical and range is obtained from six such readings which must be updated.

A mathematical study of occultation techniques is being performed at The Martin Company (Ref. 1) but an error analysis has not been completed. The general method of employing six independent pieces of measured data to determine a trajectory is being studied by the Arma Division of the American Bosch Arma Corporation. Although these methods may prove more amenable to the mechanization and computational techniques of the vehicle contained guidance system, it will require further analysis involving machine runs to obtain an error analysis and determine the smoothing and weighting techniques.

In order to obtain a preliminary error analysis so as to determine the order of accuracy that can be expected, the more conventional techniques were considered. The method of explicitly determining the trajectory involves the measurement of range from the vehicle to the geocenter and the local geocentric vertical at three discrete points along the trajectory (Ref. 2). The local geocentric vertical is obtained from measurements of the earth disc included angle or by from landmark measurements. Range can be obtained from this latter method or by triangulation techniques with respect to the local geocentric and selenocentric verticals.

## Measurement Techniques

### 1. Included Angle and Landmarks

With a knowledge of the geophysical properties of the earth and measurement of a minimum of three lines from the vehicle to the rim of the earth disc with respect to an inertial frame of reference, the local vertical and range can be computed. For simplicity, considering the coplanar case and a spherical earth, the conventions are indicated in Fig. 1 where

$\beta_1$  and  $\beta_2$  are the measured angles with respect to an inertial reference

$\theta$  is the local geocentric vertical with respect to an inertial reference

$r_e$  and  $r_{e_1}$  are the radius of the earth

$r$  is the range.

Two classes of errors will be considered:

- 1) Errors which affect the accuracy of the angle  $\beta$  and are considered to be variant with range to the earth. This will include such errors as due to optics, pickoffs, variations in the physical dimensions of the tracker due to temperature variations, etc.
- 2) Errors which affect the assumed model of the earth. This will include the effect of the earth's atmosphere, uncertainties in the contour of the earth, uncertainties in the coordinates of landmarks, etc.

Assuming that the errors  $\Delta\beta_1 = \Delta\beta_2 = \Delta\beta$  and  $\Delta r_{e_1} = \Delta r_{e_2} = \Delta r_e$ , the range and local vertical error partials are:

$$1) \quad \frac{\Delta r}{\Delta r_e} = \frac{0.707}{\sqrt{1 - r_e^2}} ; \quad \frac{\Delta \theta}{\Delta \beta} = 0.707$$

$$2) \quad \frac{\Delta r}{\Delta r_e} = 0.707 \frac{r}{r_e} ; \quad \frac{\Delta \theta}{\Delta \beta} = 0.707 \frac{r}{r_e} \frac{1}{\sqrt{1 - r_e^2}}$$

These error coefficients are presented in Figs. 2 and 3 as a function of range to the earth. The included angle technique can be considered as a special case of the landmark method where the landmarks are located near the edge of the earth disc. As the available landmarks are located closer to the local geocentric vertical, the local vertical accuracy improves for a given landmark accuracy and the range error deteriorates. The accuracy of the landmark, however, will be greater than that of the rim of the earth disc. Two conditions were selected and are shown in Figs. 4 and 5. For the included angle method where the rim of the earth disc is tracked, the uncertainty in radius ( $\Delta r_e$ ) is taken at 1 NM and an angle error ( $\beta$ ) is 10 arc seconds. For measurements employing earth landmarks, the landmark error ( $\Delta r_e$ ) was taken at 0.2 NM and an angle error ( $\Delta\beta$ ) of 4 arc seconds.

## 2. Triangulation

Utilizing the previous techniques, the local geocentric and selenocentric verticals are determined. The angle between the line of sight to the geocenter and the line of sight to each of two stars determines the direction of the local geocentric vertical in space. Similarly, the angle between the line of sight to the selenocenter and the lines of sight to two stars determines the direction of the local selenocentric vertical in space. The vehicle lies at the intersection of the two verticals. The angles between these lines of sight, together with the moon's ephemeris, fully specify the vehicle position. Position errors are a function of the characteristics of the trajectory. For a specific trajectory, machine runs at Arma determined the total position error (Ref. 3). This is indicated in Fig. 6. The increase in error in the translunar trajectory in the vicinity 25,000 naut mi range from the earth is due to the approach of the vehicle to the earth-moon line. The reduced increase in error during the transearth portion of the trajectory

is a function of the particular trajectory considered. In general, the latter must be considered as highly conservative as transearth trajectories which are mirror images of the translunar case is close to the actual situation to be expected. The magnitude and shape of the error curve, being a function of the relative location of the vehicle, earth and moon, will change somewhat for different trajectories.

Considering the translunar portion of Fig. 6 as being applicable to transearth, the included angle or landmark method of determining range is more accurate than the triangulation method for earth ranges less than 40,000 naut mi.

### Trajectory Error Analysis

This method of explicitly determining the vehicle trajectory involves the measurements of range from the vehicle to the geocenter and the local geocentric vertical at three discreet points along the trajectory (Ref. 2). The problem was reduced to that of a coplanar limited two-body case which can be represented by:

$$r = \frac{P}{1 + e \cos(\theta - \delta)}$$

where

$r$  = range from the vehicle to the geocenter

$\theta$  = local geocentric vertical with respect to an inertial reference

$P$  = semi-latus rectum

$e$  = eccentricity

$\delta$  = angle between the major axis of the ellipse and an inertial reference

This is shown in Fig. 7. The trajectory considered has an eccentricity of 0.9725 and a semi-latus rectum of  $0.4100 \times 10^8$  ft. The error partials are given in Table I. Although the actual conditions deviate from the limited

two-body assumption at long ranges from the earth, it rapidly converges to the limited two-body case as the vehicle approaches the earth. The error in neglecting the effect of earth oblateness on the gravity field was found to be 2 naut mi when the trajectory lies in the equatorial plane and 0.4 naut mi at  $45^\circ$  from the equatorial plane.

The results of the analysis are tabulated in Table II. For ranges less than 45,000 naut mi, it was assumed that the landmark and included angle method would be used. For case III where range exceeds 45,000 naut mi, range was obtained using the triangulation methods. The effect of  $\Delta e$  was small as compared to  $\Delta p$  and was ignored.  $\Delta P$  approximates the re-entry corridor. The error partial  $\Delta P / \Delta \beta$  reduces as the vehicle approaches the earth. The spacing between the three points along the trajectory is critical as indicated by cases IV and V where the ratio between the first and last reading was changed from 3/1 to 4/1 and 2/1. A decrease in this spacing, as might be expected, increases the magnitude of the error partials.

Considering cases I and II for the  $\Delta r_e$  and  $\Delta \beta$  errors previously considered, the re-entry corridor ( $\Delta p$ ) will be:

<u>Case</u>	<u><math>\Delta P</math> for <math>\Delta r_e = 1 \text{ NM}, \Delta \beta = 10 \text{ arc sec}</math></u>	<u><math>\Delta P</math> for <math>\Delta r_e = 0.2 \text{ NM},</math></u>
		<u><math>\Delta \beta = 4 \text{ arc sec}</math></u>
I	14.8 nm (1 sigma) or 44.4 nm (3 sigma)	3.5 nm (1 sigma) or 10.5 nm (3 sigma)
II	29.6 nm (1 sigma) or 88.8 nm (3 sigma)	9.9 nm (1 sigma) or 29.7 nm (3 sigma)

### Smoothing

The above 1 sigma errors are based on single sets of readings from the trackers at each of the three positions along the trajectory. By taking  $n$  readings at each measurement position, and using all measurements in the computation, the error can be reduced by  $1/\sqrt{n}$  provided that a sufficiently large sample is obtained and the errors are random and not biases. By taking multiple readings, the error can be reduced until the remaining error becomes predominately bias. Beyond that point, there is nothing to be

by obtaining additional data. Much of the equipment biases can be removed by in-flight calibration. The geophysical errors (landmarks and characteristics of the rim of the earth disc) will require further investigation to determine the portion of this value that is bias and random. In general, the trajectory error can be reduced by smoothing techniques involving multiple readings, the exact amount being a function of the distribution of random and bias errors. The increase in spacing between the three trajectory positions will also serve to reduce the error. By using past data updated and weighted to account for any intervening midcourse corrections that may be applied to the vehicle, the trajectory can be more accurately computed based on longer intervals between trajectory positions. Further work will be required to determine optimum smoothing, weighting and prediction techniques.

#### REFERENCES

1. Martin internal IDC on Occultation Techniques.
2. "An Exploratory Statistical Analysis of a Planet Approach-Phase Guidance Scheme Using Angular Measurements with Significant Error." by A. L. Friedlander and D. P. Harry III NASA TN D-471 dtd September 1960.
3. "Error Analysis for an Optical Position Fix in the Apollo Vehicle" Arma Division of American Bosh Arma Corporation Technical Report dtd February 1961.

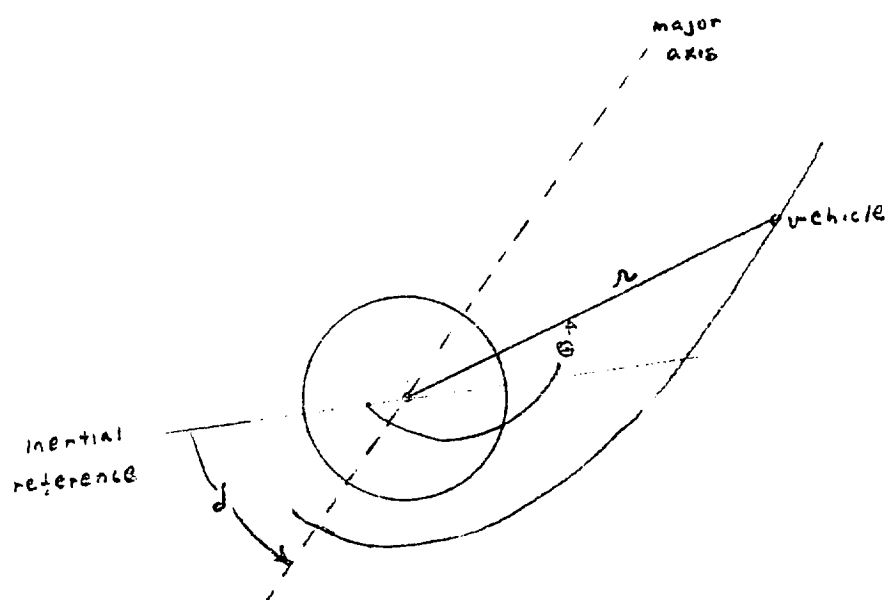
	$\Delta r_1$	$\Delta r_2$	$\Delta r_3$	$\Delta \theta_1$	$\Delta \theta_2$	$\Delta \theta_3$
$\Delta \theta_1 =$	$\frac{r_2}{r_1} \sin \left  \frac{\theta_1 - \theta_2}{2} \right $	$\frac{r_2}{r_1} \sin \left  \frac{\theta_1 - \theta_2}{2} \right $	$\frac{r_2}{r_1} \sin \left  \frac{\theta_1 - \theta_2}{2} \right $	$-\frac{r_2}{r_1} \sin \left  \frac{\theta_1 - \theta_2}{2} \right $	$\frac{r_2}{r_1} \sin \left  \frac{\theta_1 - \theta_2}{2} \right $	$-\frac{r_2}{r_1} \sin \left  \frac{\theta_1 - \theta_2}{2} \right $
$\Delta \theta_2 =$	$\frac{r_2}{r_1} \sin \left  \frac{\theta_1 - \theta_2}{2} \right $	$\frac{r_2}{r_1} \sin \left  \frac{\theta_1 - \theta_2}{2} \right $	$\frac{r_2}{r_1} \sin \left  \frac{\theta_1 - \theta_2}{2} \right $	$-\frac{r_2}{r_1} \sin \left  \frac{\theta_1 - \theta_2}{2} \right $	$\frac{r_2}{r_1} \sin \left  \frac{\theta_1 - \theta_2}{2} \right $	$-\frac{r_2}{r_1} \sin \left  \frac{\theta_1 - \theta_2}{2} \right $
$\Delta \theta_3 =$	$\frac{r_2}{r_1} \sin \left  \frac{\theta_1 - \theta_2}{2} \right $	$\frac{r_2}{r_1} \sin \left  \frac{\theta_1 - \theta_2}{2} \right $	$\frac{r_2}{r_1} \sin \left  \frac{\theta_1 - \theta_2}{2} \right $	$-\frac{r_2}{r_1} \sin \left  \frac{\theta_1 - \theta_2}{2} \right $	$\frac{r_2}{r_1} \sin \left  \frac{\theta_1 - \theta_2}{2} \right $	$-\frac{r_2}{r_1} \sin \left  \frac{\theta_1 - \theta_2}{2} \right $

Table 1

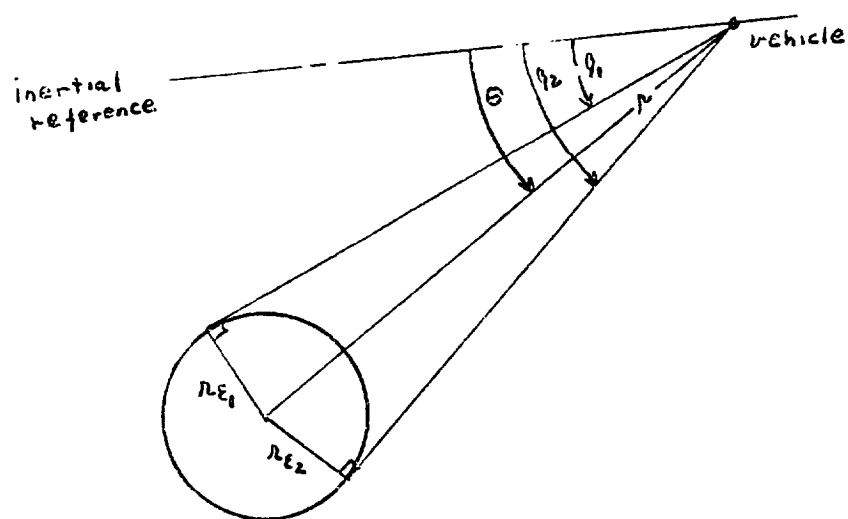
TABLE II

<u>Case</u>	<u><math>r_1</math> (nm)</u>	<u><math>r_2</math> (nm)</u>	<u><math>r_3</math> (nm)</u>	<u><math>r_1/r_3</math></u>		
I	15,000	8,660	5,000	3	13.6	1.05
II	45,000	25,980	15,000	3	18.5	4.60
III	135,000	77,900	45,000	3	15.3	11.2
IV	45,000	31,820	22,500	2	45.0	14.5
V	45,000	22,500	11,250	4	11.0	2.22





Trajectory Convention



Included Angle Measurement

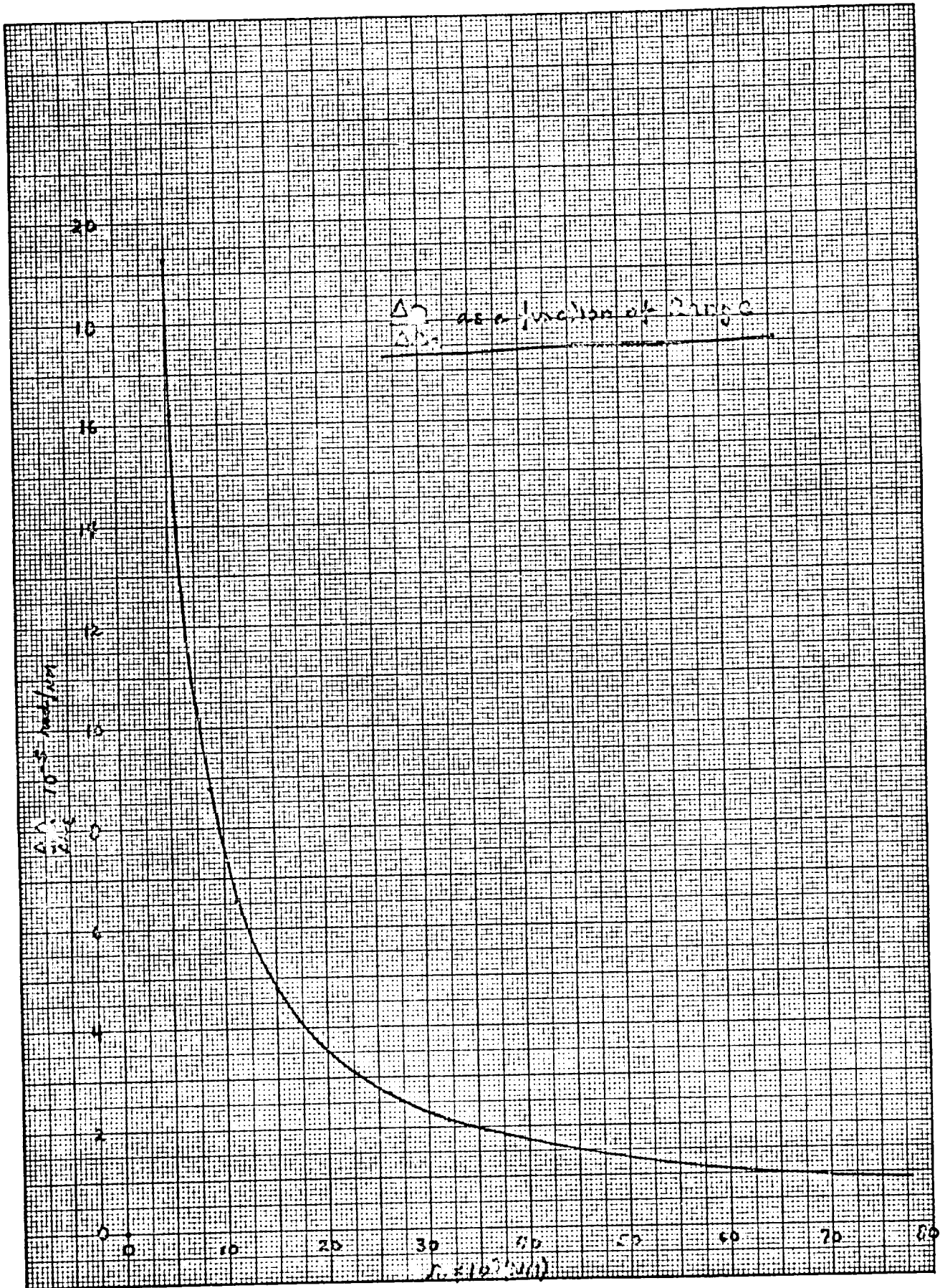


FIGURE 2

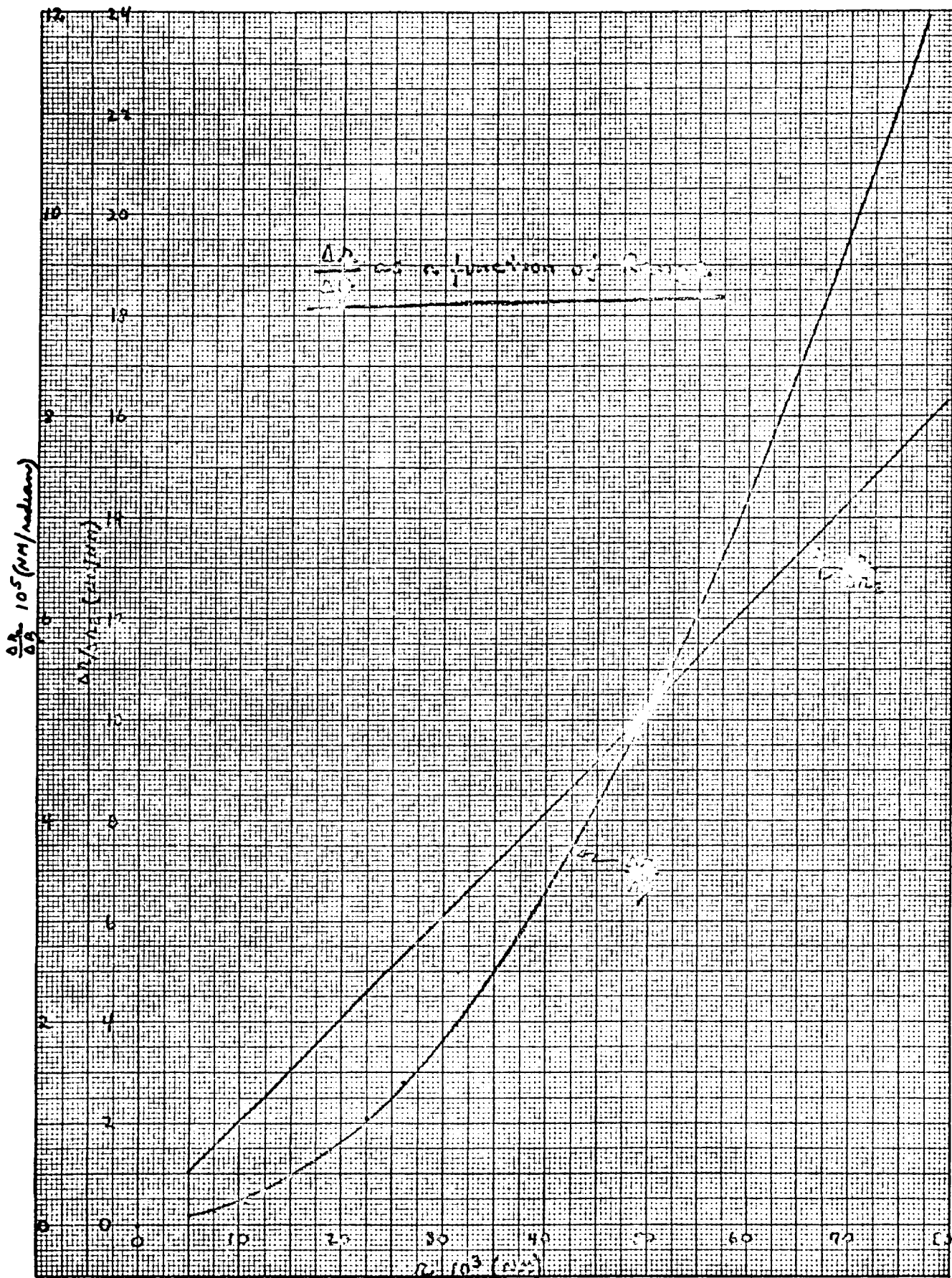


FIGURE 3

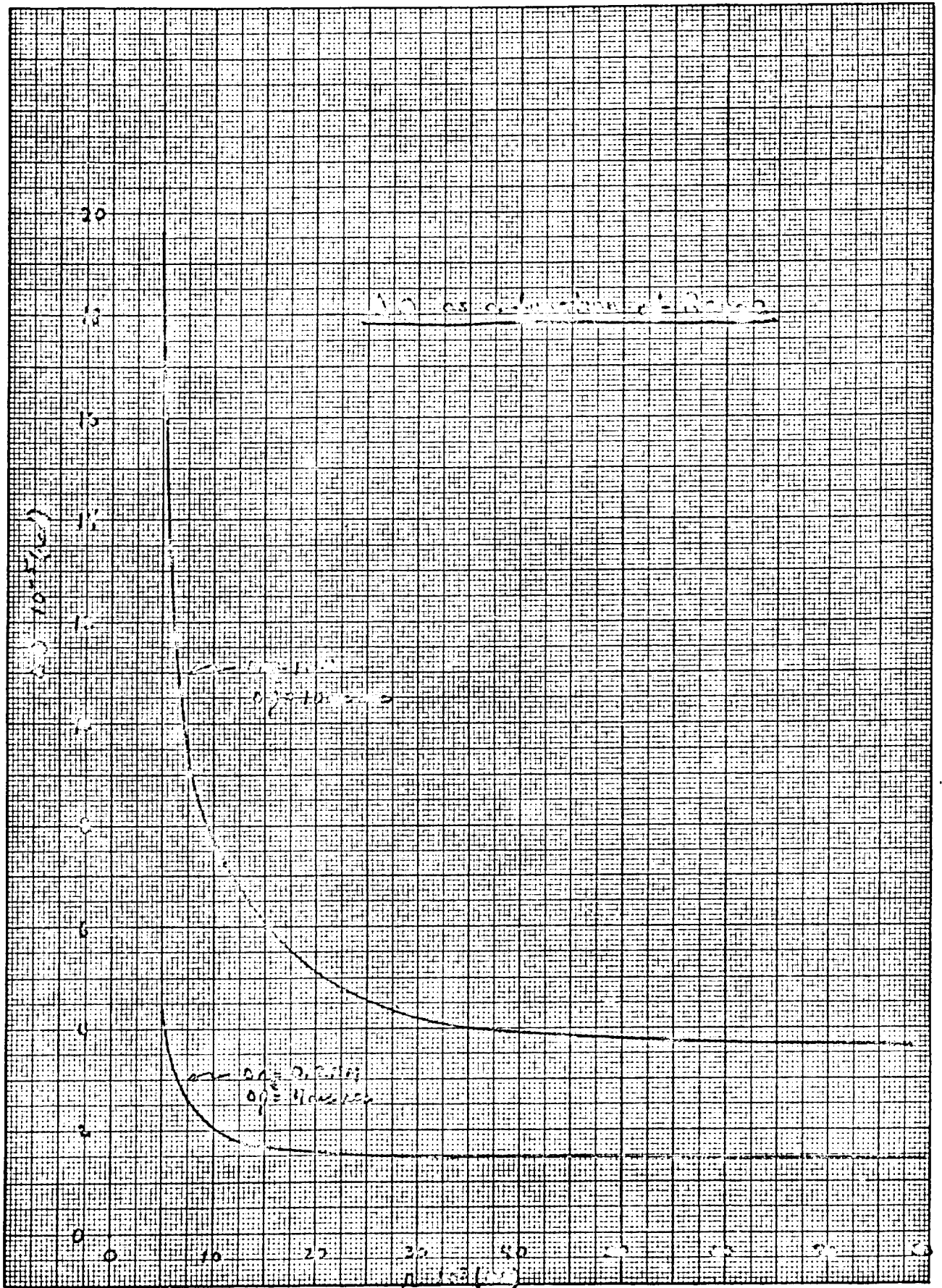


Figure 4 14



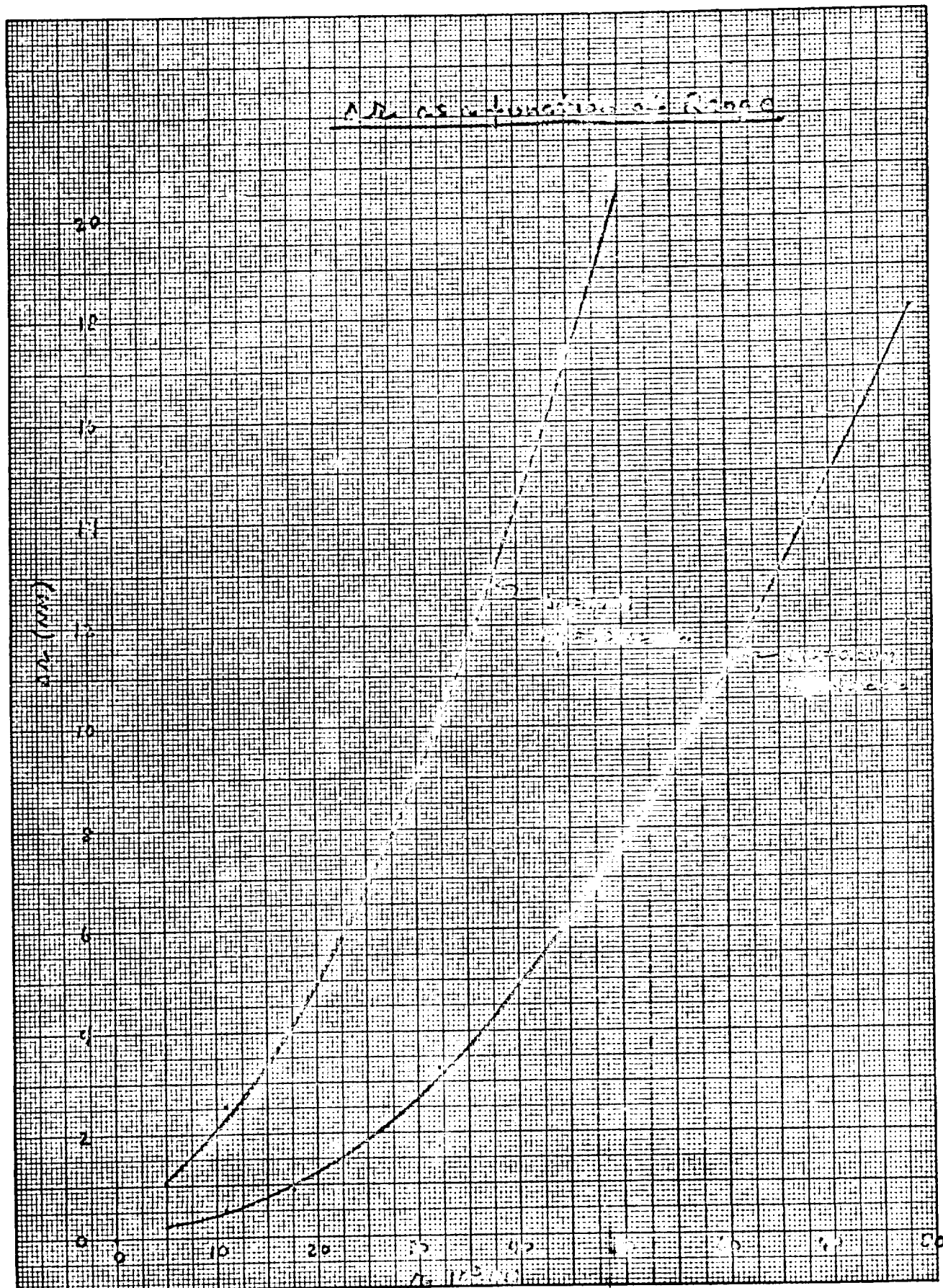
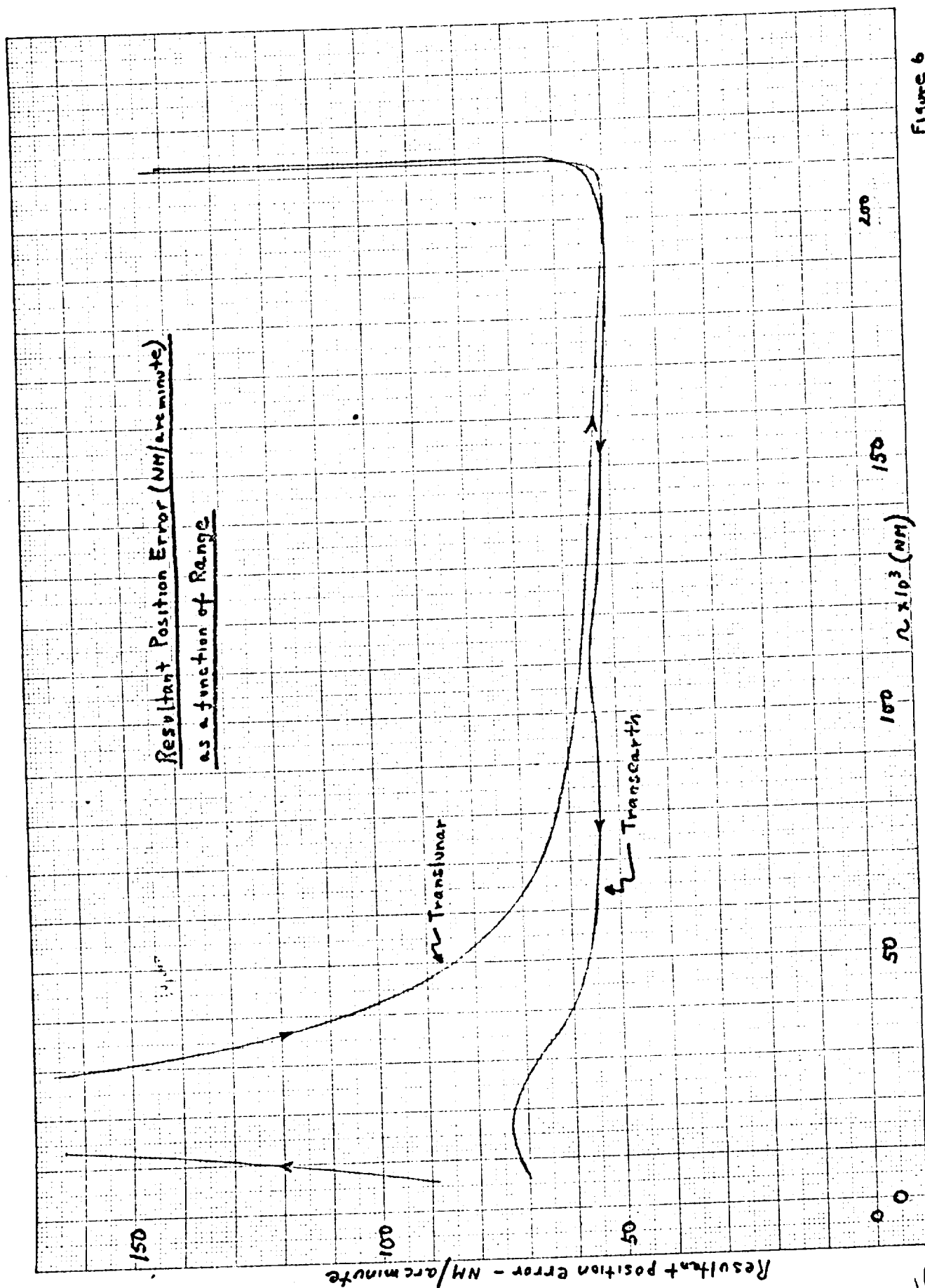


Figure 5

15

Figure 6



GUIDANCE -- OCCULTATION TECHNIQUE

Technical Memorandum 2-A.

11, March 1961

E. Lafferts

The moon moving through space eventually passes between an observer (on a vehicle) and some stars. Thus the moon occludes the light from these stars. Star occultation is the basis for an onboard technique to provide an observer with the required information to determine the parameters of his orbit.

From each occultation one obtains the surface of a cylinder with a known orientation in space. Six such occultations are sufficient to determine the orbit. If one determines where the surface of the moon occultation takes place, then the cylinder may be replaced by a half line. Three such occultations are then all that is required since from each observation the direction cosines of the half line are determined.

In terms of instrumentation, occultation is an extremely simple system. One requires an accurate clock and if one wishes to determine where occultation takes place, a telescope with rotating cross-hairs is required. One cross hair is aligned with a pair of lunar landmarks while the other is aligned with a landmark and the point on the rim where the star is occulted. The angle between these lines, the time of occultation, and knowledge of the star occulted gives all the required information.

The determination of the orbit from this data is based on the fact that the moving bodies must satisfy both geometrical and dynamical conditions. To show how these conditions are applied, a method of orbit determination will be outlined. It will be assumed that all time measurements are corrected due to the finite velocity of light which causes the apparent occultation to take place at a later time.



Let V be the vehicle rotating about the earth E and observing the moon M. We define the following coordinates:

$\lambda, \mu, \nu$  be the coordinates of V with respect to M

$x, y, z$  be the coordinates of V with respect to E

$X, Y, Z$  be the coordinates of M with respect to E

Let  $\rho$  be the distance from M to V

$r$  be the distance from E to V

$R$  be the distance from E to M

Let  $\lambda, \mu, \nu$  be the direction cosines of the line from M to V. These direction cosines are known at the times  $t_1, t_2, t_3$  which correspond to the times of occultation. Then we have:

$$\xi = \rho \lambda$$

$$\eta = \rho \mu$$

$$\zeta = \rho \nu$$

where  $\rho$  is unknown

and

$$x = \rho \lambda - X$$

$$y = \rho \mu - Y$$

$$z = \rho \nu - Z$$

We now apply the geometric property that the vectors from E to V at the times of occultation must be in a plane. This is equivalent to requiring that the determinant

$$\begin{vmatrix} x_1 & x_2 & x_3 \\ y_1 & y_2 & y_3 \\ z_1 & z_2 & z_3 \end{vmatrix} = 0$$

Expanding we obtain the three equations

$$(y_2 z_3 - z_2 y_3)x_1 - (y_1 z_3 - z_1 y_3)x_2 + (y_1 z_2 - z_1 y_2)x_3 = 0$$

$$(x_2 z_3 - z_2 x_3)y_1 - (x_1 z_3 - z_1 x_3)y_2 + (x_1 z_2 - z_1 x_2)y_3 = 0$$

$$(x_2 y_3 - y_2 x_3)z_1 - (x_1 y_3 - y_1 x_3)z_2 + (x_1 y_2 - y_1 x_2)z_3 = 0$$

which may be rewritten as

$$A_1 x_1 - A_2 x_2 + A_3 x_3 = 0$$

$$B_1 y_1 - B_2 y_2 + B_3 y_3 = 0$$

$$C_1 z_1 - C_2 z_2 + C_3 z_3 = 0$$

We now use the geometric relation between  $E$ ,  $M$ ,  $V$  to eliminate  $x_1$ ,  $y_1$  and  $z_1$  in the above

$$x_1 = \rho_\mu \lambda^\mu \quad -X_1$$

$$y_1 = \rho_\mu \mu^\mu \quad -Y_1$$

$$z_1 = \rho_\mu \nu^\mu \quad -Z_1$$

Thus the above equations become

$$A_1 \lambda_1 \rho_1 - A_2 \lambda_2 \rho_2 + A_3 \lambda_3 \rho_3 = A_1 X_1 - A_2 X_2 + A_3 X_3$$

$$B_1 \mu_1 \rho_1 - B_2 \mu_2 \rho_2 + B_3 \mu_3 \rho_3 = B_1 Y_1 - B_2 Y_2 + B_3 Y_3$$

$$C_1 \nu_1 \rho_1 - C_2 \nu_2 \rho_2 + C_3 \nu_3 \rho_3 = C_1 Z_1 - C_2 Z_2 + C_3 Z_3$$

The above equations are algebraic in the unknowns  $\rho_1, \rho_2, \rho_3$

We now make use of the dynamic conditions to determine the quantities

$A_1, B_1, C_1$ .

Each component of the vector from E to V satisfies the equation

$$\nabla^2 X = -\frac{k^2 x}{r^3}$$

If the transformation  $t = k \tau$  is made then the above may be rewritten

$$x'' = -\frac{x}{r^3} = -ux \quad \text{where} \quad u = 1/r^3$$

The solution of this equation may be expanded in a Taylor series to give

$$x = x_0 + x_0' \tau + x_0'' \frac{\tau^2}{2!} + \dots + x_0^{(n)} \frac{\tau^n}{n!}$$

The terms  $x_0, x_0', \dots, x_0^{(n)}$  may be eliminated since

$$x_0'' = -u_0 x_0$$

$$x_0''' = -u_0' x_0 - u_0 x_0'$$

$$x_0^{(4)} = -(u_0'' - u_0'^2) x_0 - u_0' x_0'$$

Thus

$$x = x_0 \left[ 1 - u_0 \frac{\tau^2}{2!} - u_0' \frac{\tau^3}{3!} + (u_0'' - u_0'^2) \frac{\tau^4}{4!} + \dots \right]$$

$$+ x_0' \left[ \tau - u_0' \frac{\tau^2}{2!} - u_0'' \frac{\tau^3}{3!} + \dots \right]$$

$$= f(\tau) x_0 + g(\tau) x_0'$$

The derivatives of  $u_0$  may be eliminated by the definitions

$$r^2_P = \frac{1}{2} \frac{d(r^2)}{d\tau} = x'x' + y'y' + z'z'$$

$$r^2_Q = \frac{1}{2} \frac{d^2(r^2)}{d\tau^2} = x''^2 + y''^2 + z''^2 - r^2 u$$

then

$$u' = -3uP$$

$$P' = Q - 2P^2$$

$$Q' = -uP - 2PQ$$

In terms of these quantities the expressions for f and g can be written

$$f = 1 - \frac{1}{2} u_0 \tau^2 + \frac{1}{2} u_0 P_0 \tau^3 + \frac{1}{24} (3u_0 P_0 - 15u_0 P_0^2 + u_0^2) \tau^4 \\ + \frac{1}{8} (u_0 P_0^3 - 3u_0 P_0 Q_0 - u_0^2 P_0) \tau^5 + \dots$$

$$g = \tau - \frac{1}{6} u_0 \tau^3 + \frac{1}{4} u_0 P_0 \tau^4 + \frac{1}{120} (9u_0 Q_0 - 45u_0 P_0^2 + u_0^2) \tau^5 + \dots$$

If  $\tau$  is picked to correspond to the second observation then

$$x_1 = f_1 x_2 + g_1 x_2 \quad y_1 = f_1 y_2 + g_1 y_2 \quad z_1 = f_1 z_2 + g_1 z_2$$

$$x_3 = f_3 x_2 + g_3 x_2 \quad y_3 = f_3 y_2 + g_3 y_2 \quad z_3 = f_3 z_2 + g_3 z_2$$

and

$$\frac{f_1}{f_2} = \frac{y_2 g_3 - z_2 y_3}{y_1 g_3 - z_1 y_3} = \frac{g_3}{f_1 g_3 - g_1 f_3} = \frac{B_1}{B_2} = \frac{C_1}{C_2}$$

$$\frac{A_3}{A_2} = \frac{y_1 z_2 - z_1 y_2}{y_1 z_3 - z_1 y_3} = - \frac{f_1}{f_1 g_3 - g_1 f_3} = \frac{B_3}{B_2} = \frac{C_3}{C_2}$$

We now have three equations in the four unknowns  $\rho_1, \rho_2, \rho_3$  and  $r_2$  which appears in the quantities  $f_1$  and  $g_1$ . We now append an additional geometric condition, namely the law of cosines at the second observation.

$$r_2^2 = \rho_2^2 + R_2^2 - 2\rho_2(\rho_1^2 + \rho_2^2 + \rho_3^2)$$

The quantities  $f_1, f_3, g_1, g_3$  are approximated by the first few terms in the series and the above system is solved to give approximate values of  $\rho_1, \rho_2, \rho_3, r_1, r_2, r_3$ . The first and second derivatives of  $r$  at  $\tau = \tau_2$  can now be found enabling one to improve on the values  $f_1, f_3, g_1, g_3$ . Iterating in this manner the position and velocity at  $\tau = \tau_2$  can be obtained, or the three positions  $r_1, r_2, r_3$  can be obtained thus enabling determination of the parameters of the orbit.

Power Supply Studies

TM-3

A P O L L O

Mid-Term

A P O L L O E L E C T R I C P O W E R S Y S T E M

Technical Memorandum TM 3

THE MARTIN COMPANY

BALTIMORE 3, MARYLAND

13 March 1961

W. Colehower

## APOLLO ELECTRIC POWER SYSTEM

### Load Analysis

The known power requirements for the Apollo mission are depicted in a sequential manner in the following four charts (Figures 1, 2, 3 and 4) in "Source Watts" that are averaged over a one minute minimum period. Instantaneous peaks are not shown, but are averaged to form blocks of energy. Peak demands of very small time duration, such as Abort Tower separation and Mission Module separation have not been included.

Changes in load have been considered to be caused by the inherent automatic operation of equipment and manual switching by crew members.

A generalized summary of the load charts indicates that power requirements near earth vary in average value between 1.6 KW and 1.9 KW while lunar phases require an average value of 2.0 to 2.2 KW. All average values shown exclude a 10% reserve factor that will determine the actual designed electrical system size. Since the maximum demand over any extended interval is 2.2 KW, the designed system size will be  $2.2 \text{ KW} + .22 \text{ KW}$  or a minimum requirement of 2.4 KW for lunar phases of the mission.

Several events that occur and are not shown on the load analysis have been omitted because they are repeats of events already shown on the charts. Lunar ejection, for example, is not shown since it is a repeat of lunar injection, from the electrical load viewpoint.

### Distribution System

A preliminary schematic of a bus system applicable to a solar array APU electrical power system is shown in Figure 5.

The basic philosophy requires a single bus (the Main D-C Bus) to service all the essential loads of the vehicle and this bus shall have



a continuous possibility of being energized at all times

The Mission Module and the Command Module will each have a non-essential bus. These two buses will service loads that are in a power emergency and will automatically be removed from the Main D-C Bus if the emergency should occur.

During the pre launch countdown, electric power will be supplied to the Main D-C Bus from the ground source and then the load will be supplied by the vehicle APU system just prior to liftoff without an interruption.

The Recovery Bus is actually a segment of the Main D-C Bus and supplies temporary emergency power by the use of the system Battery and Recovery Battery (sequentially) if the Main D-C Bus voltage should drop below the required limits during the mission. The Recovery Bus becomes the only essential bus during the recovery period; therefore, all other loads are removed automatically to conserve the output power of the two batteries that will furnish power during this period.

Essential sub-buses may prove to be desirable in the future; however, the single essential bus with radial non-essential sub-buses is a simple and reliable configuration.

All contactors shown in the schematic will be operated automatically but will have a capability of being overridden manually. The bus system of Figure 5 is also applicable to other power generation methods.

#### Comparisons

The selection of the power system for the entire flight plan may be accomplished by analyzing the power conversion method appropriate to each of the two basic flight periods: the solar-oriented period and the non-solar-oriented period. For application to the solar-oriented portion, the different solar conversion methods

two fuel consuming systems and a nuclear system have been designed, adapted to the Apollo vehicle and evaluated. The nuclear system has been eliminated from further consideration for manned short-duration missions because of its excessive weight. Fuel consuming systems, although independent of solar energy, were considered also for the sun-lit portions of some missions. For the non-solar oriented portion of flight, fuel cells, batteries and auxiliary power units using cryogenic fuels have been evaluated. The best of the four solar energy conversion methods was combined successively with each of the three methods of obtaining power during the non-solar oriented period. In addition, the continuous use of fuel cells has been evaluated.

When comparing the seven power systems potentially usable for the solar oriented period, each was sized (installed capacity) so as to provide the required 2 KW of power for two weeks. The probability of availability of qualified equipment in time for the first earth orbital flight was also considered. The weights of each system include the necessary fairing to provide aerodynamic protection to the extendable portions of the power system which are stored internally during the launch phase. It will be noted from Figure 6 that the aerodynamic fairing weight in some systems is an appreciable portion of the total weight which emphasizes the fact that comparative system studies made independent of specific vehicle configurations may be misleading and, therefore, not conclusive.

By reviewing Figure 6, it is apparent that the best of the solar conversion systems is the solar cell system. It is the lightest system (as installed) and accepts the widest orientation tolerance. In addition, the solar cell system has been in use in space since 1958, has no moving parts, is comparable in cost to the other solar systems (in small lot production), is not affected by zero gravity

and its capacity is easily expanded. Of the fuel cell systems, the Bacon system appears most promising since it probably will be lighter in weight, occupies a smaller volume, is more fully developed, operates at a high radiator temperature, and should present no problems under zero gravity conditions.

The integration of the power systems for the combined solar and non-solar oriented periods of the Apollo mission is shown in Figure 7.

The following assumptions were used in the preparation of this figure:

LOAD LEVEL - as per MLV report ER11245M

KW-HRS - moon at first quarter

shade and non-oriented periods as per revised  
load analysis

(Figures 1 to 4)

no trans lunar shade periods

#### REDUNDANCY:

Batteries	52%	
APU	100%	
Solar Cells	20%	
Fuel Cells	50%	(114 hrs use)
	100%	(336 hrs use)

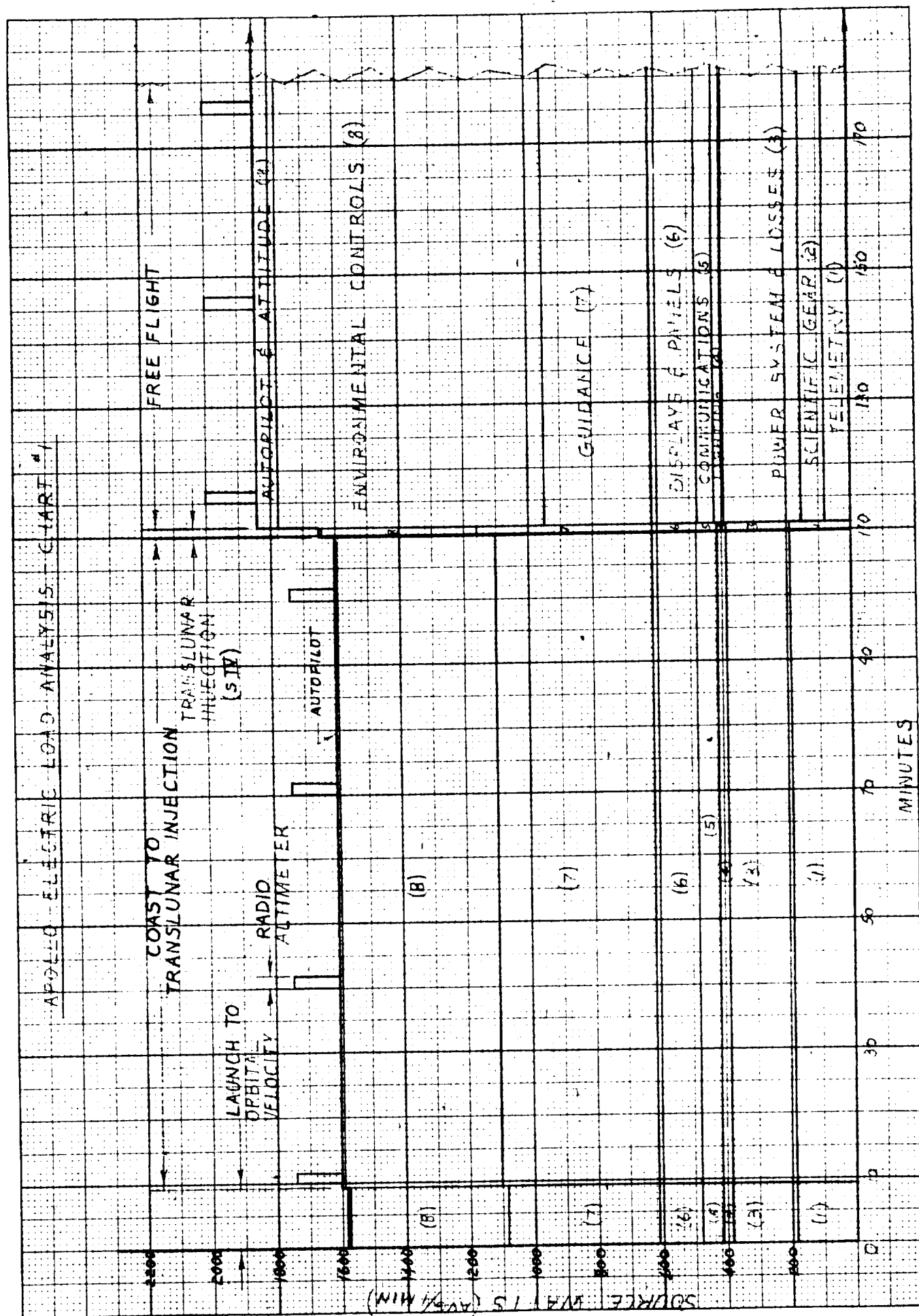
TOTAL WEIGHT includes parts of the:

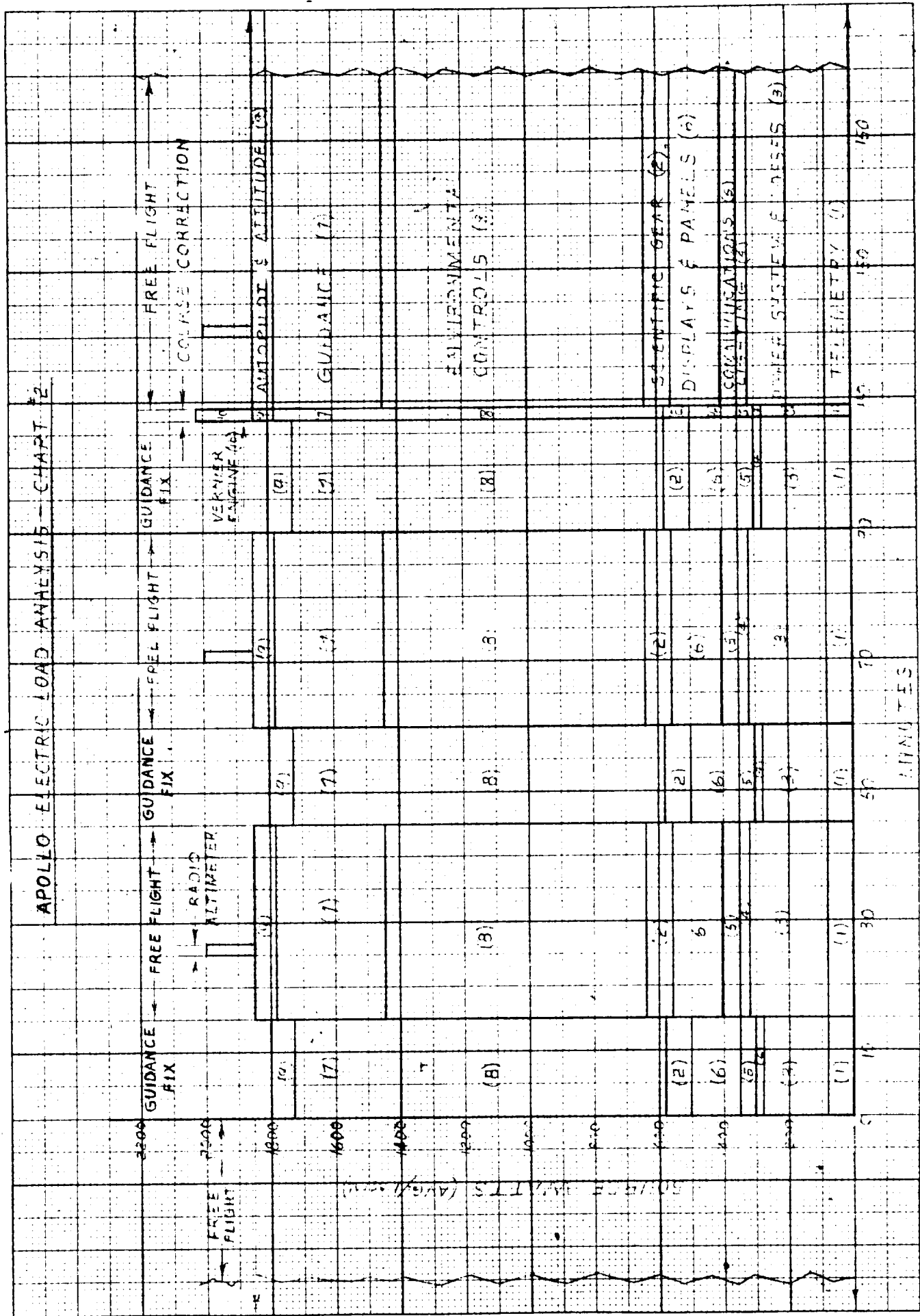
Electric Power System  
Environmental System  
Propulsion System

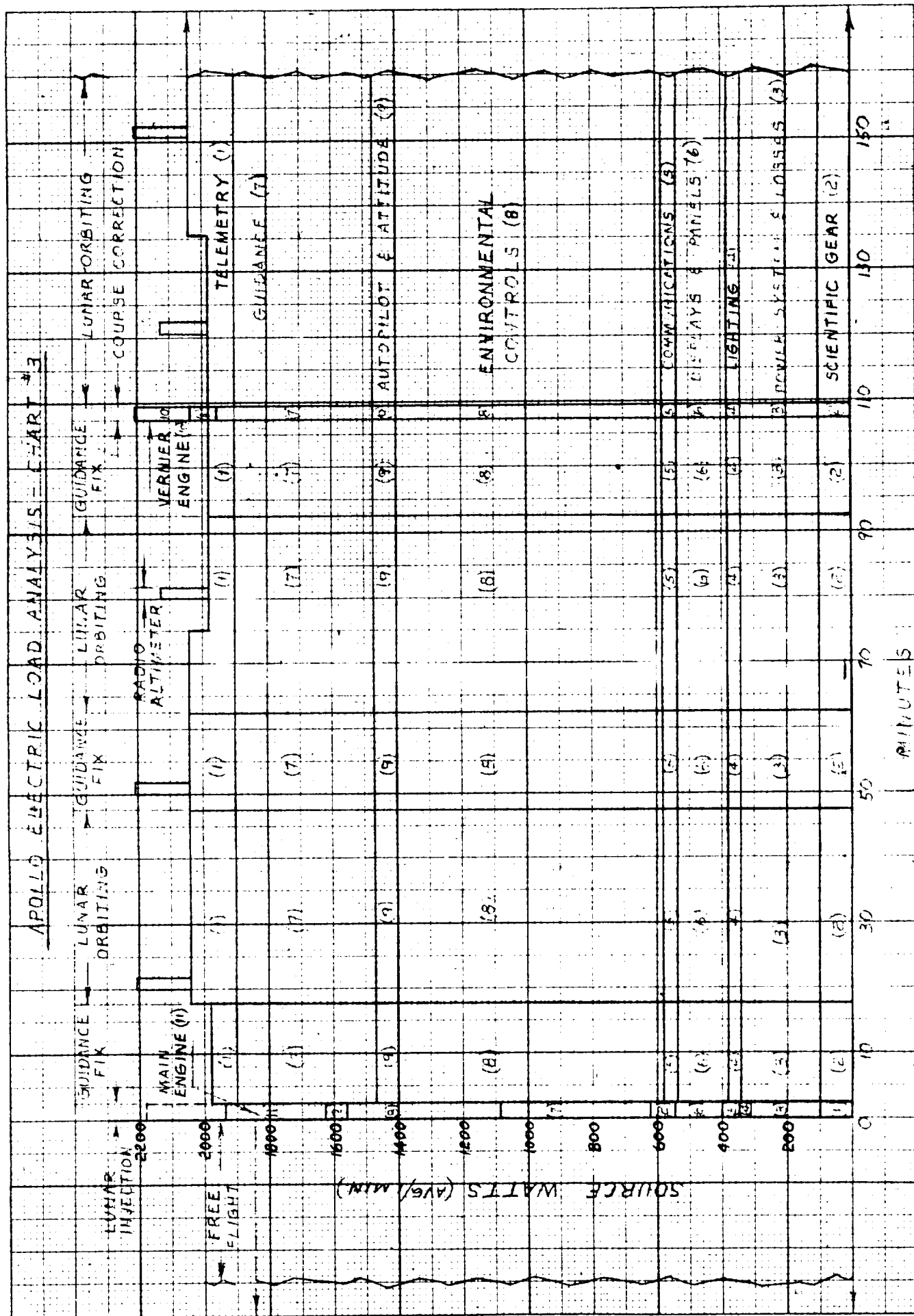
When comparing the total weights for a 14-day mission (fuel cells using main tanks), it will be observed that the last three systems are appreciably lighter than the Battery-Solar Cell system and are approximately equal to each other. The last three systems differ relative to the distribution of their total weight between the two modules. Compared to the "Fuel Cells Only" system, the Command

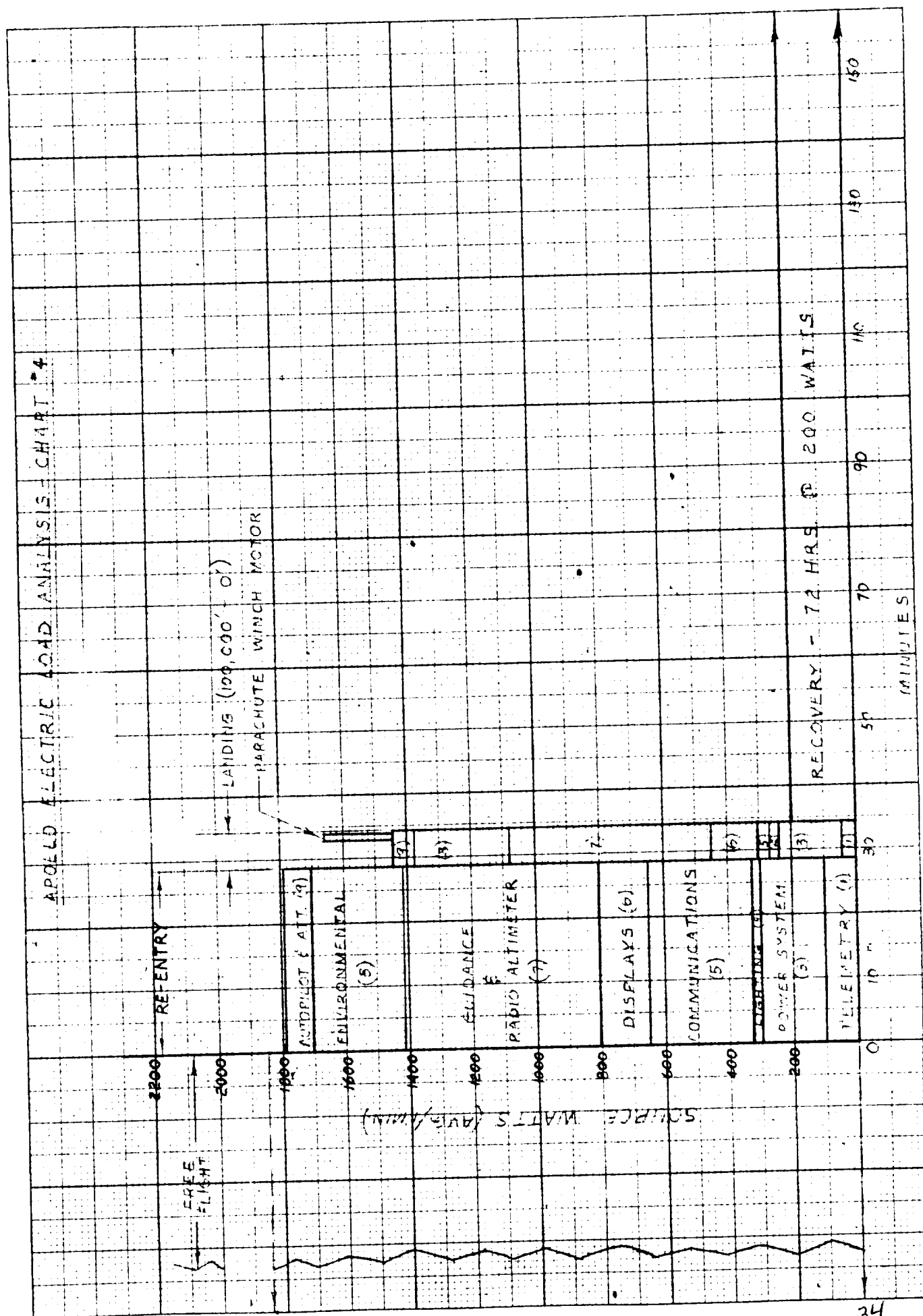
Control Module would be 92 lb. heavier for the Fuel Cell-Solar Cell system and 60 lb. heavier for the APU - Solar Cell system. Relative costs of a 23 vehicle program for each of the 4 systems are as follows:

Battery-Solar Cell	49%
APU-Solar Cell	100%
Fuel Cell - Solar Cell	71%
Fuel Cells Only	35%

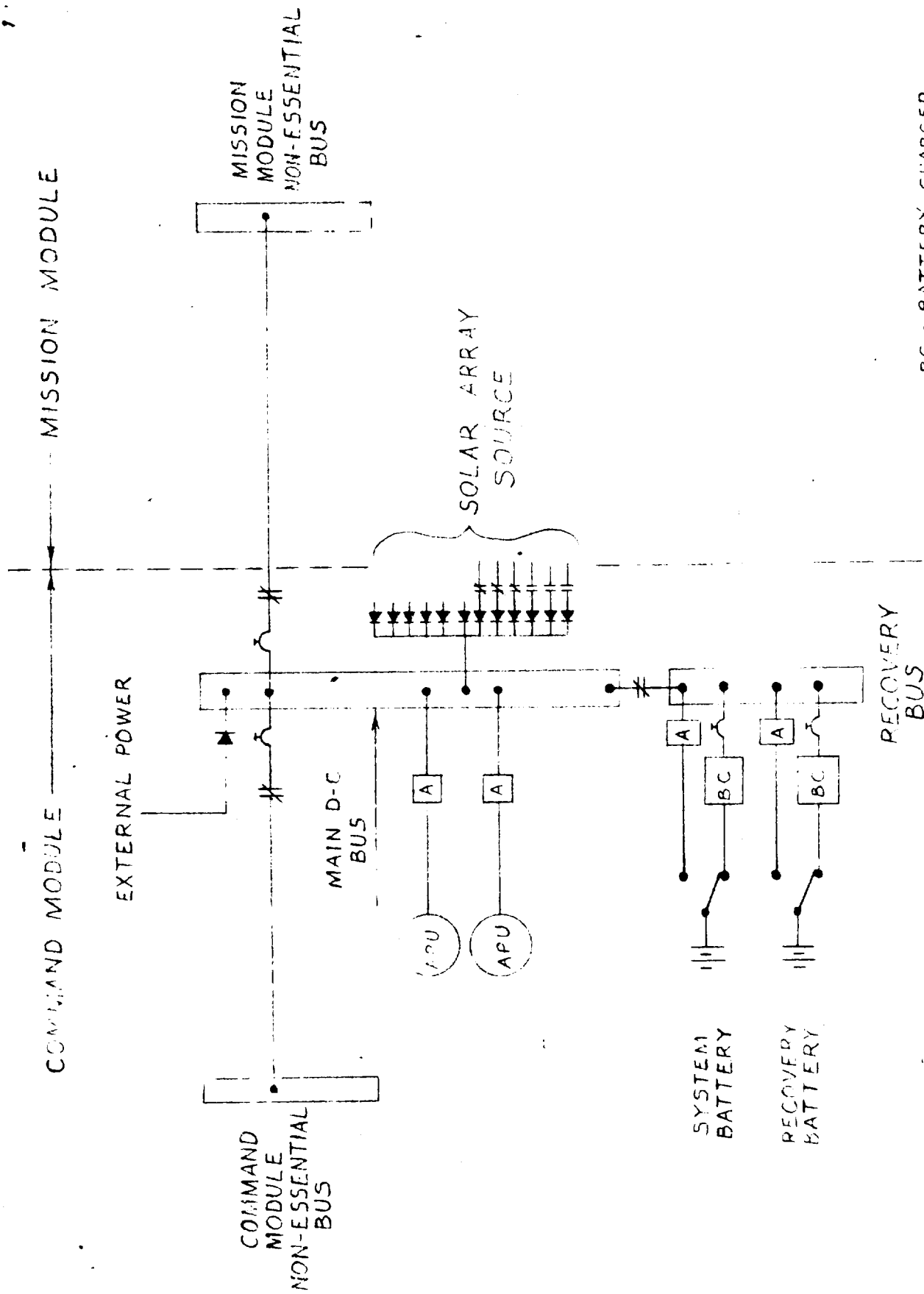














## Comparison of Integrated Electric Power System

Command Control Mod		Battery	APU	Fuel Cells	Fuel Cells
Mission Mod		Solar Cells	Solar Cells	Solar Cells	Fuel Cells
Non Solar Oriented	2 2 day Circumlunar	8-1 max. combine	26.6	25.6	328
Emergency Launch to 10 hrs of Recovery (24 Hrs)	8 2 day 12 Lunar Orbits		31.05	30.33	328
Fuel & Tankage (Independent)	24 day 24 Lunar Orbits		30.24	29.4	677
APU & Gen. (OR) Fuel Cells			187.284/19	187.284/19	150/450/715
Battery & CC Mod		205/369/569	170	400	520
- H MOD		121	36	10	
Solar Array (Basic Loads)		563/548/563	117	119	
Recovery Pwr (62 hrs. @ 130W)	Fuel	60	60	16.16/16	9
Heat Exchanger				12	12
Cooling Water				13	13
Solar Pump Motors		20		20	20
Residual (Heavy Wgt Increase)				20	
Distillation Tanks & Insulation	Variable	21/67/67	17	36	
REMARKS: General of Solar Panels, Sys					
Use of Main Tanks					
Normal	5 2 days (Circumlunar)	80"	205	205	205
Independent	12 Lunar Orbs	119"	205	205	205
Tankage)	24 days 24 Lunar Orbs	120"	1956	1956	1124
REMARKS: Heavy Main					

Cabin Leakage

TM-4



Structural Disconnect Between Command and Mission Modules - A

Flexitallic gasket will also be utilized here and the above comments on the Outside Door seal apply.

Door in Command Mission Module - will be sealed with a Flexitallic gasket. While the outside door and structural disconnect do not have to be resealed, the door in the Command Module will be operated several times and therefore, extra gaskets must be carried. To minimize gasket damage the gasket will be located in the door. The above comments on the outside door seal also apply.

Windows - Current plans are to install glazing in accordance with methods developed by Corning Glass Works under contract AF33(600)36852, AMC Project 7-654 and to seal the glass to the structure using Kovar A metal bonded to the glass and to the structure by a Narmco adhesive metal bond 302. Development tests will be run in the future to determine adequacy of sealing and other methods will also be investigated.

Cooling Tubes and Radiator Connecting Tubing - will be spliced through the pressure shell utilizing fittings fusion welded to the shell.

Vents - will use fittings fusion welded to the pressure shell.

Electrical leads - may be passed through the pressure shell by fusing conductors into glass insulators which in turn are fused to Kovar A metal base plates. These Kovar plates will be bonded to the structure. Development tests will be required.

Mechanical links may be spliced in various ways as indicated in Ref. 1 and illustrated in Fig. 2. The types required for development have not been determined as yet.

.....  
Separation Devices Controls - will involve electrical leads and will  
be handled as noted above.

Test programs are being developed and will be implemented as the various designs are evolved. After the various detail tests have been run, an analysis will be made of the composite leakage problem and a test program will be established to insure overall vehicle conformance to the requirements. Throughout the design and test development, the fact, that all items perforating the pressure shell must be separated from the command module before re-entry, must be considered.

- Ref. 1 - Space Cabin Studies, Parts I and II, Project MOVE 4-60,  
Martin Company.
- 2 - Materials Behavior in High Vacuum, ER 11441P, 7-60,  
Martin Company.
- 3 - Titan II Manhole Cover Seal Program, TM 22-5, 10-60,  
Martin Company.
- 4 - Titan II Manhole Cover Seal Program, TM 22-10, 1-61,  
Martin Company
- 5 - Investigation of High Strength Aluminum Alloys for Cooled  
Space Cabin Structures, ADA-R-197-1, 3-61, Martin Company.

- Fig. 1 - Flexitallic Seal Configuration
- 2 - Mechanical Links Thru Pressure Shell



# FLEXITALLIC GASKET WITH TONGUE & GROOVE CONFIG. ON MANHOLE COVER & RING

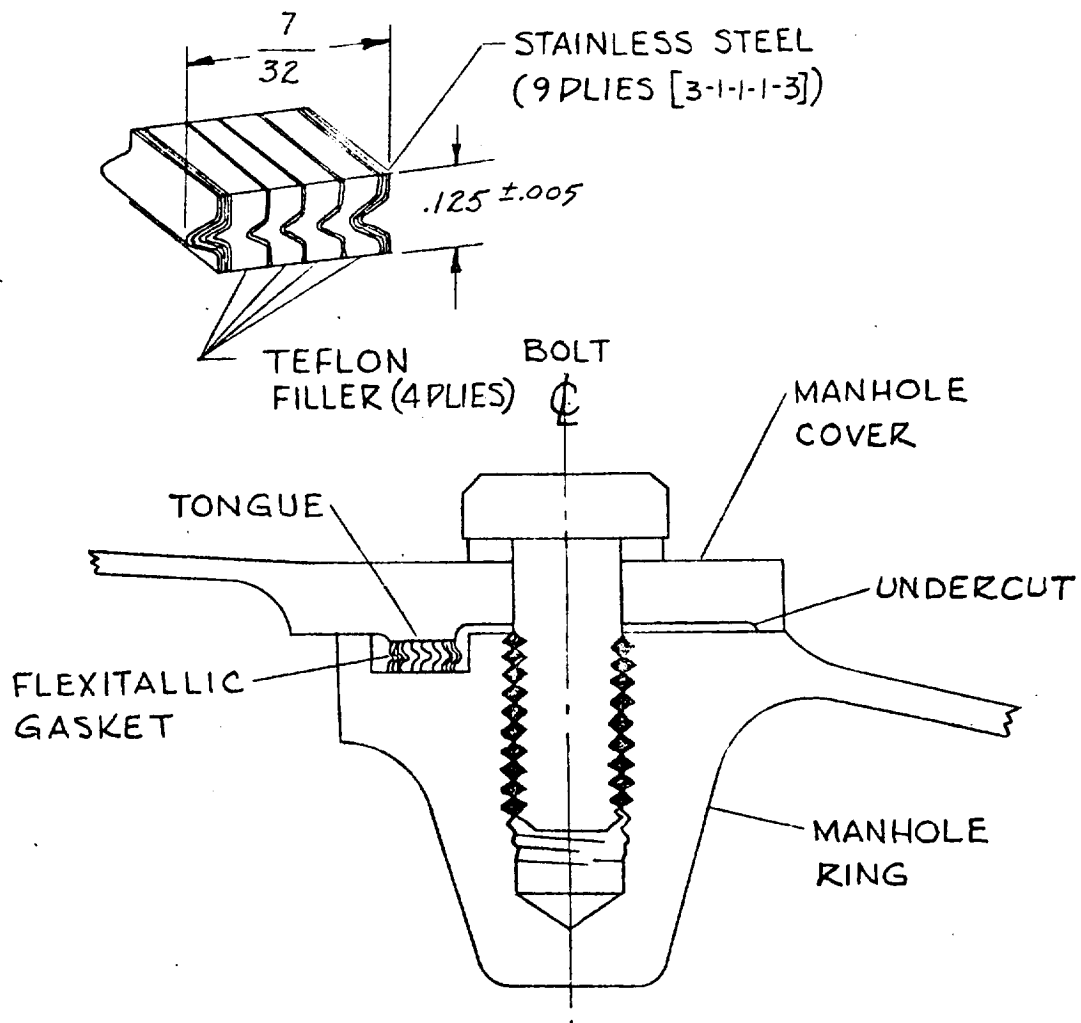
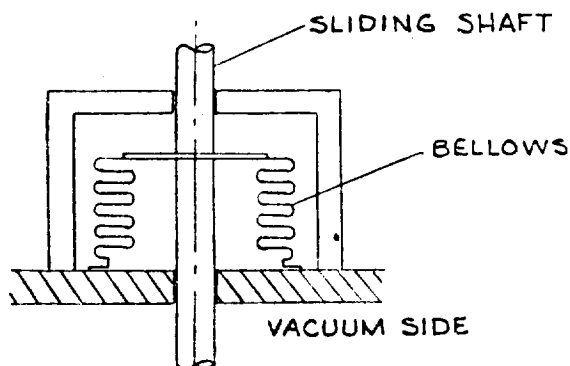
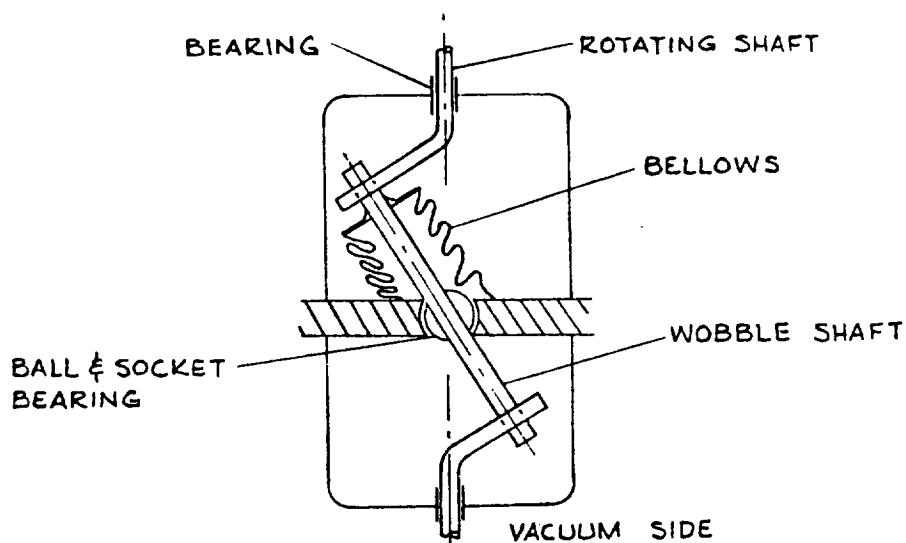


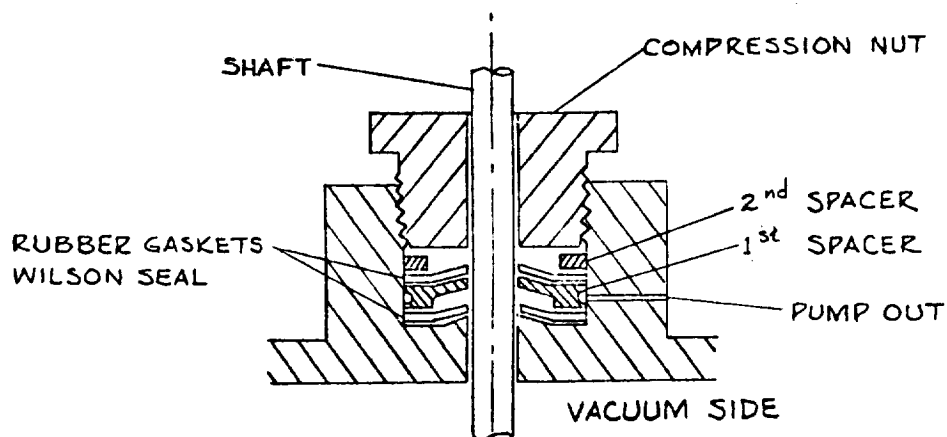
FIG. TM-4-1



SLIDING SHAFT WITH METAL BELLOWS



ROTARY MOTION



ROTARY SHAFT  
(WILSON SEAL)

Heat Shield Summary

TM-5

AERODYNAMIC HEAT TRANSFER METHODS  
(~~Technical Memorandum~~ 15 (~~Series I~~))

6 March 1911

C. Perrine

AERODYNAMIC HEAT TRANSFER METHODS

Summary

This technical memo presents the methods of analysis and results of the heat transfer studies. Results on four configurations are presented for both convective and radiative distributions.

Heat Transfer Analysis

I Introduction

The objective of the heat transfer analysis was to provide the necessary information on which to base heat shield designs and weight estimates. Because of the number of vehicle configurations being investigated in the early phase of this program, relatively simple methods for estimating heating rates were adopted. Since the primary objective of these early configuration studies was to determine significant weight differences between configurations, the approximate nature of the heating estimation procedure was considered justified.

In the latter phase of the program, when design studies have been narrowed to one or two configurations and greater accuracy in the heating estimates is required, the methods to be used will be selected accordingly.

The primary source of heating rate estimates was experimental data on similar body shapes. In cases where there were no applicable experiments, simple, proven methods were used as much as possible. Finally, in flow regions where neither experimental data nor analytical results could be relied on, consistent assumptions between configura-

these were employed in order not to incorrectly approximate any of the configurations. Examples of such uncertain areas are the base and afterbody separated flow regions and the aerodynamic control surfaces. Only experimental data on the particular areas in question can properly determine the heating levels in these regions.

## II. Methods and Results

The methods to be described have been adapted to the particular configurations so that the discussion will be divided in terms of the various vehicle shapes considered. Most of the estimation techniques which have been used were developed for the four vehicles to be described in this memorandum. These four configurations are the L-2-C, W-1, M-1-1 and L-1. Outline sketches of these four are shown in Fig. 1.

The following assumptions are applicable to all vehicle heating estimates:

1. Local convective and radiative heating rates were estimated as a ratio to a hemispherical stagnation point heating rate. In the case where no hemispherical surface existed at the stagnation point of the vehicle, a "reference hemisphere" was used to normalize the heating distributions. This distribution was assumed to apply at all flight conditions. The variation of the local absolute heating rate was then found by determining the variation of the hemispherical stagnation point heating rate and multiplying by the distribution factor.

This procedure has been substantiated, for example, by the experimental work of Heller, Ref. 1, and the

analytical results of Ref. 2, for convective heating distributions. The assumption is less accurate for the radiative heating rate distributions because of the nonlinear dependence of the radiation intensity on temperature (Ref. 3). However, by determining the distributions for radiative heating at the maximum flight velocity of interest, a conservative distribution curve could be obtained as a result of the nonlinearity.

2. The flow was assumed to be in equilibrium for both the radiative and convective heating rate estimates. The assumption of equilibrium in the boundary layer is not particularly critical since the resulting heating rates will be almost the same for equilibrium or recombination at the wall. For the case of non-equilibrium with the (questionable) assumption of no recombination at the wall, the assumption leads to conservative results.

The assumption of equilibrium behind the shock wave for radiative heating calculations is, on the other hand, very critical. The flight conditions for which non-equilibrium effects become important in radiant heating, as estimated by Yoshikawa et al and reported in Ref. 7, are shown in Fig. 2 in relation to typical overshoot and undershoot trajectories for the W-1. This figure indicates that non-equilibrium conditions might possibly occur and give greatly increased radiation intensities for these trajectories. In the present stage of analytical and experimental research on the characteristics of the non-equilibrium radiation, it is not yet possible to evaluate

- the effect of non-equilibrium flow behind the shock wave.
3. The effects of ionization on convective heating has not yet been sufficiently investigated and has therefore been neglected in these estimates.
  4. The time variation of the reference stagnation point heating rate was based on fixed range reentry and consistent lift control techniques. These two factors are very important in obtaining consistent comparisons between vehicles.
  5. In areas of the vehicle where only specific wind tunnel tests can give reliable heating values, it was assumed for this study that consistent assumptions between vehicles would be used in order not to jeopardize any vehicle in the evaluation. Examples of such areas are the base and afterbody separated flow regions and the control surface.

#### Heating Distributions For The L-2-C

The convective heating rate distribution for the L-2-C at 90° angle of attack was estimated from the experimental data on a nearly identical shape of Ref. 4 and is shown in Fig. 3. In order to establish the magnitude of the distribution with respect to the reference hemisphere ( $R = 6.4$  ft.) stagnation point heating rate, a correlation of stagnation point velocity gradients developed in Ref. 5 was used. Assuming that the stagnation point heating ratio between a sphere and a blunt shape like the L-2-C is proportional to the square root of the stagnation point velocity gradient, then a  $q/q_0$  of 0.55 is obtained. This value has been used to fix the level of the distribution shown in Fig. 3.

At angles of attack less than 90°, the stagnation point moves around the corner of configuration. The heating rates at these off-center



compressive loads were determined by the Bessho double curvature relationship; Ref. 6:

$$\frac{(s_{\text{center}})_{\text{double curvature}}}{(s_{\text{stag}})_{\text{hemisphere } R_1=R_{\text{ref}}}} = \left[ \left( \frac{R_{\text{small}}}{R_{\text{ref}}} \right) \left( 1 + \frac{R_{\text{small}}}{R_{\text{large}}} \right) \right]^{\frac{1}{2}}$$

The convective heating at the center of the blunt surface at angle of attack was estimated by three separate techniques since no directly applicable experimental data or theoretical solutions were available at these large angles of attack.

The first technique used the "cross flow" approximation of Bertram's, Ref. 1. This method has been applied to blunt delta wings at high angles of attack with apparent success. The assumption is made that the heating rate at the center of the local spanwise segment is the same as that at the stagnation point of a flat faced disk with the same corner radius and in a flow field equal to the normal component of the actual flow at the angle of attack. This method applied to the L-2-C gives the points indicated in Fig. 3 as the "cross-flow method".

The second method considered employed Eckert's reference enthalpy method at the local flow conditions found by isentropically expanding the flow from the stagnation conditions to the local conditions determined by the Newtonian pressure distribution. This calculation was done for the 50° angle of attack case and is also shown in Fig. 3.

The last method considered was the application of the results of a Mangler transformation to a known three dimensional solution to obtain the two dimensional solution approximating the present configuration. To do this, the centerline cross section of the configuration at the angle of attack of interest was obtained. This cross section was considered,

The lateral distribution of the heat shield was determined by assuming a constant angle of attack of  $10^\circ$  and the vehicle angle of attack of  $10^\circ$ . The lateral distribution of the heat shield was determined by assuming a constant angle of attack of  $10^\circ$  and the vehicle angle of attack of  $10^\circ$ . The lateral distribution of the heat shield was determined by assuming a constant angle of attack of  $10^\circ$  and the vehicle angle of attack of  $10^\circ$ . The lateral distribution of the heat shield was determined by assuming a constant angle of attack of  $10^\circ$  and the vehicle angle of attack of  $10^\circ$ .

Such a procedure has often been applied to sharp nosed flat plates and cones. The application in the blunt nose case is not entirely justified theoretically. The results of such a calculation are shown in Fig. 3.

On the basis of the limited angle of attack data on disks, which was available Ref. 8, the distribution of convective heating given by the latter method was selected for heat shield design.

The lateral distribution of the convective heating rates was assumed to be a  $\cos^2$  distribution scaled to the centerline value determined above. This is just an extension of Bertram's empirical cross flow estimate to off-centerline points.

The heating distribution over the aft portion of the vehicle was estimated very approximately in accordance with assumption 5 of the Introduction. The particular values used for this vehicle are indicated on Fig. 5 and were derived from "contemplation" of the Mercury data given in Ref. 9.

Preliminary estimates have been made on radiative heating distributions based on the assumption that the local heating rate can be computed from flow conditions in the immediate vicinity of the point in question. The assumption has been made that the local heating rate is the same as the heating rate which would be experienced at a point behind a two-dimensional thin, infinite gas layer at the "local" density and

temperature. This assumption is justified by the rapid decrease in radiation received at a point on the body for flow elements not in the immediate vicinity of the point. This decrease is due to the decrease of radiation intensity with both the square of the distance and the cosine of the incidence angle.

The static temperature distribution through the gas layer along a perpendicular to the surface drops from the value at the wall to the value immediately behind the shock wave. The effect of using the conditions behind the shock and at the wall in the radiative heating rate calculation are shown in Figure 4. The radiation intensity curves from Ref. 3 have been used and are shown in Figure 5. Near the stagnation region, the two estimates are nearly equal but as the distance from the stagnation point increases the two estimates diverge rapidly. This is due almost entirely to the rapid decrease in temperature behind the shock wave as the shock wave becomes weaker around the body. The temperature of the gas at the body, on the other hand, obtained from the isentropic expansion from the stagnation point, remains high.

The radiative heating rate distributions based on the shock wave temperature have been used for all configuration heat shield estimates to date. Calculations to obtain the temperature profile across the shock layer for use in the radiation heating calculations are presently underway. These results will be used to improve the radiative heating distribution estimates.

Part of the procedure in obtaining these distributions involves estimating the shock wave shape and location. This estimate was based on the method of Kaatari, Ref. 10, for the angle of attack region in which it was applicable. Beyond this applicable region the shock wave envelopes were estimated on the basis of experimental data shown in

Refs. 12 and 13.

#### Heating Distributions For The W-1

The W-1 configuration, shown in Fig. 1 is essentially a flat-bottomed half cone. The convective heating rate distributions on the upper conical surface were obtained from the Lee's distribution, Ref. 2, until the conical surface was "shadowed" from the flow. For higher angles of attack the upper surface heating rate estimates were based on the experimental data on the leeward side of delta wings presented by Bertram in Ref. 1. These estimates are presented in Figures 6, 6A and 6B.

The delta wing data of Bertram was also used to estimate the lower surface heating distributions at high angles of attack since the W-1 is very similar to the wings which were tested. The shape of the curves of Fig. 6A was taken from Ref. 15 data but adjustment of the magnitude was required to correlate this data with that of Fig. 6. A similar method was used to derive Fig. 6B. The basic distribution shape was taken from Ref. 13 data but, again, the magnitudes were adjusted to correlate Fig. 6B with Figs. 6 and 6A.

The control surfaces and the base heating rates were again handled in a manner consistent with previously mentioned assumption (#5). The assumed values of heating rate ratio for obtaining preliminary weights on these areas are shown in Fig. 6. It is true that the flap configuration of this vehicle, and the M-1-1 to be discussed next, are similar to those for which heating data were obtained for the M-1 shape. The probable separation and consequent reattachment of the boundary layer in front of these flaps at high deflections would make this data Reynolds Number dependent and very difficult to extrapolate to other

conclusion. Hence, this data was not used in the present estimates.

The radiative heating rate distribution was obtained in the manner described in the L-2-C discussion using the shock wave temperature in the calculation. The results are shown in Fig. 7. The shock stand off distance was assumed constant in the region of significant radiation. The stand off distance was obtained from Hayes expression (Ref. 14).

$$\frac{z}{R_w} = \frac{1}{K} \left[ 1 + \sqrt{\frac{8}{1+K}} - \frac{2.6}{K} \right]$$

Where K is the normal shock density ratio.

The extremely localized heating distribution is a result of using the shock temperature in the calculations. This result is being reevaluated at the present time by determining the effect of using the estimated shock layer temperature distribution.

#### Heating Distribution for the M-1-1

All of the techniques discussed for the W-1 heating distribution estimates are applicable to the M-1-1. The radiative heating rate distribution is the same as that shown in Fig. 6. The convective heating distribution is shown in Fig. 8.

#### Heating Distribution For The L-1

The L-1 shape was developed at the NASA Langley Research Center and has been tested there, Ref. 15. The experimental convective heating rate distributions were obtained on a modified shape but the data was easily adapted to the L-1 itself. The results are shown in Fig. 9.

The radiative distributions were obtained in the manner described earlier and the results are shown in Fig. 11.

#### III. Time Histories Of Reference Heating Rates

As an illustration of the time variation of the reference heating rates, Figs. 12 through 15 have been included. With this trajectory information and the distribution of heating rate ratio presented previously, there is sufficient information on which to base preliminary heat shield estimates.

Figure 12 is an L-2-C overshoot reentry using "roll control" to adjust the vertical component of lift with changing drag. Fig. 13 is a 60 n.mi corridor undershoot trajectory for the L-2-C. In both figures, the variation of the reference values of  $q_C$  and  $q_H$  are given.

Figures 14 and 15 is the same information for the M-1-1 vehicle.

#### IV. Concluding Remarks

The methods used to obtain the necessary aerodynamic heating information for use in the preliminary heat shield optimization studies has been presented. The methods which have been selected meet the two primary objectives:

- 1) To permit study of a number of configurations in the time available and
- 2) To provide sufficient accuracy to determine significant weight differences and heating problems between configurations.

- 1) "Joint Conference on Editing Manned Hypervelocity and Reentry  
Notes - Part I: A compilation of Papers Presented"

NASA Langley Research Center

Apr. 11-14, 1960

Langley Field, Va.

- 2) "Laminar Heat Transfer Over Blunt-Nosed Bodies at Hypersonic Flight  
Speeds" L. Lees

Jet Propulsion Vol. 26, No. 4, Apr. 1956

- 3) "Radiation From Hot Air and Stagnation Heating"

E. Rivel

AVCO Research Report R.R. 21 Oct. 1959

AF BMD-TR-59-20

- 4) "Laminar Heat Transfer Around Blunt Bodies in Dissociated Air"

H. H. Kemp, P. H. Rose & R. W. Detra

Jour. of the Aero/Space Sciences Vol 26, No. 7 July 1959 (Pg. 421)

- 5) "Some Relationships Between Shock and Body Geometry and the Stagnation  
Point Velocity Gradient for Blunt Bodies in Supersonic Flight"

Stephen Traugott

Martin-Baltimore Research Memorandum RM-37 May, 1959

- 6) "Heat Transfer to a General Three-Dimensional Stagnation Point"

Eli Reshotko

Jet Propulsion Jan. 1958 Pg. 58

- 7) "Radiative Heat Transfer at Parabolic Reentry"

K. K. Yoshikawa, B. H. Wick and J. T. Howe

(Paper No. 6 of Ref. 1)

- 8) "Aerodynamic Heating of Blunt Nose Shapes at Mach Numbers

Up to 14" K. E. Stoney

NACA RM L 58X15a April 1958

- 10) "A Survey of One-Dimensional Heat Transfer Problems in the Afterbody of the Project Mercury Capsule Reentry Configuration"  
L. C. Watson and J. E. Swanson  
NASA Project Mercury Working Paper No. 150 (CONFIDENTIAL)
- 11) "Predicted Shock Envelopes About Two Types of Lifting Atmospheric Entry Vehicles" G. B. Maftard (Preliminary)  
NASA Data Item 15 (1/13/61)
- 12) "A Review of Some Recent Developments in Hypersonic Flow"  
A. Verr. Sept. 1958  
NACA TN 53-230  
ASTIA Doc. No. AD 155-822
- 13) "Wind-Tunnel Investigation of Static Aerodynamic Characteristics of a 1/9-scale Model of a Project Mercury Capsule at High Incidence from 1.6 to 4.85"  
D. S. Shaeffer and K. L. Turner CONFIDENTIAL  
NASA TM X-291 July 1960
- 14) "Pressure and Convective Heat Transfer Problems in Three-Dimensional Hypersonic Flow" V. Zakharov  
NACA Tech Note 58-162 Sept. 1953  
ASTIA Doc. No. 155579
- 15) "Hypersonic Flow Theory"  
W. D. Hayes and R. W. Probstein  
Academic Press New York 1959
- 16) "Hypersonic Flow of a Gas over the Bell Vehicle"  
obtained from Mr. Frank Goss, NASA, Langley Field  
(1/30/61)



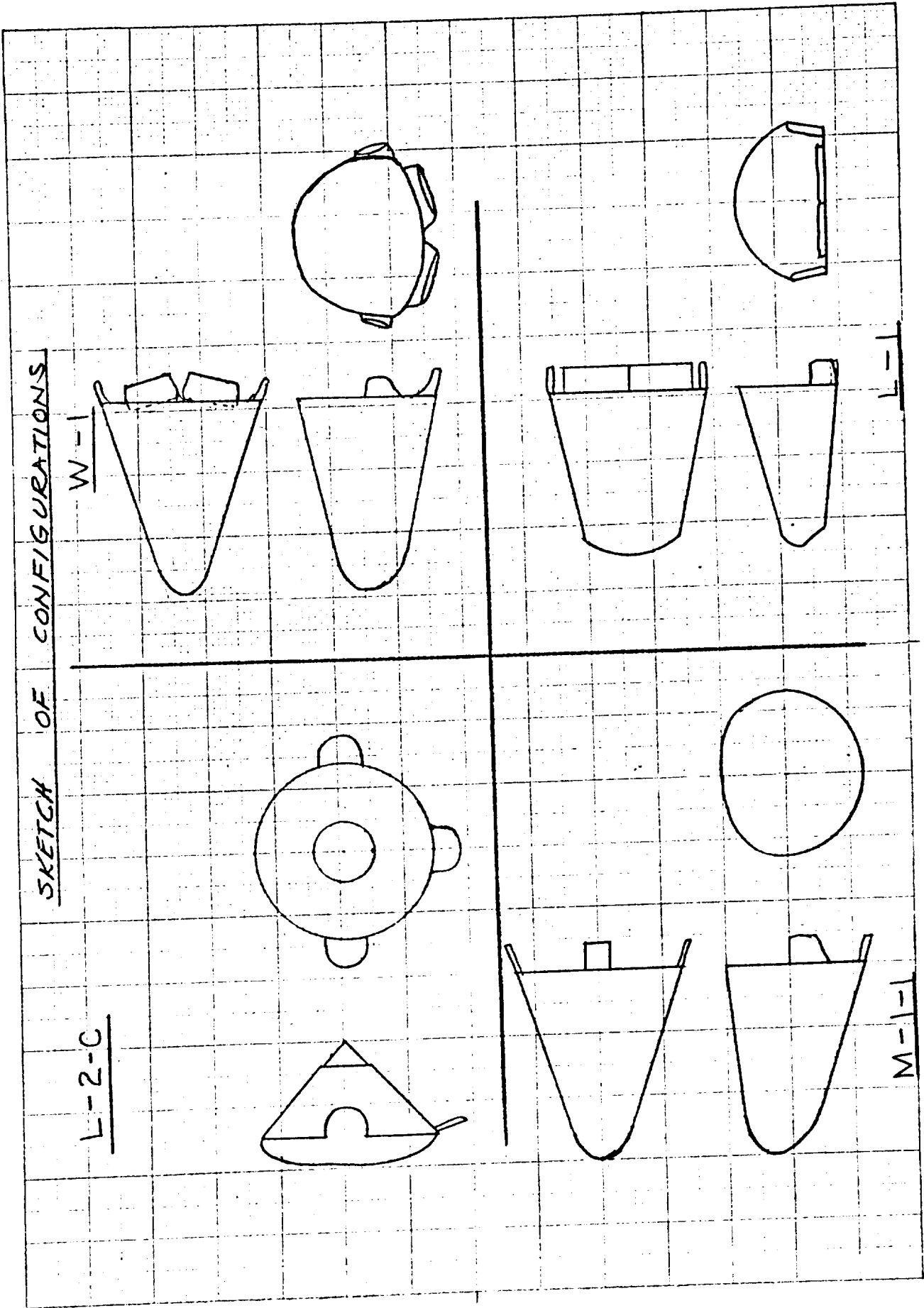
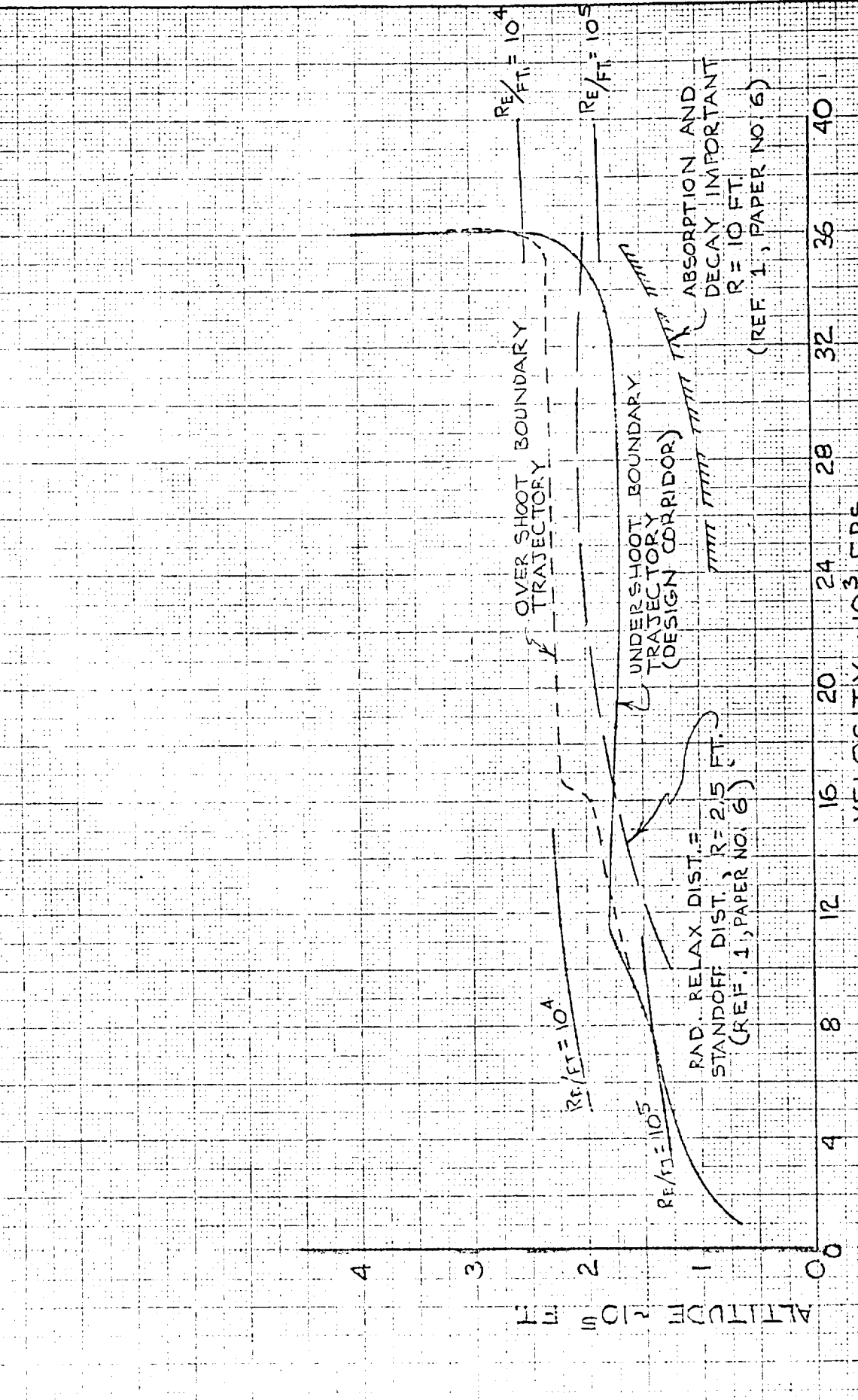


FIG 1 TM-5

# TYPICAL REENTRY TRAJECTORIES WITH IMPORTANT VELOCITY-ALTITUDE REGIONS



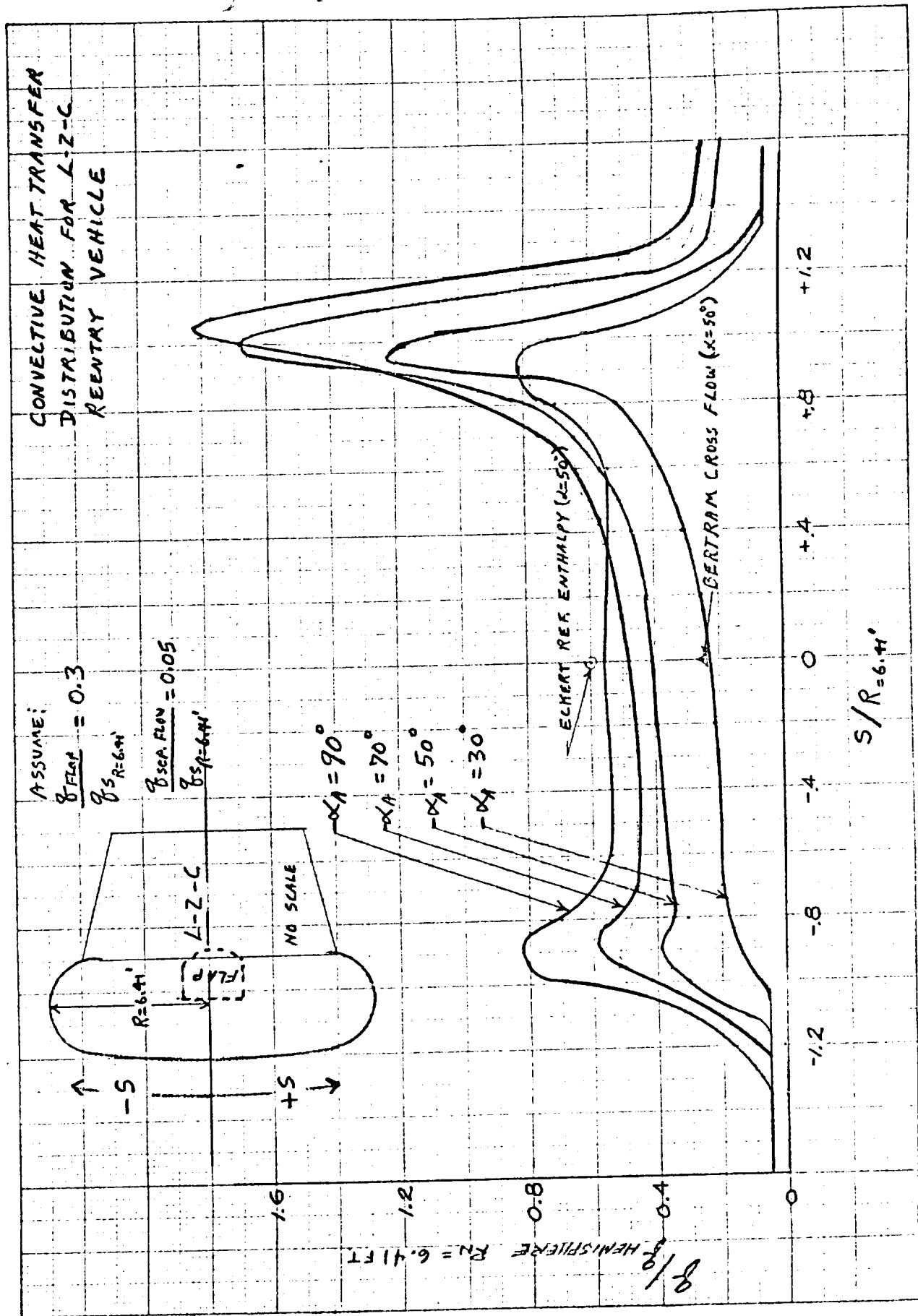


FIG 3 TM-5



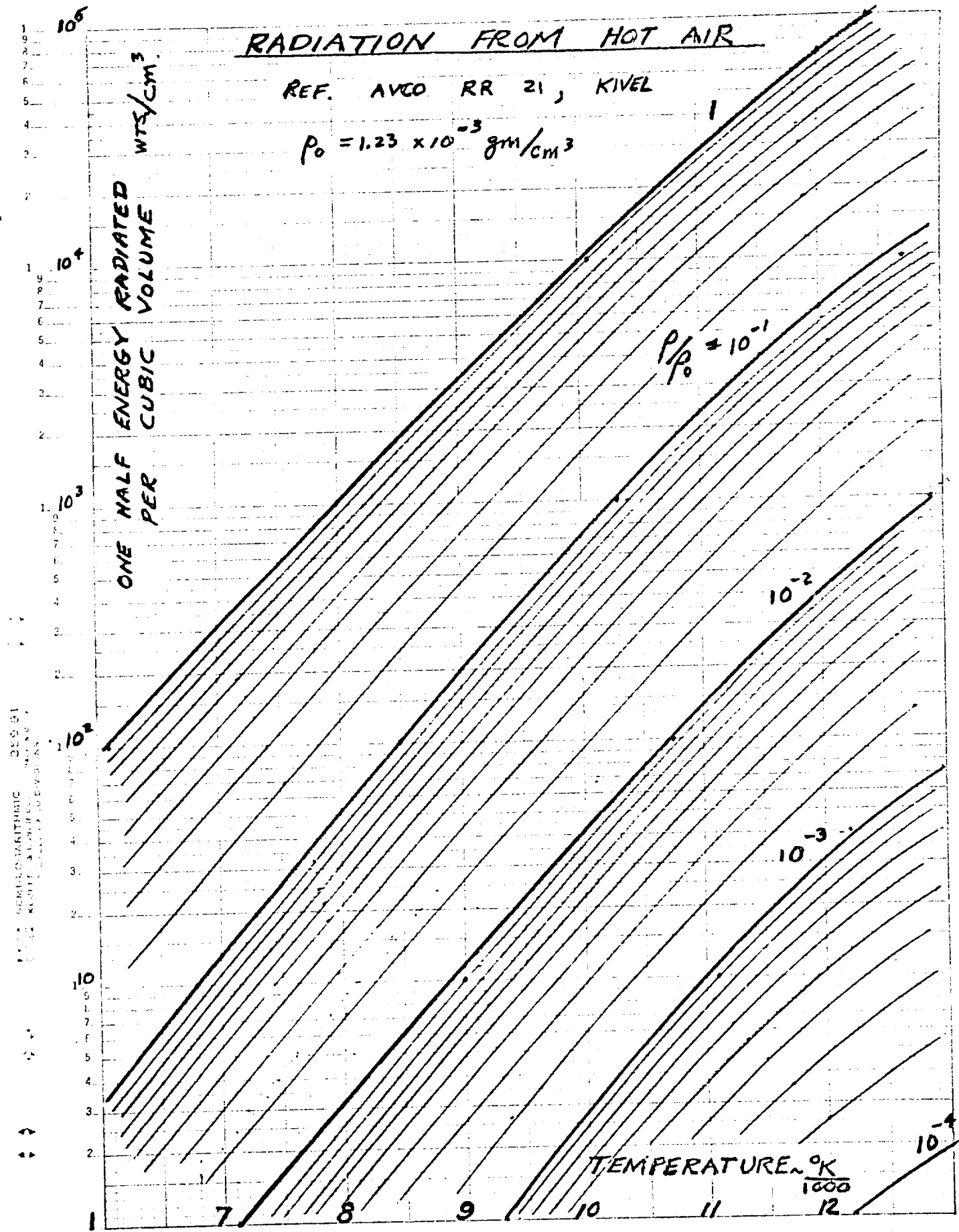


FIG 5 TM-5

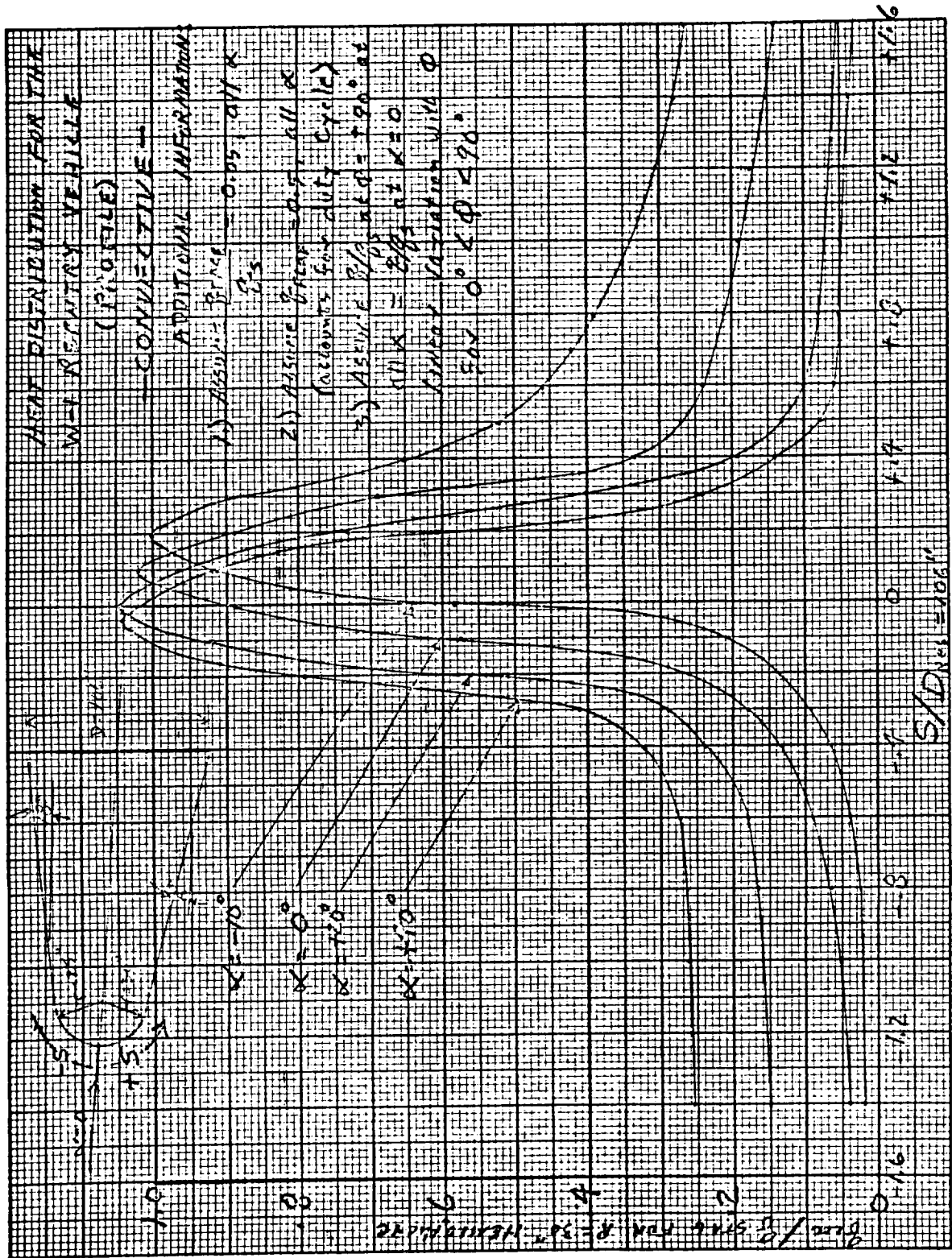


FIG 6 TM-5

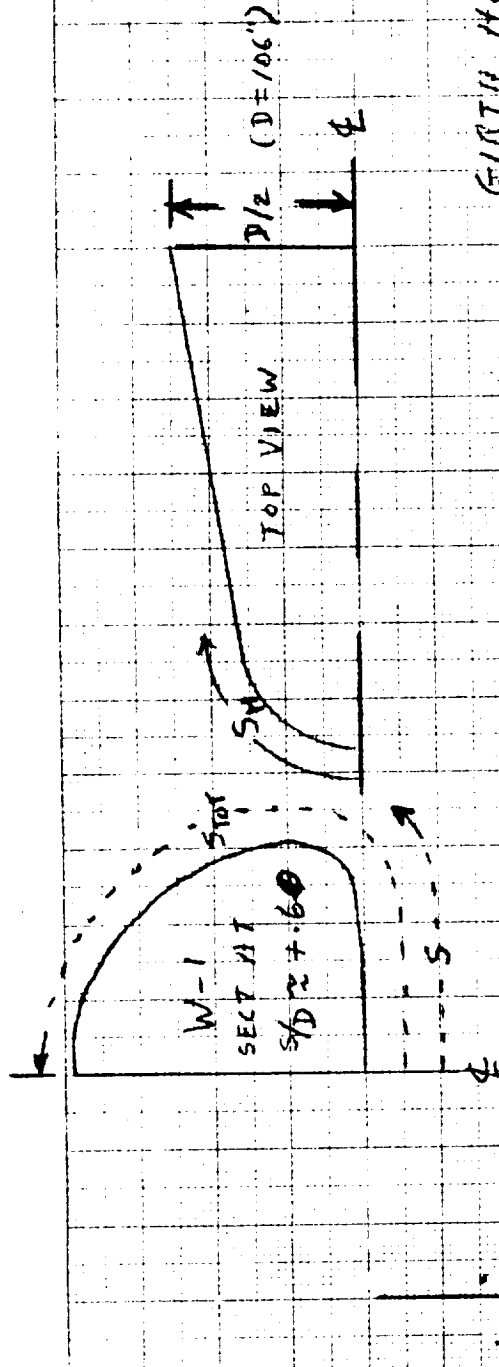
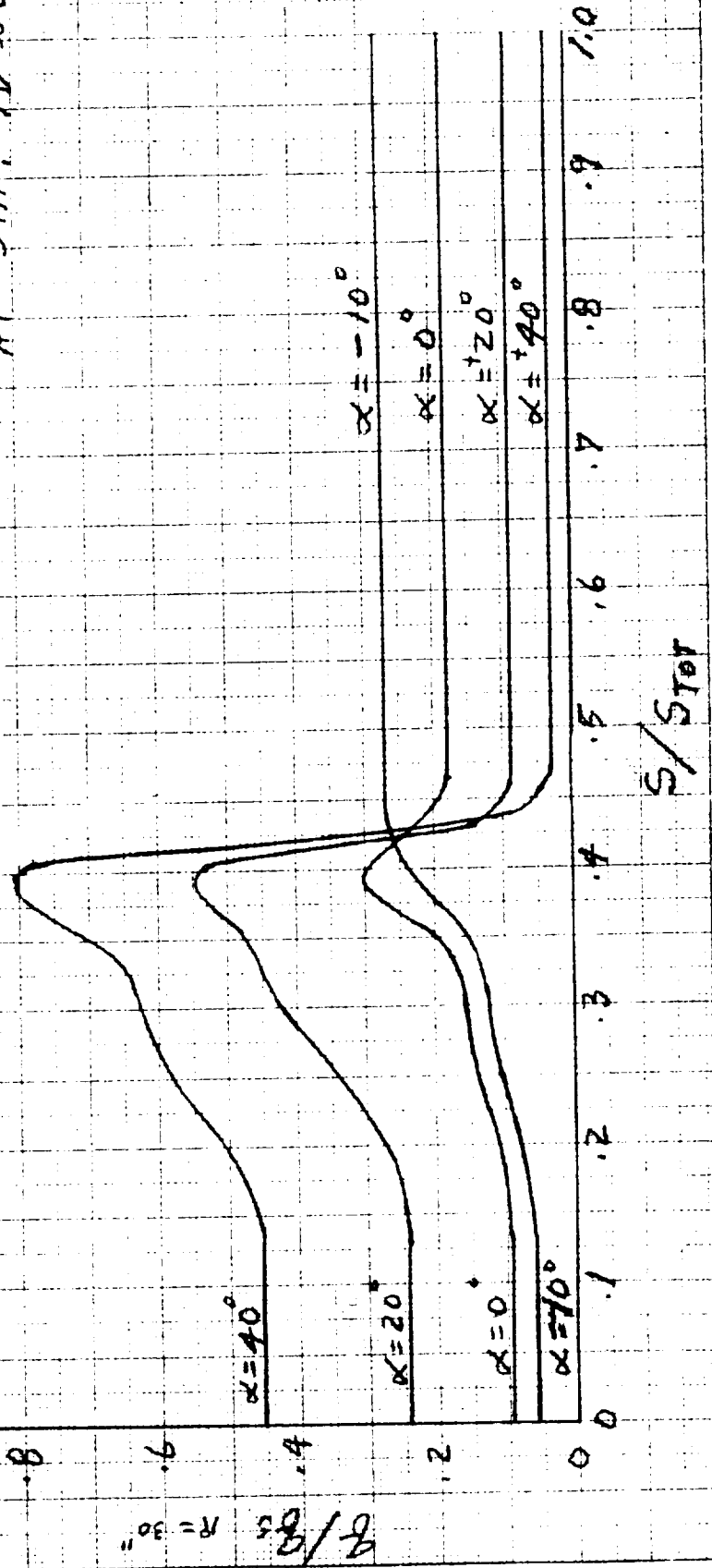


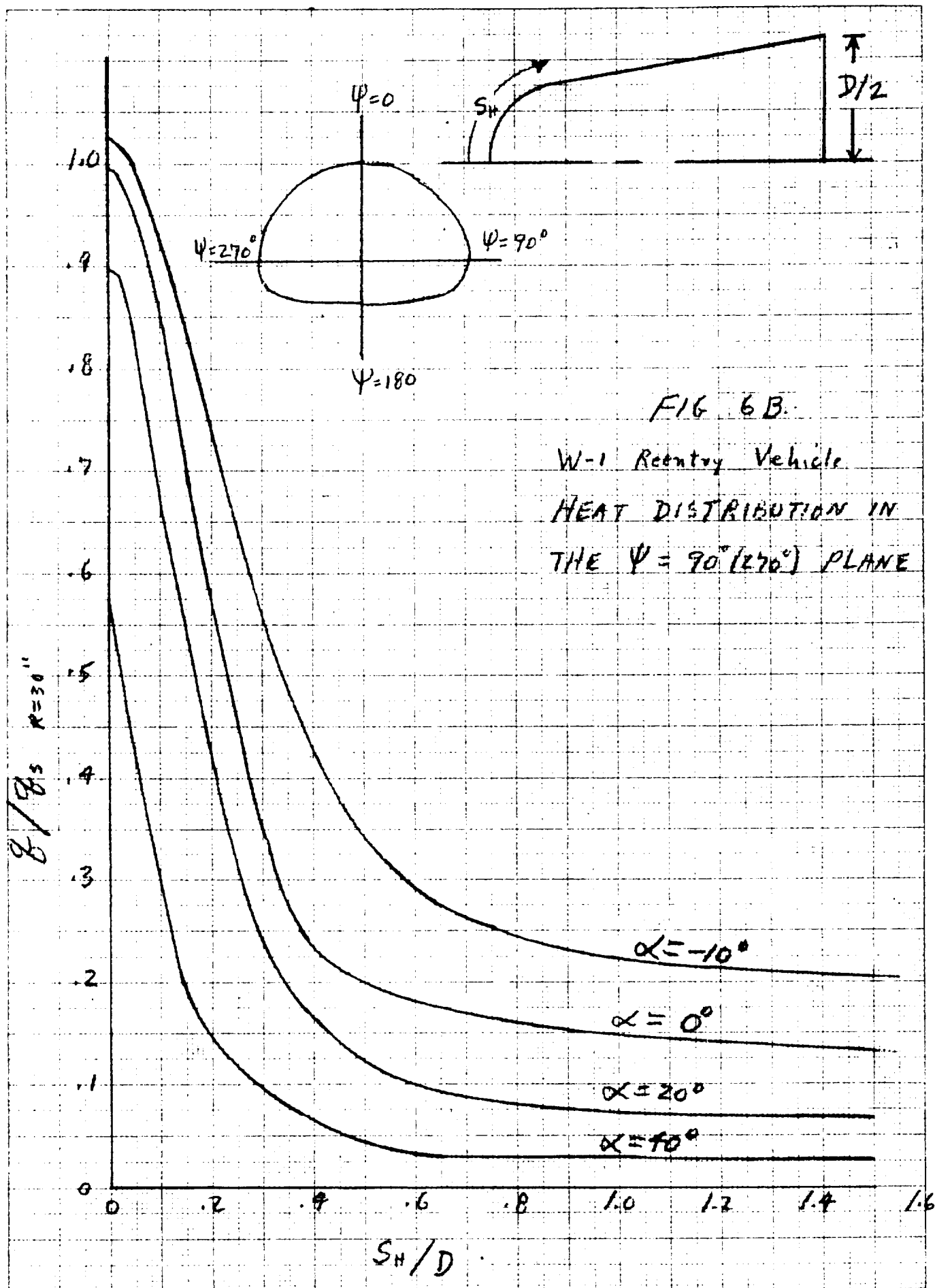
FIG. 2A

GIRTH HEAT DISTRIBUTION

W-1 REENTRY VEHICLE

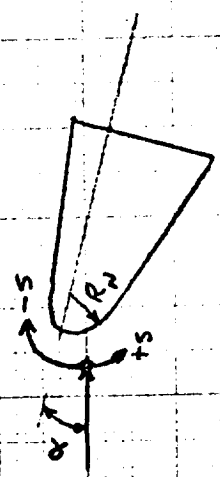
AT STA: S/D  $\approx 0.6$





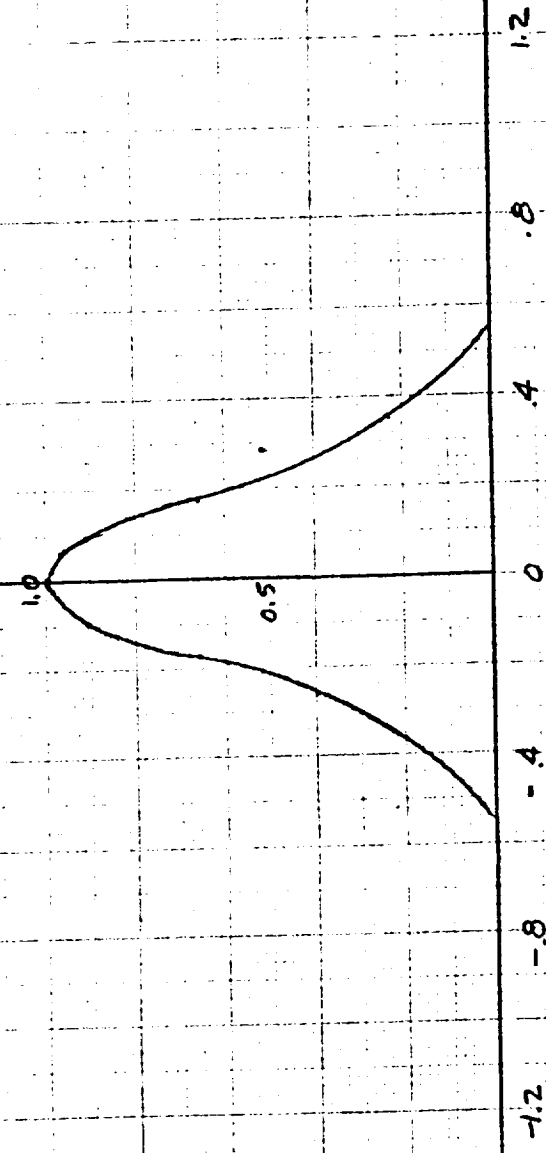


# ESTIMATED RADIATIVE HEATING DISTRIBUTION ON M-1-1 AND W-1



## ADDITIONAL INFORMATION

1. ASSUME  $q_R$  ON FLAPS IS 0.1  $q_{STAG}$ .
2. ASSUME  $q_R$  ELSEWHERE ON VEHICLE (OTHER THAN NOSE OR FLAPS) IS ZERO.



$S/R_N = 2.5 ft.$

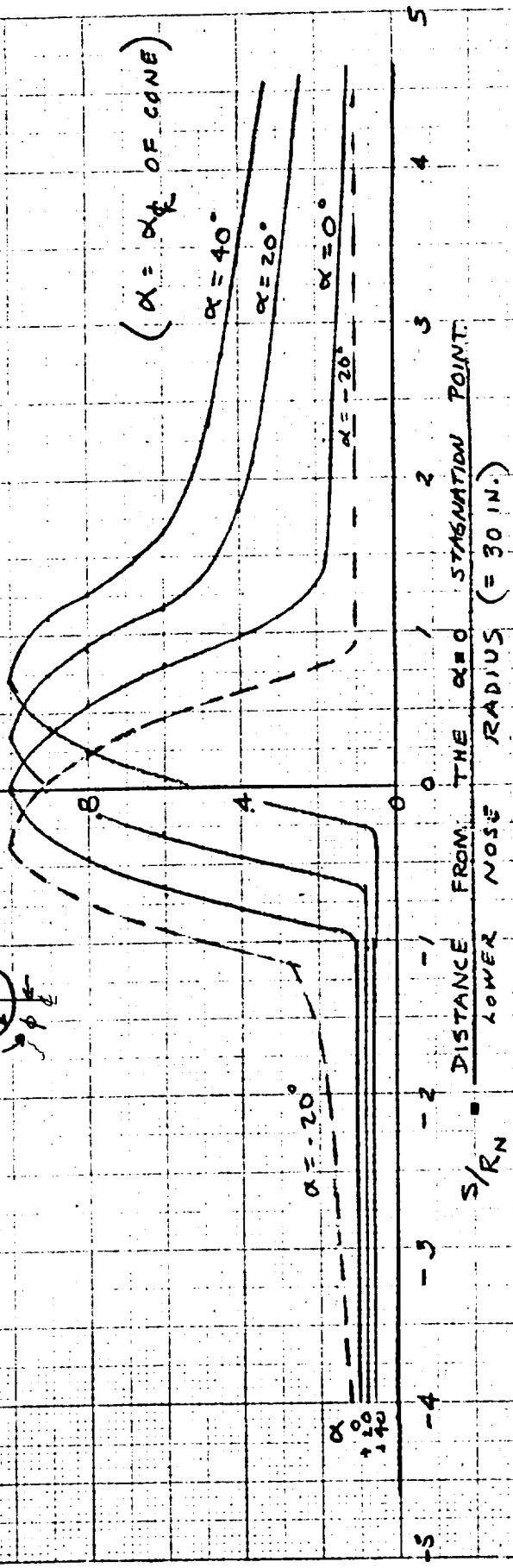
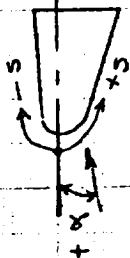
S = DISTANCE FROM GEOMETRIC STAGNATION POINT OR 1-361

FIG 7 TM-5

# M-1-1 HEATING RATE DISTRIBUTION

## ADDITIONAL INFORMATION

1. ASSUME  $\beta_{BASE} = 0.05$ , ALL  $\alpha$
2. ASSUME  $\beta_{FLIPS} = 0.5$ , ALL  $\alpha$   
(THIS ACCOUNTS FOR DUTY CYCLE)
3. ASSUME  $\beta/\beta_s$  AT  $\phi = \pm 90^\circ$   
AT ALL  $\alpha$  IS EQUAL TO  $\beta/\beta_s$  AT  $\alpha=0$   
LINEAR VARIATION WITH  $\phi$   
FOR  $0^\circ < \phi < 90^\circ$

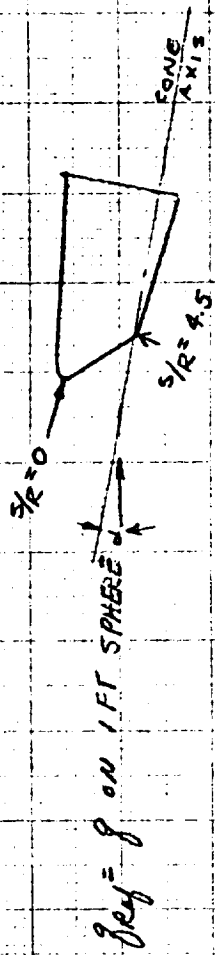


CAF 12-18-60

FIG 8 TM-5



# ESTIMATED RADIATIVE HEATING DISTRIBUTION FOR L-1



$q/q_{ref}$

ASSUME  $J_r$  ON CONTROLS  $= 1.0 J_{ref}$ .

$\alpha = 40^\circ$

$\alpha = 30^\circ$

$\alpha = 20^\circ$

$\alpha = 10^\circ$

$s/R = .075'$

CHP

FIG 11 TM-5

2011A

# L-2C +CLMAX OVERSHOOT BOUNDARY REENTRY

$\gamma_E = -5.18^\circ$

ROLL ALTITUDE CONTROL

$\alpha = 53^\circ$   $\theta_C = 7^\circ$

$R_N = 6.41$  FT.

$\frac{W}{C_D A} = 50$

$Q_C = 38200$  BTU/FT<sup>2</sup>

$Q_R = 1595$  BTU/FT<sup>2</sup>

RANGE = 3080 NM

MAX. DYNAMIC PRESS. = 74 PSF

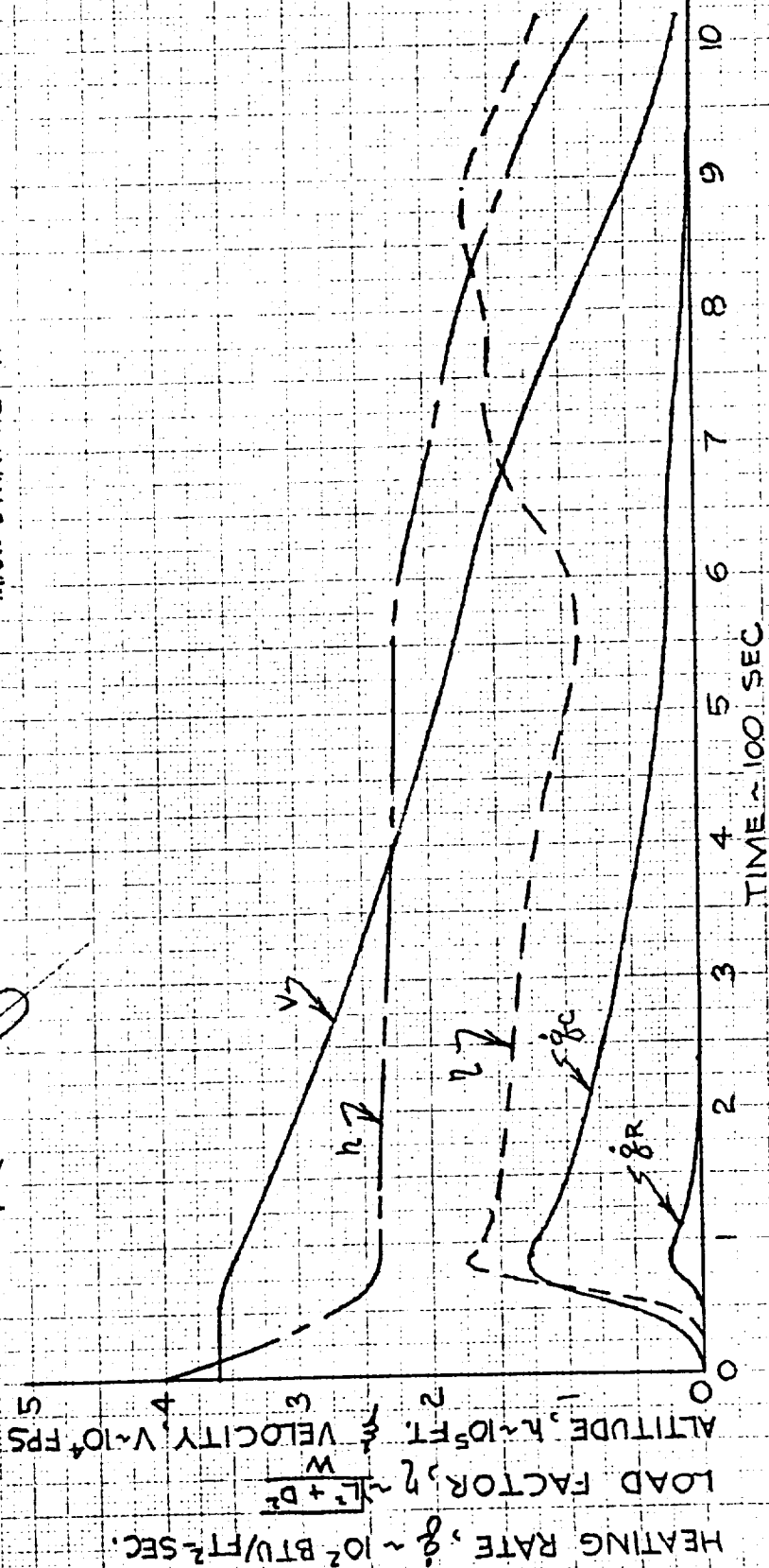
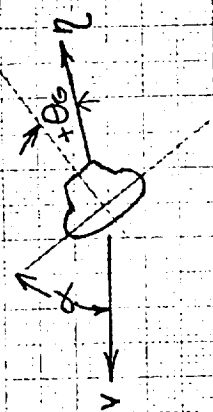


FIG12 TM-5

7017

4A

4A

3-20-60

# L-2C 60 NM. CORRIDOR UNDERSHOOT REENTRY

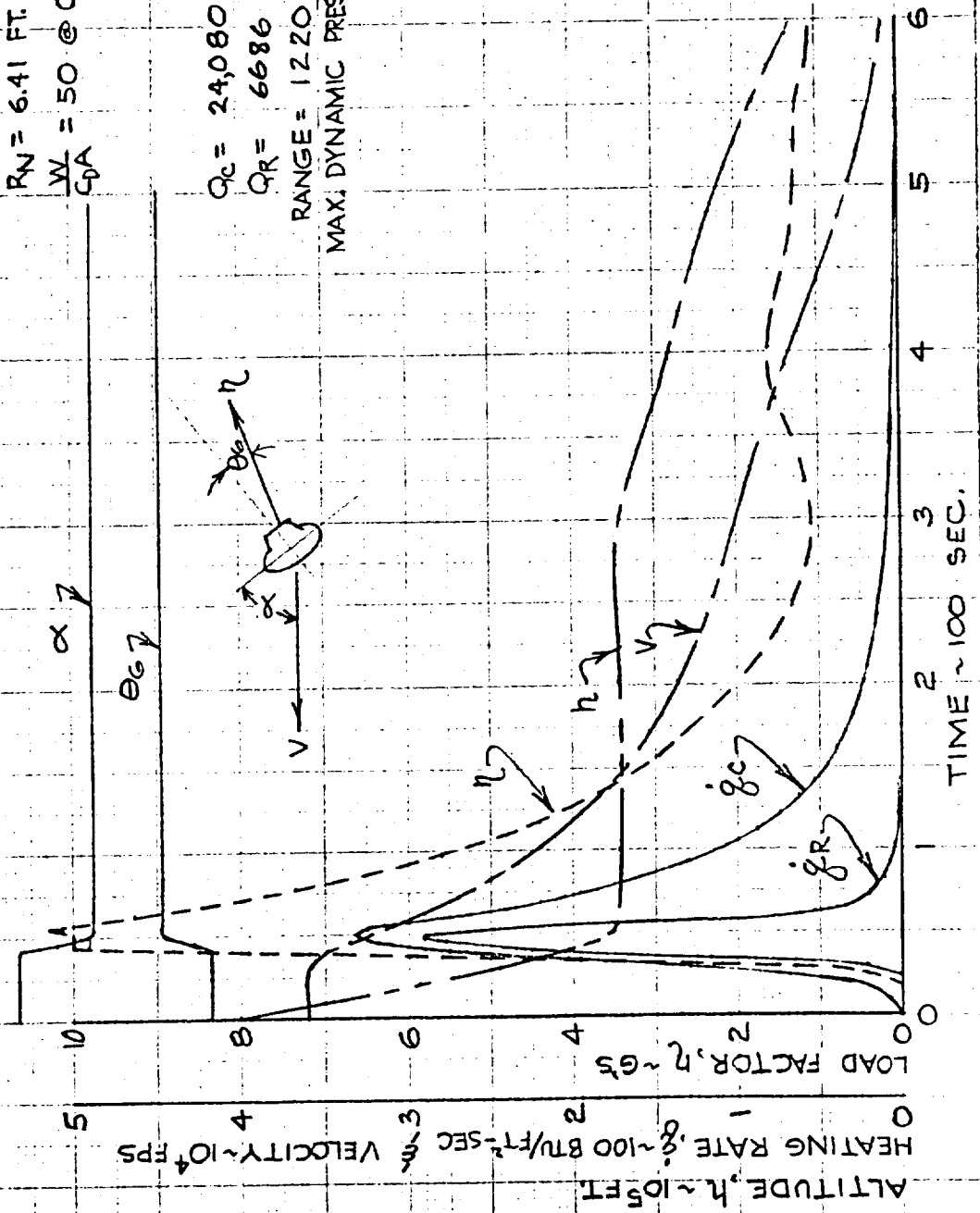
$\gamma_E = -9.0^\circ = 60 \text{ NM FROM } +C_{L\text{MAX}}$  OVERSHOOT

## ROLL ALTITUDE CONTROL

G ORIENTATION ANGLE,  $\theta_g$   
 -20  
 0  
 20  
 40  
 60  
 80  
 100

$R_N = 6.41 \text{ FT.}$   
 $\frac{W}{C_D A} = 50 @ C_{L\text{MAX}}$

$Q_C = 24,080 \text{ BTU/FT}^2$   
 $Q_R = 6686 \text{ BTU/FT}^2$   
 RANGE = 1220 NM  
 MAX. DYNAMIC PRESS. = 755 PSF



# M-1-1 +C<sub>L</sub>MAX OVERSHOOT BOUNDARY REENTRY

$Y_E = -5.3^\circ$

$R_N = 2.5 \text{ FT.}$   $\frac{W}{C_D A} = 73$

ROLL ALTITUDE CONTROL @ C<sub>L</sub>MAX ATTITUDE

$Q_C = 76,780 \text{ BTU/FT}^2$

$Q_R = 1210 \text{ BTU/FT}^2$

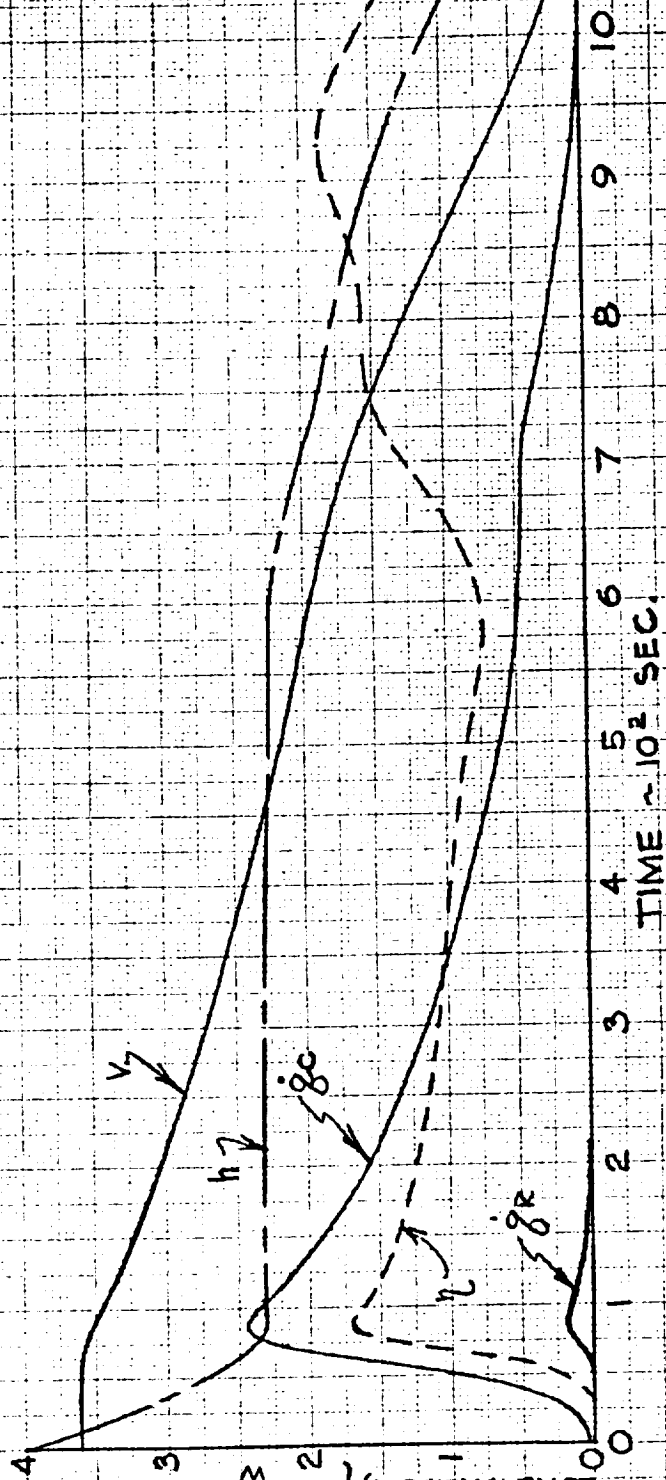
RANGE = 3530 NM

MAX DYN. PRESS  $\approx 118 \text{ PSF}$

ALTITUDE,  $h \sim 10^5 \text{ FT}$  & VELOCITY,  $V \sim 10^4 \text{ FPS}$

HEATING RATE,  $\dot{q} \sim 10^2 \text{ BTU/FT}^2\text{-SEC}$

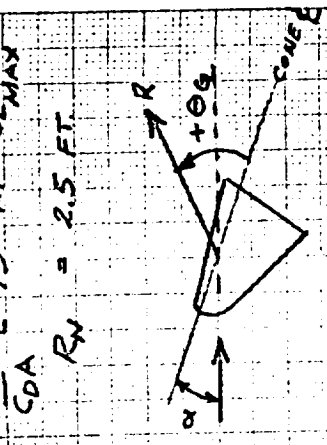
LOAD FACTOR,  $n \sim \frac{1}{1+D^2}$



# M 1-1 60 N.M. CORRIDOR UNDERSHOOT TRAJECTORY

$\gamma_E = -9.0^\circ = 60 \text{ N.M. CORRIDOR FROM } +C_{L\text{MAX}} \text{ OVERSHOOT}$

$\frac{W}{C_{DA}} = 73 \text{ AT } C_{L\text{MAX}}$   
 $R_N = 2.5 \text{ FT.}$



$Q_C = 74700 \text{ BTU/FT}^2$   
 $Q_R = 6100 \text{ BTU/FT}^2$   
 $\text{RANGE} = 1640 \text{ N.M.}$   
 $\text{MAX. DYNAMIC PRESS.} = 1180 \text{ PSF}$

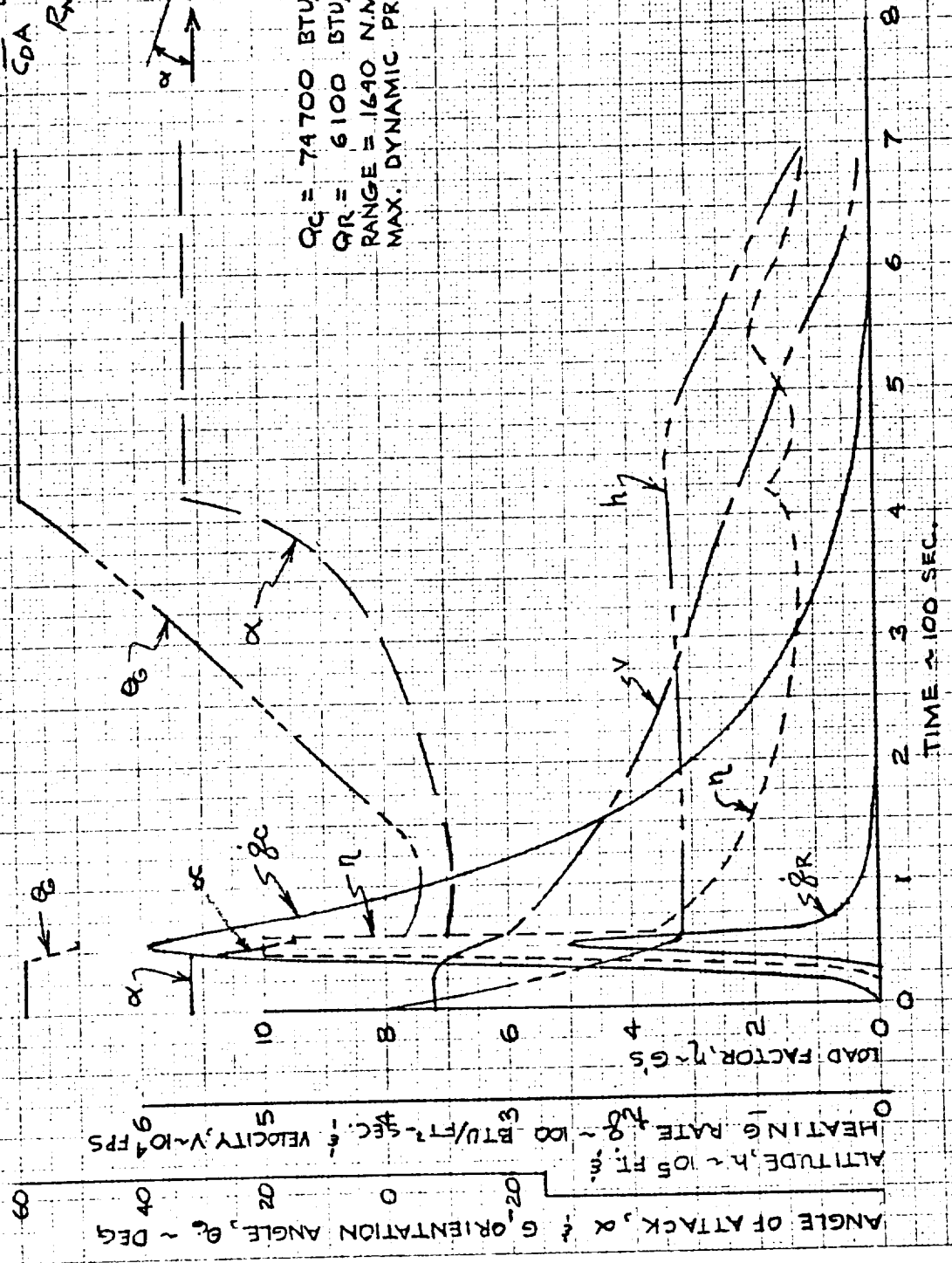


FIG 15 TM-5



## PART II - HEAT SHIELD EVALUATION AND DESIGN

It is accepted that the Apollo vehicle will require the use of ablative heat shields over a major portion of the body as shown in Figure 1. However it is possible to use composite shields of ablators over radiative type heat shields which will yield lighter heat shields than all ablative type heat shields. This is demonstrated in Reference 1. This section presents the efforts in evaluation and definition of composite heat shields for the Apollo vehicle.

### 1. Materials Selection

This section presents the selection of materials for the composite heat study on the Apollo. The materials are discussed separately as ablators, ceramics and metals.

#### a. Ablators

The selection of the type of thermal protection and of the specific material for the Apollo re-entry vehicle can be based on the stagnation point re-entry conditions enumerated below:

1. Maximum stagnation point heat transfer is approximately  $250 \text{ Btu/ft}^2\text{sec}$  (M-1-1 overshoot).
2. Heat fluxes in excess of  $100 \text{ Btu/ft}^2\text{sec}$  are encountered for approximately 300 sec. (M-1-1 overshoot-roll control).
3. Maximum stagnation enthalpy is 26,000 Btu/lb.
4. A stagnation enthalpy in excess of 10,000 Btu/lb is encountered for approximately 500 sec (M-1-1 overshoot-roll control).

- 5 The total heat pulse lasts approximately 1000 seconds and the total integrated heat input is approximately 80,000 Btu/ft<sup>2</sup>.

Item 1 requires the use of an ablator since the maximum heat flux of 250 Btu/ft<sup>2</sup>sec is higher than that which a ceramic or metal radiative shield can withstand. Once the ablation material has been selected, it must be determined whether this ablator can efficiently provide thermal protection for the entire duration of the re-entry and how far back from the stagnation point the ablator can be efficiently utilized.

The high stagnation enthalpy (Item 3) and the long exposure to stagnation enthalpies in excess of 10 000 Btu/lb (Item 4) call for a material with a large gasification ratio (weight of material which gasifies/weight of ablated material) in order to take advantage of the high mass transfer cooling available at these stagnation enthalpies.

Simultaneously, a material which operates at a high surface temperature is required in order to radiate a large percentage of the aerodynamic heat input.

Lastly, a material with a low thermal conductivity is required to minimize the amount of heat flowing through the material during the 1000 second exposure.

The above requirements are satisfied by the class of reinforced or unreinforced plastics designated as charring ablators. From the numerous combinations of plastics and reinforcements, nylon reinforced phenolic has been selected as the most likely candidate for the Apollo Heat Shield on the basis of its specific weight, thermal conductivity, chemical decomposition and effective heat of ablation.

The principal char forming plastics used for ablation are phenolics and epoxies. The highly cross linked phenolics tend to form a continuous, though fragile char structure. During tests in plasma arcs, the char tends to adhere to the uncharred plastic but it usually spalls off after the test due to thermal contractions while cooling and due to handling.

Spalling of epoxy chars during plasma arc testing has been observed. This spalling is attributed to internal pressures generated by the rapid formation of gases in the pyrolysis zone.

The properties of a number of reinforcing fibers which can be utilized with phenolic resins are listed in Table I. A comparison indicates that nylon appears to be a very desirable reinforcing material since its density and thermal conductivity are lower and its specific heat higher than that of glass, asbestos and graphite.

A nylon-reinforced phenolic generally contains 50% nylon and 50% phenolic by weight. The resulting density is approximately 1.20 g/cc. Glass and asbestos-reinforced phenolics generally contain 35-40% resin and 60 to 65% reinforcement by weight. The resulting density ranges from 1.6 to 1.8 g/cc.

When subjected to ablation, the nylon in a nylon-phenolic will completely vaporize and the char will be formed predominantly from the pyrolysis of the phenolic resin. There is evidence that some carbon is deposited in the char as a result of cracking of the nylon vapors into lower molecular weight constituents as they pass through the hot porous char. Since approximately 50% of the phenolic is pyrolyzed into gaseous decomposition products, 70 to 75% of the weight of pyrolyzed nylon-phenolic can be utilized for mass transfer cooling. An average molecular weight of 50 for nylon-phenolic pyrolysis products has been used in some analyses; however, this value varies among different investigators.

27

With a maximum heat transfer rate of  $250 \text{ BTU/ft}^2\text{-sec}$ , surface temperatures will not be high enough to vaporize glass, silica or asbestos reinforcements. Consequently, only the phenolic resin will contribute to the formation of gaseous products. On the basis of 50% gasification ratio for phenolic, only 17% to 20% of the weight of a pyrolyzed vitreous fiber-reinforced plastic contributes to mass transfer cooling.

The high loss of volatiles in nylon-phenolic is substantiated by the char properties listed in Table II. The nylon-phenolic char density of  $0.47 \text{ g/cc}$  is approximately  $1/3$  the density of vitreous fiber chars. Nylon-phenolic char densities as low as  $0.34 \text{ g/cc}$  has been reported by other investigators.

The strength of a char containing vitreous fibers is approximately 5 - 10 times as great as the mechanical strength of a nylon-phenolic char. This raises the question whether the nylon-phenolic char will adhere in turbulent flow or in a flow generating high dynamic pressures and shear forces. Consequently it is of interest to compare the effective heats of ablation of nylon-phenolic and glass-phenolic in a turbulent pipe flow test at a stagnation enthalpy of  $5000 \text{ BTU/lb}$ . After test, the internal surface of the nylon-phenolic sample exhibited a very rough appearance with deep gouges and eroded areas. Nevertheless, the effective heat of ablation of nylon-phenolic in this environment was  $3850 \text{ BTU/lb}$  as compared with an effective heat of ablation of  $3250 \text{ BTU/lb}$  for a glass-phenolic.

The greater gasification, lower conductivity and higher specific heat of nylon-phenolic should result in a lower back wall heating rate when compared to other reinforced plastics under equal exposure conditions. This is substantiated by the data in Table III. Nylon-phenolic exhibits a considerably lower temperature rise at locations of  $\frac{1}{2}$  and 1 inch below the initial front face when compared on an equal thickness basis with other reinforced plastics. If the materials were compared on an equal weight

basis, nylon-phenolic would appear even more attractive since it is considerably lighter than glass, asbestos or silica fiber-reinforced phenolics.

During the particular exposure, nylon-phenolic lost 36.5% of its initial weight. The asbestos, glass and Refrasil phenolic samples lost 16.5%, 21.8% and 9.4% of their initial weight respectively.

Some experimental data on mass loss and back wall temperature rise of nylon-phenolic at relatively low heating rates has been obtained by G.E. For a total integrated heat input of 10,000 Btu/ft<sup>2</sup> (50 Btu/ft<sup>2</sup>-sec for 200 sec) at a stagnation enthalpy of 5900 Btu/lb, the weight loss was 1.38 lb/ft<sup>2</sup>. A 0.68 inch thick specimen (4.28 lb/ft<sup>2</sup>) experienced a 60°F temperature rise on its back face at the end of the 200 sec heating period but exhibited a 300°F rise subsequent to the heating period. A 1.02 inch thick specimen (6.45 lb/ft<sup>2</sup>) exhibited a 30°F rise on its back face at the end of the heating period and a 200°F rise subsequent to the heating period.

## b. Ceramics

The temperature range of applicability for ceramics as radiative heat shield materials extends upward from the maximum service temperatures of the metallics. This defines the lower temperature of interest to ceramics as about 2200°F (selected for use of superalloys in non-structural form).

### Materials

The following discussion is included to present a brief review of ceramic materials and some of their basic characteristics. The ceramic materials of interest are classified into: (a) oxides, (b) carbides, (c) borides, (d) graphite and (e) composite materials. These materials are generally available in a high density form or a high porosity form. Certain of the manufacturing and fabrication problems of each are discussed.

#### a. Oxides

The refractory oxides are particularly attractive for this program because of their stability in an oxidizing atmosphere. However, the chemical stability of the oxides is probably the only outstanding property in their favor. Some of the less desirable traits of the oxides are: a large reduction in strength at high temperature (particularly over 3000°F); shrinkage at high temperature (although this can be alleviated by high firing temperatures); the emissivity is generally low; and thermal radiation transmissivity increases at high temperature which greatly increases the overall thermal conductance of the foamed forms of these materials. Many oxides with suitable properties are available and a few of these are available in the foamed form.

##### (1) Silica ( $\text{SiO}_2$ )

Vitreous silica possesses many desirable properties, i.e., low thermal conductivity, low density, low thermal expansion, ease of manufacture, etc. However, it is limited by melting

at a maximum temperature of 3100°F range.

(2) Alumina ( $\text{Al}_2\text{O}_3$ )

High purity alumina can be used at temperatures of approximately 3400°F. However, it experiences a large reduction in its strength around 2300°F. Alumina is readily available in the dense form in extruded or pressed shapes. Also, it is relatively easy to produce in the highly porous form and foams of this material are available in the density range of 0.5 g/cc. The material from Ipsen Industries is fairly uniform with generally spherically shaped cavities. Difficulty has been encountered with small cracks appearing throughout the material; however, the manufacturer is attempting to improve this condition and to raise the general quality of this material.

(3) Zirconia ( $\text{ZrO}_2$ )

Zirconia melts at approximately 4900°F. Dense zirconia is available in extruded or pressed shapes. The highly porous foamed form is also available but zirconia is much more difficult to foam than alumina and, for the same porosity, is much heavier. In the past, ceramic bonded porous zirconia was not available below a density of 2.5 g/cc. However, foams are now being produced with densities as low as 0.5 g/cc. For the application being considered it is expected that densities in the range of 1 to 1.5 g/cc will be most useful.

(4) Beryllia ( $\text{BeO}$ )

Beryllia melts at approximately 4660°F. Dense beryllia is available in various shapes. Foamed beryllia has been produced but only in very small bodies and the development

requirements make it currently unavailable. Also, toxicity dangers in manufacturing and testing present additional problems. Cost is high.

(5) Thoria ( $\text{ThO}_2$ )

Thoria melts at about 5500°F. Dense forms of Thoria are currently available and reports of development of a thoria foam have been received. Thoria is slightly radio-active and requires caution in use. Cost is extremely high with a severe limitation on size of dense parts.

b. Carbides

The refractory carbides possess very high melting points and the ability to retain their mechanical properties at very high temperatures. In this respect, they are superior to the oxides. However, all of the carbides are subject to oxidation with SiC possessing the greatest resistance to oxidation up to 3000°F. Therefore, for this application, the use of a carbide depends on a suitable protective coating. This can be accomplished by applying an oxide directly on the carbide, by applying a compound which converts to an oxide or by compounding the carbide with other materials such that a protective oxide layer forms on the surface. There are many possibilities of such protection methods for the carbides; however, only two appear to be available. These are the  $\text{ZrB}_2\text{MoSi}_2$  coating (The Carborundum Company) and a  $\text{ZrO}_2$  coating (The Martin Company).

Most of the carbides are available in the dense form. In the foamed form, SiC appears to be the most developed and readily available although successful foams have been made of TiC, NbC, HfC, TaC, WC and ZrC.

(1) Silicon Carbide (SiC)

SiC can be used in air at temperatures up to 3000°F. However, between 1800° and 2100° F, it oxidizes fairly rapidly.



a fact which must be recognized in the design. The oxidation resistance of SiC depends on the formation of a layer of silica on the surface. Therefore, conditions which impede the formation of  $\text{SiO}_2$ , such as low pressure, increase the oxidation rate. Also, at temperatures above the melting point of  $\text{SiO}_2$ , the oxidation resistance depends on the molten layer of  $\text{SiO}_2$ . Again, removal of this layer such as by lowering the pressure (thereby lowering the  $\text{SiO}_2$  boiling point) or high velocity air removing the liquid  $\text{SiO}_2$  can be expected to increase the oxidation rate (Ref. 2).

The melting point of SiC is approximately  $4700^\circ\text{F}$ ; however, it decomposes at approximately  $4000^\circ\text{F}$  and sublimates at  $3600^\circ\text{F}$  atmospheric pressure (Ref. 3). However, the Carborundum literature gives  $4200^\circ\text{F}$  as the maximum temperature. Therefore, the maximum operating temperature of SiC for this application may be as high as  $4200^\circ\text{F}$  or as low as  $3600^\circ\text{F}$ , depending on the effect of lower pressures.

## (2) Titanium Carbide (TiC)

The melting point of TiC is  $5600^\circ\text{F}$  and it appears that this material can be utilized to the upper temperature requirement of  $4000^\circ\text{F}$ . However, TiC oxidizes readily in air at high temperatures and therefore a protective coating is necessary. It is possible that the Carborundum coating of  $\text{ZrB}_2\text{-MoSi}_2$  would be suitable. The Carborundum Company has spent considerable effort on developing a low density (0.3 to 0.7 g/cc) TiC foam (Ref. 4). For this reason, TiC foam is probably the most readily available foamed carbide other than SiC Foam.

(3) Carbides of Nb, Hf, Ta, V, Zr, B and Cr

There is little specific information available on these materials. All have melting points over 5000°F except  $\text{Cr}_3\text{C}_2$  and  $\text{B}_4\text{C}$  which are approximately 3400° and 4100°F, respectively; all have been produced in the foamed form (however, only poor results were obtained with the chromium and boron carbides); all require oxidation protection.

c. Borides

The attractive characteristics of the borides are high chemical stability and low volatility. In general, the borides are slightly more stable than the carbides at high temperatures. However, the borides are subject to oxidation at high temperatures, being attacked readily at temperatures over 2500°F. Titanium and zirconium borides are the most oxidation resistant. Thick oxide layers are formed on the surface during exposure to high temperature oxidizing conditions; however, the layers tend to be porous. The borides of titanium, tantalum, zirconium and niobium have been foamed (Ref. 4).

(1) Titanium Boride ( $\text{TiB}_2$ )

$\text{TiB}_2$  is stable up to a melting point of approximately 4700°F.  $\text{TiB}_2$  is the most stable of the refractory borides.

(2) Zirconium Boride ( $\text{ZrB}_2$ )

$\text{ZrB}_2$  is stable up to a melting point of approximately 5400°F.  $\text{ZrB}_2$  is the second most stable of the refractory borides.

(3) Tantalum Boride ( $\text{TaB}_2$ )

$\text{TaB}_2$  decomposes to TaB plus boron upon melting. The melting points of TaB and  $\text{TaB}_2$  are not well defined. Reference 4 gives them as greater than 3600°F and Ref. 3 lists 5400°F with a question mark.

(4) Niobium Boride ( $\text{NbB}_2$ )

Like  $\text{TaB}_2$ ,  $\text{NbB}_2$  decomposes to  $\text{NbB}$  upon melting. Also, the melting point is questionable being in the range of  $3600^\circ\text{F}$  to possibly as high as  $5200^\circ\text{F}$ .

d. Graphite

Graphite possesses many desirable properties which make it a very attractive material for high temperature applications. Graphite's high strength at elevated temperatures, medium thermal expansion and low modulus of elasticity give it the ability to withstand large thermal gradients without failure. However, graphite oxidizes readily in air at elevated temperatures and a protective coating is desirable. Oxidation coatings are available for graphite but are currently limited to  $3000^\circ\text{F}$  which is insufficient to make use of the full potential of graphite.

Graphite is readily available in the dense form and many companies have experience in its manufacture and application. Also, a low density ( $0.8 \text{ g/cc}$ ) form is available (Ref. 6). This material has a very fine closed cell structure.

Pyrographite is an attractive form of graphite which possesses anisotropic properties. Its anisotropic thermal conductivity effectively allows it to be utilized as an insulator in one direction and a conductor in other directions. Thermal conductivities as low as  $0.5 \text{ Btu/hr-ft}^2\text{F/ft}$  in the insulating direction and up to  $2000 \text{ Btu/hr ft}^2\text{F/ft}$  in the conducting directions have been reported. Also oxidation rates of approximately 0.1 of the rate for normal graphite have been reported. More extensive oxidation tests are planned for a future development phase. The development of this material is progressing very fast with the Navy sponsoring a large portion of the development. Large pieces and complex shapes have been made. However, thickness in the insulating direction is limited to approximately 1/8 inch maximum and

manufacturing techniques must be developed for particular shapes. From discussions with its producers it is apparent that, at this time, this material is in a highly developmental stage resulting in high costs and relatively long procurement times; in addition, the oxidation rates are not sufficiently determined to accurately predict the effects of oxidation.

#### e. Composite materials

Some materials possess acceptable properties for the application being considered; however, no one material possesses both the most desirable physical and chemical properties including oxidation resistance. Therefore, composites of materials are considered which exhibit improved overall properties. This is accomplished by combining the chemical stability of the oxides with the good mechanical properties of other materials such as the carbides.

##### (1) Foamed SiC Impregnated with $ZrO_2$

This material has higher strength, a slightly lower thermal conductivity and improved oxidation resistance over plain SiC foam. The composite consists of approximately 50% SiC and 50%  $ZrO_2$  weight. In a test program conducted in a 5-inch hot gas facility, specimens of plain foamed SiC could not withstand the environment (3400°F for 15 minutes). In comparison, similar specimens of foamed SiC but impregnated with  $ZrO_2$  withstood not only the same but much more severe exposures. The impregnated foamed SiC appears to be capable of withstanding temperatures of approximately 3400°F in air for at least 15 minutes. With a dense thin face of  $ZrO_2$  over the cellular structure of the composite, the surface temperature capability is expected to be greater than 3400°F.

(2) Foamed SiC and  $ZrB_2 - MoSi_2$

The Carborundum Company has developed a coating material of  $ZrB_2 - MoSi_2$  which shows promise as a protective coating for foamed SiC. This material has been applied to the external surface of cubes of SiC foam and tests in air indicate surface temperature capabilities as high as 4000°F for 15 minutes.

(3) AMP Composite

American Metal Products Company has proposed a system of materials composed of a structural insulation material of porous amorphous carbon with a complex face of dense molybdenum and zirconia. The performance of this system depends on the adherence of these various layers and their resistance to flaking as well as the oxidation protection obtained from the zirconia layers. An evaluation of these characteristics would have to be conducted to determine the applicability of the composite to this program.

(4) Ceramic-Metal Honeycomb

Many companies have experimented with a single faced metal honeycomb that is partially filled with fibrous insulation and capped with a chemically bonded foamed ceramic for a temperature potential over 3000°F. Major problem area experienced by Martin with this material was the breakdown of the chemical bond at 2400 - 2600°F resulting in severe shrinkage and release of a highly corrosive gas.

(5) Resin Impregnated Ceramics

The concept of impregnating a foamed ceramic with a decomposing resin is discussed in the MLV report (Ref. 14).

Briefly this composite material incorporates the three basic

modes of thermal protection, namely reradiation, mass injection into the boundary layer and material phase changes. The impregnation with resin improves the mechanical properties of the ceramic by orders of magnitude, improves its thermal shock resistance and provides a non-shape changing heat shield. Materials under study for this composite are the use of SiC,  $Al_2O_3$ ,  $ZrO_2$ , and BeO ceramic foams with various resins such as phenylsilane. See section 5 for further discussion of this material.

Table IV presents a summary of some of the available materials and their characteristics of interest to heat shield design.

### High Strength Porcelain

It is important to consider now the effect that density has upon practical designs. Since the dense materials have relatively high  $\rho k$  values, heat transfer considerations dictate that these materials be used in thin sections and insulated from the basic structure. Schematics of typical designs for small and large radii parts using the dense materials are shown in Fig. 2. Special attention must be given to the method of support to insure that the attachment is made at a reasonable temperature. In the case of the small radii parts, attachment is accomplished aft of the stagnation point where the heat rates are substantially lower than at the stagnation point. For the large radii parts, this approach is not possible and the attachment is made by extending ceramic legs from the hot face. In both the small and large radii designs, the ceramic part must have high strength since, with a limited number of supports, a mechanical failure is likely to be catastrophic.

The highly porous forms of ceramic (ceramic foams) have relatively low  $\rho k$  values, thus allowing the use of thick sections without a large weight penalty. The attachment to the substructure can then be made at a temperature substantially lower than the surface temperature. However, due to the low strength of the ceramic foam, a continuous attachment is more preferable than the concentrated attachment used with the dense ceramics. Since the attachment is continuous, a mechanical failure is less likely to be catastrophic. Examples of the construction of small and large radii parts using the ceramic foams are shown in Fig. 3.

Another important factor is that manufacturing techniques are markedly different for the dense and foamed forms of ceramic. The dense forms of the oxides and carbides are generally manufactured by

casting and sintering with little or no machining accomplished after the firing cycle. Thus, each dense part is essentially made-to-order and design changes can be costly both in time and expense. In contrast, the ceramic foams are made in slab form and shipped to the user where it can be easily shaped by machining; design changes can be incorporated at a nominal cost.

Two heat shield designs are considered with foamed ceramic; the full depth module where the attachment of the ceramic is made directly to the cooled substructure; and the partial depth module where the attachment of the ceramic is made at a high temperature point with additional insulation provided between this point and the cooled substructure.

For either type of design, the attachment concept used is:

- (1) Continuous or semi-continuous support to increase reliability if cracking of the ceramic should occur.
- (2) Flexibility, particularly in the direction normal to the attachment plane, to reduce thermal stresses which arise due to the large thermal gradient in the ceramic.

In general, the full-depth ceramic design is heavier and has higher thermal stresses, disadvantages which are somewhat offset by the problem of achieving a high temperature attachment to the ceramic in the partial depth ceramic design.

There are generally three basic problem areas in working with ceramic foams, (1) obtaining a high surface emissivity, (2) sealing the surface against hot gas flow (since these are open-celled foams), and (3) attaching the ceramic to the metallic support. The solutions to these problems for  $\text{SiO}_2$  and  $\text{SiC}$  are discussed below.

#### $\text{SiO}_2$

In the case of  $\text{SiO}_2$ , the surface sealing and high emissivity



coating were combined by adding iron oxide to a silica slip and slip casting a thin dense face onto the foam. The attachment of the ceramic to the metallic support was dependent upon the type of panel.

Full Depth Design Fig 4a - the attachment was made to the cooled aluminum substructure by bonding with a silicon rubber. The thickness of this rubber was established by requirements that it be thick enough to absorb thermal deformations but still thin enough that a large temperature drop would not occur through the bond. The temperature limit of the rubber bond at the ceramic to rubber interface was selected as 600°F.

Partial Depth Design Fig 4b - the operating temperature of the ceramic-to-metal joint was chosen as 2000°F. The metal honeycomb was slip cast in place allowing sufficient space between the material and the slip for expansion as the temperature increased. The attachment of the other face of the metal honeycomb to the cooled substructure was achieved by brazing. The honeycomb was filled with a fibrous insulation, e. g., Refrasil, to reduce radiative heat transfer between the ceramic and the cooled substructure.

#### SiC

For the SiC-ZrO<sub>2</sub> material, a ZrO<sub>2</sub> paste is used to seal the face against hot gas flow. Emissivity measurements of the face, as sealed with the ZrO<sub>2</sub> paste, indicated that an emissivity of 0.7 is obtained with this technique. Therefore, no attempt was made to raise this emissivity by addition of new materials to the surface coating. Attachment to the cooled substructure in the full depth design is accomplished with the same rubber bond as used with SiO<sub>2</sub>, however, the hot attachment for the partial depth design is achieved in a different manner.

Experiments with ceramic bonds and metal brazes as methods of achieving this high temperature bond resulted in the selection of brazing as the more practical method. The properties of the brazes used currently limit this type of attachment to a temperature of about 1500°F; however, it is not considered impossible, with the proper brazes, to raise this temperature limit to 2000°F.

Currently solutions to these same problems are being developed for the specific case of  $Al_2O_3$  and  $ZrO_2$  foam at The Martin Company under AF contract AF 33(616)-7497 Refs 12 and 13.

## Fabrication

Some of the methods of fabrication have been discussed above. Generally it may be stated that machining and fabrication of the ceramic foams has been studied and essentially solved. No major difficulties are expected in this area.

### c. Metallics

The metallic heat shields can be separated into two major types -- one the structural type in which the metal is at a high temperature and is used to react overall vehicle loads as well as local loads and two, the non-structural type in which the metal is at a high temperature and is used to react all or part of the local loads but does not react overall vehicle loads.

Since the APOLLO vehicles being studied are blunt bodies with the underlying structure being the environmentally controlled space cabin for the crew, the non-structural approach is obviously the best approach. Exceptions to this are the control flaps which may prove, upon detail analysis, to be most amenable to a structural radiation cooled type structure. Future discussion will be limited to the major surface areas of the APOLLO vehicle on which the non-structural type metal radiative shield will be studied.

Superalloys, such as L-605, are suitable for this application at temperatures up to a maximum of 2200°F while refractory metals, such as the  $\frac{1}{2}$ T; molybdenum alloy and the F-48 columbium alloy are suitable for much higher temperatures. The specific useful service temperature of any of the refractory metal alloys will depend almost entirely on the oxidation protection coating provided. The results of a literature survey are given in section 5b. To date, these seem to indicate a maximum service temperature

of about 2500 to 2600 F. No great detail on the characteristics of the various super alloys or refractory metal alloys is presented since, for this part of the APOLLO study, these characteristics will affect only the  $\Delta$  Wing discussed in section 2c. These metals are used for the outer panels of the heat shield. A comparative study was made of the weights per square foot of surface area for three structural configurations as a function of service temperature and external air load. This information is presented in section 5b.

The thermal analyses to be performed place greatest emphasis on the peak value of the insulation material to be used between the hot outer surface and the cooled cabin wall. For the range of temperatures of the super alloy heat shields, the most efficient insulation appears to be the A.D. Little vacuum packaged powder insulation originally developed for the Dyna-Soar. Ref. 15 presents data on this material which is summarized in section 5b. Thus ADL-17 insulation was used with all super alloy heat shield studies.

For the range of temperatures of the refractory metals ADL-17 cannot be used. The most efficient insulations appear to be the fibrous inorganic fibers such as Refrasil, Min-k, potassium titanate, etc. In using these materials it would be most economical to allow them to be evacuated as the vehicle left the atmosphere thus reducing the air conduction and convection modes of heat transfer during re-entry. The feasibility of such an approach requires detail study of the specific vehicle, method of heat shield support and trajectory. For all refractory metal heat shield studies the fibrous insulation selected was Refrasil. Very little effort was assigned to this study since oxidation protection seems to be a major problem especially when complicated by the unknown chemical reactions with the decomposed

ablators. In addition a brief study of overall heat shield weights indicated that minimum weights would be achieved with the super alloys plus additional ablators.

## 2. Analysis Methods

The external data inputs required to calculate heat shield weights consist of trajectory data (altitude, Mach No., cold wall stagnation heat rate input, angle of attack) and heating rate distribution around the body as a function of stagnation point heating and angle of attack. Since the angle of attack varies during the trajectory, the heat rate at some local spot is not a constant function of the stagnation point heating rate. In order to reduce the amount of effort required to study the heat shields for the many vehicles being compared in the first part of the APOLLO study, it was decided to assume that the aerodynamic heating at any point on the vehicle is a constant fraction of the stagnation point aerodynamic heating. This fraction was calculated by the following method.

$$f \equiv \left[ \frac{\dot{q}_w}{\dot{q}_{sw}} \right] = \frac{\int_0^{t_{max}} \left( \frac{\dot{q}_w}{\dot{q}_{sw}} \right) \dot{q}_{sw} dt}{\int_0^{t_{max}} \dot{q}_{sw} dt}$$

This was done for both undershoot and overshoot trajectories for both convective and radiative heating.

The heat shield analysis methods used consisted of computing both ablative and radiative heat shield weights separately and then using these data in a specified way to obtain composite heat shield weights. This approach was selected since it would have been impossible to study integrated

heat shields for several different vehicles, several different trajectories and at many locations on the vehicle.

## a. Ablative Analysis

The ablative analyses were performed on an IBM 709 structural heating program. The program applies a finite difference technique for the thermal balance based upon initial condition at each time increment.

Encompassed in the program are the practical types of surface boundary conditions, including the following: aerodynamic heating, solar radiation, surface re-radiation, bow shock radiation, and the transpiration cooling effect of the ablative gas. Internal thermal effects accounted for include: conduction, radiation, convection, and the thermal effect on internal equipment, whether it be electronic (heat generation), structure, or fuel tanks (variable weight).

The stagnation point heat transfer theories of Detra, Kemp, and Riddell, for continuum flow and Kemp and Riddell for free molecule flow are used in the program. The variation of heating around blunt nose bodies may be included. The program also provides for the calculation of heat transfer coefficients on flat plates at arbitrary angles of attack.

Bow shock radiative heating is calculated using the following equations as noted

$$q_r = 6110 R_N \sigma^{1.78} \left( \frac{V}{10^4} \right)^{12.5}$$

FOR  $V > 35,000$

$$q_r = 0.9 R_N \sigma^{1.78} \left( \frac{V}{10^4} \right)^{19.5}$$

FOR  $25,000 \geq V \geq 30,000$

$$q_r = 2040 R_N \sigma^{1.78} \left( \frac{V}{10^4} \right)^{12.5}$$

FOR  $30,000 > V$

$$q_r = \text{RADIATIVE HEAT RATE} \sim \frac{6110}{R_N} R$$

$\sigma = \text{DENSITY RATIO}$

$$R_N = \text{NOSE RADIUS} \sim \text{INCHES}$$

$V = \text{VELOCITY} \sim \text{FT/SEC}$

Inputs required for a typical problem.

1. The trajectory of the vehicle (i.e., velocity and altitude vs. time).
2. The nose radius of the body.
3. The position on the body to be analyzed.
4. The thermal properties of all materials employed.
  - a. Thermal conductivity vs. temperature.
  - b. Specific heat vs. temperature.
  - c. Density
  - d. For the ablating surface the following additional information must be provided: temperature at which the material ablates, heat of ablation, relative amount of ablated material that vaporizes, emissivity, heat of combustion, and boundary layer factor.
5. Heat generation vs. time for electronic equipment.
6. Weight vs. time for fuel tanks.

In general, the program is applicable to pure melting or subliming ablators but is not capable of handling a charring ablator. However, since this was the only program available it was utilized in the following manner.

The particular materials under study are nylon phenolic and a secondary material of glass phenolic. Both materials start to decompose about 1000 to 1500°F and form char type layers on the surface. The function of the char layer is to provide a high temperature insulation, forcing surface temperatures up and increasing the reradiation heat transfer component. Since in the present IBM program, the surface temperature is assumed to be

the decomposition temperature, the high reradiation term would be lost if the decomposition temperature were set at a realistic figure of 1000 - 1500°F.

The re-entry heating pulses of the APOLLO vehicles have high initial rise rates with equilibrium temperatures well over 1500°F. Also with a charring ablator, the surface temperature is a function of the char thickness. Since so little was known about the capability of these materials to retain char layers under the APOLLO re-entry conditions and because of the reradiation problem discussed above it was decided to set the melting temperature in the IBM program at 3000°F instead of 1000 - 1500°F in order to partially account for the high reradiation from the char layer. The properties assumed for the two materials studied are given in Table V. To allieviate this problem a char layer IBM program is being compiled (see section 5a).

Thick slabs were analyzed on the IBM for various  $\frac{h}{T}$  factors ( $\frac{h}{T}$  = ratio of local heat rate to stagnation point heat rate) for specific re-entry trajectories. From these analyses time histories were plotted of the weight of material ablated, the weight of material required to obtain attemperature of 1000°F and 200°F. Typical plots are shown in section 4. In addition these same weight figures were plotted versus  $\frac{h}{T}$  factor for the conditions at the end of the trajectory. The use of these curves is explained in section 2c.

#### b. Radiative Shield Analyses

The following method of analysis was used to minimize the weight of an insulated and cooled radiative heat shield. The method parallels quite closely the method of Swann (ref. 1) except that the square heating



pulse is replaced by a triangular pulse which seems to be more easily applied to the APOLLO re-entry trajectories.

The following assumptions have been made:

1. The  $Q$  vs. time curve that is to be used for the radiative shield is approximated by a right triangle shaped pulse, defined by

$$Q = Q_0 (1 - Bt) \quad (1)$$

where:

- $Q_0$  = the maximum value of the triangular distribution  
 $1/B$  = the time duration of the triangular dist.

This assumption is very adequate for the pulses under consideration, especially when an ablator is required to handle the large  $Q$  that occurs early in the actual  $Q$  vs.  $t$  distribution. When no ablator is to be used, the rapid rise rate occurring early in the trajectory still validates the assumption.

2. A steady state condition is assumed to occur throughout, the heated face being at the wall-equilibrium temperature and the back face being cooled to  $T_1$ .
3. Assume the product of the density times the thermal conductivity

is  $\rho k = \gamma + \alpha T^3$

where

$$\gamma, \alpha = \text{constants}$$

$$T = ^\circ K$$

4. A mean  $\rho$  is used, picked at a mean temperature defined by

$$T_m^2 = \frac{1}{2} (T_0^2 + T_1^2) \quad (T_0 + T_1) \quad (3)$$

where

$$T_0 = \left( \frac{q_{\text{cool}}}{\sigma \epsilon} \right)^{1/4}$$

$T_1$  = cooled back face temperature

Equation (3) has been obtained in a rigorous manner that is consistent with (1) and (2).

The total weight of the cooled radiative shield is the sum of the weight of the shield itself plus the weight of the cooling system considered on the basis of a unit area of shield. (This does not consider the weight of coatings, attachments, or any other items which are constant and hence should not be considered in the optimization).

$$W = \rho z + \frac{1}{L_{\text{eff}}} \int_0^z q_{\text{cool}} dt \quad (4)$$

where:

$\rho$  = density of shield material

$z$  = thickness of the shield

$L_{\text{eff}}$  = latent heat of cooling, including a factor for the system weight

$q_{\text{cool}}$  = the instantaneous rate of heat being conducted through the shield

Minimizing (4) with respect to the thickness,  $z$ , the following minimum weight formula results:

$$W_{\text{min}} = \left\{ \frac{1}{\sigma L_{\text{eff}}} \left[ \alpha \left( \frac{T_0^4}{2} - T_1^4 \right) + 4 \delta \left( \frac{1}{2} T_0 - T_1 \right) \right] \right\}^{1/2} \quad (5)$$

In proceeding from equation (4) to equation (5) it is observed that the minimum weight system is the one in which the weight of the shield is equal to the weight of the cooling system, or:

$$W_{\text{Shield}} = W_{\text{Cooling System}} = \frac{1}{2} W_{\text{Min.}} \quad (6)$$

The application of this equation to a specific trajectory requires knowledge of the heat rate history as a function of time. Having this for a given point on the vehicle, the time in the trajectory at which the equilibrium temperature was equal to the maximum operating temperature of the radiative heat shield material was determined. From this a triangular pulse was fitted to the remaining part of the trajectory and the minimum weight calculated. The properties of the radiative materials considered are shown in Table VI and Figures 5 and 6.

Using this method, it was possible to plot the minimum insulation and cooling weight for a given material and re-entry trajectory versus  $\frac{1}{t}$  factor. Examples are shown in section 4. Use of these curves are discussed in section 2c.

#### c. Composite Heat Shield Analysis

The approach used to calculate the weights of the composite heat shields was to utilize the data derived by the methods outlined in 2a and 2b above in a specific manner. Since the design criteria affects this approach, the design criteria are listed.

- a) A safety factor of 1.25 is applied to all aerodynamic heat rates to provide for the unknowns in calculating aerodynamic heat rates, material property variations, etc.

- b) Whenever an ablator is used over a radiator, sufficient ablative material is provided to insure that  $T_{eq} = (T_{max} \text{ of radiator } - 200^{\circ}\text{F})$  at the time the ablator is consumed.
- c) The radiator is designed for the latter portion of the trajectory starting at the time when  $T_{eq} = T_{max} \text{ of radiator}$ .

Also affecting the calculation of these composite heat shield weights are practical considerations. These practical engineering considerations require that a weight increment be charged to each type heat shield for various reasons listed below.

- a) A self insulative layer to maintain the bond between the ablator and the radiator at a temperature consistent with reasonable adhesive strengths. This temperature was chosen as  $1000^{\circ}\text{F}$ . For this reason a  $1000^{\circ}\text{F}$  curve appears on the ablative weight charts versus  $\frac{F}{B}$ . As can be seen this represents a considerable weight penalty per square foot. Examination of the method of calculating this self insulative layer reveals that it is derived from a thick slab IBM ablator analysis in which the  $T_{melt}$  has been selected as  $3000^{\circ}\text{F}$ . Therefore this represents a temperature drop of  $2000^{\circ}\text{F}$  through the self insulative layer. This is extremely conservative since the ablator chosen was nylon phenolic which, although it may have surface temperatures as high as, or in excess of  $3000^{\circ}\text{F}$ , has a pyrolysis temperature of  $1000$  to  $1500^{\circ}\text{F}$ . This means that the self insulative layer should only have to provide a drop of  $500^{\circ}\text{F}$  maximum. This, in conjunction with the confidence that development of a more efficient self insulation is feasible, led to the decision to use a weight increment of only 25% of the weight increment calculated by the thick slab IBM program. Currently effort on a better definition of this self insulative layer and the type bond to be applied is in progress.

b) Studies over the past several years in the design of porous ceramic heat shields have shown that weight must be added, to the theoretical optimum calculated, to provide for a ceramic coating, used to fill the exposed surfaces of the porous ceramic. This is applied to restrict flow of hot gases into the open celled porous ceramics. In addition the attachment of the ceramic to the substructure requires the use of a flexible, continuous type support, usually a high temperature silicone rubber for low temperature substructure or a brazing material for the high temperature support. Experience has shown that these items result in a weight increase of about 1 #/ft<sup>2</sup>. This number was used for all ceramic radiative shields.

c) Review of the work accomplished by Bell Aircraft and others in the design, fabrication and test of metal radiative heat shield of the double wall insulated and cooled approach have shown that considerations of the metal panel weight, the support clip weight etc., result in a weight penalty of about 1 #/ft<sup>2</sup>. This number was used in all superalloy metal heat shield studies.

d) Use of an active water cooling system on the internal support structure requires that allowance be made for the weight of the system hardware, such as tubes, valves, pumps, heat exchangers, trapped coolant etc. In this study an original cooling system factor ( $r_c$ ) of 1.75 was used. This is defined as:

$$r_c = \frac{\text{Weight of water and weight of cooling system}}{\text{Weight of water}}$$

Later studies by Farox (Part XII) for vehicles of the blunt lifting body shape, have yielded the curve of  $r_c$  versus maximum cooling rate shown in Fig. 7. For this reason the results of the radiative heat shield studies were adjusted to reflect this later data. This was

accomplished by multiplying the insulation and cooling weight by

$\sqrt{\frac{r_c}{1.75}}$  as suggested by the theoretical analyses which show that the weight of the insulation and cooling is proportional to the  $\sqrt{r_c}$ . A new  $r_c$  of 2.3 was chosen as representative.

Using the above discussed methods of analysis, design philosophy, and practical weight increments, the unit heat shield weight at any position on the vehicle was selected as follows.

- (1) Using the  $f$  factor  $\left(\frac{f}{f_c}\right)$  curves derived, select both undershoot and overshoot factors, namely  $f_o$  and  $f_u$ .
- (2) Using the criteria of  $q = \sigma \epsilon (T_{max} - 200)^4$ , select times,  $t_c$  and  $t_u$ , in the overshoot and undershoot trajectories at which the radiative shield becomes effective.
- (3) Multiply  $f_o$  and  $f_u$  by 1.25, then using  $1.25f_o$  and  $1.25f_u$  as calculated, plus  $t_o$  and  $t_u$  from (2) go to the curves of  $W_{abl}$ ,  $W_{abl}$  versus  $F$  versus time for 1000 overshoot and undershoot and read out  $W_{abl_o}$ ,  $W_{abl_o}$ ,  $W_{abl_u}$ ,  $W_{abl_u}$ .
- (4) Calculate the ablator and self insulator weight by
 
$$W_o = W_{abl_o} + \frac{1}{4} [W_{abl_o}^{1000} - W_{abl_o}]$$

$$W_u = W_{abl_u} + \frac{1}{4} [W_{abl_u}^{1000} - W_{abl_u}]$$
- (5) Again using  $1.25 f_o$  and  $1.25 f_u$  go to the curves of radiation weight versus  $f$  and select  $W_{RAD}$  and multiply by  $\sqrt{\frac{2.3}{1.75}}$
- (6) Using whichever ablative and self insulative weight is greater from (4), (either  $W_o$  or  $W_u$ ) calculate the total heat shield weight by

$$W_{TOTAL} = W_o \text{ (or } W_u) + W_{RAD} \sqrt{\frac{2.3}{1.75}} + \Delta W_{INC}$$

where the  $\Delta W_{INC}$  is discussed above.

As can be seen, the above procedure makes several assumptions. It reflects the heat flow on the ablator that has passed the 1000 °F line. This is unconservative. It assumes that the surface temperature is at the equilibrium temperature and neglects the heat required to bring the radiative heat shield up to steady state conditions. These are conservative assumptions. It also neglects the heat removal required to maintain steady state conditions as the surface temperature is forced to follow  $T_{eq}$ . This is conservative. Summing up the effects of all these conservative and unconservative assumptions in light of the long time heating history, it appears that any errors introduced should be small.

Secondly, in view of the fact that these figures are to be used only to calculate heat shield weights for the first phase of the Apollo study (vehicle comparison), their use seems justified.

### 3. APOLLO Vehicles Studied

Three APOLLO vehicle configurations have received significant heat shield effort to date; these being the M-1-1, the L-2C, and the W-1. Each of these vehicles is described below with remarks as to significant heat shield problem areas.

M-1-1 - A modified Eggers-Wong vehicle having a geometry midway between the M-1 and M-2 vehicles. Re-entry weight = 6400#,  
 Ref. area = 78.5 Ft<sup>2</sup>,  $C_{D@L/D_{max}} = 0.49$ ,  $(L/D)_{max} = 0.731$

- Problem areas:
1. Escape tower loads must be transmitted through heat shield in high heat rate region.
  2. Landing bag stowage in forward area requires incorporation of blow off heat shield, again in region of high heat rate.

3. Location of top forward parachute attachment point requires design of removable raser run along top of vehicle.
4. Hatch must be provided in back for entrance to mission module. Less severe problem since this is low heat rate region.
5. Basic heat shield is exposed to micrometeorites during entire 14-day mission.

I-2C - A modified Mercury shape - NASA design. Re-entry weight = 6000#, Ref. area = 129.5 ft<sup>2</sup>,  $C_{L@L/D_{max}} = 0.51$ ,  $(L/D)_{max} = 0.737$

- Problem areas:
1. Hatch for access to mission module goes through forward heat shield area. Sealing plus structural integrity poses severe problem.
  2. Attachment to the boost vehicle is accomplished at critical heating region.
  3. Using landing bags in forward area will cause support structure for the heat shield to be heavy and will complicate internal cooling system.

L-1: A flat-bottomed vehicle - NASA design. Re-entry weight = 6000#, Ref. area = 92.6 ft<sup>2</sup>,  $C_{D@L/D_{max}} = 0.845$ ,  $(L/D)_{max} = 0.615$

Problem areas: roughly the same as the M-1-1 except that a planned side by side arrangement with the mission module will require a hatch through a high heat rate region for access to the mission module.

General comment on all vehicles:

1. Heating on control flaps not well known either in magnitude



of this history (One third turn) measurement on the N-1  
measured a value for the clay of 1.5 g/g and a possible shock  
for content of the clay.

2. For clay distribution across vehicles, particularly on back  
side, not well defined.

## L. Final Heat Shield Computations

The detail weight calculations derived for three vehicles are discussed in this section. The vehicles studied were the M-1-1, the L-2c and the W-1 for two reentry trajectories, namely the positive  $CL_{max}$  overshoot and the 60 nautical mile (vacuum perigee corridor width) undershoot.

As stated previously the heat shield configuration under study is composed of an ablator laminated over a radiative heat shield which is insulated and cooled. Porous ceramics and superalloy metals were considered for the radiative heat shield. The properties of these materials are given in Table VI. In light of the tentative results discussed in 4-a only a super alloy or structural insulation sub-structure was assumed for the bulk of these studies. Also, as discussed in 1c, no specific studies were made of the control flaps in each vehicle, rather the thermal protection required as the flaps was taken as 50 per cent of the stagnation point heat shield weight.

### a. General Study of various type composite heat shields

Early in the study a comparison was made of a glass phenolic ablator laminated on top of either a porous ceramic or a metallic shield. Since foamed zirconia had the lowest  $k$  value and the highest temperature potential of the foamed ceramics, it was chosen as the ceramic. The super alloy shield utilized the ADL-17 vacuum powder insulation. Both shields were water cooled at the attachment to the primary pressure shell.

The basic data used is shown in fig. 8, 9, and 10 for the glass phenolic and in fig. 11 and 12 for the zirconia and super alloy shields. The composite heat shield weights were calculated by the methods described in section 2. These calculations are shown in Table VII and VIII. These calculations reveal several facts.

(1) The ablator plus super alloy and ADL-17 composite shield weighs considerably less than the ablator plus foamed zirconia composite shield.

(2) In the case of the super alloy and ADL-17 composite shield, the heat rate at which the radiation shield becomes effective is so low that ablation has ceased at that time.

Based on these conclusions no further studies were made of porous ceramics composite heat shield weights and the calculations for the super alloy composite heat shield weights were simplified by eliminating the step of calculating  $t_o$  and  $t_u$ , using instead the single curve of total weight ablated for any  $F$ .

b. Calculation of final composite heat shield weights.

Using the integrated heat rate distributions shown in Figure 13 thru 17, the nylon phenolic ablator weights shown in figure 18 thru 21, and the super alloy plus ADL insulation and cooling weights shown in fig. 11, 12, 22, 23 composite heat shield weights were calculated for the M-1-1, L-2c and the W-1 vehicles as shown in Table IX thru XI. The M-1-1 ablative and radiative weights versus  $F$  were used for the W-1. It should be noted that these are minimum heat shield weights along certain specific center lines, usually vertical and horizontal. These figures are then used by the weight group to calculate the overall heat shield weight of each vehicle taking into account specific problem areas on each vehicle.

In addition Tables XII and XIII show the calculated cooling rates as derived from the analysis procedure presented in section 2c. These figures are subject to certain limitations but certainly can be used as representative of the maximum cooling rates which can be encountered. These figures were used in the study of the cooling system presented in Part III.

c. Study of Nose Section of M-1-1 and W-1

On the M-1-1 (and W-1) vehicles, review of the overall vehicle design approach led to the conclusion that it would be very desirable to be able to obtain access to the nose section by removal of the entire nose heat shield and support structure. Equipment is located in the nose section to pull the center of gravity of the vehicle forward. Since this section was to be removeable the question of whether this section had to be cooled arose. Therefore a study was made of the weight of a cooled versus uncooled nose. This study showed that the heat rate is sufficiently high at the stagnation point that a small weight penalty of only  $0.6 \text{ \#/ft}^2$  is required to eliminate the cooling. This is shown in Fig. 24. Since this is only a small section of the vehicle in terms of surface area, this weight penalty does not seem excessive.

d. Evaluation of Heat Shield Concept Proposed

One factor noted from the results of the above calculations was that for the insulated and cooled superalloy shields the weight of the insulation and cooling is about the same as the weight increment added for the metal hardware. Also several reservations about use of an ablator on top of metal radiative shields have been uncovered in considering the actual usage of this type of heat shield.

(1) This concept accepts the fact that a fairly large piece of undecomposed resin will fly off downstream as the bond temperature reaches the critical temperature. This "flying" hardware could damage aft portions of the vehicle such as the control flaps.

(2) In addition, these pieces will probably not be removed uniformly and may seriously affect the aerodynamics of the vehicle if a significant portion should leave a critical area prior to other areas.

For these reasons it has been decided to study a "structural insulation" approach whereby a material such as glass phenolic is used in place of the metal radiative shield. This should allow a phenolic to phenolic bond with the ablator which should raise the temperature limit at that location to almost the pyrolyzation temperature. It is accepted that this will not be as efficient an insulator as the ADL-17 and will result in an increase in the insulation and cooling weight. Offsetting factors justifying this increase in insulation weight are

- (1) A more structurally practical design results.
- (2) The self insulative layer on the ablator can be eliminated
- (3) The metal hardware weight increment can be partially eliminated (only partially since obviously this type heat shield will also be found to have some practical weight increments)
- (4) The higher cooling rates resulting should lower the cooling system factor  $r_c$ .

Currently effort is progressing on evaluation of various reinforced phenolic materials in different geometric combinations to serve as structural insulation. The strengths of these non-metallics at high temperatures is being studied as well as their insulative properties.

111

References:

1. "Composite Thermal Protection System for Manned Reentry Vehicles" by Robert T. Swann - presented at ARS 15<sup>th</sup> Annual Meeting, 5-8 December 1960
2. "Basic Chemistry of Silicon Carbide," The Martin Company, ER 10640-14.
3. Handbook of Chemistry and Physics, Chemical Rubber Publishing Company, 39<sup>th</sup> Edition, 1958.
4. "Development of Non-Oxidic Refractory Foams," (Final Report), The Carborundum Company, (AF 33(616)-6294), April 1960.
5. High Temperature Technology, John Wiley and Sons, Inc., New York, 1956.
6. Letter from Great Lakes Carbon Corp., dated 1 September 1960.
7. The Reactor Handbook, Vol. 3, Section 1, USAEC, March 1955.
8. Quarterly Progress Reports on AF 33(616)-6034--"Investigation of Feasibility of Utilizing Available Heat Resistant Materials for Hypersonic Leading Edge Applications."
9. Progress Reports on AF 33(616)-5542--"Development and Evaluation of Materials for High Temperature Applications."
10. Quarterly Progress Reports on AF 33(616)-5930--"Refractory Inorganic Materials for Structural Applications."
11. Progress Reports on AF 33(616)-6294--"Development of Non-Oxidic Refractory Foams."

14. "Manned Lunar Vehicle System", The Martin Company ER 11245M
  15. "Manufacturing Methods for Insulated and Cooled Double Wall Structure" Bell Aerosystems Company
- AF TR 7-799 (II) - Oct. 1960

TABLE I

## Properties Of Fiber Reinforcements For Organic Resins

Reinforcing Material	Density g/cc	Thermal Conductivity Btu-in/hr-ft <sup>2</sup> -°F	Specific Heat Btu/lb - °F
Asbestos	2.5	---	0.27
Glass	2.2	6.7	0.20
Graphite	1.8	900	0.20
Nylon	1.15	1.7	0.40

TABLE II

## Char Properties Of Ablators

Material	Initial Density g/cc	Char Density g/cc	Char Porosity %
Asbestos-Phenolic	1.50	1.31	46
Glass-Phenolic	1.83	1.36	32
Silica-Phenolic	1.64	1.65	27
Nylon-Phenolic	1.17	0.47	72



TABLE III

Comparison of Internal & Backwall Temperature Rise  
In Reinforced Plastics Tested By CML

Heating Time 600 sec

(500 sec Low Flux Heating  
100 sec High Flux Heating)

Total Heat Input - 10,000 Btu/ft<sup>2</sup>

Thermocouple Reading at End of Heating Period

Material	Location of Thermocouple Below Stagnation Point			
	0.166"	0.333"	0.500"	1.000" (Back Wall)
Nylon-Phenolic	Burned Out	797 °F	183 °F	111 °F
Asbestos-Phenolic	1843 °F	355 °F (Internal Delamination)	256 °F	154 °F
Glass-Phenolic	Burned Out	1172 °F	341 °F	265
Refrasil-Phenolic	2079 °F	970 °F	265 °F	150 °F

TABLE IV

Material	Limiting Temperature (°F)	Available	State of Development	Reproducibility Quality Control	Cost of Material Specimen	Chemical Stability	Oxidation Resistance	Mechanical Properties	Thermal Properties	Density gm/cc
1 SiC foam	3100 no coat- ing, 4000 with coating	Yes	2*		\$25 per 4-1/2 x 2-1/2 x 9		4**	Fair	Good	0.25-0.3
2 SiC dense (NT)	3100 no coat- ing, 4000 with coating	Yes	1		\$50 per 1 x 1 x 3 in.		4	Good	Fair	3.1 (dense 3.22)
3 ZrO <sub>2</sub> foam (Zircos)	Over 4000	?	4		~\$80 per 6 x 6 x 1-1/2	Stable in both oxidizing and reducing atm.	1	?	?	1.4 (pos- sibly 0.5)
4 Al <sub>2</sub> O <sub>3</sub> foam (Iperin)	~3300	Yes	3		\$5 per 4-1/2 x 2-1/2 x 9		1	Good	Good	0.5
5 SiC-ZrO <sub>2</sub> foam	~3300	Yes	3		\$60 per 4-1/2 x 2-1/2 x 9		2	Good	Good	0.5
6 Pyro graphite	Over 4000	?	2 N/A problems depend on de- sign		High cost		Approximately 1/10 of Graphite	Good	Good	1.8 to 2.3
7 Graphite	Over 4000	Yes	1		?		No coat avail for our req.	Good	Good	1.7
8 ZrO <sub>2</sub> -Mo, SiC-TiC-graphite, Amorphous C (AMP system)	Over 4000	?	5		~\$140 per 1/2 in. x 1 in. spec		?	Good	Fair	Approx- imately 1.7
9 ZrO <sub>2</sub> -Mo TiB <sub>2</sub> -TiC Amorphous C (AMP system)	Over 4000	?	5		Approximately same as 8		?	?	?	Approx- imately 1.7
10 MoSi <sub>2</sub> -Zr B <sub>2</sub> hot pressed	Approximately 4000° F	?	4		\$175 per 1 x 1 x 3	Slowly con- verts to ZrO <sub>2</sub> and SiO <sub>2</sub>	3	?	?	6.0
11 MoSi <sub>2</sub> -Zr B <sub>2</sub> coating	Approximately 4000° F	Yes	4		Development	Stable in oxidizing and reducing atm volatilized by water 1850° C	1	?	?	0.3-0.4
12 HfO foam	Over 4000	?	6			Same as 10	3	?	?	5-5.5
13 HfO dense	Over 4000	Yes	1		\$152-195 per 6 x 6 x 1-1/2 in.	Same as 12	1	Good	Fair	2-2.9
14 ZrO <sub>2</sub> dense	Over 4000	Yes	1				1	Good	Fair	4.5
15 Al <sub>2</sub> O <sub>3</sub> dense	~3300	Yes	1		\$50 per 1-1/2 x 6 in. rod		1	Good	Fair	3.7
16 SiO <sub>2</sub> dense	~3100° F	YES	1		?	PHASE CHANGE OVER 2000° F	1	Good	Good	2.1

1. Does not oxidize  
2. Acceptable rate  
3. May be acceptable  
4. Not acceptable

1. Fully developed  
2. Fairly well developed, subject to change  
3. Large pieces have been made, little  
improvement  
4. Small pieces only have been made  
5. Not been produced, considered practical  
6. Designing, but not yet produced

17 SiO <sub>2</sub> foam	~3100° F	YES	2		\$30 per 11 in x 4 x 3 in	PHASE CHANGE OVER 2000° F	1	Fair	Good	1.5
--------------------------	----------	-----	---	--	------------------------------	------------------------------	---	------	------	-----

TABLE V  
PROPERTIES OF MATERIALS EMPLOYED FOR  
APOLLO HEAT SHIELD STUDY

<u>Material</u>	<u>Phenolic Refraisil</u>	<u>Phenolic Nylon</u>
K, Btu/hr/ft/F	0.14	0.144
C <sub>p</sub> , Btu/lb/F	0.38	0.45
$\rho$ , lb/ft <sup>3</sup>	112	76
Emissivity	0.8	0.8
Heat of ablation, Btu/lb	1000	1500
Temp. of ablation, F	3000	3000
Ratio of vaporized material to total ablated material	0.3	0.6
$\beta$ =	0.5	0.5

$$\beta = a \frac{M_{\text{vapor}}^b}{(M_{\text{air}})^b}$$

$a = 2/3 \quad b = 1/4 \text{ for laminar}$   
 $a = 1/3 \quad b = 1/4 \text{ for turbulent}$

TABLE VI

Material	Max Service Temperature	$\rho \left( \frac{\text{lb}}{\text{cu ft}} \right)$	$k \left( \frac{\text{BTU ft}}{\text{sq ft-hr-}^\circ \text{F}} \right)$ @ ½ max service temp.
ZrO <sub>2</sub> foam	4000°F	50	.106
SiCZrO <sub>2</sub> foam	3500°F	33	.169
Al <sub>2</sub> O <sub>3</sub> foam	3300°F	33	.238
SiO <sub>2</sub> foam	2600°F	33	.102
Refrasil	2800°F	6	.114
ADL 17	2200°F	12	.0152



M-1-1 VEHICLE  
GLASS PHENOMIC - VIRGINIA SHIELD

[illegible]

# TABLE VIII

13 Feb 61

ENG. REP. NO.

**PAGE**

1-1-1

## NIGHT BREAKDOWN

Horizontal

Vertical  $\Phi$

Harriet

[illegible]

TABLE IX

Table IV

**06 0501**

121

L-2C

WEIGHT BREAKDOWN

$r_c = 2.30$

VERTICAL  $\Delta$

S/R <sub>0</sub>	W <sub>ABL</sub>	W <sub>SA</sub>	W <sub>INS</sub>	W <sub>COOL</sub>	W <sub>TOTM</sub>	S/R <sub>0</sub>	W <sub>ABL</sub>	W <sub>SA</sub>	W <sub>INS</sub>	W <sub>COOL</sub>	W <sub>TOTHL</sub>
-1.2	—	1.0	.23	.23	1.46	0	1.48	—	.50	.50	2.48
-1.0	.42	1.0	.27	.28	1.97	.2	1.43	—	.50	.50	2.43
-.8	.43	1.0	.26	.26	2.00	.4	1.38	—	.50	.50	2.38
-.6	.43	1.0	.26	.26	2.00	.6	1.33	—	.50	.50	2.33
-.4	.50	1.0	.25	.25	2.00	.7	1.52	—	.50	.50	2.52
-.2	.80	1.0	.25	.25	2.30	.8	2.24	—	.50	.50	3.24
0	1.48	—	.50	.50	2.48	.9	2.95	—	.50	.50	3.95
.2	1.54	—	.50	.50	2.54	1.0	2.24	—	.50	.50	3.24
.4	2.56	—	.50	.50	3.56	1.1	.47	1.0	.26	.26	1.99
.6	4.01	—	.50	.50	5.01	1.2	.24	1.0	.29	.29	1.82
.8	5.51	—	.50	.50	6.51	1.3	.13	1.0	.29	.29	1.69
.95	9.68	—	.50	.50	10.68	2.14	—	1.0	.23	.23	1.46
1.0	9.47	—	.50	.50	10.47						
1.1	6.34	—	.50	.50	7.34						
1.2	4.08	—	.50	.50	5.08						
1.4	.15	1.0	.30	.30	1.75						
1.6	.15	1.0	.30	.30	1.75						
1.7	.15	1.0	.30	.30	1.75						
1.8	.13	1.0	.31	.31	1.75						
2.0	.13	1.0	.31	.31	1.75						
2.2	.11	1.0	.32	.32	1.75						

TABLE X

IV



W-1  
WEIGHT BREAKDOWN  
K<sub>2</sub> = 2.30

S/D	W <sub>HAL</sub>	W <sub>SA</sub>	W <sub>INS</sub>	W <sub>COOL</sub>	W <sub>TOTAL</sub>	%	W <sub>ADL</sub>	W <sub>SA</sub>	W <sub>INS</sub>	W <sub>COOL</sub>	W <sub>TOTAL</sub>	POINT AROUND GIRTH AT 45° FROM VERTICAL
-1.4	0.3	1.0	.35	.35	2.0							
-0.4	0.3	1.0	.35	.35	2.0							
-0.2	2.8	—	.50	.50	3.8							
-0.1	8.0	—	.50	.50	9.0							
0	12.0	—	.50	.50	13.0							
0.1	14.9	—	.50	.50	15.9							
0.2	12.3	1.0	.17	.17	13.6							
0.3	10.9	1.0	.17	.17	12.2							
0.4	7.3	1.0	.17	.17	9.1		0.4	13.8	.17	.17	15.1	
0.6	3.4	1.0	.17	.17	4.7		0.6	9.5	.17	.17	10.8	
1.0	1.6	1.0	.17	.17	2.9		1.0	4.5	.17	.17	5.8	
1.6	1.0	1.0	.23	.23	2.4		1.6	2.8	.17	.17	4.1	
0	12.0	—	.50	.50	13.0							
0.1	10.4	—	.50	.50	11.4							
0.2	7.1	—	.50	.50	8.1							
0.3	2.0	—	.50	.50	3.0							
0.4	.4	1.0	.35	.35	2.1							
0.8	.3	1.0	.35	.35	2.0							
1.5	.3	1.0	.35	.35	2.0							

TABLE XI

V<sub>2</sub>

## TABLE XI.

A-1-1

<u>Alumina</u>					
$t = P.S. \times \frac{2}{\sqrt{g}}$	Ablation Ends	Shield Design Starts	$\Delta t$ Triangle	Secs	Secs
.1	0 sec.	0 sec.	780 sec.	2.09 $\frac{870}{\text{ft-sec}}$	1.26 $\frac{870}{\text{ft-sec}}$
.2	0	0	780	2.56	1.66
.3	0	0	780	3.02	1.85
.5	195	140	740	3.57	2.44
.7	300	230	650		
.9	385	315	610		
1.0	420	350	590		
1.25	480	425	535		

<u>Superalloy</u>					
.1	215 sec.	140 sec.	745 sec.	.36 $\frac{870}{\text{ft-sec}}$	.23 $\frac{870}{\text{ft-sec}}$
.3	575	475	495	.47	.31
.5	780	735	225	.82	.54
.7	830	780	180		
.9	855	805	155		
1.0	865	815	145		
1.25	850	840	130		

TABLE XIII

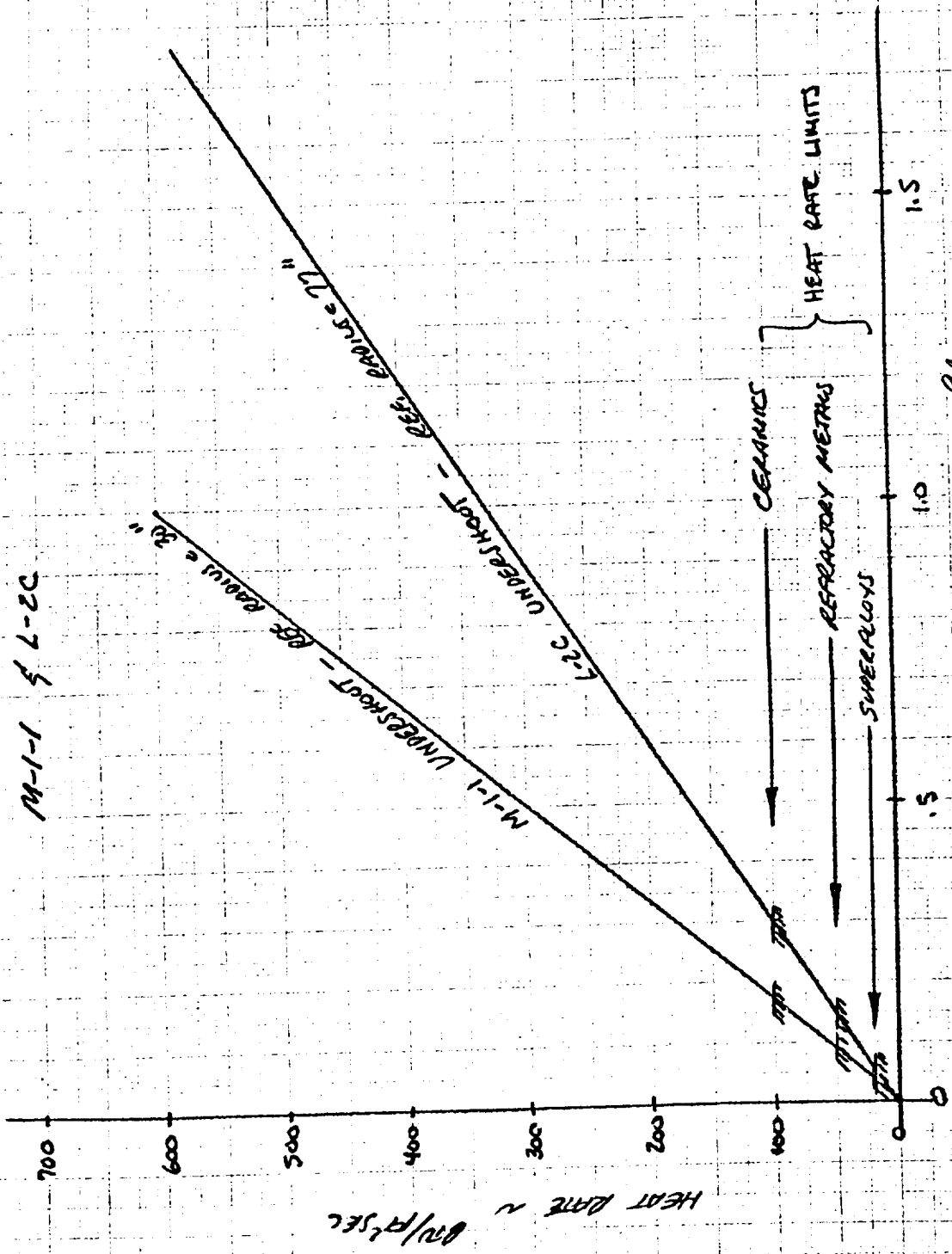
L-2C

<u>Zirconia</u>						
$f = F.S. \times \frac{S_2}{S_1}$	Ablation Ends	Shield Design Starts	$\Delta t$ Triangle	$\frac{Q_{cool}}{t_{00}}$	$\frac{Q_{cool}}{t_0} \frac{\Delta t}{2}$	
.1	0 sec.	0 sec.	670 sec.	1.73 $\frac{BTU}{ft^2 sec}$	1.26 $\frac{BTU}{ft^2 sec}$	
.3	0	0	670	2.56	1.65	
.5	0	0	670	3.08	1.91	
.6	0	0	670	3.36	1.96	
.7	115	0	670	3.55	2.13	
.9	180	115	600	↓	↓	
1.0	220	150	580	↓	↓	
1.25	285	220	490	↓	↓	

<u>Superalloy</u>					
.1	0 sec.	0 sec.	670 sec.	.36 $\frac{BTU}{ft^2 sec}$	.24 $\frac{BTU}{ft^2 sec}$
.2	240	150	580	.48	.32
.3	360	280	500	.50	.33
.5	480	420	440	.54	.36
.7	590	490	400	.58	.39
.9	690	575	330	.67	.45
1.25	750	700	225	.80	.55

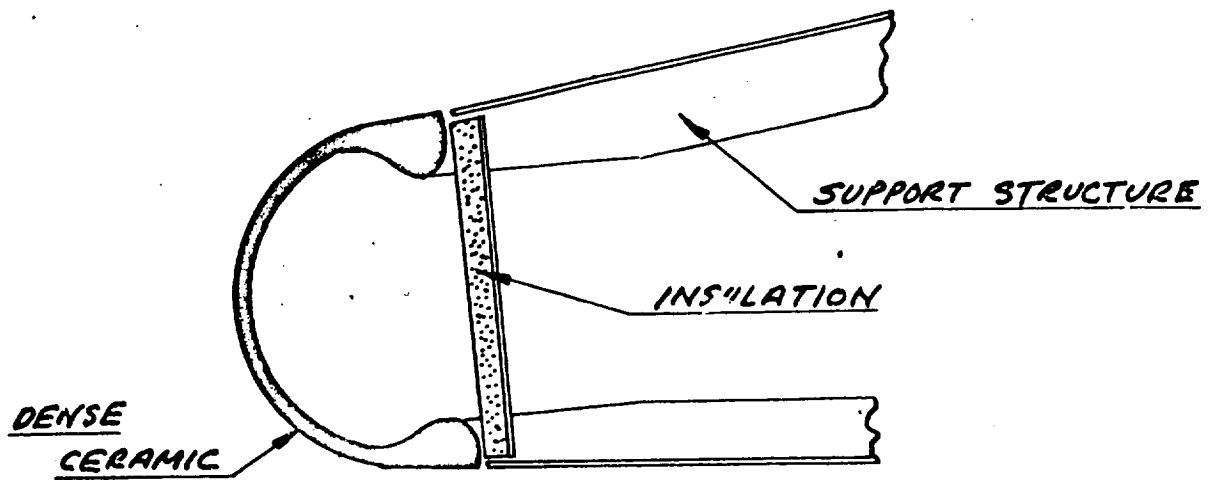
# HEAT RATE VERSUS LOCAL f FACTOR

M-1-1 § L-2C

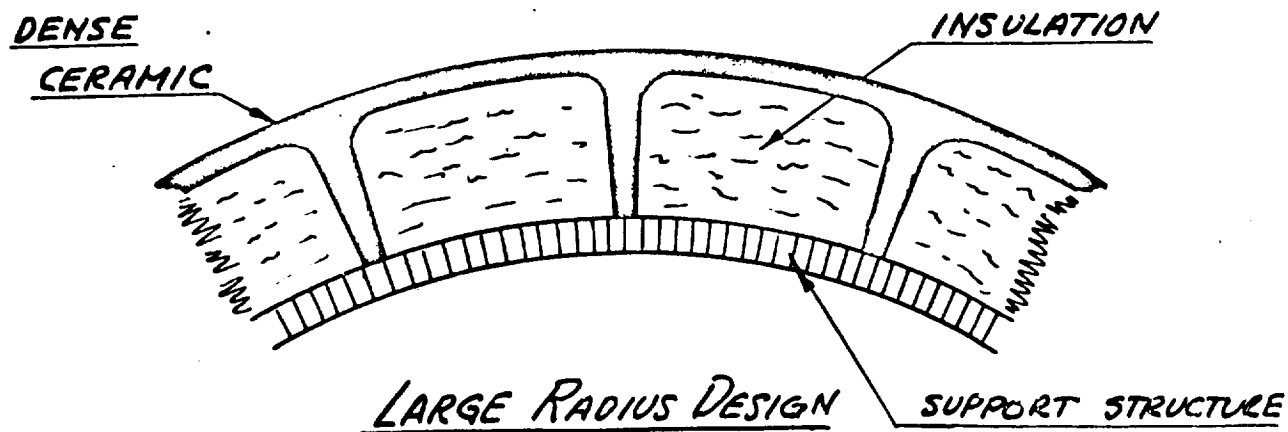


LIMIT f FACTOR =  $\frac{91}{91}$  BASED ON REF. RADIUS

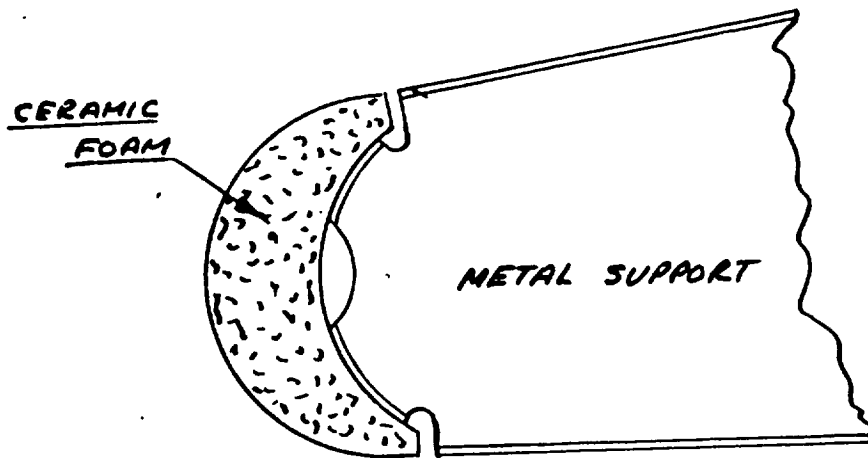
Fig 1



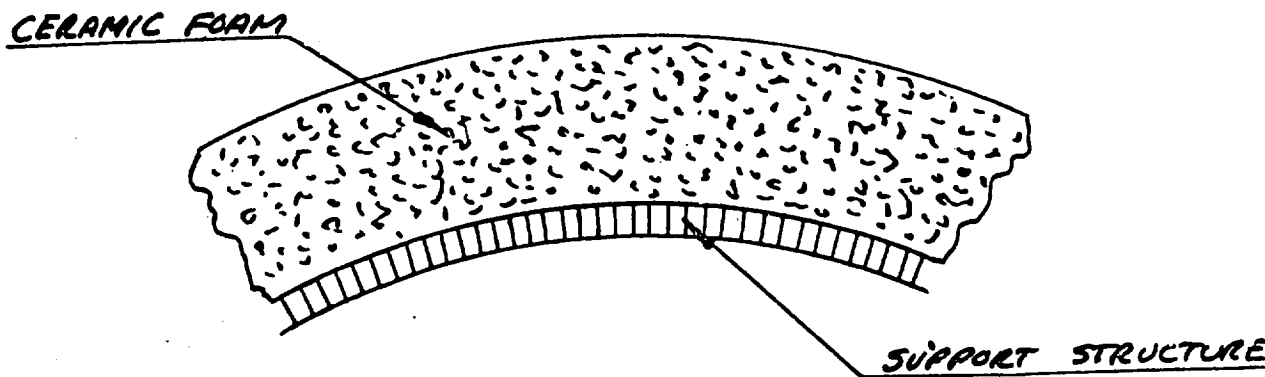
SMALL RADIUS DESIGN



<sup>2</sup>  
FIG. # SCHEMATIC OF DENSE CERAMIC RADIATIVE SHIELDS

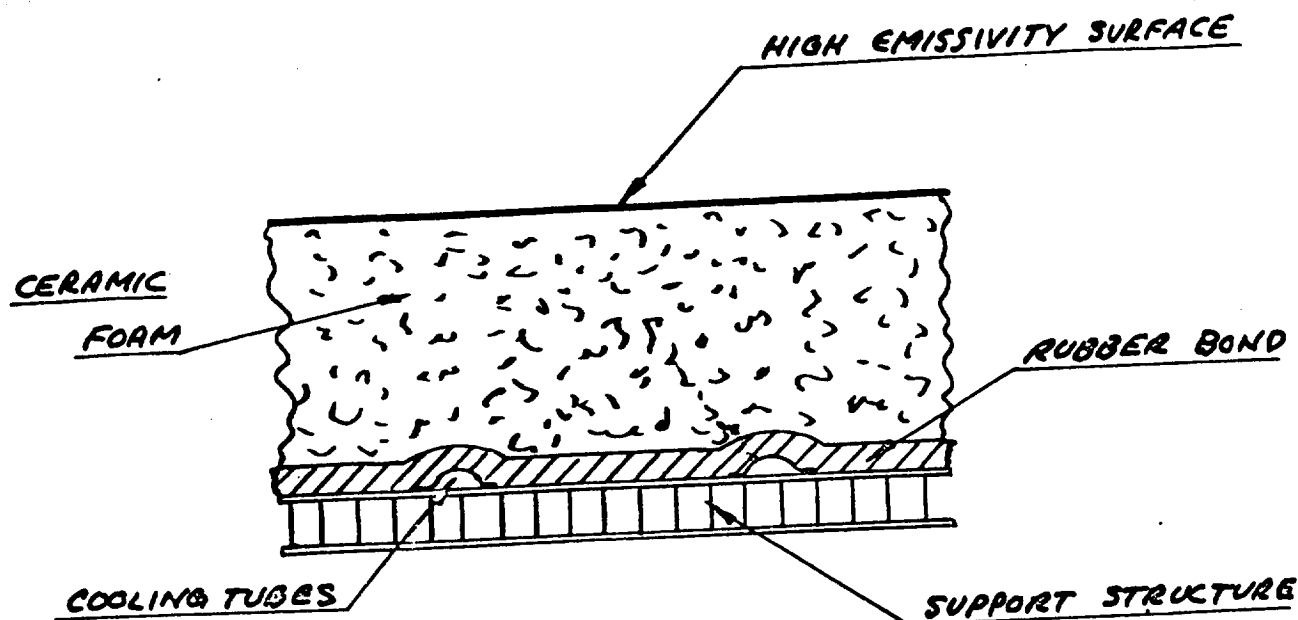


SMALL RADIUS DESIGN

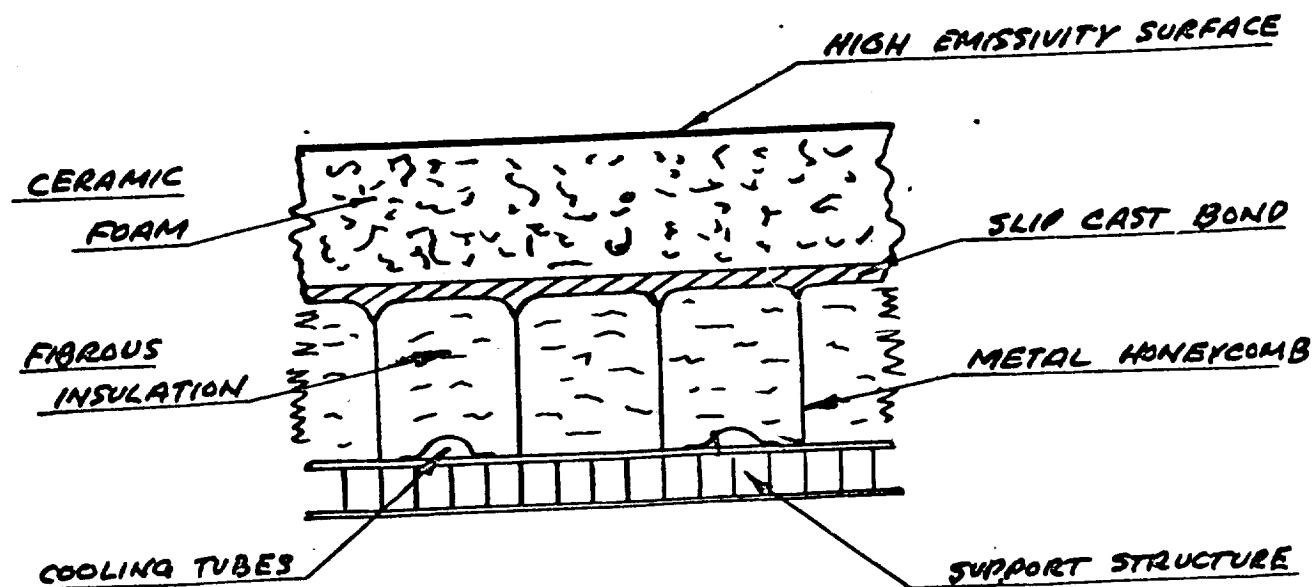


LARGE RADIUS DESIGN

3  
FIG. 3 SCHEMATIC OF CERAMIC FOAM RADIATIVE SHIELDS



a. FULL DEPTH DESIGN



b. PARTIAL DEPTH DESIGN

4  
FIG. 6 FULL AND PARTIAL DEPTH DESIGNS

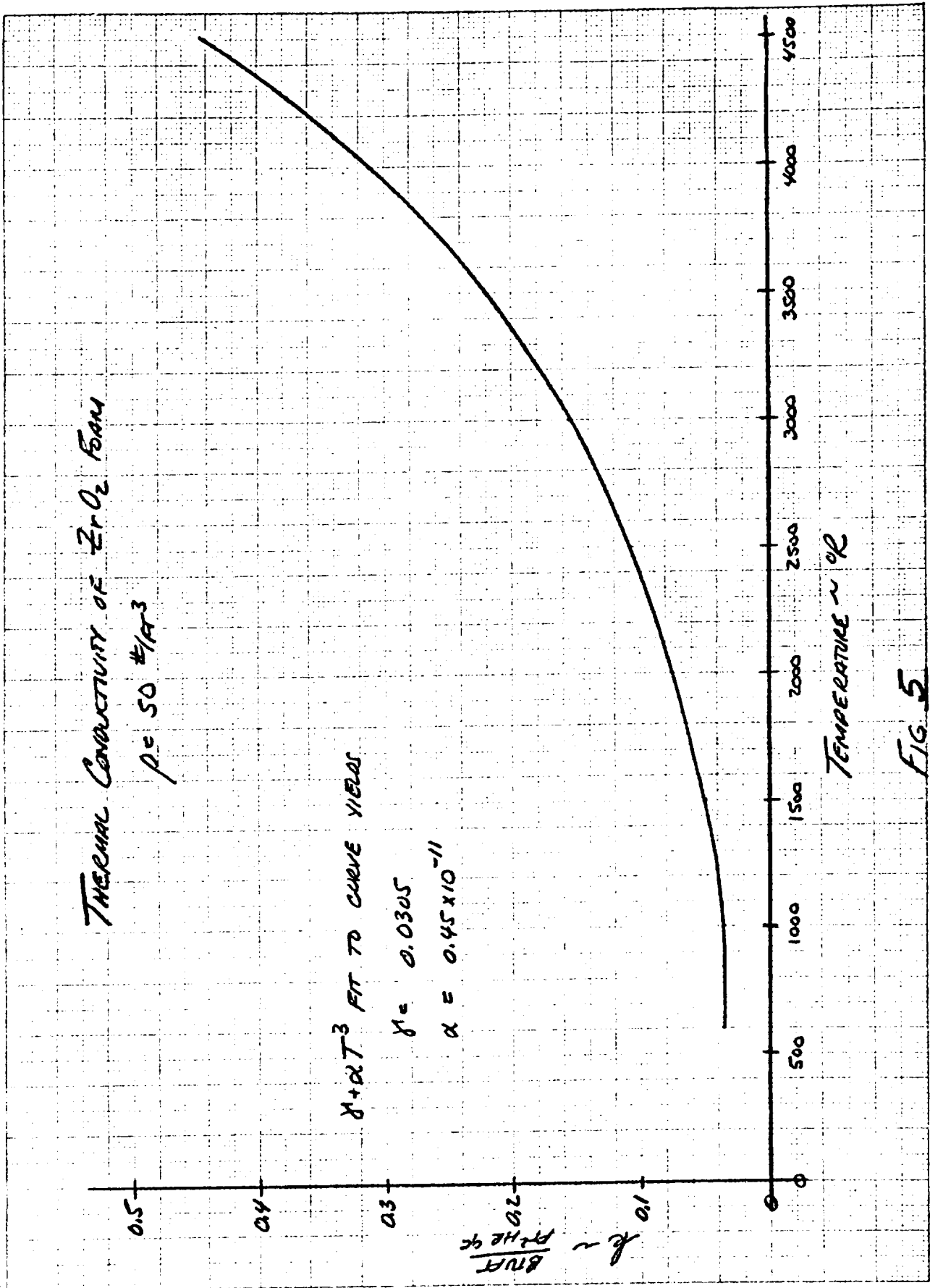


FIG. 5



# Thermal Conductivity of ADL-17

$\rho = 12 \text{ #/ft}^3$ ,  $P = 100 \text{ mm Hg}$

$\gamma + \alpha T^3 \text{ FIT YIELDS}$

$\gamma = 0.0112$

$\alpha = 0.135 \times 10^{-11}$

$k = \frac{BTU}{ft^2 hr ft}$

0.220

0.020

0.018

0.016

0.014

0.012

0.010

500

1000

1500

2000

2500

TEMPERATURE  $^{\circ}R$

Fig. 6

# PRELIMINARY COOLING SYSTEM FACTOR

M-1-1 VEHICLE

ACTIVE TIME = 700 SECONDS

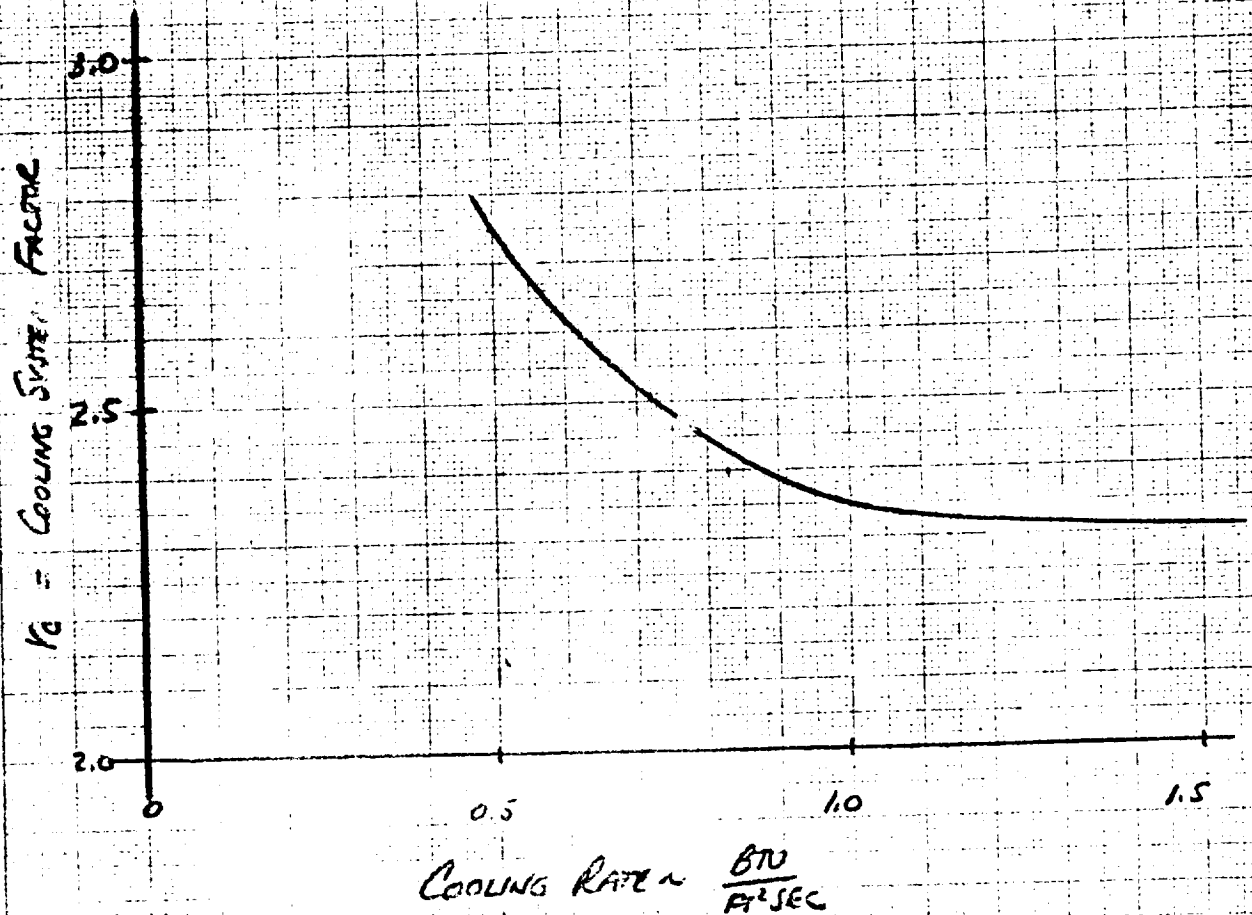
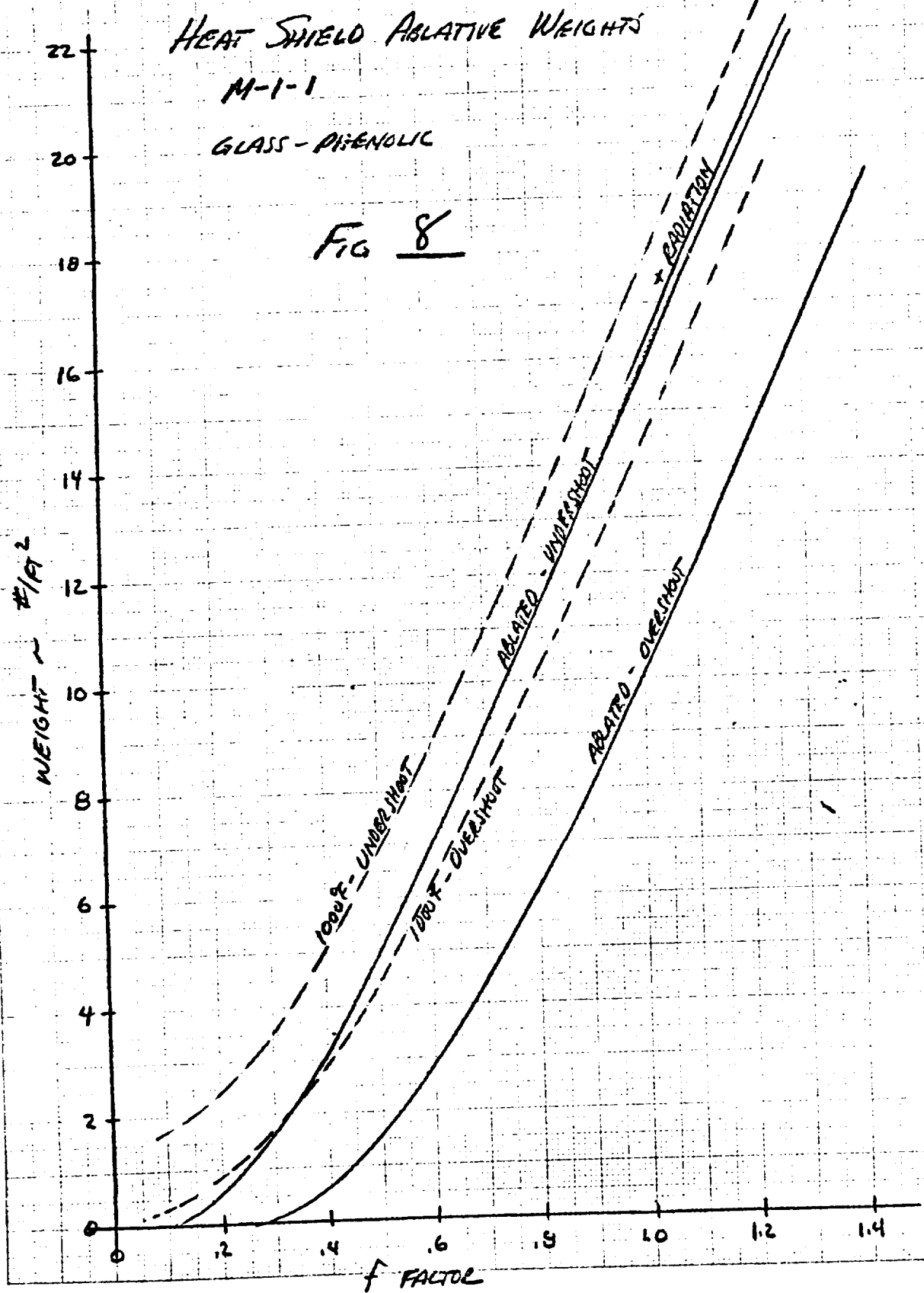


FIG 1



1000°F for  $f_c = 1.25$

RELATIVE WEIGHT FOR M-1-1

OVERSHOOT - RIGIDNESS Phenolic  
(NO RADIATION)

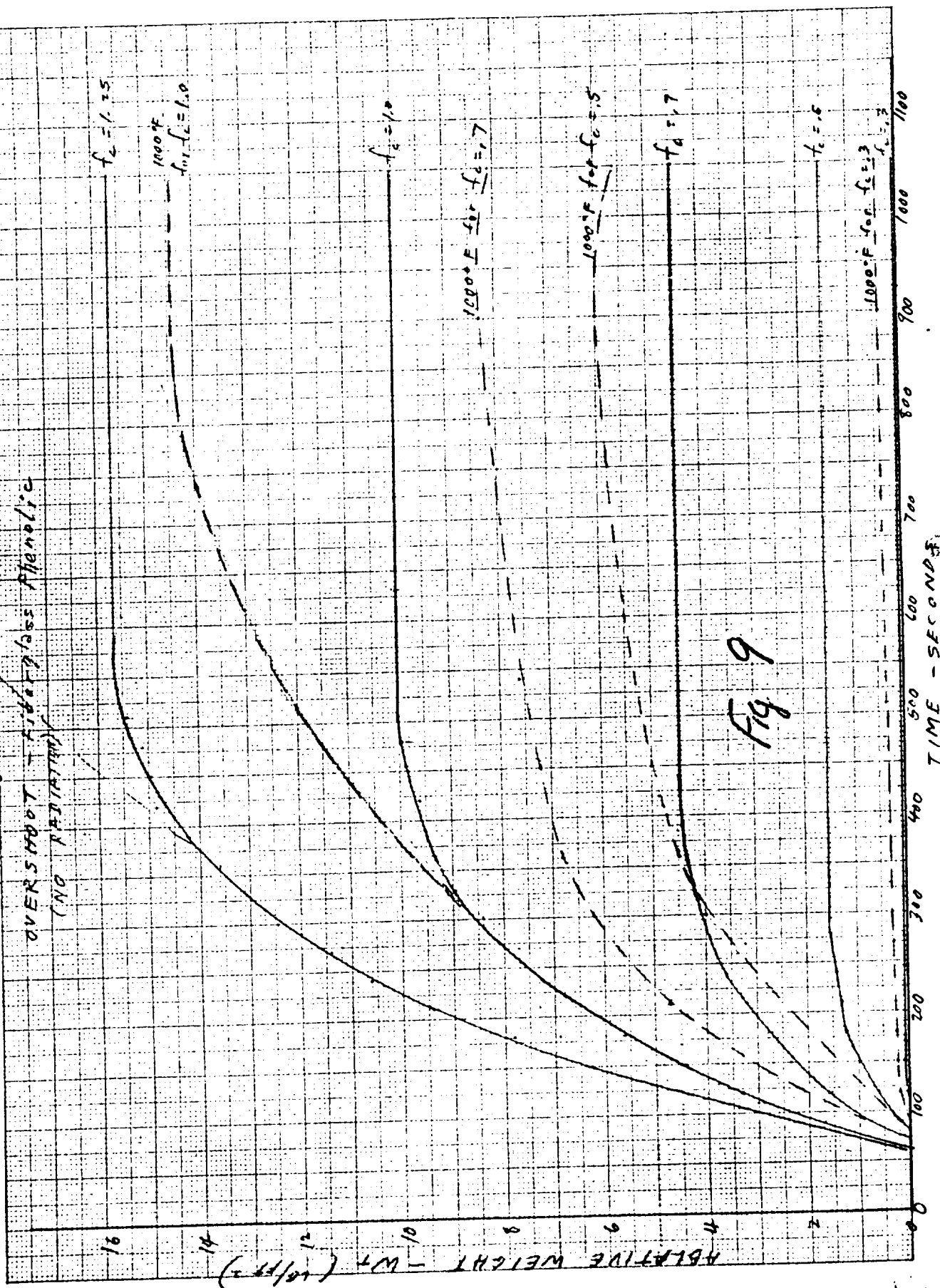
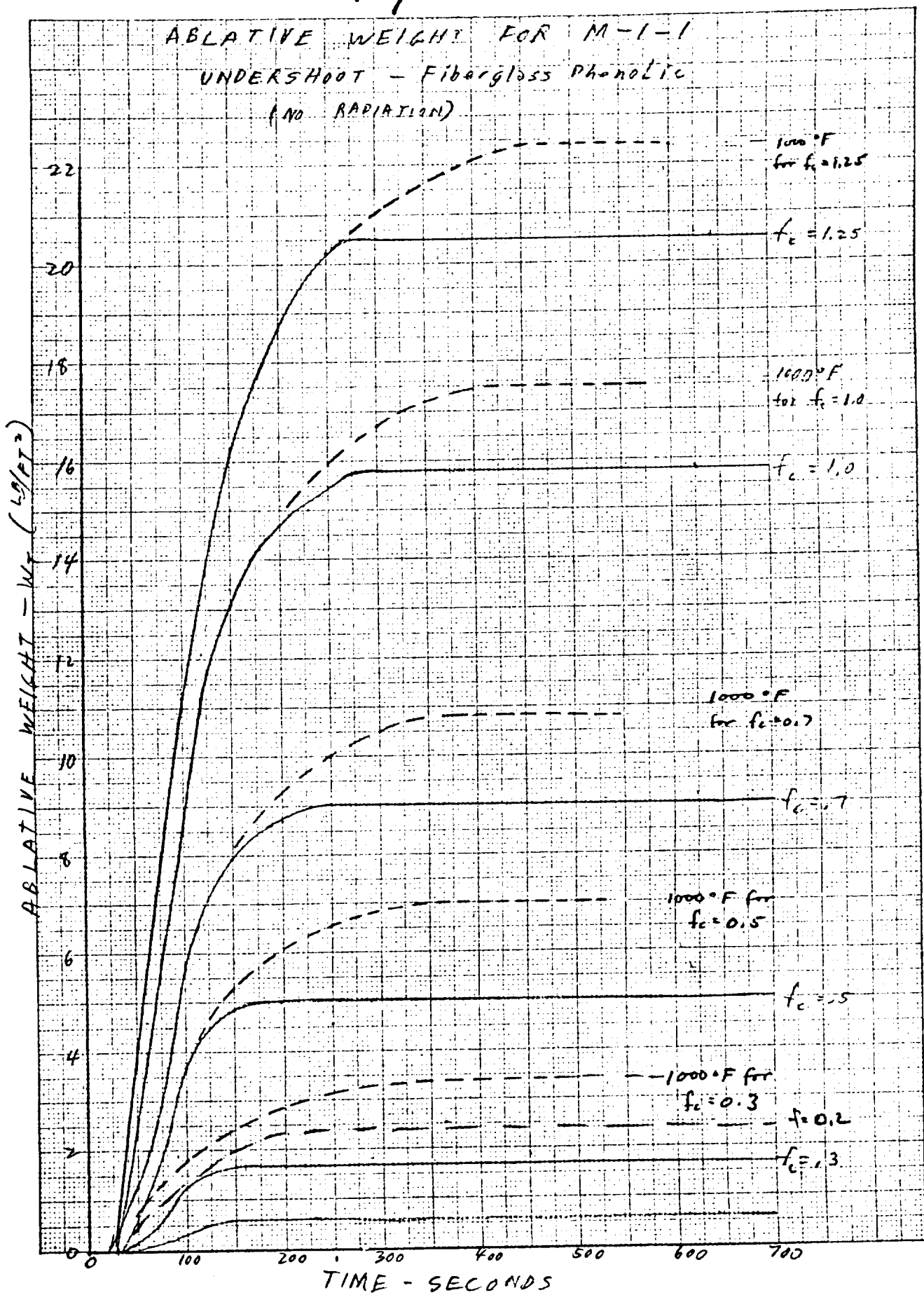


Fig 9

# Fig 10



M-1-1 HEAT SHIELD WEIGHTS

ZrO<sub>2</sub> FOAM CERAMIC

OVERSHOOT TRAJECTORY

$\tau_c = 1.75$

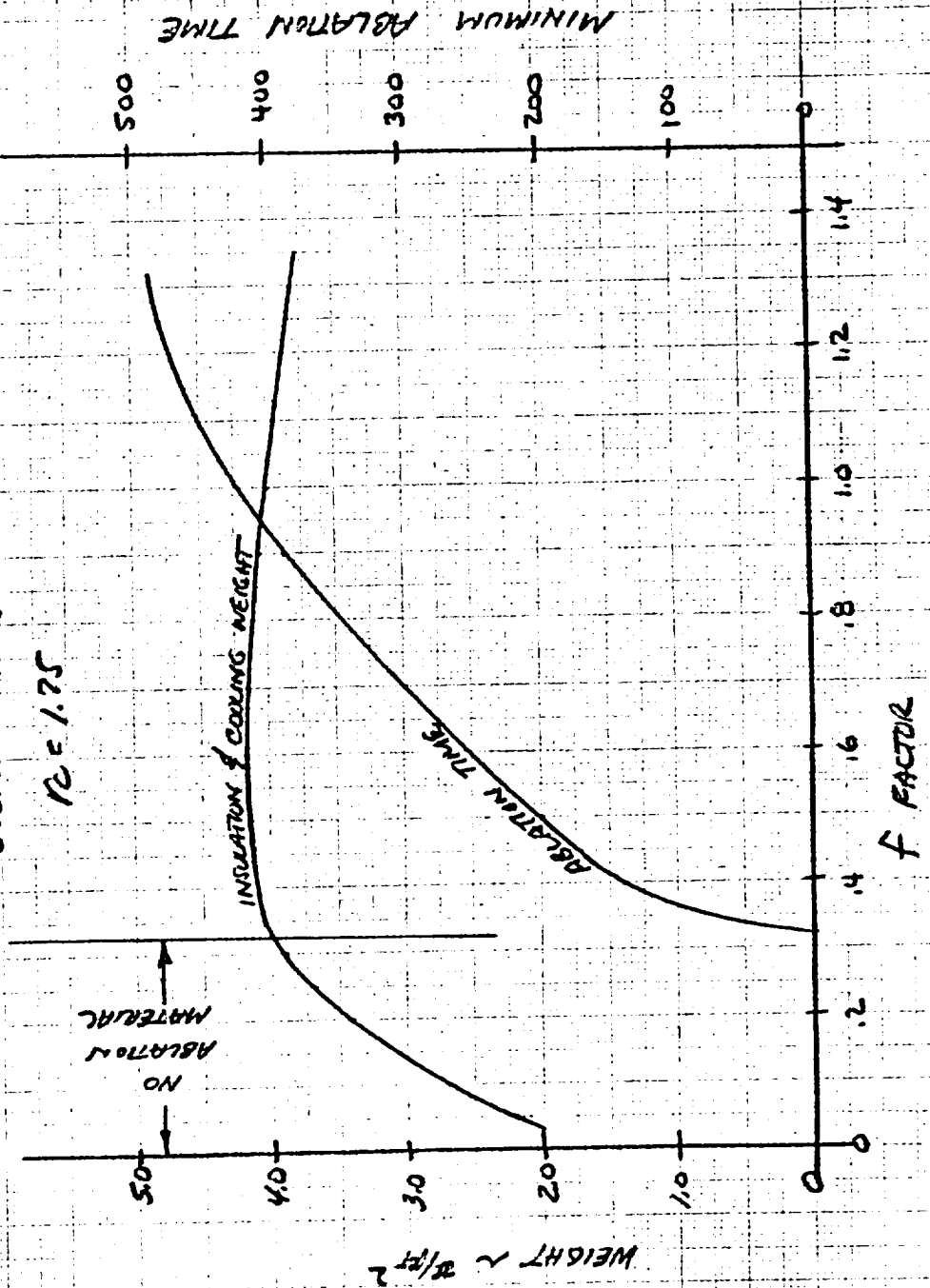


Fig 11

M-1-1 HEAT SHIELD WEIGHTS

SUPERALLOY + AOL-17

OVERSHOOT TRAJECTORY

$\gamma_c = 1.75$

MINIMUM ABLATION TIME ~ SECONDS

1000  
500  
0

1.4  
1.2  
1.0  
.8  
.6  
.4  
.2  
0

ABLATION TIME

INSULATION AND COOLING WEIGHT

WEIGHT DURING ABLATION

NO ABLATION

WEIGHT ~  $\frac{W}{\text{lb}}$

10  
5.0  
0

f factor

FIG 12

# M-1-1 HEAT DISTRIBUTIONS

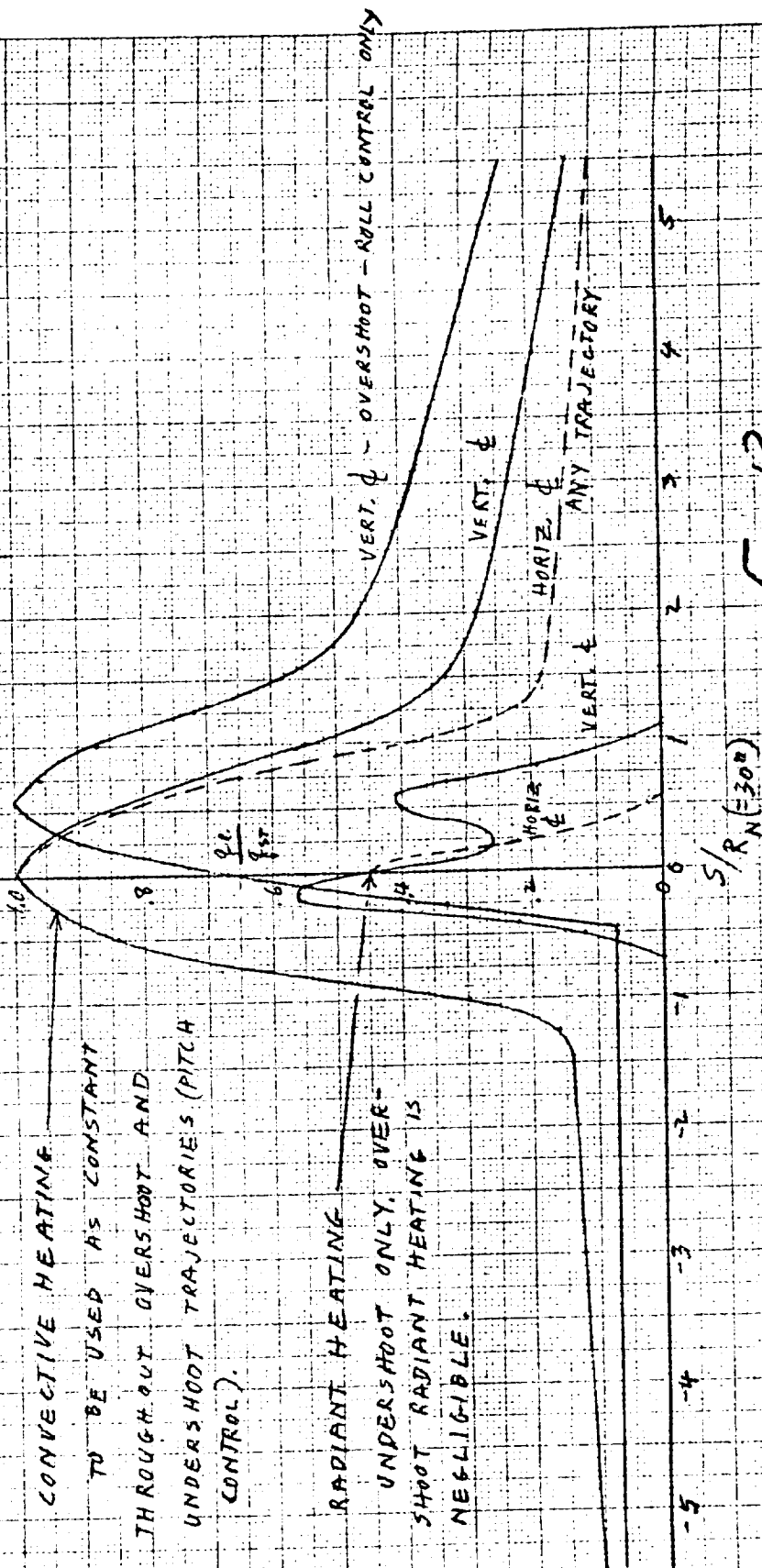
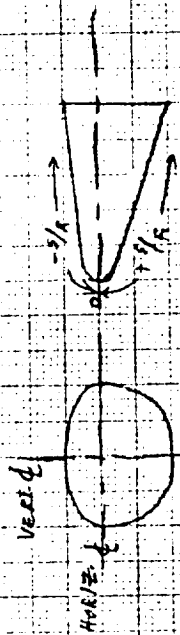
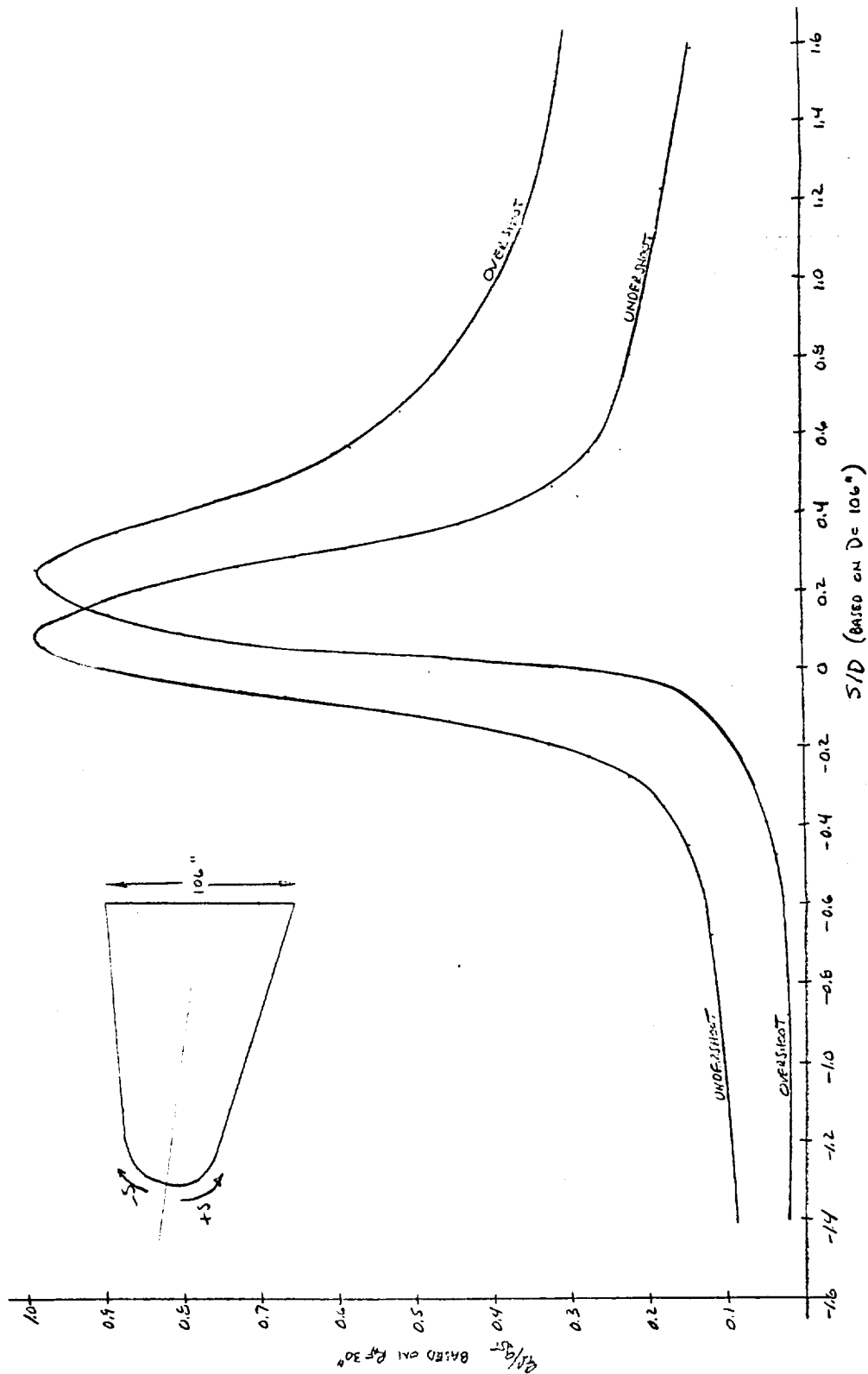


Fig 13





# PRELIMINARY HEAT SITUATIONS FOR THE W-1 VEHICLE



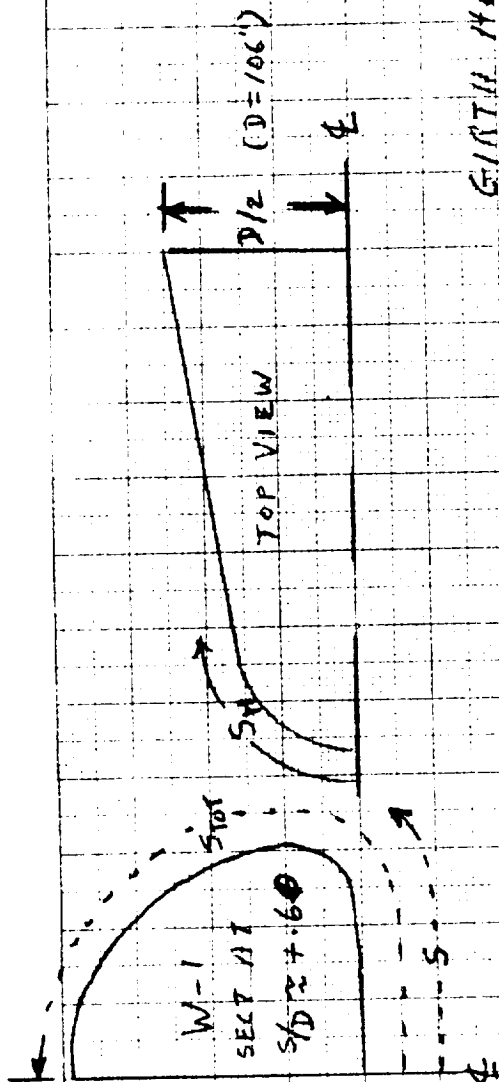
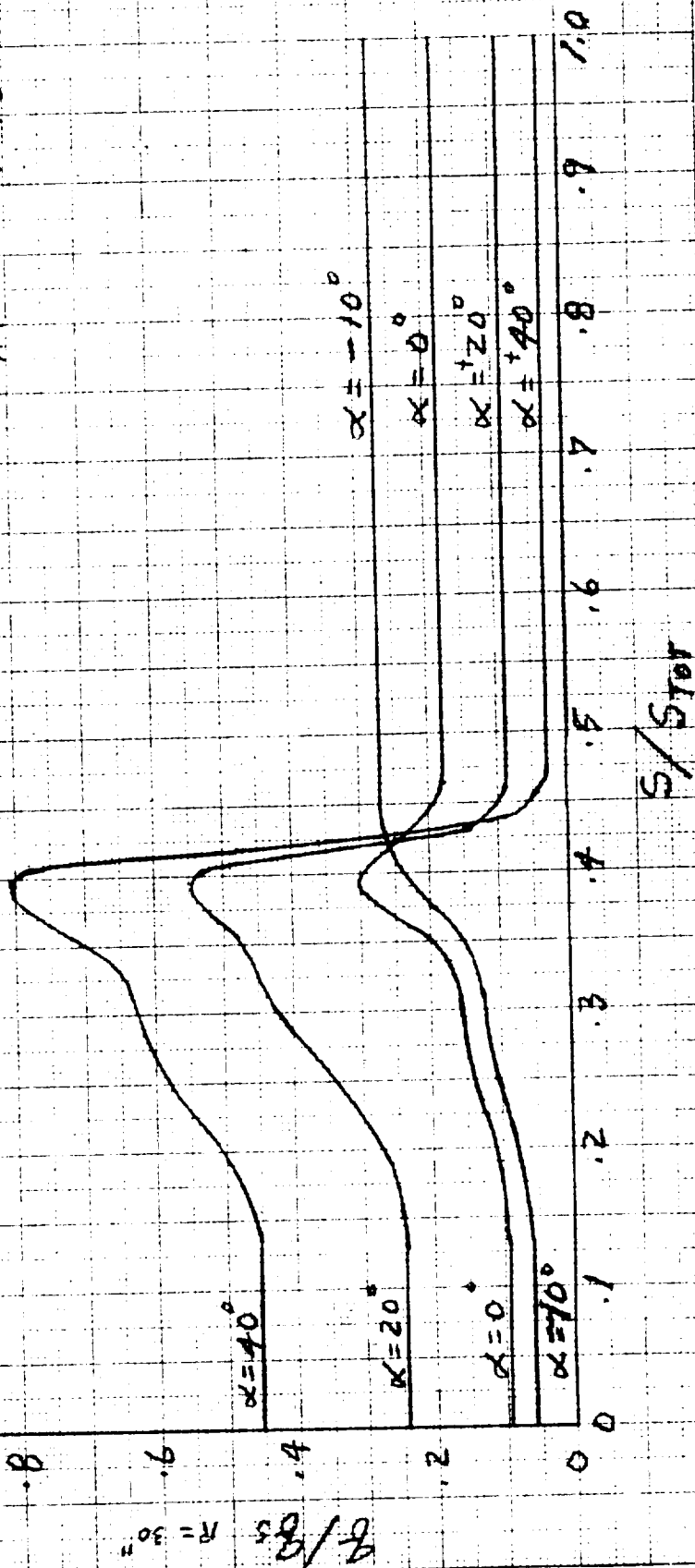


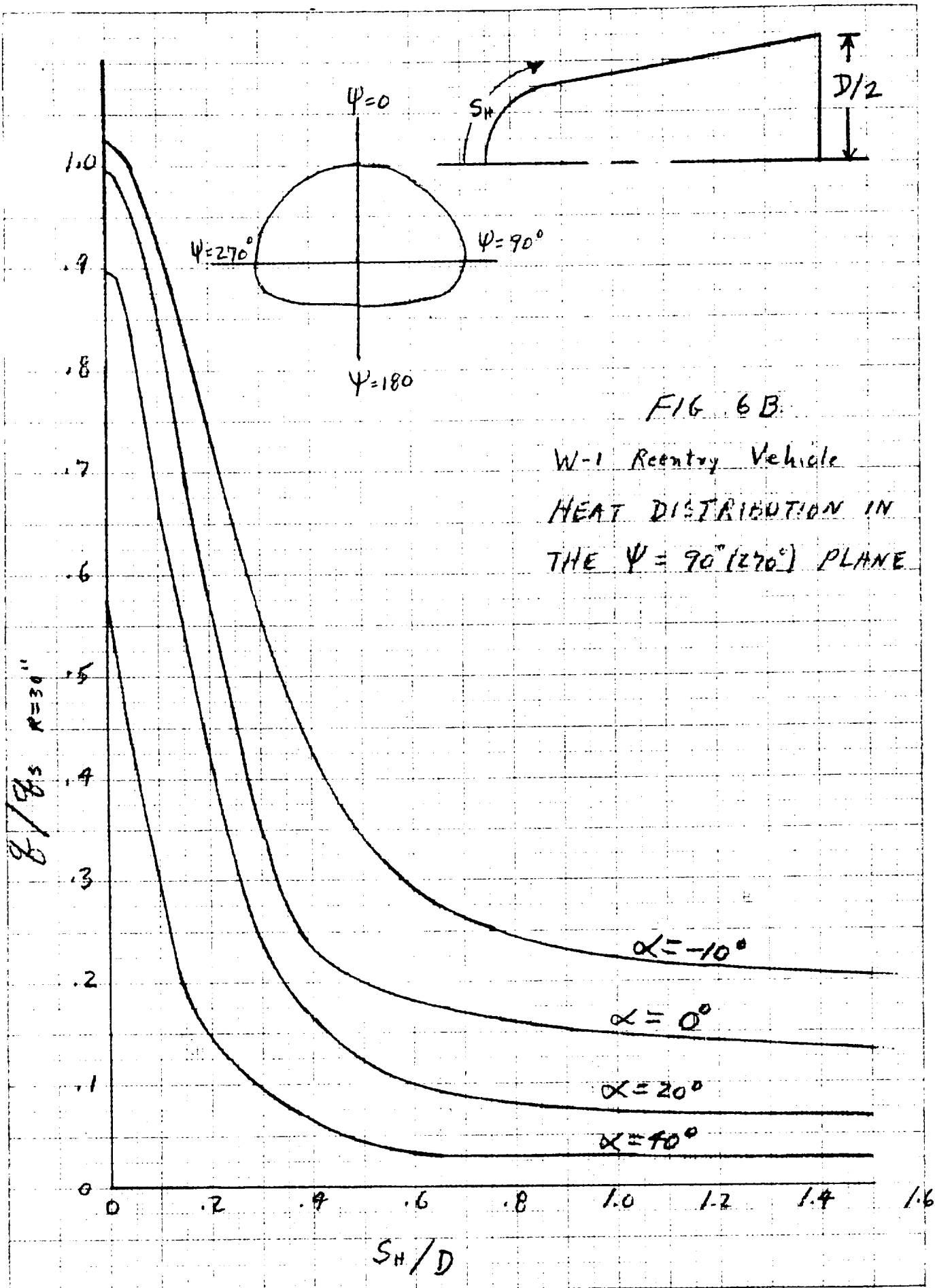
FIG. 6A

GIRTH HEAT DISTRIBUTION

W-1 REENTRY VEHICLE

AT STA: S/D  $\approx 0.6$





M-1-1

ABLATIVE WEIGHTS, OVERSHOOT,  
NYLON PHENOLIC

Fig 18

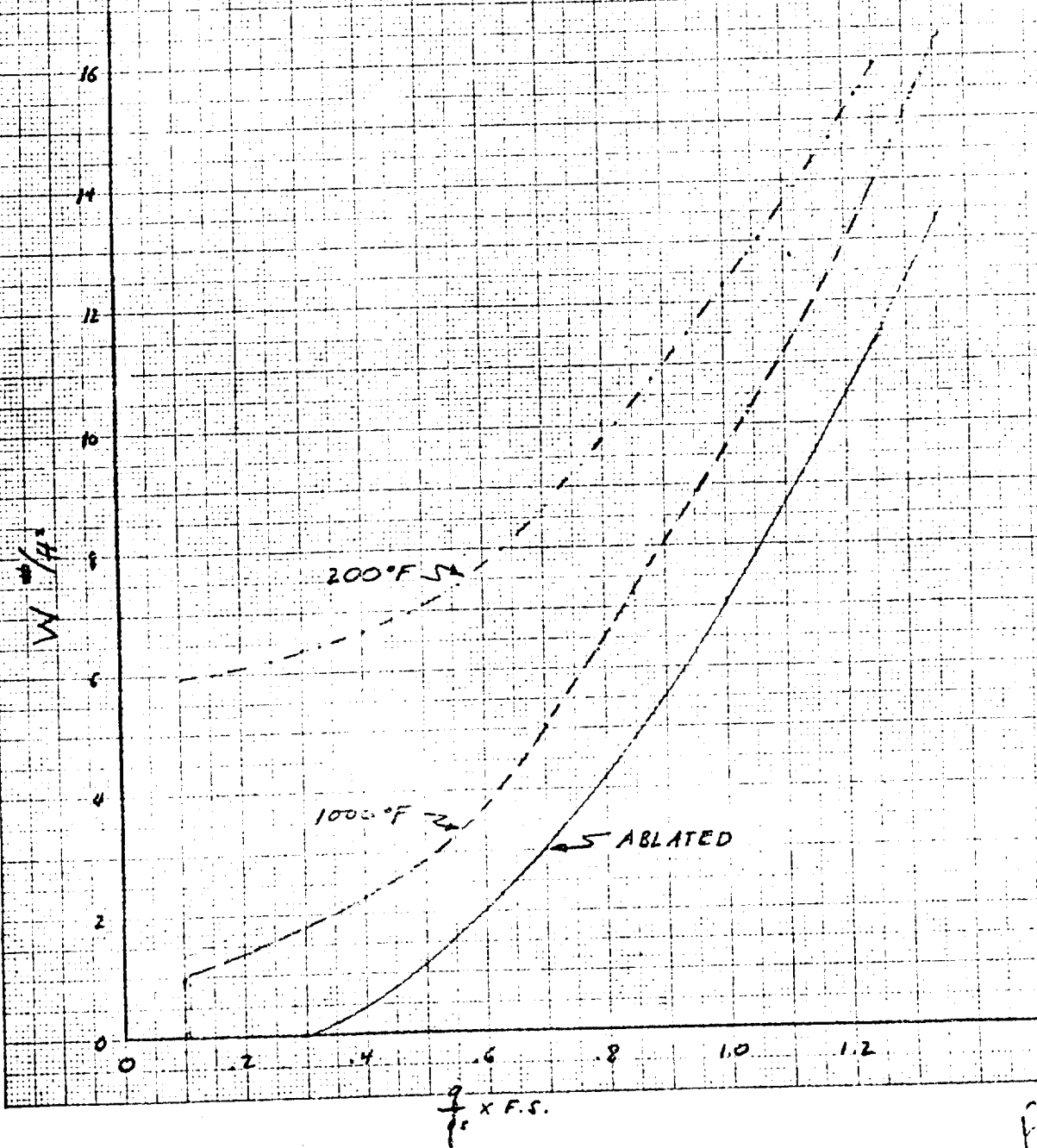


Fig 1843

# HEAT SHIELD ABLATIVE WEIGHTS FOR M-1-1 NYLON-PHENOLIC — UNDERSHOT (60 NM.)

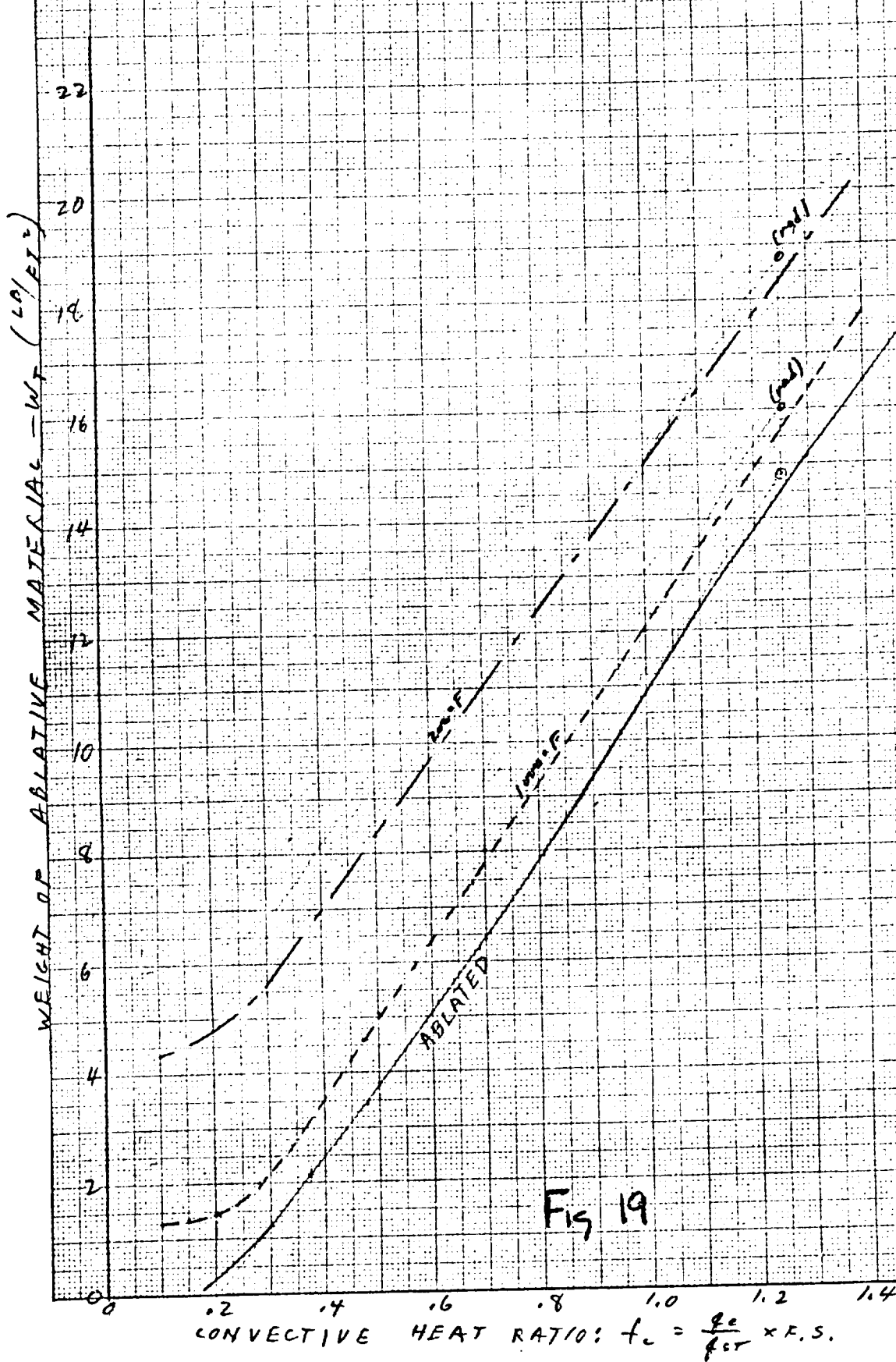


Fig 19

# L-2C OVERSHOOT, NYLON PHENOLIC ABLATIVE WEIGHTS

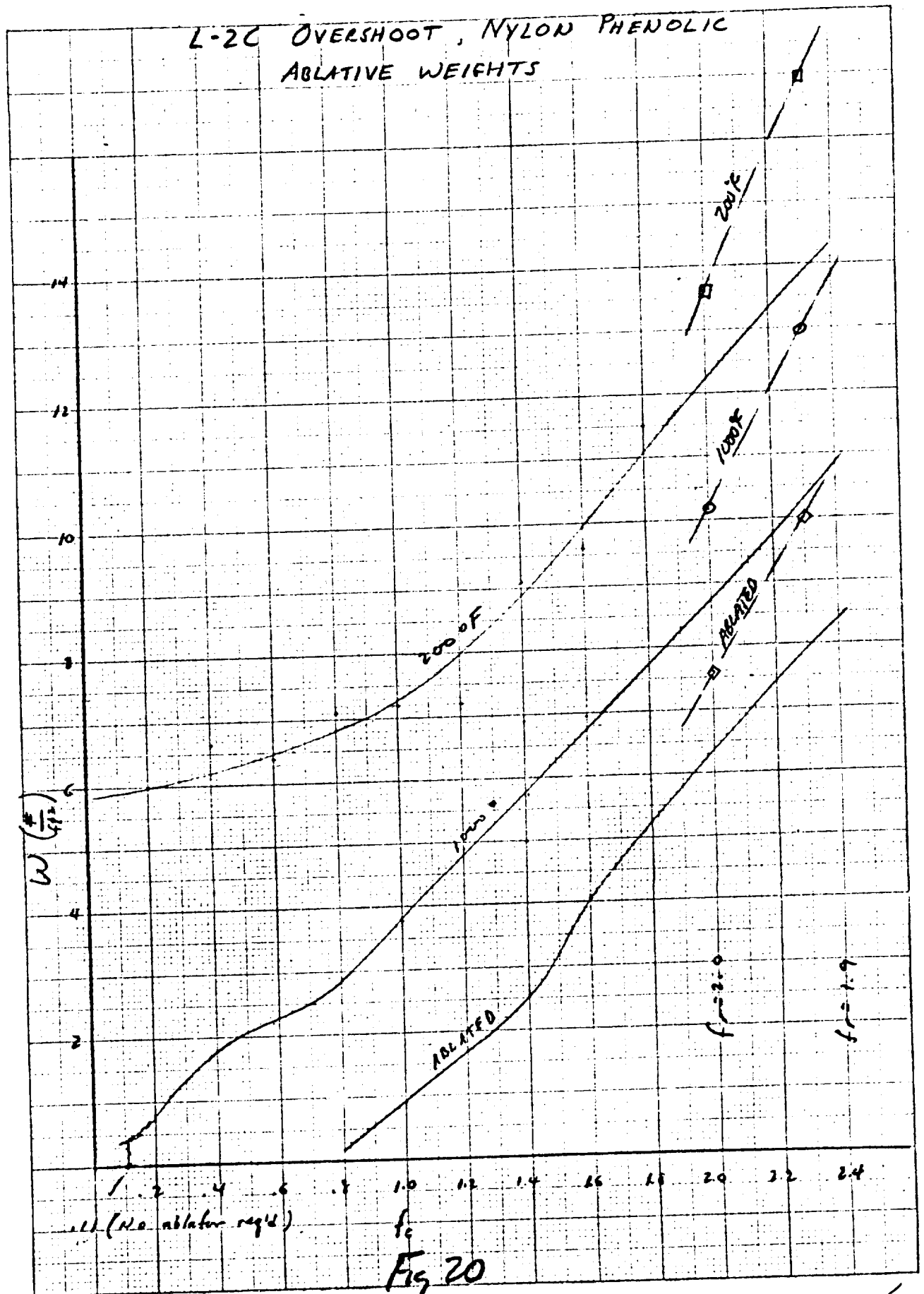


Fig 20

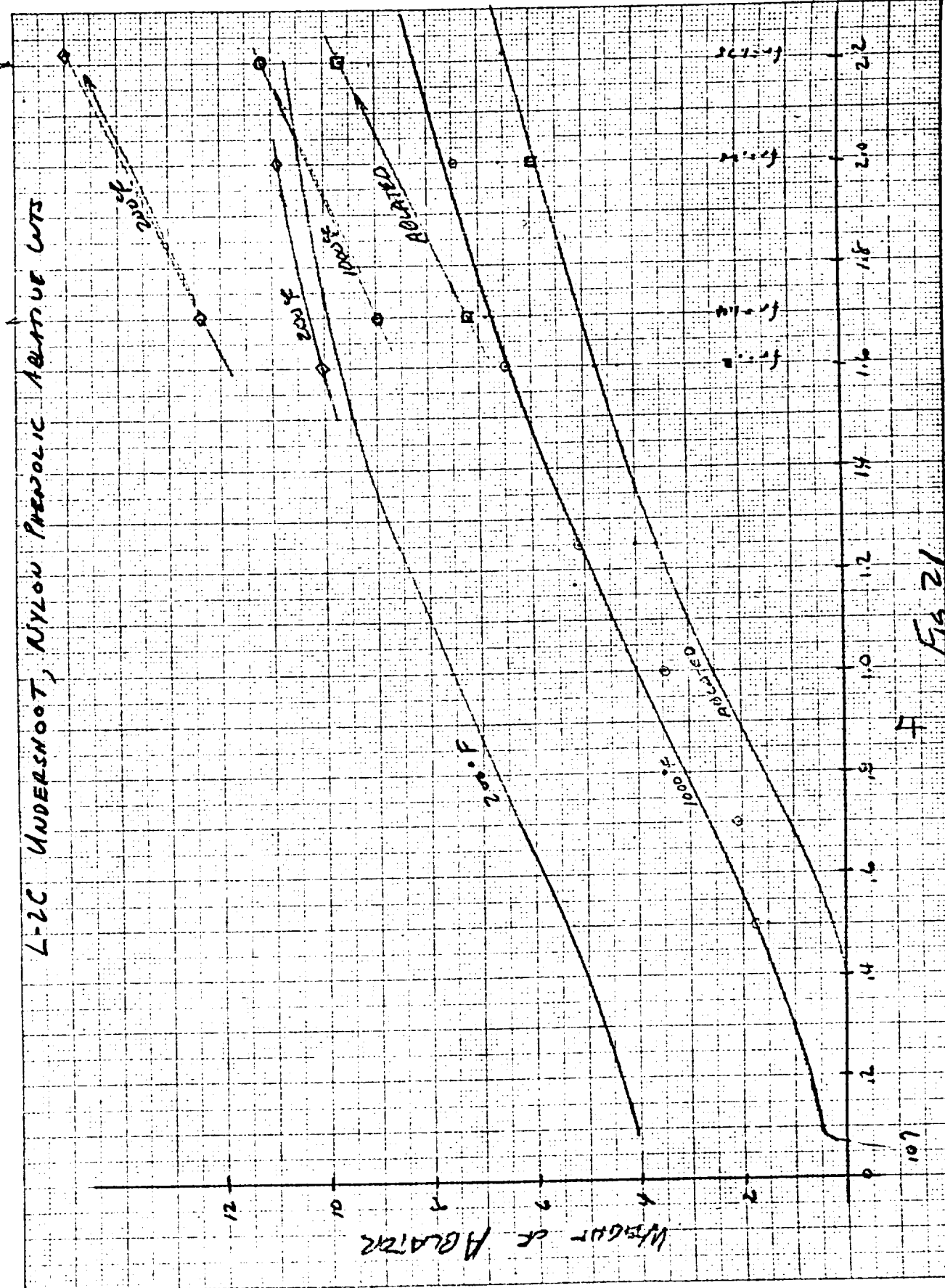


Fig 21



L-2C HEAT SHIELD WEIGHT

SUPERALLOY + ADL-17

OVERSHOOT TRAJECTORY

$\gamma_c = 1.75$

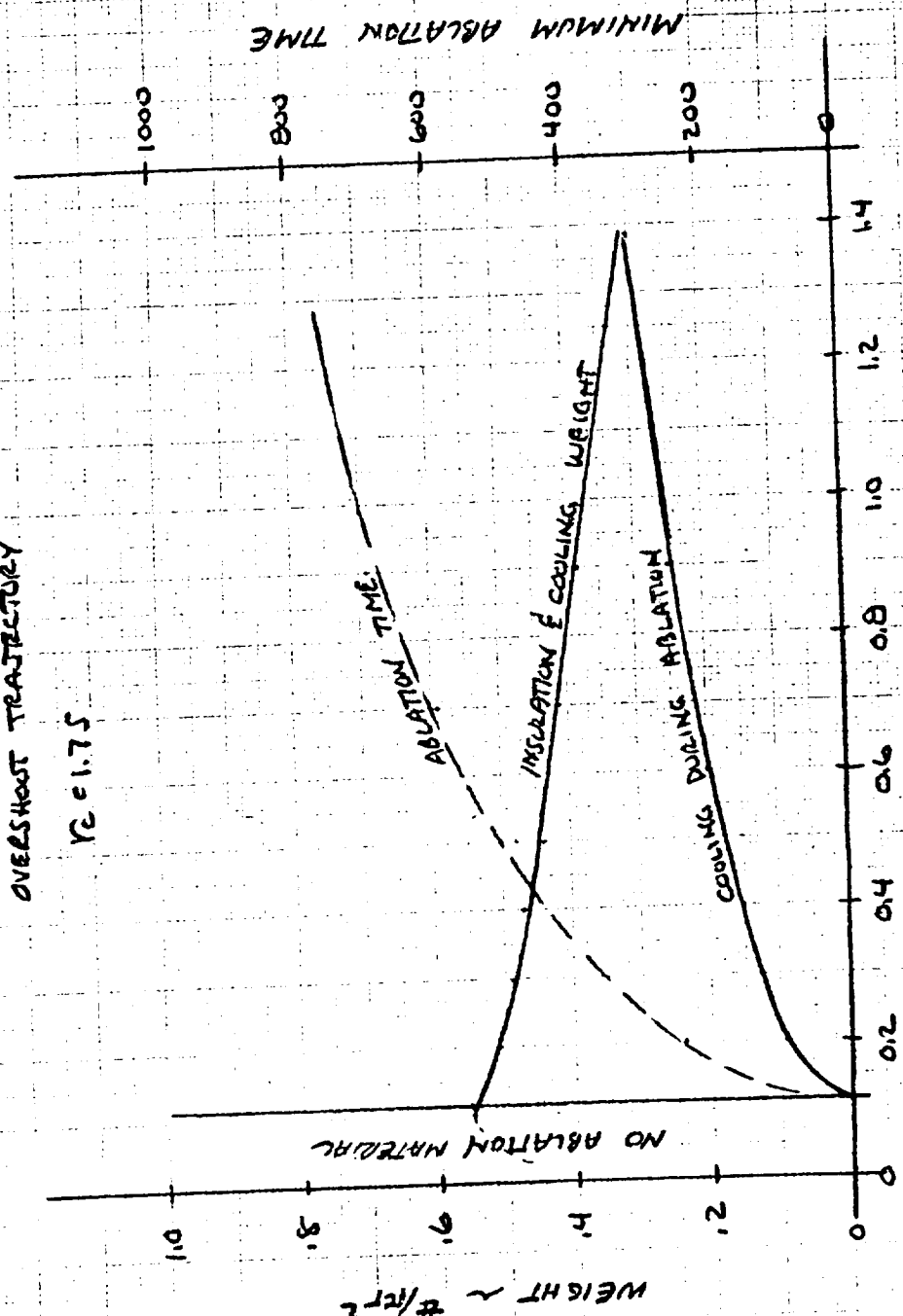


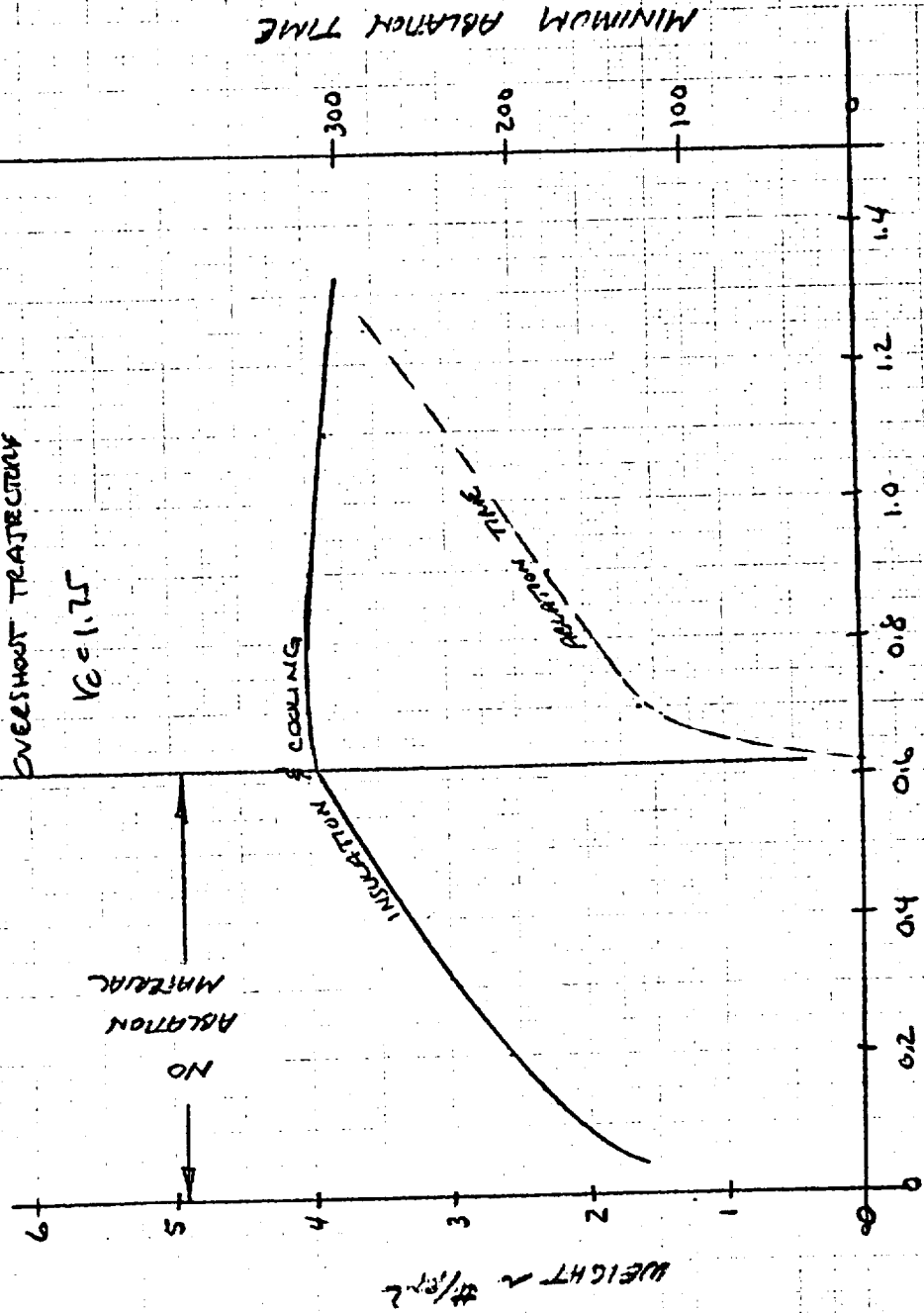
Fig 22

# L-2C HEAT SHIELD WEIGHTS

ZNO<sub>2</sub> FOAM

OVERSHOOT TRAJECTORY

$$V_c = 1.75$$



F FACTOR

Fig 23

# WEIGHT OF ABLATOR & WATER COOLING SYSTEM FOR M-1-1 (UNPERSHOOT)

NYLON-PHENOLIC

$$f_p = 1.25$$

$$f_R = 1.0$$

$$f_c = 2.3$$

FOR ABLATOR + SELF-  
INDICATIVE LAYER  
WITH BACK FACE AT 200°F

$$W = 18.8 \text{ LB/FT}^2$$

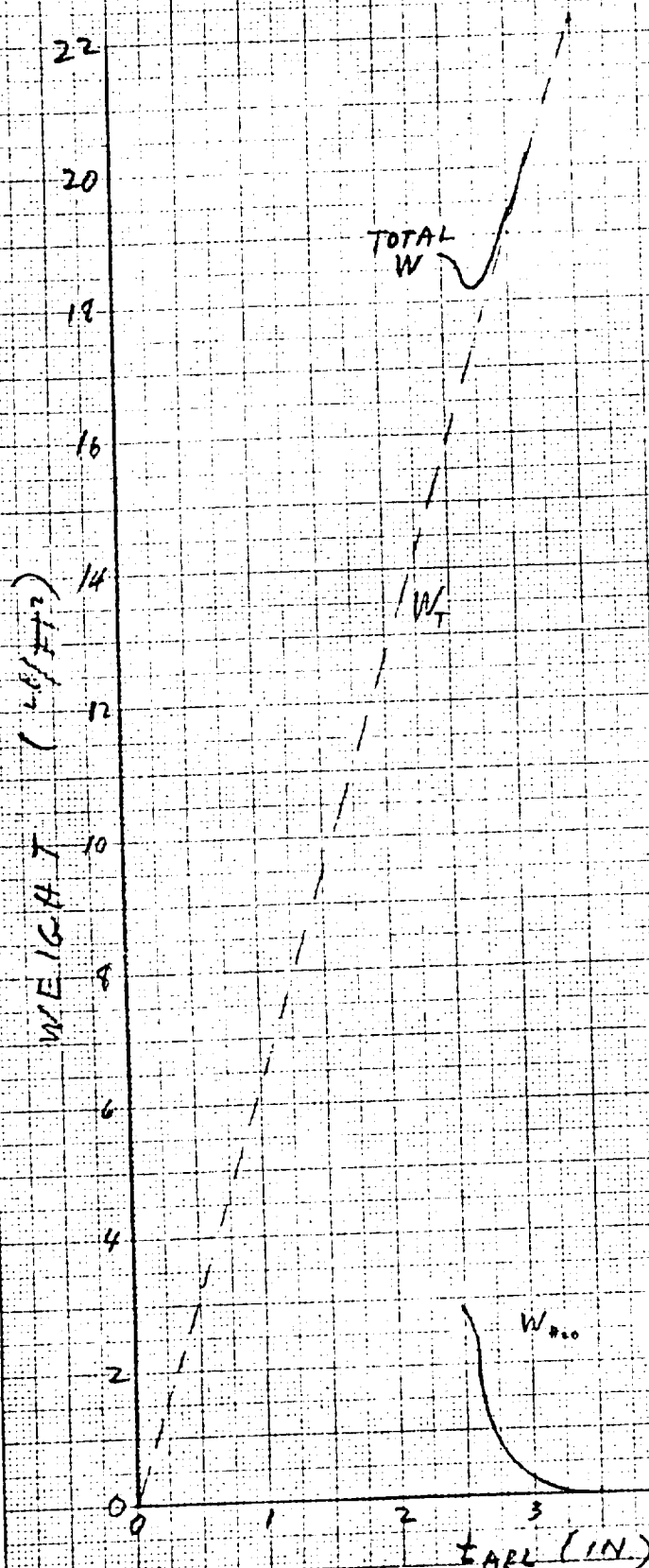


Fig 24

## 5. Supplementary Efforts

Several of the studies performed or being performed in support of the APOLLO heat shield program are described herein.

### a. Char Layer Ablators

Two IBM programs capable of handling ablative materials are currently available within Martin-Baltimore, however, neither of these programs can adequately handle a charring ablator. Since review of ablator materials indicates that char layer ablators are the most attractive materials for use on APOLLO, it was decided to put emphasis on the development of such a program. This is being actively manned and is progressing satisfactorily.

The program as currently conceived will be able to handle both charring ablators and the resin impregnated ceramic material. Literature is being reviewed from the aspect of understanding the influence of such factors as chemical reactions between the gaseous material and the char, combustion of the gaseous material in the boundary layer and combustion of the char surface. Some of these effects will be included in the program as inputs even though the proper form is not known at this time. Mechanical removal of the char will also be included.

The program status is such that, optimistically, the first binary deck will be compiled and an example problem run by 1 April '61.

### Approximate Steady State Analysis

An approximation to the steady state heat transfer analysis of a char layer ablator has been formulated.

The analysis is known to be crude, but is felt to be useful in understanding how a charring ablator may function. Of particular interest is the fact that for a given heat rate input  $\dot{q}_w$ , as the char layer thickens, the surface temperature increases and the effectiveness (effective heat of ablation  $h_{eff}$ ) increases.

# APPROXIMATE CHLORINE ABLATOR ANALYSIS

$T_s$	= surface temperature of char	$^{\circ}R$
$T_p$	= pyrolyzation temperature of resin	$^{\circ}R$
$\delta$	= thickness of char layer	$ft.$
$k$	= thermal conductivity of char	$\frac{BTU \ ft.}{ft.^2 \ Sec. \ ^{\circ}F}$
$\epsilon$	= emissivity of char	
$h_p$	= heat of pyrolyzation of resin	$\frac{BTU}{\# \ of \ Resin}$
$h_c$	= heat of combustion of char	$\frac{BTU}{\# \ of \ Char}$
$\dot{M}$	= total mass loss rate	$\frac{\#}{ft.^2 \ Sec.}$
$\dot{m}_v$	= vaporized mass loss rate	$\frac{\#}{ft.^2 \ Sec.}$
$\dot{m}_c$	= char mass loss rate	$\frac{\#}{ft.^2 \ Sec.}$
$M$	= ratio of molecular weight of air to that of injected mass	
$h_{st}$	= stagnation air enthalpy	$\frac{BTU}{\#}$
$h_{aw}$	= enthalpy of air at wall temperature	$\frac{BTU}{\#}$
$C_p$	= specific heat of vaporized products	$\frac{BTU}{\# \ ^{\circ}F}$
$C_{pc}$	= specific heat of char	$\frac{BTU}{\# \ ^{\circ}F}$
$K$	= constant in blocking term	

## ASSUMPTIONS

1. Steady State temperature distribution
2. Heat conducted into resin is ignored
3. Char thickness remains constant either by mechanical erosion or by combustion
4. Vaporized products are heated up to surface temperature prior to injection into the boundary layer
5. the combustion products injection is not included in the blocking effect
6. The combustion of the char term is probably an upper bound and may be much less if available oxygen is not sufficient to result in this rate of combustion. For this reason, the analysis was carried out with and without this term.

At Gas Surface

$$Q_{\text{conducted into}} = Q_{\text{radiated}} + Q_{\text{conducted}} + Q_{\text{absorbed}} - Q_{\text{combustion}}$$

$$Q_{\text{radiated}} = \sigma \epsilon T_s^4$$

$$Q_{\text{conducted}} = \frac{k_{\text{gas}} (T_s - T_g)}{\delta} \quad \text{where } k_{\text{gas}} \text{ is mean } k$$

$$Q_{\text{absorbed}} = A(M)^{\text{acc}} \epsilon_g (T_{\text{sr}} - T_{\text{wg}})$$

$$Q_{\text{combustion}} = \dot{m}_c h_c$$

At Resin Interface

$$Q_{\text{conducted}} = Q_{\text{absorbed by pyrolysis}} + Q_{\text{absorbed by } \dot{m}_p \text{ temp rise}} + Q_{\text{absorbed by } \dot{m}_c \text{ temp rise}}$$

$$Q_{\text{absorbed by pyrolysis}} = \dot{m} \dot{m}_p$$

$$Q_{\text{absorbed by } \dot{m}_p \text{ temp rise}} = \dot{m}_p (T_s - T_v)$$

$$Q_{\text{absorbed by } \dot{m}_c \text{ temp rise}} = \dot{m}_c (T_s - T_v)$$

at resin interface

$$\dot{m}_c = \dot{m}_p + \dot{m}_c \quad \text{Rate of ablation reaction}$$

$$\dot{m}_c = \frac{Q_{\text{conducted}}}{h_c} = \frac{Q_{\text{radiated}} + Q_{\text{conducted}} + Q_{\text{absorbed}} - Q_{\text{combustion}}}{h_c}$$

$$\begin{aligned}
 q_{\text{conducted}} &= \dot{m} h_p + \dot{m}_v C_{pv} (T_s - T_v) + \dot{m}_c C_{pc} (T_s - T_v) \\
 &= \dot{m}_v \left[ \frac{h_p}{F} + (T_s - T_v) (C_{pv} + \frac{1-F}{F} C_{pc}) \right] \\
 \therefore \dot{m}_v &\propto q_{\text{cond.}}
 \end{aligned}$$

At char surface

let  $q_o = q_{\text{Boundary layer}}$

$$q_o = \sigma \epsilon T_s^4 + q_{\text{conducted}} \left[ 1 + \frac{K(M)^{0.25} (H_{sr} - H_w) - \frac{1-F}{F} h_c}{\left[ \frac{h_p}{F} + (T_s - T_v) (C_{pv} + \frac{1-F}{F} C_{pc}) \right]} \right]$$

Let  $H_w = C_{pa} T_s$

where  $C_{pa}$  = avg. specific heat of air

$$q_o = \sigma \epsilon T_s^4 + \frac{h_m (T_s - T_v)}{\tau} \left[ 1 + \frac{K(M)^{0.25} (H_{sr} - C_{pa} T_s) - \frac{1-F}{F} h_c}{\left[ \frac{h_p}{F} + (T_s - T_v) (C_{pv} + \frac{1-F}{F} C_{pc}) \right]} \right]$$

$$\therefore q_o = f(T_s, H_{sr}, \tau)$$

$$H_{eff} = \frac{q_o}{\dot{m}} = f q_o \frac{\left[ \frac{h_p}{F} + (T_s - T_v) (C_{pv} + \frac{1-F}{F} C_{pc}) \right]}{\frac{h_m (T_s - T_v)}{\tau}}$$

$$\therefore H_{eff} = f(T_s, H_{sr}, \tau)$$

Note:

To account for surface removal by mechanical erosion only -

set  $h_0 = 0$

Also, any fraction of the surface removal can be considered combustion by multiplying  $h_0$  by that fraction.

For the present analysis a mean thermal conductivity is assumed.

For the following variation of  $k$  with temperature  $k_m$  is selected as shown:

$$k = k_0 = \text{constant}$$

$$k_m = k_0$$

$$k = b T$$

$$= a + b T$$

$$\left. \begin{aligned} k_m &= b \left( \frac{T_s + T_v}{2} \right) \\ k_m &= a + b \left( \frac{T_s + T_v}{2} \right) \end{aligned} \right\}$$

$$k = b T^2$$

$$= a + b T^2$$

$$\left. \begin{aligned} k_m &= \frac{b}{3} \frac{(T_s^3 - T_v^3)}{(T_s - T_v)} \\ k_m &= a + \frac{b}{3} \frac{(T_s^3 - T_v^3)}{(T_s - T_v)} \end{aligned} \right\}$$

$$k = b T^3$$

$$= a + b T^3$$

$$\left. \begin{aligned} k_m &= \frac{b}{4} (T_s^2 + T_v^2)(T_s + T_v) \\ k_m &= a + \frac{b}{4} (T_s^2 + T_v^2)(T_s + T_v) \end{aligned} \right\}$$



Example

For nylon phenolic

assume

$$h_c = 14,250 \text{ BTU/}$$

$$h_g = 1500 \text{ BTU/}$$

$$\epsilon = 0.85$$

$$T_v = 1400^\circ\text{F} = 1860^\circ\text{R}$$

$$C_{p1} = 0.40 \frac{\text{BTU}}{\text{lb}^\circ\text{F}}$$

$$C_{p2} = 0.20 \frac{\text{BTU}}{\text{lb}^\circ\text{F}}$$

$$F = 0.72$$

$$k_m = 0.8 \frac{\text{BTU Ft.}}{\text{Ft}^2 \text{HR } ^\circ\text{F}} = 2.22 \times 10^{-4} \frac{\text{BTU Ft.}}{\text{Ft}^2 \text{Sec. } ^\circ\text{F}}$$

$$M = 0.2$$

$$K = 2/3 \text{ for laminar flow}$$

$$C_{p2} = 0.27 \frac{\text{BTU}}{\text{lb}^\circ\text{F}}$$

For cases of  $T_b$  from  $2000^\circ\text{F}$  to  $5000^\circ\text{F}$

$\tau$  from 0.030 in. to 0.090 in.

$$M_{\text{cr}} = 20,000 \frac{\text{BTU}}{\text{lb}} \text{ and } 10,000 \frac{\text{BTU}}{\text{lb}} \text{ } 5,000 \frac{\text{BTU}}{\text{lb}}$$

The following curves have been worked out with and without combustion.

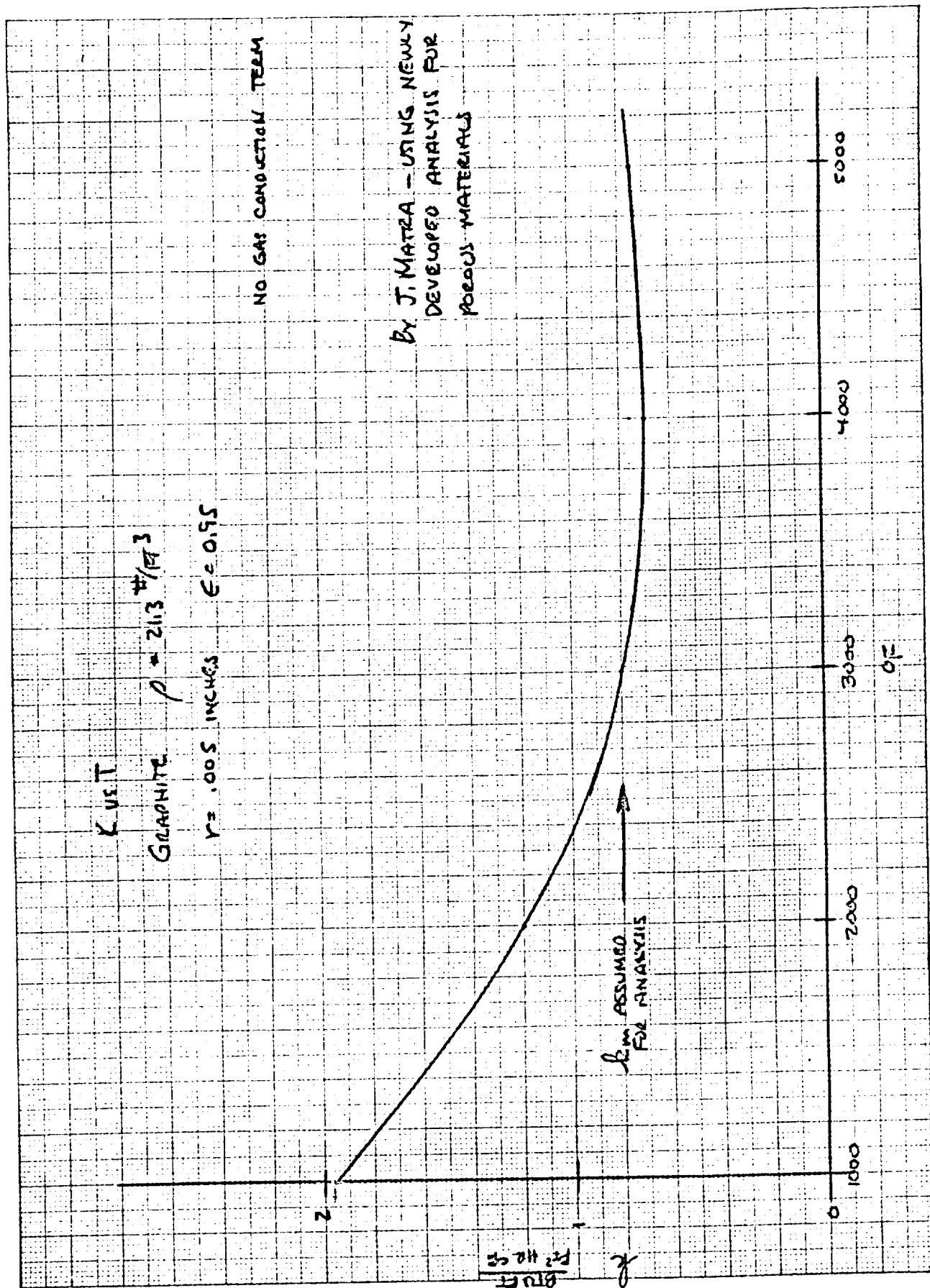


Fig 1

$H_{ST} = 5000$   
WITH COMBUSTION

1000

100

10

1

2000

3000

$T_c (^{\circ}R)$

4000

5000

Fig 2

157

$\gamma_{CHARGE} = .030$

$.060$

$.090$

$\gamma_{CHARGE} = .090$

$.060$

$.030$

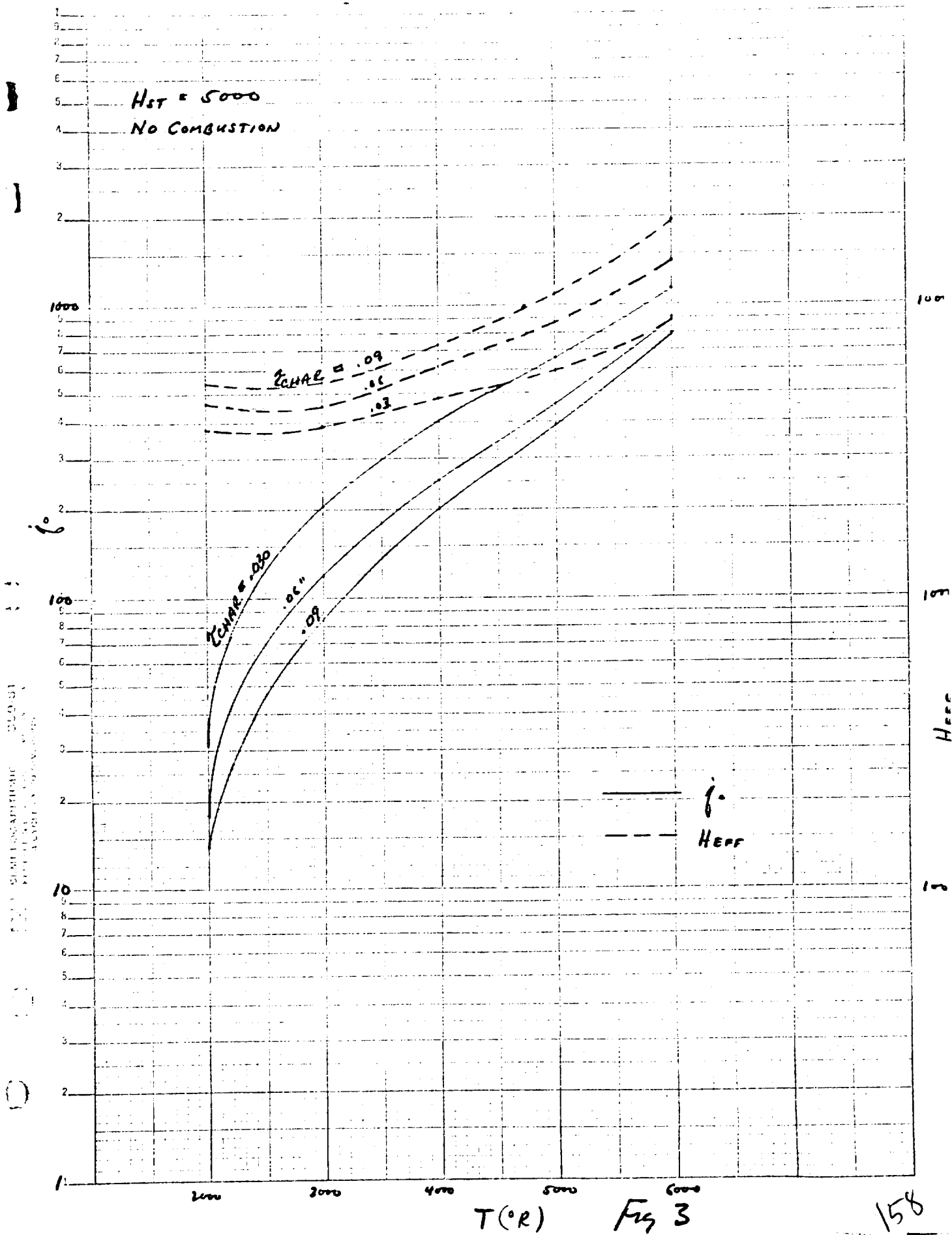
$\delta$   
H<sub>EFF</sub>

10,00

1,000

H<sub>EFF</sub>

100



WITH COMBUSTION

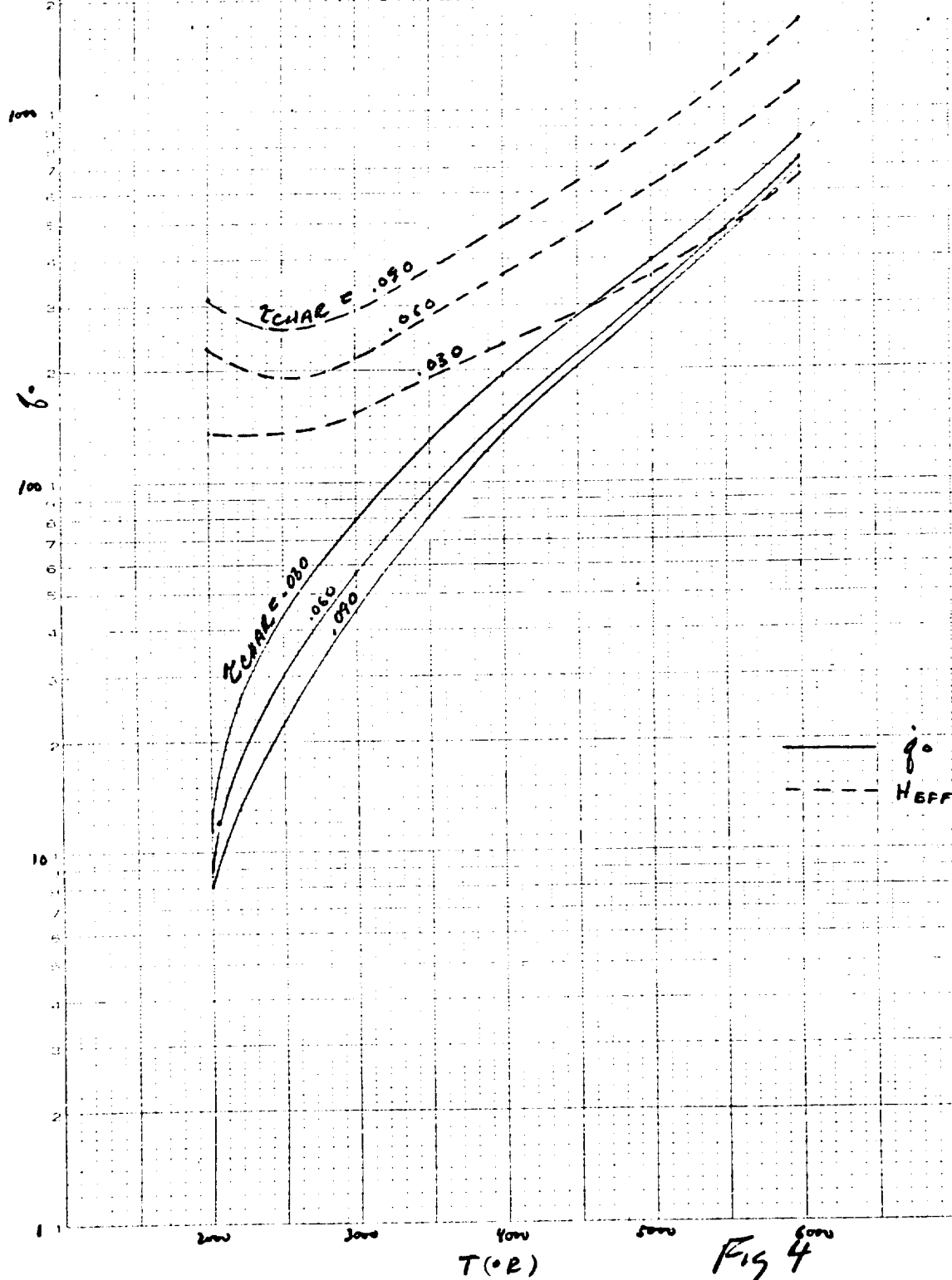
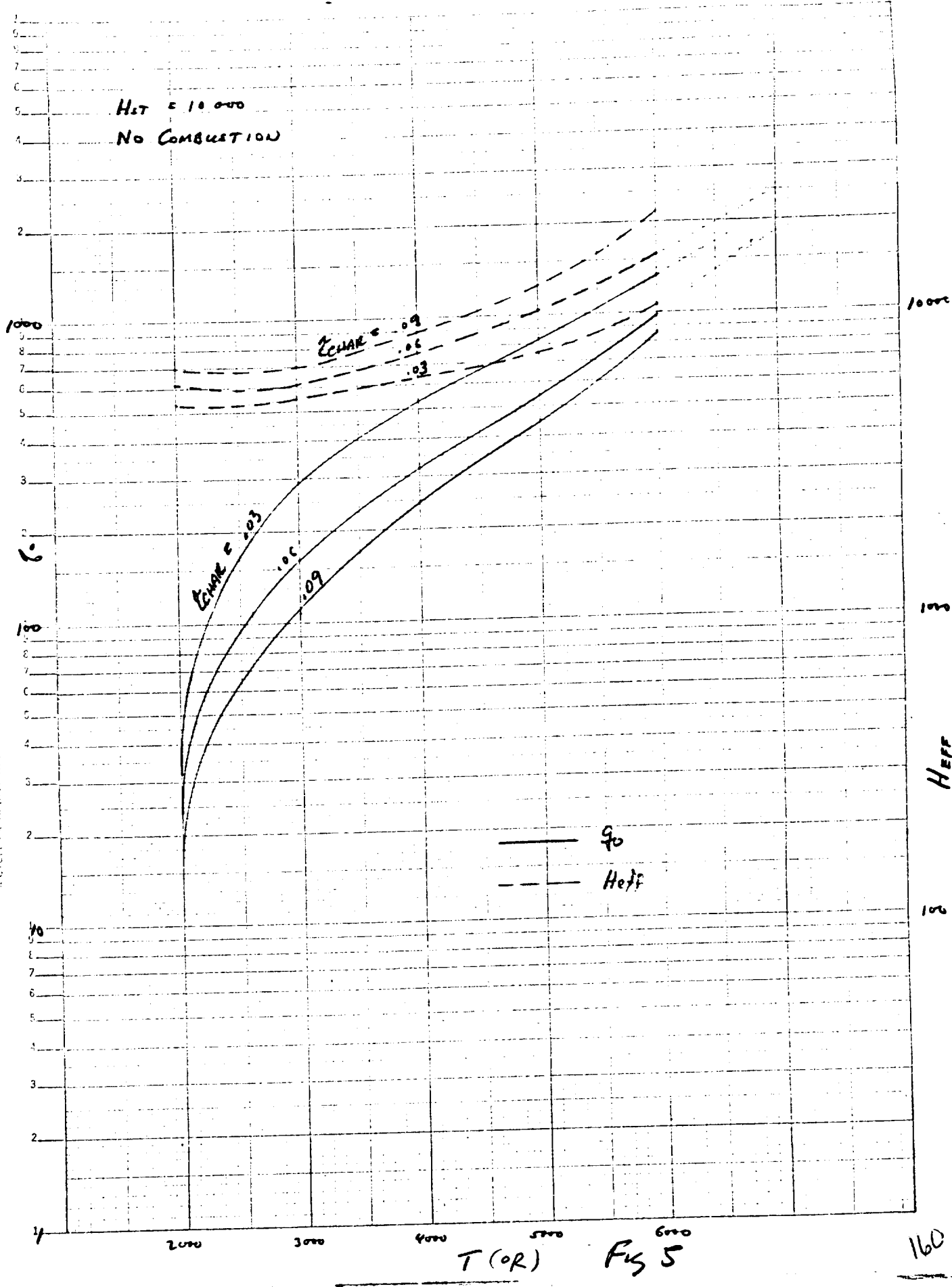


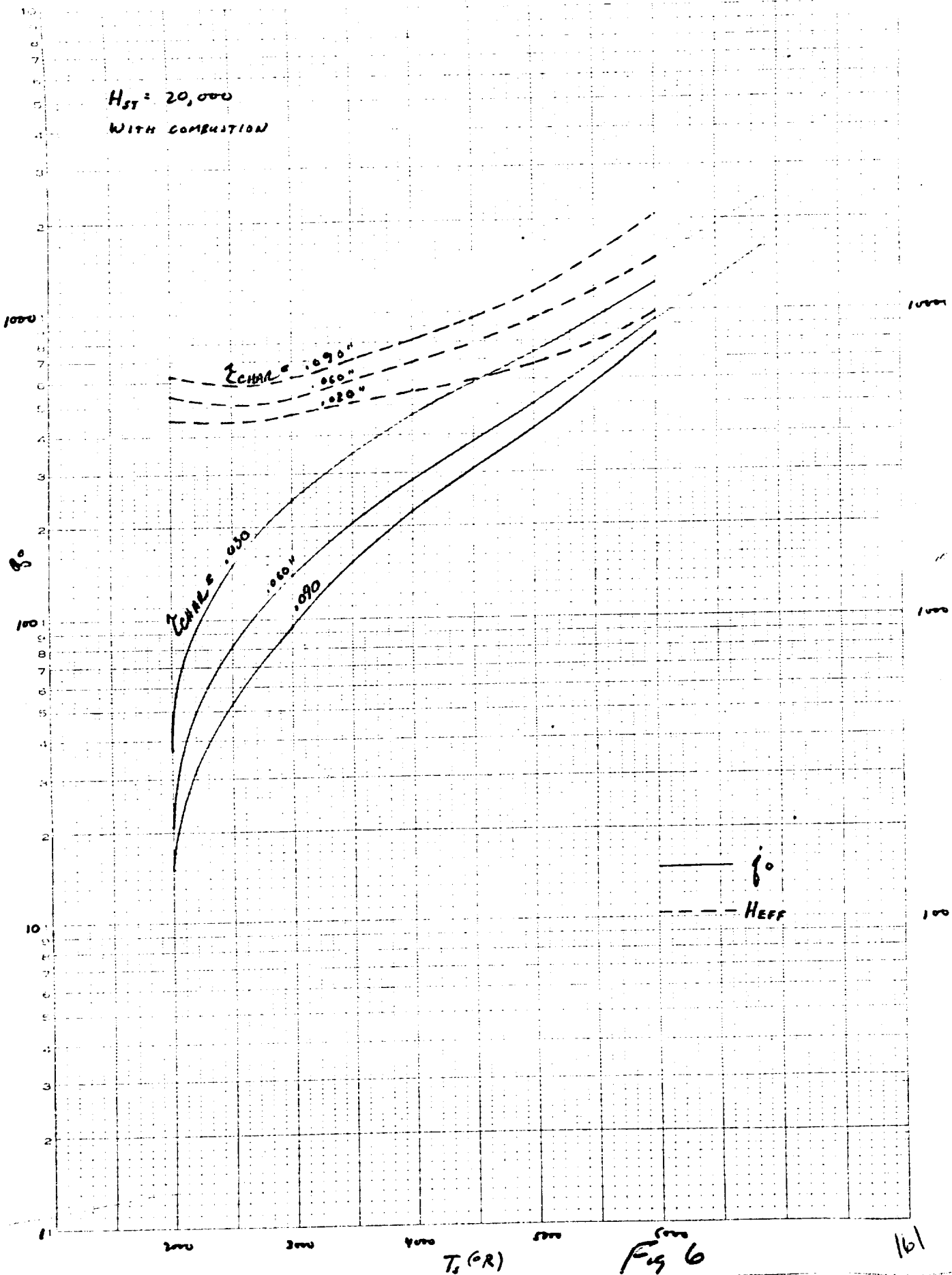
Fig 4<sup>cont</sup>

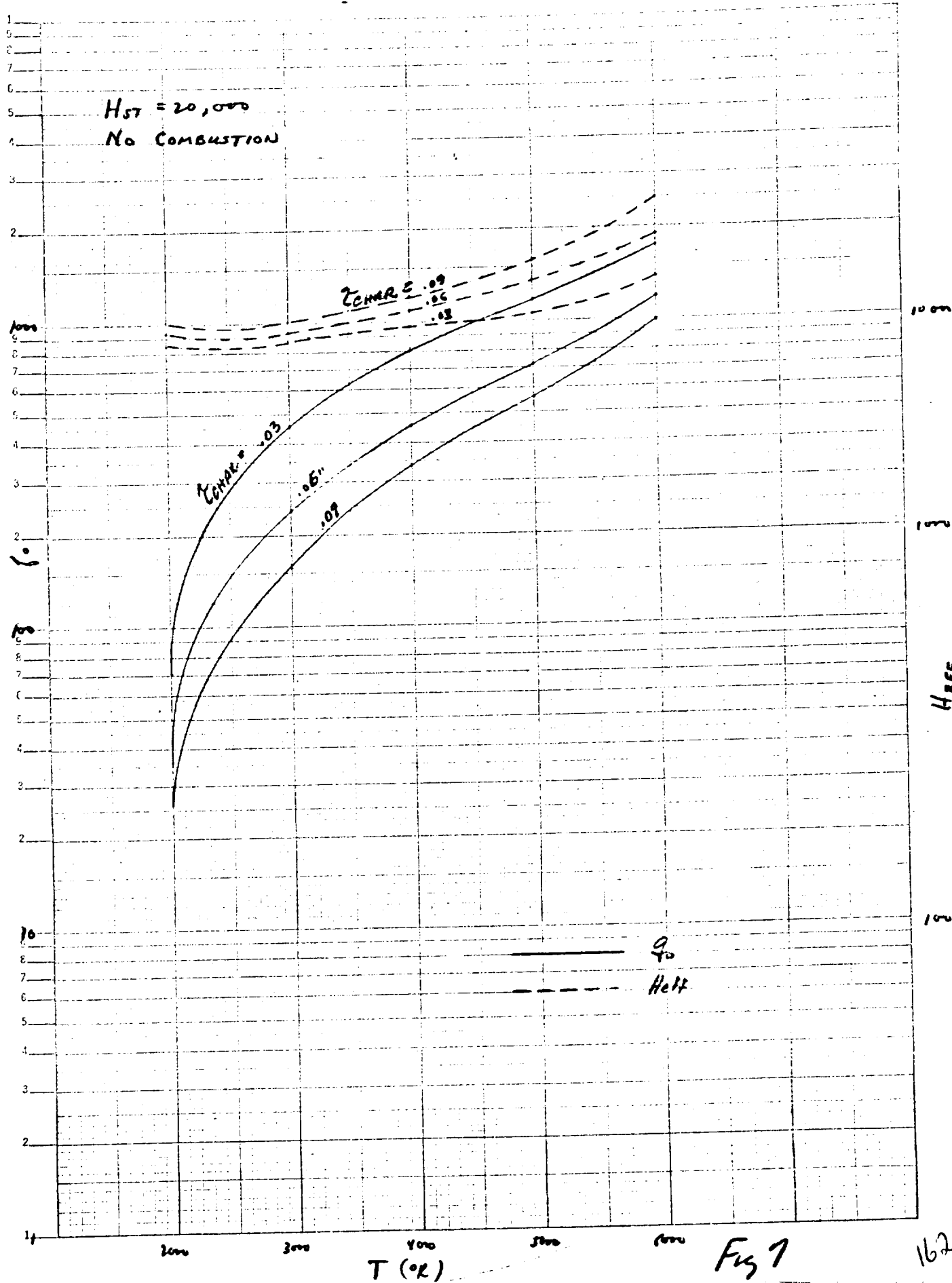


T (°R)

Fig 5

$H_{ST} = 20,000$   
WITH COMBUSTION







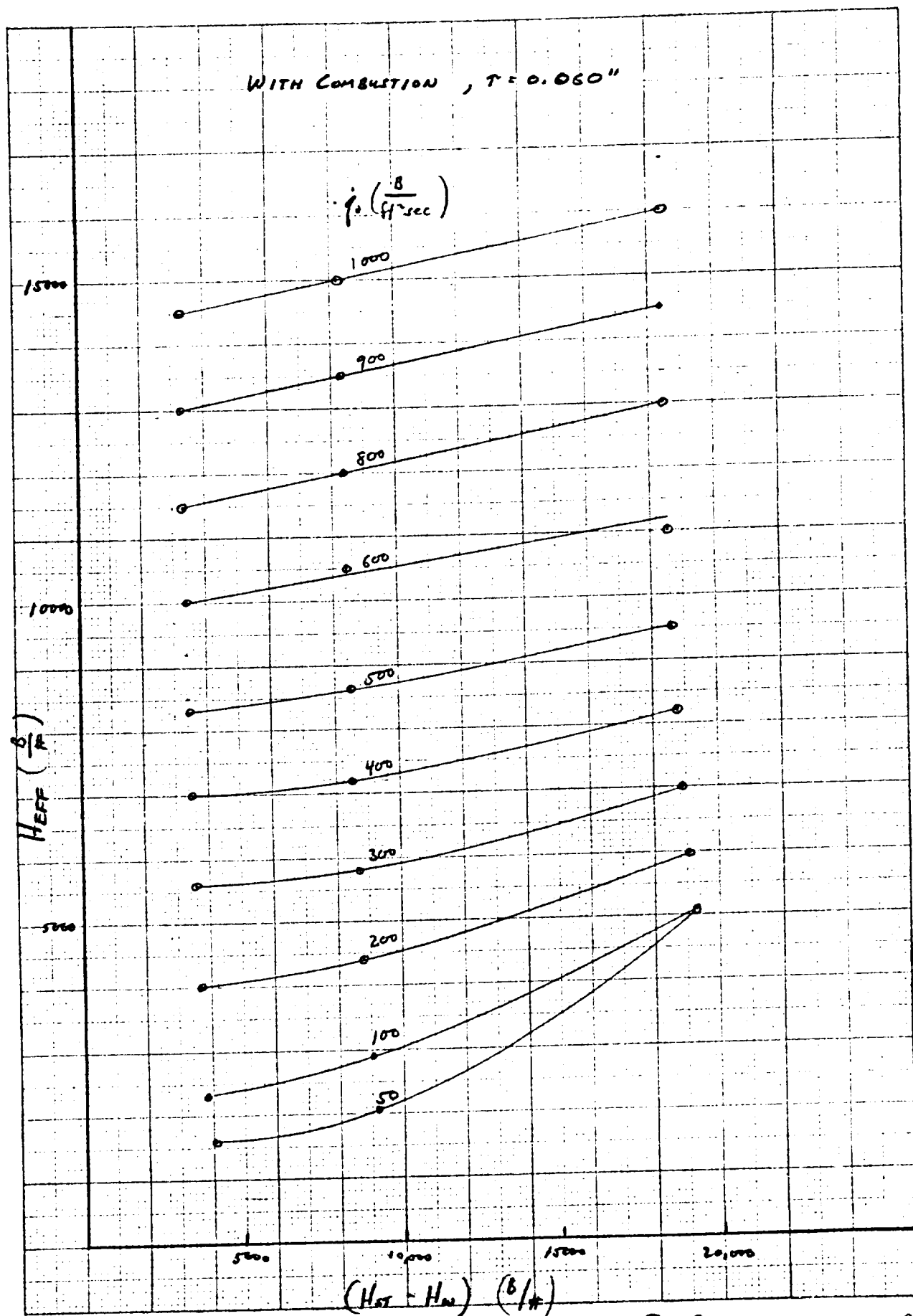


Fig 8

b. Data on Metal Radiative Shields.

A review of the progress in metal radiative heat shields was initiated with the purpose of studying at least the following programs.

- a) NASA experimental studies in support of Dynasoar.
- b) Bell-AMC Contract for cooled double wall type construction.
- c) Boeing-AMC Contract for superalloy hot structure approach.
- d) McDonnell-WADD Contract for refractory metal hot structure approach.

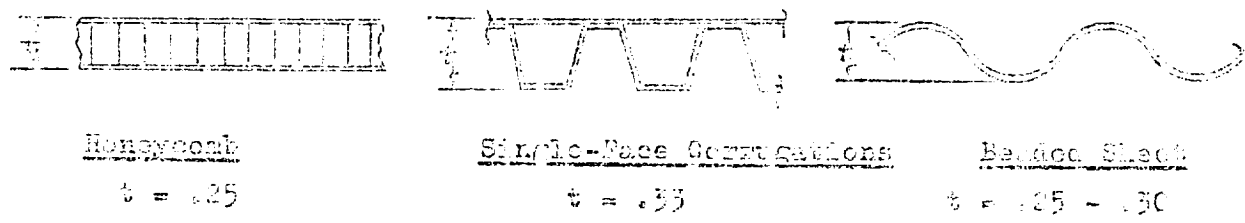
This activity resulted in the following pieces of data.

- a) Preliminary weight study of various types of outer metal panels for the cooled double wall approach. Rene 41, L-605 and F-48 alloys in a honeycomb, single face and corrugation and a beaded sheet configuration were studied as a function of service temperature and external pressure.
- b) Review of refractory metal alloy oxidation protection coatings.
- c) Summary of insulation data on ADL-17 vacuum insulation.

# METALLIC HEAT SHIELD WEIGHT STUDY

The following study was conducted to obtain preliminary weights of metallic heat shields for the Apollo Study. Composite outer panel weights are dependent on:

- (1) The type of shield construction - which in turn is influenced by alloy selection and vehicle design. The following types of construction are evaluated:



- (2) Local dynamic pressure - Values of 2, 4, and 6 psi. Ult. are used as variables
- (3) Panel temperature - Values of 1600°F, 1800°F, 2000°F, 2200°F, and 2500°F are assumed.
- (4) Panel support geometry - Supports used for 12x12 in. panels are shown in figures (2) and (3).

Table I presents general properties and information pertinent to the super alloys and refractory metal used in the study.

Table II presents some advantages and disadvantages reflected in the methods of shield construction.

Figures (2) and (3) present the metallic heat shield weights for various temperatures and external pressures dependent on the type of construction selected.

It should be noted that no attempt to optimize a particular construction was made, thus, the weight values shown may be conservative by as much as 10-20%.

TABLE I - MATERIALS

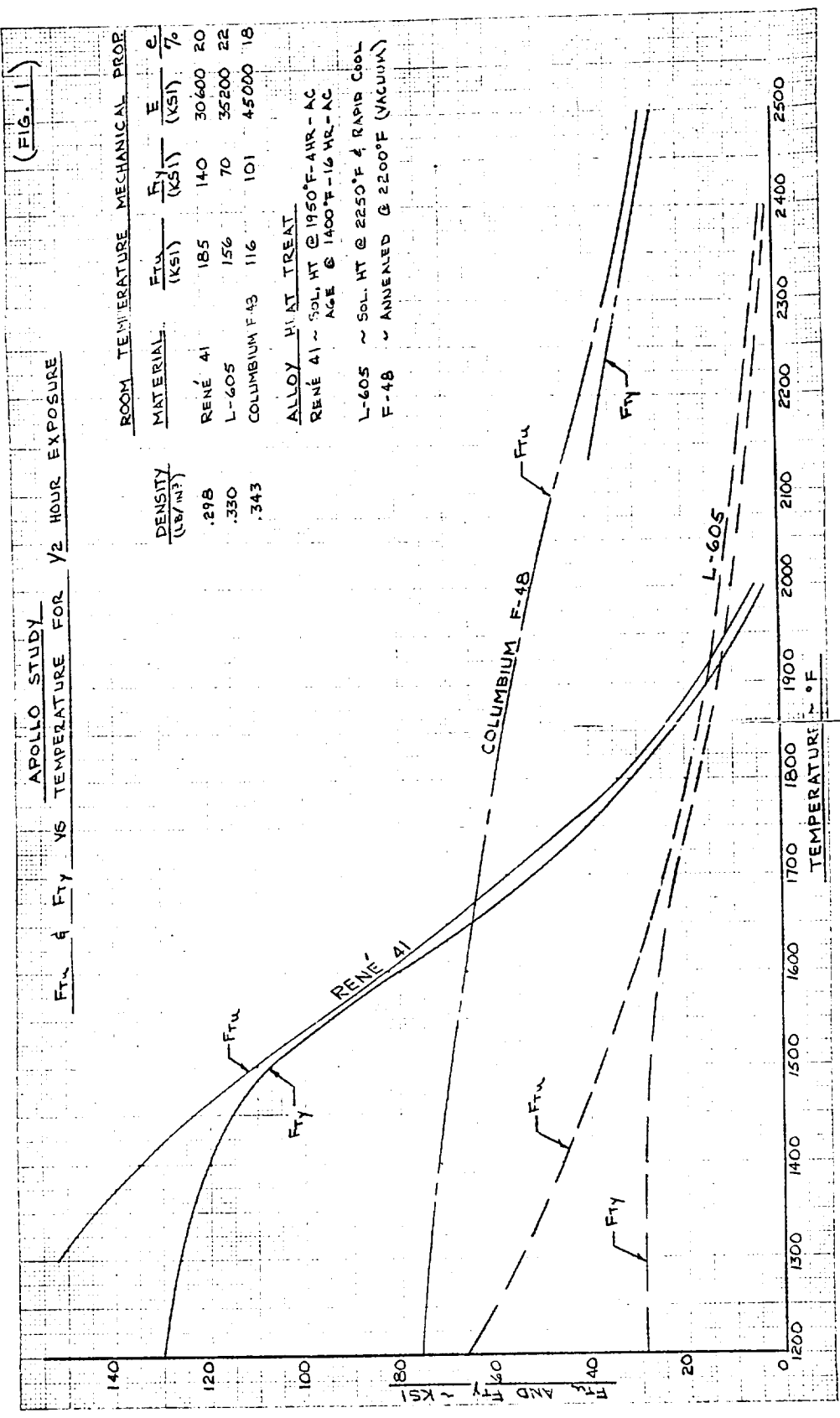
	RENN: 41	Columbiar (W 48)	
		2470-2500°F	2200°F - 2800°F (Recrystallization Temp.)
Melting Range	Up to 1900°F	2425-2570°F	1900-2300°F
Useful Temp. Range			
(See Figure 1)			
Mechanical Properties			
Density (70°F)	.298 #/in. <sup>3</sup>	.330 #/in. <sup>3</sup>	.343 #/in. <sup>3</sup>
Thermal Expansion (70-1800°F)	$9.35 \times 10^{-6}$ in/in/°F	$9.41 \times 10^{-6}$ in/in/°F	
Thermal Conductivity (1600°F)	175 BTU/in/Ft <sup>2</sup> /Hr/°F	181 BTU/in/Ft <sup>2</sup> /Hr/°F	
Specific Heat (70°F)	0.108 BTU/lb./°F	.092 BTU/lb./°F	
Oxidation Resistance (100 Hr. Exposure @ 2200°F)	.008 in. Mat'l. Affected	.050 Mat'l. Affected	Coating Reduc.
Forming	Gold-Forming similar to Stainless Steels	Gold-Forming with Intermediate Stages of Solution H.T.	.025 Metal Loss/Side Not Forming Good
Machineing	Machinable with Carbide or Cobalt Tools	Machinable with Tungsten Carbide Tools	Good
Welding	Tungsten Inert Gas Welding Only (Requires Additional Stress Relief @ 750°F)	Can be Fusion or Resistance Welded	Resistance - Fair Fusion - Good
Cost	\$17.96/lb.	1.14/lb.	
Weight	7.95/lb.	6.77/lb.	
Strength	66,000 psi	66,000 psi	
Impact	7.63/lb.	6.77/lb.	
Hardness	49 Rockwell C	49 Rockwell C	
Other Notes	0.00 in.	0.00 in.	Very Limited for Parts 0.20 in.

TABLE II - TYPES OF CONSTRUCTION

<u>HONEYCOMB</u>		<u>BEADED SHEET</u>		<u>SINGLE-FACE CORRUGATIONS</u>	
<u>Advantages</u>	<u>Disadvantages</u>	<u>Advantages</u>	<u>Disadvantages</u>	<u>Advantages</u>	<u>Disadvantages</u>
1. Extremely light wt. (See Fig. 2).	1. Difficult to fabricate, especially for complex contours.	1. Average wt. (See Fig. 3).	1. Requires excessive support structure.	1. Easy fabrication.	1. Heavy (See Fig. 2)
2. Easy to Attach		2. Can be formed to most contours.	2. Bumpy M.L.	2. Easy to attach.	2. Difficult to contour form.
3. Sonic Fatigue resistant.	2. Limited to L-605 foil gages at present.	3. Small thermal gradients thru single sheet.	3. Poor ability to withstand thermal stresses.	3. Adaptable to design changes.	3. Spotwelds subject to sonic fatigue damage.
4. Low Stresses due to Thermal Gradients.	3. Braze Alloy is weakest Temp. link & limited to 2200°F Max.	4. Inexpensive & adaptable to incorporation of design changes.	4. Sonic Fatigue & Flutter susceptible at ends of beads in flat sheet.	4. Compatible with superalloys & refractory metals.	4. Large thermal gradients for rapid heating rates.
5. Smooth M.L.	4. Simple Design Changes impossible to incorporate except to make new panels.	5. Compatible with superalloys & refractory metals.		5. Smooth M.L.	
	5. Difficult to inspect braze quality.				

APOLLO STUDY  
F<sub>TU</sub> & F<sub>TY</sub> VS TEMPERATURE FOR 1/2 HOUR EXPOSURE

(FIG. 1)



ROOM TEMPERATURE MECHANICAL PROP.				
MATERIAL	F <sub>TU</sub> (KSI)	F <sub>TY</sub> (KSI)	E (KSI)	e %
RENE 41	185	140	30600	20
L-605	156	70	35200	22
COLUMBIUM F-43	116	101	45000	18

ALLOY HEAT TREAT

RENE 41 ~ SOL. HT @ 1950°F - 4HR - AC  
 AGE @ 1400°F - 16 HR - AC  
 L-605 ~ SOL. HT @ 2250°F & RAPID COOL  
 F-48 ~ ANNEALED @ 2200°F (VACUUM)

1680

(FIG 2)

APOLLO STUDY  
METALLIC HEAT SHIELD WEIGHTS FOR VARIOUS TEMPERATURES & EXTERNAL PRESSURES

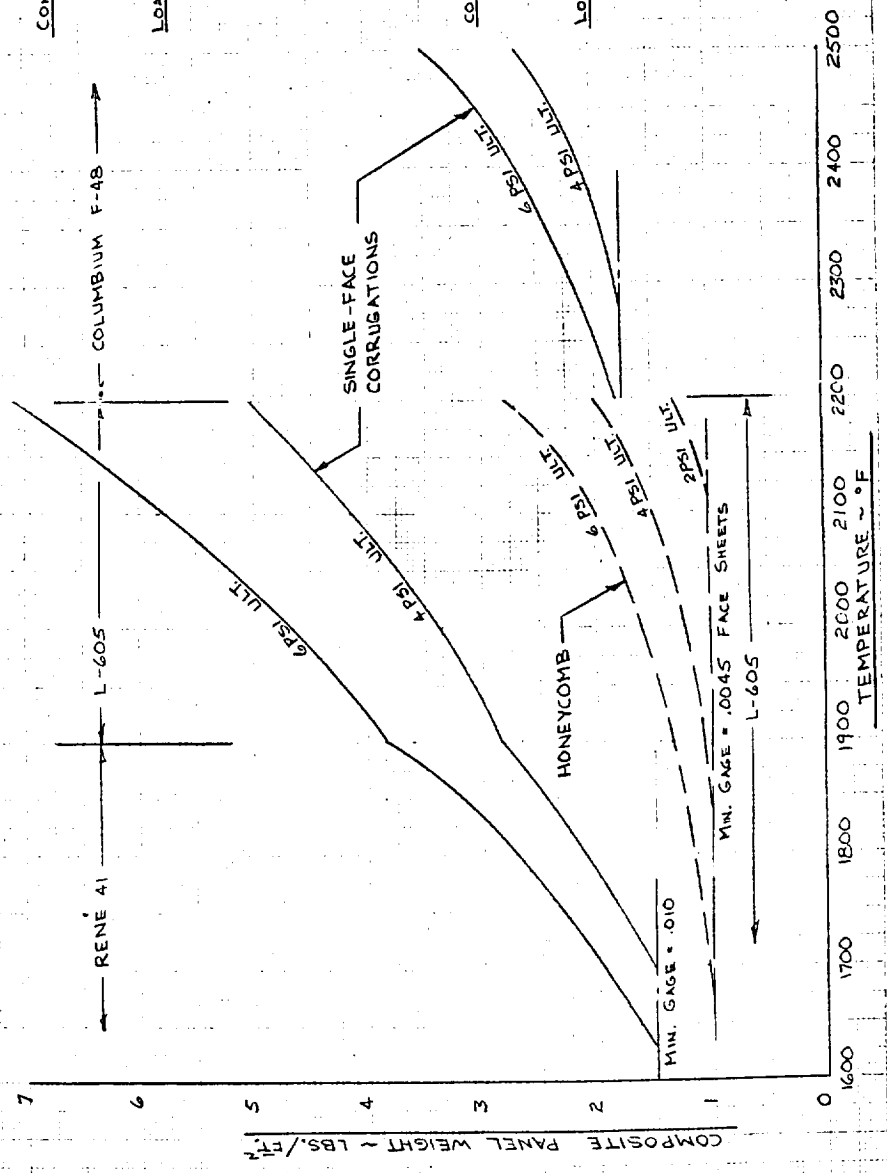
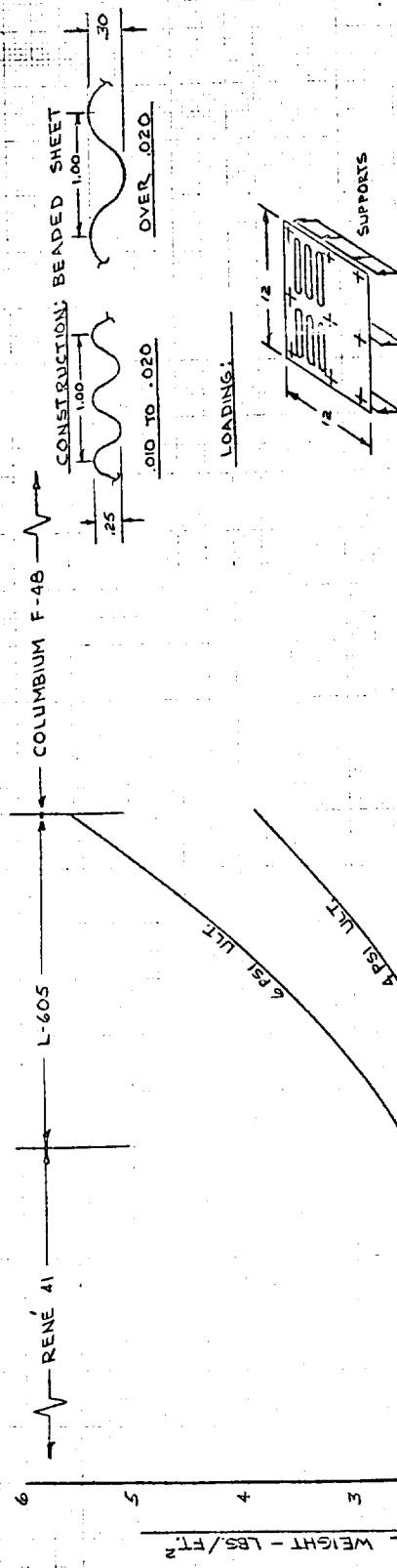


(FIG. 3)

APOLLO STUDY  
METALLIC HEAT SHIELD WEIGHTS FOR VARIOUS TEMPERATURES & EXTERNAL PRESSURES





## SUMMARY OF REFRACTORY METALS COATING DEVELOPMENT

References: The following references were prepared notes for the Fourth Refractory Composite Working Group Meeting - Cincinnati, Ohio. November 15, 16, 17, 1960.

- (a) Boeing Aero-Space Division
- (b) Chance Vought Aircraft
- (c) North American Aviation Inc.
- (d) General Electric - Flight Propulsion Division
- (e) Bell Aero Systems Company
- (f) Chrom Alloy Corporation
- (g) University of California - Ernest O. Lawrence Radiation Laboratory

Additional references include:

- (h) McDonnell Aircraft Refractory Metals Development Program (1st, 2nd, 3rd, and 4th quarterly progress reports)
- (i) Martin Evaluation of Coatings for Molybdenum (ER-11462-1-2-3)

It is a known fact that the refractory metals cannot be used for extended periods of time at elevated temperatures (above 1500°F) in an oxidizing atmosphere without adequate surface protection. A great deal of effort has gone into the study of coatings for the refractory metals during the past several years and development of a substantial variety of coating systems and application methods have been developed. These efforts, however, have not been integrated either in respect to the overall area of high temperature-time relationships, or in considering the range of problems confronting any single coating.

It should be emphasized that most of the encouraging reports of progress in the field of high temperature coatings are based on small numbers of samples which are submitted to simple static oxidation tests perhaps in combination with thermal cycling or tensile strains of moderate stress levels. Such coatings are far removed from having been successfully applied to complex joined structures such as those involved in the Apollo Vehicle.

A review of references (a) thru (i) is presented in Table I and reflects the present coating state-of-art for molybdenum and columbium alloys with pertinent test results and/or comments.

TABLE I - REFRACTORY METAL COATING SUMMARY

## COLUMBIUM ALLOY OXIDATION PROTECTION (F-48, F-50, FANSTEEL 82)

Ref.	Coating	Application Technique	Test Data		Comments
			Temp.	Time	
(a)	Disil 2 (AL-12%Si)	Hot Dip	3000°F 2600°F	10 min. 60 min.	Ductility & other base metal properties remain unchanged.
	Disil 3	Pack Cementation	3000°F 3200°F	60 min. Short time	Laboratory Development Stage.
(b)	Vaught Cementation Coatings	Pack Cementation	-----	-----	Size or shape of component does not limit application. Good self-sealing characteristics.
(c)	Aluminum Slurry	Spraying, Dipping, Brushing	2500°F	120 min.	Laboratory Development Stage.
(d)	LB-2 (10 Cr-Si-Al)	Hot or Cold Dip	2500°F	120 min.	Does not embrittle base alloy. Resists impact damage. Easily applied to complex shapes.
(e)	Vaught V-2 Silicon-Aluminum-Chromium with .005 covering of Rokide "A"	Pack Cementation	2200°F (Moving air @ 1500 ft/sec.)	120 min.	Rokide coating appears to protect coating from erosive effects of flow.
(f)	Aluminizing	Cold Slurry Application	2500°F	120 min.	Stress-Rupture Data, Oxidation-Stress Data, & assembly sequence of composite structures.

TABLE I CONTINUED

## MOLYBDENUM ALLOYS (MO - 0.5 Ti.)

Ref.	Coating	Application Technique	Coating Thickness	Test Data		Comments
				Temp.	Time	
(a)	Disil 1 (Mo Si <sub>2</sub> )	Pack Cementation	.0015	3000°F 3200°F	60 min. Short time	Ductility of base metal not appreciably altered. Process in semi-production.
(b)	Vaught Cementation Coating	Back Cementation	---	---	---	Tensile Element Stresselongation data-fatigue data-riveted joint data.
(c)	Vapor Deposited Silicide	---	---	2800°F	---	Preliminary Test Data Only
(e)	Chromolloy W-2	---	---	3000°F 2750°F 2500°F 2250°F 2000°F 3000°F 2750°F 2500°F 2250°F 2000°F	40 min. 130 min. 225 min. 270 min. 300 min. 15 min. 60 min. 150 min. 175 min. 140 min.	Average Life from limited number of samples exhibiting large variations in protective coating performance in oxidation resistance. Most coating failures occurred at edges or corners of the specimens
(f)	Durak MG	---	---	---	---	Some plating of complex structure for MAC Refractory Metals
	Chromalloy W-2	---	.001 (Spot welded corrosion specimen) .002 (Sheet Specimen)	2600°F 2800°F	7200 min. 1800 min.	Program completed.

INSULATION PACKAGE DATA TAKEN FROM BELL AEC INT. RPT. 7-799(II)

(1) Percent By Wt. of Constituents (ADL-17)

Alumina	40%
Aluminum Flakes	13.33%
Carbon	13.33%
Silicon Nitride	13.33%
Fibrous Asbestos	20%
	<hr/>
	99.99%

(2) Settling Characteristics (54,000 Paps @ 100 u Pressure)

8 lb/ft. <sup>-3</sup> Density	Segregation & Densifying
10- 12 lb/ft. <sup>-3</sup> Density	Partial Segregation
16 lb/ft. <sup>-3</sup> Density	No Segregation

(3) Liquid Oxygen Compatibility (Explosion Hazard)

Insulating powder when compared to carbon, is definitely a very small hazard and is termed compatible with liquid oxygen.

(4) Thermal Conductivity Tests

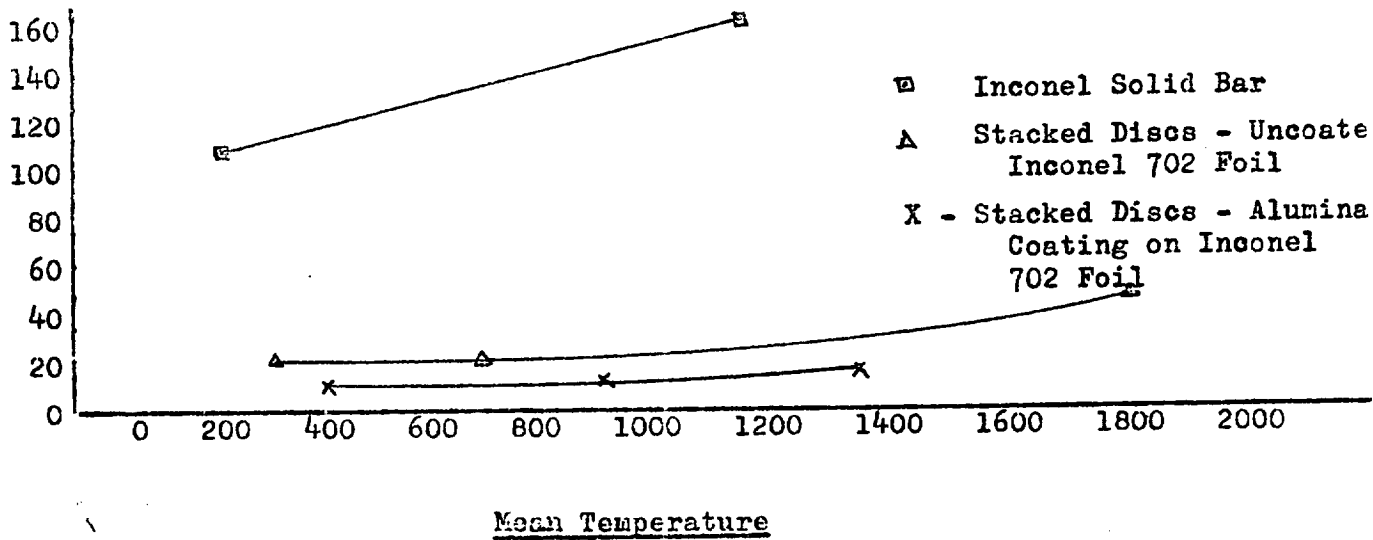
See Figures 1 & 2

(5) Insulation Packaging

Placed in .005 Inconel (Annealed) Foil with filters to relieve internal pressures. A "Bag" type package was found not satisfactory as a container unless clamped between the outer wall and primary structure. Final design used corrugated beading and channel beams to stiffen the bottom of the package. Coil Springs are used to support the package against the outer wall.

(6) Outer Wall Supports

Stacked metal foil discs coated and uncoated are used between the cooled inner wall and support to minimize the short circuit heat flux. Test results of lin. height discs are shown on the following page.



(7) Insulation Total System Weights

Total System Wt. for 0.75 in. layer of ADL-17 Powder with insulating effectiveness of the powder in a vacuum

$$= 1.545 \text{ Lbs./Ft.}^{-2}$$

© Sea Level

$$= 1.96 \text{ Lbs./Ft.}^{-2}$$

The wt. penalty reflects only the amount of coolant required to offset the additional heat transmitted to the primary structure.

1/16/61

EFFECT OF TEMPERATURE & PRESSURE ON  
KP OF ADL-17 INSULATING POWDER

COLD SIDE TEMP. = 100°F  
 $\rho = 12 \text{ LBS./FT.}^3$

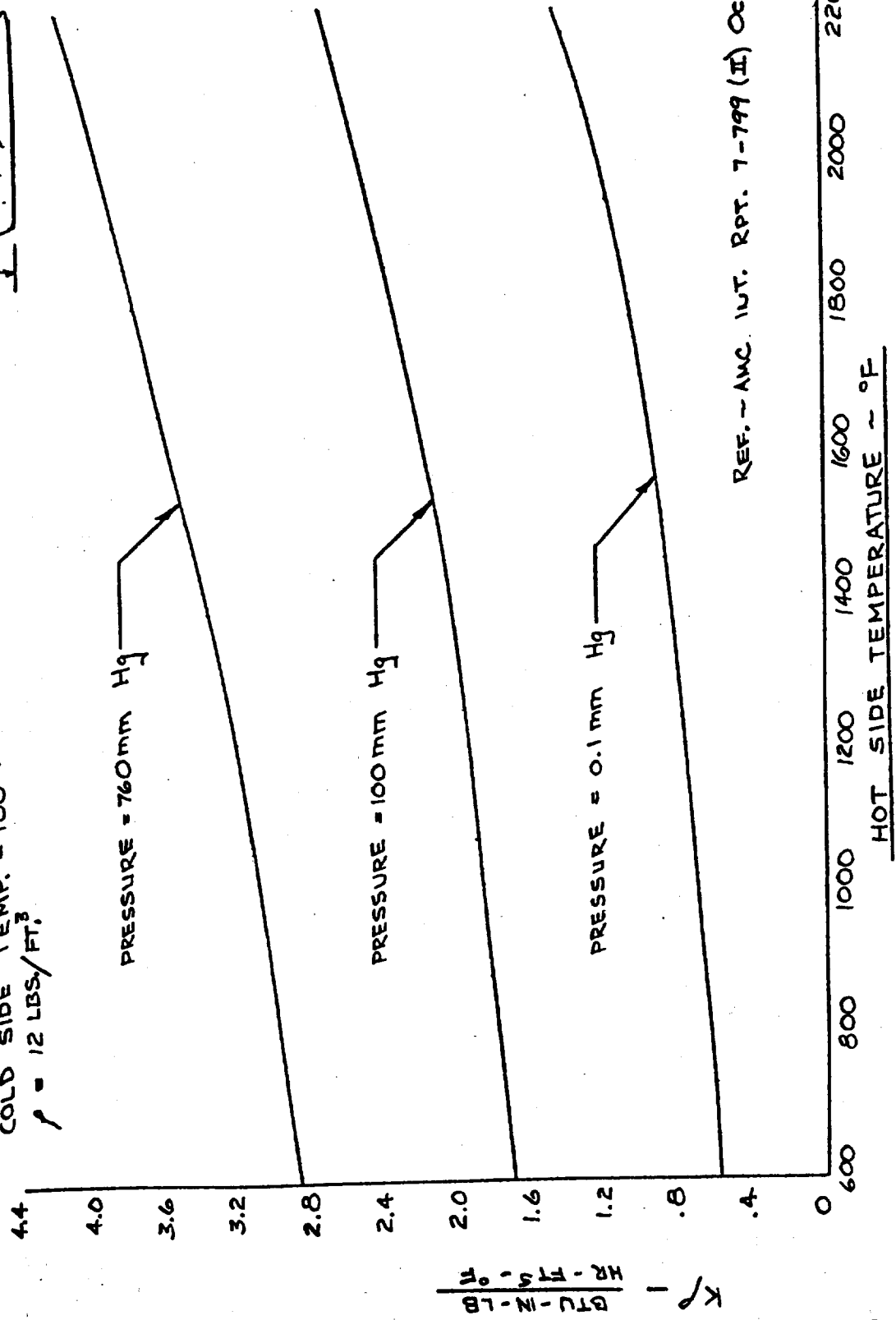
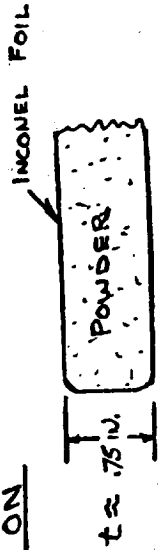


FIGURE 1

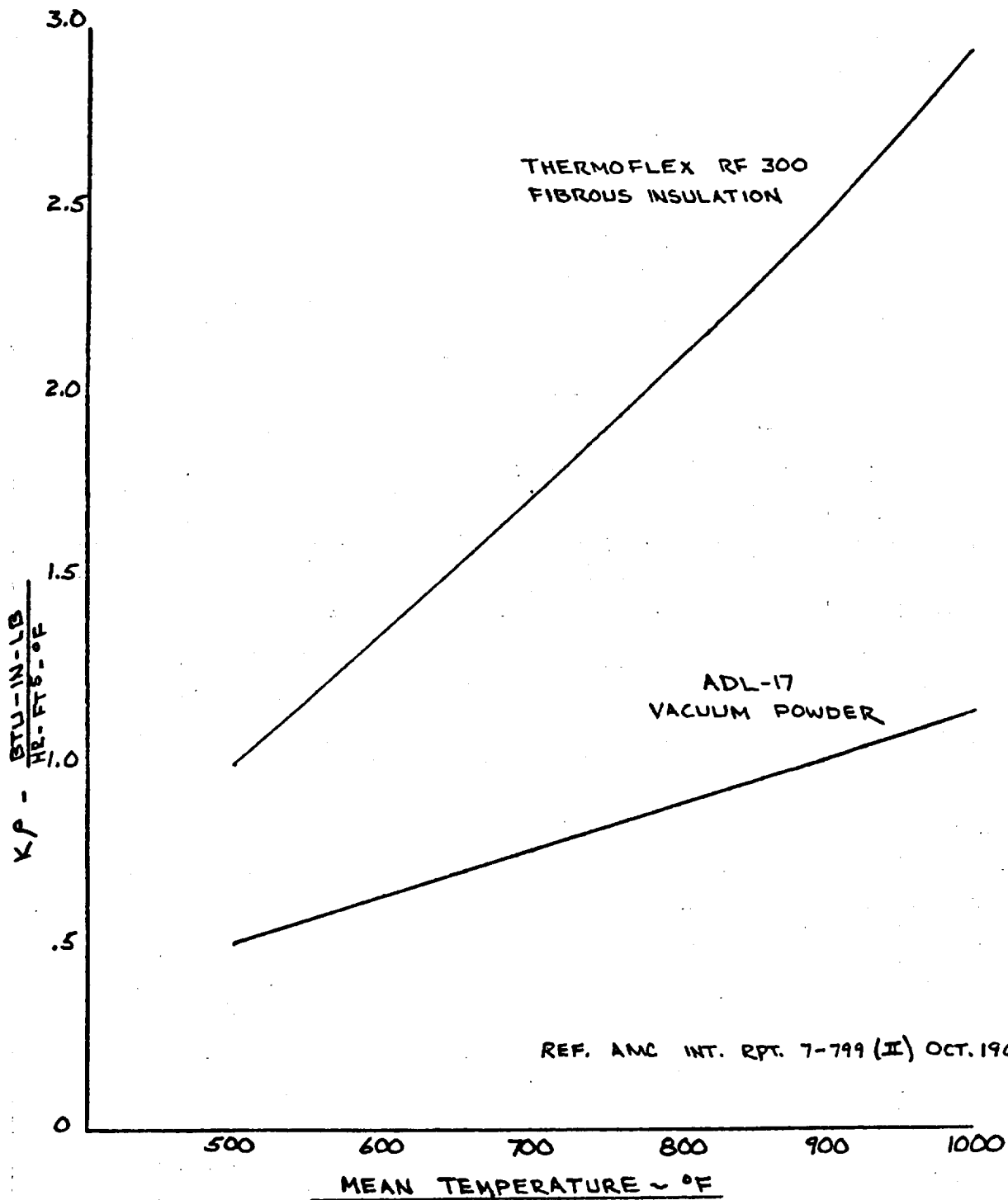
REF. - AWC. INT. RPT. 7-799 (II) OCT. 1960

HOT SIDE TEMPERATURE - °F

FIGURE 2

KP COMPARISON AT ALTITUDE

PRESSURE = 500 MICRONS



C. Resin Impregnated Ceramic Nose Cap

Activity in the area of resin impregnated ceramics was very limited due to lack of a good method of analyzing the material - either by IBM or by hand calculation. In an attempt to bracket the potential of the material, an analysis was performed using the data presented in the MLV report on mass loss rate as a function of surface temperature for a SiC foam impregnated with a phenolic resin. Steady state conditions were assumed and no attempt was made to calculate the heat conducted into the substructure. This analysis presented in the enclosed IDC is crude at best and is far from adequate to satisfy the immediate needs of APOLLO. The char layer ablator program currently being compiled for the 709 should relieve this situation if material properties are available.

It was also decided early in the APOLLO program that a large ceramic specimen should be fabricated as early as possible to demonstrate the construction of such heat shields and to gain experience in fabricating a large ceramic part. The material selected for this part was the phenolic resin impregnated SiC ceramic since it is much stronger, is less susceptible to mechanical or thermal shocks, and has a high heat rate input potential.

The part designed, and currently scheduled for completion by 1 April '60, was a 16 inch base chord segment of a 20 inch diameter sphere. The ceramic is laid up in modules bonded to a water cooled steel substructure. In the process of the assembly of this part fabrication methods and tools have been developed for the machining of the porous ceramics, and an improved method of resin impregnation has been developed. In all cases the methods and tools developed are applicable to any ceramic material and can therefore be quickly applied to any new designs with other materials such as  $Al_2O_3$  or  $ZrO_2$ .



Current plans are to test this part in the 14" hot gas jet  
now under construction if

- (a) the 14" calibration program yields results that  
would make such a test meaningful.
- (b) the final article manufactured is suitable for  
testing.
- (c) analysis of the material shows that such a test would  
have some merit.

Using basically the data presented in the MLV report by Strauss, an analysis of a resin impregnated ceramic material has been formulated using as the basic information the experimental mass loss rate measured by Strauss.

The results for the phenyl silane filled SiC ceramic are presented in carpet plot form for ease of use.

$\epsilon$  = emissivity of surface

$T_s$  = surface temperature  $\sim$   $^{\circ}\text{R}$

$\dot{m}_v$  = vaporized mass loss rate  $\sim \frac{\#}{\text{Ft.}^2 \text{ Sec.}}$

$\dot{m}_R$  = resin mass change rate  $\sim \frac{\#}{\text{Ft.}^2 \text{ Sec.}}$

$\dot{m}$  = total mass change rate  $\sim \frac{\#}{\text{Ft.}^2 \text{ Sec.}}$

$K_1$  = constant in blocking term

$K_2$  = constant in blocking term

$H_{ST}$  = stagnation enthalpy  $\sim \frac{\text{BTU}}{\#}$

$H_w$  = enthalpy of air at wall temp.  $\sim \frac{\text{BTU}}{\#}$

$h_p$  = heat of pyrolysis of resin  $\sim \frac{\text{BTU}}{\#}$

$T_v$  = pyrolyzation temperature of resin  $\sim$   $^{\circ}\text{R}$

$T_o$  = initial temperature of shield  $\sim$   $^{\circ}\text{R}$

$C_R$  = specific heat of resin and ceramic  $\sim \frac{\text{BTU}}{\text{\#}^\circ\text{F}}$

$C_C$  = specific heat of char and ceramic  $\sim \frac{\text{BTU}}{\text{\#}^\circ\text{F}}$

$C_v$  = specific heat of vaporized products  $\sim \frac{\text{BTU}}{\text{\#}^\circ\text{F}}$

$M$  = ratio of molecular weight of air  
to that of injected mass

In the MLV report, Strauss gives an experimental fit to the mass loss rate of a phenyl silane filled SiC foam material as

$$\dot{m}_v = 2.43 \times 10^{-4} (T_s - 2235) \quad T_s \sim ^\circ\text{R}$$

and also that for a typical brick the material percentages are

SiC - 28%

ZrO<sub>2</sub> - 10%

Resin - 62%

Using this data an equation is formulated for a total heat balance as

$$\begin{aligned} \dot{Q}_0 = & \textcircled{1} \epsilon \sigma T_s^4 + \dot{m}_v K_1 M^{K_2} (H_g - H_w) + \textcircled{2} h_p \dot{m}_a + \dot{m} C_R (T_v - T_0) + (\dot{m} - \dot{m}_c) \left( \frac{T_s - T_v}{2} \right) C_{Re} \\ & + \dot{m}_v C_v (T_s - T_v) \end{aligned}$$

- ① heat radiated away
- ② heat blocked by mass injection
- ③ heat absorbed in pyrolyzing resin
- ④ heat absorbed in raising resin and ceramic to pyrolyzation temperature
- ⑤ heat absorbed in raising temperature of char and ceramic
- ⑥ heat absorbed in raising vaporized mass up to surface temperature prior to injection

An example is presented where the values used were:

$$\dot{m}_w = 2.43 \times 10^{-6} \quad (T_s = 2235)$$

$$\epsilon = 0.80$$

$$K_1 = 0.71 \quad K_2 = 0.4 \quad M = 0.2$$

$$H_{wv} = 0.27 T_s \quad h_p = 1000 \quad \dot{m}_e = 2.22 \dot{m}_w$$

$$\dot{m}_i = 3.59 \dot{m}_w \quad T_v = 1860^\circ R \quad T_o = 0$$

$$C_{p1} = 0.21 \quad C_{p2} = 0.21 \quad C_{p3} = 0.40$$

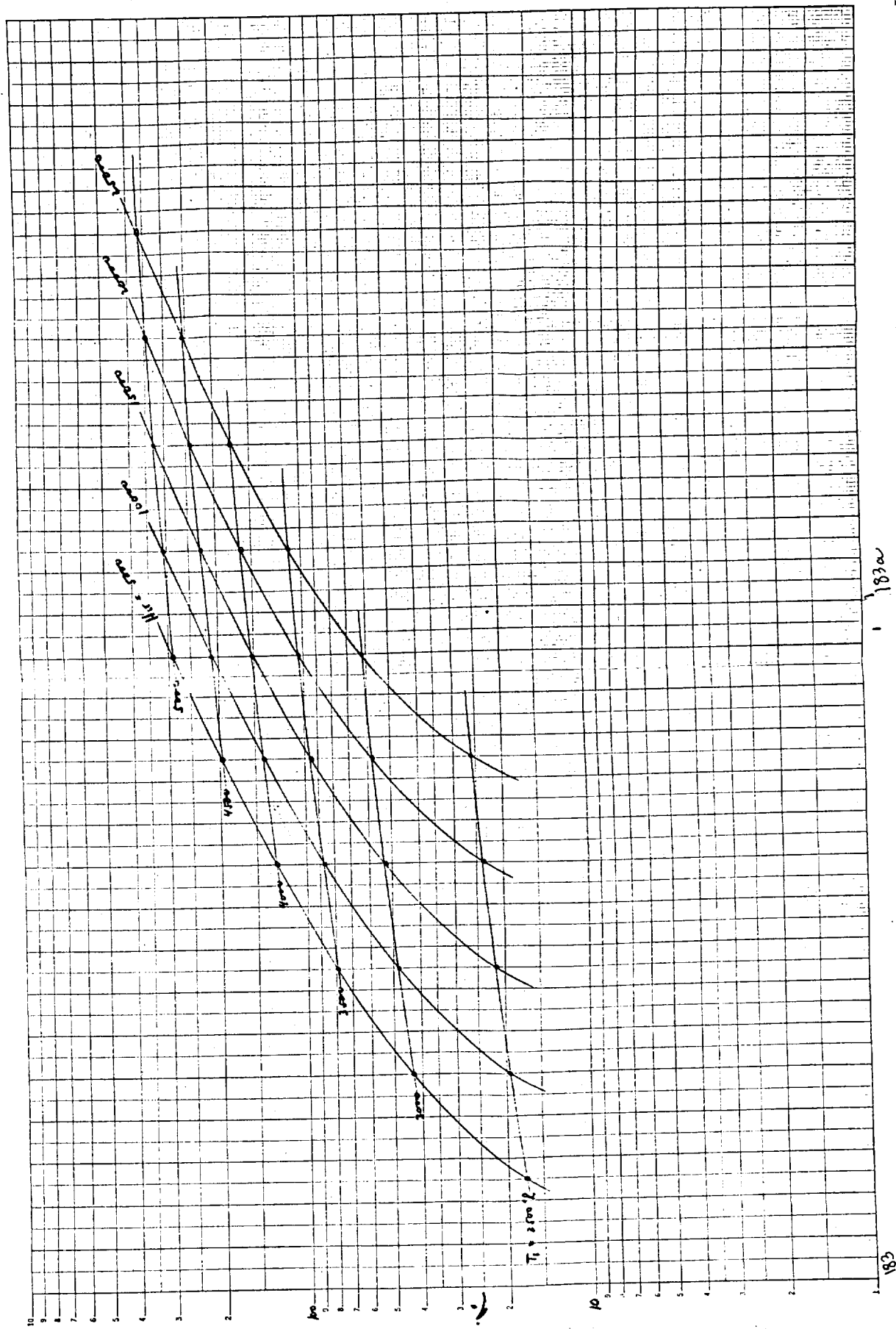
$$H_{ST} = 5,000, 10,000, 15,000, 20,000, 25,000$$

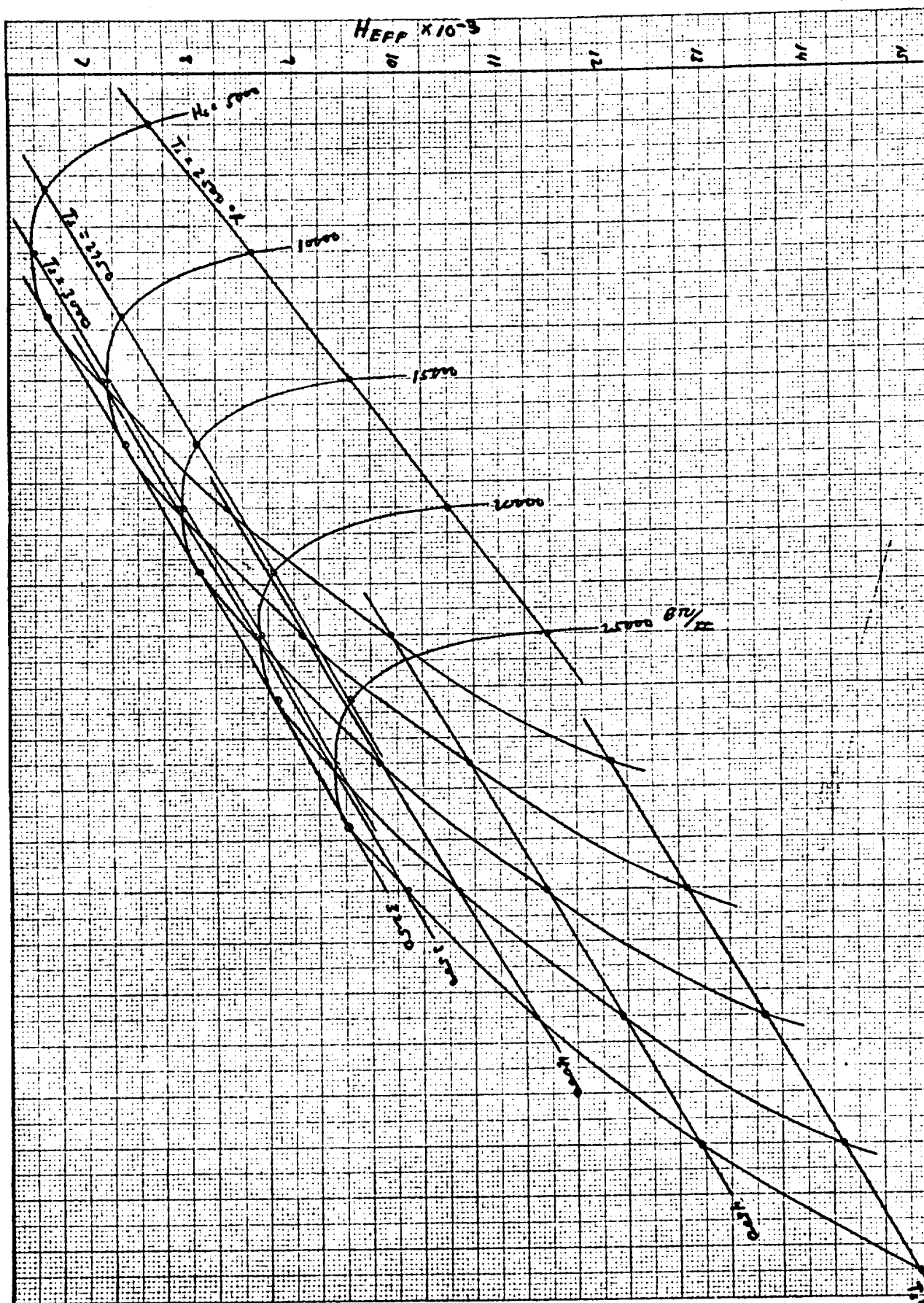
RESULTS IN  
FIGS. 1 & 2

For  $Q_o = 125 \text{ BTU}/\text{ft}^2 \text{ Sec}$ ,  $H_{ST} = 8000 \text{ BTU}/\text{#}$ , Figs 1 AND 2 YIELD

$$T_s = 3900^\circ R, \quad H_{eff} = 8600 \text{ BTU}/\text{#}$$

This compares with Strauss's analysis for about the same case  
of  $T_s = 3960^\circ R$  and  $H_{eff} = 8300 \text{ BTU}/\text{#}$ .





## TM-5 Part III

### Structural Cooling System

Basically, there are two possible approaches to the removal of heat flowing from the outer surface towards the primary structure during re-entry:

(1) Local evaporation of a coolant which is stored within the primary structural panels in quantities adequate to absorb the total heat flowing towards the respective panels during re-entry.

(2) Circulation of a secondary coolant within the primary structural panels, which serves as a carrier of heat from the structure to a remotely-located evaporative heat exchanger, where heat is dissipated by the evaporation of an expendable coolant.

The most suitable expendable coolant in both cases is water, which has the advantages of high latent heat, ready availability and suitable temperature characteristics for aluminum structures. Therefore, the weight of expendable coolant necessary for removal of the heat reaching the primary structure during re-entry is identical for both approaches. However, the difference lies in the equipment that are needed in conjunction with each approach. For the first, some type of wicking material is needed to retain the water before evaporation, as well as adequate passages to carry away the low density vapor to suitable locations where it can be ejected overboard. The equipment required in connection with the second approach include a coolant storage vessel, circulating pump, evaporative heat exchanger, manifolds and supports, etc.

It is quite likely that the second approach would involve a higher weight penalty than the first. However, it was selected for Apollo, on a preliminary basis, mainly due to its advanced stage of development.

This development effort, undertaken mostly by Bell Aircraft Corporation over the past few years, was preceded by a careful examination of direct evaporation schemes, which were found to be less desirable at the time. It is the intention of the Martin Company to re-assess the merits of direct evaporation schemes before making a final choice between a circulating system and a direct evaporation system. At this time, however, we shall base our weight estimates on the circulating system which rejects its heat through a remotely-located evaporative heat exchanger.

The principal items comprising the structural cooling system are (1) the evaporant, (2) storage tanks, (3) heat exchanger, (4) circulating pump, (5) residual coolant, (6) manifolds and supports and (7) valves, sensors and controls. The weights of the first two items are mainly dependent on the total cooling load (in Btu) for the overall mission. On the other hand, the weights of items (3), (4), (5) and (6) are strongly influenced by the maximum cooling rate ( $\text{Btu/sec ft}^2$ ) anticipated at some interval during the mission. The weight of item (7) is relatively independent of both the total cooling load and the maximum cooling rate.

Analysis shows that an optimum heat flow rate to the primary structure is realized when the weight of insulation required to produce that heat flow rate is equal to the weight of the cooling system necessary to dissipate that heat flow rate. In order to establish these weights, it was necessary to develop a factor representing the ratio of the cooling system weight (including the evaporant) to the evaporant weight.

Preliminary design calculations were performed, based on three different uniform cooling rates, namely  $\frac{1}{2}$ , 1 and  $1\frac{1}{2}$   $\text{Btu/sec ft}^2$ . Reasonable assumptions were made with regards to thermal conductivity, thickness and



configuration of primary structure, length and cross-section of coolant passages and headers, coolant flow velocity, maximum acceptable structural temperature and pressure drop in the expendable coolant exhaust circuit. Based on these assumptions, the cooling system weight factors were computed to be 2.73, 2.33 and 2.30, respectively for cooling rates of  $\frac{1}{2}$ , 1 and  $1\frac{1}{2}$  Btu/sec ft<sup>2</sup>.

Studies currently in progress are aimed at the determination of the variation of the cooling rate with respect to both location on the vehicle surface and mission time interval. With the results of these studies, it will be possible to develop a more refined estimate of the cooling system weight factor.

**Radiation Summary**

**TM-6**

A P O L L O  
Mid-Term  
R A D I A T I O N  
Technical Memorandum No. 6

THE MARTIN COMPANY  
Baltimore 3, Maryland

✓ March 13, 1961

In our earlier work, we had partially evaluated and scaled the design and operational implications of solar flare particles. Data obtained since that time have indicated that such outbursts may be more frequent than was estimated and that some of the characteristics that looked earlier to be common from event to event may be quite variable. These include possible variations in time of the energy spectrum and flux decays and also a lowering of the low energy limit to perhaps 1-2 Mev. The variability of the spectrum changes the radiation safety efficiency of any given shielding design and complicates the analysis and of course the increased frequency of these events has increased our concern for them.

We know most definitely what is required to give man the same degree of protection he has on earth  $\sim 1000 \text{ gm/cm}^2$  ( $2000\#/ft.^2$ ) - that is the shielding afforded by the earth's atmosphere. The questions are how much less than this is satisfactory and how do we provide this mass of shield. Looking at the second question first - the most obvious way to shield is to utilize the 15000 lbs. of the vehicle to the greatest extent possible. Previously our studies and all others that we had seen considered shielding within idealized spheres of elementary material - aluminum, carbon, etc. We have taken the actual M-1-1 and L2C configurations, broken them down into hundreds of area elements and used the actual materials (as many as eight different layers of inorganic compounds) to compare the shielding inside each of the command modules together with the effects of the mission and propulsion modules. This is illustrated in Figure 1. We have also considered a radiation shelter within the mission module.

The comparison indicates that the dose within the M-1-1 is about 78% of the dose within the L2C. More specifically considering the severe event that occurred following the class 3+ solar flare on May 10, 1959, the total incident proton dose would have been about 34 Rad. in the M-1-1 command module and about 43 Rad. in the L2C command module. The distribution of

dose over the surface of the spacecraft is shown in Figure 2.

In these calculations, we considered command module equipment uniformly spread out in the cabin. In the next step, we will use the results obtained without the equipment to guide us in positioning the equipment to give better radiation protection. This we can do easily by looking at the dose through each area element to determine where the additional masses of material could be most efficiently utilized.

The shielding afforded by the equipment is very significant. The calculations of dosage made without the equipment installed, of course, show higher doses but also emphasize the differences in the structural material shielding effects of the two configurations. Table I summarizes the results of these calculations.

TABLE I

PROTON DIFFERENTIAL SPECTRUM	DOSE INSIDE H-1-1 COMMAND MODULE		DOSE INSIDE L2C COMMAND MODULE		DOSE INSIDE MISSION MODULE STORM CELLAR BEHIND L2C (WITHOUT EQUIPMENT)		
	WITH EQUIPMENT	WITHOUT EQUIPMENT	WITH EQUIPMENT	WITHOUT EQUIPMENT	PLUS 2000 # A1	PLUS 1000 #A1	PLUS 500 #A1
-2.5 E@20-100 Mev. -4.8 E@101-700 Mev.			21.140 + 13.121 34.261				
-3.5 E@20-100 Mev. -4.8 E@101-700 Mev.			24.151 13.121 37.272				
-4.0 E@20-700 Mev.		$2.333 \times 10^2$	$3.289 \times 10$	$5.829 \times 10^2$			
-4.5 E@20-700 Mev.		$3.512 \times 10^2$	$3.886 \times 10$	$10.496 \times 10^2$			
-4.8 E@20-700 Mev.	33.6	$4.528 \times 10^2$	42.77	$14.89 \times 10^2$	4.04	14.2	67.5
-5.0 E@20-700 Mev.		$5.405 \times 10^2$	$4.620 \times 10$	$19.053 \times 10^2$			
-5.5 E@20-700 Mev.		$8.238 \times 10^2$	$5.487 \times 10$	$34.615 \times 10^2$			

Interior proton doses measured at the chest of the middle crewman (Rad.).

Data obtained using the measured spectrum following the solar flare on May 10, 1959. ( $E^{-4.8}$ ). For other spectra, the data are standardized to the flux of protons between the measurement interval of 110-220 Mev.

Within the M-1-1, the dose without considering attenuation through the on-board equipment would be 452.8 Rad. Within the L2C considered similarly, the dose within the command module would be 1489 Rad. A less detailed analysis was performed considering the dose inside the mission module behind the L2C configuration. At this point, the crew is heavily shielded front and back by the L2C and the massive tankage and propellants. The calculations showed that the dose decreased from about 67.5 Rad. to 14.7 Rad. to 4.04 Rad. as we wrap aluminum weights of 500, 1000 and 2000 lb. respectively in the form of an open ended cylinder within the mission module. The absorber thicknesses and dose distribution are shown on Figure 3. The axis of this "storm cellar" would coincide with the vehicle primary axis and its dimensions would be 46" dia. by 65" long. This analysis did not consider on-board equipment or material in the mission module. We may conservatively allow for this by reducing the aluminum shield plates by 350 lbs. It appears that the mission module "storm cellar" has merit, although there is a large variation in the dose distribution.

Since the energy spectrum may vary from the  $E^{-4.8}$  or  $E^{-5.0}$  once thought characteristic, we calculated the dose in Rad. for a number of different spectra. The manner in which the spectrum is changed is very critical to the result. For example, if we change the spectrum from  $E^{-2}$  to  $E^{-6}$  and keep the total number of particles above 10 Mev. constant, the number of particles between 10 Mev. (cut-off energy) and 100 Mev. (mean range in aluminum =  $10 \text{ gm/cm}^2$ ) would be  $10^4$  greater for the  $E^{-2}$  differential spectrum than for the  $E^{-6}$ . Therefore,  $10^4$  more particles would pass through  $10 \text{ gm/cm}^2$  of aluminum using the flatter spectrum than would pass through using the  $E^{-6}$  relationship. We changed the spectra by standardizing on the measured number of protons between 110-220 Mev. following the May 10, 1959 flare. This tends to conserve the energy flux and the observational data but enables us to evaluate the effects of variation in its distribution.

The fluxes were extended down to 20 Mev. (less than the mean range in the thinnest layer of either configuration) and up to 700 Mev.

Another factor involved in the spectral distribution is the RBE. Although the Rad. doses may be very comparable, there may be enough differences for the distribution of protons near termination energy (high RBE) to effect the mean RBE. We are presently calculating emergent energy spectra and will know both the mean RBE and also the dose for each area element. This will show us how the dose is distributed over essentially as many parts of the body as there are area elements. This is important because of the relative sensitivity of different organs. If necessary, we can also add in the man as a number of layers of appropriate material and evaluate the physical and biological dose at a number of depths into the body for each area element. The extent to which such detail will be necessary is dependent upon the variability around the mean emergent spectra (mean RBE) with and without the equipment together with the extent to which the equipment distribution can be optimized.

In the next few weeks, we will complete our analysis of secondary radiations and can evaluate the configuration and shielding with respect to these factors jointly. This will also include the particles that are present in the Van Allen belts. We have no indication to believe that the secondaries from solar flare protons will significantly increase the dose.

It appears at present that an event such as followed, the solar flare on May 10, 1959, will not expose the crew in these vehicles to more than 35-45 Rad. A small mass of "spot" or close proximity shielding can reduce the dose to 25 Rad. in the mission module. The question still remains as to whether this represents an adequate "design" event for Apollo. Our estimate for an event of this intensity or greater was twice in two years. For a 7-day mission, this is an encounter probability of less than 1/50.

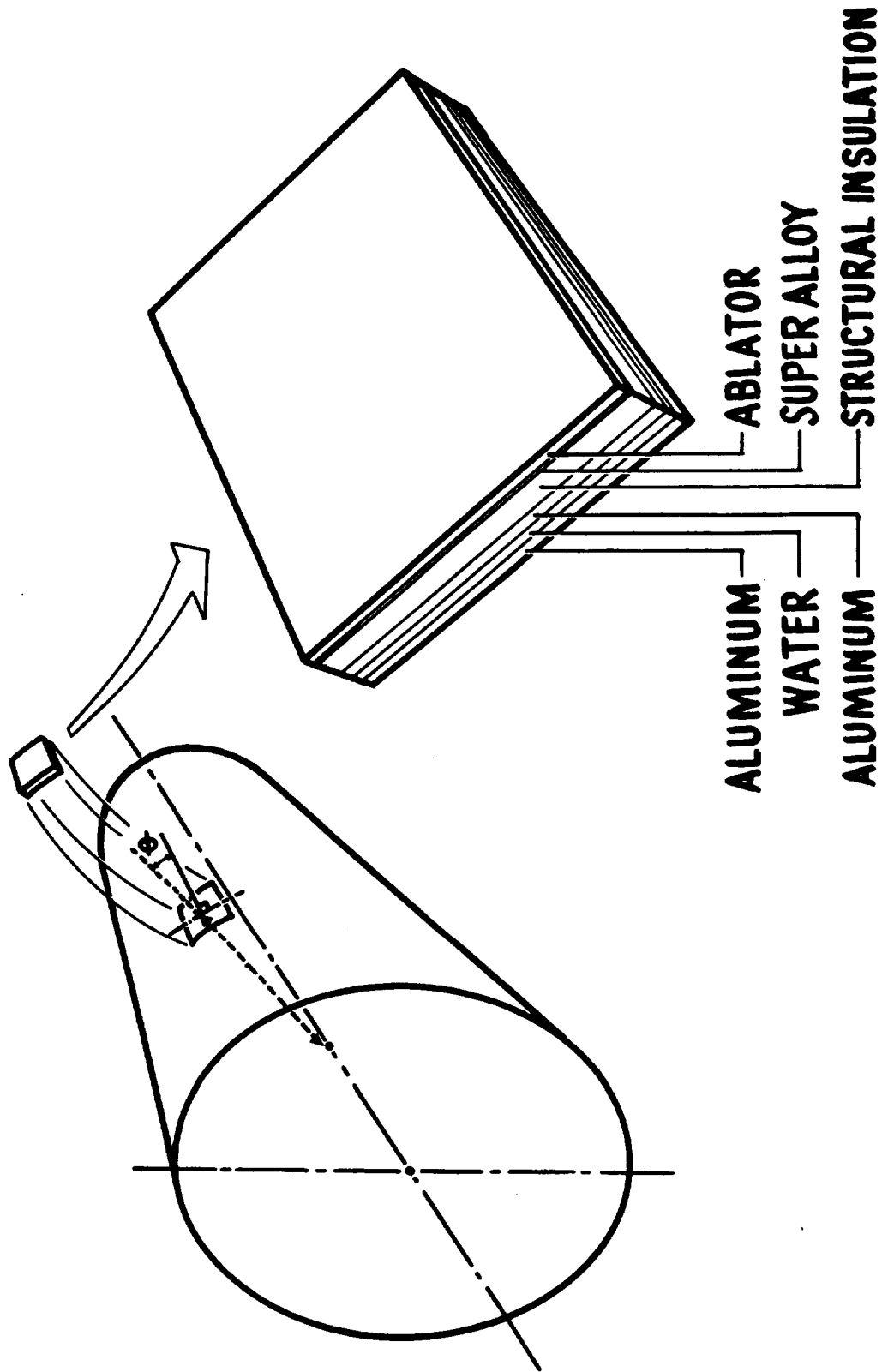
For a 14-day mission, the probability is about 1/27. If the frequency of



these events is much higher say 4 per year, then the probability of encounter becomes  $1/7$ . Until we have more data, we cannot definitely answer the first question- or how much less than 1 atmosphere of effective shielding is necessary. However, it still appears that a design adequate for the May, 1959 flare is sufficient.

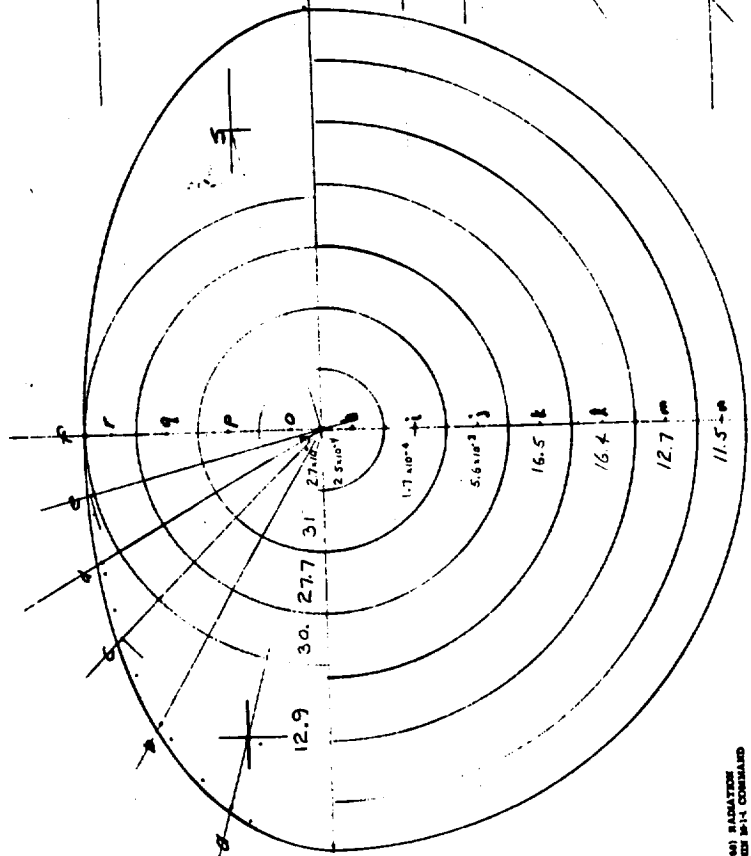
The prediction of specific flare events as an operational aid to Apollo does not as yet seem feasible within the next ten years. This does not preclude using indices of solar activity as launch schedule guides. Although less effective in reducing solar proton encounter probabilities, they are more feasible. There are at least a dozen different solar activity indicators in present use. Some of these go back over many years of record; others only to the IGY or more recently. The proper evaluation and utilization of such data may be expected to reduce the proton encounter probability by a factor of two to four. This utilization of solar "climatology" appears possible for Apollo whereas basing any hopes on specific predictions of solar "meteorology" is at present too optimistic.

CONFIDENTIAL



Radiation Dose Calculation Schematic

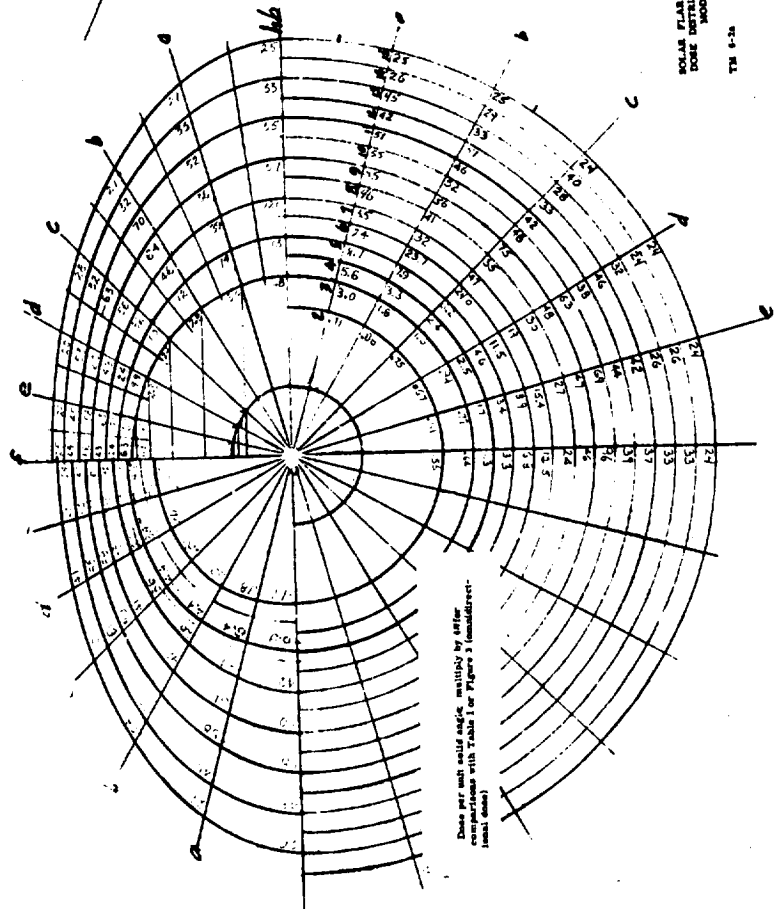
CONFIDENTIAL



SOLAR FLARE (RAY 18.1MM) RADIATION  
DOSE DISTRIBUTION WITHIN 1:1 CONICAL  
MODULE (RAD)

TM 6-34

1972

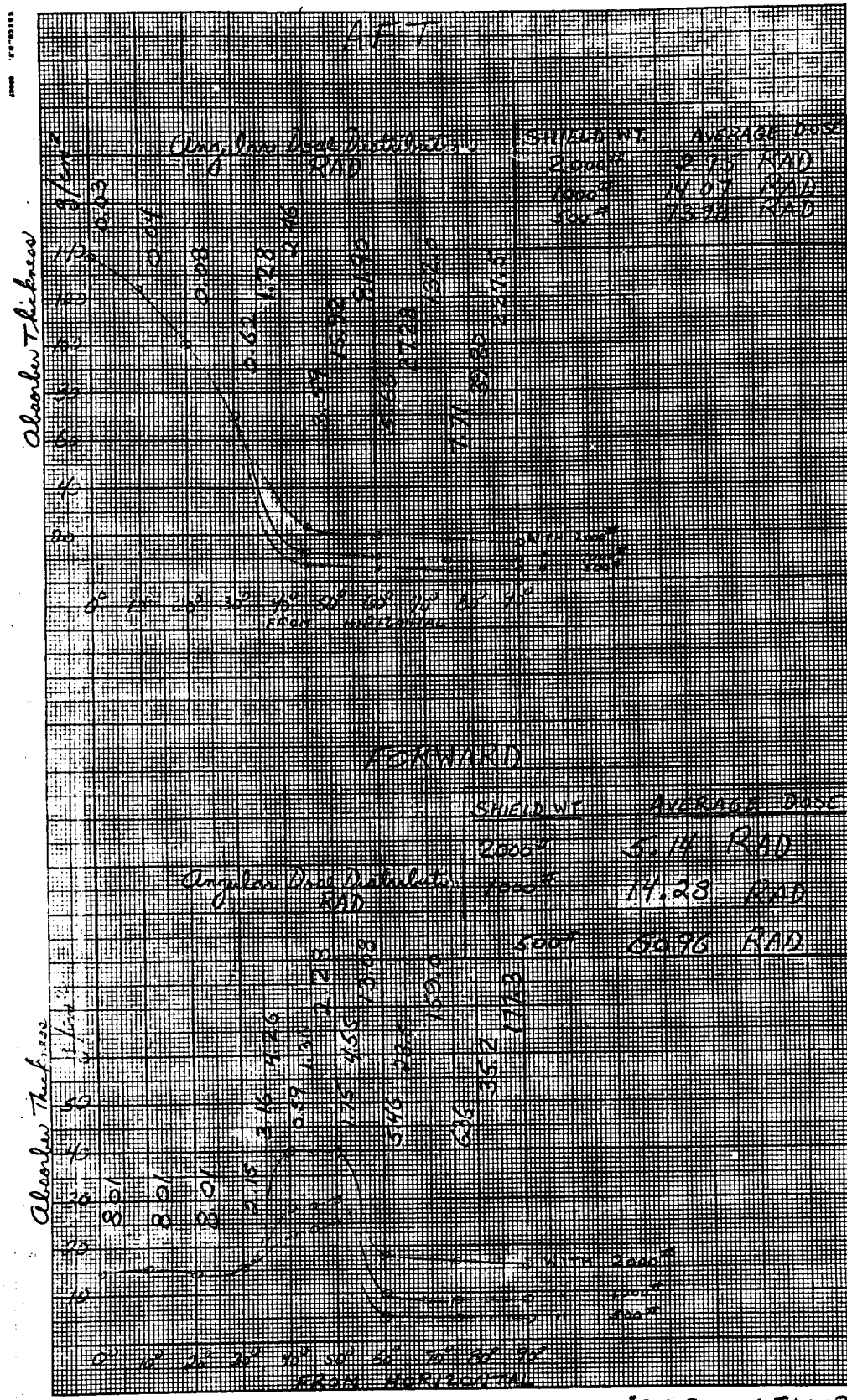


These per unit solid angle, multiplied by either  
cosine of angle with Table 1 or Figure 3 (normal direct-  
normal dose)

FRONT VIEW

197





SOLAR FLARE RADIATION DOSE INSIDE "STORM CELLAR"  
 L2C CONFIGURATION  
 TM 6-3  
 NO MISSION MODULE EQUIPMENT CONSIDERED  
 CLASS 3+ FLARE - 5/10/59

199w

191

Reliability Story

TM-7

~~CONFIDENTIAL~~

Technical Memorandum

TM - 7

Apollo Spacecraft Reliability Analysis

March 14, 1961

W. L. Hadley *and*

Apollo Spacecraft Reliability Manager

C. D. Hoover

Apollo Reliability Engineer

~~CONFIDENTIAL~~

## TABLE OF CONTENTS

	PAGE
INTRODUCTION	1
OVERALL VEHICLE RELIABILITY STATUS	2
RELIABILITY ANALYSES	
Recovery Gear and Communications	4
Flight Control	11
Power Subsystem	17
Display Instruments	21
Environmental Controls	26
Reaction Controls, and Mission Control and Abort Propulsion	34
Guidance	41
Structures	48
Communications and Telemetry	49
APOLLO MISSION RELIABILITY	52
CREW SAFETY	54
APPENDIX A- Reliability	



## Introduction

- I. The Apollo reliability effort emphasizes the successful accomplishment of seven technical tasks during the course of the complete program through lunar mission accomplishment. The scheduling, control and integration of these seven tasks with other program efforts is essential to their successful accomplishment. This technical memorandum covers work performed in completing the first two of the seven tasks: those involved with determination of numerical reliability requirements and with evaluation of alternate system designs to optimize reliability for the selected configuration.

A complete description of all seven tasks of the Apollo reliability effort is contained in the appendix of this technical memorandum.

## OVERALL VEHICLE RELIABILITY STATUS

Preliminary analyses of the various major subsystems comprising the Apollo System Spacecraft have been made. Reliability estimates for Apollo, along with assigned goals, are shown in Fig. 1.

Failure rates were based on data from equipments currently in use; items of equipment uncommon to current hardware were estimated on a basis of parts similarity. Equipment reliability values do not assume use of components of improved reliability. Mission times used were in accordance with current concept of a fourteen-day mission.

The primary purpose of the analyses made was to detect major problem areas and institute corrections in the design for these problems. In keeping with the known accuracy of predicted values of reliability at this phase in a program, major stress was placed on the value of reliability estimates for comparison purposes. This emphasis led to more significant conclusions in selecting the most favorable of several alternate system configurations.

From the early analyses, it was evident that major problem areas existed particularly in the Flight Control and Environmental Control Subsystems. In the Flight Control Subsystem, hydraulic leakage to hard vacuum during free flight constituted a serious reliability hazard; in the Environmental Controls Subsystem, gas leakage to hard vacuum caused the greatest reliability degradation.

Additionally, the former distribution of redundant equipment between the mission module and the command module resulted in serious reliability degradation. On equipment used during free flight and re-entry, redundancy would have been lost on separation prior to re-entry, and a non-redundant system required to operate throughout the total mission.

In the current design, necessary changes have been made to systems and to the distribution of equipment between the Mission and Command modules to improve the probability of mission accomplishment. Yet to be accomplished during the reliability study phase are the following tasks:

1. Safety analysis of the Apollo Spacecraft in conjunction with the Saturn Booster.
2. Continued reliability evaluation of alternate designs originating from system optimization studies.
3. Final reliability analysis of the recommended design and an estimate of the overall Apollo Spacecraft reliability.

The major problem area yet remaining is the Reaction Control and Mission Control and Abort Subsystem. In view of the fact that this subsystem analysis has just been completed, time has not been available to correct reliability discrepancies. With design changes indicated, this subsystem should meet the required goal.

From studies completed thus far, it is concluded that reliability values of the order of magnitude required are possible and within practical limits of achievement. Further refinements to the systems will alter estimated values slightly but are not expected to change the foregoing conclusion.

Structure	400	99.95	2000
Recovery, Repair & Communications	1	99.95	
Communications & Navigation	100	99.95	51.3
Guidance & Navigation	100	99.95	
Flight Control System	1	99.95	287
Reaction & Control Inboard Promissory	1	99.95	10.3
Power System	300	99.95	
Display Instruments	300	99.95	
Environmental Controls	300	99.95	
Crew	400	99.95	
Abort System	1000	99.95	
Overall Synecraft	480	99.95	84.91

\* Estimate based on contemplated changes

SECRET

## Recovery Gear and Communications

1. The configurations used in the first reliability analysis were based on the following:

a. Required items of equipment

- (1) MLV Feasibility Survey, Vol. I, Part 2
- (2) Apollo "Base line Recovery System"

b. Parachute Equipment

- (1) RSVP-2 Volume II-Mechanical Type System, Page VI-10
- (2) Dyna Soar I
- (3) "Base line Recovery System"

c. Descent Directional Control

- (1) Pilot operated, open parachute gore steering; simple drift sight and float lights for drift reference.

d. Landing Gear

- (1) "Base line Recovery System" - Helium-inflated bag with variable orifice vent

e. Ventillation Equipment and Electrical Power-

- (1) Currently planned systems

f. Oxygen Equipment

- (1) MLV Feasibility Survey, modified in conformance with currently planned systems

g. Communications, Pyrotechnics, and Survival Equipment

- (1) MLV Feasibility Survey

2. With an allocated mission reliability is 99.95%, the estimated reliability of the current configuration is 99.94%

3. Although no significant problem areas have been found, substantial reliability improvement can be achieved as follows:

a. Parachute Equipment

From the analysis (see Parachute Equipment Reliability Diagram) Lines and Fittings ( $f_0$  and  $f_{31}$ ) and Drogue Release ( $f_{32}$ ) contribute approximately 99% to the unreliability of the Parachute Equipment. It is recommended, therefore, that components be manifolded and prepackaged into a number of self-contained modular units so that a minimum number of lines and fittings will be employed and that necessary interconnecting lines may be short, welded units. Further, redundant drogue release components should be incorporated. It is estimated that these two changes alone will increase Parachute Equipment reliability from 7246 Missions between Failure to approximately 33,000 Missions between Failure; and that the Recovery Gear and Communications Subsystem "One Mission" Reliability will improve from 99.94% to approximately 99.95%.

b. Ventillation Equipment

From the Apollo Statement of Work; Para. 1.1.2.1.2 (c):

"Postlanding Survival Period. The spacecraft should be designed for crew survival for at least 72 hours after landing"

Present power available will permit operation of the ventillation system for a period of only 12 hours and not for a period of 72 hours.

If a 12 hour operating period is a requirement, then the presently contemplated ventilating equipment will contribute 37% to the unreliability of the Subsystem. Redundant ventilating equipment will reduce the ventillation equipment's contribution to unreliability to substantially zero, and improve Recovery Gear and Communications Reliability from 99.94% to approximately 99.96%. However, if the operating period requirement for the ventillation equipment is 72 hours, the present configuration will result on a total spacecraft mission reliability of 00% because of the total lack of power after 12 hours of the 72 hour survival period. Resolution of this problem is required at the earliest possible date.

4. A second reliability analysis was made of a modified Subsystem employing smaller main parachute canopies (70 ft/sec. descent rate) and retro rockets for final touchdown deceleration in place of the larger parachute canopies (30 ft./sec. descent rate) and landing bag for final touch-down deceleration. It appears

that a small gain in Subsystem reliability might be achieved (from an estimated 99.94% to 99.96%). There are, however, possible safety hazards involved with the modified Subsystem due to the higher descent rates, improper rocket-firing times, and fire hazard. Study is continuing and will be satisfactorily resolved on the final configuration.

# A P O L L O   S Y S T E M

## PRELIMINARY RELIABILITY ESTIMATE FOR SPACECRAFT

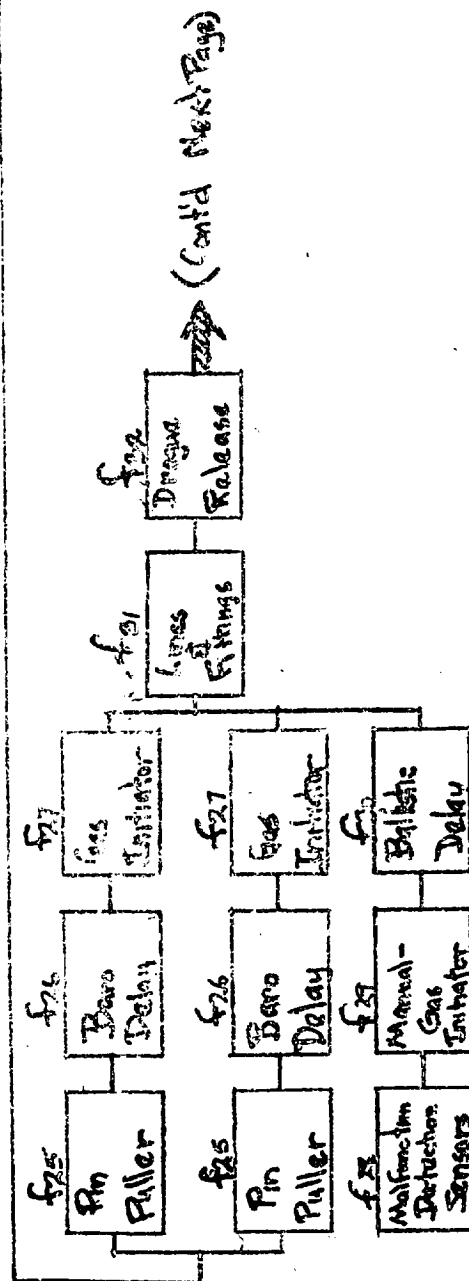
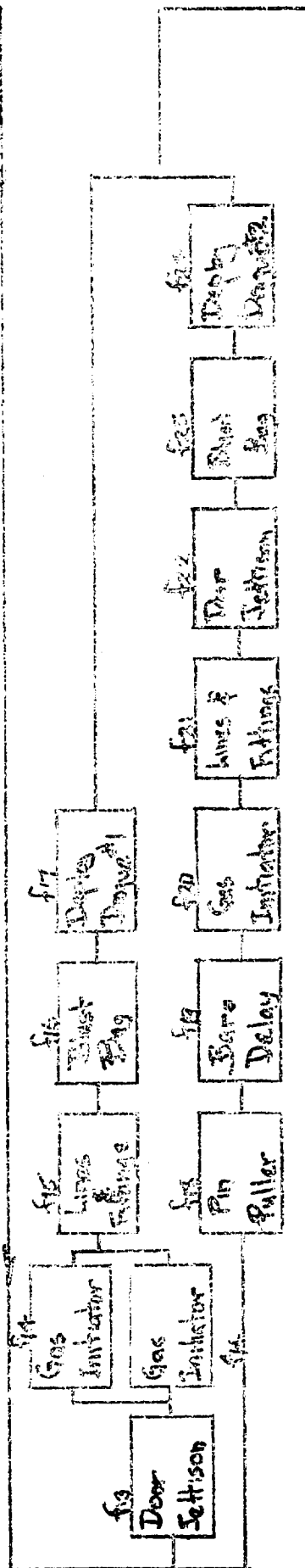
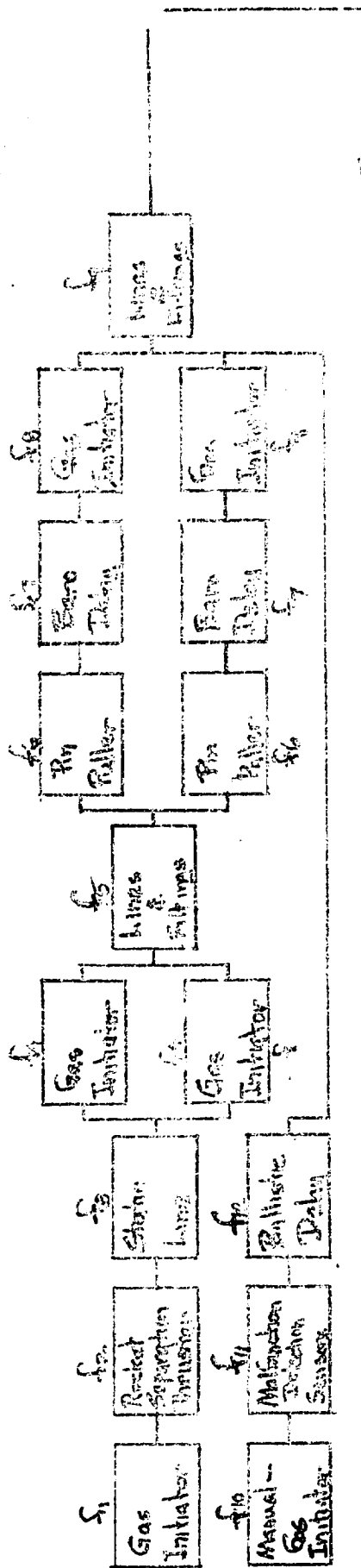
### RECOVERY GEAR AND COMMUNICATIONS

ONE MISSION RELIABILITY GOAL - 99.95%

ONE MISSION PREDICTED RELIABILITY - 99.94%

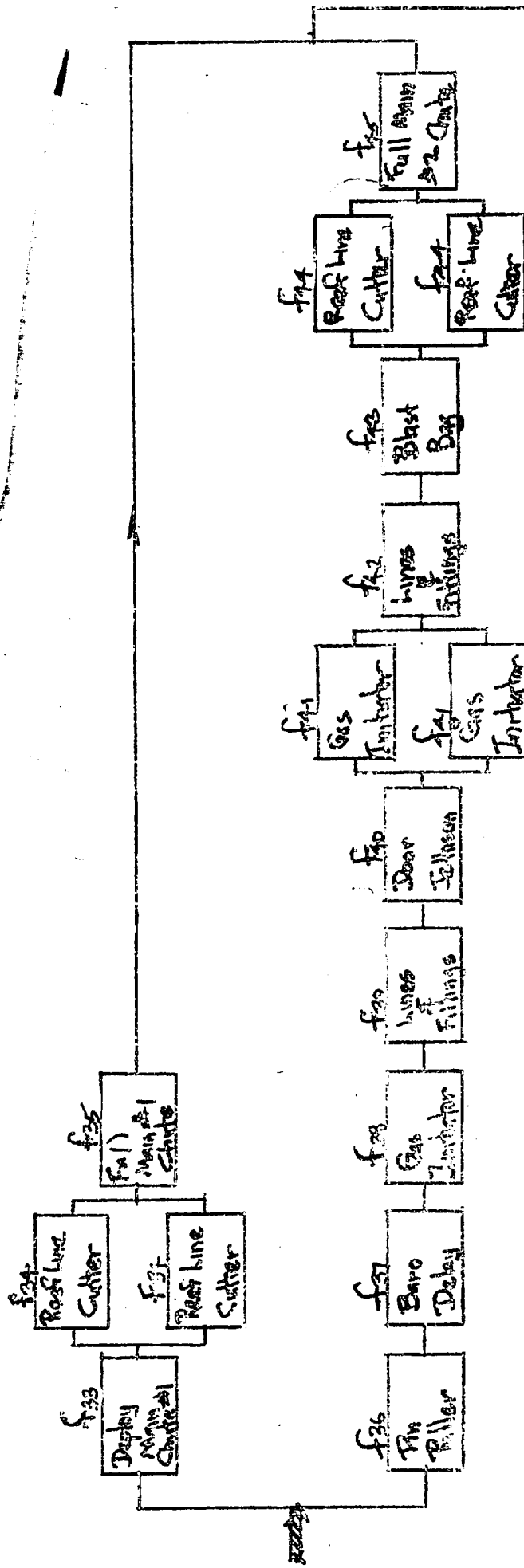
C O M P O N E N T	Operating Time Per Mission (Hrs)	Predicted Failure Rate per Mission	% of Total Subsystem Failure Rate per Mission	Predicted Reliability in Missions Be- tween Failure
Parachute Equipment	one cycle	.000138	21.296	7246
Descent Directional Control	0.2	.000015	2.315	66667
Landing Gear	one cycle	.000117	18.056	8547
Oxygen Equipment	0.4	.000055	8.488	18182
Ventillation Equipment	12	.000240	37.037	4167
Pyrotechnics, Explosives, Markers	one cycle	---	---	---
Electrical Power	12.4	.000010	1.543	100000
Radio/Radar (Comm & DF)	72.4	.000001	0.154	1000000
Survival Equipment	72	.000072	11.111	13889

# PARACHUTE EQUIPMENT RELIABILITY DIAGRAM



(Cont'd Next Page)





$$[f_1 + f_2 + f_3 + f_4]^2 + f_5 + (f_6 + f_7 + f_8)^2 [f_6 + f_7 + f_8]^2 + f_9 +$$

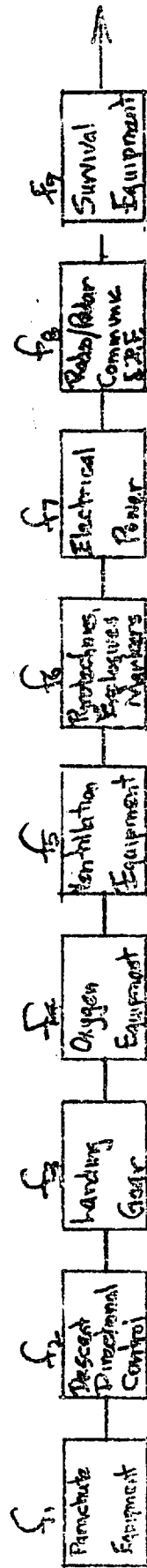
$$[f_{15} + (f_{14})^2 + f_{15} + f_{16} + f_{17}] (f_{18} + f_{19} + f_{20} + f_{21} + f_{22} + f_{23} + f_{24}) +$$

$$(f_{25} + f_{26} + f_{27})^2 (f_{28} + f_{29} + f_{30}) + f_{31} + f_{32} +$$

$$[f_{33} + (f_{34})^2 + f_{35}] [f_{36} + f_{37} + f_{38} + f_{39} + f_{40} + (f_{41})^2 + f_{42} + f_{43} + (f_{44})^2 + f_{45}] +$$

$$f_{46} (f_{47} + f_{48}) = \text{Mission failure rate} = .000135$$

# RECOVERY GEAR & COMMUNICATIONS RELIABILITY DIAGRAM



$$f_1 + f_2 + f_3 + f_4 + f_5 + f_6 + f_7 + f_8 + f_9 = \text{mission failure rate}$$

$$f_1 = 1/1000000 \quad t_1 = 0.2 \quad t_2 = 1 \text{ (cycle)} \quad t_3 = 0.4 \quad t_4 = 0.00055 \quad t_5 = 0.000240 \quad t_6 = 0.0001 \quad t_7 = 0.00010 \quad t_8 = 12.4 \quad t_9 = 12$$

$$f_1 t_1 = 0.00000038 \quad f_2 t_2 = 0.00015 \quad f_3 t_3 = 0.00017 \quad f_4 t_4 = 0.00055 \quad f_5 t_5 = 0.000240 \quad f_6 t_6 = 0.0001 \quad f_7 t_7 = 0.00010 \quad f_8 t_8 = 0.00012 \quad f_9 t_9 = 0.00012$$

$$= 0.000648$$

### Flight Control

1. The first reliability analysis for the flight control subsystem was based on the following:
  - A. Auto pilot and back up - Dyna Soar I.
  - B. Hydraulic Circuitry and Control - MLV Feasibility Survey, Vol. I, Part 2.
  - C. Hydraulic servo actuators and Surface Controls - RSVP-2, Vol. II.
2. With an allocated mission reliability of 99.65%, the estimated reliability of this configuration was only 93.06%.
3. Several reliability problems were encountered and had to be corrected as shown in the Flight Control Subsystem summary and the Reliability diagrams.
  - A. The six dual servo actuators were exposed, during free flight, to hard vacuum as well as temperature extremes for 338 hours; after which they were activated and used 1.2 hours during re-entry. Failures would have resulted from complete loss of hydraulic fluid with resultant out-gassing and destruction of organic seals, rod galling due to evaporation of hydraulic fluid lubricant, gas entrainment in the hydraulic fluid, etc. Hydraulic system degradation due to actuator leakage alone during free flight contributed 84.549% to the unreliability of the flight control and sub-system. The elimination of this source of unreliability by some means such as frangible or flexible actuator covers was necessary. If the leak failures could not be substantially reduced, it became expedient to consider other type control systems, i.e. hot gas servos, etc.
  - B. The auto pilot back-up switch and common electrical components each contributed 4.86% to control system unreliability. It was feasible to improve the missions between failure from 286 to 358 (threefold gain) by careful design and selection of components and parts.
  - C. The system employed one auto pilot and one manual back-up control system. Redundant auto pilots and/or manual back-up control would improve reliability from 93.06% to approximately 93.38%. Although this was a significant gain, it was small compared with the gain to be made by actuator leak elimination.
4. Design changes were made and the hydraulic flight control equipment were replaced by hot gas servo actuators; improved electrical

### Flight Control

components and redundant autopilots were also incorporated. A second reliability analysis (see Flight Control Subsystem - Hot Gas Summary and the accompanying Reliability Diagram) was made and reliability improved from 93.06% to 99.65%. This later estimate equals the goal; with careful design fabrication and use, it appears that no major problems will be encountered and that the goal could be met in the operational Apollo.

# A P O L L O   S Y S T E M

## PRELIMINARY RELIABILITY ESTIMATE FOR SPACECRAFT

### FLIGHT CONTROL SUBSYSTEM

ONE MISSION RELIABILITY GOAL        - 99.65%

ONE MISSION PREDICTED RELIABILITY - 93.06%

C O M P O N E N T		Operating Time per Mission	Predicted Failure Rate per Mission	% of Total Subsystem Failure Rate per Mission	Predicted Reliability in Missions Between Failure
Auto Pilot	Free Flight Orbit	338	.003552	4.936	282
	Reentry	1.2	.000004	0.006	250000
	Total	339.2	.003556	4.942	282
Auto Pilot Backup Switch	Free Flight Orbit	338	.003380	4.697	296
	Reentry	1.2	.000120	0.167	8333
	Total	339.2	.003500	4.864	286
Common Electrical	Free Flight Orbit	338	.003380	4.697	296
	Reentry	1.2	.000120	0.167	8333
	Total	339.2	.003500	4.864	286
Common Hydraulics-Reentry		1.2	.000252	0.350	3968
Servo Actuator Switch Reentry		1.2	.000180	0.250	5556
Actuator Hyd. Subsystem - Reentry		1.2	.000019	0.026	52632
Servo Actuators-Reentry		1.2	.000030	0.042	33333
Electrical Subsystems- Reentry		1.2	.000009	0.013	111111
Surface Controls-Reentry		1.2	.000072	0.100	13889
Hydraulic Leaks-Free Flight		338	.060840	84.549	16

CONFIDENTIAL

215

# A P O L L O   S Y S T E M

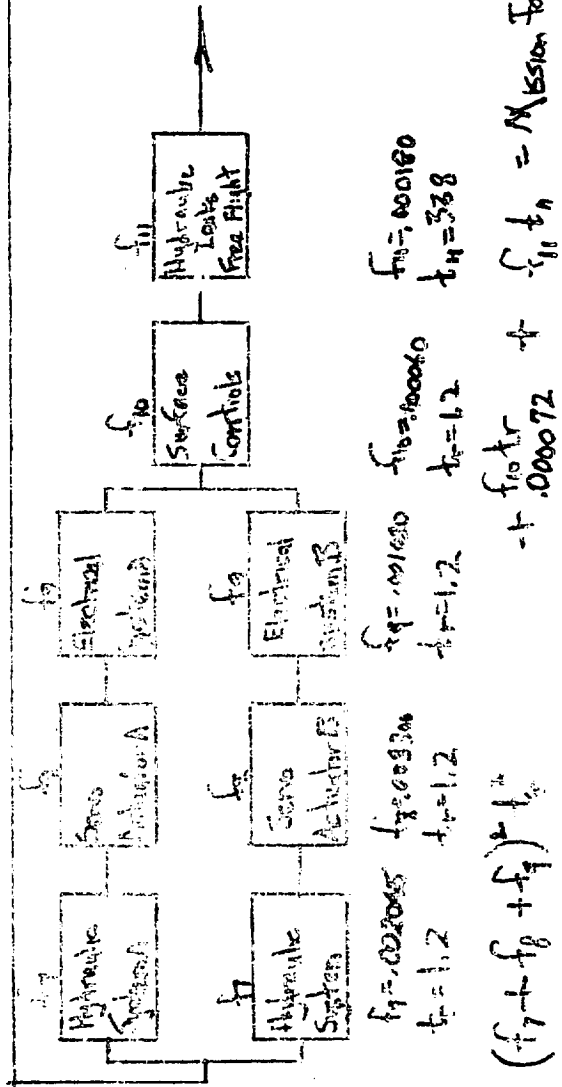
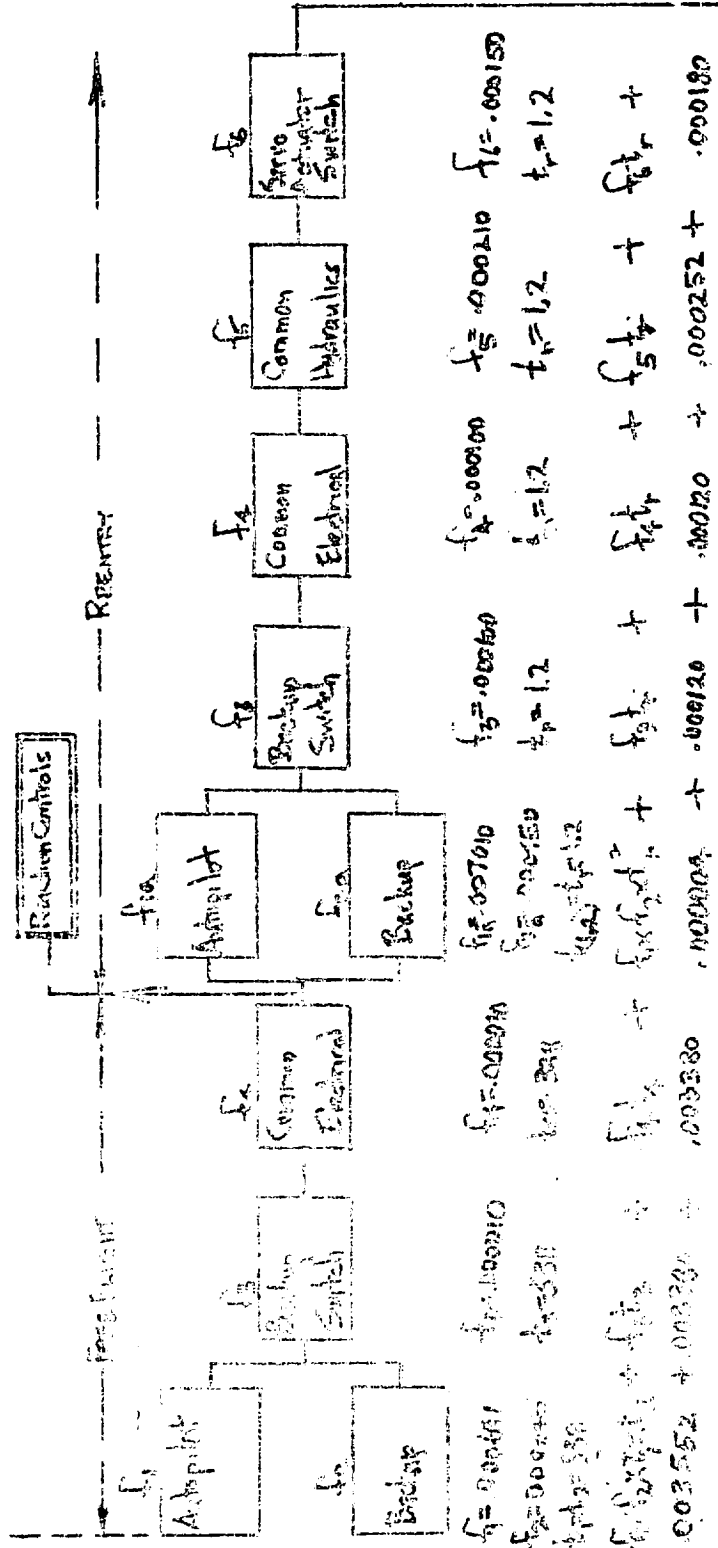
## PRELIMINARY RELIABILITY ESTIMATE FOR SPACECRAFT FLIGHT CONTROL SUBSYSTEM - HOT GAS

Goal - 99.65%  
Estimated - 99.65%

C O M P O N E N T		Operating Time per Mission	Predicted Failure Rate per Mission	% of Total Subsystem Failure Rate per Mission	Predicted Reliability in Missions Between Failure
Auto pilot with Manual Backup	Free Flight Orbit	338	.000010	0.28	100,000
	Reentry	1.2	0.000000	0	----
	Total	339.2	.000010	0.28	100,000
Common Electrical	Free Flight	338	.001690	48.55	592
	Reentry	1.2	.000060	1.72	16,667
	Total	339.2	.00175	50.27	571
Hot gas generator Reentry		1.2	.000580	16.66	1724
Servo actuator Switch Reentry		1.2	.000180	5.17	5556
Servo actuators - Reentry		1.2	.000870	24.99	1149
Electrical Subsystems Reentry		1.2	.000009	.25	111111
Surface Controls-Free Flight		1.2	.000072	2.07	13889

CONFIDENTIAL

# FLIGHT CONTROL SUBSYSTEM RELIABILITY DIAGRAM

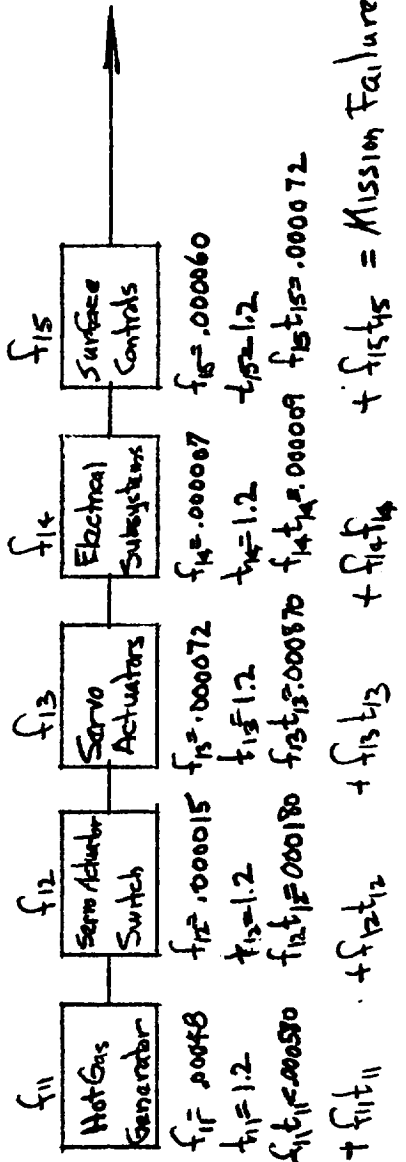
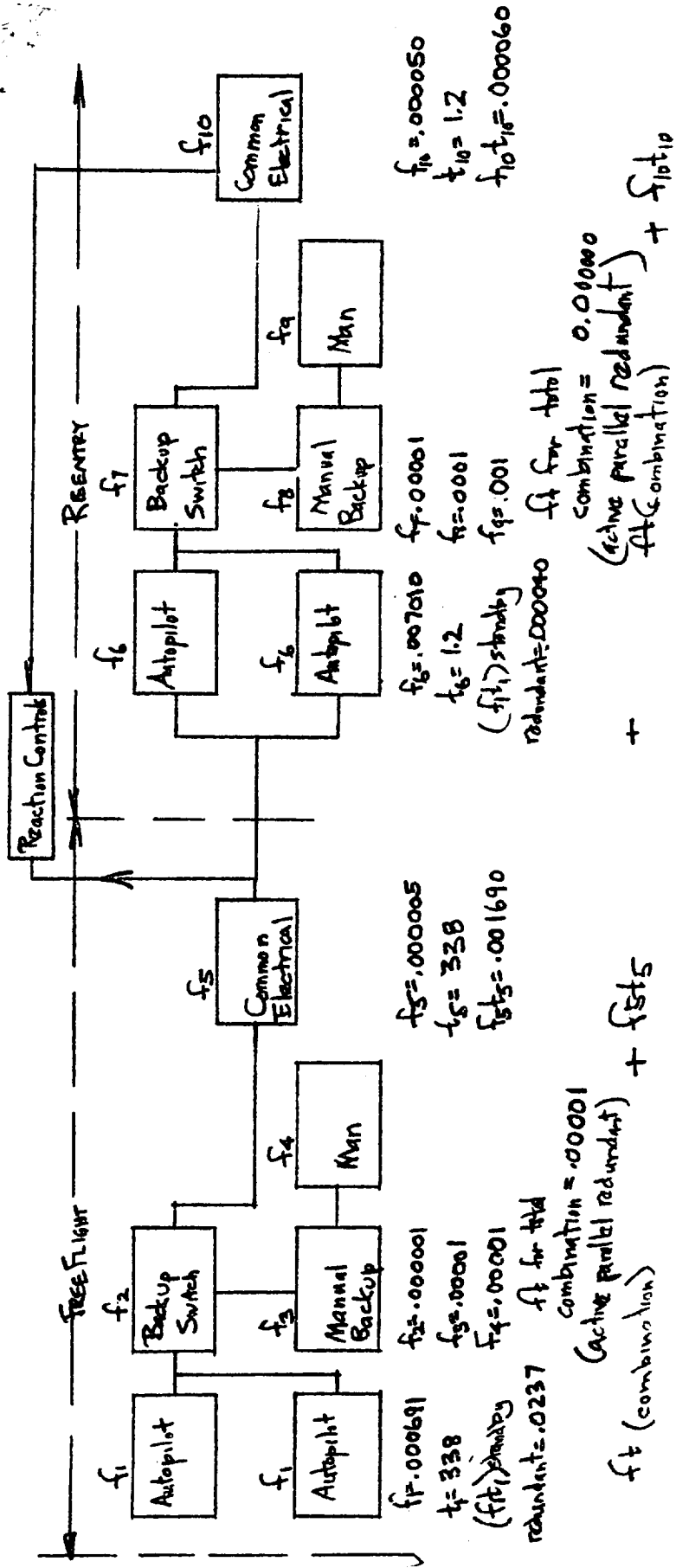


CONFIDENTIAL

217  $(f_1 + f_2 + f_3) \cdot t_1$

$f_{10} + f_{11} = \text{Mission Failure Rate}$

# FLIGHT CONTROL SUBSYSTEM (HOT GAS) RELIABILITY PROGRAM



CONFIDENTIAL



~~CONFIDENTIAL~~

Power Subsystem

1. The first reliability analysis for the power subsystem was based on the MLV Feasibility Survey, Vol. I, Part 2. In this configuration, primary electrical power was supplied from solar cells during illuminated flight and from reciprocating internal combustion engine D. C. generator power sources during periods of darkness; during reentry, the reciprocating engines coupled to the D.C. generators and to hydraulic pumps were used to meet reentry power loads. The total time of operation of the reciprocating engines was assumed to be approximately 4 hours.
2. With an allocated mission reliability of 98.75%, the estimated reliability of this first configuration was 98.74%.
3. No significant problem areas were noted from this analysis, although it appeared that improvement could be made in the following areas:
  - a. The static inverters, although redundant, contributed 35.8% to subsystem unreliability. Definite reliability improvement should be possible and reasonably expected.
  - b. The reciprocating engine hydraulic power equipment contributed approximately 50% to subsystem unreliability. It appeared possible that definite improvement could be made in this equipment.
4. Subsequent spacecraft design and mission employment changes have made power supply changes necessary. For example, hydraulic power requirements were eliminated when hot gas servo actuators were substituted for hydraulic servo actuators in the flight control subsystem; the elapsed time of flight during dark periods was increased substantially. It therefore became necessary to study alternate power sources in order to arrive at an acceptable spacecraft power configuration.
5. One electrical power source trade off study has been made comparing solar cells, thermoelectric generators, thermionic generators, and fuel cells (see comparison chart). These trade off studies will continue as necessary until the desired equipment have been selected. Reliability analyses of the complete power subsystem are being coordinated with trade off studies and will continue for the remainder of the period.

~~CONFIDENTIAL~~

APOLLO SYSTEM  
PRELIMINARY RELIABILITY ESTIMATE FOR SPACECRAFT

Power Subsystem

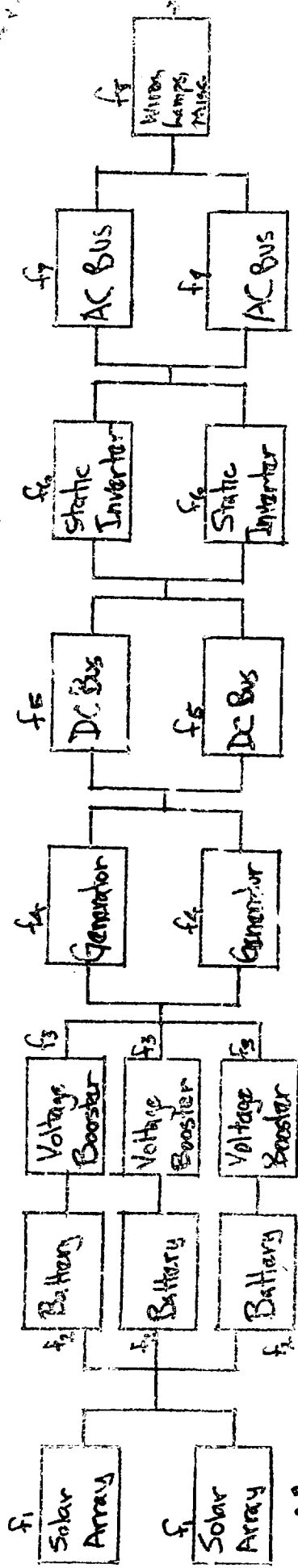
ONE MISSION RELIABILITY GOAL - 98.75%

ONE MISSION PREDICTED RELIABILITY - 98.74%

COMPONENT	Operating Time per Mission (Hrs)	Failure Rate Per Mission Predicted	% of Power Subsystem Failure Rate Per Mission	Predicted Reliability in Missions-Between-Failure
Solar Arrays	335	$7.17 \times 10^{-10}$	$6 \times 10^{-6}$	$1.395 \times 10^9$
Battery-Booster Combination	335	$1.24 \times 10^{-10}$	$1 \times 10^{-6}$	$8.064 \times 10^9$
Generators	3.65	$4.352 \times 10^{-7}$	.003	$2.29 \times 10^6$
D. C. Bus	335	---	---	---
Static Inverter	335	$4.48896 \times 10^{-3}$	35.8	223
A. C. Bus	335	---	---	---
Wires, lamps, switches, outlets, connectors, etc	335	$1.6850 \times 10^{-3}$	13.4	593
Reciprocating Engine / Hydraulic Power	3.65	$6.382199 \times 10^{-3}$	50.8	157

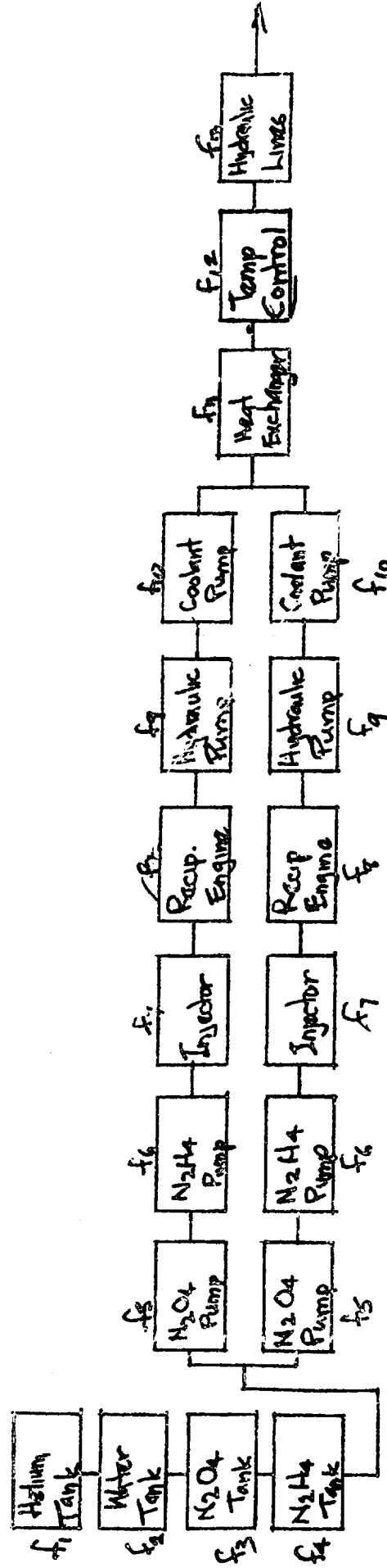
CONFIDENTIAL  
220

# POWER SUBSYSTEM RELIABILITY DIAGRAM



$$\frac{f_1^2}{4} + \frac{(f_2 + f_3)^2}{9} + f_4^2 + \frac{f_5^2}{4} + \frac{f_6^2}{4} + \frac{f_7^2}{4} + \frac{f_8^2}{4} = f_{\text{subsystem}}$$

## Electrical Power



$$f_1 + f_2 + f_3 + f_4 + (f_5 + f_6 + f_7 + f_8 + f_9 + f_{10} + f_{11} + f_{12} + f_{13}) = f_{\text{subsystem}}$$

CONFIDENTIAL

# A P O L L O   S Y S T E M

## COMPARISON OF ESTIMATED RELIABILITY OF VARIOUS TYPES OF PRIMARY ELECTRICAL POWER SOURCES

Primary Power Source Type		Call Connection Schematic	Parallel Elements Required	Parallel Elements Installed	Mission Operating Time (hrs)	Predicted Reliability-mission-between-failure
Solar Cells			10	10	340	150
			10	11	340	40,000
			10	12	340	10 <sup>7</sup>
Thermoelectric			8	8	340	1.8
			8	12	340	1522
FUEL CELLS	Single O <sub>2</sub> -H <sub>2</sub> eqpt, Fuel Cells & H <sub>2</sub> O Removal Eqpt (same)		40	40	340	25.6
	Two isolated single systems		40	80	340	685
	Parallel O <sub>2</sub> -H <sub>2</sub> eqpt., and H <sub>2</sub> O Removal eqpt, Fuel Cell of 42 elements		40	42	340	2857
Thermionic			8	8	340	1.4
			8	12	340	1180

CONFIDENTIAL

## DISPLAY INSTRUMENTS

1. The display instruments configuration used in the reliability analysis are based on the MLV Feasibility Survey, Vol. I, Part 2.
2. It has been assumed that they are necessary for the safe conduct of the mission and are therefore classed as a subsystem. Additionally, various other subsystems are equipped with instruments necessary for proper equipment operation - these instruments are separate from the display instruments and their unreliability has been charged against their respective subsystems.
3. The types of displays that will ultimately be used have been assumed to be as follows:
  - a. Galvanometer Type
    - (1) Velocity
    - (2) Altitude
    - (3) Position and Course
    - (4) Structural Temperature with Thermocouples
    - (5) Control Position
    - (6) Electrical power, Voltage and Current
    - (7) Cabin Temperature
  - b. Cathode Ray Tube
    - (1) Attitude
  - c. Bourdon Type Pressure Gage
    - (1) Suit Pressure
  - d. Cabin pressure indicators use a pressure transducer and a galvanometer type indicator. Rate of change of pressure is indicated by an aneroid type indicator similar to a rate of climb indicator.
  - e. CO<sub>2</sub> partial pressure and O<sub>2</sub> partial pressure is indicated by Beckman Instruments Inc. gas analyzers consisting of CO<sub>2</sub> and O<sub>2</sub> sensors, high gain amplifiers and galvanometer type meters.
4. As shown in the Display Instruments summary, single instrument reliabilities were first analyzed (Non-Redundant I) (see Reliability Diagram I-no redundancy). The one mission predicted reliability for the non-redundant equipments was 97.69%, well below the goal of 99.55%.
5. By adding redundancy to those instruments which operate for 340 hrs. during the mission, (see Reliability Diagram II-limited redundancy), the one mission estimated reliability was improved to 99.96%.

CONFIDENTIAL

DISPLAY INSTRUMENTS

6. It was concluded that the reliability goal could be met and probably exceeded if adequate redundancy is maintained while using simple standard aircraft type instruments. It must be pointed out that the choice of complex sophisticated instruments could substantially reduce reliability.

CONFIDENTIAL

A P O L L O   S Y S T E M  
PRELIMINARY RELIABILITY ESTIMATE FOR SPACECRAFT  
DISPLAY INSTRUMENTS

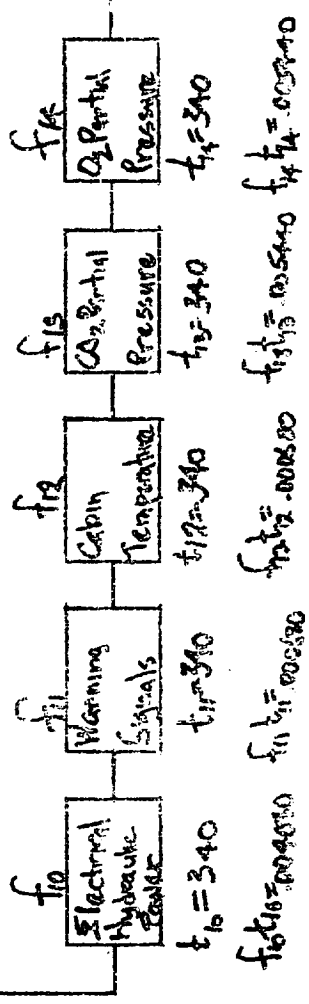
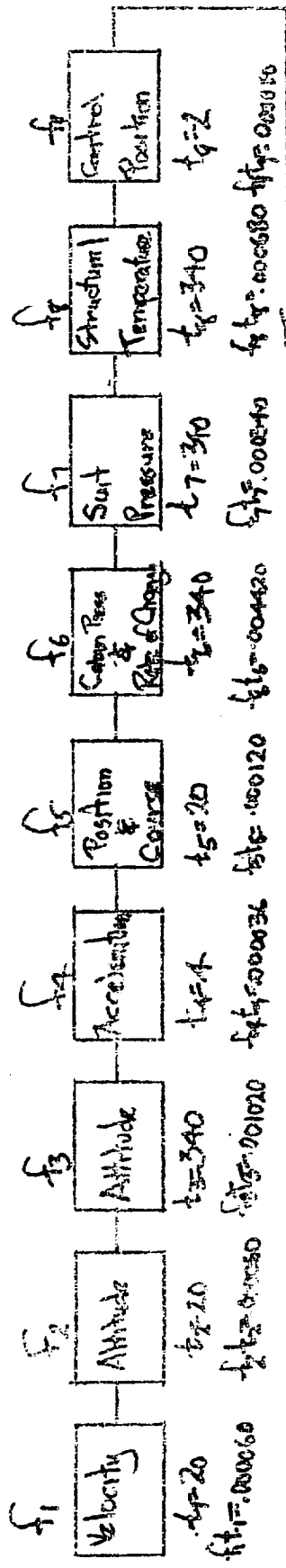
ONE MISSION RELIABILITY GOAL - 99.55%

ONE MISSION PREDICTED RELIABILITY { Non-Redundant - 97.69%  
Limited Redundancy - 99.96

C O M P O N E N T	Opr Time per Mis- sion hrs	Non-Redundant I			Limited Redundancy II		
		Predicted Failure Rate per Mission	% Total Subsystem Failure Rate per Mission	Predicted Reliabil- ity in Mis- sions Be- tween Fail	Predicted Failure Rate per Mission	% Total Subsystem Failure Rate per Mission	Predicted Reliabil- ity in Missions Bet. Failure
Velocity	20	.000060	0.259	16667	.000060	13.216	16667
Altitude	20	.000060	0.259	16667	.000060	13.216	16667
Attitude	340	.001020	4.409	980	.000001	0.220	1000000
Acceleration	4	.000036	0.156	27778	.000036	7.930	27778
Position & Course	20	.000120	0.518	8333	.000120	26.432	8333
Cabin Pressure & Rate of Change of Pressure	340	.004420	19.104	226	.000019	4.185	52632
Suit Pressure	340	.000340	1.470	2941	.000000	0.0	---
Structural Temp.	340	.000680	2.939	1470	.000000	0.0	---
Control Position	2	.000080	0.346	12500	.000080	17.621	12500
Electrical/Hydraulic Power	340	.004080	17.635	245	.000017	3.744	58824
Warning Signals	340	.000680	2.939	1471	.000001	0.220	1000000
Cabin Temperature	340	.000680	2.939	1471	.000000	0.0	---
CO <sub>2</sub> Partial Pressure	340	.005440	23.513	184	.000030	6.608	33333
O <sub>2</sub> Partial Pressure	340	.005440	23.513	184	.000030	6.608	33333

~~CONFIDENTIAL~~

# DISPLAY INSTRUMENTS RELIABILITY DIAGRAM (NO REDUNDANCY)



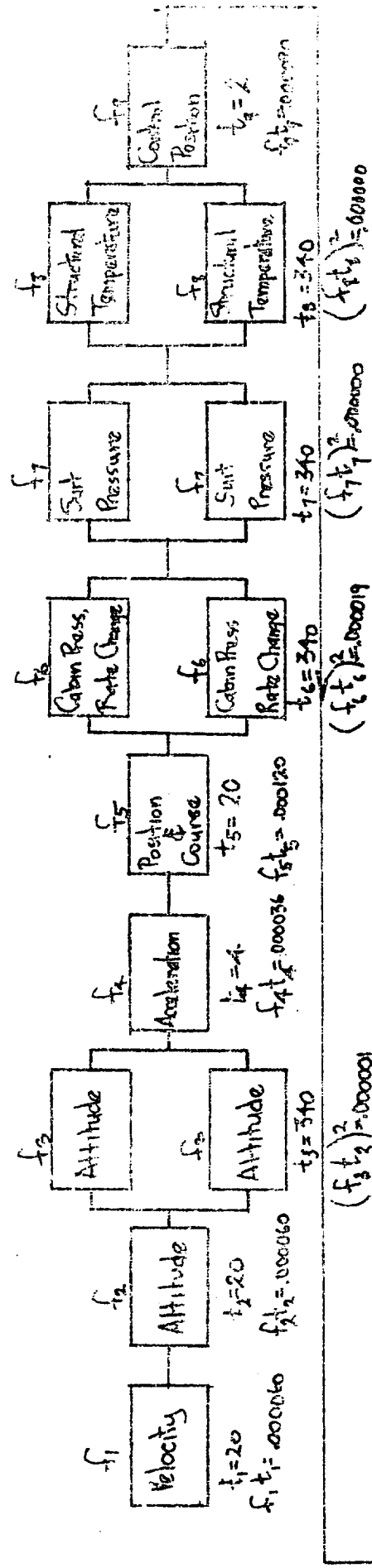
$$f_1 t_1 + f_2 t_2 + f_3 t_3 + f_4 t_4 + f_5 t_5 + f_6 t_6 + f_7 t_7 + f_8 t_8 + f_9 t_9 + f_{10} t_{10} + f_{11} t_{11} + f_{12} t_{12} + f_{13} t_{13} + f_{14} t_{14} = \text{Mission Failure rate}$$

$\Sigma = .023136$



# DISPLAY INSTRUMENTS RELIABILITY DIAGRAM (REDUNDANCY EMPLOYED FOR

INSTRUMENTS IN USE FOR 340 HOURS.) III



$$f_1 t_1 + f_2 t_2 + (f_3 t_3)^2 + f_4 t_4 + f_5 t_5 + (f_6 t_6)^2 + (f_7 t_7)^2 + (f_8 t_8)^2 + f_9 t_9 + (f_{10} t_{10})^2 + (f_{11} t_{11})^2 + (f_{12} t_{12})^2 + (f_{13} t_{13})^2 + (f_{14} t_{14})^2 + (f_{15} t_{15})^2 =$$

~~Failure rate~~

$$= 0.000454$$

## ENVIRONMENTAL CONTROLS

1. The first reliability analysis for the environmental control subsystem was based on the MLV Feasibility Survey, Vol. 1, Part 2 plus the addition of a molecular sieve CO<sub>2</sub> absorbing device.
2. With an allocated mission reliability of 98.5%, the predicted reliability of the original configuration was 83.88%. The failure rate required reduction by a factor of 11.7 in order to meet the goal.

Analysis indicated that significant gains in reliability could be made in the following areas:

### a. Molecular Sieve

- 1) From published data, it appeared that both the synthetic zeolite and the silica gel cycle absorption times could be modified so that the equipment could operate at a reduced capacity in case of partial subsystem failure. By slight changes in plumbing, operation with greatly improved reliability could be achieved. This would not increase the electrical load.
- 2) Three of six valves were continuously exposed to hard vacuum. If this number would be reduced, significant gain in reliability and safety would result. Further, a reduction in weight might be realized since hard vacuum plumbing would be heavier than ventilation ductwork.
- 3) Silica gel heaters heat 100% of air passing through the system. Direct oven type heating with minimum air circulation can be equally as effective. No gain in direct system weight but a significant reduction in electrical and heat exchange loads can be realized. This would directly improve power system reliability (greater safety margin).
4. It appeared that the controls system could be simplified and some redundancy incorporated. Further, standby means could be incorporated to permit manual operation of the system.

### b. Gas Supply

The mission module is intended to be discarded prior to re-entry. This technique makes the location of redundant equipment critical since a backup system

may have to be discarded when it is critically needed. Those backup systems needed for re-entry, therefore, must be located in the command module. In the original configuration, the backup oxygen and nitrogen supplies were located in the "throw away" mission module. In the current configuration, a high pressure backup supply has been incorporated in the command module for use during re-entry or during any emergency. ,

3. After the incorporation of changes, a reliability analysis was made of the second configuration. This design incorporated the following modifications.
  - a. Coolant circulating pumps were changed from positive displacement pumps to submerged centrifugal pumps.
  - b. Rearrangement of plumbing
  - c. Manual cycling of the molecular sieve
  - d. Modification of valves in the molecular sieve
  - e. Reduction in the number of lines and fittings by use of welded plumbing in modular equipment units
  - f. Use of gaseous  $N_2$  and  $O_2$  equipment for reentry gas supply.
4. In order to take full advantage of the molecular sieve modifications, a redundant blower had to be added; without it, a 1% reduction in reliability was estimated.
5. The second configuration analyzed has an estimated reliability of 99.54%, somewhat better than the subsystem goal of 98.50%. In view of the results of this analysis, it appears that the operational Apollo Spacecraft should meet its reliability goal.

# A P O L L O   S Y S T E M

## PRELIMINARY RELIABILITY ESTIMATE FOR SPACECRAFT

### ENVIRONMENTAL CONTROLS SUBSYSTEM

ONE MISSION RELIABILITY GOAL      98.50%

ONE MISSION PREDICTED RELIABILITY   83.88%

Date December 14, 1960

COMPONENT	Operating Time per Mission	Predicted Failure Rate per Mission	% of Total Subsystem Failure Rate per Mission	Predicted Reliability in Missions Between Failure
Ground Cooling (in use)	4	.0000424	0.0241	23600
Ground cooling flight degradation of reliability	336	.0008736	0.4972	1150
TOTAL Ground Cooling, Ground & Flight	340	.0009160	0.5213	1090
Molecular Sieve	340	.1013440	57.6723	9.86
Cabin & Equipment Cooling - Launch & Free Flight	339	.0151919	8.6453	66
Cabin & Equipment Cooling - Re-entry	1.2	.0002486	0.1414	4000
TOTAL Cooling Equipment	340	.0154405	8.7867	65
Oxygen Supply - Launch & Free Flight	339	.0088619	5.0431	113
Oxygen Supply - Re-entry	1.2	.0001748	.0994	5720
TOTAL Oxygen Equipment	340	.0090367	5.1425	111
Nitrogen Supply - Launch & Free Flight	339	.0052306	2.9766	190
Nitrogen Supply - Re-entry	1.2	.0001032	.0587	9700
TOTAL Nitrogen Equipment	340	.0053338	3.0353	188
Humidity Control - Launch & Free Flight	339	.0017990	1.0238	556
Humidity Control - Re-entry	1.2	.0000354	.0201	28250
TOTAL Humidity Control Eqpt.	340	.0018344	1.0439	545
Atmospheric Residuals - Launch & Free Flight	339	.0001333	0.0758	7500
Atmospheric Residuals - Re-entry	1.2	.0000024	.0014	416000
TOTAL Atmospheric Residuals Equipment	340	.0001357	0.0772	7380

C O M P O N E N T	Operating Time per Mission	Predicted Failure Rate per Mission	% of Total Subsystem Failure Rate per Mission	Predicted Reliability in Missions Between Failure
Lines, Fittings, Controls - Launch & Free Flight	339	.0020989	1.1944	476
Lines, Fittings, Controls - Re-entry	1.2	.00004114	.0236	24100
TOTAL Lines, Fittings, Controls	340	.0021403	1.2180	467
Tunnel - Re-entry	1.2	.0000120	0.0068	83300
Separation Coupling, Valves	1.2	.0001512	0.0860	6620
Re-entry Cooling Degradation During Free Flight	336	.0393792	22.410	25

# A P O L L O   S Y S T E M

## PRELIMINARY RELIABILITY ESTIMATE FOR SPACECRAFT

### ENVIRONMENTAL CONTROLS SUBSYSTEM

ONE MISSION RELIABILITY GOAL            98.50%  
 ONE MISSION PREDICTED RELIABILITY    99.54%

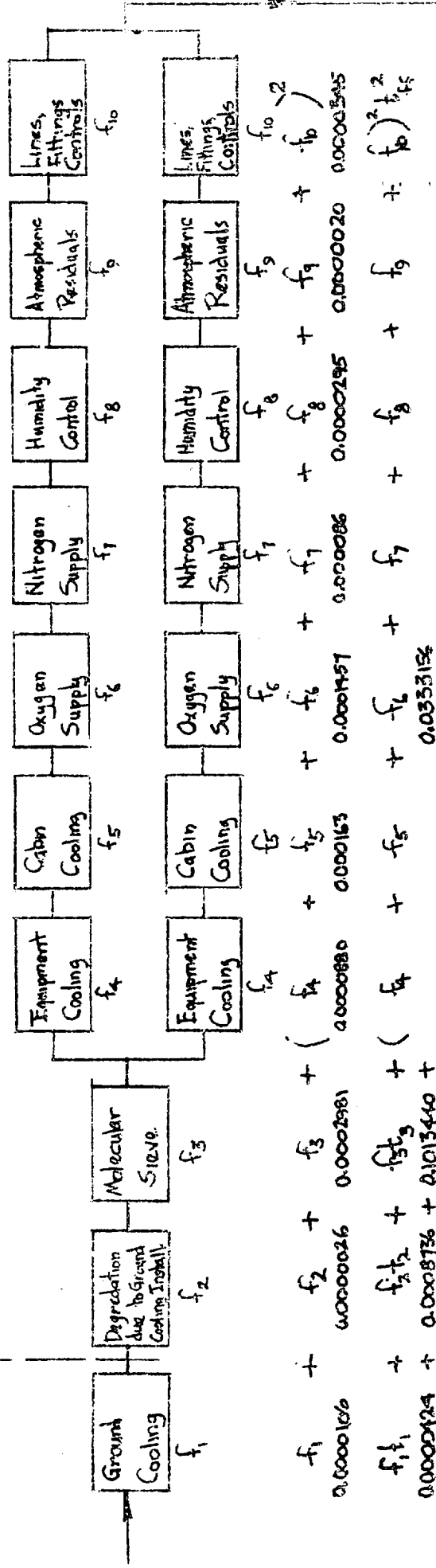
C O M P O N E N T	Operating Time per Mission	Predicted Failure Rate per Mission	% of Total Subsystem Failure Rate per Mission	Predicted Reliability in Missions Between Failure
Ground Cooling (in use)	4	.000042	.91	23809
Ground cooling flight degradation of reliability	336	.000169	3.67	5917
TOTAL Ground Cooling, Ground & Flight	340	.000211	4.58	4739
Molecular Sieve (LiOH Backup)	340	.000001	.02	1,000,000
Cabin & Equipment Cooling Launch & Free Flight	339	.000440	9.55	2272
Cabin & Equipment Cooling Re-entry	1.2	.000180	3.90	5555
TOTAL Cooling Equipment	340	.000620	13.45	1612
Oxygen Supply - Launch & Free Flight	339	.001200	26.04	833
Oxygen Supply - Re-entry	1.2	.000052	1.12	19230
TOTAL Oxygen Equipment	340	.001252	27.16	798
Nitrogen Supply - Launch & Free Flight	339	.000460	9.98	2173
Nitrogen Supply - Re-entry	1.2	.000004	.09	250000
TOTAL Nitrogen Equipment	340	.000464	10.07	2155
Humidity Control - Launch & Free Flight	339	.000099	2.15	10,101
Humidity Control - Re-entry	1.2	.000035	.76	28571
TOTAL Humidity Control Eqp.	340	.000134	2.91	7462
Atmospheric Residuals - Launch & Free Flight	339	.000001	.02	1000000
Atmospheric Residuals - Re-entry	1.2	.000002	.04	500000
TOTAL Atmospheric Residuals Equipment	340	.000003	.06	333333

232

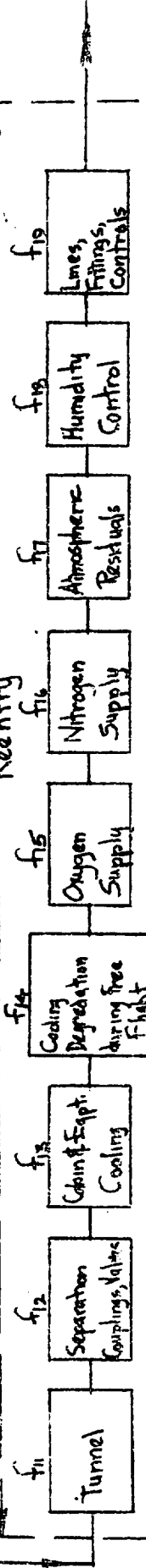
C O M P O N E N T	Operating Time per Mission	Predicted Failure Rate per Mission	% of Total Subsystem Failure Rate per Mission	Predicted Reliability in Missions Between Failure
Lines, Fittings, Controls Launch & Free Flight	339	.001690	36.67	591
Lines, Fittings, Controls Re-entry	1.2	.000041	.89	24390
TOTAL Lines, Fittings, Controls	340	.001731	37.56	577
Hatch	1.2	.000006	.13	166667
Separation Coupling Valves	1.2	.000076	1.65	13157
Re-entry Cooling, De- gradation During Free Flight 336		.000111	2.41	9009

# ENVIRONMENTAL CONTROLS RELIABILITY DIAGRAM

## Launch & Free Flight



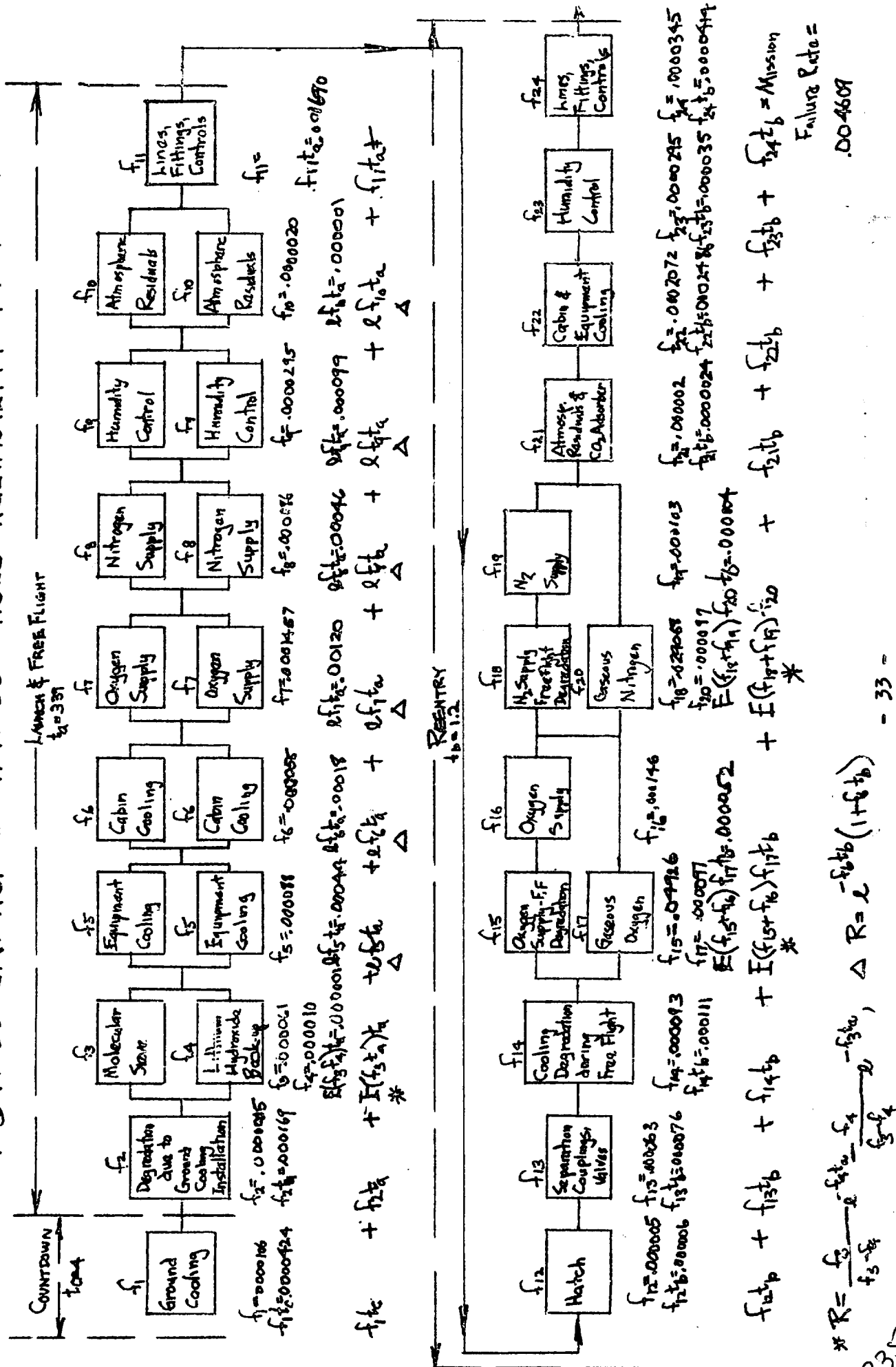
Reentry


$$f_{\text{subset}}^{\text{Hourly}} = f_{12} + f_{13} + f_{14} + f_{15} + f_{16} + f_{17} + f_{18}$$
$$0.00001 + 0.0001260 + 0.0002372 + 0.001172 + 0.001457 + 0.000086 + 0.000020 + 0.000295 + 0.0000345$$
$$f_{11}t_{11} + f_{12}t_{12} + f_{13}t_{13} + f_{14}t_{14} + f_{15}t_{15} + f_{16}t_{16} + f_{17}t_{17} + f_{18}t_{18} + f_{19}t_{19} = \text{Mission Failure Rate}$$

234



# MODIFIED ENVIRONMENTAL CONTROLS RELIABILITY DIAGRAM



\*  $R = \frac{f_3}{f_3 - f_4} e^{-f_4 t_{CD}} - f_3 t_{CD}$ ,  $\Delta R = e^{-f_4 t_{CD}} (1 + f_4 t_{CD})$

235

## Reaction Controls and Mission Control and Abort Propulsion

1. The configuration used in the reliability analysis is the current design described in TM-17 "Apollo Orbital Rendezvous Study".
2. With an allocated mission reliability of 99.5% the estimated reliability of this configuration is only 73.57%.
3. Several gross reliability problems were encountered as shown in the subsystem reliability summary and the reliability diagram, and are listed below along with suggested corrective action recommendations:
  - a. Common pressurization - This is a conventional single helium pressurization system used for propellant feed to the attitude and vernier engines as well as for control of the mission control and abort engine. Pressurization failure can result in complete loss of all spacecraft control and total loss of space abort capability. Complete standby redundant pressurization equipment would reduce the mission failure rate from .023870 to approximately .00031 failures per mission.
  - b. Common Bumping - A loss of function or a leakage failure in either  $N_2O_4$  or  $N_2H_4$  lines and fittings will result in a complete loss of attitude and vernier control along with all space abort capability. Suitable bypass and isolation valves along with appropriate redundancy should decrease the mission failure rate from .122760 to approximately .0069.
  - c. Attitude Control Engines - The present configuration incorporates two complete sets of attitude control engines in active parallel redundancy which have a total effective failure rate of .08450 for mission. If the engine sets were isolated by suitable valving, the complete set of control engines could be used in standby redundancy and the mission failure rate would decrease to .0449. If the engine sets were so arranged that each engine were isolated one from the other, the mission failure rate would decrease to approximately .0081.
  - d. Mission Control and Abort Propulsion - It is estimated that the combination of pumps, turbine, and reduction gear contributes approximately 49% to mission control and abort propulsion unreliability. Further, it is estimated that the mixture ratio valve and the thrust valve contribute approximately 39% to the engine unreliability. It appears that a combination of improved component reliability plus appropriate redundancy can be incorporated into the engine so that a substantial reduction in unreliability can be achieved.
  - e. Attitude, vernier, and mission control and abort propulsion Electronic Control - A preliminary analysis indicated that one single set of reaction engine controls would yield a reliability of only 95.75%. It was therefore necessary to

assume that each set of 6 attitude engines, the vernier engines, and the mission control engine each utilize sequential redundant electronic control equipment.

4. Based upon the analysis it is reasonable to assume that with suitable design modifications, the reliability of the reaction controls and mission control and Abort Propulsion Subsystem should meet the assigned reliability goal of 99.50%. A subsequent analysis will be made of the subsystem during the study phase.

# PRELIMINARY RELIABILITY ESTIMATE FOR SPACECRAFT

REACTION CONTROLS AND MISSION CONTROL AND ABORT PROPULSION

ONE MISSION RELIABILITY GOAL 79.5%

ONE MISSION PREDICTED RELIABILITY 73.57%

COMPONENT	Operating time per mission	Predicted Failure Rate per mission	% of Total subsystem failure rate per mission	Predicted Reliability in missions-between failure
Common Pressurization	158			
Trans Lunar Flight	158	.001580	5.6043	90
Injection, orbit	24	.001580	5.6043	595
Trans Earth Flight	158	.001580	5.6043	90
Reentry	1	.000010	.0228	14,285
Total Pressurization		.003870	7.7789	42
N <sub>2</sub> O <sub>4</sub> Supply				
Trans Lunar Flight	158	.001580	5.6043	633
Injection, orbit	24	.000240	.0782	4,167
Trans Earth Flight	158	.001580	5.6043	633
Reentry	1	.000010	.0033	100,000
Total N <sub>2</sub> O <sub>4</sub> Supply		.003410	1.1113	293
N <sub>2</sub> H <sub>4</sub> Supply				
Trans Lunar Flight	158	.001580	5.6043	633
Injection, orbit	24	.000240	.0782	4,167
Trans Earth Flight	158	.001580	5.6043	633
Reentry	1	.000010	.0033	100,000
Total N <sub>2</sub> H <sub>4</sub> Supply		.003410	1.1113	293

# A P O L L O   S Y S T E M

## PRELIMINARY RELIABILITY ESTIMATE FOR SPACECRAFT

### REACTION CONTROLS AND MISSION CONTROL AND ABORT PROPULSION

ONE MISSION RELIABILITY GOAL 99.5%

ONE MISSION PREDICTED RELIABILITY 73.57%

C O M P O N E N T	Operat- ing time per mission	Predicted Failure Rate per mission	% of total subsystem failure rate per mission	Predicted Reliability in missions- between- failure
<del>Common Plumbing</del>				
Trans Lunar Flight	158	.056880	18.5365	17.6
Injection, orbit	24	.008640	2.8157	115
Trans Earth Flight	158	.056880	18.5365	17.6
Reentry	1	.000360	.1173	2,778
Total Common Plumbing		.122760	40.0060	8.1
Attitude Control				
Trans Lunar Flight	158	.000090	.0293	11,111
Injection, orbit	24	.000080	.0261	12,500
Trans Earth Flight	158	.000126	.0411	7,936
Reentry	1	.000400	.1303	2,500
Total Attitude Control		.000696	.2268	1,437
<del>Attitude Control Engines</del>				
Trans Lunar Flight	158	.039500	12.8726	25.3
Injection, orbit      9	24	.003900	1.2711	256
Trans Earth Flight	158	.039500	12.8726	25.3
Reentry	1	.001500	.5214	625
Total Attitude Control		.084500	27.5377	11.8

239

# APOLLO SYSTEM

PRELIMINARY RELIABILITY ESTIMATE FOR SPACECRAFT  
REACTION CONTROLS AND MISSION CONTROL AND ABORT PROXUSION  
ONE MISSION RELIABILITY GOAL 99.5%  
ONE MISSION PREDICTED RELIABILITY 73.57%

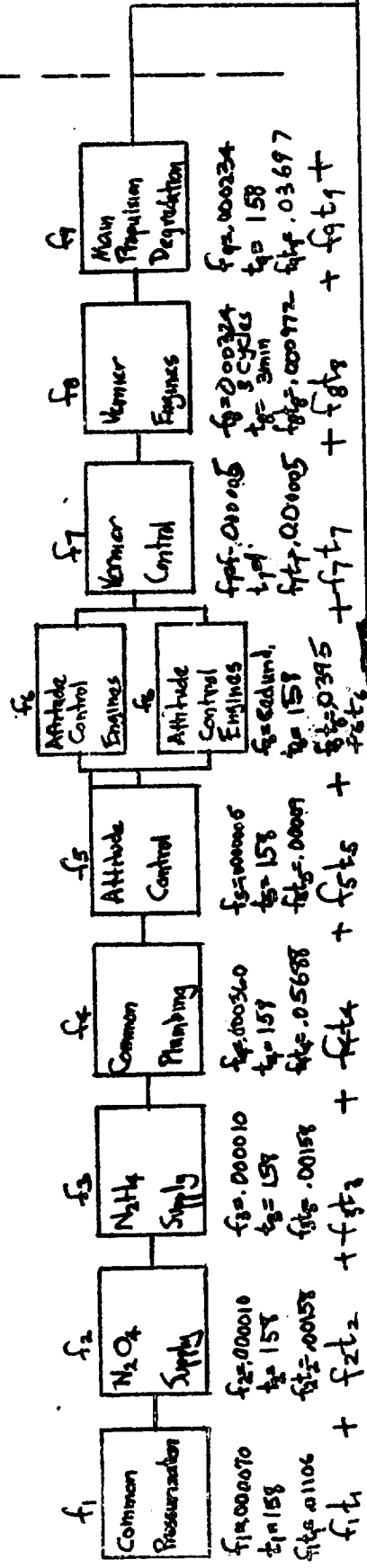
COMPONENT	Operating time per mission	Predicted Failure Rate per mission	% of total subsystem failure rate per mission	Predicted Reliability in missions between failure
Vernier Control				
Trans Lunar Flight	1	.000005	.0016	200,000
Injection, orbit	1	.000005	.0016	200,000
Trans Earth Flight	2	.000010	.0033	100,000
Reentry	1	.000004	.0013	250,000
Total Vernier Control		.000024	.0078	41,667
Main Propulsion				
Total Degredation-Trans Lunar Flight	158	.036970	12.0480	27.0
Main Propulsion Control	2 cycles	.000010	.0032	100,000
Main Propulsion Engine	2 cycles	.030870	10.062	32.4
Total Main Propulsion		.067850	22.184	14.73
TOTAL O <sub>2</sub> SUPPLY INJECT.	1	.000167	.0544	5,988
TOTAL H <sub>2</sub> SUPPLY	1	.1000167	.0544	5,988
TOTAL RATE PER MISSION		.306854		3.259

240

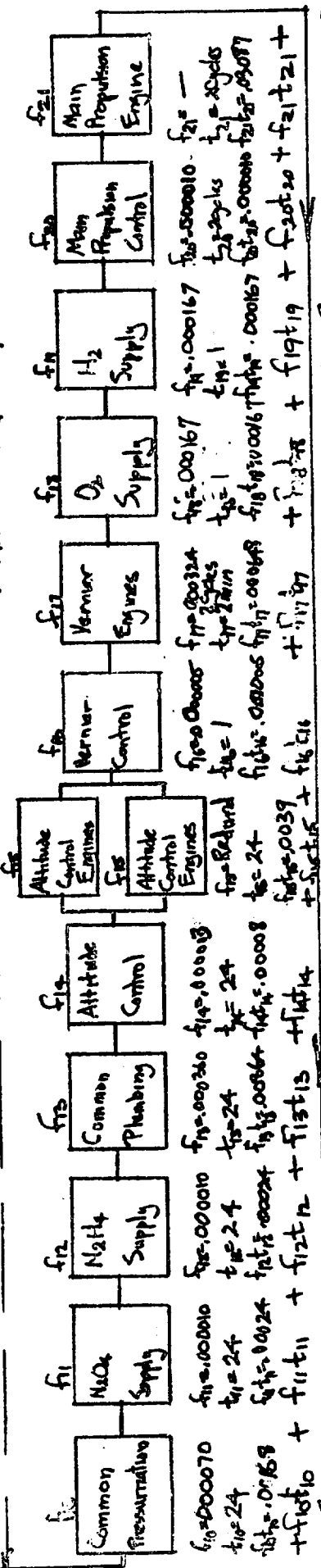
(1)

# REACTION CONTROLS & MISSION CONTROL & ABORT PROPULSION

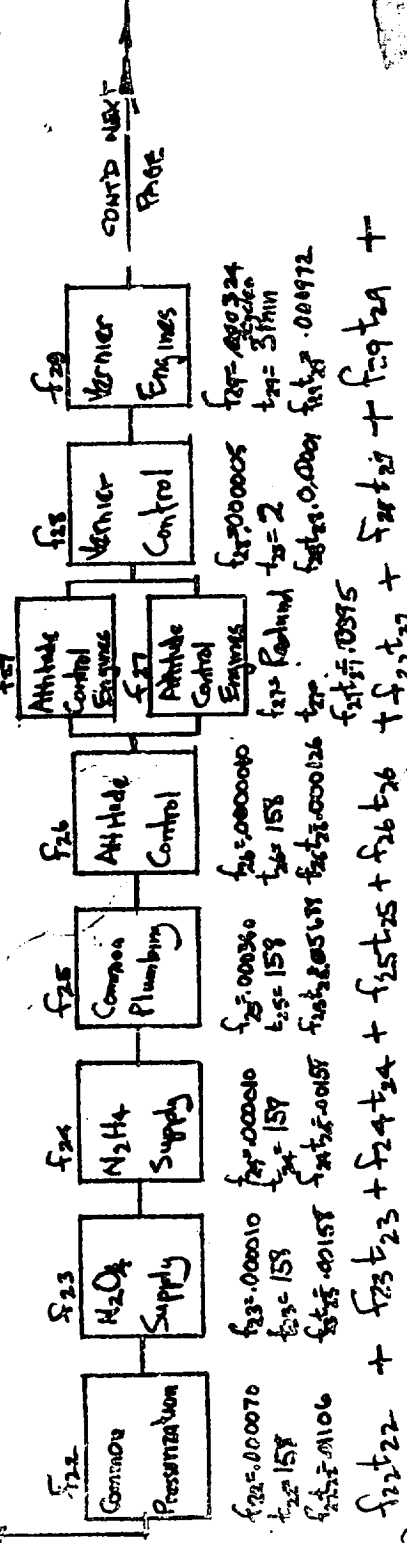
TRANS LUNAR FLIGHT



LINEAR INTERSECTION & ORBIT TRANSFER INJECTION



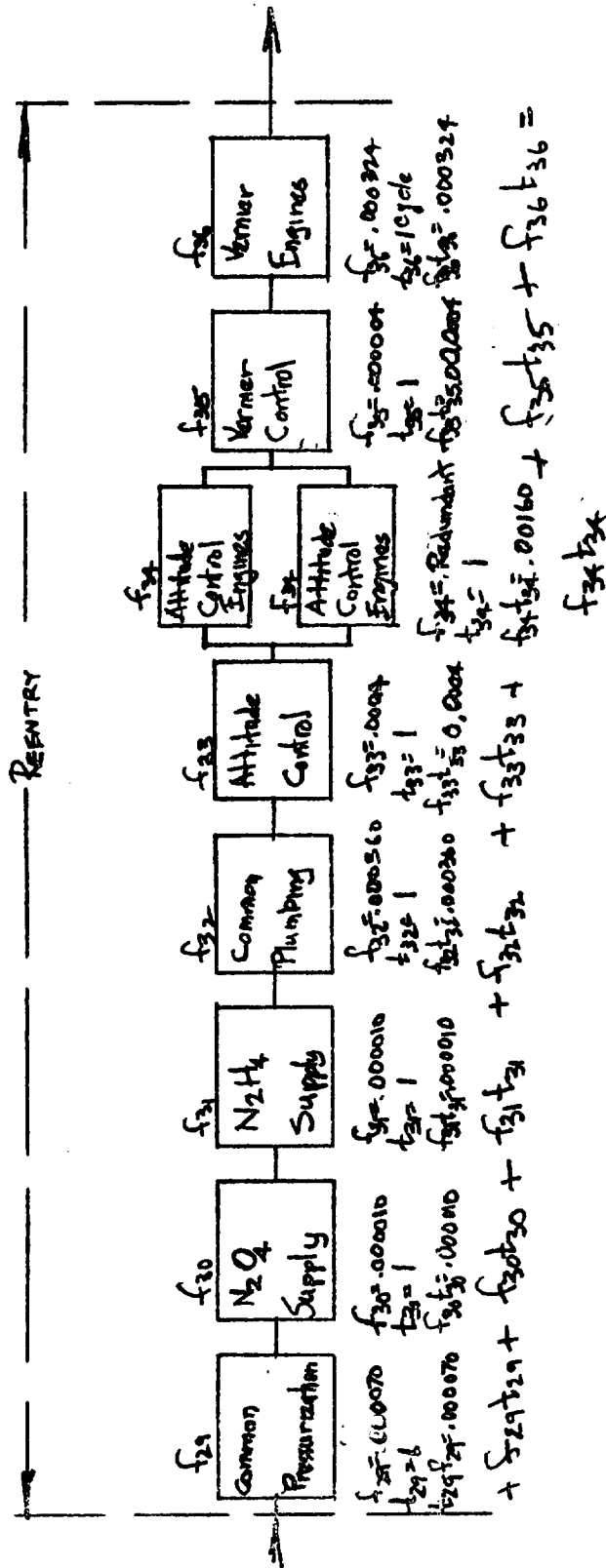
TRANS EARTH FLIGHT



CONT'D NEXT PAGE

(H)

# REACTION CONTROLS & MISSION CONTROL & ABORT PROPULSION





~~CONFIDENTIAL~~

Guidance

1. The first reliability analysis made of the guidance subsystem was based on the MLV Feasibility Survey, Vol. I, Part 2.
2. Specific component analyses were based upon the following:
  - a. Star Tracker. GPE, KS-50 Kollaman, ITT Laboratories
  - b. Horizon sensor. Conical Scan Sensor designed by Barnes Engineering Company, Stamford, Connecticut.
  - c. Computer
    - (1) DYNA-SOAR I
    - (2) Kearfatt CGHS used in Navy WV-2 and Air Force RC-121 Early Warning Search Aircraft
  - d. Inertial Platform
    - (1) DYNA-SOAR I
    - (2) Kearfatt CTRS as in C (2) above.
3. It was assumed that the guidance subsystem would be in operation as follows:
  - a. Launch Boost - Star Tracker, Horizon Sensor, Inertial Platform, and Computer - 0.208 hours.
  - b. Free-flight and Lunar Orbit - Star Tracker, Horizon Sensor, Inertial Platform, and Computer - 20 hours.
  - c. Reentry-Inertial Platform and Computer - 1.2 hours
4. As shown in the summary, single component reliabilities were first analyzed (See Reliability Diagram, Non-Redundant). The one mission predicted reliability for the non-redundant components was 92.25%, well below the goal of 97.55%. By duplicating all equipments and adding back-up switches, the one mission estimated reliability was improved to 99.72%. It appeared that the reliability goals could be met only if redundant components were employed.
5. A second reliability analysis was made subsequent to a design change. This subsystem is described in TM - Guidance. Based on this configuration, the following assumptions were made:
  - a. The digital computers are in active parallel redundancy when operating. They are operating for 34 hours during trans lunar flight lunar orbit, and trans earth flight.

~~CONFIDENTIAL~~

- b. The astro inertial platform is assumed to be operating full time during the mission. The back up platform is in active parallel redundancy during pre coast and post coast boost, during injection into trans earth trajectory, and during reentry. It is in sequential redundancy during all other periods.
  - c. The auto-manual tracker is assumed to be operating a total of 34 hours during trans lunar flight, lunar orbit, and trans earth flight.
6. As shown in the summary, the one mission predicted reliability was 97.55%, exactly equal to the goal. It appears that this estimated reliability may be significantly improved in at least two ways:
- a. Use the digital computers in sequential redundancy rather than active redundancy.
  - b. Include earth back up guidance information for certain specific mission phases.
7. In view of the results of the first two analyses, it appears that the reliability goal for the guidance subsystem can be met.

~~CONFIDENTIAL~~

# A P O L L O   S Y S T E M

**CONFIDENTIAL**

## PRELIMINARY RELIABILITY ESTIMATE FOR SPACECRAFT

### GUIDANCE SUBSYSTEM

ONE MISSION RELIABILITY GOAL - 97.55%

ONE MISSION PREDICTED RELIABILITY

Non-Redundant - 92.25%  
Redundant - 99.72%

C O M P O N E N T		Opr. Time per Mission hrs.	Non-Redundant			Redundant		
			Predicted Failure Rate per Mission	% Total Subsystem Failure Rate per Mission	Predicted Reliability in Mission Between Failure	Predicted Failure Rate per Mission	% Total Subsystem Failure Rate per Mission	Predicted Reliability in Mission Between Failure
Inertial Platform	Launch-Boost	.208	.002300	2.855	435	.000005	0.181	200000
	Free Flight Orbit	20	.002220	2.755	450	.000005	0.181	200000
	Reentry	1.2	.013270	16.470	75	.000176	6.386	5682
	Total		.017790	22.080	56	.000186	6.749	5376
Computer	Launch-Boost	.208	.006171	7.659	162	.000038	1.379	26316
	Free Flight Orbit	20	.005940	7.373	168	.000035	1.270	28571
	Reentry	1.2	.035600	44.186	28	.001267	45.972	789
	Total		.047711	59.218	21	.001340	48.621	746
Back up Switching	Launch - Boost	.208	---	---	---	.000081	3.018	11905
	Free Flight Orbit	20	---	---	---	.000800	29.028	1250
	Reentry	1.2	---	---	---	.000288	10.450	3472
	Total		---	---	---	.001172	42.526	853
Horizon Sensor	Launch Boost	.208	.004372	5.426	229	.000019	0.689	52632
	Free Flight Orbit	20	.004200	5.213	238	.000018	0.653	55556
	Total		.008572	10.639	117	.000037	1.342	27027
Star Tracker	Launch Boost	.208	.003316	4.116	302	.000011	0.399	90909
	Free Flight Orbit	20	.003180	3.947	314	.000010	0.363	100000
	Total		.006496	8.063	154	.000021	0.762	47619

# APOLLO SYSTEM

PRELIMINARY RELIABILITY ESTIMATE FOR SPACE

REACTION CONTROLS AND INJECTION PROPULSION SUBSYSTEM

ONE MISSION RELIABILITY GOAL 99.5%

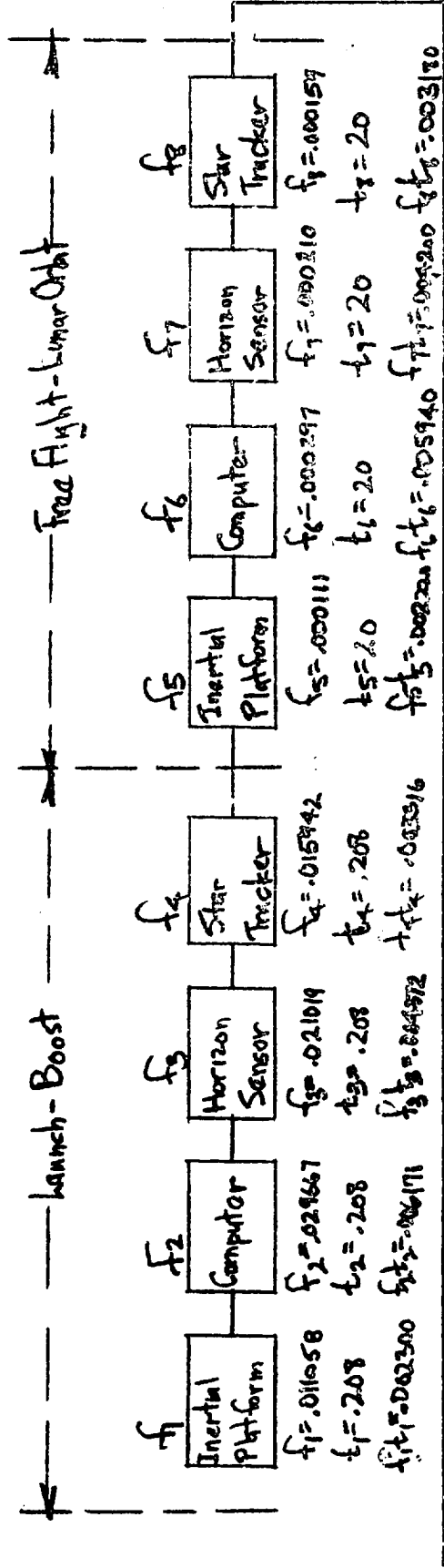
ONE MISSION PREDICTED RELIABILITY 99.56

C O M P O N E N T	Operat- ing time per Mission	Predicted Failure Rate per Mission	% of Total Subsystem Failure Rate Per Mission	Predicted Reliability in missions bet- ween failure
Astro-Inertial				
Pre Coast	.21	.000000	0	
Coast	.139	.000000	0	
Post Coast Injection	.052	.000000	0	
Trans Lunar Flight	168	.000980	3.959	1020
Lunar Orbit	2.4	.002430	9.817	411
Injection Trans Earth	.1	.000095	.383	10,526
Trans Earth Flight	164	.001700	6.867	588
Reentry Maneuvers	.1	.000010	.0403	100,000
Reentry	1	.001240	5.009	806
TOTAL Astro-Inertial		.006455	26.075	155
DIGITAL COMPUTER				
Translunar Flight	17	.004300	17.37	233
Transearth Flight	17	.011600	46.86	86
TOTAL Digital Computer		.015900	64.22	63
Auto-Manual Tracker				
Translunar Flight	17	.001200	4.847	833
Transearth Flight	17	.001200	9.847	833
TOTAL Auto-Man. Tracker		.002400		

24

# GUIDANCE SUBSYSTEM RELIABILITY DIAGRAM

## NON-REDUNDANT COMPONENTS

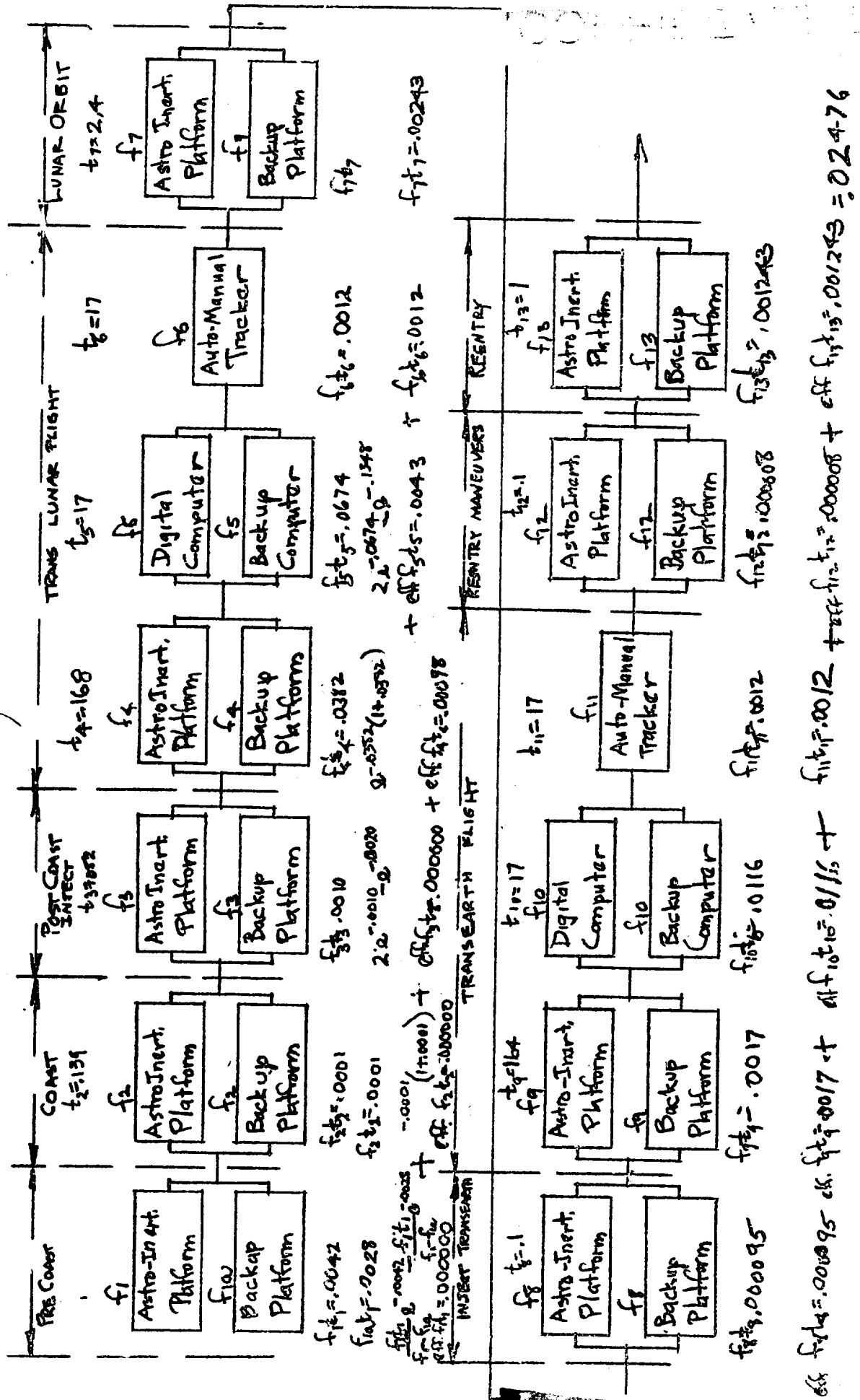


$$f_1 t_1 + f_2 t_2 + f_3 t_3 + f_4 t_4 + f_5 t_5 + f_6 t_6 + f_7 t_7 + f_8 t_8 +$$

$$f_9 t_9 + f_{10} t_{10} = \text{Mission Failure Rate} = .080569$$



## GUIDANCE SUBSYSTEM RELIABILITY DIAGRAM II.



## Structures

Assuming that strength will be normally distributed, and that the Factor of Safety is 1.4

Reserve strength = difference between load and strength distribution

$$\text{Then} \\ R = 1 - \frac{1}{FS \cdot Cv}$$

Where:

Cv = coefficient of variation of reserve strength

FS = Factor of Safety

R = Number of standard deviations (directly convertible to reliability value.

Let Cv = .075 (based on good quality control, workmanship, machine process control, etc.)

$$R = \frac{1 - \frac{1}{1.4}}{.075} = \frac{.286}{.075} = 3.8093 \text{ standard deviations}$$

$$R = .99993$$



CONFIDENTIAL

### Communications and Telemetry

1. The reliability analysis for the communications and telemetry subsystem was based on the Apollo proposal configurations. It was assumed that two requirements had to be met in order to successfully accomplish a mission:
  - a. The first requirement assumed that command reception, voice reception and transmission, and range transmission were necessary up to injection into lunar orbit.
  - b. The second requirement assumed that range and command functions were necessary from the beginning of injection into lunar orbit up to reentry; i.e. voice reception and transmission was not required after injection into lunar orbits. It was further assumed that the telemetry and range transponders could, when necessary, perform the same function, and that both could also substitute for the voice transponder.
2. With an allocated mission reliability of 99.0%, the estimated reliability was 98.05%.
3. The reliability estimate for the first requirement was found to be .9851 - somewhat below the .99 requirement selected for the communications and Telemetry System.

The range code modulator was found to be the major unreliability contributor.

Several solutions exist. A concentrated effort might be made to improve the reliability of the range code modulator or redundancy could be utilized. The latter solution would increase the weight

CONFIDENTIAL

and could increase the power consumption depending upon the type of redundancy selected.

Using time sequenced redundancy for the range code modulator, incorporating a switching device having a reliability of about .9645 would result in a .9907 reliability at this point.

The reliability for the second requirement was estimated to be .8983. Again several solutions exist including a concentrated design effort.

Again the range code modulator is the major unreliability contributor. Utilizing time sequenced redundancy for the range code modulator incorporating a "perfect" switching device increases the reliability to .9519.

Utilizing time sequenced redundancy in the transponder combination (with a perfect switching device) along with time sequencing the range code modulator increases the reliability to .9803 for the second requirement. It was assumed that the time sequenced unit would begin to operate after both the range and telemetry transponders had failed.

Simple redundancy above then is not sufficient. A combination of a concentrated design effort in the range code modulator and transponder areas, selection of improved parts as well as redundancy utilization will be necessary to meet the goal under the assumed conditions and requirements.

Countdown	1st stage Ign.	2nd stage Ign.	3rd stage Ign.	Coast	3rd stage Helign & Injection	Trans Lunar Orbit & Lunar Orbit Trans.	Lunar Orbit Injection	Injection Trans.	Birth Traj.	Trans Earth Flight	Maneuvers for Re-entry	Re-entry	Landing	Post Landing
72 hr	.033	.044	.131	.139	.053	.168	2.4	.1	.164	.1	1.2	1	72	
Forward reception														
Return Trans.														
Return Trans.	.9985		.986		.966	.976		.168	.986	.986	.986	.986	.986	.986
Range Transmission			.997	.997	.997	.997		.997	.997	.997	.997	.997	.997	.997
Refinery Data														
Refinery														
Range Tracker														
Computer														
Horizon Sensor														
Command Reception														
Voice Trans.														
Range Trans.														
Command Reception														
Range Transmission														

### Apollo Mission Reliability

The mathematical expression for Apollo lunar mission reliability is:

$$R_B R_S R_E$$

where  $R_B$  = reliability of the Saturn C-2 booster

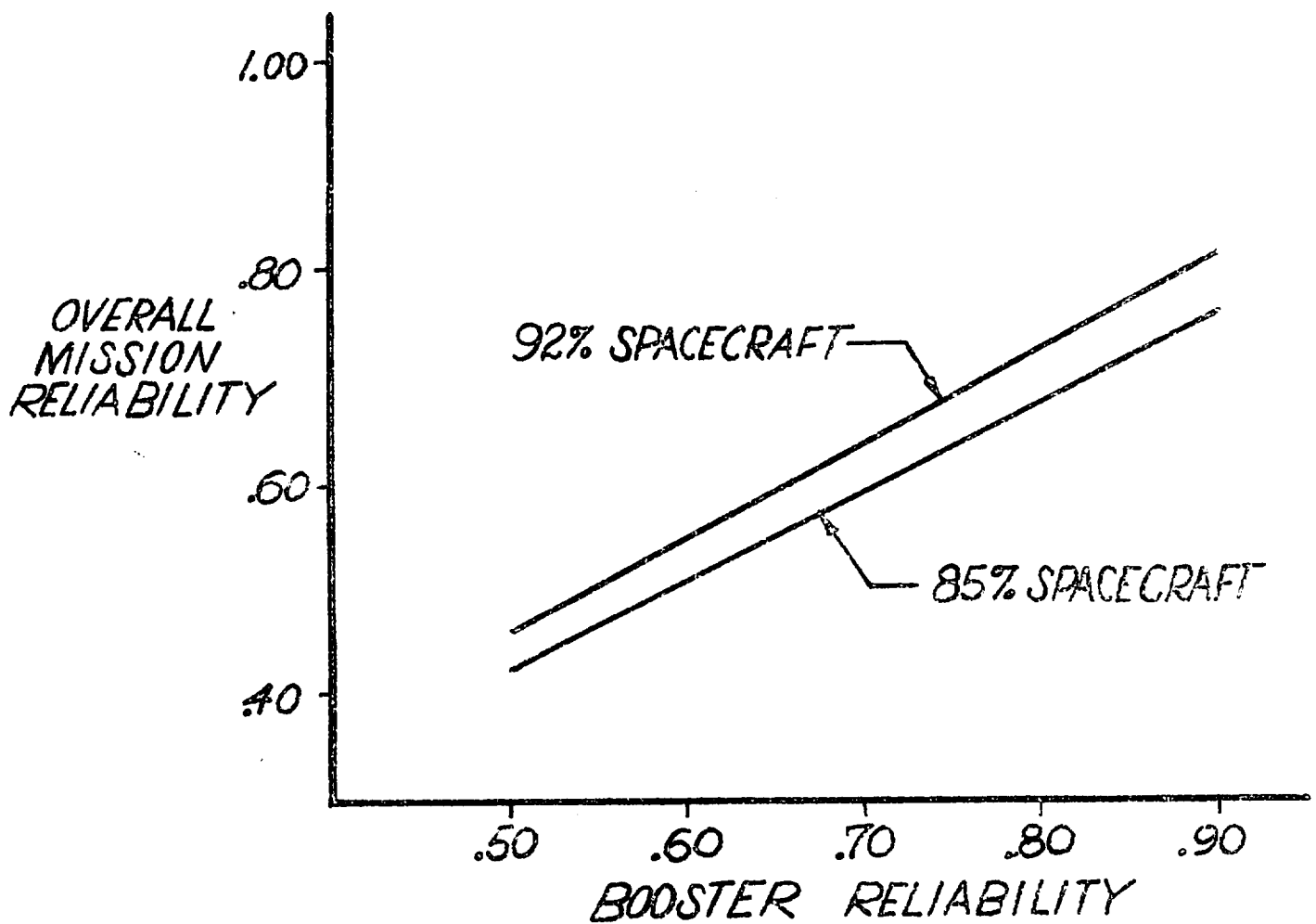
$R_S$  = reliability of the Apollo Spacecraft

$R_E$  = probability of no unexpected mission environmental conditions.

The figure entitled "mission reliability" shows the product,  $R_B R_S$ , as a function of booster and spacecraft reliability. At this stage, a firm number for  $R_S$  is expected by the end of the study. Further coordination with NASA personnel is required, however, to obtain a value for  $R_B$  the mission reliability of the Saturn C-2 booster. The resultant product  $R_B R_S$  must be multiplied by  $R_E$  to obtain total probability of mission accomplishment. Some estimates are expected for certain environments by the end of the study but a considerably greater quantity of data will be required in the future to fully assess  $R_E$ .

The full evaluation of all three of these factors will yield the desired prediction of the probability of lunar mission accomplishment and a series of sub-numbers which will represent probability of accomplishment of each individual flight phase. This basis matrix of numbers can be used to assess reliability of alternate mission and to indicate those flight phases where abort is most likely to occur.

## MISSION RELIABILITY



### Crew Safety

The attached technical paper demonstrates the basic mathematical method developed for evaluating crew safety. With the completion of the matrix of reliability numbers by flight phase and the evaluation of the probability of emergency return in a failed vehicle a vigorous determination of crew safety can be made for the Apollo mission. Both of these tasks are scheduled for the current study contract and will result in a numerical prediction of crew safety for the Apollo system.

### Introduction

Achieving reliability in space vehicles is one of the most difficult problems which we face today. This problem can only become more acute as we attempt manned space flight in less than perfect vehicles. Some of these problems of reliability are now being met by the analysis of vast amounts of failure information and the application of this knowledge to the design of new vehicles. One factor that stands apparent in designing a manned space vehicle which depends on present day components is that we must expect failures and we must incorporate safety provisions into the design which will permit the man to return safely when these vehicle failures occur. The prime questions in providing adequate safety provisions concern the level of crew safety desired, the type of safety provisions required, and the environmental conditions under which the safety provisions will have to operate.

Many of these questions facing us in the design of manned space vehicles can be successfully answered by information presently in existence on the levels of human safety which are acceptable and on the time distribution and nature of failures which occur in equipments of the type to be used in manned space vehicles. The application of this existent information to new designs can have a profound impact on the design itself and can yield a valuable index on the level of safety provided by the design. The techniques of safety evaluation and improvement in safety during the configuration design phase of a program can be handled in a manner analogous to that now being successfully used to predict and improve reliability in new design equipments. This paper discusses the steps to be followed in the prediction of crew safety and shows examples of methods of prediction which have been successfully applied to determine the adequacy of safety provisions in manned space vehicles.

### Defining of the Relationship Between Mission Reliability and Crew Safety

The first step in the evaluation of crew safety involves defining the relationship between mission reliability and crew safety. For manned space vehicles an adequate definition of mission reliability covers the phases of launch, boost, orbiting flight and return to a designated spot on the earth. A mission reliability definition as the 'ability of the system to remain within the desired flight envelope and return to base X' can establish that mission reliability,  $R$ , equals the product of the system reliability in each phase of a typical mission or

$$R = R_1 \cdot R_2 \cdot R_3 \cdot R_4$$

where

- $R_1$  = system reliability during the launch phase
- $R_2$  = system reliability during powered boost phases
- $R_3$  = system reliability during the orbiting phase
- $R_4$  = system reliability during the landing phase

An adequate definition of crew safety, on the other hand, need only imply safe return of the vehicle crew from any point in the flight envelope once the mission has been initiated. The reliability,  $R$ , once stated, establishes two important factors. The first is that a system with mission reliability,  $R$ , will return the crew safely  $R\%$  of the time. The second factor is that unless  $R$  is an extremely high value then  $Q = (1-R)\%$  of the time some auxiliary means must be provided to return the crew safely from the mission. Let this auxiliary means have a reliability of  $R_A$  when used, then crew safety,  $R_S$ , (or probability of survival) can be written as

$$R_S = 1 - Q \cdot Q_A \quad (Q_A = 1 - R_A)$$

For mathematical reasons it is more convenient to think in terms of crew hazard,  $Q_S = 1 - R_S$ , so that  $Q_S = Q \cdot Q_A$ .

1 HANLEY

As an example, if system reliability,  $R$ , for one mission equals 90% and the reliability  $R_A$  of some auxiliary means of returning the crew safely equals 99% then

$$Q_g (\text{crew hazard}) = \frac{1}{10} \cdot \frac{1}{100} = \frac{1}{1000}$$

or 1000 missions between fatalities. In actual experience the formula  $Q_g = QQ_A$  is not used directly, as the reliability,  $R_A$ , of the safety provisions varies considerably during the different phases of a mission and the safety provisions themselves may, in fact, be different for various phases of flight. As an example, a parachute may suffice for escape from a space vehicle in certain flight phases but cannot be used for the majority of the flight. It is common practice therefore to write the formula for crew hazard as

$$Q_g = \sum QQ_A$$

letting the phases of flight be subdivided into as many phases as there are different reliabilities,  $R_A$ , for the safety provisions. It is also common to further modify the above expression for crew hazard by letting

$$Q_g = \sum QQ_A + Q_R$$

where the  $Q_R$  value represents the probability of failure for which no safety provision exists. This is particularly appropriate when the safety provisions are thought of as an emergency means of returning the crew from any point on the trajectory. In this case,  $Q_R$  might represent the probability of failure of the crew environmental control system, a type of failure for which the safety provisions cannot compensate.

ROCKET ENGINE PROBABILITY OF SURVIVAL  
AS A FUNCTION OF OPERATING DURATION

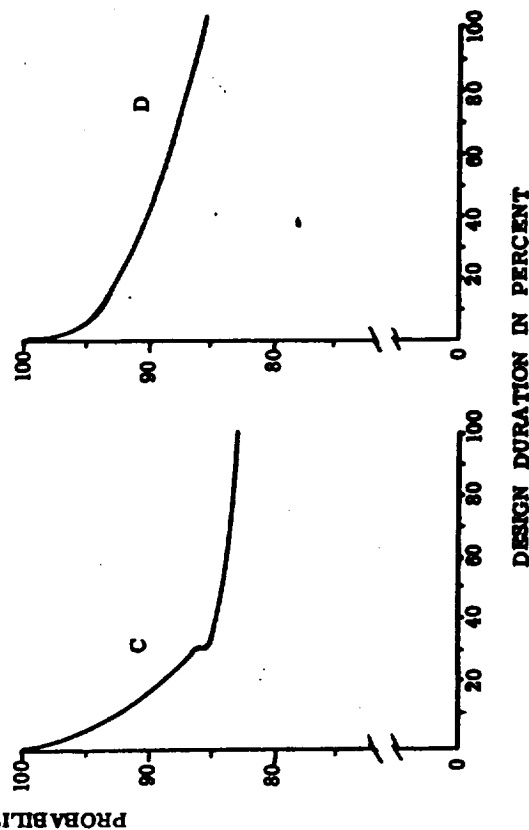
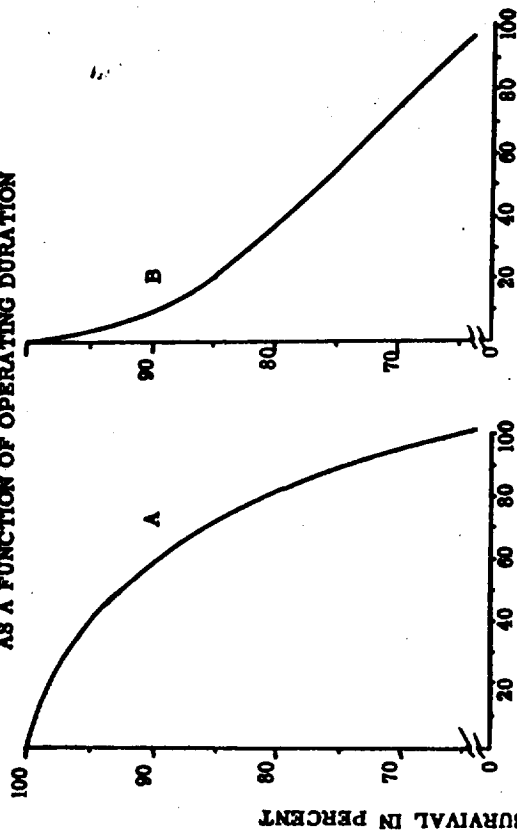


Figure 1

2 HADLEY



### Estimation of Frequency of Use of the Vehicle Safety Provisions

The estimation of the frequency of use of the vehicle safety provisions during the configuration design phase of a space vehicle is one of the typical current-day problems being successfully handled by reliability prediction techniques. These prediction techniques provide the answer by determining what equipment must operate successfully in each phase of a mission and what reliability can be expected from this equipment as a function of operating duration and component interrelationships. For orbiting space vehicles, by far the most interesting flight phase for reliability prediction is the powered boost phase. This stems from the fact that multiple stage vehicles are in common use, each different in operating duration, equipment complexity and even different in propellant combination. An additional factor of extreme interest is the 'proneness' of the liquid rocket engine to early failures occurring during or shortly after the start transient. Another factor which can cause a drastic variation in failure rate within the boost phase of flight is the trend toward liquid rocket engine redundancy in several proposed space vehicles. As a general rule, this redundancy becomes effective 't' seconds after rocket fire when sufficient propellants have been consumed to increase the vehicle thrust-to-weight ratio above 1.0 with n-1 thrust chambers operating.

To show the trend of rocket engine failure rate vs. operating duration, several sets of data have been examined and are shown in Figure 1. Engines B, C, and D are of the acid-gasoline type while engine A is of liquid oxygen type. Engines B, C and D are of the 10,000# to 20,000# thrust class while engine A is of less than 5000# thrust. A constant failure rate, or probability of survival, over the operating duration of each engine would be denoted by a straight line from 100% at zero time to the reliability at full duration. It is noted that each of the engines (except A) exhibits a curve depressed from the straight line showing its proneness toward early failures. Experience shows the trend to be even more pronounced as a liquid rocket engine completes development. In the case of engine A, an uncooled chamber, the trend is reversed as 'near-out' type of failure is experienced near the end of the operating duration.

For manned space vehicles of the near future, such failure rate curves dominate the picture during a mission. The rocket engine remains as the major contributor to vehicle failure rate during the powered phases of flight.

For the purpose of clear illustration of the use of these curves, let us define a rocket-powered manned space vehicle of three stages with single engines in the second and third stages and a first stage with two thrust chambers. With this configuration the following engine reliabilities are assumed:

- Stage I      95% each barrel for the full Stage I duration
- Stage II     96% for the full Stage II duration
- Stage III    98% for the full Stage III duration

The reliability  $R_B$  for powered boost thus becomes

$$R_B = R_I R_{II} R_{III}$$

$$\text{or } R_B = (.95)^2 (.96) (.98) = 85\%$$

Ten times in every 67 missions an engine failure will occur and will require use of the safety provisions. If the trajectory is further broken down into such terms as altitude, velocity, dynamic pressure, and vehicle attitude at time 't' then this information, combined with engine failure rate as a function of time, will provide a prediction of the frequency of certain initial conditions under which the safety provisions will operate. It might be determined, for example that the failure distribution as a function of time is such that it follows the trend shown in Table I.

3 HADLEY

Specification of a Numerical Safety Requirement for the Vehicle Configuration

The choice of a numerical goal for crew safety in a manned space vehicle is best based on examination of current levels of safety provided by aircraft. In specifying this numerical goal it is desired to achieve as high a level of crew safety as possible while not choosing a level so high as to be unobtainable. Data from three classes of manned aircraft are readily available as a guide in the choice of a safety goal. Commercial airliners, for example, have a major accident record of one per 60,000 flights, high performance military fighter planes have a major accident every 4,000 flights. Rocket powered aircraft of the X series have a record of one major accident per 100 flights. Thus, a range of numbers is established on a per mission basis which can permit the selection of a crew safety goal for a manned space vehicle.

Suppose it is felt that a proposed space vehicle design will be less safe than high performance military fighter aircraft but should be more safe than previous models of rocket powered aircraft. The numerical safety goal then might be 99.8% or 99.9%. Converted to terms of crew hazard,  $Q_S$ , these numbers imply one accident per 500 missions and one accident per 1000 missions respectively.

If we now revert to the previously mentioned 85% reliable booster and the formula for crew hazard

$$Q_S = Q Q_A$$

then the permissible probability of failure,  $Q_A$ , for the vehicle safety provision is

$$\begin{aligned} \frac{1}{500} &> Q_S > \frac{1}{1000} \\ \frac{1}{500} &> \frac{10}{67} Q_A > \frac{1}{1000} \\ \frac{1}{75} &> Q_A > \frac{1}{150} \end{aligned}$$

4 HADLEY

Table I: Frequency of Use of Vehicle Safety Provisions During the Powered Boost Phases of Flight

Flight Phase	Velocity Range in fps	Altitude Range in feet	Time in Secs.	Mean No. of Missions Between Safety Provision Use	
				Between Safety Provision Use	
Boost I	0-100	0-500	0-10	20	
	100-3,000	500-200,000	10-120	100	
Boost II	3,000-8,200	200,000-230,000	120-125	25	
	8,200-17,000	230,000-900,000	125-220	100	
Boost III	17,000-17,200	900,000-920,000	220-230	33	
	17,200-25,000	920,000-1,200,000	230-320	100	
Overall Frequency of Safety Provision Use During Boost Phase --- 1 per 6.7 missions					

Such a table as shown above provides an estimate of the frequency of use of the safety provisions for a given range of flight conditions. The choice of six flight phases in the table is arbitrary and can be expanded to any number consistent with the different modes of escape from the vehicle. It may be, for example, that during the first 50 seconds of booster operation subsequent to launch an ejection seat serves as the primary mode of escape while later phases of boost use an ejectable capsule. In this case, a different subdivision of flight phases would be desirable.

The desired reliability of the safety provisions is therefore established as ranging from 96.65% to 99.35%. This reliability in the vehicle safety provisions will provide a crew hazard level for the manned space vehicle of from one per 500 missions to one per 1000 missions.

#### Numerical Evaluation of Crew Safety

Having defined crew safety in terms of probabilities and having set a numerical goal of crew safety, a manned space vehicle configuration can now be evaluated for adequacy of safety provisions. Table 2 shows a hypothesized vehicle configuration for the three stage booster previously mentioned. In this case, it has been assumed (1) that an aircraft has been placed on top of the booster, (2) that capsule provides the sole means of escape below some minimum altitude at which the airplane can be successfully separated from the booster (designated flight phase I), (3) that above this minimum altitude the airplane serves as the primary mode of escape with the escape capsule providing backup capability. (Flight Phase II)

The expansion of the basic crew hazard formula  $Q_S = Q_A Q_C$  to take into account the particular configuration can be written as

$$Q_S = Q_1 Q_C + Q_2 (k Q_A Q_C + (1-k) Q_C)$$

where

$$Q_1 = 1/20$$

$$Q_2 = 1/10$$

$$Q_A = 1/100$$

$$Q_C = 1/10$$

and  $k$  = the proportion of failures in flight phase II for which the aircraft can be used as a safety provision.

If  $k = 90\%$ , for example, crew hazard becomes

$$Q_S = \frac{1}{20} \cdot \frac{1}{10} + \frac{1}{10} \left[ \frac{9}{10} \cdot \frac{1}{100} \cdot \frac{1}{10} + \frac{1}{10} \cdot \frac{1}{10} \right]$$

$$Q_S = \frac{1}{200} + \frac{9}{100,000} + \frac{1}{1000}$$

$$Q_S = \frac{1}{165} \text{ per mission}$$

In literal terms, the formula for crew hazard tells us:

1. That once every 200 missions a fatality will result from use of the escape capsule during the first 60 seconds of flight ( $Q_1 Q_C$ )
2. That once every 110 missions the airplane will fail when being used for escape and will require initiation of capsule escape ( $Q_2 k Q_A$ )
3. That once every 100 missions the failures in flight phase II will be of such a nature that airplane escape cannot be initiated [ $Q_2 (1-k)$ ]
4. That capsule use frequency is one per 16.5 missions [ $Q_1 + Q_2 k Q_A + Q_2 (1-k)$ ]; therefore, the aircraft will return the crew ~~about~~ 94% of the time (including landing at unscheduled destinations).

From the aspect of improving crew safety, the major effort should be to reduce the probability of capsule use during flight phase I or to improve the reliability of the capsule when used under the conditions of flight phase I as this phase of flight is the prime contributor to crew hazard. The former course of action, reducing the frequency of capsule use, is obviously the preferred method as this results in a direct increase in the proportion of successful missions. Improving the capsule reliability, on the other hand, does not improve the basic mission reliability.

Where two alternate means of escape are available in a vehicle, the formula for crew hazard

$$Q_S = Q_2 [k Q_A Q_C + (1-k) Q_C]$$

is worthy of careful analysis. As previously stated, such a formula is applicable during flight phase II for the vehicle configuration shown in Table 2. Let us examine what happens to crew hazard,  $Q_S$ , as we change the values of  $k$ ,  $Q_A$  and  $Q_C$ .

5 HADLEY

Missions Between Fatalities For  
Values of  $k$ ,  $Q_A$  and  $Q_C$

	$Q_A$	$Q_C$
Case A	1/10	1/100
Case B	1/100	1/100
Case C	1/100	1/10

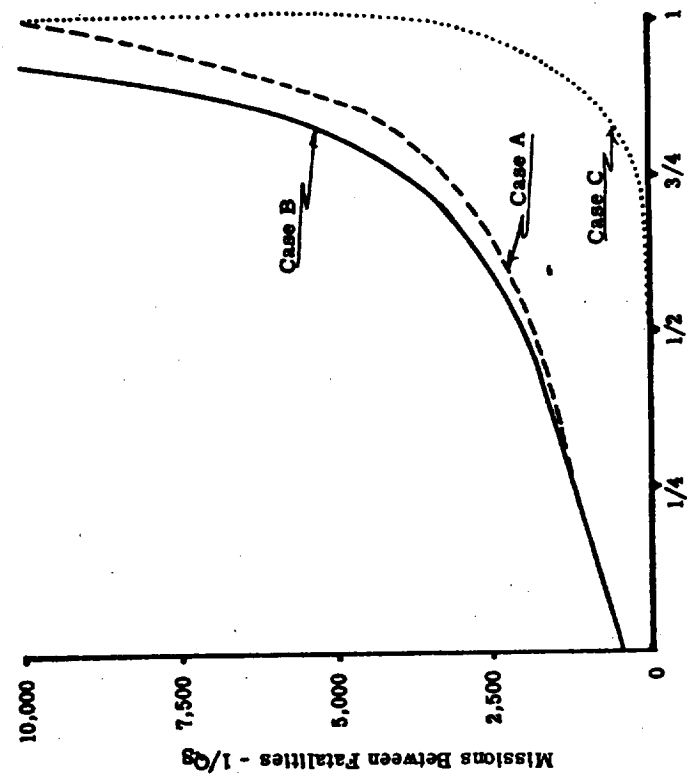


Figure 2

Assumptions are:

Case A

$$Q_A > Q_C$$

let  $Q_A = 1/10$  (90% reliable airplane)

let  $Q_C = 1/100$  (99% reliable airplane)

Case B

$$Q_A = Q_C$$

let  $Q_A = Q_C = 1/100$  (99% reliable airplane and capsule)

Case C

$$Q_A < Q_C$$

let  $Q_A = 1/100$  (99% reliable airplane)

let  $Q_C = 1/10$  (90% reliable capsule)

The results for varying  $k$  are shown in Figure 2.

Table 2 - Assumed Vehicle Configuration			
Flight Phase	Probability of Vehicle Failure - $Q_1, Q_2$	Mode of Escape	Escape System Probability of Failure when Used - $Q_A, Q_C$
I. Launch Pad to + 60 seconds	1/20	Capsule Only	1/10
II. + 60 seconds to Boost III shutdown	1/10	Aircraft	1/100
		Capsule Backup to Aircraft	1/10

6 HADLEY

For the configuration discussed, it is seen from Figure 2 that major gains in crew safety are realized by having the capsule escape mode substantially more reliable than the airplane or by having the proportion of failures for which airplane escape can be used as close to 1.0 as possible. In terms of design of rocket boosters, an increase in  $k$  would amount to reduction in the frequency of failure modes which are destructive to the airplane or which otherwise prevent successful separation of the airplane from the booster under conditions of rocket engine malfunction. A typical example of a failure mode which lowers the value of  $k$  is the occurrence of divergent vehicle instability following unscheduled loss of thrust. Such conditions make successful separation of an aircraft extremely difficult and therefore would result in capsule ejections for the configuration shown. The addition of fins on the booster would provide a more favorable environment for separation, thus increasing  $k$ .

### Conclusion

In the examples shown, many simplifications have been made for ease of illustration and to obtain a first approximation to the index of crew safety for a vehicle configuration. In actual practice, a substantial number of refinements are needed. It is obvious, for example, that the reliability of the airplane escape mode is not constant throughout boost phase as shown in the example. This reliability must be modified for modes of vehicle failure, for initial conditions under which emergency separation can occur, for the point on the trajectory where maximum dynamic pressure occurs, for the severity of heating conditions encountered subsequent to escape and for adverse landing conditions not compensated for by aircraft maneuverability. Similarly, the reliability of the capsule escape mode must consider refinements for separation, stability, re-entry, landing impact and post-landing recovery capability, all dependent on the time at which separation occurs or on the nature of the failure warranting separation. The omission of these refinements does not imply that they cannot be assessed in a manner which is rigorous. Considerable information is available to enable a first approximation for all factors listed. The use of these numerical methods of evaluating crew safety will contribute substantially to the design of manned space vehicles of optimum reliability and safety.

## APPENDIX

### A. RELIABILITY

The Apollo reliability effort is a technical task directed at elimination of trouble. During the study contract, problem areas and weaknesses have been anticipated and corrected by means of evaluation of proposed designs. During subsequent program plans, emphasis will change to the analysis of test data and the solution of known problems. This present concentration on evaluation of design, coupled with careful planning for subsequent program phases, is essential to the conduct of a successful reliability effort on Apollo.

The tasks which must be performed on subsequent phases have been identified and form an important part of the overall program plan.

During the present Apollo contract, reliability work has concentrated on:

- (1) Support of the design effort to arrive at a configuration with high inherent reliability.
- (2) Support of the program planning effort to define the conduct of a follow-on contract for the system.

As a result of this effort the technical and management aspects of the reliability program have received serious attention.

The program comprises seven tasks:

#### 1. Determination of Numerical Reliability Requirements

Values of reliability consistent with the desired probability of mission accomplishment must be established as a basis for evaluating proposed systems.

#### 2. Definition of Design Requirements

The required numerical values of reliability must be translated into requirements which the designer can fulfill through known design techniques. At the present state in reliability, only gross rules are available to identify design features which will yield given numerical values of reliability. Considerable negative data is available, however, to identify design features which will not yield a specific required value of reliability.

#### 3. Conduct of Design Evaluation Studies

Alternate methods of performing a system function must be evaluated to select the superior method. Reliability effort in this area yields high dividends because the emphasis is on comparative analysis rather than on absolute values of predicted reliability.

#### 4. Conduct of Design Review

For the selected system design, compliance or non-compliance with design requirements must be documented. Most significant is the identification of requirements for which compliance cannot be ascertained when the design review is in progress. The program should be carefully reviewed at this point to provide proof of compliance in these unknown areas prior to flight.

#### 5. Identification of Critical Product Characteristics

As part of design review on the selected configuration, this task provides a means of controlling the product during procurement, manufacture, shipping, handling and storage. Failure to identify significant product characteristics will result in generalized types of control methods in the above areas which do not anticipate causes of product degradation.

#### 6. Demonstration of Control of Critical-Product Characteristics

Every inspection or test performed on an article of flight configuration hardware is intended to prove that certain product characteristics are under control. This task insures that inspection and testing does, in fact, provide such proof.

#### 7. Reliability Data Collection and Utilization

Reliability data on tests conducted, equipment operating time and equipment discrepancies must be collected and analyzed to determine status in achieving system reliability and to provide an organized method for improving system reliability in the areas yielding the biggest dividends.

The management aspects of the program are associated with accomplishing these seven tasks on schedule and insuring that the information resulting from each task is used to influence decisions in the conduct of the program.

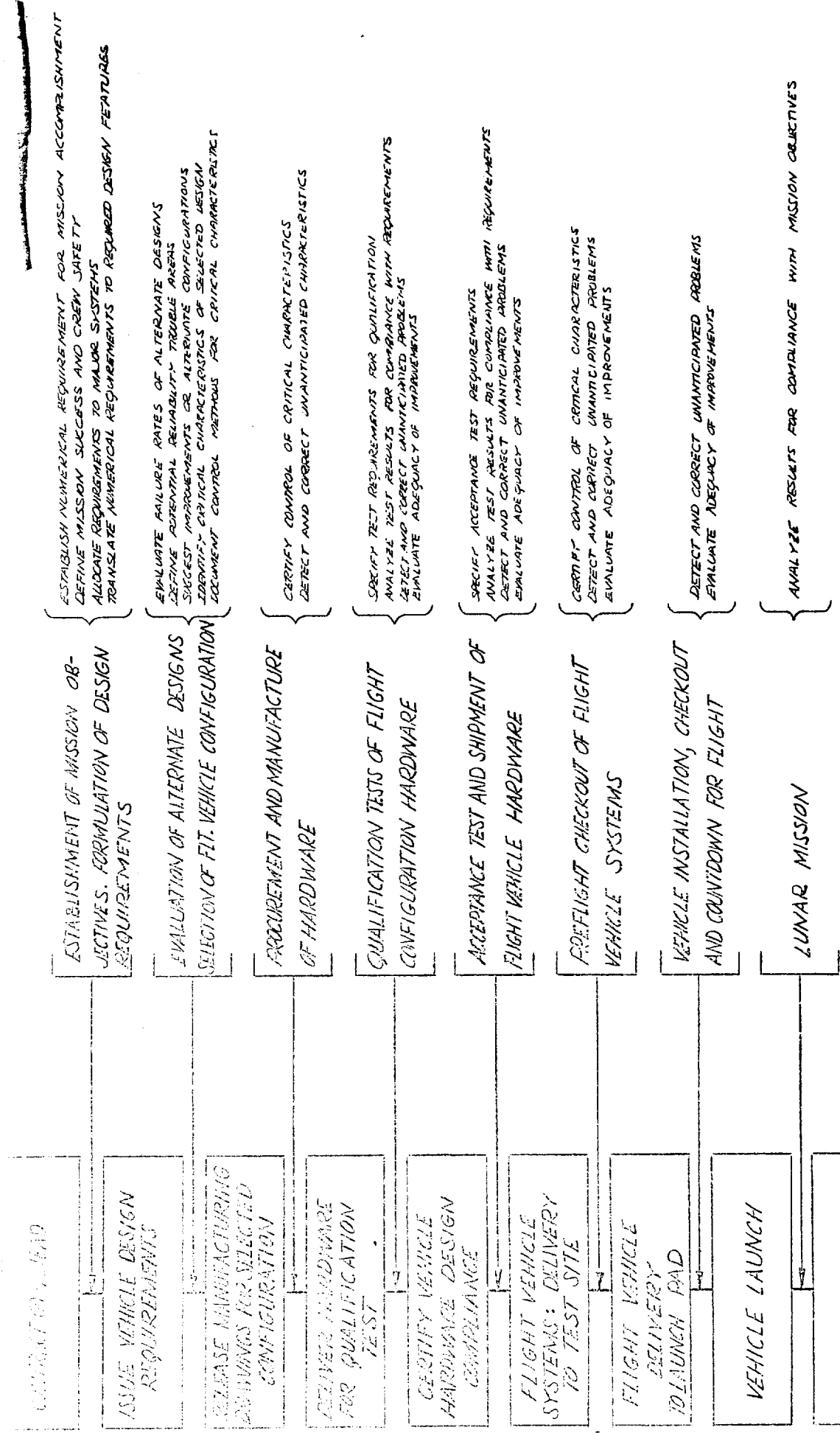
How these tasks apply to Apollo may be seen in Fig. IV-7, which shows the key events during the life cycle of the Apollo vehicle, the program activity required to make each event occur and the specific reliability effort which takes place as a part of the program activity.

The present reliability effort on Apollo will result in a specification which documents requirements for the conduct of the Apollo reliability effort, a program plan showing the specific tasks which will meet the requirements of the specification and the detailed reliability analysis performed on the spacecraft systems. Subsequent figures and text show the nature and format of the system analyses which have been conducted since program inception.

265

# RELIABILITY REPORT

3.



RELIABILITY • FLIGHT • DESIGN • ADMIN • LIFE • NOISE

266w



**Mock-ups with Painting of Controls**

**TM-8**

## Technical Memorandum 8

## Apollo 3-D Layouts

Two devices known at the Martin Company as "3-D Layouts" are being used to advantage in developing the internal arrangement of the Apollo spacecraft. These layouts consist of inexpensive wood and cardboard structures which represent the full scale internal contours of the vehicle. Their value lies in their use as engineering layouts, in three dimensions, as the name implies.

A 3-D layout of the Command Module has been constructed for the modular L-2C configuration and for the modular W-1 configuration. Because of the type of construction used, these layouts are very flexible in application. The L-2C for example, could be converted to almost any configuration, having basically circular cross sections, and a size compatible with Apollo requirements. The W-1 layout could likewise be readily used to represent other unsymmetrical body shapes, and was in fact converted from the M-1-1 configuration. The contours resulting from this conversion are sufficiently accurate to be very useful. Should still greater accuracy be necessary to solve some local problem, it can be readily attained.

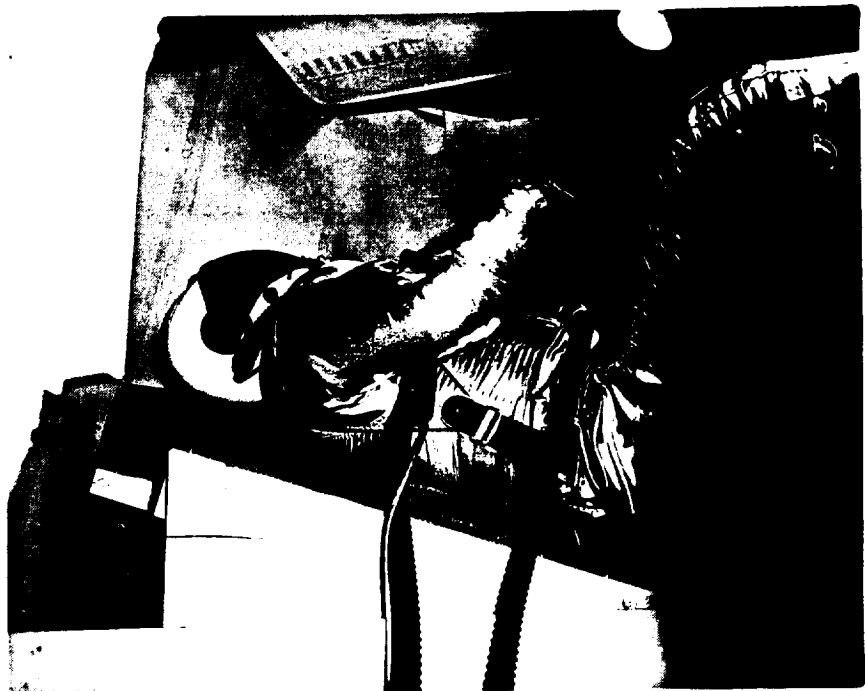
Both 3-D Layouts have suffered numerous minor changes. In attempting to determine an overall optimum arrangement, seats have been moved, instrument panels reoriented and/or moved, and various equipment arrangements have been considered.

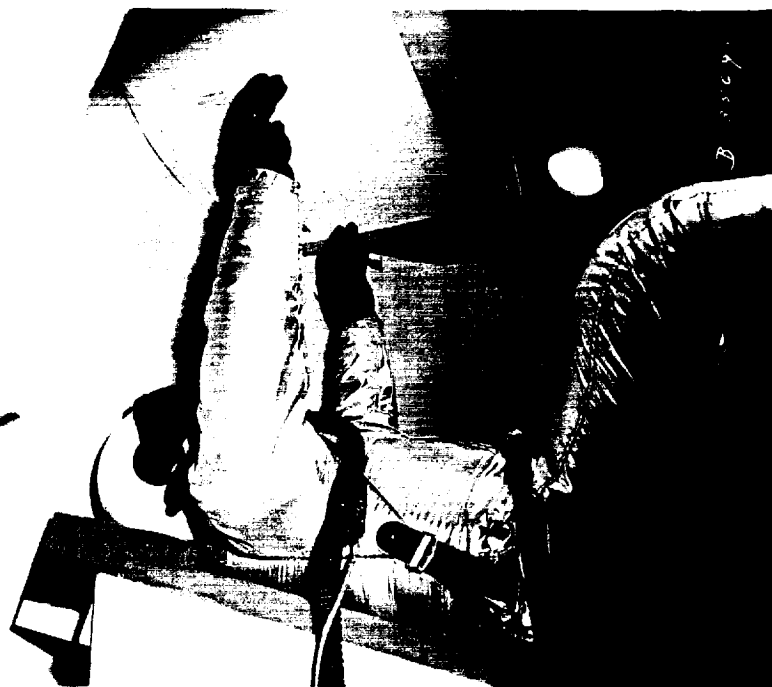
Such questions as: "Is it visible?"..... "Can it be reached?"... "Is there sufficient room to use it?"... can be answered quickly and completely by entering the layout and examining the item or area in question. Problems involving motion are handled better in this fashion than by any other method.

Very recently an answer to one major question has been determined in this manner. The question: "In an emergency situation, could the Apollo crew enter the Command Module, then put on a pressure suit?" No such requirement exists for vehicles in current use and little or no data was available regarding time and space minimums for donning the suit, under the conditions mentioned. The number and complexity of motions required to put on a pressure suit are such that drawings can not be used with confidence to determine the adequacy of an area for such use. The 3-D Layout, however, is well suited to answering questions of this type. A demonstration conducted within the confines of the W-1 Layout showed quickly and conclusively that the suit can indeed be put on in the available area.

During the above demonstration, a suspicion formed earlier, was verified: the side instrument panels must be hinged. An additional problem was also brought to light: The additional rigidity of the suit when pressurized prevented a foot and leg motion which is necessary if the crew member is to pass from the aft to the forward seat; accordingly, the seat will either be moved slightly, or the support structure altered to provide the necessary clearance.

As work on Apollo progresses to a more detailed state, other problems must be expected. They will be more detailed in type, but the 3-D Layout will continue to provide the best possible solution to many of these problems.





**Landing System Story**

**TM-9**

LANDING SYSTEM STUDIES

TECHNICAL MEMORANDUM 79

10 March 1961

R. Chandler &

J. Miller

TECHNICAL MEMORANDUM #9

LANDING SYSTEM STUDIES

1. Introduction -- The landing system normally brings the vehicle from the post re-entry condition to a planned earth location. However, it can be used under all flight conditions including escape from the launch pad. The system provides stability augmentation and deceleration, on-board terminal trajectory control, surface contact shock attenuation, and automatic location aids for land or water touchdowns. The first phase of the landing maneuver starts at approximately 80,000 feet altitude with the vehicle speed around Mach 2. At 10,000 feet the terminal phase commences using a steerable gliding parachute and ends with retro-rocket deceleration to touchdown.

With the exception of the retro-rocket, the system is designed for proper operation with any single sub-system failure. Although dual ignition systems (including dual pyrotechnic igniters) will be provided to insure retro-rocket operation, this device is too sensitive to ignition altitude and energy absorption requirements to allow complete redundancy. Crew survival under all situations is of paramount importance. The best approach to this achievement appears to be to reduce horizontal and vertical velocity to as nearly zero as possible at the touchdown point. The high rate-of-descent gliding steerable parachute and two thrust level (retro-sustainer) retro-rocket provide this soft landing capability.

2. Systems Considered -- In the effort to obtain the landing technique which best satisfied the aforementioned considerations, a wide range was explored. Considerable industry and government-agency consultation yielded basic data. Studies progressed from ridiculous methods, to possibilities, to practicalities, and finally to the selected system.

Those in the ridiculous category were a buoyant, on-board inflated, hydrogen-filled balloon (42 ft. diam.), an inflated spherical bag around the vehicle (53 ft. diam.), and an unassisted retro-rocket system. All of these with their gas or propellant stowage containers weighed nearly as much as the vehicle to be landed. Another in this category was the Barish "Flexi-rotor" which consisted of a vortex-ring parachute as the hub of a rotor formed of unrolled, tip-weighted fabric panels. This was eliminated by inherent de-

-----  
RECEIVED  
-----

274



ployment problems, non-controlability, and excessive development requirements.

In the possible category were horizontal landing vehicles. The fixed wing, "Dyna-Soar" type vehicle involves a weight penalty on the order of 50 per cent and was, therefore, not considered. However, the lentic shaped and elongated Eggers (M-2) bodies may be made subsonically stable by incorporation of retractable or inflatable fins and "winglets". These vehicles land at about 130 knots and require 5000 foot runways but offer many miles of glide range (4 to 6 times initial altitude based on low super-or subsonic maneuvering speeds). In addition to their weight penalties, the "abort off the pad" and the ability to land on unprepared surfaces require a vertical landing capability not met by the winged vehicles. Therefore, they were discarded.

As mentioned in the "Apollo Mid-Term Review" report (Martin Co. Engineering Report No. 11686), rotor blade systems were evaluated and discarded because of their excessive weight and packaging difficulties. A stowable Rogallo Kite was also seriously considered and will be discussed further.

### 3. Rogallo Kite - Skid Landing System

The glide range, maneuverability, and particularly the conventional horizontal landing technique of this configuration make it most attractive. From NASA research data, it appears that system weight is competitive and that the stowage problem can be solved. The only serious unknown quantity of this device is its deployment and erection under in-flight conditions. This complication arises from stowage limitations imposed by the lifting re-entry body configuration. An inflated-tube Keel configuration was briefly considered, but the uncontrollable buffeting of a large mass of fabric, suspension lines, and inflating conduits during the few seconds of inflation seemed rather disenchanted.

So a controlled unfolding 4-section rigid Keel system was designed from data obtained from D.E. Hewes, Spin Tunnel Branch, Langley Research Center. This device is packaged in a trailing pylon stowed in the mission module during most of the flight and requires heat protection during re-entry. A 1/10-scale model has been built to evaluate the unfolding technique and membrane stowage conditions within the box structure formed by the

collapsed I-section keel and leading edges. The wing area is limited mainly by the quarter-keel stowable length since more than four folding sections was considered impractical. The wing area is 1000 sq. ft. with a 50-degree leading edge sweep and 37.6 ft. keel and leading edge length. The maximum lift-drag ratio of this configuration is estimated to be 4.11 incorporating the drag of the vehicle and the wing loading is 6 psf. A larger wing area with respect to the vehicle size would result in improved L/D (the max. L/D of the wing alone is approx. 7). A larger area would also reduce the 40-knot landing speed by the square root of one-sixth the modified wing loading. However, ground stability then becomes a problem as well as stowage and deployment. Smaller wing areas become less efficient and result in higher landing speeds so were discarded.

The flexible wing uses aluminum alloy and steel I-section structural beams with 2, 3, and 4 inch webs and 4 inch flanges. The leading edges are modified by a semicircular outer section for improved aerodynamic drag characteristics. These Keel sections are erected and locked by explosive gas actuating cylinders, cables, and latches. The beam load distribution is triangular from the hoop-tension of the Mylar-coated nylon-fabric membrane. The maximum membrane tension is 35.3 lb/in. at 5 g's.

Landing loads are taken on the vehicle lower surface control flaps, designed for skidding with **air-oil shock struts**.

Control is accomplished by fore-and-aft or lateral movement of the system c.g. with respect to wing center of pressure. This is done with pilot controlled electrically powered winches. In this case, the vehicle must move 14.3 feet fore-and-aft to change the angle of attack from 20 to 45 degrees for cruise-glide and landing stall respectively. Lateral movement required is only 5 feet for a 30 degree bank resulting in an 850 foot turning radius at the 116 knot glide speed at 20,000 ft. altitude.

The flexible wing deployment might best be described by discussing the reverse or packing sequence from the erected position down to the stowed pylon. Assuming that the wing is in a zero angle of attack (horizontal) plane, the leading edges (pivoted at the nose or wing apex) are rotated in the horizontal plane to become tangent and parallel to the center keel. The membrane is pleated and collapsed into the cavity between the beams. This "box-beam" and the stowage pylon on which it is mounted are rotated in the vertical plane of symmetry aft to the trailing position. This

- "T-shaped" structure is the second step of the deployment sequence and is used as a first stage drag device -- both for vehicle stabilization and deceleration to reduce opening shock loads on the membrane. The "box beam" is then unlatched and the quarter-length sections (pivoting about their end hinge-points) are rotated in the plane of symmetry to become tangent and parallel to each other and the web of the H-section stowage pylon. Thus the entire assembly is compactly packaged within a 1 ft. square, 10 ft. long H-beam.
4. Steerable Parachute System Trade-offs

Figure 1 shows the weight-velocity trade-offs of parachute and landing impact absorption equipment. The parachutes are the Ringsail type. The pneumatic bags are neoprene-coated nylon pressurized with helium gas stored at 3000 psi in fiberglass spherical containers -- bag system weight includes the latter. The retro-rocket is a solid propellant wire-wound steel case type. The fixed weight includes drogue chutes and their risers, main chute risers, glide control and steerability equipment, and landing system sequencing equipment.

It is apparent that relatively slow rates of descent are necessary to avoid prohibitive system weights with para-bag systems -- even for bags designed for 16-g landing loads. The 100-foot diameter practical limit on parachute size arises from opening time requirements for escape from the pad, low gliding velocity (12 knots), packing complications, and excessive weight for redundancy. Excessive weight and poor performance eliminated para-bag systems from further consideration.

Figure 2 shows the proposed gliding steerable parachute and its operation. An electric winch of approximately one horsepower provides actuation of the chute control flap for glide or turning control at the pilot's command. It is significant that the horizontal velocity vector may be controlled in magnitude from 0 to 50 ft/sec. as well as being variable in direction.

## 5. Steerable Parachute Piloting Techniques

The steerable parachute previously described will be pilot controlled during the descent from 8500 ft. to ground surface - 2300' at Edwards Air Force Base. The selection of the landing point will normally be made by the pilot through a visual ground reference system. Selection of the ground contact point and landing direction is desirable for these reasons - to avoid local ground hazards, such as excessive slope, marsh, trees, etc. and to achieve a minimum horizontal velocity.

The determination of the ground contact point will be a more difficult problem. If the wind profile is known, the periscope can be slewed to the descent angle produced by the average wind and the descent velocity of the vehicle. The ground area observed would then be the area in which the pilot could maneuver during the descent.

Due to wind variation during descent, the velocity within the maneuver range would vary and produce apparent complication for the piloted landing. However, the pilot could reach any point within the glide range on the view screen. This technique would require a means of programming the wind profile into the optical system to maintain the ground contact area in the field of view. Another method would be the use of an average wind, slew the periscope as previously described, and then require the optical system to hold this field of view.

278

Attainment of the selected landing point depends upon the pilot's capability to see the vehicle movement on the field of view and to make the necessary corrections in direction and velocity to reach the desired landing point and have a touchdown horizontal velocity of approximately zero.

Vehicle velocity can be measured by knowing the altitude and rate of change of the angle between a reference point at time  $t_1$  and its position at time  $t_2$ . Parachute descent during this same time period will also produce an increase in this reference angle. This would be interpreted as ground speed by the optical system. Figure 3 shows the time required to pass through an angular displacement of 1 minute of arc vs. altitude. Also provided are the time limits during which the change in altitude does not produce an error in horizontal velocity greater than 1/2 ft/sec.

It is seen from Figure 3 that there is an excess of time over that required to observe the displacement due to one minute of arc and therefore the altitude error need not be considered and its complication in determining horizontal velocity can be eliminated.

Another problem is the capability of the pilot to discern movement on the view screen within the range of 50 to 0 feet/sec.

The rate threshold of man's ability to perceive motion, as determined by Aubert in 1888 is 1-2 minutes of arc per second. Later work by J. F. Brown in 1931 indicated 2 to 6 minutes of arc per second were required. Assuming the maximum value of 6 minutes of arc per second, an 18" distance between the eyes and the view screen, and a view screen diameter of 10", the following table shows the threshold velocities at various altitudes.

#### THRESHOLD VELOCITY FOR EYE PERCEPTION

Alt. (Ft.)	8000	5000	2000
Velocity (ft/sec)	15	10	4

279

The pilot can, therefore, perceive the rates of motion concerned in this problem without magnification. If lower threshold velocities become desirable, they can be achieved through magnification. The displacement threshold is approximately one minute of arc. Since 20 minutes of arc can be achieved before reaching the accuracy limit due to descent, this threshold will not be restrictive.

In the event of an abort in weather, the landing selection point cannot be made; however, by previously dropping a radio beacon (serving a major purpose in assisting search and retrieval), the second function of achieving minimum ground velocity can be accomplished. Equipment that would determine direction and distance to the beacon would also be required.

If ground communication, providing knowledge of vehicle predicted contact point and existing surface winds can be made, the pilot could maneuver the vehicle to reach a horizontal velocity of approximately zero at touchdown.

The following landing procedure demonstrates a possible typical landing. While a total glide distance of 2000 ft. is shown, this distance can be increased to 2600 ft. by omitting the wind orientation maneuver.

#### LANDING SEQUENCE

<u>Time</u> Sec.	<u>Time</u> Sec.	<u>Alt.</u>	<u>Maneuver</u>	<u>Function</u>	<u>Remarks</u>
0	5	8500	Determine desired landing area.	Parachute closed.	Pilot decision only.
5	2	8125	Turn input to desired landing.	Open flap.	Pilot controlled system.
7	10	7975	Turn 180°	Adjust flap for Max. velocity.	Maximum turn assumed

<u>Time</u>	<u>Time</u>	<u>Alt.</u>	<u>Maneuver</u>	<u>Function</u>	<u>Remarks</u>
17	20	7225	Straight glide at max. speed.	Maintain max. speed. Deter- mine possibil- ity of making initially selected landing area. Make first wind estimate.	Covered 1000' @ 50'/sec.
37	5	5725	Turn 90°	Cant Flap.	Pilot decision. Turn to new heading for improved landing.
42	20	5375	Straight glide at max. speed.	Open flap.	Covered 1000' @ 50'/sec.
62	12	3975	Fly wind star (2 - 60° turns 7 sec.) 1 - 5 sec. leg	Move flap as req'd.	This maneuver was included as a typical wind orientation maneuver. If wind are known by surf. observation or communication, a glide maneuver would replace thi
72	12	3135	Turn to wind heading and adjust to 0 velocity.	Move flap as req'd to reach desired heading and velocity for zero touch- down.	Flap must be set at predetermined position to nullify wind velocity.
84	-	2300 (50' ground clearance)	Fire Rockets	Automatic system - altitude sensing and rocket ignition.	

## 6. Retro-Rocket Requirements

Figure 1 indicates that para-retro landing system weight is minimum at a descent velocity of 80 ft/sec. However, current gliding steerable parachute data require a 70 ft/sec. rate-of-descent to counteract the guideline horizontal wind velocity of 30 knots (50.7 ft/sec.). This value came from parachute glide angle test data by Milton T. Kane of Sandia Corp., Albuquerque, New Mexico. Later Radioplane (Div. of Northrop Corp.) test data indicate that this glide angle may be improved allowing a lower rate of descent while still maintaining up to 50 ft/sec. horizontal speeds. However, a retro-rocket based on a rate-of-descent of 70 ft/sec. was sized and later decreased in weight by a Thiokol Corp. design.

An error analysis was performed to determine the ignition altitude tolerance and the residual energy that must be absorbed by a sustainer phase of rocket burning. Assuming normal distributions of occurrence, statistical tolerances were established as follows. Rate-of-descent decreased to 61.8 ft/sec. when a 5400 lb. suspended weight is considered with the previously designed main chute.

### One sigma rate-of-descent Error Contributions (about 61.8 ft/sec. at sea level)

+1.2	ft/sec.	due to variation of atmospheric density at sea level.
+0.8	"	" " " " " " " " with altitude to 5000'.
+0.85	"	" " " " " " parachute drag coefficient. (.70 ± .02)
+2	"	" " " " " " unsteady air (gusts, etc.)
+0.8	"	" " " " " " vehicle weight. (5400 ± 135 lb.)

RMS =  $\pm 2.73$  ft/sec. ( $\pm 4.4\%$ ).

### One sigma Rocket Ignition Timing Tolerances (about 50 ft. altitude, 2 sec. burn)

+0.0084	sec.	due to pendulum action of suspended system ( $\pm 7^\circ$ ).
+0.0253	"	" " " " terrain roughness ( $\pm 1.5$ ft.).
+0.0169	"	" " " " sensor error ( $\pm 1$ ft.).
+0.0052	"	" " " " contact switch.

RMS =  $\pm .032$  sec. ( $\pm 1.6\%$ ).



### One Sigma Rocket Burning Time Tolerances (about 2 sec.)

$\pm .10$  sec. due to rocket thrust variation ( $\pm 2.5\%$ ).  
 $\pm .126$  " " " variation of vehicle weight ( $\pm 2.6\%$ ).  
 $\pm .087$  " " " " " descent velocity ( $\pm 4.4\%$ ).  
 $\pm .05$  " " " " " soak temp. and manuf. ( $\pm 2.5\%$ ).  
 RMS =  $\pm .1895$  sec. ( $\pm 9.5\%$ ).

The root-mean-square altitude error was computed from the sum of the squares of the products of the ignition timing tolerance and descent velocity and the burning time tolerance and one-half the descent velocity (average during burn). The result was  $\pm 6.2$  feet. It is significant that ignition error contributed less than  $\pm 2$  feet to the above relation. The retro-burning phase needs the major improvement.

A sustainer phase with a thrust slightly less than the vehicle weight accounts for this error by lowering the vehicle slowly to the surface such that the resultant velocity can be absorbed by structure crushing.

The foregoing error analysis will be refined during the remaining study period. It is recognized that some parameters may be interdependent or may have skewed distributions of occurrence causing the computed error to be misleading. However, it is significant that accurate knowledge of parachuted rate-of-descent and vehicle weight with corresponding correction to retro-ignition altitude can considerably reduce contact velocity and nearly eliminate structural energy absorption.

7. Impact -- The work that has previously been accomplished in impact theory has been applied primarily to spherical entry bodies. However, the work accomplished by NASA with the Mercury shape gives some insight as to impact g's that can be expected. In these studies a small change in attitude was found to have considerable effect in reduction of the acceleration along the vertical axis. This reduction occurred in both sand and water impacts. The reduction <sup>in sand</sup> was from 74 g's to approximately 47 g's at 10° attitude and 30 g's at a 30° attitude. In water the maximum g's of 35 reduced to 10 at a 30° attitude.

These values were the result of tests made at an impact velocity of 30 ± 1 fps.

Using the NAVORD Report 3533, a rough estimate of g's during the flow establishment phase was made and the load factor for the W-1 configuration at 30 fps was approximately 10 g's. The drag coefficient determined from this study was for spherical bodies. Therefore, this value is low.

Determination of the actual load factor at various points in the W-1 configuration at various impact velocities and attitude would require a more detailed study and test program than can be made during this study.

However, it is felt that the test programs conducted by NASA have shown a range of load factors that will have some application in the Apollo vehicle.

Using crushable honeycomb, at a velocity of 30 fps and a load factor of 27, a stroke of 12 inches will be required. In addition, a structure that is capable of taking a pressure of 27 psi. is also necessary.

Multiples of retro-rockets were examined to insure impact attenuation with the following results:

1. If two rockets, each of which can do the job, are fired, the vehicle accelerates up - at 123'/sec. (2 sec. burn, 12,000 # each).
2. If two rockets are used, the combination of which does the job, and only one fires, the vehicle hits the ground at 61.9'/sec.

The only solution using two rockets is that only one fires. If both fire, because of malfunctioning the vehicle is accelerated upward. Conclusion - make one rocket reliable enough to fire once ignited.

Therefore, it appears that a lower contact velocity must be assured rather than attempting to absorb the high impact energies associated with the higher velocities.

8. First Phase Drag Device -- The drogue parachute diameter has been based primarily on the drogue parachute used in the Mercury. Its function is to provide stability from Mach 2 at 80,000 feet to the main parachute opening at 10,000 feet. It will also provide a means of main parachute deployment and will reduce the main parachute opening loads through additional drag.

It has been designed for an opening load of 92,500# ultimate. This is based on a  $q$  of 700 psf.

11 ft. diameter First ribbon drogue parachute will provide a force of approximately 6600# at Mach 2 and an altitude of 80,000 ft.

The present riser length places the skirt five base diameters from the base of the vehicle. A study of the literature indicates that this is a minimum distance for parachutes. If data from the Cree missile tests indicate that this distance must be increased, each additional base diameter will require 7 lb. of riser.

#### 9. Flotation Model Tests

a. Wooden models 1/20 scale were constructed and floated to empirically determine:

- (1) Stable floating positions and their waterlines,
- (2) Static roll stability limits (roll-over angle from vehicle horizontal reference plane).

The L-1, L-2C, and M-1-1 models were ballasted to weigh .75 lb. (6000 lb. full scale) and to centers of gravity obtained on 1/25/61. Models were floated on 1/27/61. On the L-1 model the c.g. was 6.8 in. (full scale) above the desired point due to physical limits of wood construction. A photograph was taken of each model in its two floating positions. Figures 4, 5, and 6 show typical positions.

#### b. Results

	Roll-over Angle-degrees from normal position	C.G. Location-in.	
		X	Z
L-1	90	75	21.6 (28.4 on model)
L-2C	85	30.8 above base on centerline	
M-1-1	85	97	6.8 below

#### c. Conclusions

- (1) All models floated in two positions -- normal upright and inverted.
- (2) All models were extremely stable -- had to be rolled almost vertically before they would capsize to their alternate floating position.

285

- (3) L-1 and M-1-1 floated such that the back face (door opening area) was always exposed to the atmosphere.
- (4) L-2C most stable flotation attitude was cone-end submerged (escape door area).

~~CONFIDENTIAL~~

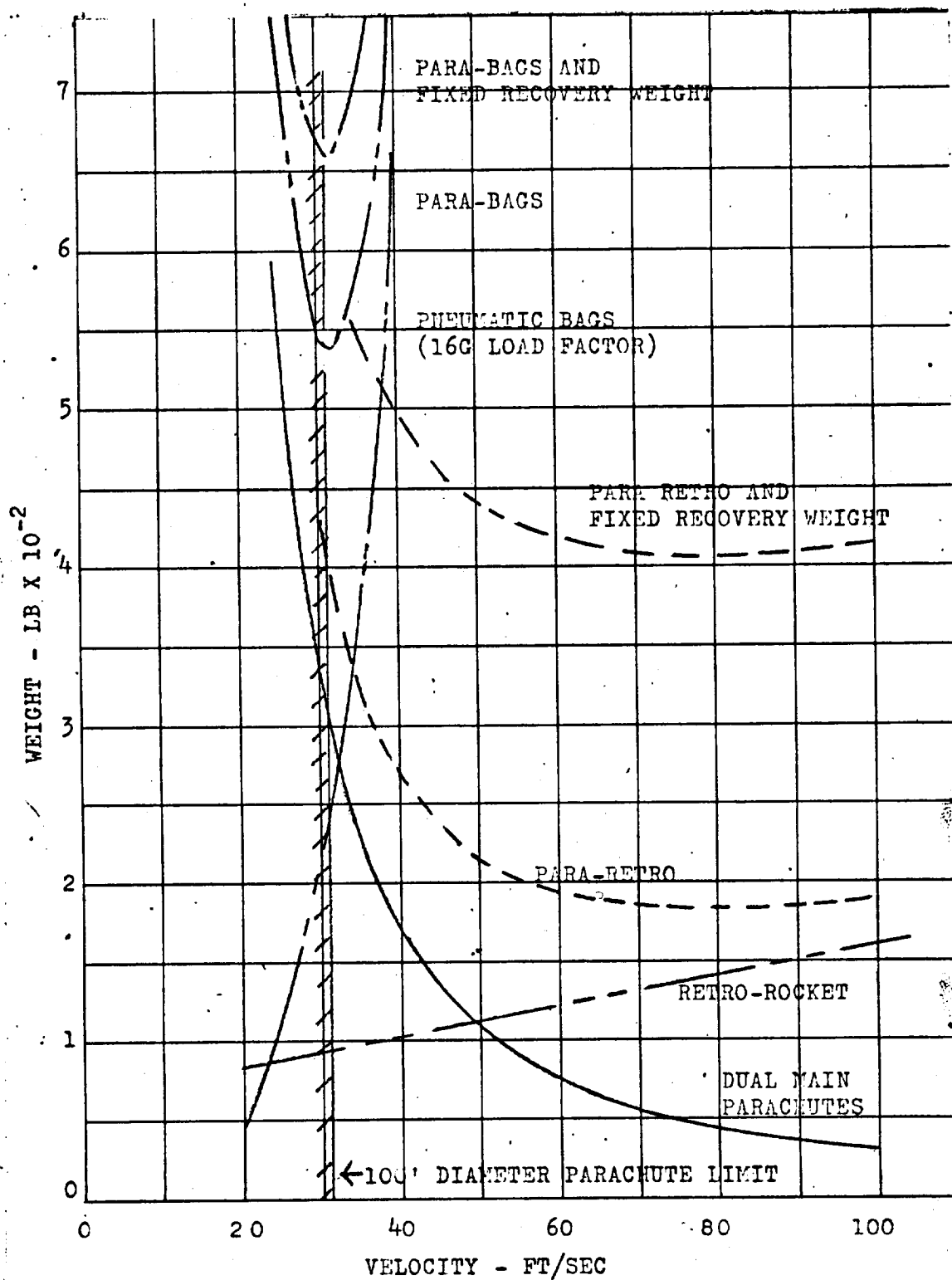
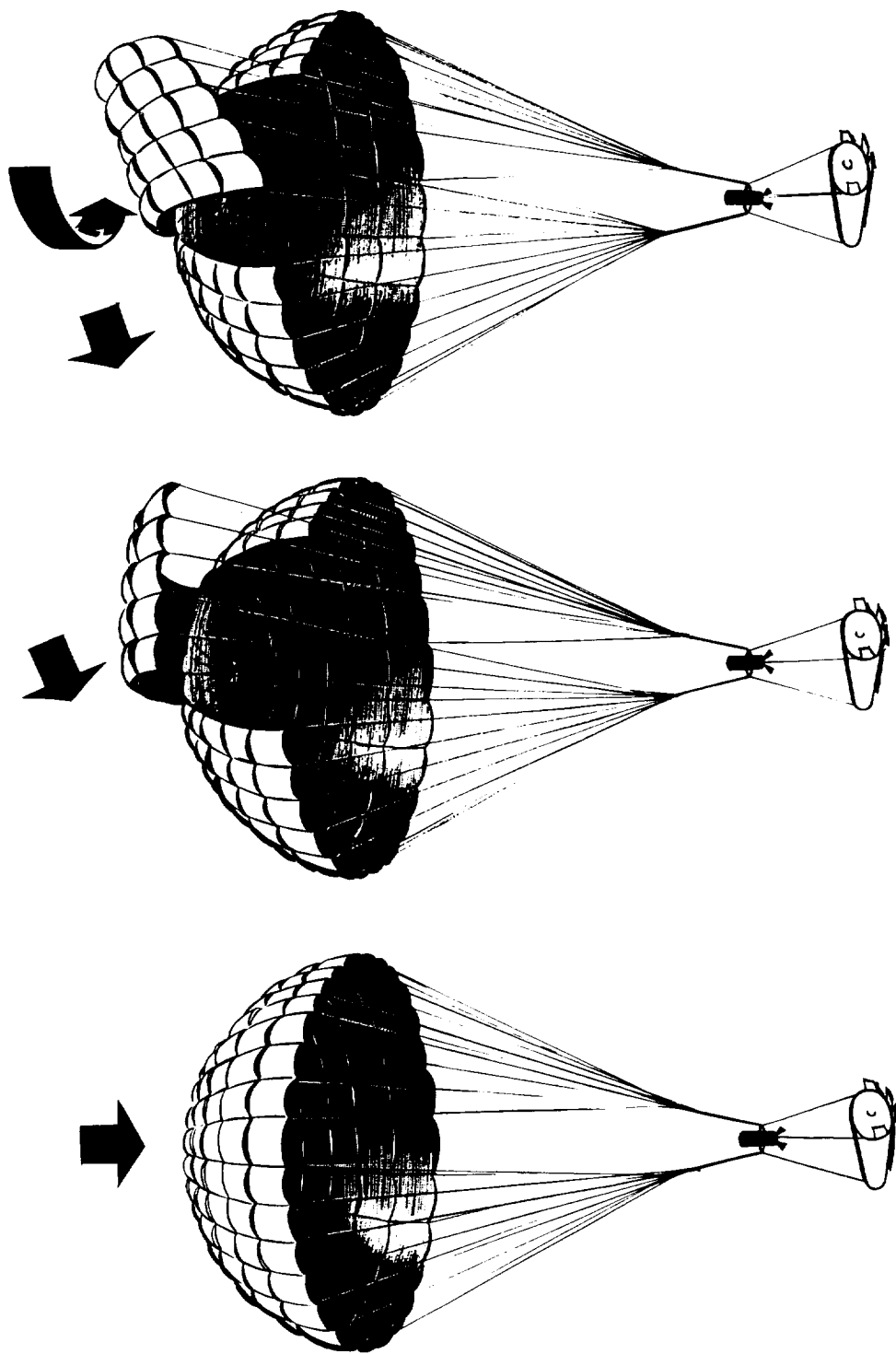


Figure 1 Landing System Weight vs Descent Velocity

# GLIDING STEERABLE PARACHUTE



**TURNING**

**GLIDE**

**DESCENT**

FIGURE 2

CONFIDENTIAL

CONFIDENTIAL

CONFIDENTIAL

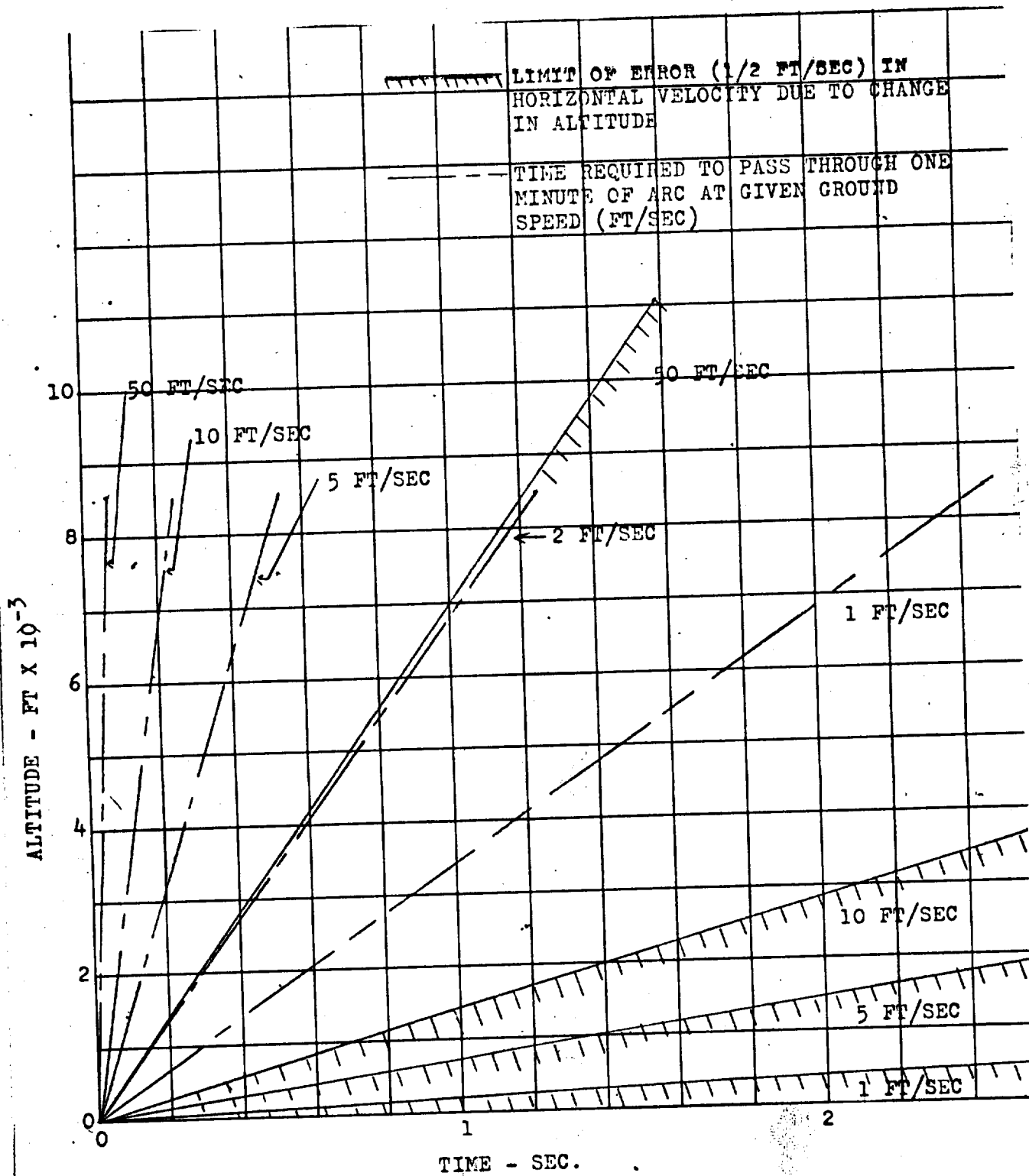
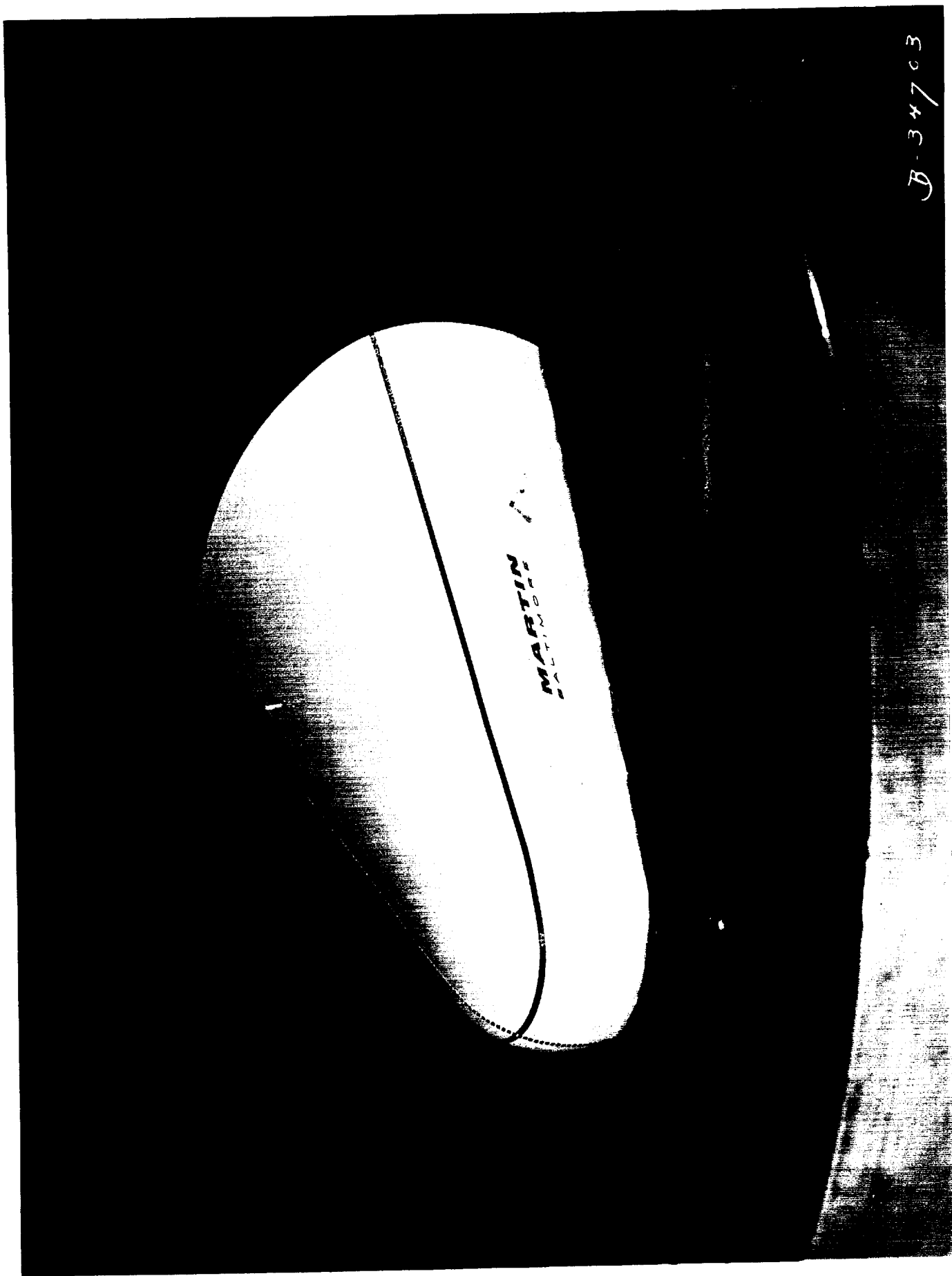


Figure 3 Time to Pass Thru A One Minute Angle vs Altitude



B-34703

FIG. 4



B-34704

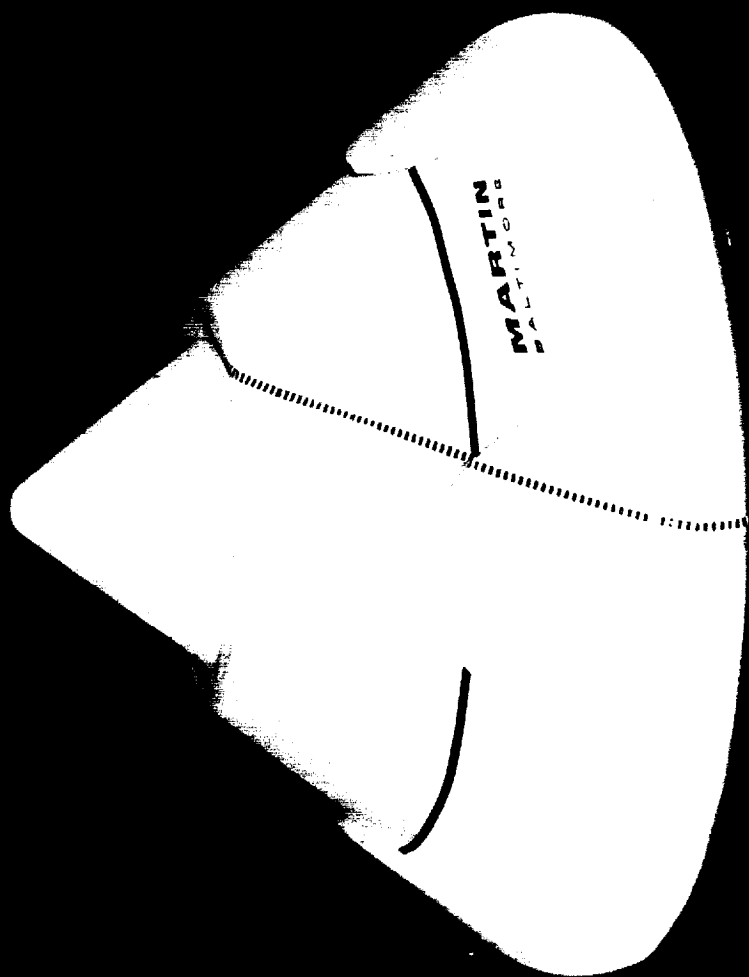
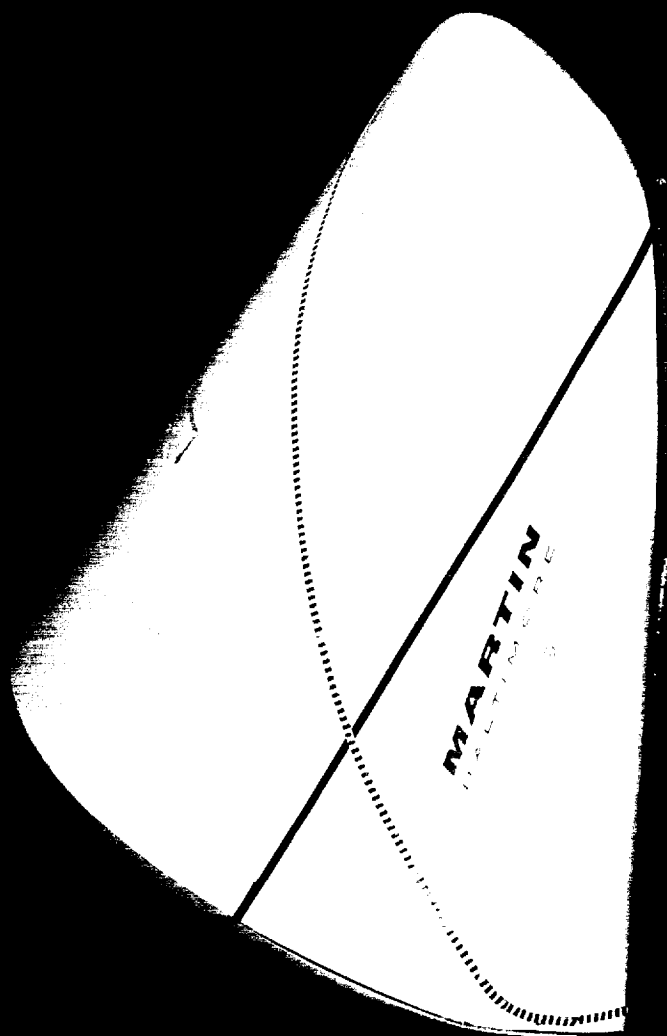


Fig 5

B-34702



Environmental Control

TM-10

10 Mar 1961

## TM-10 - ENVIRONMENTAL CONTROL SYSTEMS

1. System Design, Safety, and Reliability

The initial system proposed in the MLV study has been refined and reviewed for functional reliability. A preliminary reliability analysis estimate of 83.88% (based on the MLV system plus a molecular sieve) has been increased to a current estimated value of 99.54. The major changes included revisions in the molecular sieve system configuration and addition of gaseous emergency oxygen and nitrogen supply in the command module. The basic system modifications were primarily in valving needed for proper system operation during various modes of system operation. The proposed configuration is shown on TM-10-1 and TM-10-2.

2. Molecular Sieve CO<sub>2</sub> Absorption Systema. Alternate Approaches

The systems currently under study are modifications of that proposed by Hamilton-Standard (Ref: EP 60707). The modifications include a cycle time compatible with the Apollo earth orbital mission, as well as heatless desorption, continuous heating and alternate heating and cooling for the silica gel bed. Use of a freeze-out approach in lieu of the silica gel bed has also been considered. A general schematic is shown on Fig. TM-10-2.

b. Power and Cooling Penalties

Summaries of the characteristics of the systems under consideration are listed in table TM-10-1. Direct weight saving over lithium hydroxide absorption would be about 140 pounds. This is subject to reduction by the power and cooling penalties noted in the table. The high peak load of the heatless desorption approach imposes a significant penalty during the lunar portions of the mission.

c. Development Problems

The basic development problem in this system is with the molecular sieve bed valves, since these are exposed to hard vacuum

# SYMBOLS

VA



FILL VALVE



VENT (O.B. - OVERBOARD)



CHECK VALVE



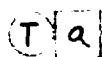
QUANTITY INDICATION



ACCUMULATOR-EXPANSION  
TANK

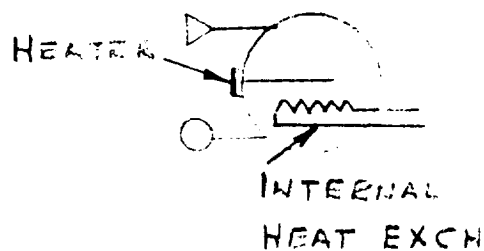


PUMP



WATER SEPARATOR  
ACTUATOR/TIMER

CRYOGENIC - SUPERCRITICAL  
O<sub>2</sub> - N<sub>2</sub> STORAGE TANK



A- SNORKEL IN  
B- SNORKEL E  
C- SHUTOFF  
D- SEPARATION  
E- COMPARTME  
F- AIRFLOW E  
G- PRESSURE  
H- VACUUM RE  
J- CABIN SAF  
K- PRESSURE  
L- COMPARTM

1- SHUTOFF  
2- BYPASS  
3- RELIEF  
3a- HIGH PRES.  
4- PRESSURE  
5- OXYGEN PA  
6- NITROGEN  
7- PRESSURE S  
8- SEPARATIO

11- CREW TEMPE  
12- SHUTOFF  
13- (REENTRY) C  
14- (REENTRY) E  
15- HELIUM PRE  
16- HIGH PRES  
17- LOW PRESS  
18- FILL-VENT  
19- EQUIPMENT  
20- EQUIPMENT

# LVE IDENTIFICATION

LET (BAROMETRIC)  
 CHAUST (BAROMETRIC)

U SHUTOFF  
 INT SHUTOFF (BAROMETRIC)  
 BYPASS  
 RELIEF  
 ELIEF  
 ETY  
 SUIT PLUG-IN/CHECK  
 TENT SAFETY

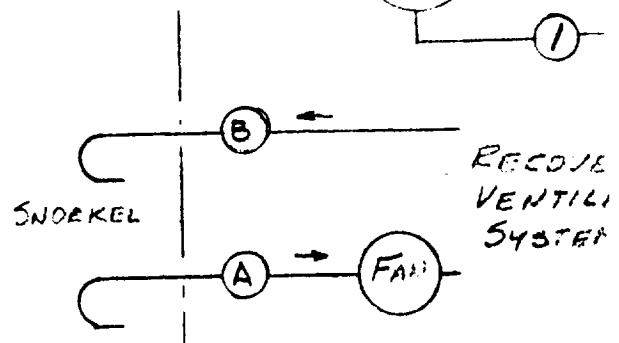
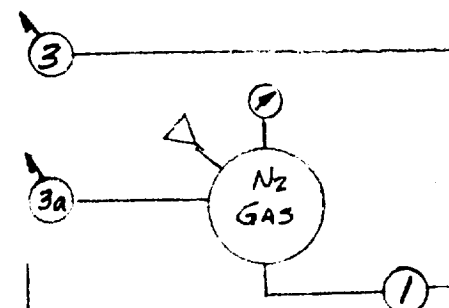
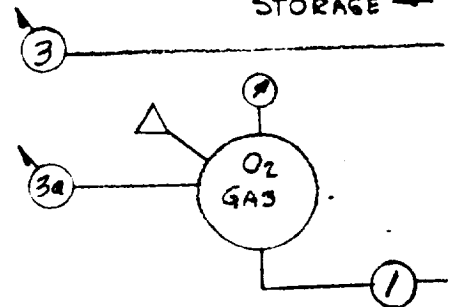
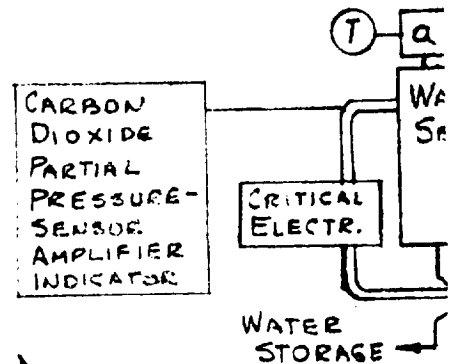
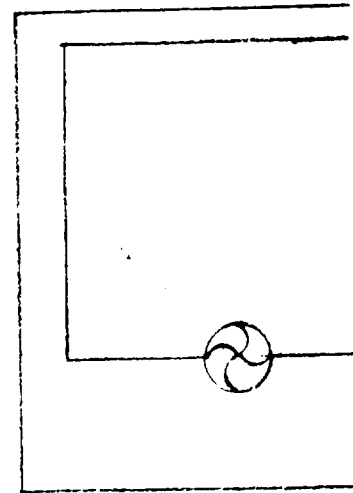
SURE RELIEF  
 REDUCER  
 RTIAL PRESSURE  
 TOTAL PRESSURE)  
 TUIT PLUG IN/CHECK  
 IN SHUTOFF

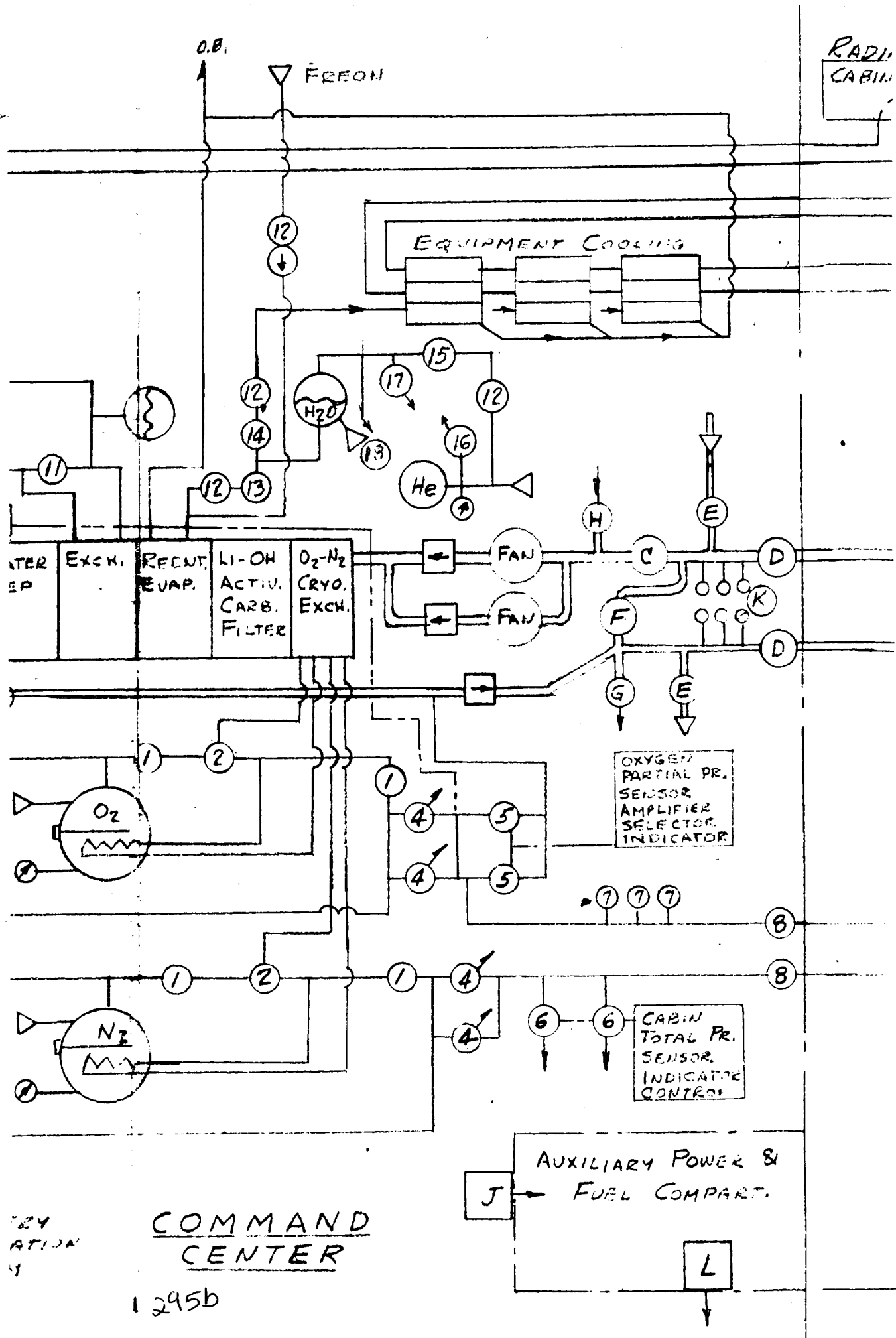
IRETARE CONTROL

RAIN TEMPERATURE CONTROL  
 EQUIPMENT TEMPERATURE CONTROL  
 PRESSURE REDUCER  
 SURE RELIEF  
 URE RELIEF

TEMPERATURE CONTROL  
 GROUND COOLANT

1 2950

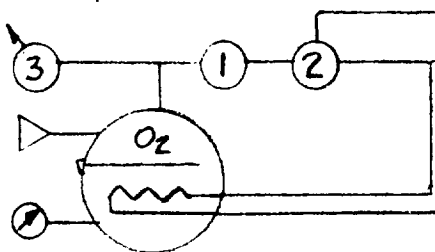
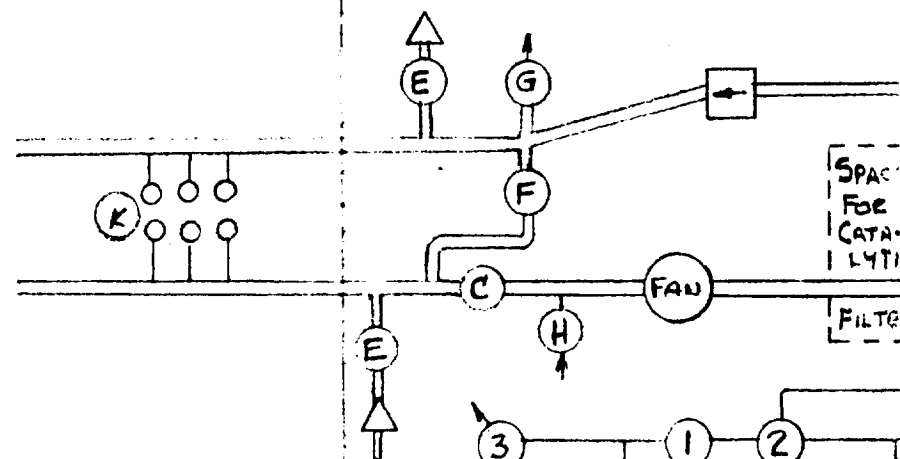
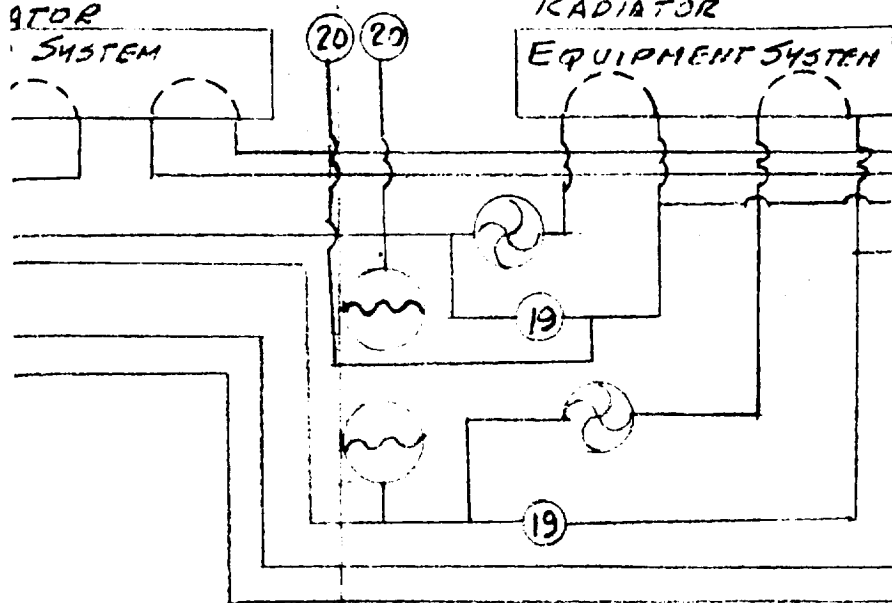




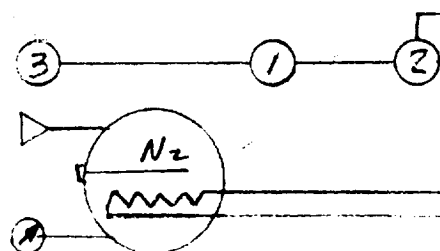
COMMAND  
CENTER  
1295b

STOR  
SYSTEM

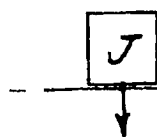
RADIATOR  
EQUIPMENT SYSTEM



7 7 7

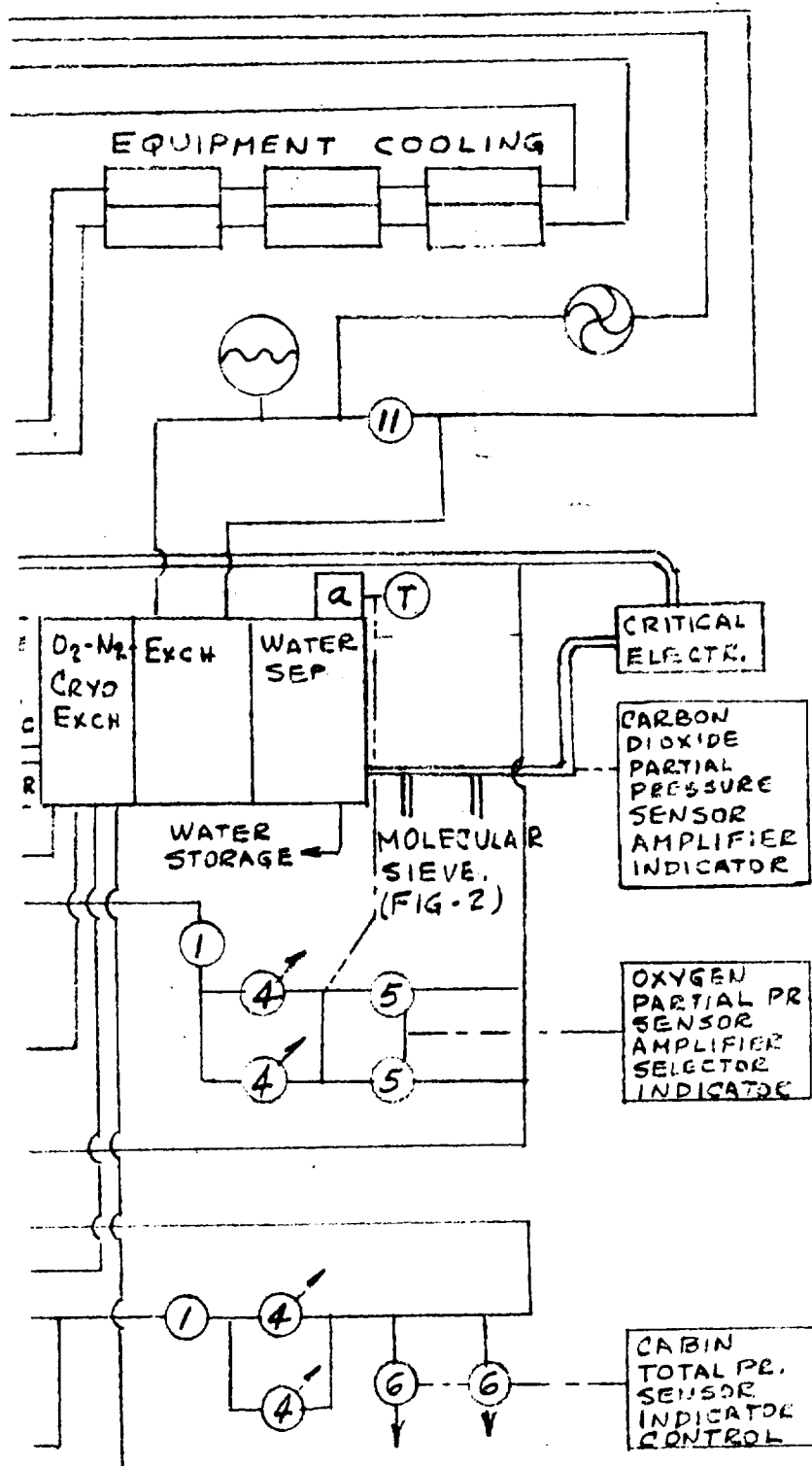


MISSION  
MODULE



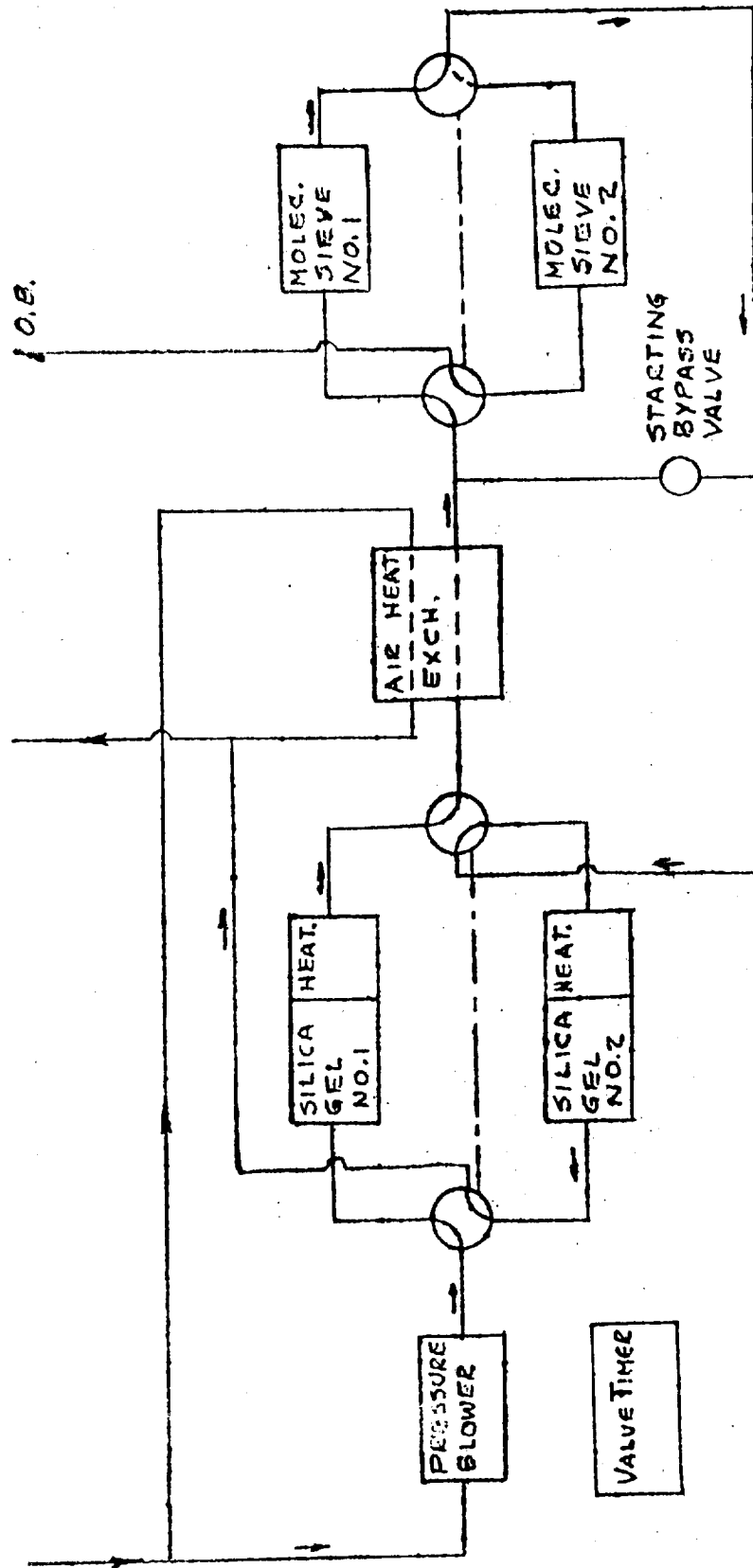
295e





## ENVIRONMENTAL CONTROL SYSTEM

FIGURE TM-10-1 2-9-61  
RLR



# MOLECULAR SIEVE SYSTEM

FIG. TM-10-2

(REF: HAMILTON STANDARD LETTER 12-19-60 & PHONE MODIFICATIONS)

ALTERNATE REACTIVATION LOOP. 2  
 PARTIAL HEATING OF SILICA GEL  
 FROM EQUIPMENT COOLANT  
 LOOP (BALANCE FROM ELECTRICAL  
 HEAT), THEN COOLING SILICA  
 GEL FROM CABIN COOLANT  
 LOOP. IF USED, DELETE AIR  
 HEAT EXCHANGER UNLESS NEEDED  
 IN GROUND BYPASS OPERATION.

and must operate approximately 1000 cycles during the mission. Basic reliability of the system can be improved by the addition of a manual override on all valves which will permit partial operation of the system while repairs are made to the malfunctioning items. During this type of emergency operation, the carbon dioxide level will be about twice normal value (but less than 1%).

Table TM-10-1

Molecular Sieve		Hamilton Standard		American Machine & Foundry	
Type		Silica Gel Dryer		Silica Gel Dryer	13X Mol. Sieve Dryer
Weight		54.0		49.0	45.0
Size		Appx. 18" cube			
Power Peak		1168 <sub>w</sub> El. (20 min/ 3 hrs.)	728 <sub>w</sub> + 1685 BTU	230 <sub>w</sub> Continuous	*Probably about the same
Fan		90 <sub>w</sub> El.	90 <sub>w</sub>	110 <sub>w</sub>	
Average		218 <sub>w</sub>	139 <sub>w</sub>	340 <sub>w</sub>	
Ground-Predry		1028 <sub>w</sub> - 2 hrs.	Same		
Heat Load - BTU/Hr.					
Desorb. Heat		477		785	
Fan		307		375	
Total		784		1160	
ΔH over LiOH System (BTU/Hr.)		479		855	

\*Based on lower weight flow  
in 13X bed.

### 3. Heat Sinks

#### a. Passive/Semi-Passive Systems

The extent to which internal heat could be dissipated by passive means from the mission module was evaluated using the basic configurations shown on Fig. TM-10-3 for an internal heat generation of 10,000 BTU/Hr. The surface areas and physical configuration used in early studies (original configuration) of the mission module would permit this heat dissipation if internal air velocities were high enough to transfer the heat to the internal shell. This would necessitate the use of an internal skin and blower configuration and would result in an internal radiator using air as the heat transfer medium (Semi-passive system).

With the present configuration, the controlling factor is the interior radiation exchange between the inner and outer vehicle shells. Approximately 4200 BTU/Hr. can be dissipated through this configuration at the required temperature level, using a semi-passive system arranged in a similar manner to that of the original configuration. This capacity would be further reduced if equipment is installed in the annular area between the shells.

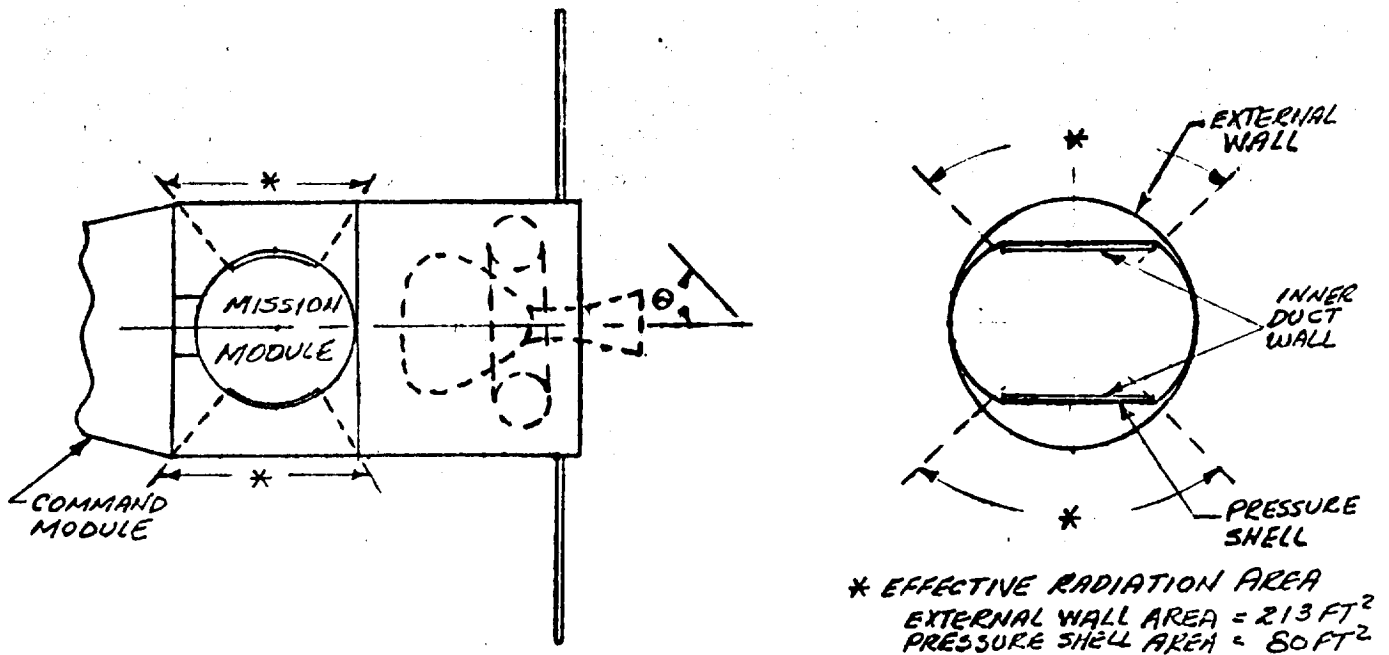
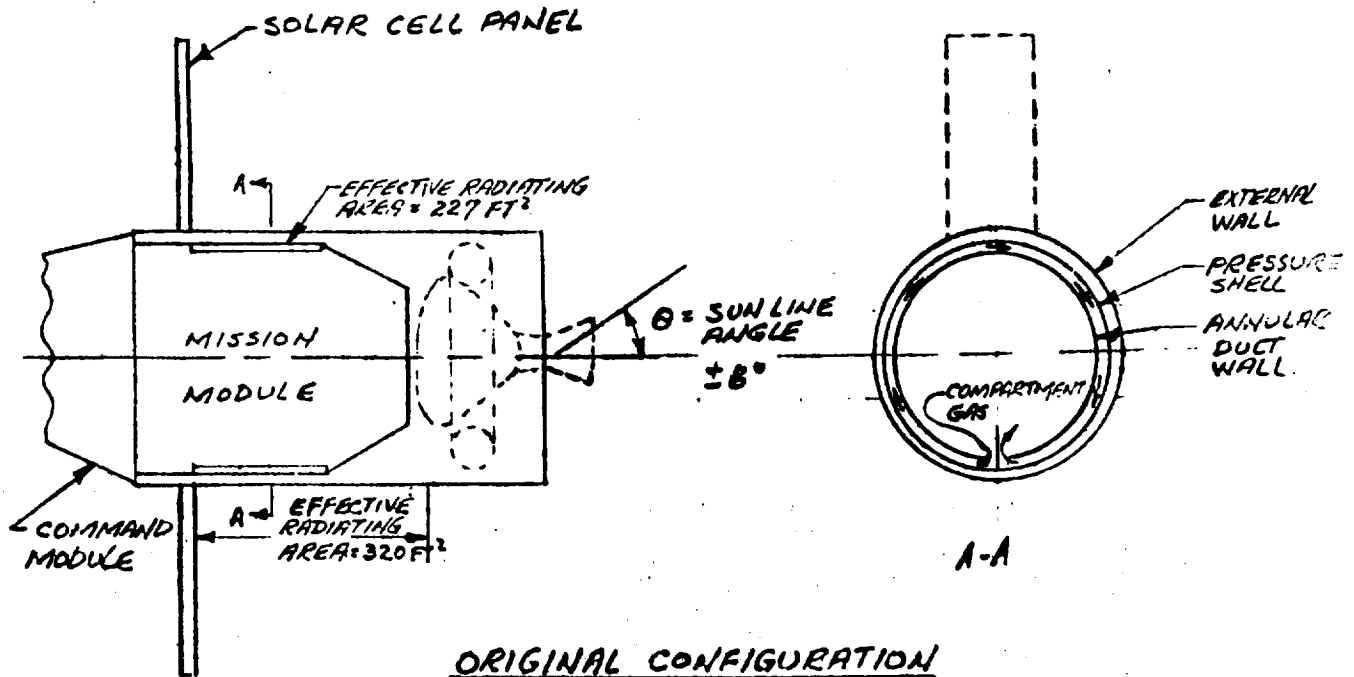
Practical problems resulting from the use of a semi-passive system would include:

- (1) Lack of positive control of compartment humidity level. The internal skin temperature is below cabin dew point and condensation on the skin would occur. Practical fan pressure drop considerations would limit annular duct velocities to values too low to guarantee condensed moisture pickup under weightless conditions.
- (2) Loss of cabin pressure unless the inner skin was readily removable to permit access to puncture damage. Loss of pressure would also result in loss of cooling because of inability of fans to operate in very low cabin pressures.

#### b. Radiative Systems

Preliminary evaluation of both internal and external heat transfer properties has been made. The controlling factor is the external radiation.

# PASSIVE TEMPERATURE CONTROL GEOMETRY



PRESENT CONFIGURATION

The radiators are oriented to see deep space at all times (Fig. TM-10-4, Position 2). Figure TM-10-4 shows several configurations which were considered. Figures TM-10-5 and TM-10-6 indicate a preliminary analysis of the radiator operating temperature levels which could possibly result with the heat dissipation rates which have been assumed. (These curves are preliminary and will be subject to significant changes after final evaluation of the configuration.)

External heat transfer from the radiators will be adequate for the circumlunar mission except during the near-earth and low lunar orbit portions of the mission. During these periods the temperature level of <sup>the</sup> cabin system radiator will be too high for moisture control and adequate heat dissipation. Use of water evaporation during these periods to boost cooling system capacity in order to reach the desired temperature levels is feasible with a low expenditure of water. Use of this approach during the earth-orbital mission would involve large amounts of water and integration of the cooling load with cryogenic fuels for an auxiliary power unit is being studied.

Since the external radiation heat transfer is the controlling factor, the internal heat transfer can be evaluated on the basis of pumping power, wet weight of the heat transfer loop, practical passage limits for the heat loads under consideration, and material thickness needed for meteorite protection. After evaluation of the above factors, ethelene glycol was selected as giving the minimum vehicle weight penalty.

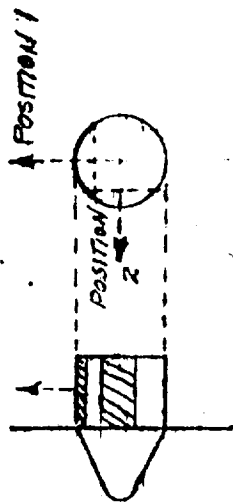
#### 4. Water Recovery System

A review of the possible systems for recovering water from urine and wash water indicates that only the vacuum distillation and compression distillation techniques have reached a development status which would make their use feasible on the Apollo vehicle.

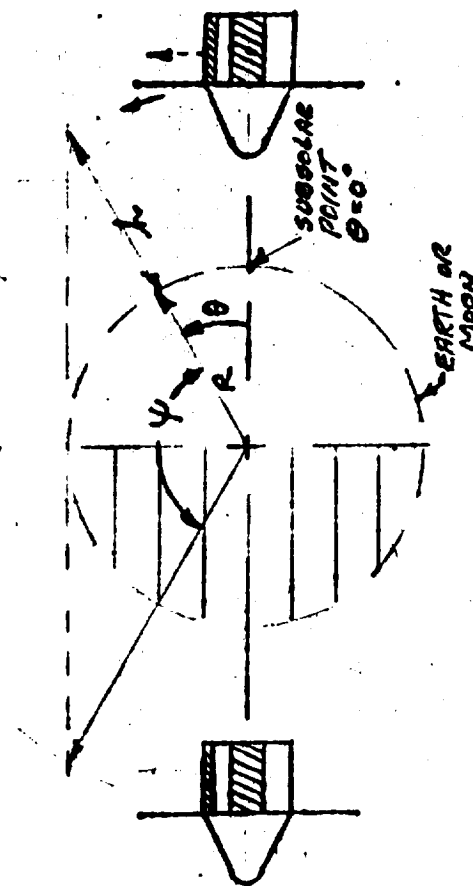
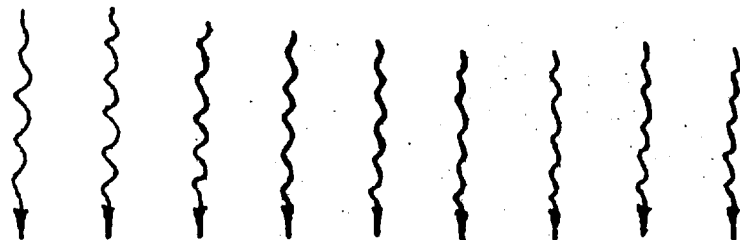
Data taken from nuclear submarine tests indicate that condensate from the air conditioning system can be used for drinking after being

# RADIATOR ORIENTATION GEOMETRY

POSITION 1. VEHICLE ORIENTED SO THAT NORMAL TO PLANE THROUGH EDGE POINTS OF RADIATOR LIES IN ORBITAL PLANE.



POSITION 2. VEHICLE ORIENTED SO THAT NORMAL TO PLANE THROUGH EDGE POINTS OF RADIATOR IS PERPENDICULAR TO ORBITAL PLANE



R = RADIUS OF EARTH OR MOON

h = ORBITAL ALTITUDE

theta = ANGULAR POSITION DURING ORBIT STARTING AT SUBSOLAR POINT

psi = ANGULAR PORTION OF ORBIT DURING WHICH RADIATOR DOES NOT RECEIVE DIRECT AND REFLECTED RADIATION

psi = 36 DEGREES

$$= 2 \cos^{-1} \left( \frac{R}{R+h} \right) \text{ (FOR POSITION 1)}$$

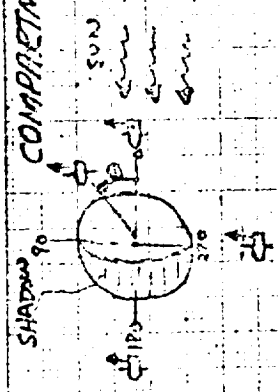
TM-10-4



LUNAR ORBIT PERIOD = 5.35 HRS @ 1000 MILE  
(6.125 DEGREES/HR)

METHODS & DATA: REF  
ORACREBT  
M 1501-2

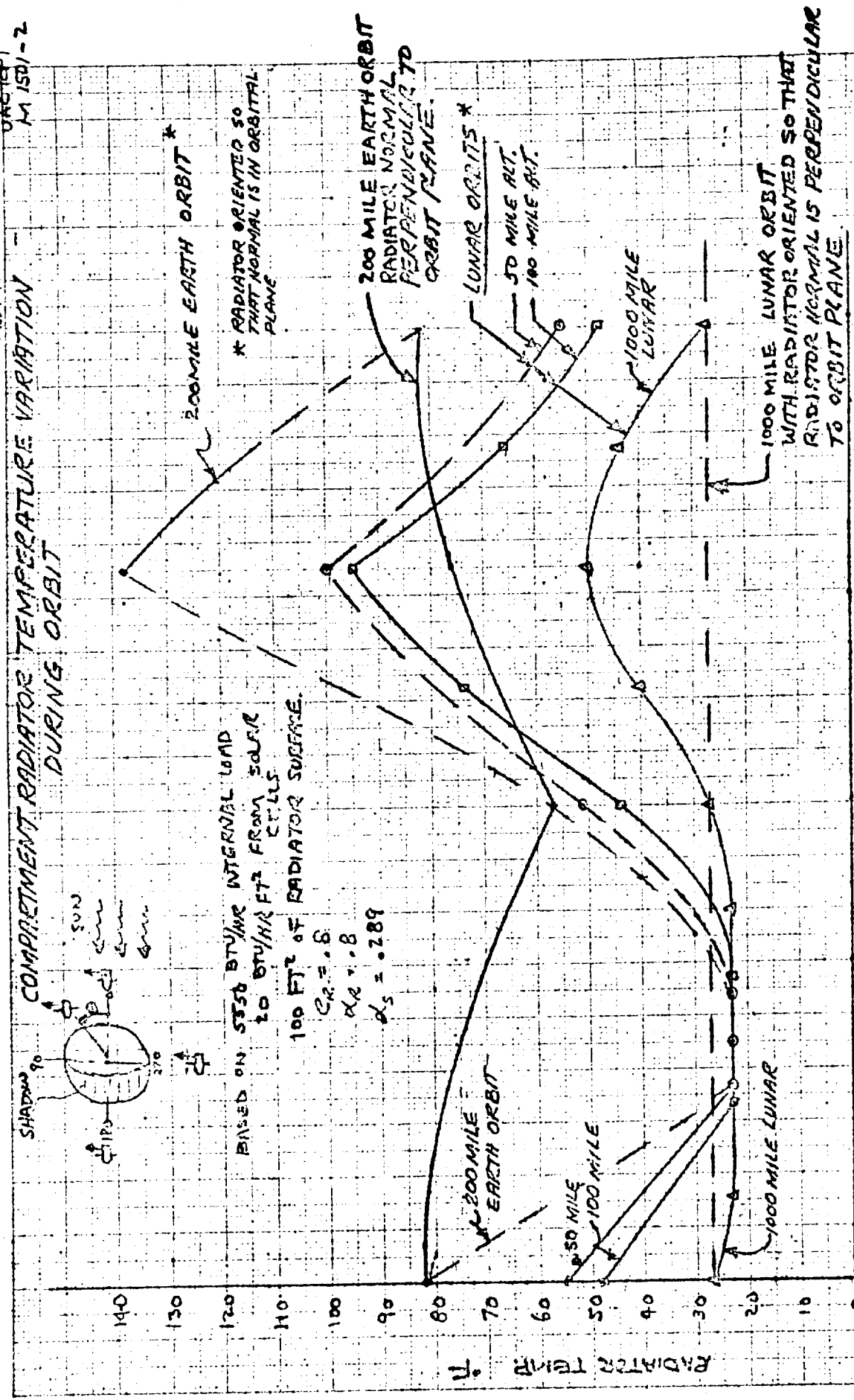
# COMPARTMENT RADIATOR TEMPERATURE VARIATION DURING ORBIT



BASED ON 5350 BTU/HR INTERNAL LOAD  
20 BTU/HR FT<sup>2</sup> FROM SOLAR  
CELLS

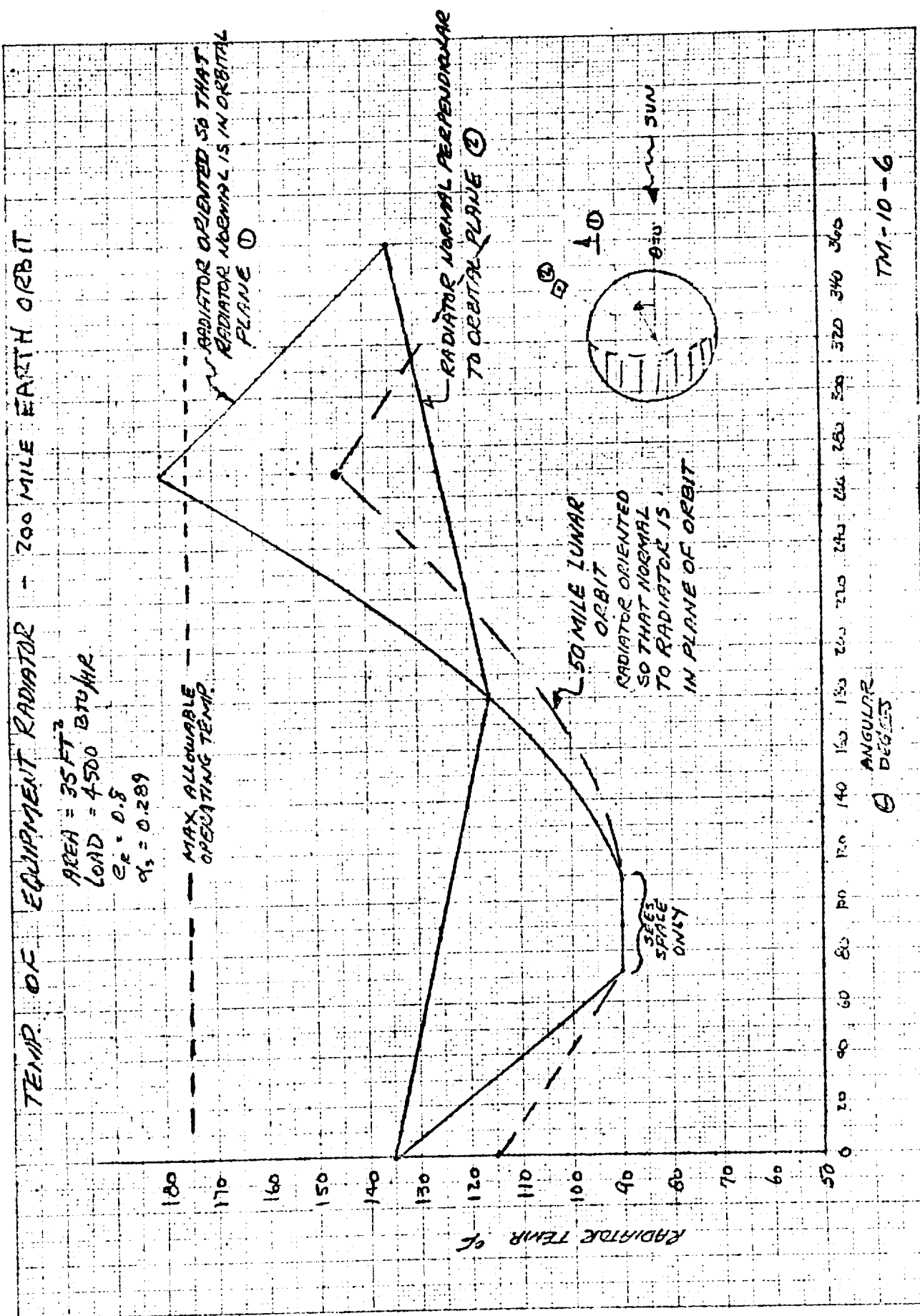
100 FT<sup>2</sup> OF RADIATOR SURFACE

$C_{R} = .8$   
 $A_{R} = .8$   
 $d_s = .289$

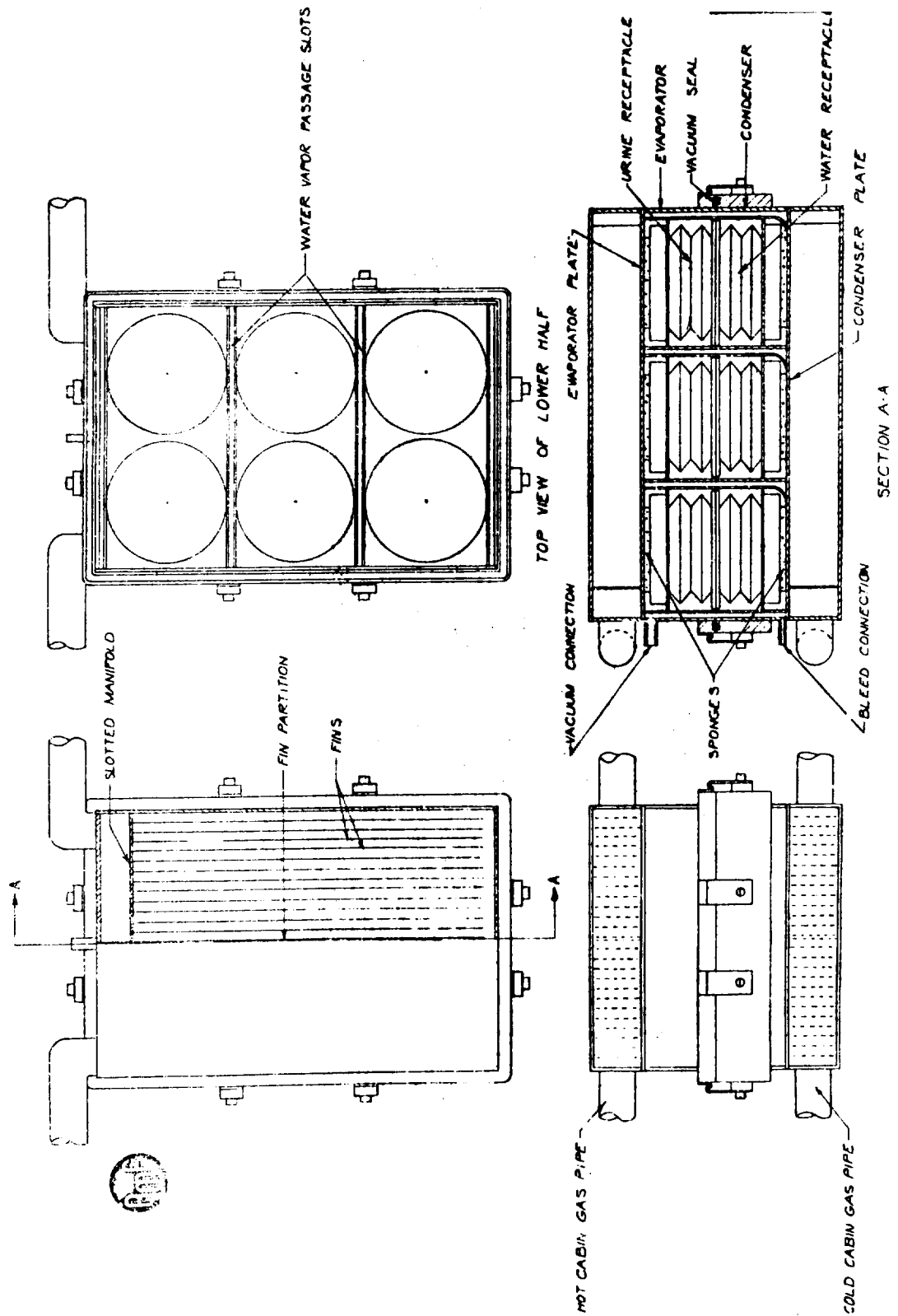


ANGULAR  
θ, DEGREES

TM-10-5



✓ treated chemically and does not need to be processed in the water recovery system. The proposed vacuum distillation system (Fig. TM-10-7) and compression distillation system (Fig. TM-10-8) were sized to process a fluid rate of 4.2 pounds in 8 hours, thus requiring essentially continuous operation for the mission, but giving the minimum size equipment. To process an additional 2 pounds of water per day per man (for washing) would increase the size of the units about 50%. Processing water on a batch basis would require a further increase in size. Pertinent data on the proposed units are included in table TM-10-2.



TM-10-7

VACUUM DISTILLATION UNIT

AMERICAN MACHINE & FOUNDRY COMPANY

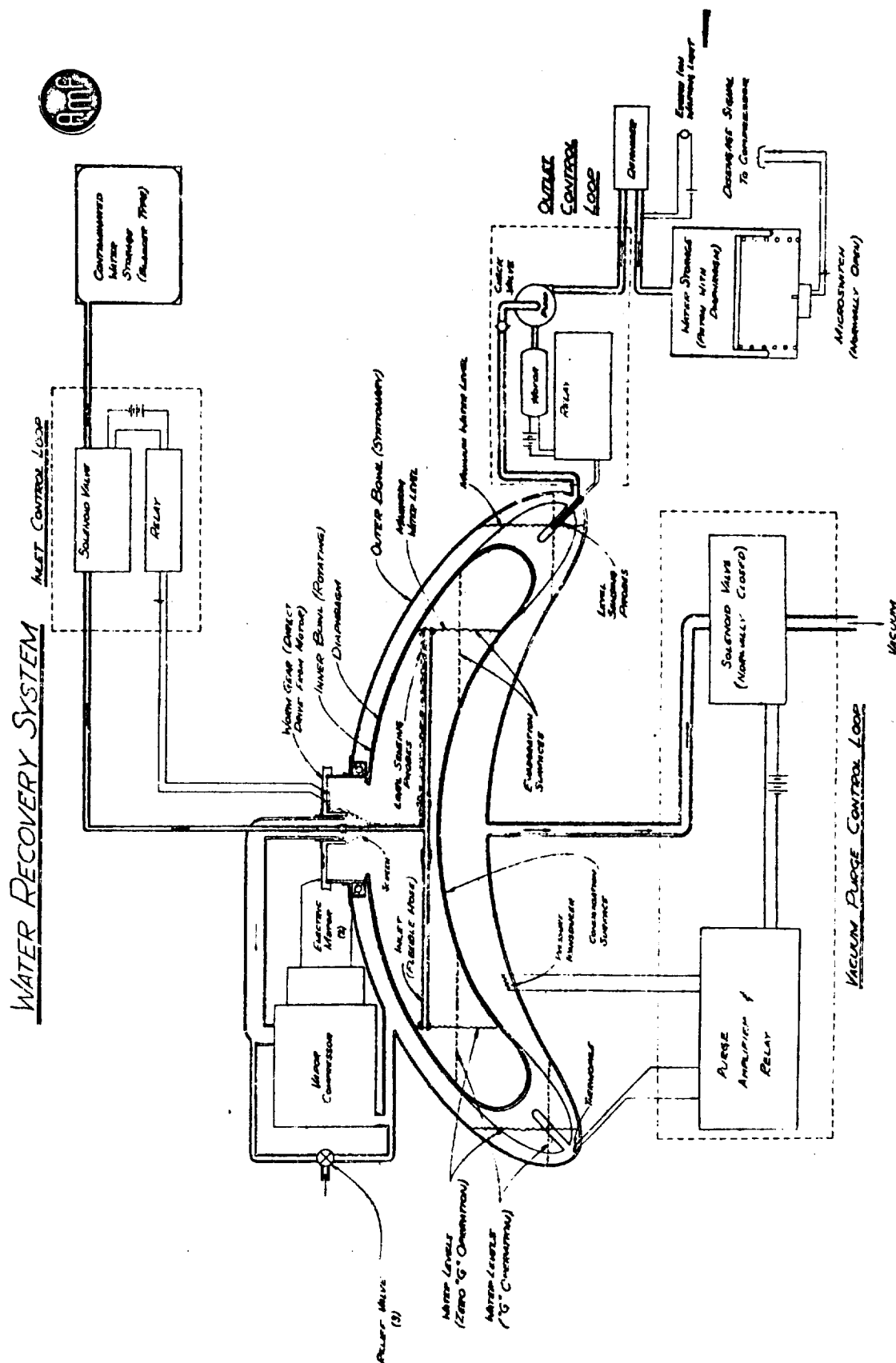


Table TM-10-2

Type	Vacuum Distillation		Compression Distillation	
Figure	TM-10-7		TM-10-8	
Capacity #H <sub>2</sub> O/8 hrs.	4.2	6.2	4.2	6.2
Weight - Lb.	26	35	49**	55**
Size	12"x12"x16"	12"x18"x16"	1.2 Ft. <sup>3</sup> (16" dia. x 10")	1.5 Ft. <sup>3</sup> 1.9 Ft. <sup>3</sup>
Power - Watts	None or 21*	Same	113	120 to 150
Cooling Required BTU/Hr.	555	835	385	460
				512

\*\* Based on AMF estimates plus allowance for water storage container weight based on water amounts.

\* Automatic operation (controls power).

## 5. Secondary Power Prime Mover

Two basic types of hydrogen-oxygen fueled secondary power units have been studied for possible application during dark or unoriented periods of vehicle operation. These are the conventional turbine cycle (AiResearch) and the reheat cycle (Sundstrand hypercycle). Either system would drive an alternator and re-entry cooling system water pump and would be comprised of dual prime mover units and controls coupled to a single set of fuel tankage. Since the systems would normally operate less than 10% of the vehicle mission time, the additional complexity needed to use the cycles for additional cooling over that used for the basic power generation unit appears unwarranted.

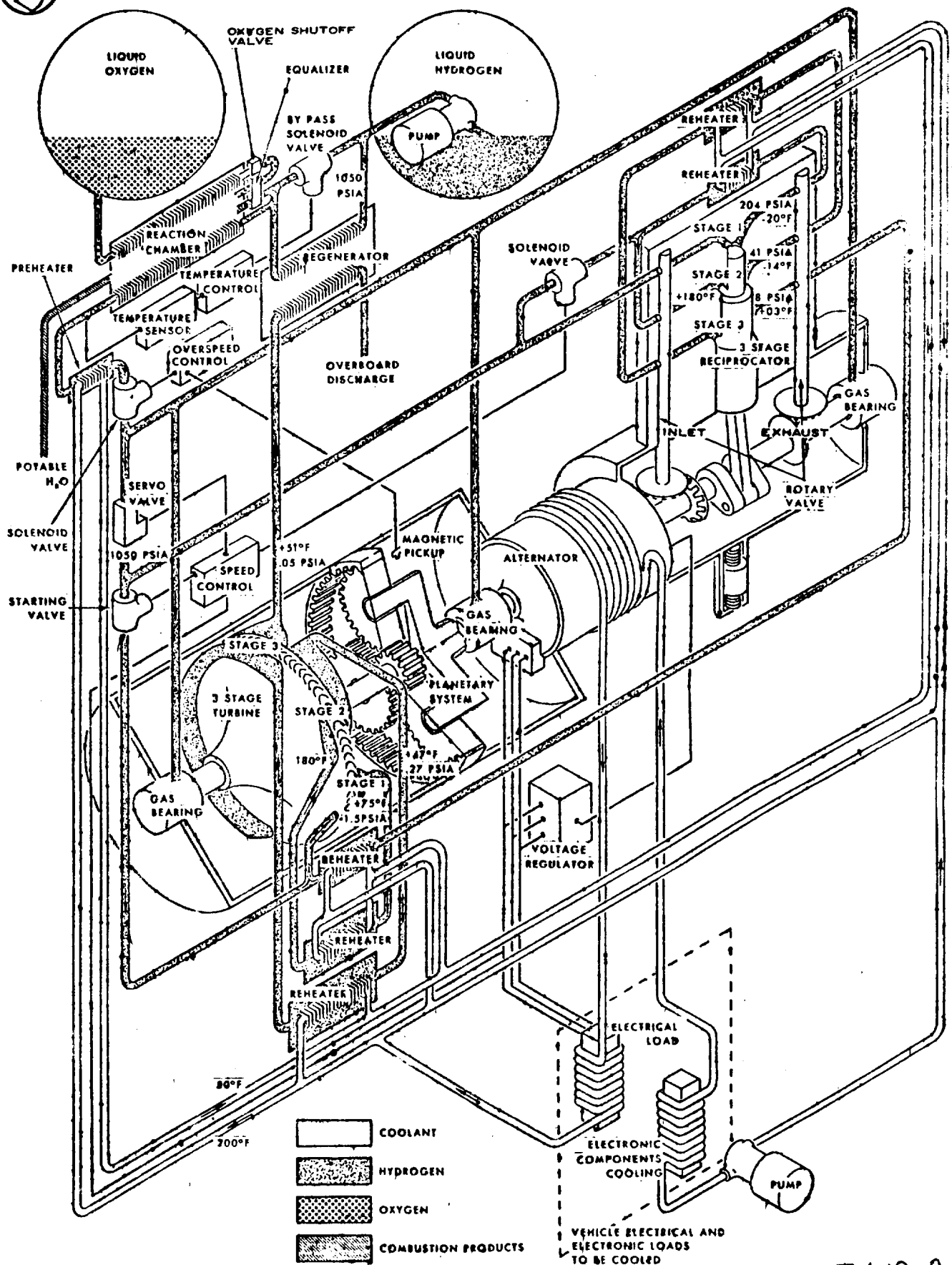
The basic cycle used by AiResearch is based on heating the hydrogen fuel by heat from the alternator and power unit lubricating system. Oxygen is then added and the combustion output is passed through a four stage multiple re-entry turbine, exhausting to vacuum. Fuel is stored in supercritical cryogenic form, thus eliminating pumping. Turbine operating temperature is nominally 1600°F.

The reheat cycle (Hypercycle) proposed by Sundstrand for this application (see Fig. TM-10-9) is based on a six stage unit - three stages reciprocating and a three stage multiple re-entry turbine. The turbine speed of 60,000 RPM is geared down to a 6000 RPM shaft speed on the reciprocating portion of the unit. The cycle is basically a hydrogen expansion cycle, with oxygen being used only to supply enough heat to close the cycle thermodynamically. The turbine operating temperature is 160°F. The 20,000/1 expansion ratio requires a fuel inlet pressure of 1050 PSIA which requires hydrogen pumping. Since positive pump inlet pressure under weightless conditions would be required, use of supercritical cryogenic stowage or an expulsion fuel tank system would be required. Use of an expulsion system appears undesirable because of the low temperature problems occurring with any bladder material.

309



DENVER



SYSTEM SCHEMATIC

TM-10-9  
310



Aerodynamics of W-1

TM-11

A P O L L O

Mid-Term

AERODYNAMIC CHARACTERISTICS OF THE W-1 AND L-2-C

Technical Memorandum No. TM - 11

THE MARTIN COMPANY

Baltimore 3, Maryland

✓ March (13) 1961

C. Perrine  
P. Frank

# AERODYNAMIC CHARACTERISTICS OF THE W-1 AND L-2-C

## Summary

This technical memorandum presents the estimated, and in some case experimental, aerodynamic characteristics for the W-1 and L-2-C configurations. Subsonic transonic and hypersonic estimates have been made and are presented.

## I Introduction

During the early phase of the Apollo study, various aerodynamic characteristics have been required for evaluation of W-1 and L-2-C configuration. Hypersonic characteristics were required for reentry performance, heating and control studies. Transonic and subsonic characteristics were required for launch abort studies. This document summarizes the estimates which have been made to date. Figure 1 shows a sketch of the two vehicles of interest.

## II W-1 Aerodynamics

### A. Hypersonic

The hypersonic aerodynamic characteristics of the W-1 reentry vehicle were obtained by calculations using Newtonian Impact Theory. All force and moment coefficients are referenced to the circular base area and the body length. The angle of attack is measured with respect to the cone center line.

The longitudinal characteristics are shown in Figs. 1 through 3. The lift and drag coefficients and lift to drag ratio are plotted as functions of angle of attack in Fig. 1. The maximum lift coefficient ( $C_L = .585$ ) occurs at approximately  $50^\circ$

angle of attack and at an  $L/D = 0.51$ . The maximum  $L/D$  is 0.80 at  $26.5^\circ$  angle of attack. The zero lift angle of attack is  $+5.5^\circ$ . The important force parameters are summarized in the table below.

$\alpha$ DEG.	$C_L$	$C_D$	$L/D$	$W/C_{DA}$	$W/C_{LA}$
0	0	.275	0	216	$\infty$
26.5	.41	.51	.80	117	146
50	.585	1.17	.51	51	100

The pitching moment coefficient about the center of gravity is also plotted in Fig. 1 as a function of angle of attack. The data includes the effects of two undeflected longitudinal control flaps whose total area is equal to 10% of the vehicle reference area. The pitching moment coefficients were calculated for center of gravity locations on the cone center line at 60%, 65%, and 70% of the body length (measured from the nose).

At the 70% location, the vehicle is neutrally stable at the angle of attack for  $(L/D)_{max}$ , and is marginally stable as the angle of attack increases to  $C_{L_{MAX}}$ . The 70% c.g. location therefore represents the aft limit for static longitudinal stability.

With the c.g. located at 65% of the body length, the W-1 is statically stable throughout the usable angle of attack range.

The forward limit of the c.g. location is determined by the requirement to trim the vehicle at  $C_{L_{MAX}}$ . This forward limit is closely related to the control surface characteristics. Since the control surfaces are located on the lower aft edge of the body, positive pitching moments, (nose up) cannot be obtained. The control surfaces are in the body "shadow" when positive deflections

(trailing edge up) exceed the angle of attack. For these reasons the most forward c.g. location is obtained when the surfaces are deflected, completely out of the air stream, and are exerting no negative moments. An analysis was made of the size of the longitudinal control surfaces required. This analysis was based on longitudinal trim and damping requirements plus an allowance for roll control. Since all of the information required to make this estimate was not known, it was necessary to make certain assumptions. These assumptions were:

1. Maximum deflection =  $\pm 60^\circ$
2. C.g. located at 65% of body length on the cone center line.
3. Pitch damping requirement on deflection =  $20^\circ$
4. Roll control requirement on deflection =  $10^\circ$
5. Trim requirement is based on angle of attack change from  $C_{L_{MAX}}$  to  $(L/D)_{MAX}$ .

The results of this analysis showed that a flap area of 10% of the reference area would be required. This value for flap area was used in the determination of the longitudinal characteristics of the vehicle.

The control surface deflections required to trim versus angle of attack are shown in Fig. 2 for a c.g. location of 65% of body length. Note that about  $30^\circ$  of positive deflection margin is maintained over most of angle of attack range of interest. This margin is sufficient to supply the estimated pitch damping and roll control requirements. The positive trim deflections will result in relatively low control surface heating rates.

The directional stability characteristics at zero angle of attack are shown in Fig. 3. The vehicle has directional static stability without side flaps at a c.g. location of 65% of the body length. The characteristics at angle of attack <sup>are</sup> presently being determined.

It will be necessary to add side flaps for directional damping and to trim out the effects of yaw due to roll. These side flaps will probably be required for adequate directional stability at large angles of attack. The size of the flaps required for these purposes has not yet been determined. The present size shown in the detailed drawings are based on estimates using unpublished NASA Langley wind tunnel data on a flat bottom configuration similar to the W-1.

#### B. Transonic

Transonic pitching moment characteristics of the W-1 were required for studying abort gyrations at maximum dynamic pressure during boost. Maximum dynamic pressure occurs at a Mach Number of about 1.3. Although it is not possible to calculate exactly the aerodynamic coefficients for this velocity range the attempt was made to evaluate the transonic pitching moment coefficients of the W-1 escape configuration by comparing with test results of the Mercury escape configuration for  $M = 1.3$ .

The Mercury test data are given below

M	$\frac{dC_m}{d\alpha}$	$\frac{dC_N}{d\alpha}$	$C_X$
1	-.0085	.0288	.780
1.1	-.0107	.0312	1.050
1.3	-.0125	.0450	.920
1.4	-.0110	.0400	.890
1.6	-.010	.0300	.760
6.0	-.0137	.0400	.270
9.6	-.0150	.0450	.235
30	-.0150	.0450	.235

316

These data indicate that the pitching moment coefficients and the normal force coefficients for  $M = 1.3$  and  $M = 6$  to  $30$  are about the same. The large difference in axial force coefficients between  $M = 1.3$  and  $M = 30$  is partly caused by base drag.

Based on the comparison of the above Mercury data normal force and moment coefficients were taken from hypersonic calculations. The result is shown in Fig. 5.

In the calculated  $\alpha$  - range from  $-15^\circ$  to  $+15^\circ$ , the escape configuration is stable from  $\alpha = -6^\circ$  to more than  $+15^\circ$ .

### C. Subsonic

The requirement for subsonic static stability in the escape configuration was the determining factor in the design of the escape system. In order to estimate the subsonic characteristics, of the escape configuration, a technique was developed which when checked against the Mercury wind tunnel data gave the results shown in Figure 6.

With this estimation technique, a number of methods for obtaining a stable subsonic W-1 escape configuration were investigated. The results are shown in Fig. 7. It was found that adding ballast to the tower or stabilizing fins required excessive weights to be added to the vehicle. However, by retaining the transition fairing behind the vehicle during escape, it was possible to achieve a stable subsonic configuration with only slightly increased weight due to the additional thrust requirements from the escape rocket. Additional subsonic data is given in Fig. 8 for the flared configuration.

### III L-2-C Configuration

#### A. Hypersonic

The hypersonic characteristics of the L-2-C configuration have been taken from unpublished NASA Langley  $M = 6.7$  wind tunnel test. The untrimmed lift and drag characteristics are shown in Fig. 9.

The effects on  $L/D$  of various c.g. off-sets and flap deflections required to trim are shown in Fig. 10. A 3% offset in c.g. has been selected for design requirements in order to provide trim with low control deflections in the angle of attack region of interest.

#### B. Transonic

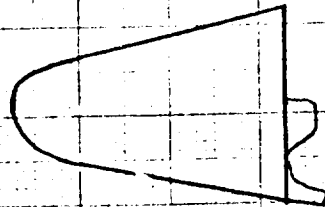
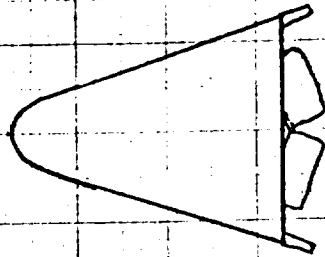
The transonic characteristics were estimated for use in the abort during boost studies and are shown in Fig. 11 through 14. The  $\alpha$  reference line is rotated  $90^\circ$  in these curves. Mercury data is also included in Fig. 11 and 12 for comparison.

#### C. Subsonic

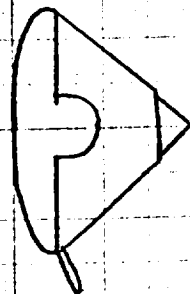
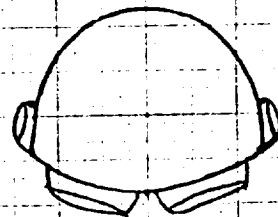
Subsonic characteristics were estimated for the L-2-C escape configuration to determine the tower length required to stabilize the vehicle. The method used was the same as that which gave the results for Mercury shown in Fig. 6. The pitching moment vs angle of attack for two tower lengths is shown in Fig. 15. The 200 inch tower length was selected to provide a small margin of stability at subsonic speeds. The stability in the escape configuration improves with increasing Mach number.



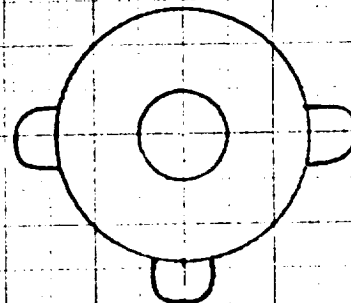
# REENTRY CONFIGURATIONS



W-1

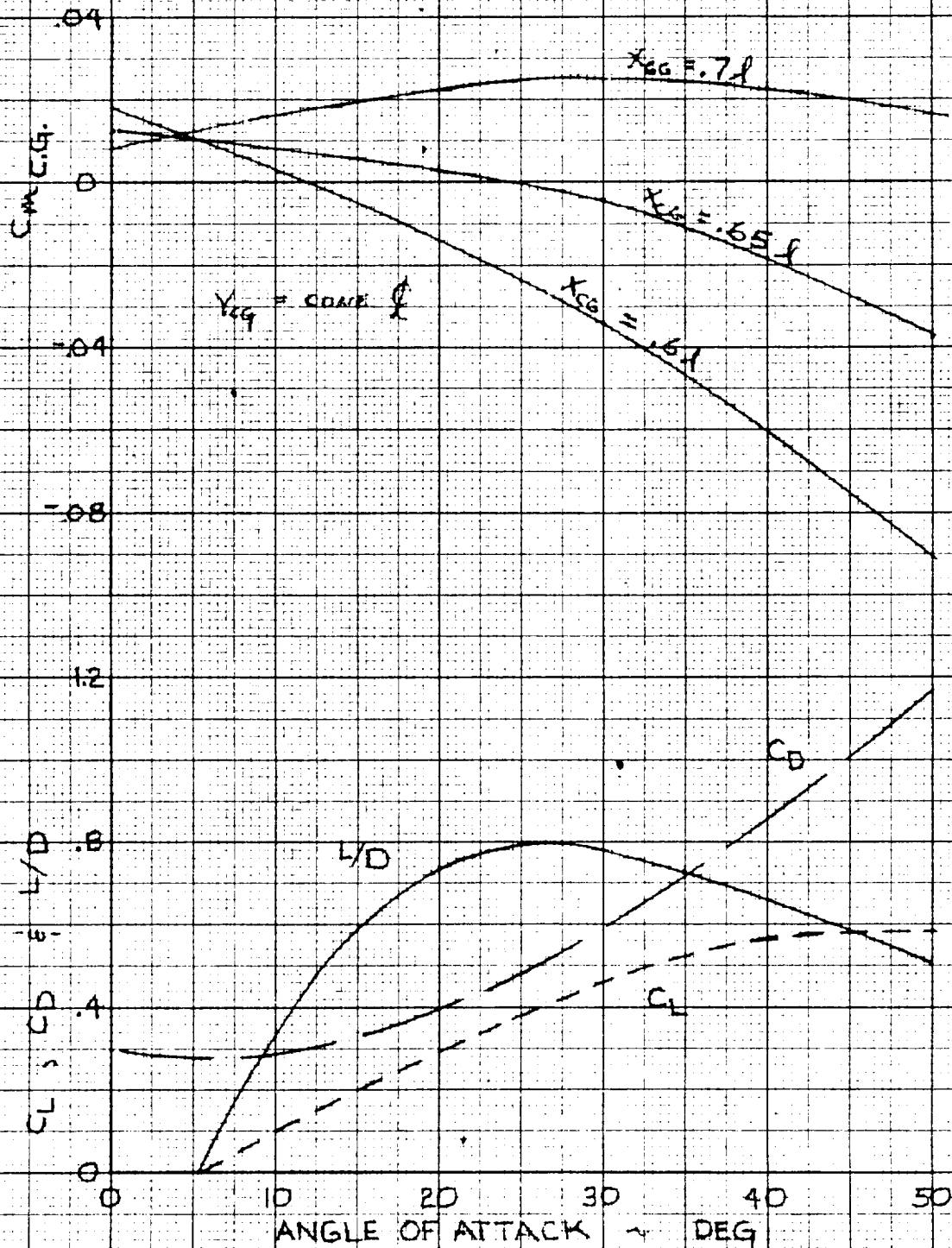


L-2-C

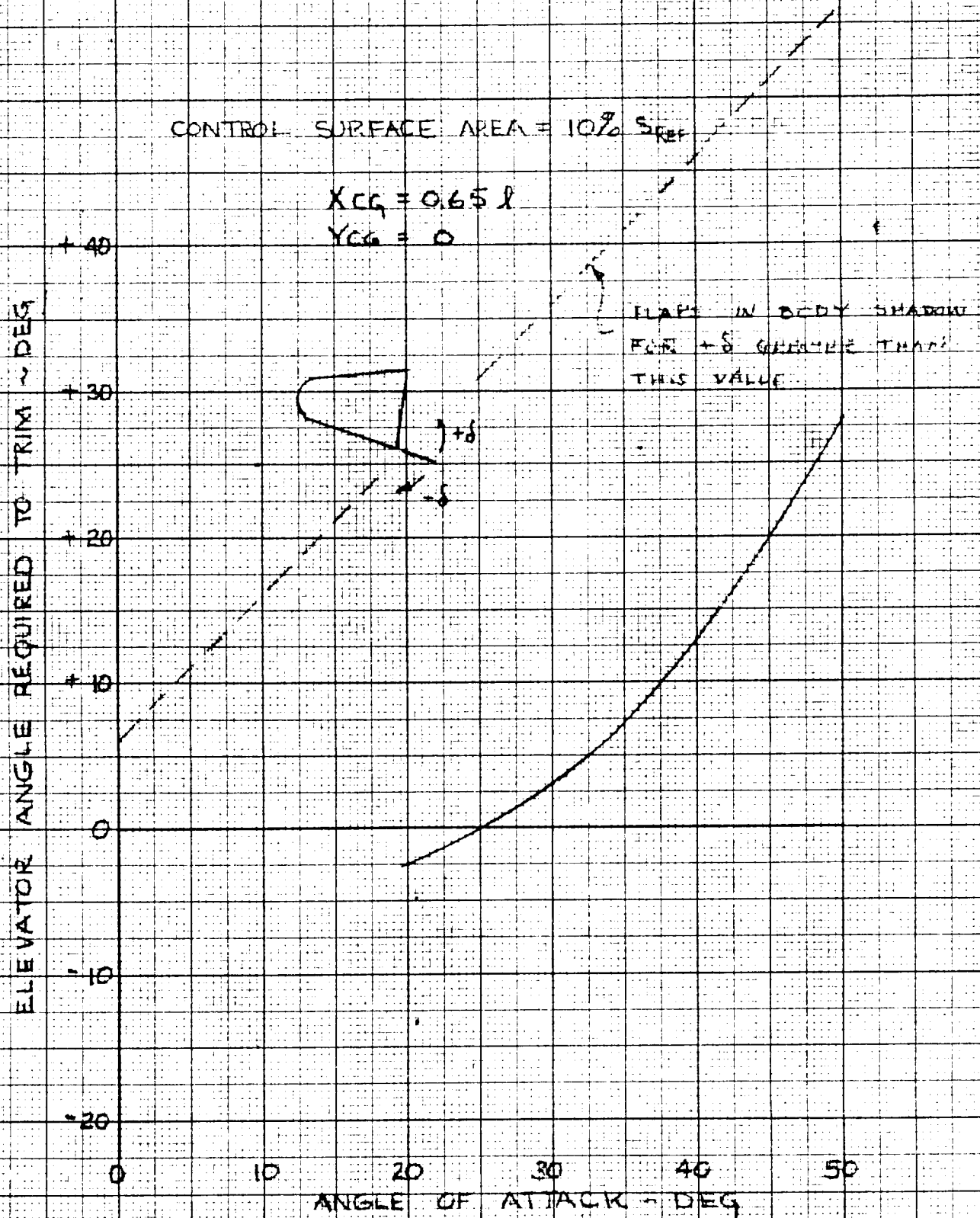


# W-1 VEHICLE LONGITUDINAL CHARACTERISTICS

$$S_{\text{FLAP}} = 10\% S_{\text{REF}}$$



# W-1 VEHICLE ELEVATOR ANGLE REQUIRED TO TRIM



# W-1 VEHICLE

## DIRECTIONAL STABILITY PARAMETER

### (NO SIDE FLAPS)

$$\alpha = 0^\circ$$

$$X_{CG} = 0.65 \lambda$$

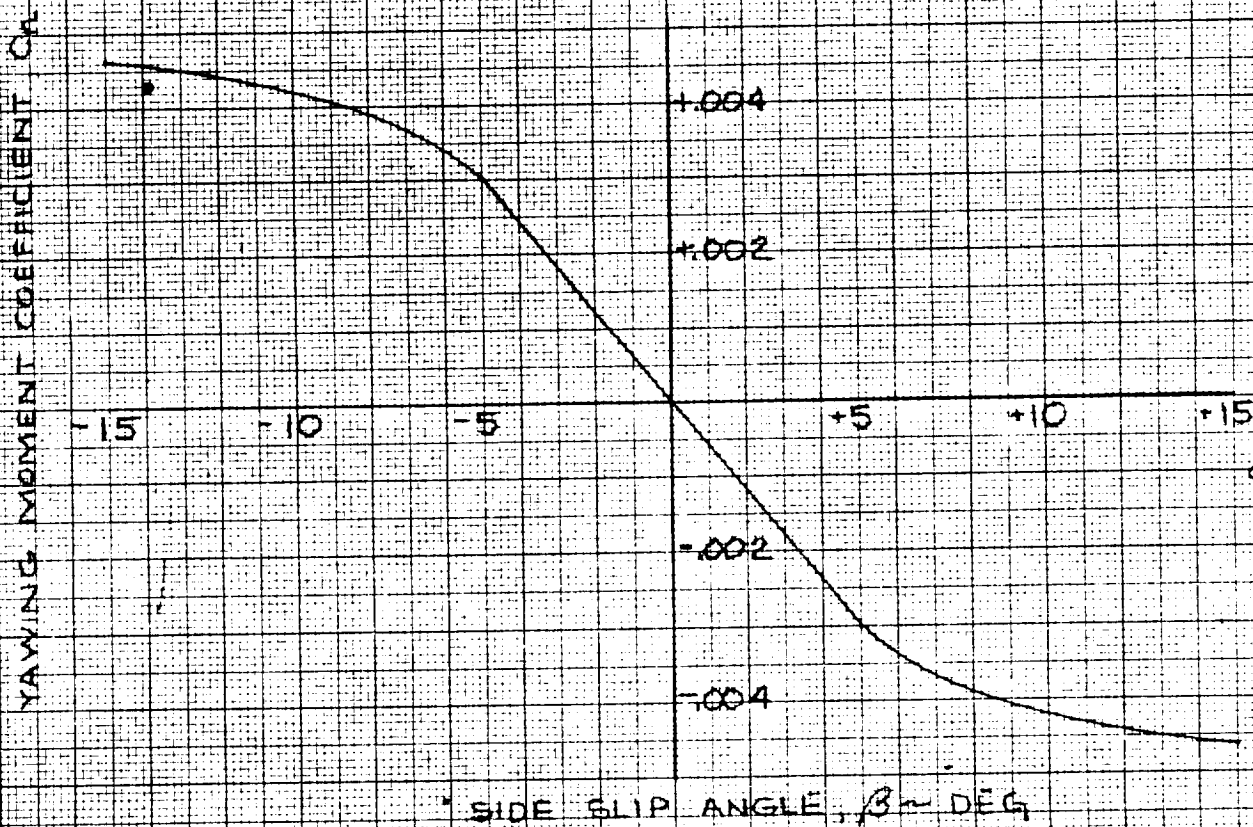


Fig. 5

W-1 Escape Configuration

150" tower + 250# tower ballast

Mach-Number  $M = 1.3$

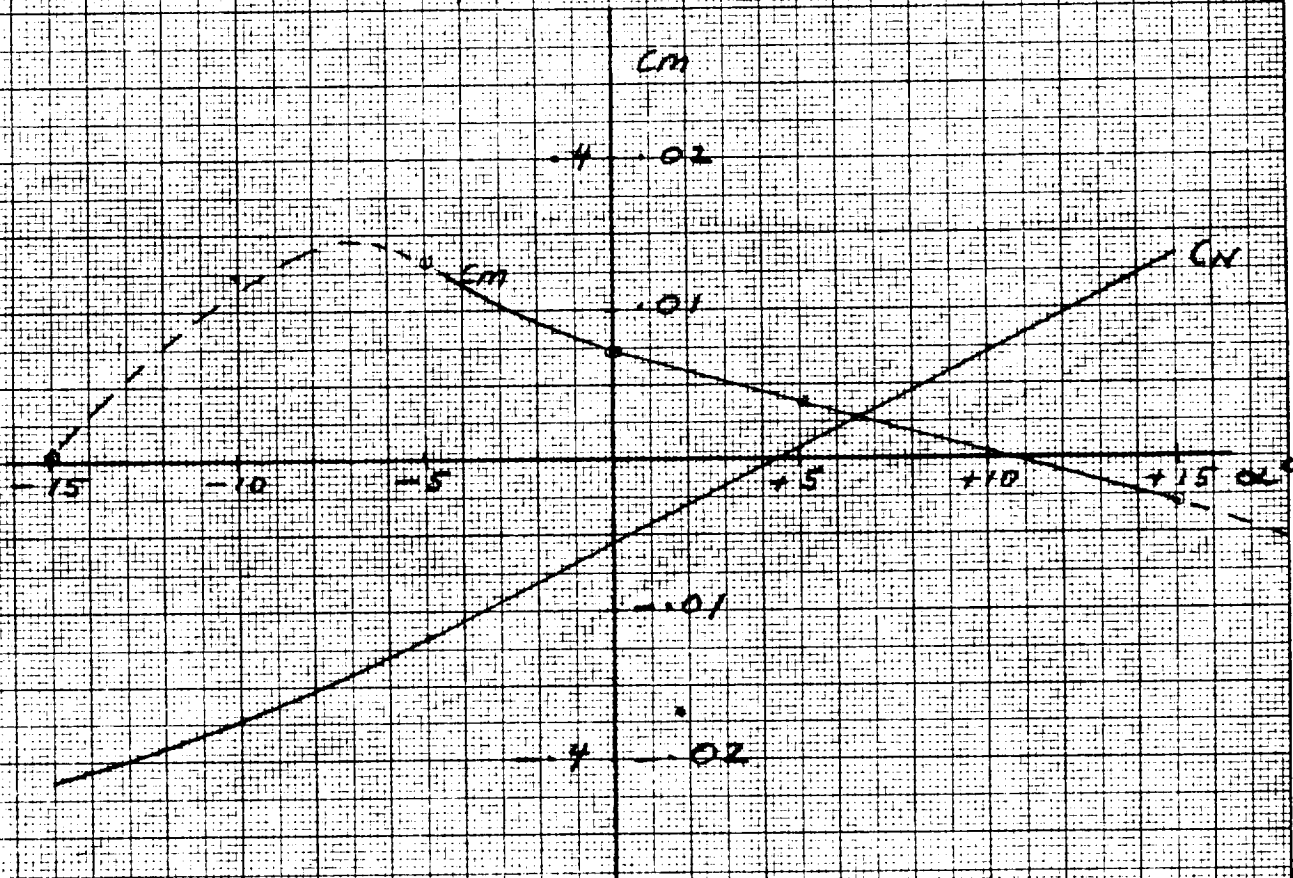
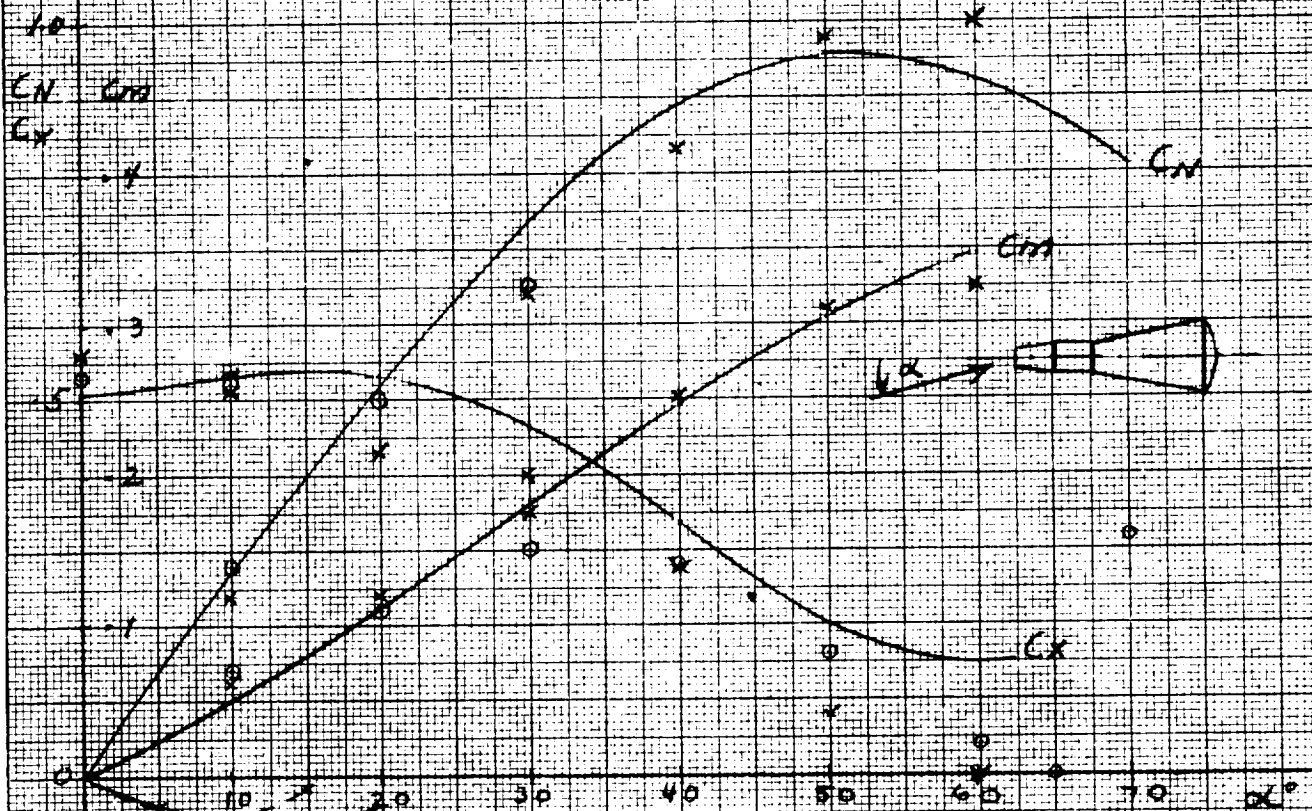


Fig. 6

$C_N$ ,  $C_x$ ,  $C_m$  of Mercury Exit Configuration

calculated subsonic

$M = .05$  } tested  
 $M = .5$  }



$C_m$  of Mercury Escape Configuration

calculated  
 tested

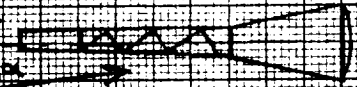




Fig. 7

W-1 Escape Configuration  
and Exit configuration

subsonic

— Capsul without tower,  
with  $2 \times 13 \text{ ft}^2$  flaps on  
lower and upper side  
flap angle  $\delta = 45^\circ$

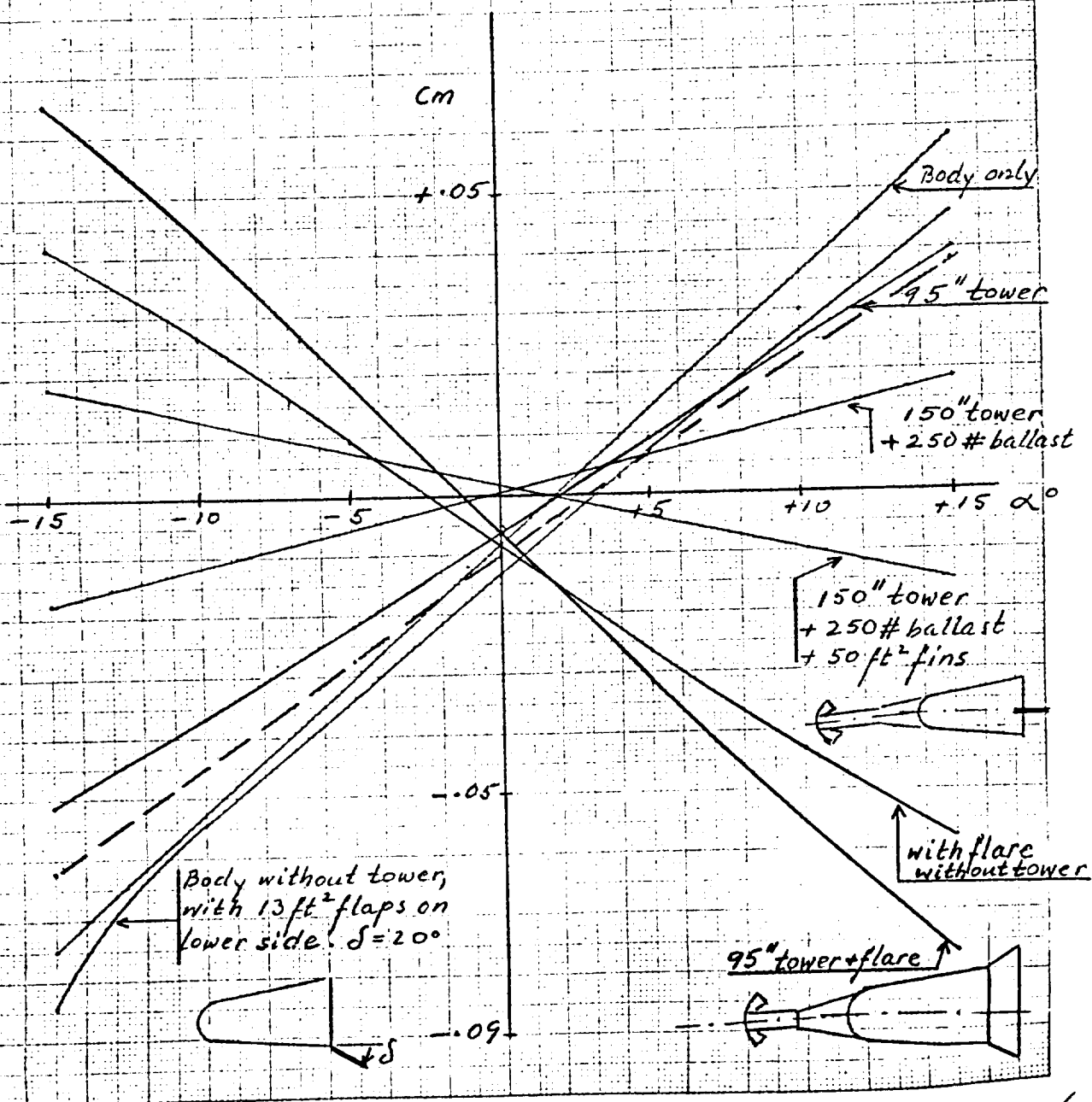
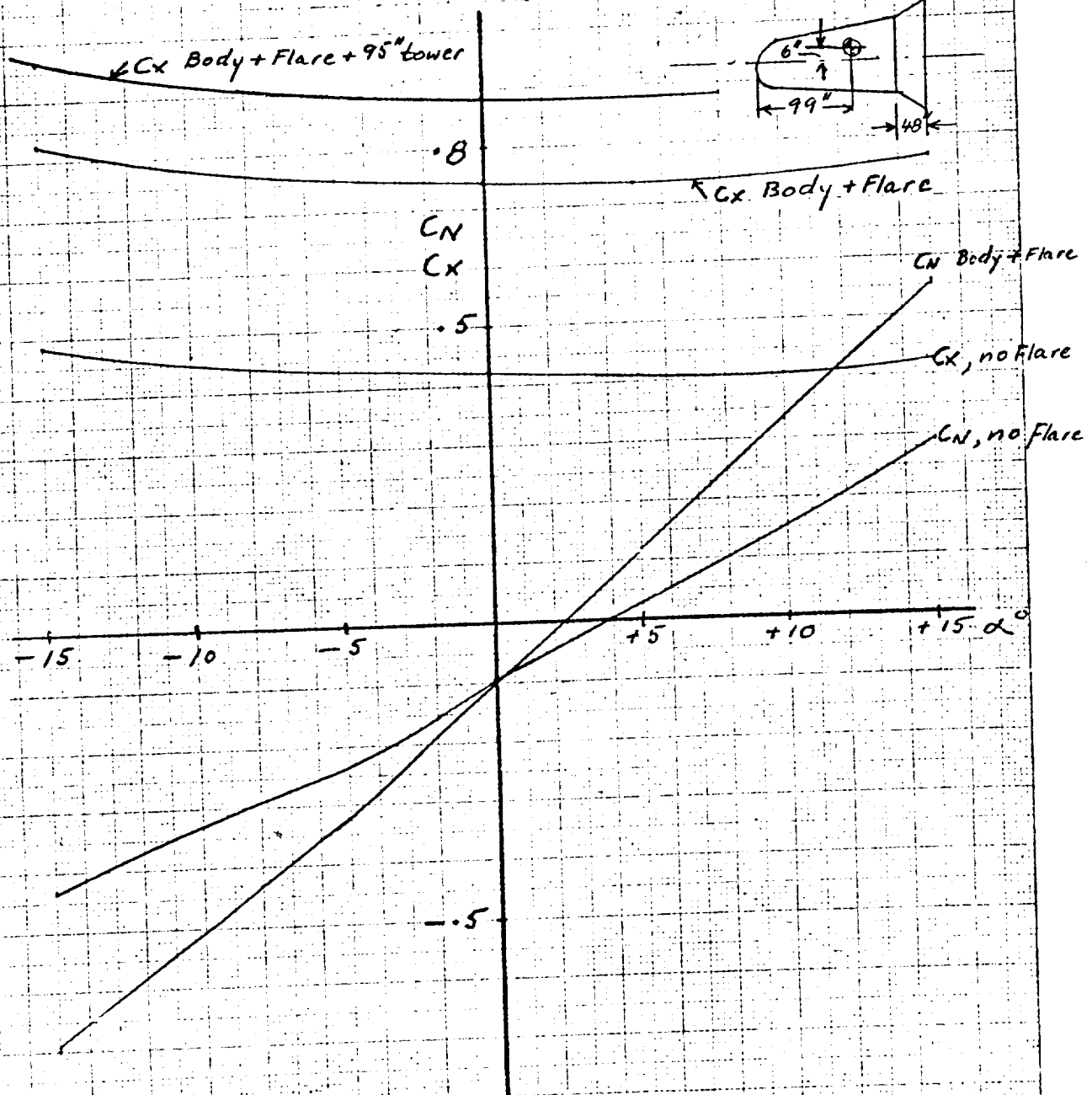


Fig. 8

W-1, Body with flare, no tower

subsonic

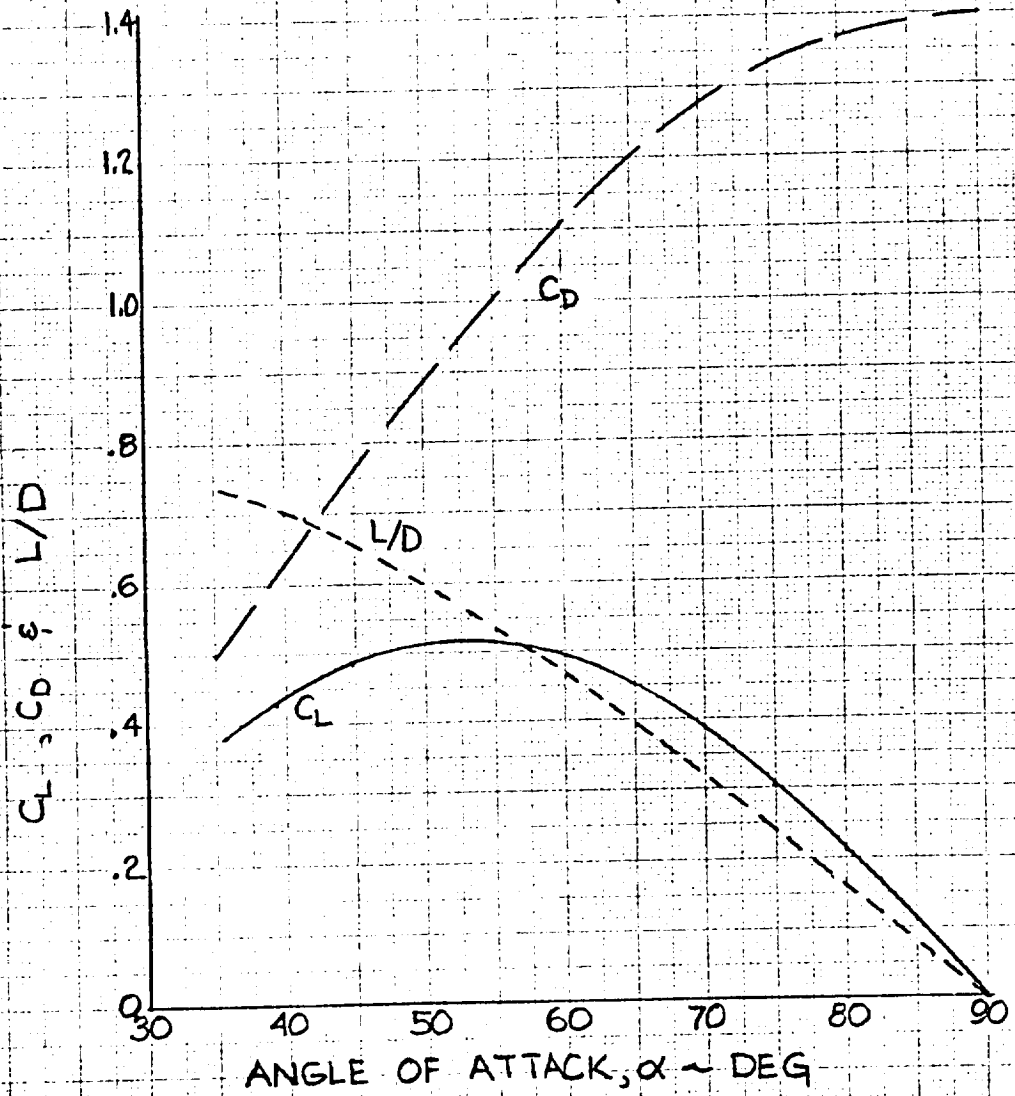
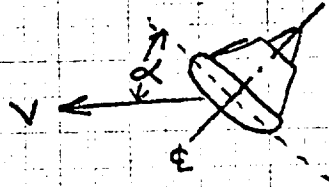
Normal force and axial force coefficients





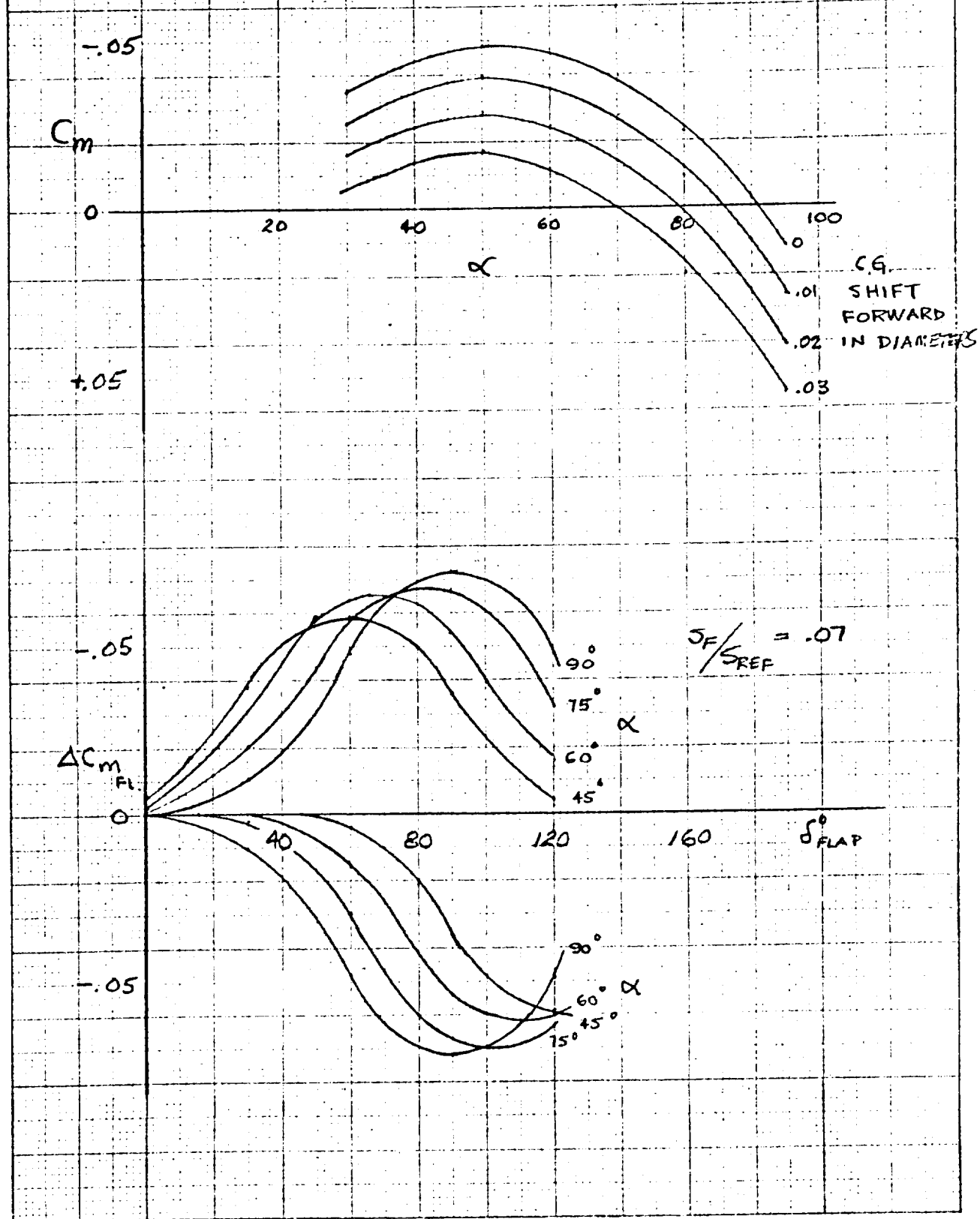
# L-2-C REENTRY VEHICLE

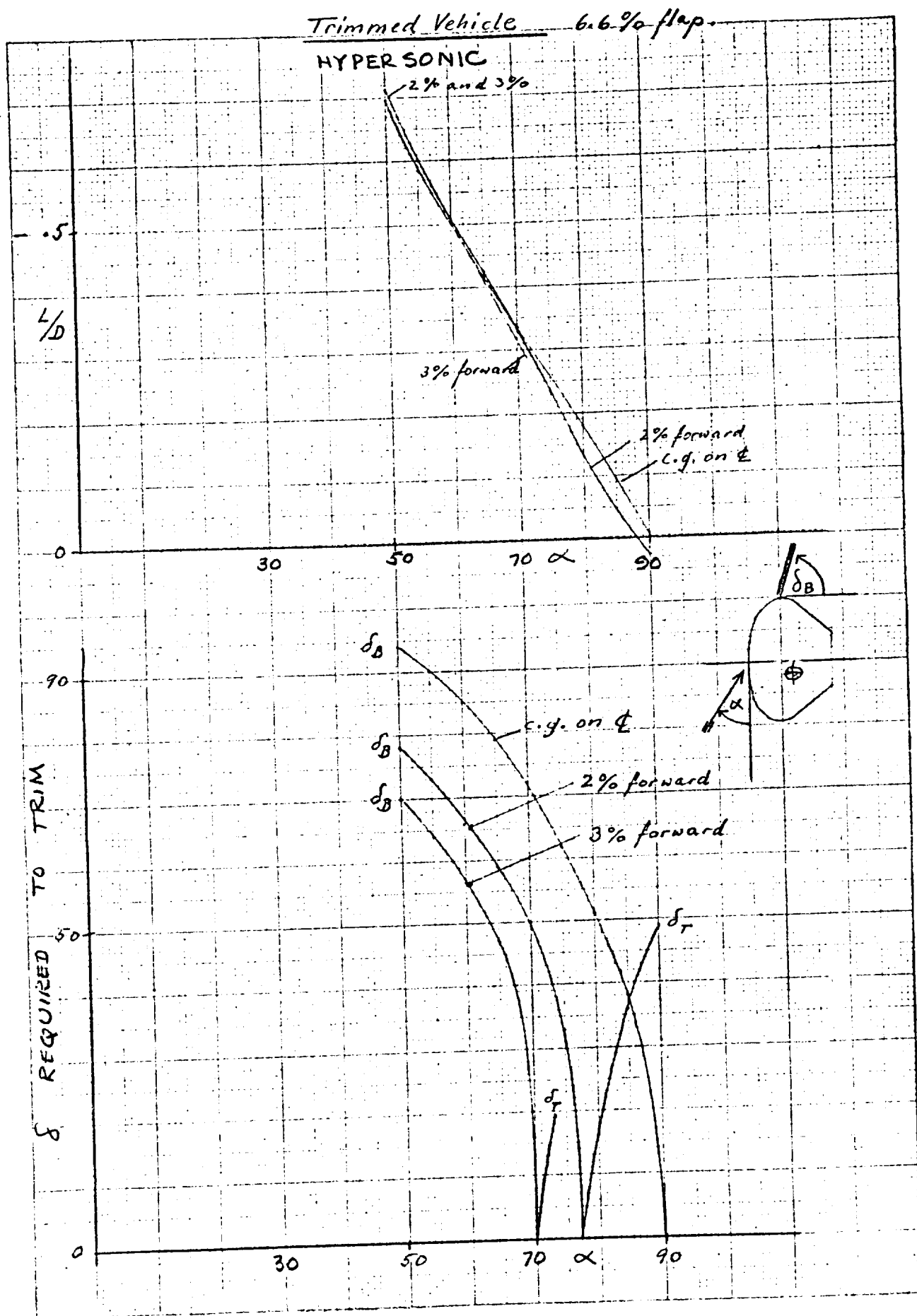
REF. AREA = 129.5 FT.<sup>2</sup>



TM-11 FIG-9

# L-2-C LONGITUDINAL CONTROL

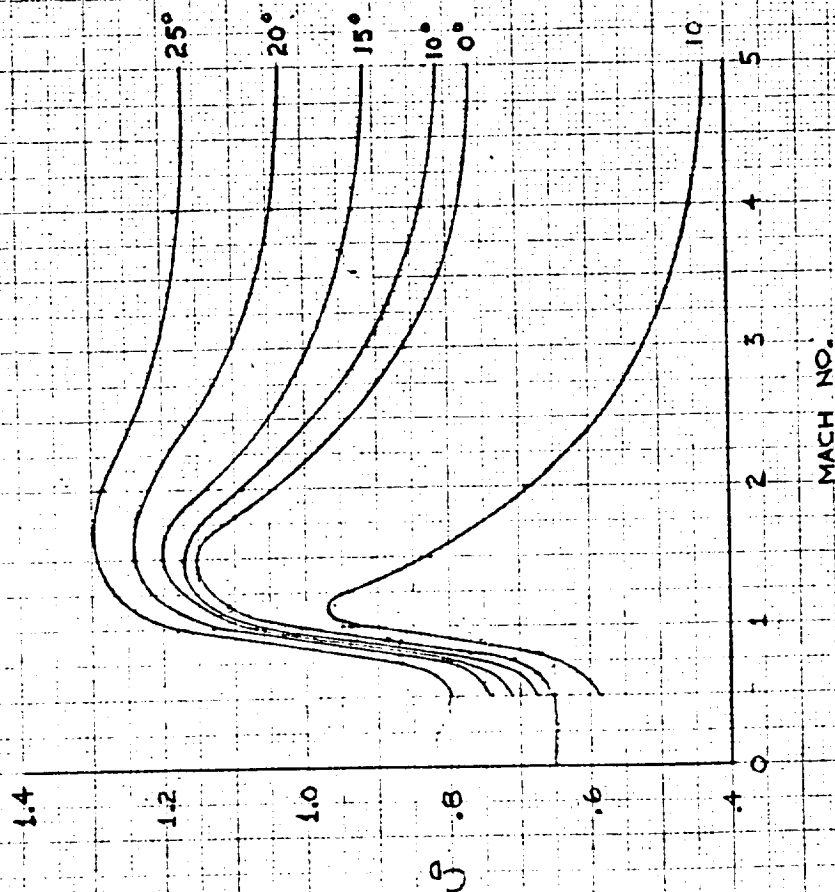
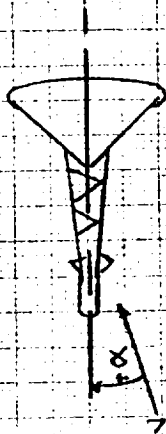




DRAG COEFFICIENT ( $C_D$ ) VS. MACH NO.

CONFIGURATION ~ L-2C (ESCAPE)

$A_{REF} = 130 \text{ FT}^2$



LIFT COEFFICIENT ( $C_L$ ) VS. MACH NUMBER

CONFIG: ~ L-2C (ESCAPE)

$R_{REF} = 130 \text{ FT}^2$

WING LOADING — 10

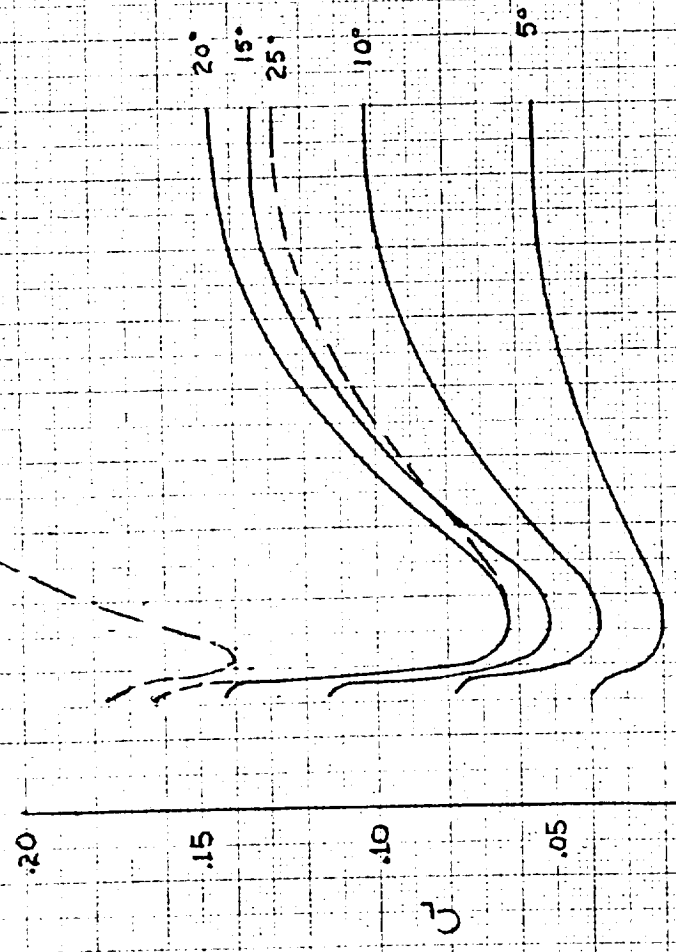


FIG 12 TM-11

LIFT COEFFICIENT ( $C_L$ ) VS. MACH NUMBER

CONFIGURATION ~ L-2-C (RE-ENTRY)

$Q_{REF} = 130 \text{ FT}^2$

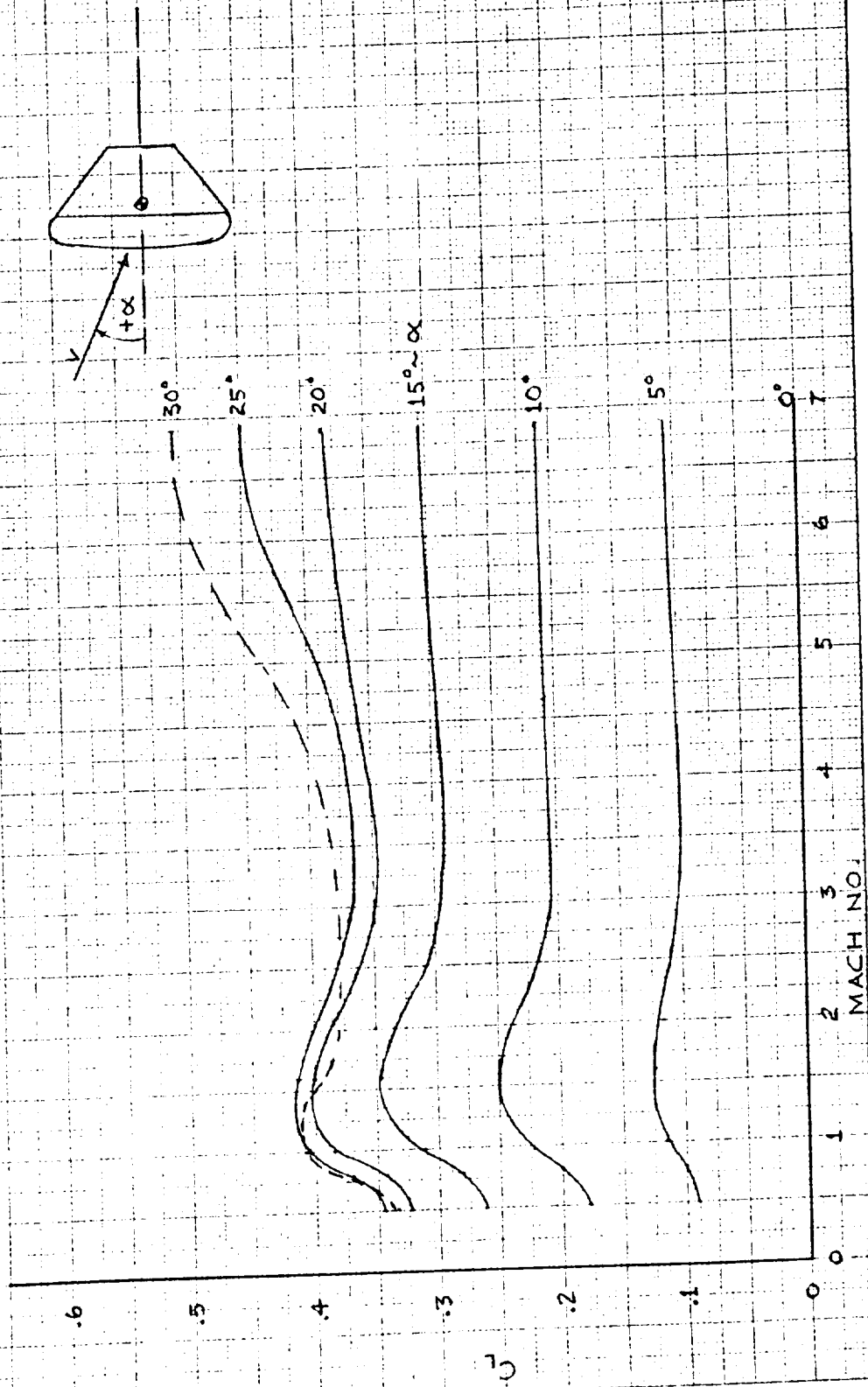


FIG 13 TM-11

DRAW COEFFICIENT ( $C_D$ ) VS. MACH NUMBER

CONFIGURATION ~ L-2-C (RE-ENTRY)

$Re_F = 130 \text{ Ft}^2$

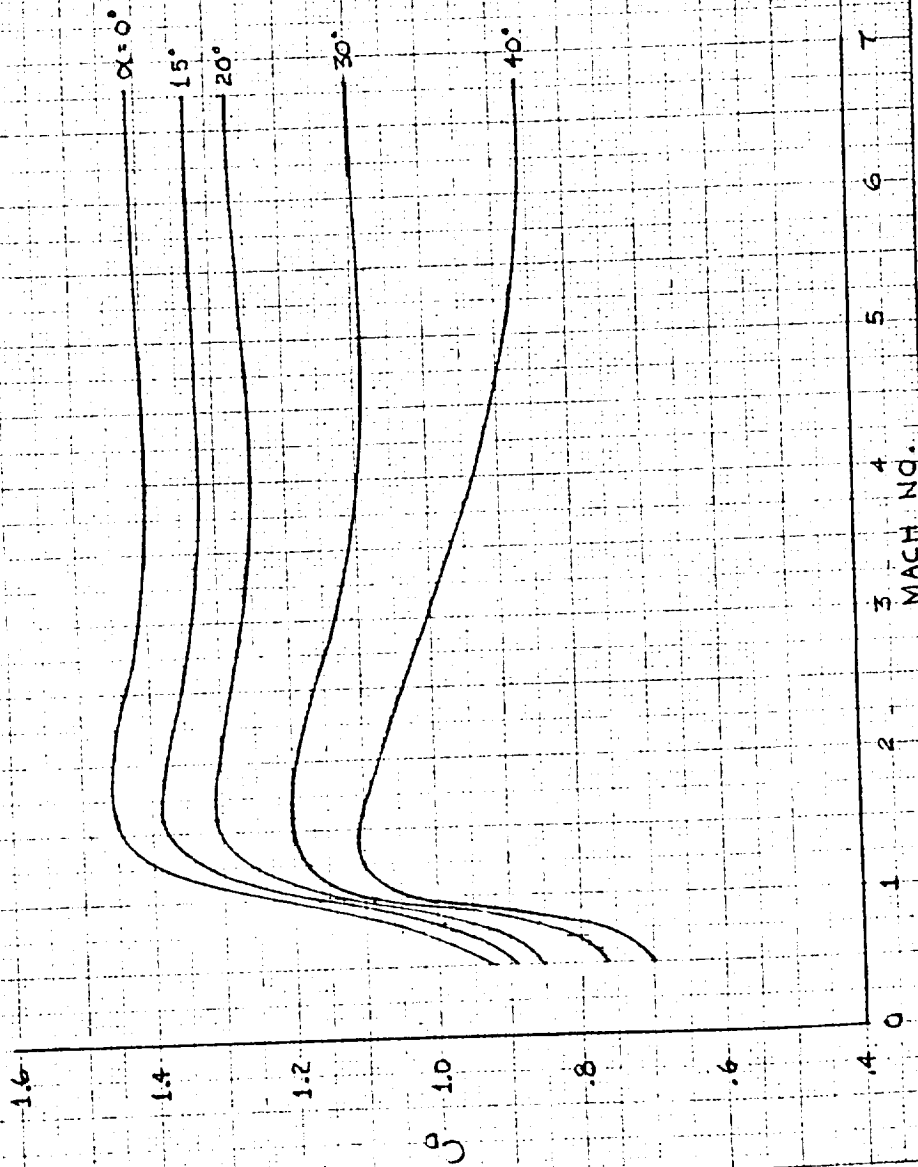
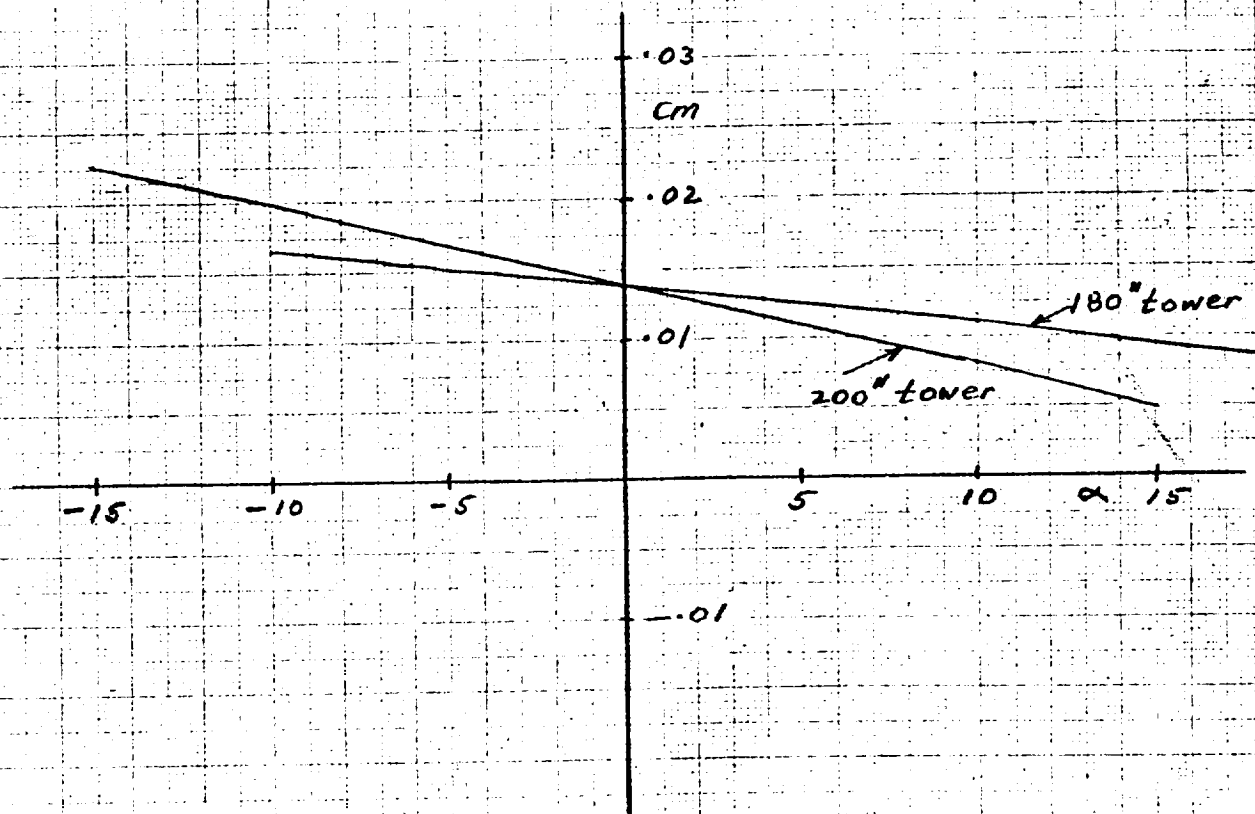
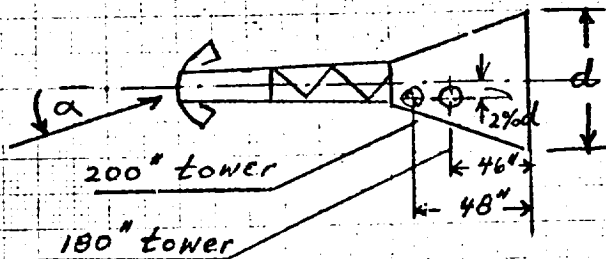


FIG 14 TM-11

Fig. 15

LC-2 Escape Configuration

no ballast subsonic





Reentry Controls

TM-12

APOLLO RE-ENTRY CONTROL  
Technical Memorandum No. 12  
March 13, 1961

J. Hinson  
J. Bryant

### Summary

The re-entry stability analysis conducted to-date for the L-2-c and W-1 Apollo vehicles which have been selected for further study, has resulted in the selection of a feasible autopilot configuration. The effect of aerodynamic surface actuation rate limiting due to hot gas servo power limitations has been analyzed by describing function techniques and a minimum required surface rate established. The autopilot configuration selected has been based on a restricted linear analysis but experience gained from a thorough six-degree of freedom program (reference 1) on a similar configuration was used extensively in the study. Linear analyses indicate that a constant gain system will be acceptable but a variable gain autopilot is presently being packaged which will be married with an analog simulation of the re-entry aerodynamics to provide a means of studying the effect of non-linearities and cross coupling during re-entry.

Re-entry Guidance studies have been initiated on several different concepts which include both prediction and the error-null type techniques. The most promising of these techniques to date is based on solving Chapman's (reference 2)  $\Xi$  function continuously to predict range, load factor, total heat, etc. Preliminary results of a parametric study of this technique which has been conducted for both skip and non-skip re-entry are presented.

## CONTENTS

### Summary

- I. Introduction
- II. Re-entry Aerodynamic Control
- III. Re-entry Glide System (REGS)
  - A. Range Prediction Based on Constant  $\gamma_D$  and Bank Angle
  - B. Ballistic Control Followed by Equilibrium Glide
  - C. Skip Into Near Orbit
  - D. Method of Steepest Descent (Adjoint Method)

### References

## I. Introduction

A safe re-entry of the Apollo vehicle into the earth's atmosphere from both the earth orbital and lunar missions must be assured. In addition, flight path control must be provided with sufficient accuracy to land at a pre-selected landing site. These two requirements have reflections on every sub-system within the Apollo vehicle. For the purposes of this study a safe re-entry infers that g limitations of the crew and heat limits of the structural design must be observed during re-entry. One of many possible techniques can be utilized to meet these two requirements from a flight path control as well as vehicle stability standpoint.

Re-entry from an earth orbital mission has been extensively studied by The Martin Company previously on a typical lifting body configuration (reference 1). Previous studies on a re-entry from a lunar orbital mission (reference 3) have indicated that range variation as a function of small changes in initial conditions and with the particular method of lift control utilized during re-entry were highly sensitive. For this reason a broad and comprehensive investigation of the re-entry control problem was initiated during the present Apollo study.

In order to instrument this program, a number of analog simulation programs have been mechanized. Both a two-dimensional and three-dimensional program have been programmed in the Martin analog facility which incorporate heat rate and load factor limits along with a total heat calculation, and are capable of being coupled with various control laws.

The purpose of this memorandum is to present the results to date on both attitude and flight path control studies and to explain the purpose and status of those studies still under investigation.

The configurations which have been investigated during the program have been limited to the low ( $\pm 0.7$ )  $\gamma_D$  class. These vehicles typically have low aerodynamic damping, natural frequencies on the order of 1-10 rad/sec., inertia and aerodynamic cross coupling, and from a preliminary stability standpoint can be considered very similar. An autopilot configuration can be selected which in general will meet the requirements of the Apollo re-entry vehicle and the gains within the autopilot varied to meet the specific vehicle requirements.

Re-entry guidance techniques which provide control over the re-entry landing point for both skip and non-skip type trajectories are under study. For purposes of this memorandum, a skip trajectory will be defined as one which exits beyond a point in the re-entry profile where dynamic pressures less than 5 psf are encountered. One of these techniques employs an explicit closed form guidance law, similar to that proposed for trans-lunar and trans-earth guidance, followed by an equilibrium glide phase of flight. A somewhat more complex technique under study employs the continuous prediction of that  $\gamma_D$  desired to hit the landing sight based on the solution of Chapman's  $Z$  function (reference 2). A still more complex but more flexible technique is under study which utilizes the method of steepest descent to continuously select the optimum trajectory from the standpoint of several constraints, for example load factor, total heat and range. In addition to these studies on landing point control a study has been conducted on a tangent steering law which would skip the Apollo re-entry vehicle (by use of aerodynamic forces) into a new orbit condition

340

between  $4 \times 10^5$  ft and  $2 \times 10^6$  ft. A general block diagram of the re-entry control system is shown in figure 1.

## II. Re-entry Aerodynamic Attitude Control

The aerodynamic characteristics, in terms of damping and natural frequencies, of the selected Apollo re-entry configurations (the L-2-c and W-1), are similar. Stability derivatives on the asymmetric W-1 configuration are under development to be used in a first estimate of the re-entry autopilot requirements for this body. The stability analysis of the re-entry portion of flight has been concentrated to-date on the L-2-c configuration. Aerodynamic test data obtained from NASA, Langley Field, was used in the analysis. This information consisted of  $C_n$ ,  $C_a$ ,  $C_{m\alpha}$  and  $C_{m\dot{\alpha}}$  vs angle of attack ( $\alpha$ ) data which were obtained at Mach 6.7. These coefficients were assumed to be invariant with Mach number for the purposes of this analysis.

The aerodynamic stability analysis to-date has been restricted to the pitch axis dynamics with the assumption being made that the stability in yaw would be analogous because of the symmetry of the L-2-c configuration and also because of unavailable lateral coefficient data. With the present configuration both roll attitude, control and roll damping will be accomplished by reaction jets since the present control surfaces are not designed to produce rolling moments.

From observation of the  $C_{m\alpha}$  and  $C_{m\dot{\alpha}}$  vs angle of attack curves for various off-set c.g. locations, it was decided that it would be desirable to limit control surface deflections to  $\delta = 90^\circ$  max. In order to trim at max  $C_L$  with this limitation requires a 2% forward location of the c.g. using flap configuration F-1 ( $b = 1.748$  ft.  $c = 2.32$  ft). It was necessary to develop  $C_{m\alpha}$  and  $C_{m\dot{\alpha}}$  curves for the 2% location from the 1% and 3% locations for which data was available. This data is presented in figure 2. Since the stability

342



analysis was to be conducted for the angle of attack producing max  $C_L$  ( $\alpha = 55^\circ$ ) the slope of  $C_m$  vs  $\alpha$  was determined for this angle of attack. The pitching moment coefficient per deflection of the control surfaces was determined by constructing a plot shown in figure 3 of  $C_m$  vs  $\delta$  and taking the slope at a deflection of  $90^\circ$  and  $\alpha = 55^\circ$ . Damping derivatives ( $C_{m\dot{\alpha}}$  and  $C_{m\dot{\delta}}$ ) were assumed to be negligible in this analysis as was the  $C_{n\delta}$  and  $C_{a\delta}$ .

The aerodynamic transfer function  $\Theta/\delta$  was developed and examined under various flight conditions. The general form of  $\Theta/\delta$  is shown below:

$$\frac{\Theta}{-\delta} = \frac{M_\delta / I_{yy} (s + \frac{1}{A})}{s \left[ s^2 + \left( \frac{M\dot{\delta}}{I_{yy}} + \frac{1}{A} \right) s + \frac{M\dot{\delta}}{I_{yy} A} + \frac{M\alpha}{I_{yy}} \right]}$$

A good approximation for this transfer function has been found to be:

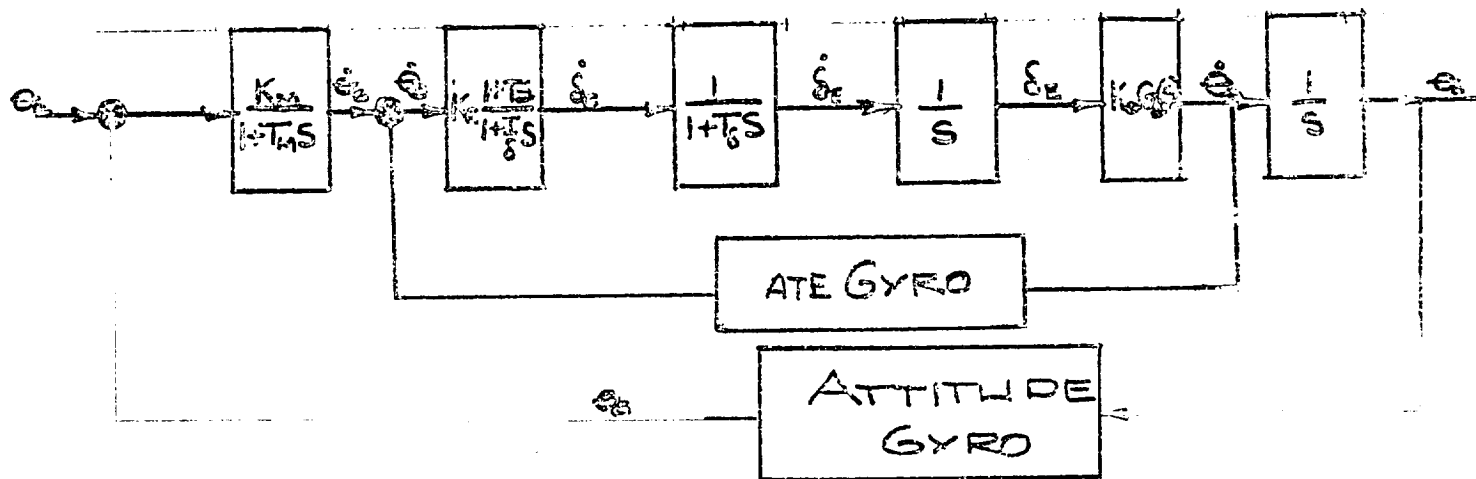
$$\frac{\Theta}{-\delta} \approx \frac{K_a}{s^2 + \omega_n^2}$$

in which  $K_a = \frac{q S C C_{m\delta}}{I_{yy}}$  and  $\omega_n^2 = \frac{q S C C_{m\alpha}}{I_{yy}}$ .

A plot of  $\omega_n$  and  $K_a$  vs  $q$  (dynamic pressure) was made and is shown in figure 4.

Because of the wide variations in the dynamic pressures to be encountered in a typical re-entry the rate damping gain necessary for satisfactory damping would normally be programmed to change with a change in  $K_a$ . In order to avoid this gain programming, it was decided

to investigate a pseudo adaptive autopilot design similar to that employed in reference 4. This autopilot has the general form shown below:



For the analysis conducted to-date the following data has been used:

$$T_s = 0.01 \quad \omega_0 = 26 \text{ CPS} \quad f_0 = 0.5$$

$$\frac{\dot{\theta}_0}{\theta_0} = \frac{\omega_0^2}{s^2 + 2f_0\omega_0 s + \omega_0^2}$$

Root locus plots were constructed for  $\dot{\theta}_e / \dot{\theta}_0$  from which  $K_r$  and the lead circuit design requirements were established.

The principal of the above design is to minimize the effect of airframe dynamics on the overall stability and response characteristics. This is accomplished by achieving high performance of the inner loop  $\dot{\theta}_0 / \dot{\theta}_e$  over a range of frequencies from zero to beyond the actual frequency of the outer loop  $\theta_0 / \theta_e$  ( $\dot{\theta}_0 / \dot{\theta}_e = 1$ ). The following

values have been selected for  $K_p$  and the lead circuit:

$$K_p = 107$$

$$T = 0.1075$$

$$n = 13$$

The root locus for the inner loop is shown in figure 5.

This analysis was conducted in order to determine the complexity of the autopilot requirements during re-entry and to produce preliminary system requirements to the Electronic Design Support Section which is breadboarding the re-entry autopilot design.

The configuration of the roll autopilot is much like the cis-lunar attitude control system in the mission module. Pulse width jet systems are utilized to achieve fast response and approximately linear operation. The size of the system was selected on the basis of the speed of response required for lateral damping and heading changes required for lateral range control. In order to arrive at this desired speed of response some discussion is required on the technique to be used for heading control. Two methods for accomplishing lateral heading change are immediately apparent. First, the vehicle can be controlled by a pitch-roll technique in which the angle-of-attack and bank angle

are controlled by guidance commands to produce the desired combination of lateral and longitudinal range. Second, the vehicle can be maintained at a desired trim angle of attack and rolled about the trim velocity vector to produce the desired vertical and lateral forces to achieve the displacements required to arrive at the target. Both of these techniques are under study and some of the advantages of each will be discussed in the Re-entry Guidance Section of this memorandum.

345

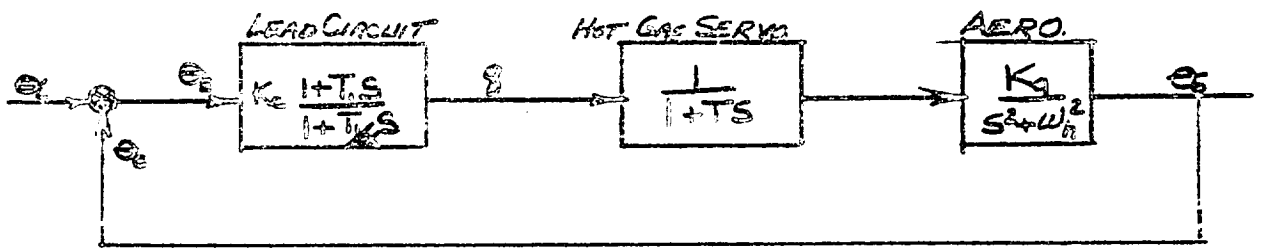
The roll response felt to be necessary from a review of the Re-entry trajectories and heading change requirements is  $180^\circ$  in ten seconds. The thrust requirements were established as 37.75 lbs and total fuel based on the desirability of twenty such rolls during a typical re-entry. These numbers will be revised pending results of the three-dimensional analog program presently under study.

In addition to the preliminary design of the autopilot, an investigation of the control system rate saturation limits has been conducted in an attempt to reduce control power requirements during re-entry. Since rate saturation acts like a non-linear element, the usual linear analysis techniques must be modified. This can be done by use of describing functions (reference 5 and 6). The purpose of this investigation was to specify the minimum surface deflection rates necessary to assure a stable operation in the frequency range of interest.

The effect of the rate-limiting in the pseudo-adaptive design is to produce a high frequency chatter at small amplitudes. The magnitude of this chatter is directly related to  $\dot{\epsilon}_{\max}$ . It can be seen then that the  $\dot{\epsilon}_{\max}$  limitation will not affect vehicle stability since even a limit-cycle oscillation at high frequency and low amplitude will have very little effect on the vehicle dynamics. Reducing  $\dot{\epsilon}_{\max}$  will affect the vehicle response but this effect, using the pseudo adaptive autopilot, is difficult if not impossible to analyze unless the system is evaluated on an analog computer.

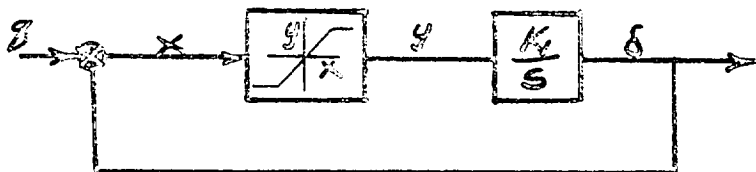
In order to have some basis for establishing  $\dot{\epsilon}_{\max}$  by hand analysis another approach was necessary. The autopilot design used for

this analysis is based on the simple system shown below:



$$T = 0.05$$

### NON LINEAR HYDRAULIC SERVO



$$S/q = \frac{1}{1 + \frac{S}{NK_1}}$$

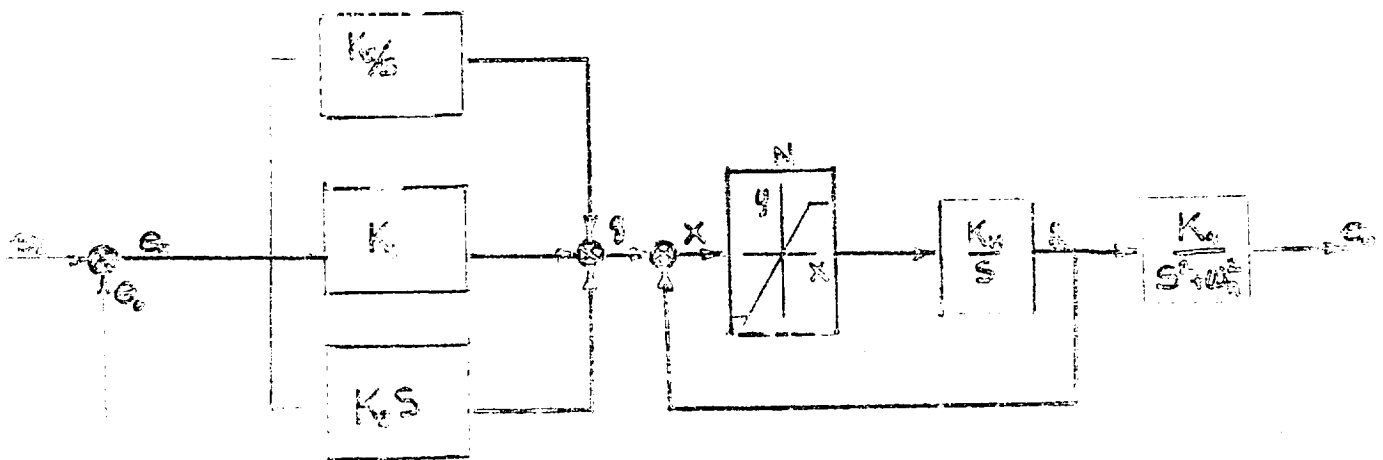
$$\text{FOR } N=1, K_1=20$$

$$T = \frac{1}{NK_1} = 0.05$$

By use of describing function techniques, the above system can be analyzed to establish the minimum value of  $\delta'$  required for a stable operation. The root locus of the open loop linear analysis of is shown in figure 6 in which  $K_c$  has been established as 7.55 to give a 0.4 damping at the maximum dynamic pressure flight condition. The effect of the rate saturation in the hot gas servo is to move the pole toward the imaginary axis and thus cause the locus of the open loop to bend toward this axis. The resultant effect is to cause an instability to occur as a function of the amplitude of  $\theta_c$ . This value of  $\theta_c$  which would cause an unstable operation in the present

situation ( $\dot{\theta}_{\max} = 1 \text{ rad/sec}$ ) is extremely small, on the order of 2 degrees. For this reason, along with the fact that the lead circuit type of autopilot would require programming of gains, a third autopilot configuration was studied.

Previous studies conducted on the autopilot requirements of a lifting body returning from an earth orbital mission indicated from a linear analysis that a position-rate-integral type of autopilot would provide a stable re-entry operation. This analysis was later substantiated by a six degree of freedom analog simulation which included non-linearities, cross coupling, and the vehicle dynamics. Because of the similarity of the aerodynamic transfer functions of the L-2-c and W-1 with the configuration previously studied this type of autopilot was investigated as a possible configuration for the Apollo re-entry vehicle, and is shown below in block diagram form.



$$\frac{K_0}{K_1} = \frac{K_1}{K_2} = 0.5 \omega_n^2 \quad \omega_n = \frac{NK_1K_2}{1 + \frac{NK_1K_2}{s}} = \frac{1}{\frac{1}{NK_1} + 1} = \frac{NK_1}{s + NK_1}$$

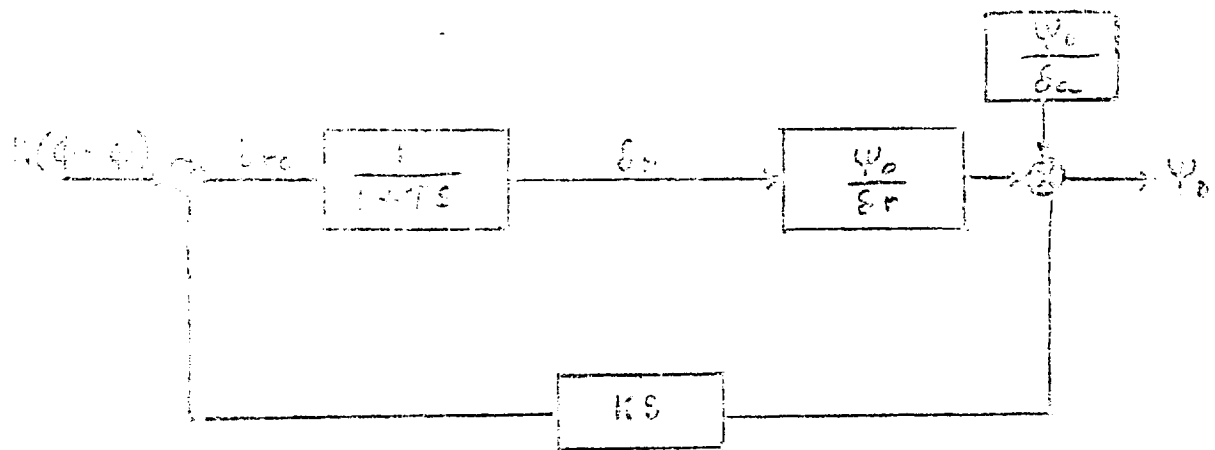
$$K_H = 20$$

$$\frac{\theta_0}{\theta_i} = \frac{(K_0 s^2 + K_1 s + K_2) \omega_n^2 (1/s^2)}{1 + \frac{(K_0 s^2 + K_1 s + K_2) \omega_n^2 (1/s^2)}{s^2 + NK_1}}$$

The gains in the above pitch loop autopilot were determined by root locus analysis techniques. A typical root locus is shown in figure 7 for one flight condition during re-entry. This autopilot configuration represents the recommended system for the pitch control loop for both the L-2-c and W-1 configurations. It is presently being breadboarded for a demonstration in an analog simulation of the moment equations during a typical Apollo re-entry.

An investigation of the effect of rate-saturation on this autopilot design was conducted in order to establish the minimum rate required of the hot gas servo actuation system. Typical root locus plots are shown in figures 8 and 9 which demonstrate the effect on the locus of the system of this saturation. The minimum rate has been established as 0.5 rad/sec. in order to have a system capable of a stable operation with damping of greater than 0.3 during all flight conditions. It is felt that a constant gain system in the autopilot would give satisfactory operation rather than the variable gains indicated on the block diagram. Final decisions on this matter will be made after an analog simulation, which will be used to evaluate the effects of non-linearities and cross coupling in the system, is completed.

The recommended yaw autopilot is shown below and consists of a yaw compensation and damping loop.



Cross-fer terms are incorporated to reduce the effect of adverse yaw which is expected when the vehicle is rolled about its velocity vector in the process of making a lateral range correction.



1. Atmosphere and planet are spherically symmetric.
2. Variations in atmospheric temperature and molecular weight with altitude are negligible compared to any variation in density.
3. Peripheral velocity of the earth is negligible compared to the velocity of the Apollo vehicle.
4. The small change in distance from the planet center is negligible compared to the fractional change in velocity in a given increment of time.
5. The flight path angle  $\delta$  is sufficiently small that the component of drag is large compared to the component of lift in the horizontal direction.

#### Equations of Motion

The two component equations of motion which Chapman has collapsed are the classical:

$$-\frac{d^2b}{dt^2} = -\frac{d^2r}{dt^2} = g - \frac{v^2}{r} - \frac{L}{m} \cos \delta + \frac{D}{m} \sin \delta$$

or

$$\frac{d^2b}{dt^2} + \frac{v^2}{r} = -\frac{D}{m} (\cos \delta + \frac{L}{D} \sin \delta)$$

where:

$b$  = altitude

$v$  = vertical velocity component

$u$  = circumferential velocity component normal to radius vector.

$y$  = distance from earth center

### III. Re-Entry Glide System (REGS)

#### A. Range Prediction Based on Constant 40 and Bank Angle

##### Introduction

The complete equations of motion for a vehicle entering the earth's atmosphere are by nature complex and difficult to solve even with large high-speed digital computers. The in-flight solution of these complete equations for the purpose of controlling range, deceleration and heat absorption becomes practically impossible because of the restrictions placed upon the size and complexity of airborne type computers. It is, therefore, both mandatory and desirable to reduce the mathematical and computational complexity of the entry guidance and control scheme to a minimum.

Among the different approaches investigated, the method developed by Chapman (Ref. 2) to approximate the solutions obtained with the complete equations of motion offers a substantial saving in computational complexity. In essence he has reduced the motion equations to a single, ordinary, nonlinear differential equation of second order by rejecting terms which contribute only negligibly to the solution and by the introduction of a particular mathematical transformation.

##### Assumptions

The physical and mathematical assumptions made in the development of the "Chapman" equation restrict its application to a particular range of altitudes and initial conditions which are, however, within the range of extremes predicted for the Apollo mission. The basic assumptions are:

L = Lift force

D = Drag force

m = Mass of vehicle

$\alpha$  = Flight path angle relative to local horizontal

Initially, the term  $\frac{d\alpha}{dt}$  in equation (2) is dropped. This is equivalent to the restriction of assumption 4. Next, an independent variable  $\bar{r}$  (ratio of horizontal to circular satellite velocity  $u/u_c$ ) is introduced and employed as the independent variable along with a new dimensionless dependent variable  $Z$  formed through a transformation of the two original motion equations.  $Z$  is defined as:

$$Z = \frac{\rho}{2(C_D A)} \sqrt{\frac{r}{\beta}} \bar{u}$$

where:

$\rho$  = density of fluid

$C_D$  = Drag coefficient

$\beta$  = Atmospheric density decay parameter

Through the process of mathematical manipulation, Chapman's final  $Z$  function results:

$$\ln \bar{r} - \left(2 + \frac{\beta}{2}\right) = \frac{1 - \bar{u}^2}{2\bar{u}^2} \cos^{-1} \bar{u} - \sqrt{\beta r} \frac{1}{\bar{u}} \cos^{-1} \bar{u}$$

The physical meaning of each of the terms is perhaps helpful:

$\ddot{z}$  = vertical acceleration

$-\left(\frac{F_D}{m} \cos \theta\right)$  = vertical component of drag force

$\frac{1}{R} \dot{z}^2$  : gravity + centrifugal force  
 $-\frac{F_L}{m} \sin \theta$  : lift force

A brief investigation of the analytic strength of the Z function and its ability to predict almost all of the important trajectory parameters associated with an Apollo type entry, has led to a detailed study of the possibility of using it as the primary entry range control law for the Apollo mission. With this one differential equation it is possible to closely predict for example the following important motion parameters if the initial flight path angle ( $\gamma$ ), flight path circumferential velocity ( $\dot{\theta}$ ), and lift - drag ratio (L/D) are known:

Circumferential Distance (range)

$$\Delta \theta = \frac{1}{\dot{\theta}} \int \frac{L/D}{R} \cos \theta \, dz$$

Corresponding Elapsed Time

$$t = \frac{1}{\dot{\theta}} \int \frac{L/D}{R} \sin \theta \, dz$$

A dimensionless function proportional to total heat absorbed

( $\bar{Q}$ )

$$\bar{Q} = \frac{\int_{u_0}^{u_1} \frac{u^{3/2} du}{\bar{z}^{1/2} \cos^2 \gamma}}$$

Horizontal component of deceleration

$$a_x \approx g \frac{\sqrt{\beta} \bar{z}}{\cos \gamma}$$

Flight path angle  $\gamma$  as a function of velocity

$$\sin \gamma = \bar{z}' - \frac{\bar{z}}{\sqrt{\beta} u}$$

#### Approach

Inasmuch as the  $Z$  function affords only an approximation of the solution of the complete equations of motion, the philosophy thus far has been to check in detail the  $Z$  function solutions with results





probably lower this value.

The analog mechanization employed to study this technique is represented in figure 21.

The construction of the ground trajectory plot or "footprint" is currently in process. The lateral range capability as a function of longitudinal range is calculated with the following equation:

$$R_y = Y_1 + Y_2$$

where

$$Y_1 = \frac{L}{R} (60 + 57.295) \ln W \sin \phi_E \sin \phi_C$$

$$Y_2 = 620 \left( \frac{L}{R} \right)^{1.78} \sin 2\phi_E$$

and where:

$$\begin{aligned} \phi_E &= \text{Vehicle bank angle about the velocity vector} \\ \phi_C &= \text{Earth's central angle} \\ \frac{L}{R} &= \frac{\text{Longitudinal range}}{\text{Earth Radius}} \end{aligned}$$

The derivation of these equations is based upon curve matching techniques employed by Frank and Perrine and have shown good correspondence with results obtained on the IBM 709 with the complete equations of motion. Some representative plots are shown in figures 12 through 26 for flight path angles near the undershoot boundary (-6.35° at 250,000 ft). After completion of plots for flight path angles near the overshoot boundary (-2.1° at 250,000 ft) the various curves will be combined into plots representative of initial entry angles and the maximum load



restrictions applied. The final result will be a series of "footprints" representative of flight path angles within the overshoot and undershoot boundaries that will define the lateral and longitudinal maneuver capability of the vehicle with critical load and heat factors taken into account. Plans are presently under way to mechanize this series of ground traces into a pilot display so that manual control of flight range will be afforded.

This display will be coupled with an existing three-dimensional analog simulation of the Apollo re-entry which is presently being utilized to study automated re-entry techniques.

The ground traces shown in figures 22 through 33 represent various L/D trim conditions and the longitudinal and lateral range as a function of roll angle. For example, in figure 22 a range of greater than 22,000 N.M. is possible if a constant L/D of .56 is flown and this is the 0° bank L/D condition. For a bank angle of 45° the longitudinal range drops to 13,200 N.M. for L/D constant = .56 while a lateral range of 40 N.M. to the right of the initial flight path is realized. It should be pointed out once more, that these plots do not as yet have maximum skip apogee, load, or heat factors superimposed. The place of the Chapman Z function in the overall atmospheric entry control loop is shown in figure 34.

The assumptions in the mechanization of this scheme are:

1. Initial conditions at re-entry in terms of velocity, flight path angle and range to go will be supplied by the mid-course guidance system.
2. Continuous knowledge of the range to the target as computed by the inertial system.

With these restrictions in mind, the operation of the entry control system would be roughly as follows:

1. With the initial conditions enumerated above supplied by either ground fix or the inertial platform, an initial L/D (bank angle) is chosen for entry based upon the range to the target. Insertion of this parameter into the computer along with the initial conditions supplied by the inertial platform will indicate the correctness of the selection by computing range for a selected series of L/D ratios and comparing the results with the original choice. The comparator ratiometer will present this information to the pilot in the form of the footprint display in addition to commanding a new L/D ratio through the vehicle dynamics. The pilot will be able to override the control loop and take primary command at any time.

B. Ballistic Control Followed By Equilibrium Glide

This technique uses guidance steering which has been developed for hitting a fixed point in space followed by an equilibrium glide to the target. Altitude damping is required in the transition from the free-fall to the equilibrium glide portion of re-entry. This system is expected to be extremely effective in controlling skip type re-entry. We limit ourselves to a two-dimensional consideration of the problem in the guidance plane. In a cartesian frame centered at the center of the earth, the vehicle position and velocity will be denoted  $X_H, Z_H$  and  $\dot{X}_H, \dot{Z}_H$  at any time  $t$ . The target point will be denoted  $X_T, Z_T$  and the desired hit time  $T$ .

The equation of a Keplerian ellipse (with focus at the origin) through the vehicle position can be written

$$(1) \quad aX_H + bZ_H + C = (X_H^2 + Z_H^2)^{1/2} \equiv r_H$$

The derivative of this expression

$$(2) \quad a\dot{X}_H + b\dot{Z}_H = \frac{1}{r_H} (X_H \dot{X}_H + Z_H \dot{Z}_H)$$

provides another relation between the constants  $a$ ,  $b$ ,  $c$ , and this is all the kinematics can say. The third relation depends upon the dynamics and is called Kepler's Second Law:

$$(3) \quad C = \frac{1}{G} (\dot{X}_H Z_H - X_H \dot{Z}_H)^2$$

where  $G$  is the product of the universal gravitational constant and the mass of the earth. These three equations completely define  $a$ ,  $b$ , and  $c$ , and, hence the free-fall trajectory for given  $X_H, Z_H, \dot{X}_H, \dot{Z}_H$ . Our problem however, is to determine  $\dot{X}_H, \dot{Z}_H$  so that the resulting path goes through  $X_T, Z_T$  at the time  $T$ . The requirement that the trajectory pass through the target point gives

$$(4) \quad aX_T + bZ_T + C = (X_T^2 + Z_T^2)^{1/2} \equiv r_T$$

Equations (1) through (4) constitute four equations in the five unknown  $a, b, c, \dot{X}_H, \dot{Z}_H$ . At this point the usual procedure is to introduce the expression for the free-fall time as the fifth relation. This system cannot be solved in closed form for  $\dot{X}_H, \dot{Z}_H$ ; thus an iteration technique is employed. A velocity is guessed which goes through the target point since this can be solved. Then the flight time is checked against  $T-t$ . The velocity is modified in successive

steps until a match is obtained.

The objections to this procedure are as follows:

- (a) The expression for time is complicated hence iterating it is undesirable.
- (b) Even after the perfect or correlated velocity is computed the vehicle can only steer to null one component or else to establish a preferred ratio of components. Then, as the non-zero component(s) are driven to zero by the acceleration, the rocket thrust is terminated.

An obvious alternative suggests itself at this point; i.e. re-define the correlated velocity so that we simply steer to hit the target point, regardless of the time of arrival there. In this manner, the troublesome expression for time is eliminated from the steering computation, permitting a solution in closed form. The procedure then would be to monitor the flight time resulting from this steering.

We now consider equations (1) through (4) and

$$(5) \quad \begin{cases} \dot{x}_H = V \cos \Gamma \\ \dot{z}_H = V \sin \Gamma \end{cases}$$

as six equations in the unknowns  $a, b, c, \dot{x}_H, \dot{z}_H, \Gamma$ . In addition to the target position  $x_T, z_T, \tau$ , the vehicle speed  $V$  is assumed known. These equations can be solved to yield a single equation in the desired flight path angle. First of all  $a, b, c$  can be eliminated from equations (1) through (4) leaving a cubic equation in  $\dot{x}_H, \dot{z}_H$ . From physical considerations, it was guessed that this equation must be factorable, eliminating the one root which is always real. When

the speed is less than minimum energy there should be no real root and when it is greater, there should be only two real roots. The linear factor was found (it corresponded to the degenerate case of two straight lines from the center of the earth to the points  $X_H, Z_H$  and  $X_T, Z_T$ ) and the resulting quadratic equation was

$$(6) \quad G(Z_H Z_T - r_H r_T + X_H X_T) + r_H [(Z_H - Z_T) \dot{X}_H + (X_T - X_H) \dot{Z}_H] (\dot{X}_H Z_H - X_H \dot{Z}_H) = 0$$

Finally substituting (5) into (6) and dividing through by  $-r_H V \cos^2 \Gamma$  yields

$$(7) \quad L \tan^2 \Gamma + 2M \tan \Gamma + N = 0$$

where

$$(8) \quad \begin{aligned} L &= X_H (X_T - X_H) - K \\ M &= \frac{2X_H Z_H - Z_H X_T - X_H Z_T}{2} \\ N &= Z_H (Z_T - Z_H) - K \\ K &= \frac{G}{r_H r_T} (Z_H Z_T - r_H r_T + X_H X_T) \end{aligned}$$

The solution for  $\tan \Gamma$  is

$$(9) \quad \tan \Gamma = \frac{1}{L} [-M \pm (M^2 - LN)^{1/2}]$$

The sign ambiguity is easily settled--we want the smallest  $\tan \Gamma$ .

The steering law can then be written as

$$(10) \quad \tan \Gamma - \frac{\dot{Z}_H}{\dot{X}_H} = \theta_0$$

The above equation for  $\tan \delta_d$  has been mechanized in an analog program and combined with a two dimensional trajectory simulation. The evaluation of this steering law is presently being conducted and preliminary results indicate that skip trajectories can be effectively controlled.

When the vehicle velocity has become sub-orbital for either direct or skipping type re-entry, a transition to equilibrium glide is initiated by an altitude damping control law of the form

$$\dot{Q}_d = K_h (h'_a - h'_d) \quad \text{where } h'_d = \frac{K_g}{K \dot{h}_d}$$

Following the altitude damping phase, an equilibrium glide will be made to the target using a control law of the form:

$$(\dot{h}_d)_d = \frac{2\sigma_T}{\ln \frac{1}{1-\mu^2}}$$

$$(\dot{h}_d)_c = K [(\dot{h}_d)_a - (\dot{h}_d)_d]$$

This type of control has been thoroughly evaluated for sub-orbital velocities in previous studies. It is very effective in controlling the impact point and is easily controlled by a human operator.

The evaluation of this guidance technique will be completed within the next month.

#### C. Skip Into Near Orbit

During the early portion of the Apollo program an operational concept was evolved which required a skip into orbit upon returning to the earth from a lunar mission. This concept has many attractive

364

features from a control standpoint such as good control over landing site selection, updated re-entry conditions during orbit by means of ground tracking or airborne measurements and the fact that the vehicle could use developed techniques during the re-entry from an earth orbit. The obvious disadvantage of such a concept would be the weight of propellant required to achieve and de-orbit from the desired near-earth orbit and the added complexity required of such a system. In order to evaluate this concept a program was initiated on the Martin analog facility which incorporated a control steering law to modulate lift during the initial re-entry from the parabolic approach speeds in such a manner that a minimum impulse would be required to achieve an orbit whose perigee was greater than 400,000 ft and whose apogee was less than 400 miles. A parametric study has been completed utilizing a special form of the control law developed in section II-B of this memo referred to as tangent steering. This steering law attempts to modulate lift so as to produce a trajectory that is tangent to a target orbit of a desired perigee altitude. The steering law commands a change in lift proportional to the error between the  $\gamma_d$  ( $\gamma$  desired) and  $\gamma_a$  ( $\gamma$  actual) through the relationship

$$\tan \gamma_d - \tan \gamma_a = \tan \gamma_e$$

$$C_L = K \tan \gamma_e$$

$$\text{where } \tan \gamma_d = \pm \sqrt{C/A}$$

$$\text{and } C/A = 1 + \frac{r^2 V^2}{r_c \mu (2 \frac{r}{r_c} - \frac{r V^2}{\mu} - 2)}$$

$$r_c = \text{desired tangent target radius}$$

In order to simplify the mechanization of this law on the analog computer an approximation was developed which is of the form

$$C/A = - \frac{2\Delta h}{r^2 V^2}$$

73 runs were made on the analog program in which the initial conditions within the 40 mile design corridor were varied. The target orbit radius was varied as was the gain,  $K$ , in the steering law to study the effects of these parameters on the  $\Delta V$  requirement. Figures 34, 35 and 36 show the  $\Delta V$  requirements as a function of the steering law gain and initial conditions for various target orbit altitudes.



#### D. METHOD OF STEEPEST DESCENT (ADJOINT METHOD)

During re-entry of the Apollo vehicle, certain requirements must be fulfilled by the guidance system. Included in these requirements are maximum heating restrictions, satisfactory acceleration levels for the vehicle occupants and equipment and specified landing position. An ideal guidance scheme should determine the trajectory which minimizes the heat input to the body surface, constrain the flight path to one having acceptable acceleration limits and specified landing position and finally, provide signals to the control system to accomplish such a re-entry trajectory.

A promising technique for achieving such an optimum guidance system is the Calculus of Variations. In past years, resort to variational techniques for providing guidance equations has been practically impossible due to the complicated nature of the indirect methods and their associated split boundary conditions. Tedious iteration schemes are an unfortunate necessity for obtaining **extremal** arcs by the indirect methods of variational calculus.

Recently, several breakthroughs have occurred which show promise of applying direct methods of variational calculus to future guidance systems. Nearly simultaneously Kelley (Reference 7) and Bryson et al (Reference 8) published methods incorporating direct variational techniques for obtaining **extremal** solutions with an associated reduction in computing time. Both methods make use of the system of equations about a nominal trajectory. This adjoint system yields influence coefficients which, in turn, correct the nominal trajectory in an optimum fashion. Convergence of the method to the true optimum is accomplished by "steepest descent" methods.

These direct variational methods are actually linearized solutions to the Mayer Problem of the indirect method of the Calculus of Variations. The approximation involves replacing the non-linear trajectory equations of motion by a nominal trajectory and a linear, small perturbation system of equations. The adjoint system of equations of the direct method corresponds to the Euler Lagrange equations of the indirect method and the influence coefficients in the direct method correspond to the Lagrange multiplier in

the indirect method. The significant advantage of the direct method is its ability to determine near optimum solutions in relatively few computer cycles.

To apply a direct variational technique to the Apollo vehicle, an on-board computer would be programmed to determine the lift commands which, in turn, would be inputs to the control system. Boundary conditions consisting of position, rate and altitude data would be provided the computer by either on-board sensing devices or ground control linkages. To account for errors in the system (primarily input position and rate data) the trajectory could be continually optimized from the vehicles present position to the desired touch-down point. The system would become increasingly accurate as the impact point is neared. The significant advantage lies in the ability to guide the vehicle in a manner which would optimize some pertinent physical parameter such as minimizing the heat input to the body, minimizing the flight time, etc.

Since the methods of References (7) and (8) are the first direct trajectory optimization methods to show promise for future guidance schemes, work is continuing to evolve a simple, direct optimum (or at least near optimum) guidance technique to be applicable for the Apollo vehicle.

An interesting alternate application of such a guidance technique would be in the rendezvous mission. An optimum guidance technique such as discussed above would have an advantage in controlling the thrust magnitude and direction of the intercept vehicle. Such a system would be programmed to minimize the flight time and fuel consumption from launch of the intercept vehicle to actual intercept with the target satellite.

#### Status of Investigation

A direct variational method capable of optimizing load factor, heat input and range is presently being developed and prepared for programming on the Master IBM 709 computer. The program will provide a means of determining the optimum re-entry trajectory from a performance standpoint as well as serving as a tool for studying optimum re-entry guidance techniques.

In order to evaluate this technique for the Apollo re-entry during this study phase, a working agreement has been arranged with Raytheon, who

367

has a direct variational method (reference 8) programmed presently on an IBM 704, to supply typical re-entry trajectories tailored to the Martin Operational Concept. These trajectories will be analyzed to evaluate the advantage of using an optimization approach by comparing them with the results of the other re-entry techniques under study. Specifically the total heat, of time history and range capability will be compared and the resultant advantages offered by the direct variational method weighed against the increased computer size, weight and complexity required to mechanize this technique. \*These studies will be completed during the present Apollo program.

### REFERENCES

1. Martin Company Report No. ER 10784 P (Secret)  
"Recoverable Space Vehicle, Piloted."
2. National Aeronautics and Space Administration Technical Report R-11  
"An Approximate Analytical Method for Studying Entry Into Planetary Atmospheres" by Dean R. Chapman.
3. Martin Company Report No. ER 11245 M -- "Manned Lunar Vehicle System"
4. IAS Paper No. 59-124, "Synthesis and Flight Test of a Ballistic Missile-- Adaptive Flight Control System" by Ordway B. Gates, Jr. and Orrin C. Kaste.
5. Martin Company Report, Undesignated number. "Use of Describing Functions in Analysis of Non-linear Control Systems." by W. H. Foy, Jr., January, 1959.
6. Truxal, "Automatic Feedback Control System Synthesis," McGraw Hill Co., 1955

\* To further assist in the evaluation of this technique for re-entry guidance, Raytheon is supplying an estimate on the airborne computer required for the optimization technique including the problem solution time, required in-puts, computer development time and the physical characteristics of the computer.

7. American Rocket Society Preprint No. 1230-60  
"Gradient Theory of Optimal Flight Paths" by H. J. Kelley
8. Institute of Aero. Sci. Preprint No. 61-6.  
"Determination of the Lift or Drag Program that Minimizes Re-Entry Heating with Acceleration or Range Constraints Using a Steepest Descent Computation Procedure" by A. E. Bryson, W. F. Denham, F. J. Carroll and K. Mikhlin.

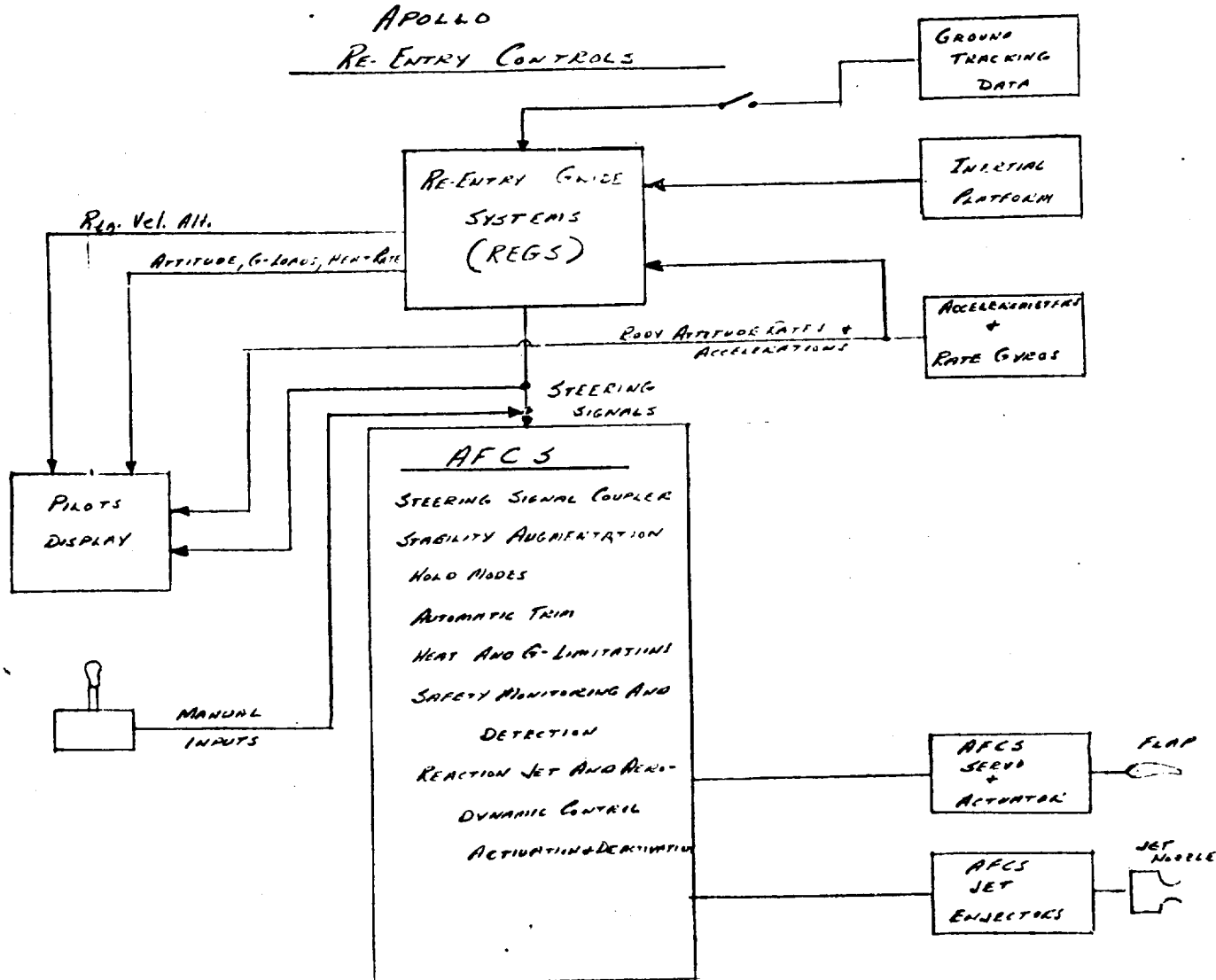


FIGURE 1

L-1-C Configuration  
 $C_m$  vs  $\alpha$

C.G. 20% D<sub>1</sub> Forward

$F=1$   $\delta_B = 45^\circ$   
 $F=1$   $\delta_B = 90^\circ$   
 $F=1$   $\delta_B = 135^\circ$

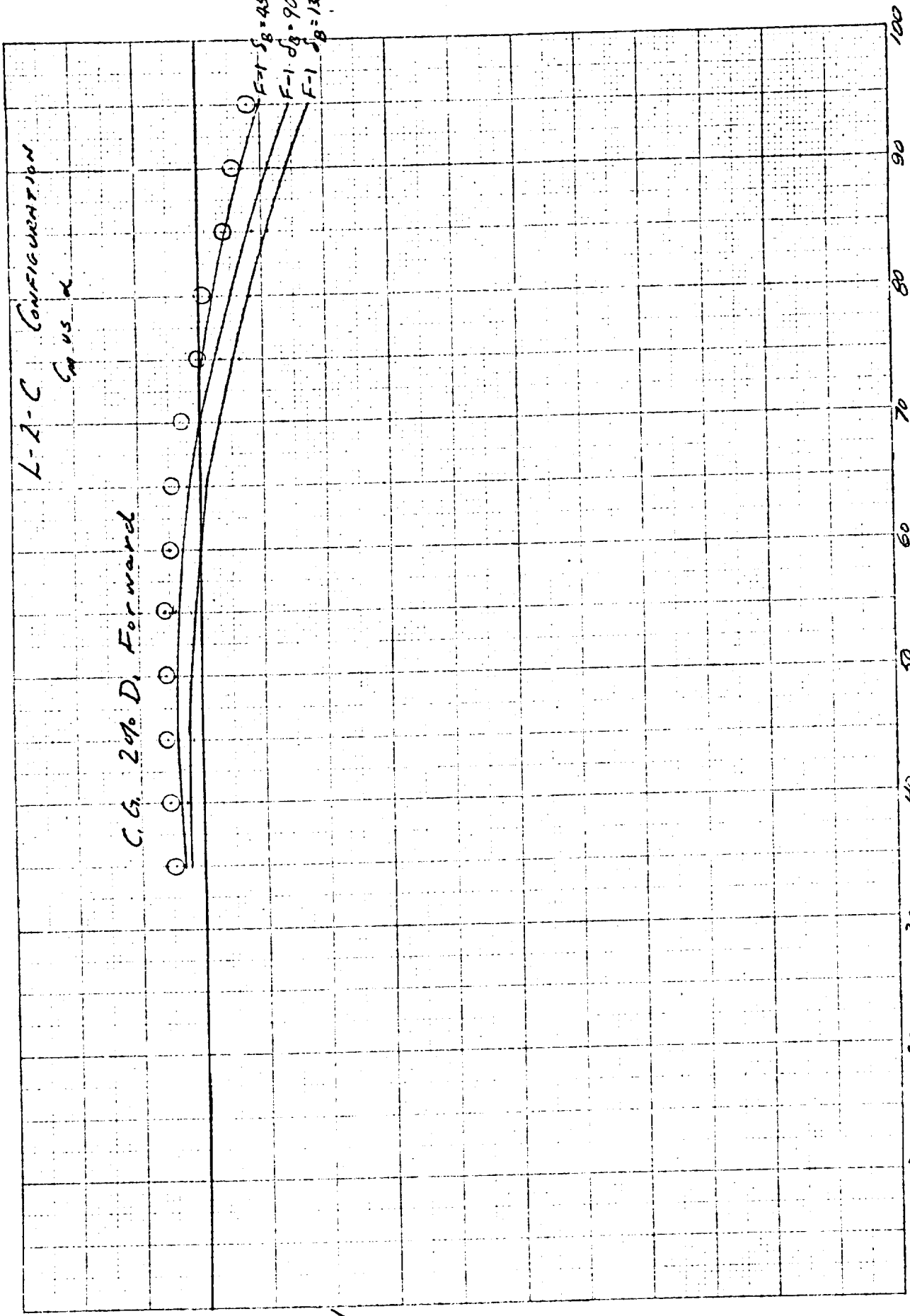


FIGURE-2

T.M-12

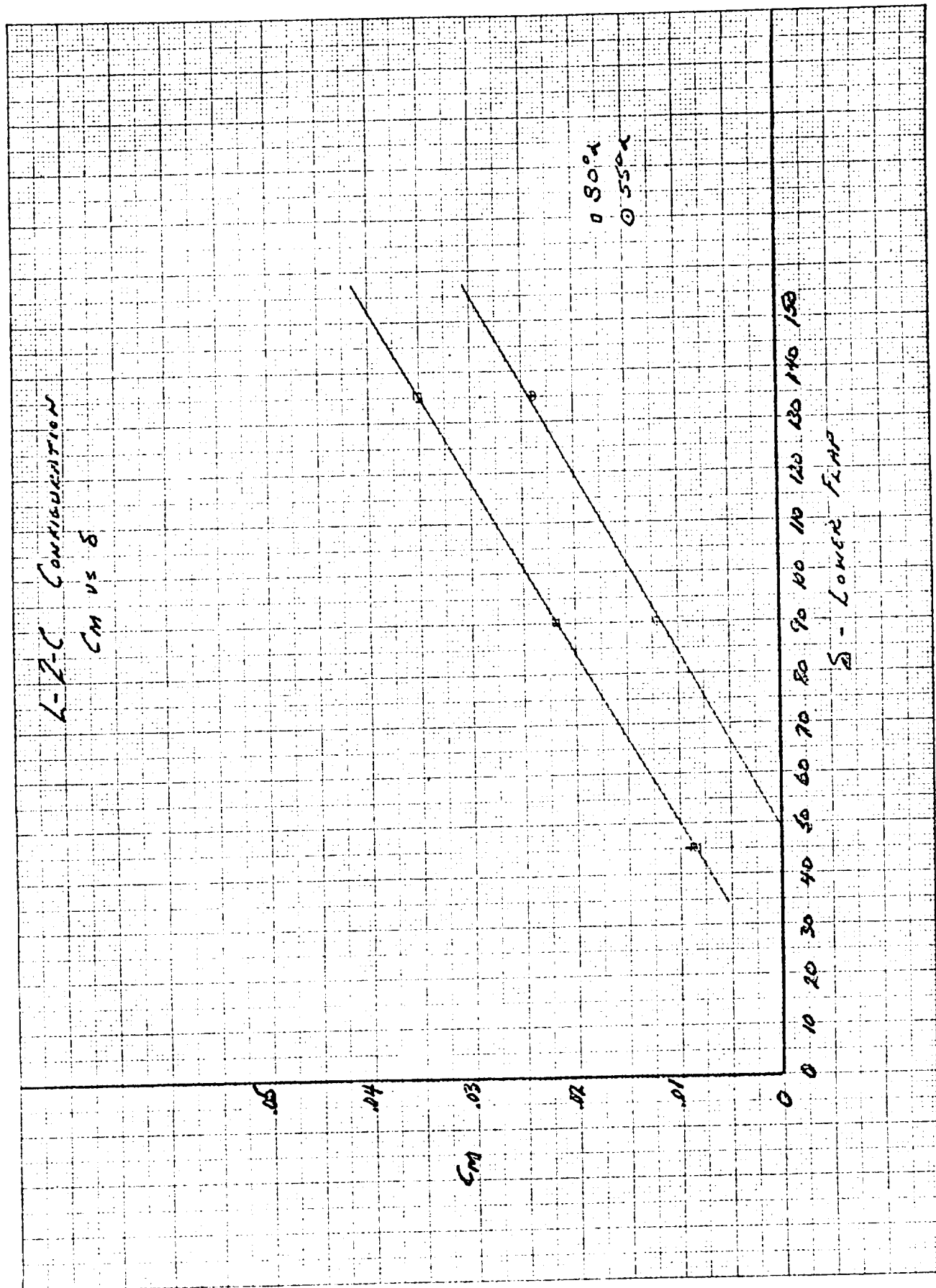


FIGURE-3

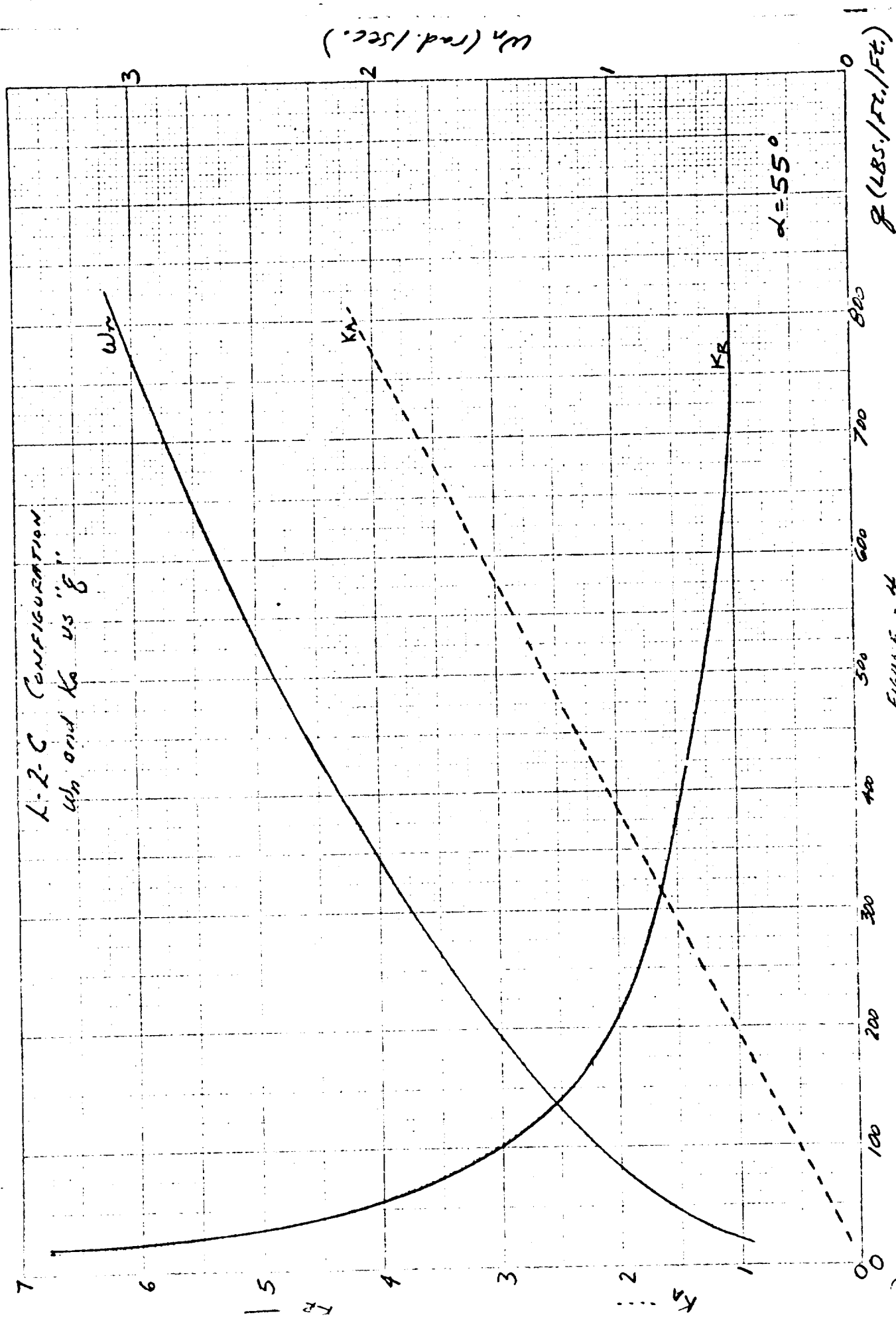


FIGURE - 4



$$G.H. = \frac{K(1 + 0.1075s)}{(1 + 0.008275s)(1 + 0.015s)(s^2 + w_n^2)(5 + 81.5 + j14j)(5 + 81.5 - j14j)}$$

Upper half of root locus with lead network.

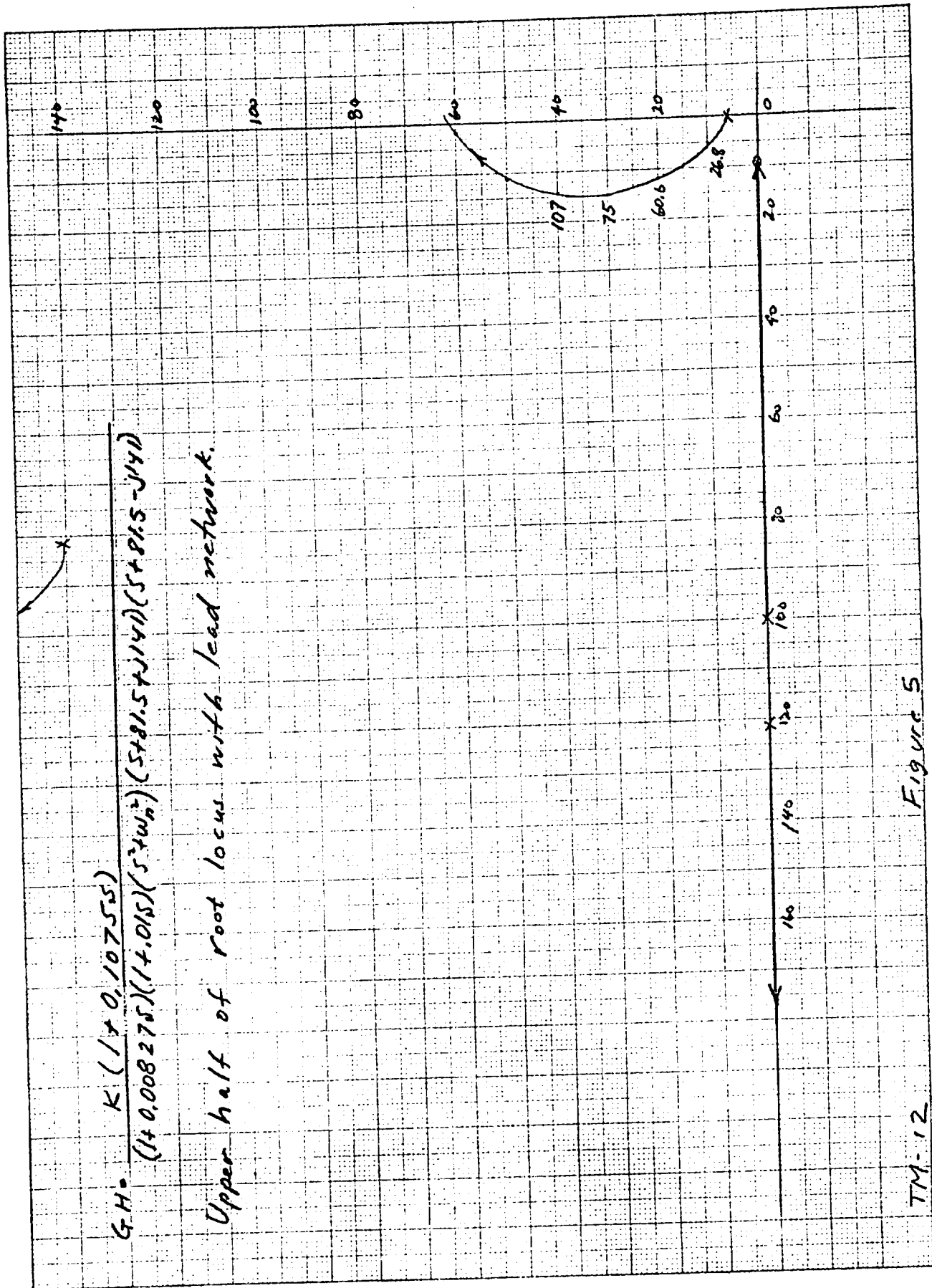
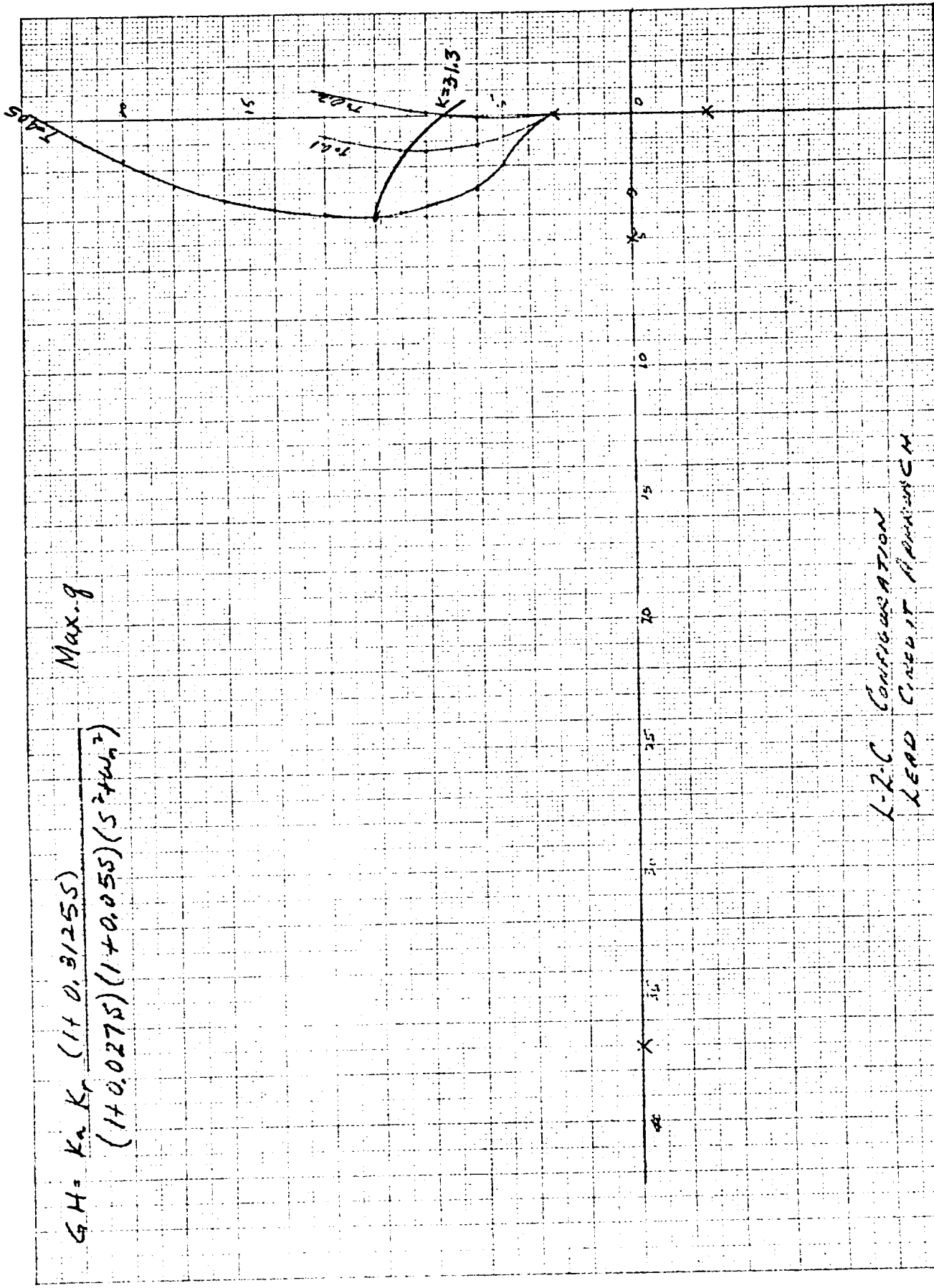


Figure 5

TM-12

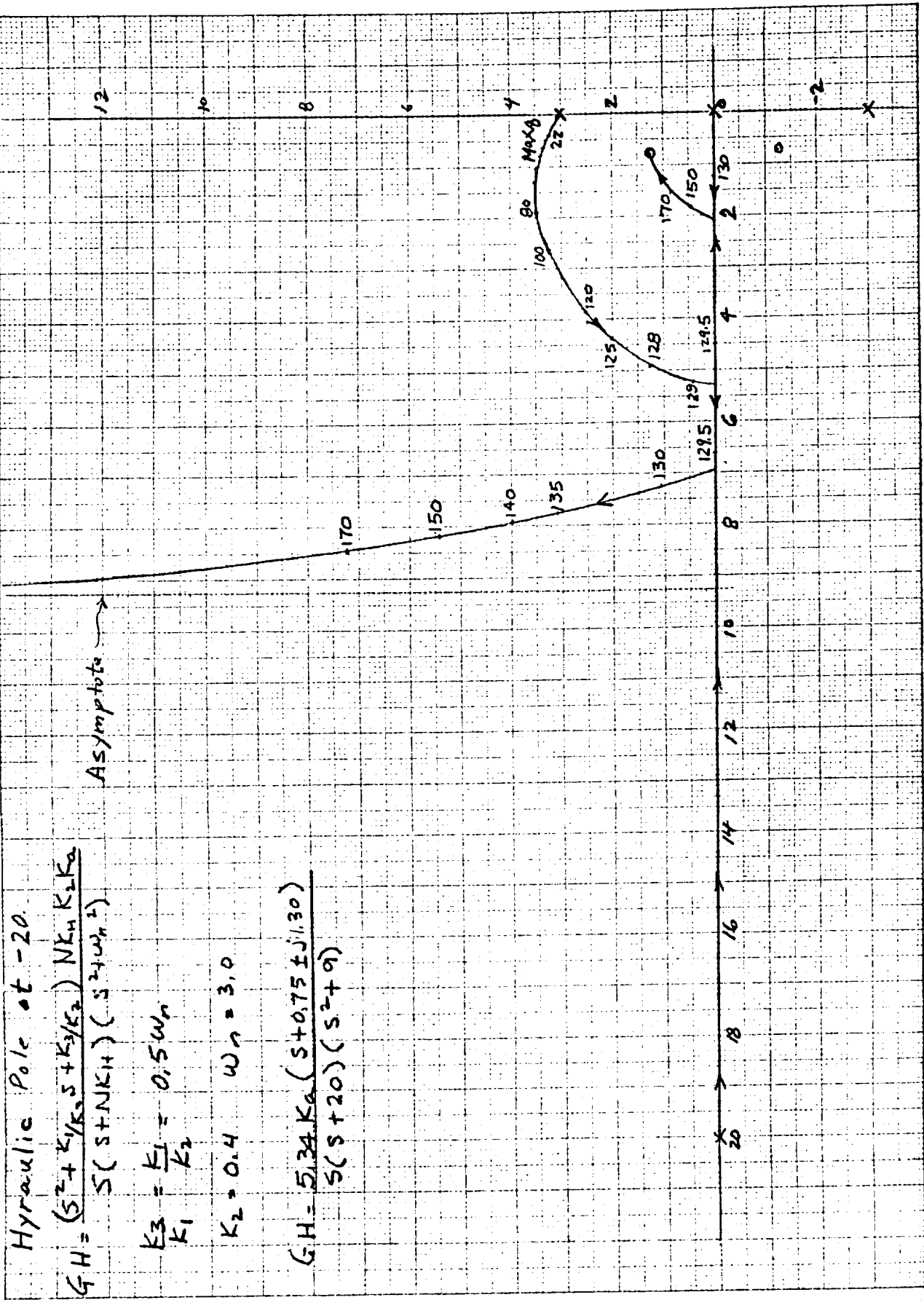
$$GH = K_a K_r \frac{(1 + 0.3125s)}{(1 + 0.0275s)(1 + 0.055s)(s^2 + \omega_n^2)}$$

Max. g



L-R-C CONFIGURATION  
LEAD CREDIT APPROXIMATION

Run 1



Hydraulic Pole at -20.

$$GH = \frac{(s^2 + \frac{K_1}{K_2}s + \frac{K_3}{K_2}) NK_1 K_2 K_0}{s(s + NK_1)(s^2 + \omega_n^2)}$$

$$\frac{K_3}{K_1} = \frac{K_1}{K_2} = 0.5 \omega_n$$

$$K_2 = 0.4 \quad \omega_n = 3.0$$

$$GH = \frac{5.34 K_0 (s + 0.75 \pm j1.30)}{s(s + 20)(s^2 + 9)}$$

Figure - 7

TM-12

Run 3

Hydraulic Polkat -5

$$GH = \frac{(s^2 + K_1/K_2 s + K_3/K_2) NK_H K_2 K_a}{s(s + NK_H)(s^2 + \omega_n^2)}$$

$$\frac{K_2}{K_1} = \frac{K_2}{K_2} = 0.5 \omega_n$$

$$K_2 = 0.4 \quad \omega_n = 3.0$$

$$GH = \frac{1.335 K_a (s + 0.75 \pm j/3.0)}{s(s + 5)(s^2 + 9)}$$

Asymptote →

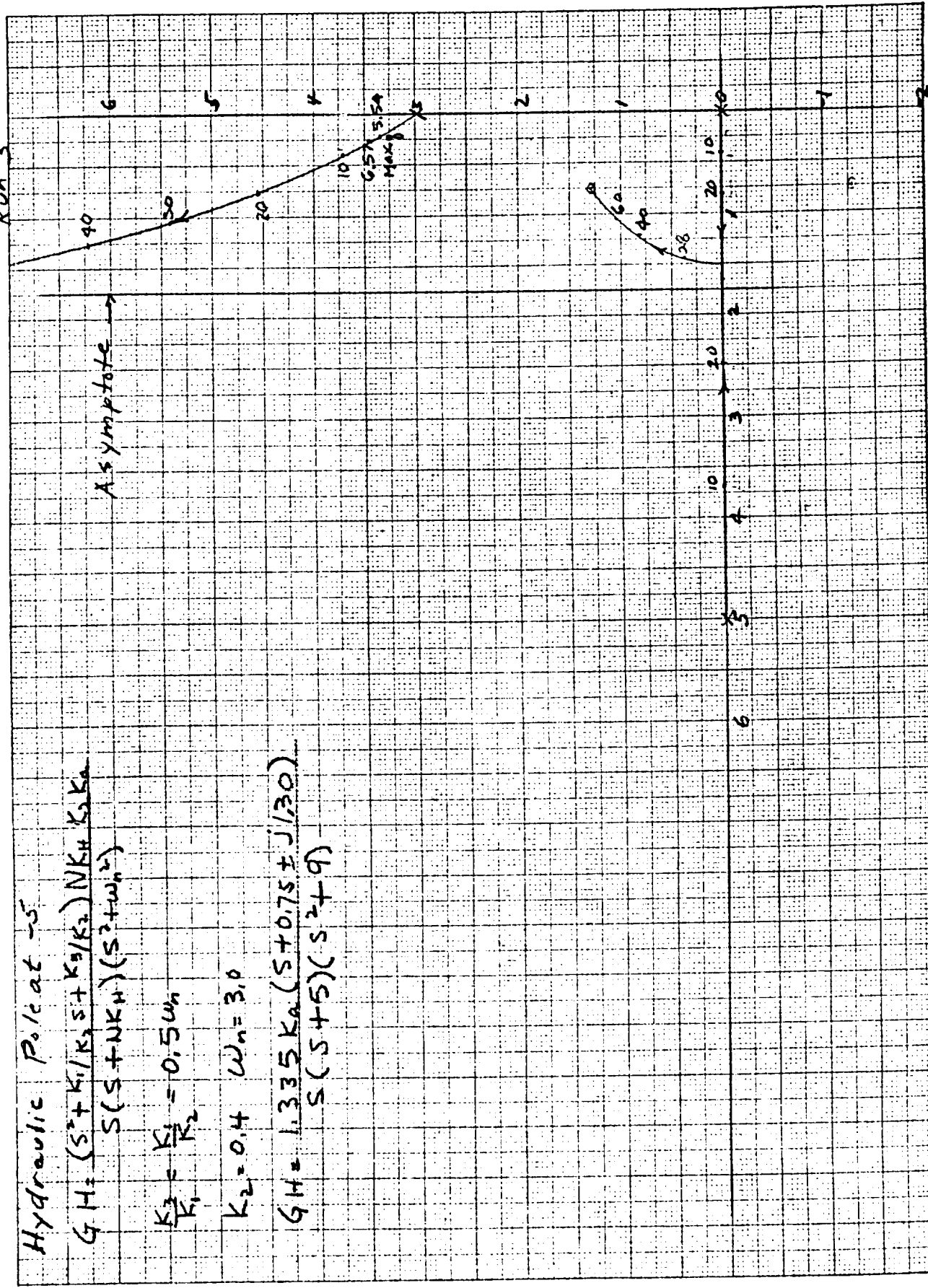
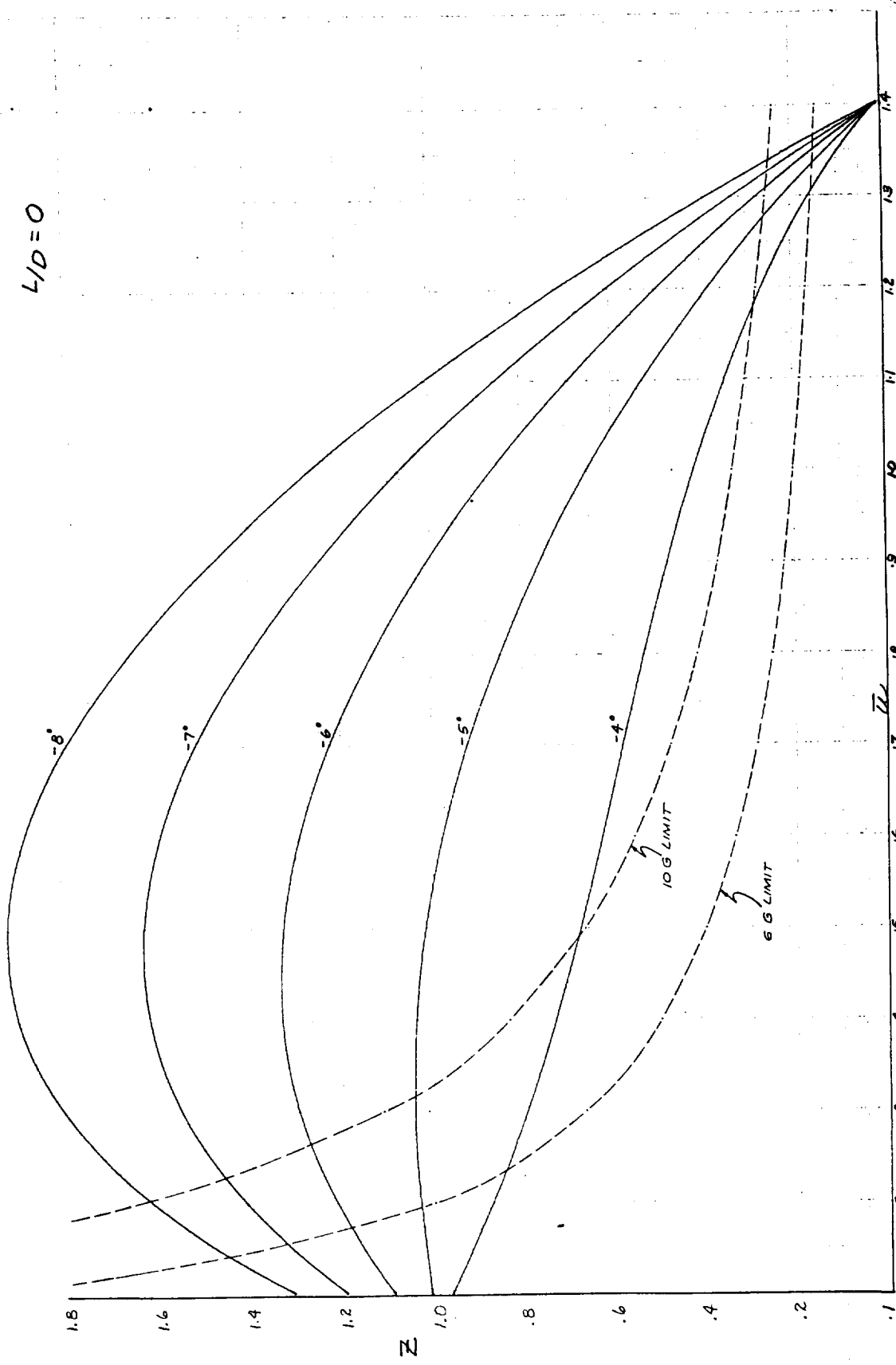


Figure-8

$L/D = 0$



$$\begin{aligned} L/D &= 0 \\ \bar{u}_i &= 1.4 \\ \bar{z}_i &= .01 \end{aligned}$$

$\chi_i = -4^\circ$	$A_{\chi_i} = .1571$	$\bar{u} = .101$	481 MM.
$-5^\circ$	.0996	.101	342 "
$-6^\circ$	.0812	.101	279 "
$-7^\circ$	.0692	.101	238 "
$-8^\circ$	.0604	.101	203 "

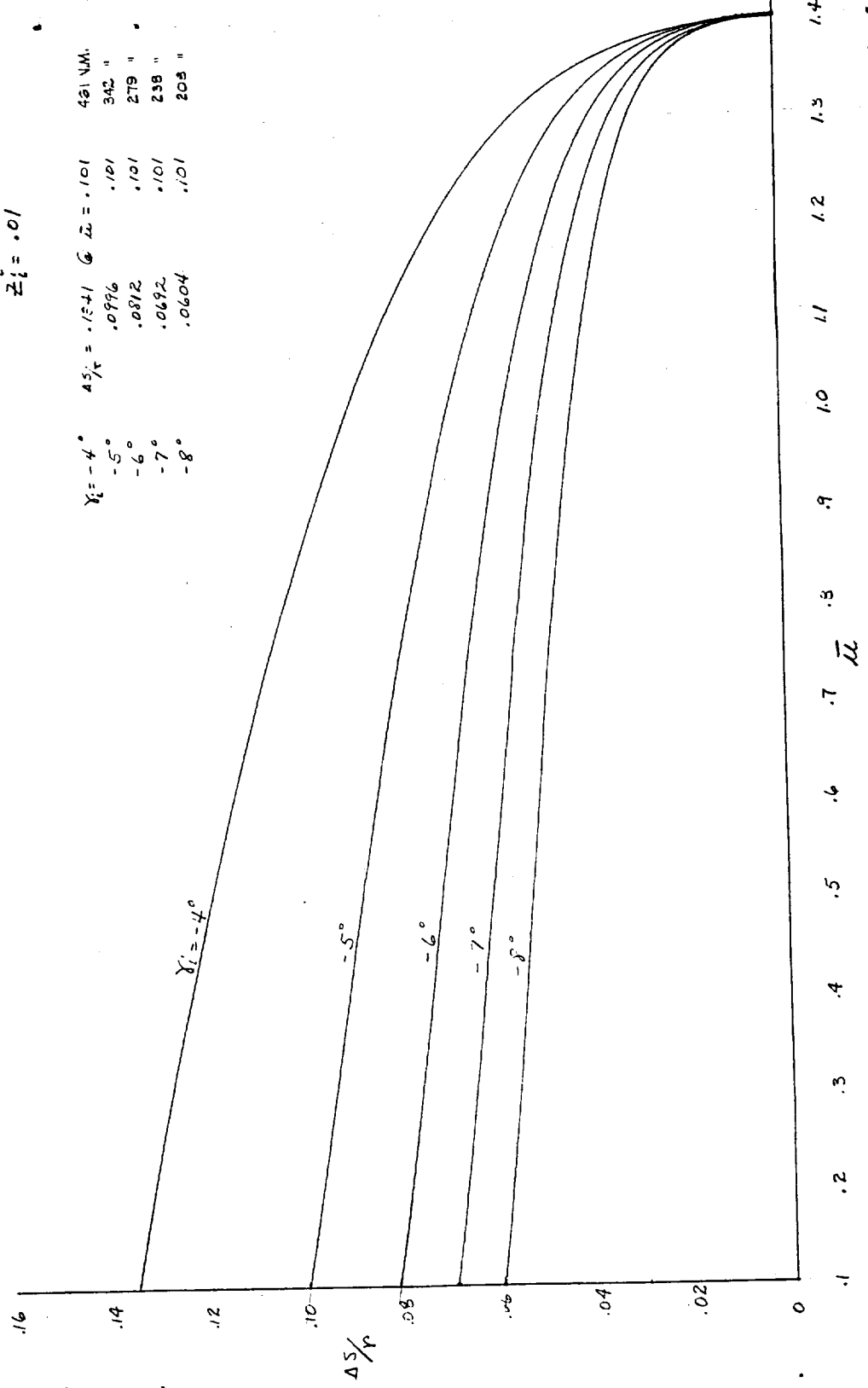
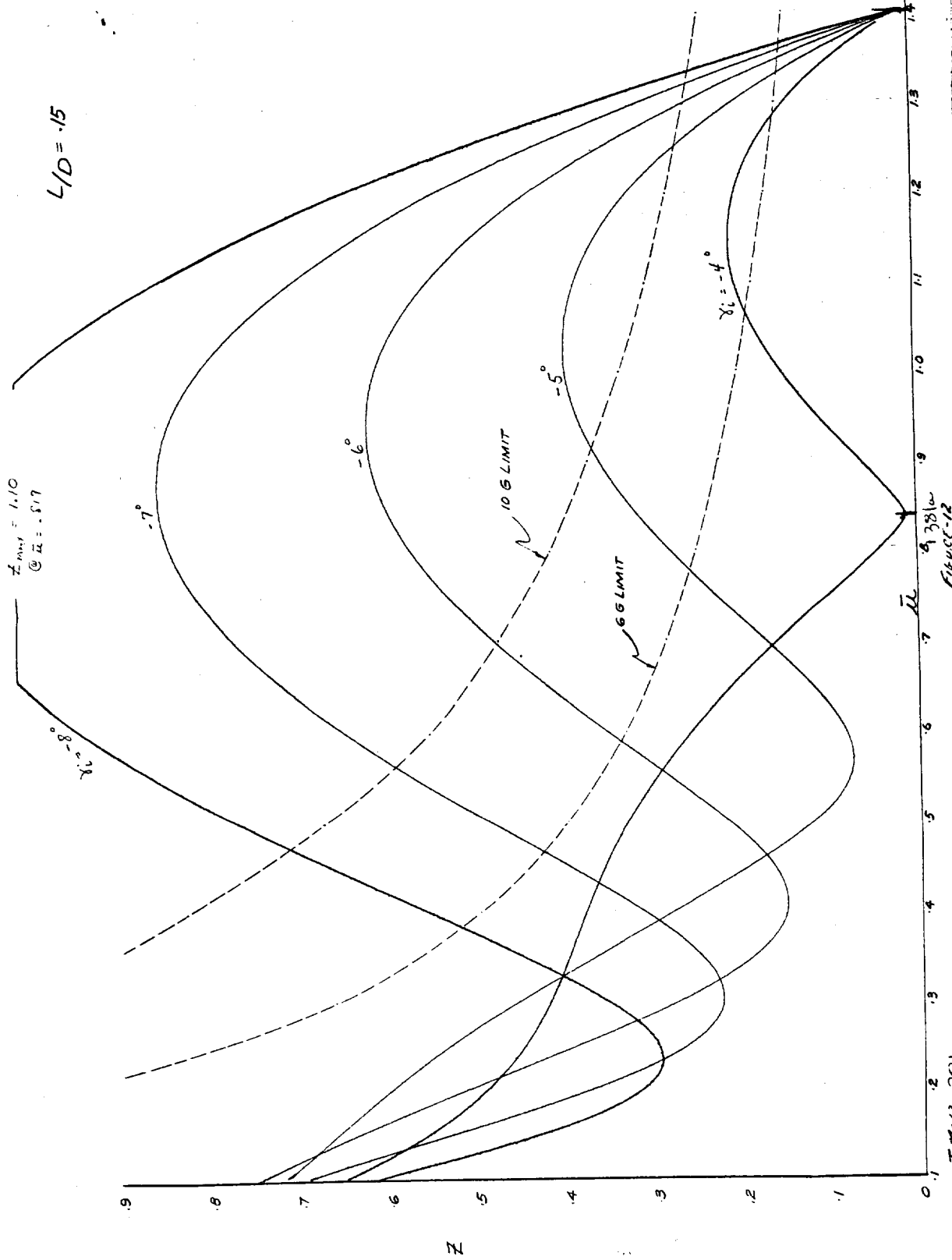


FIGURE 11

D

3



$L/D = .15$   
 $M_i = 1.4$   
 $Z_i = .01$

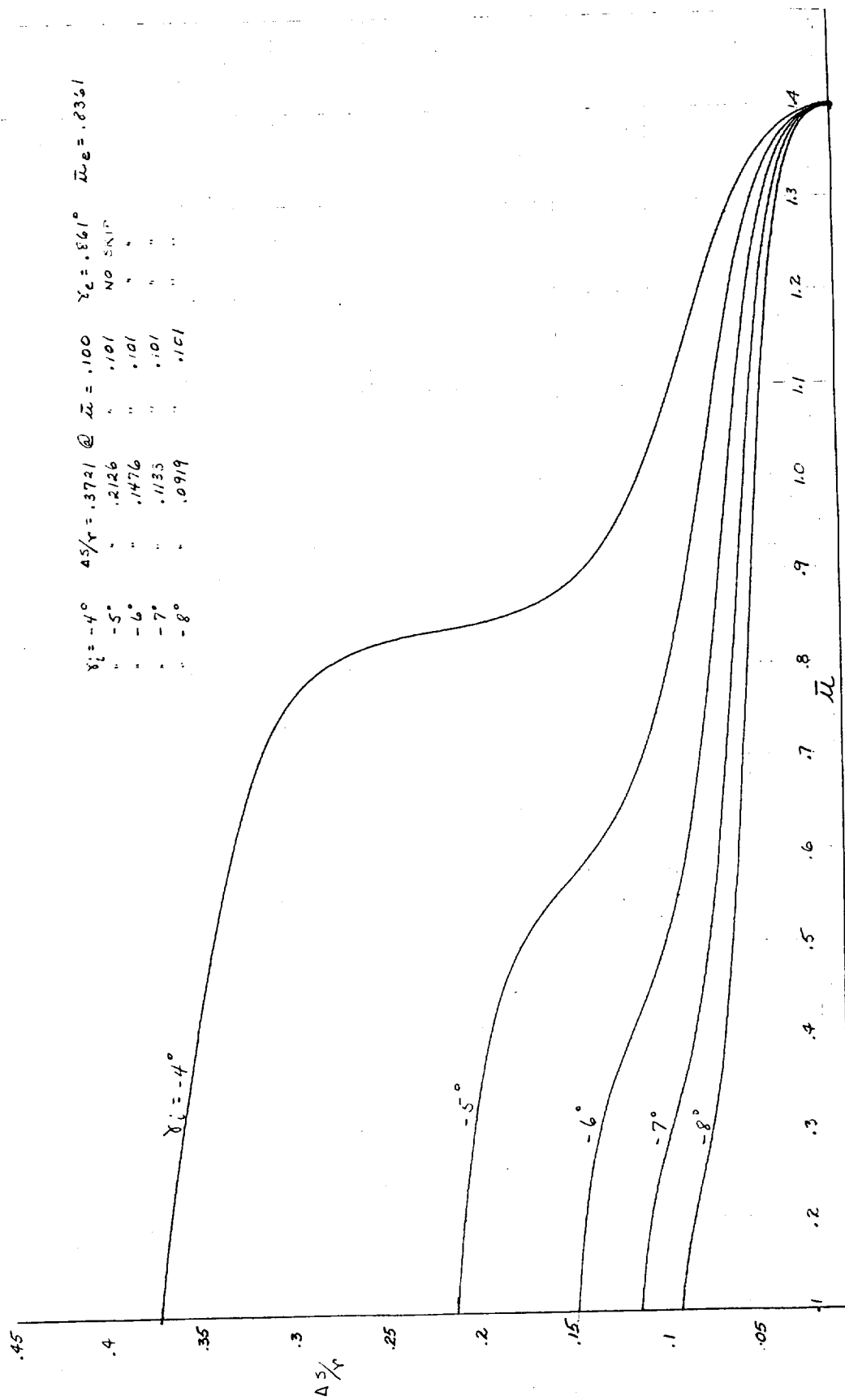
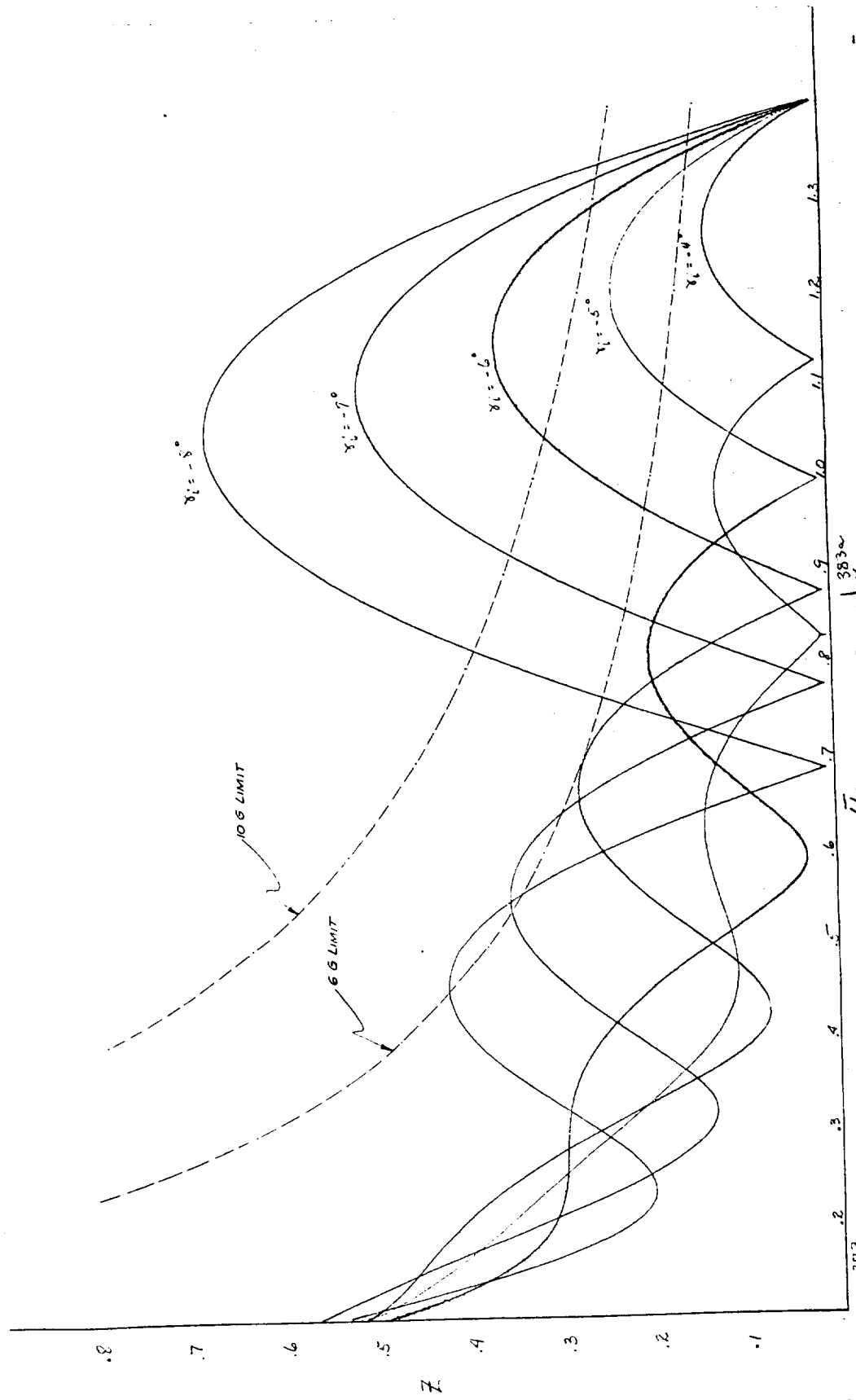


FIGURE 13-1382w



$$\frac{L/D}{\lambda} = .25 \quad \frac{L}{\lambda} = 1.4 \quad \frac{Z_1}{\lambda} = .010$$



383

TM-12

11

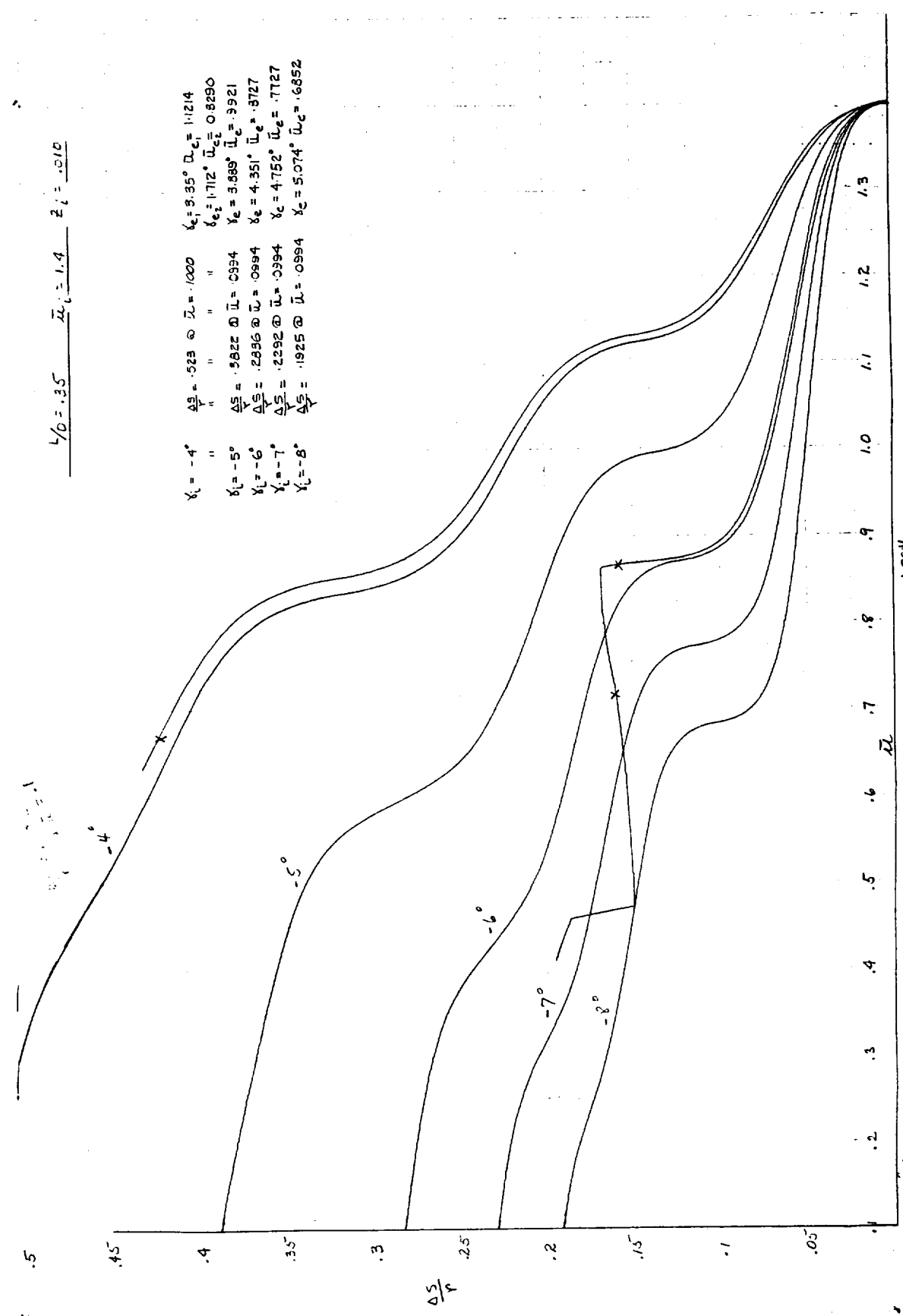
FIGURE 14

383~

$L/O = .35 \quad \bar{u}_L = 1.4 \quad Z_L = .010$

$\bar{u}_L = 1.4$   
 $Z_L = .010$

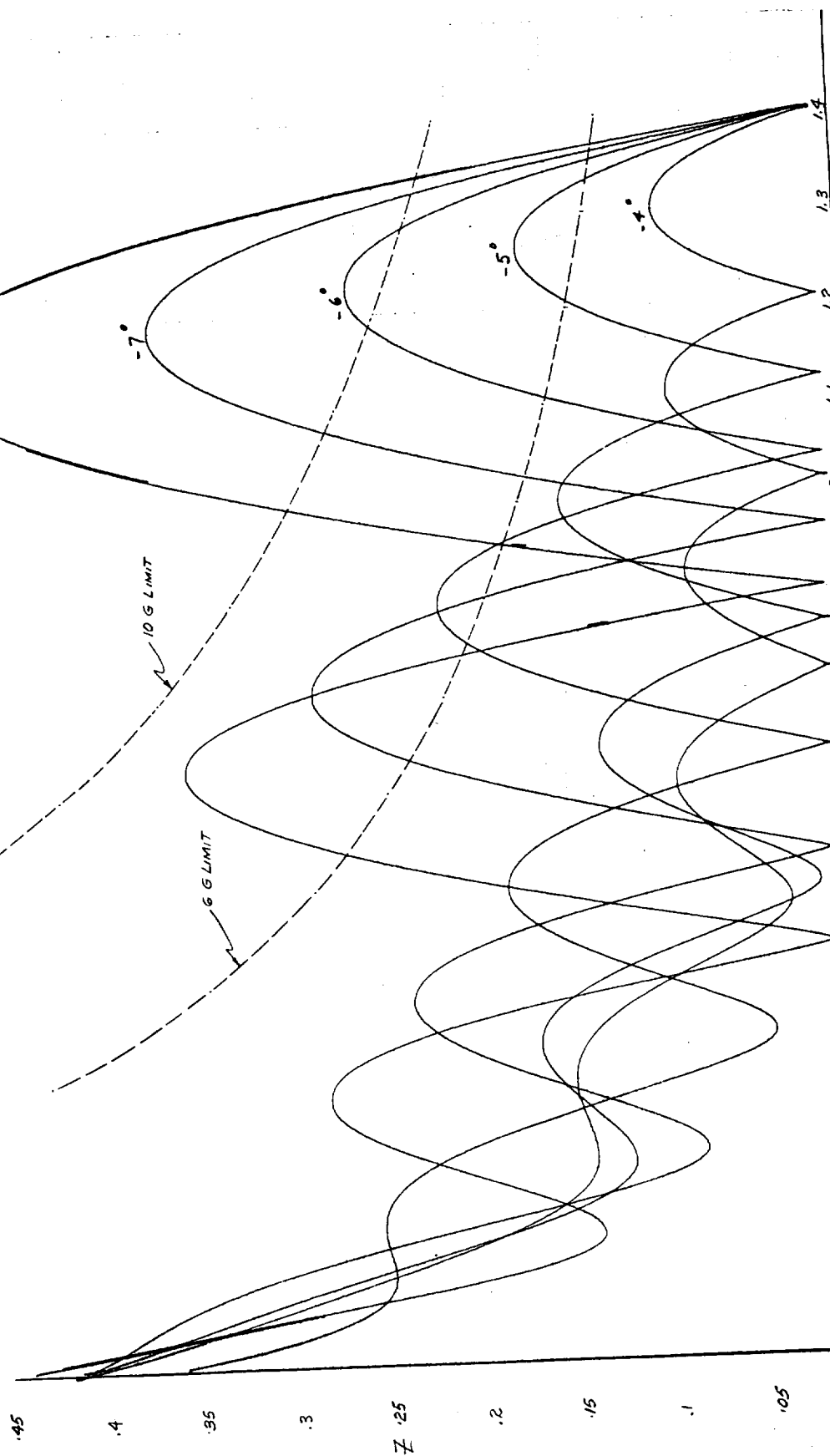
$\chi_L = -4^\circ$	$\Delta S = .523$	$\bar{u} = .1000$	$\chi_L = 3.35^\circ$	$\bar{u}_L = 1.1214$
"	"	"	$\chi_L = 1.712^\circ$	$\bar{u}_L = 0.8290$
$\chi_L = -5^\circ$	$\Delta S = .5822$	$\bar{u} = .0994$	$\chi_L = 3.589^\circ$	$\bar{u}_L = .9921$
$\chi_L = -6^\circ$	$\Delta S = .2356$	$\bar{u} = .0994$	$\chi_L = 4.351^\circ$	$\bar{u}_L = .8727$
$\chi_L = -7^\circ$	$\Delta S = .2292$	$\bar{u} = .0994$	$\chi_L = 4.752^\circ$	$\bar{u}_L = .7727$
$\chi_L = -8^\circ$	$\Delta S = .1925$	$\bar{u} = .0994$	$\chi_L = 5.074^\circ$	$\bar{u}_L = .6852$



384  
 7M-12

$\gamma_c = -9^\circ @ 250 \text{ K FT.}$

$L/D = .56 \quad \mu_c = 1.4 \quad z_c = .010$



ALL FIGURE - 161 385a

TM-12 385

$$\frac{L_0}{D} = .56 \quad \bar{\mu}_1 = 1.4 \quad Z_1 = .010$$

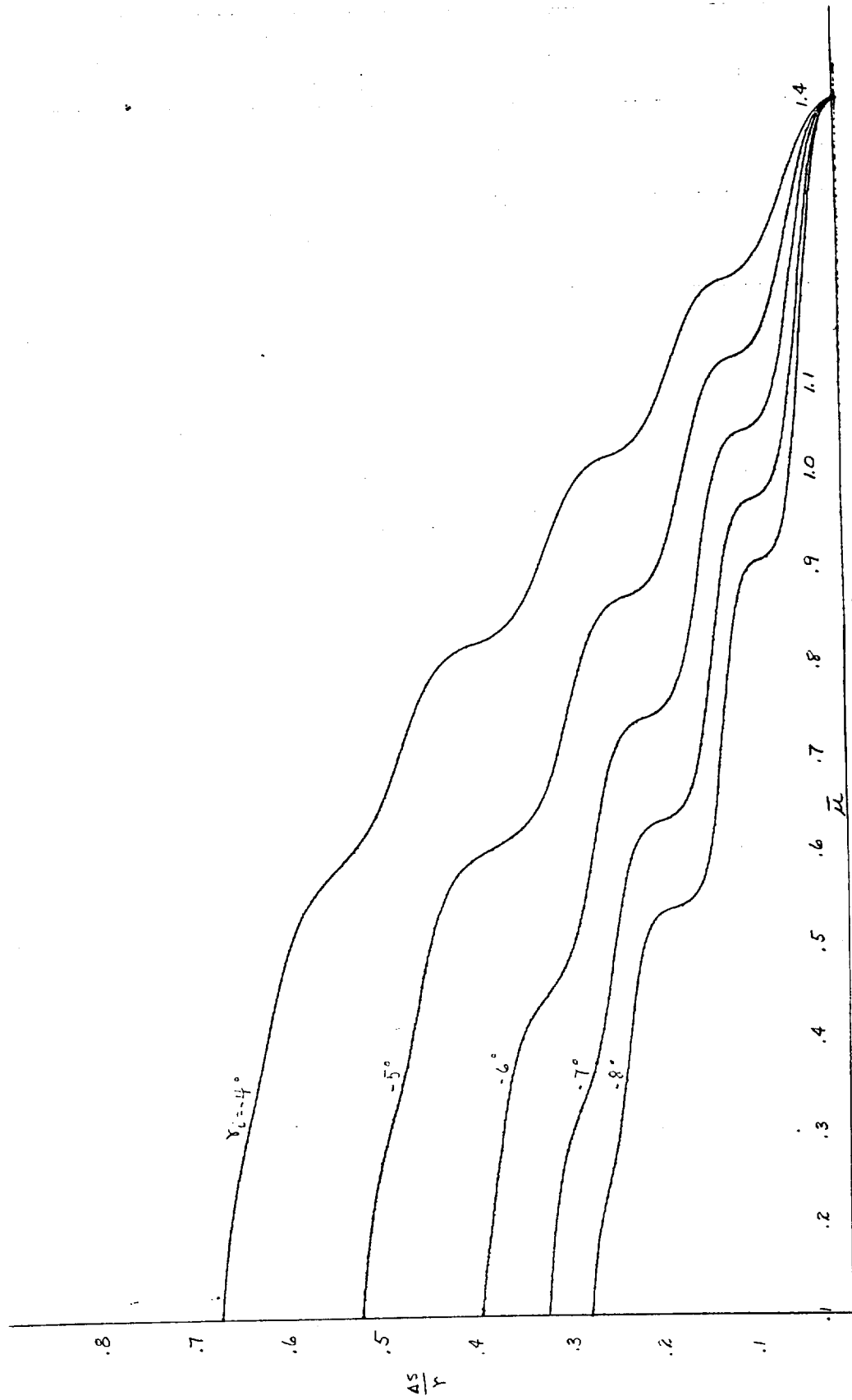
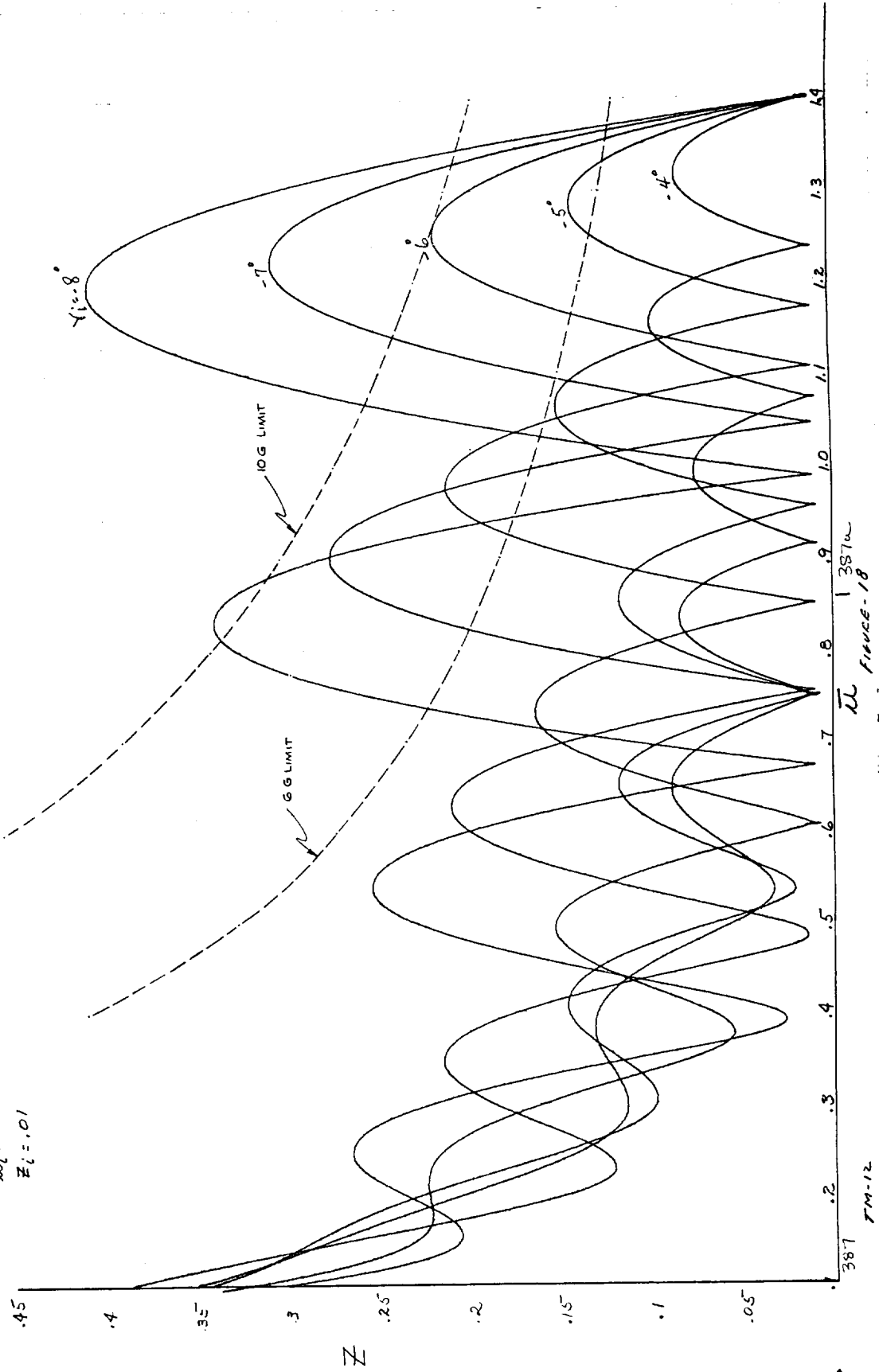


FIGURE-17 | 386a

$\gamma_D = .7$   
 $\bar{\mu}_i = 1.4$   
 $\bar{\pi}_i = .01$



387  
 FM-12  
 387w  
 FORCE-18

$L/D = .7$   
 $\bar{U}_i = 1.4$   
 $Z_i = .01$

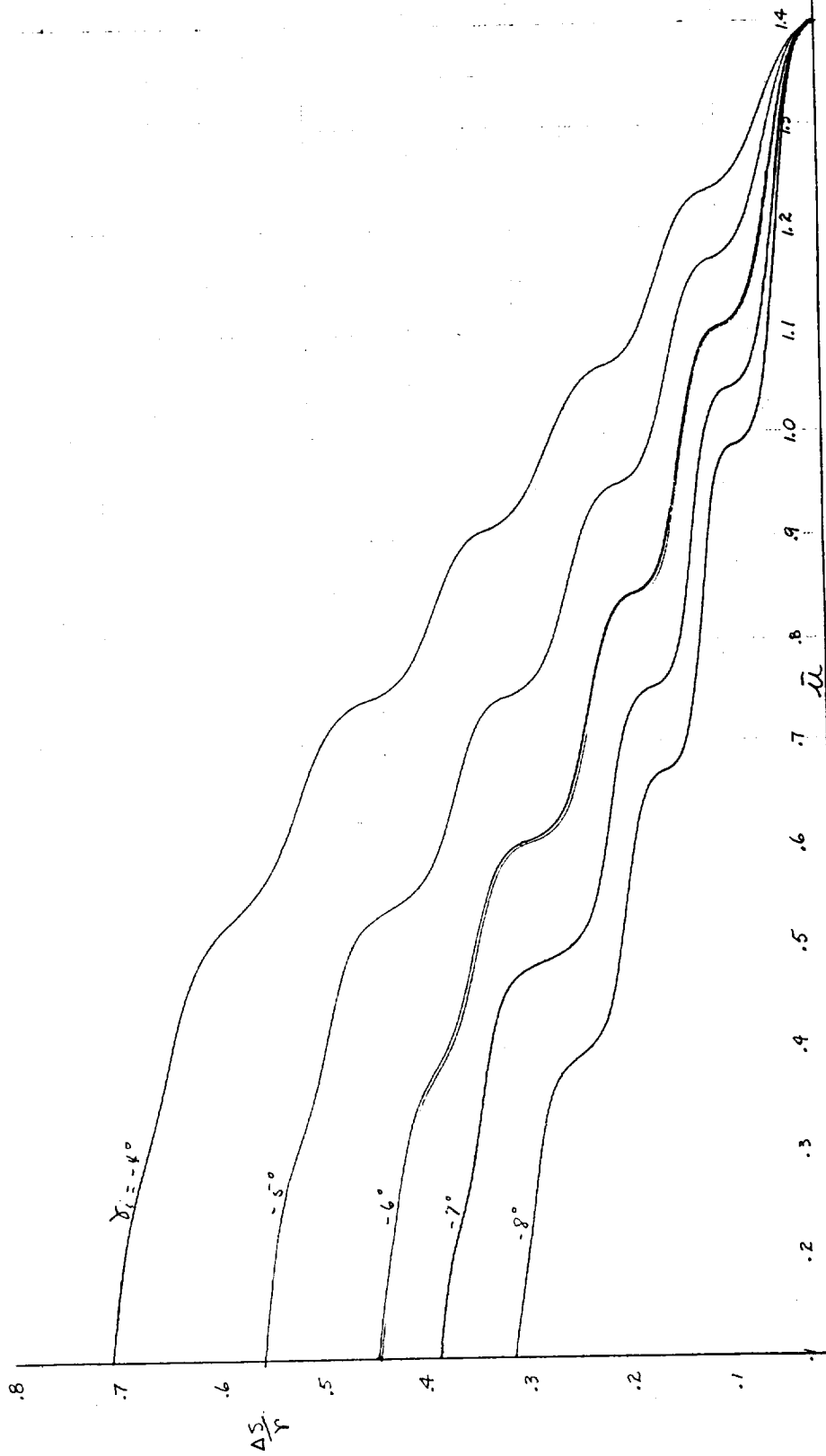
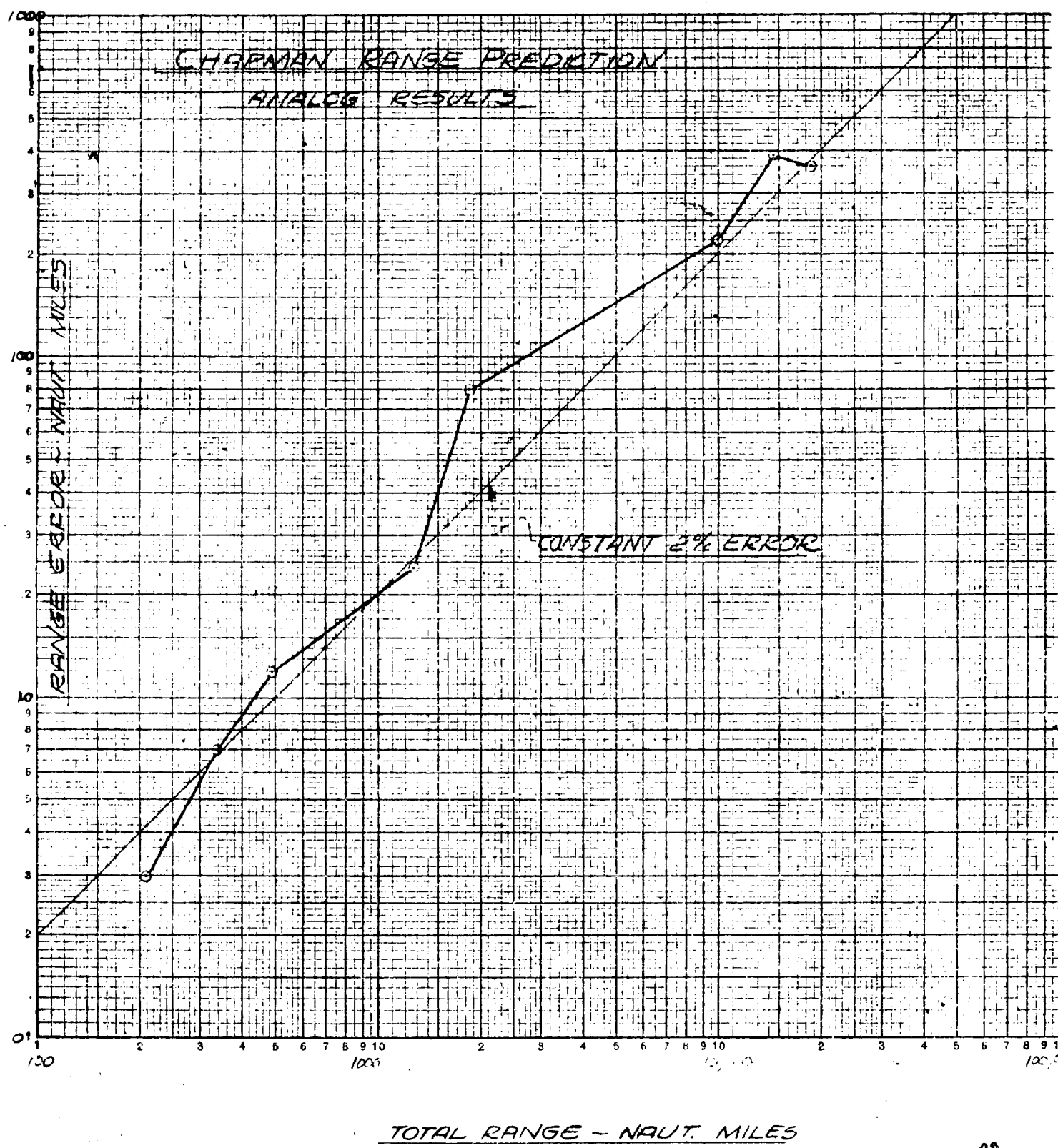


FIGURE 19 388a

K&E LOGARITHMIC 359-120  
KEUFFEL & ESSER CO. MADE IN U.S.A.  
3 X 7 CYCLES







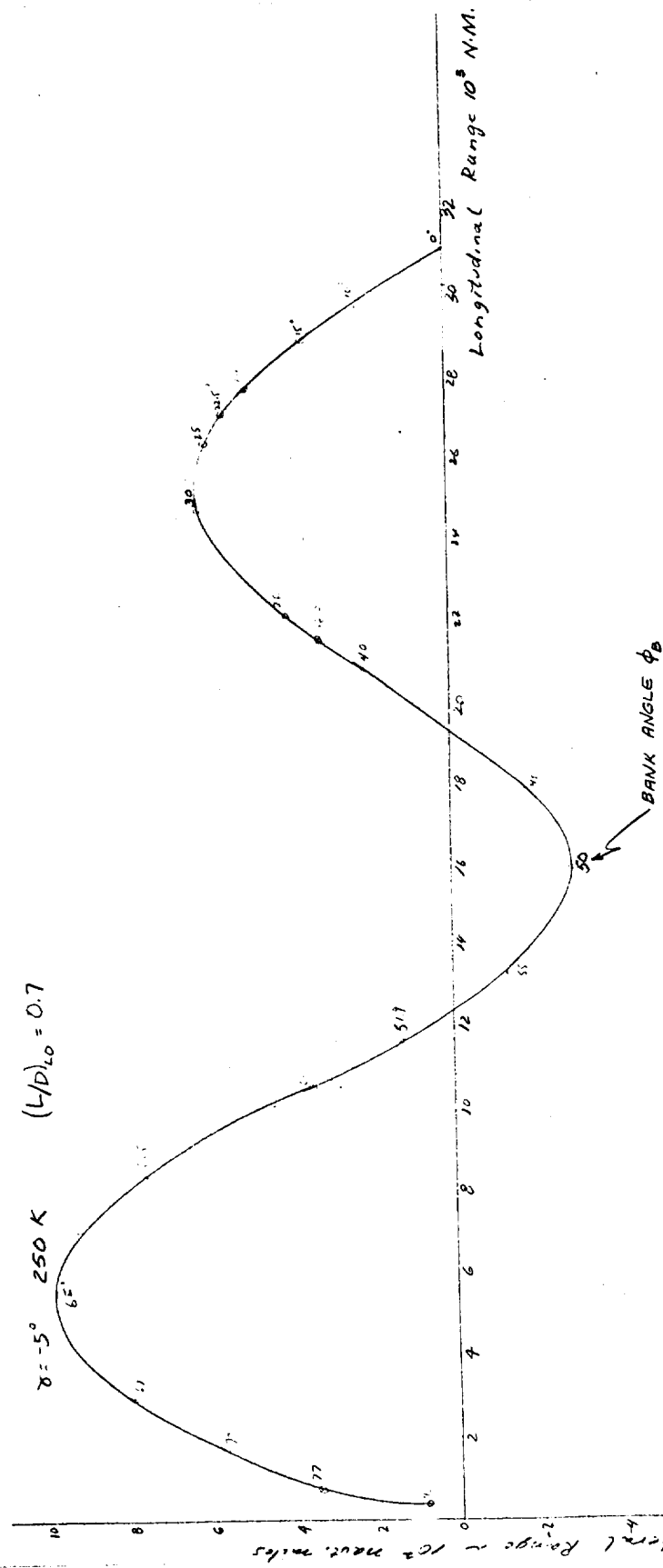
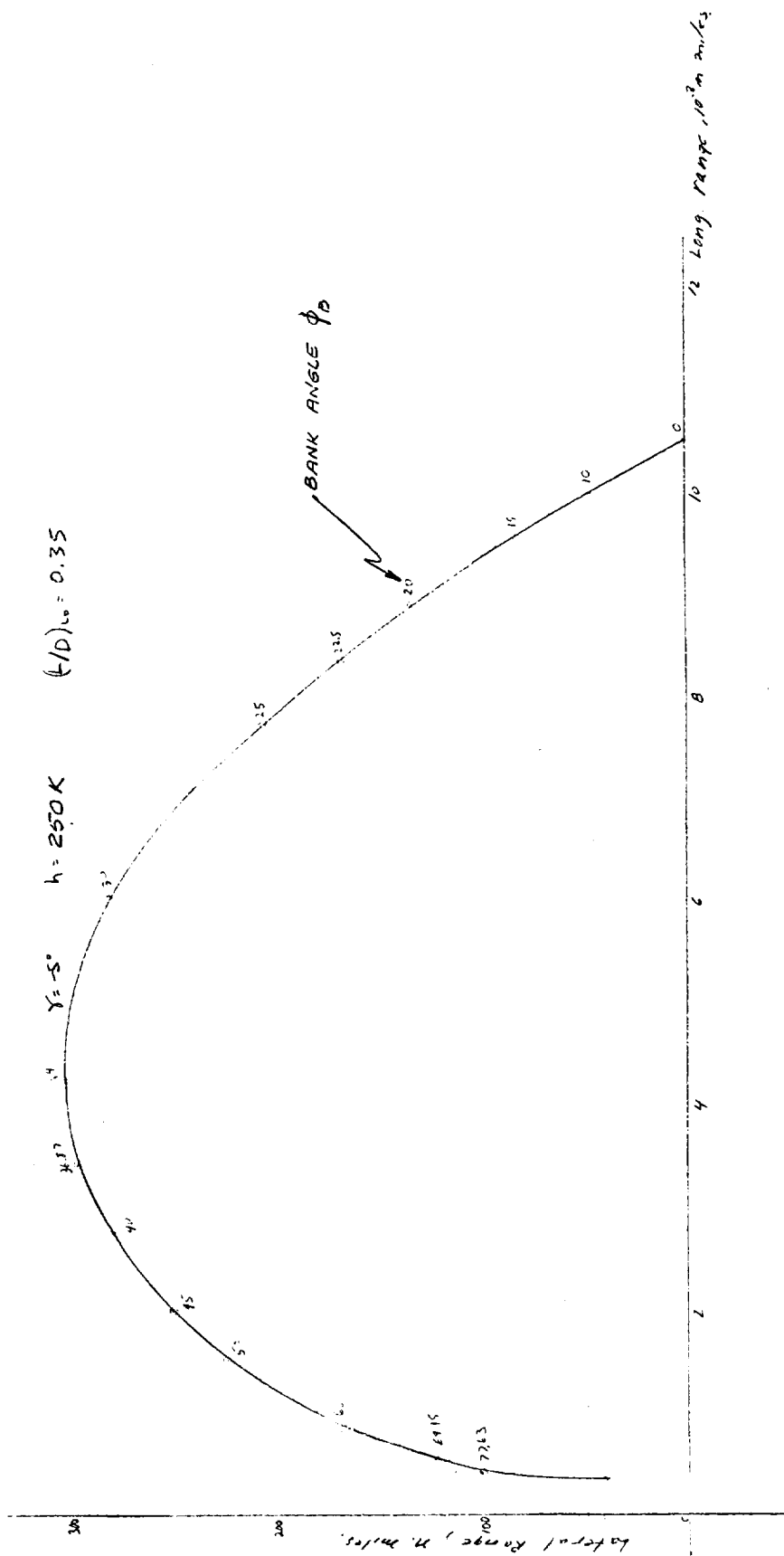
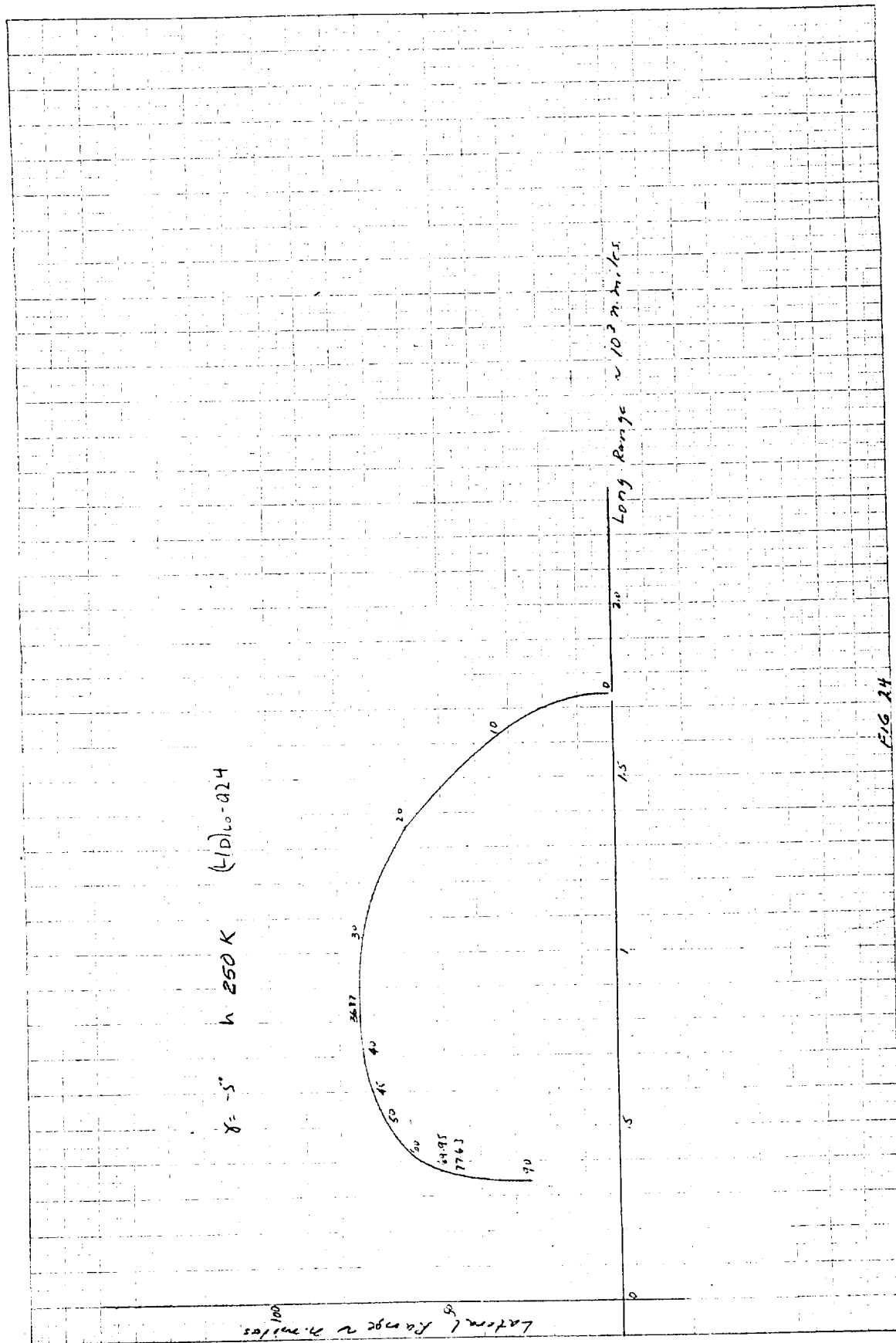


FIG 21

1 3912







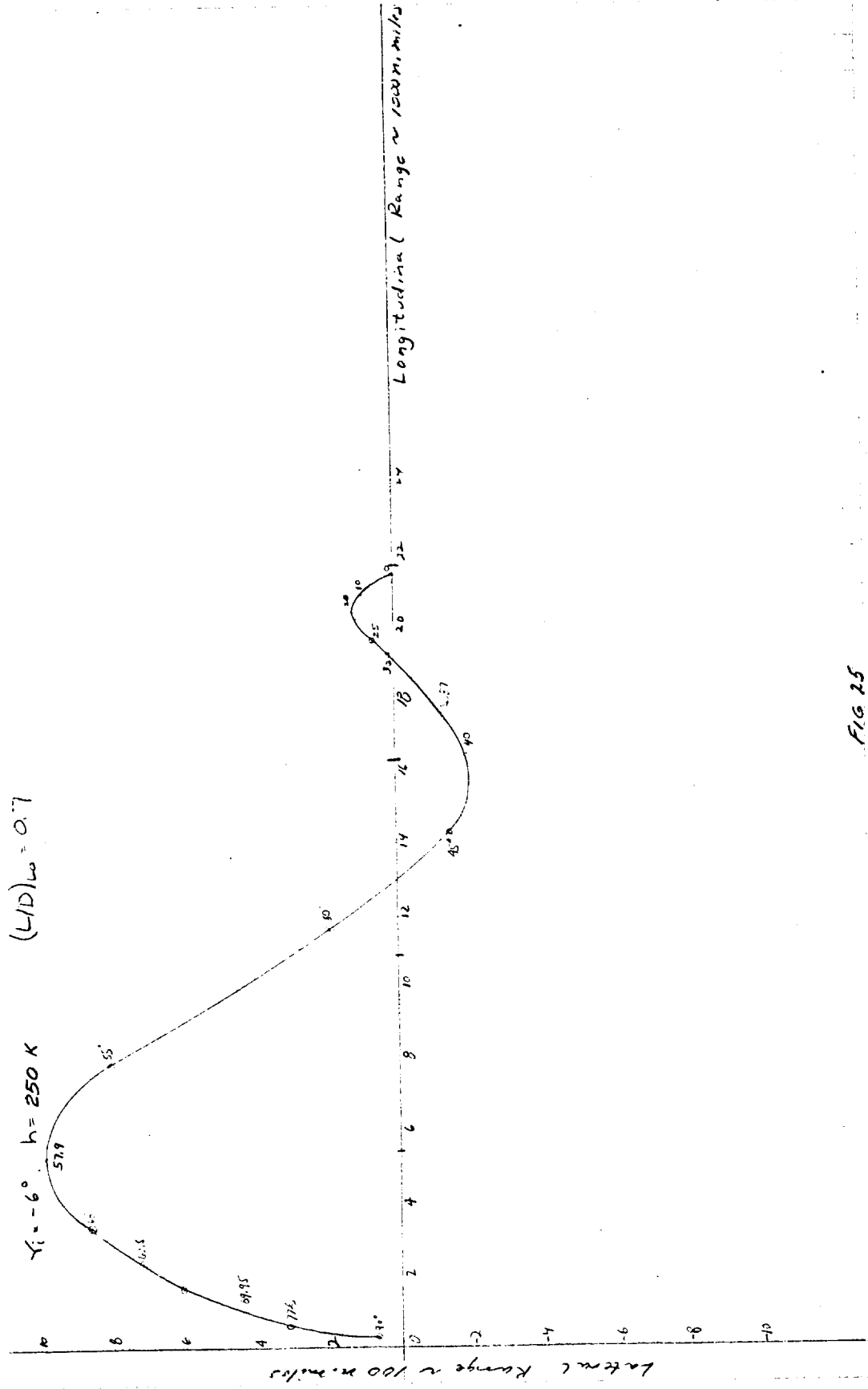


FIG 25 1395a

$\gamma = -6^\circ$      $h = 250K$      $(\gamma/D)_\infty = 0.56$

Lateral Range ~  $10^2$  m. miles

Long. Range ~  $10^3$  m. miles

FIG 26

396a

396

TM-12

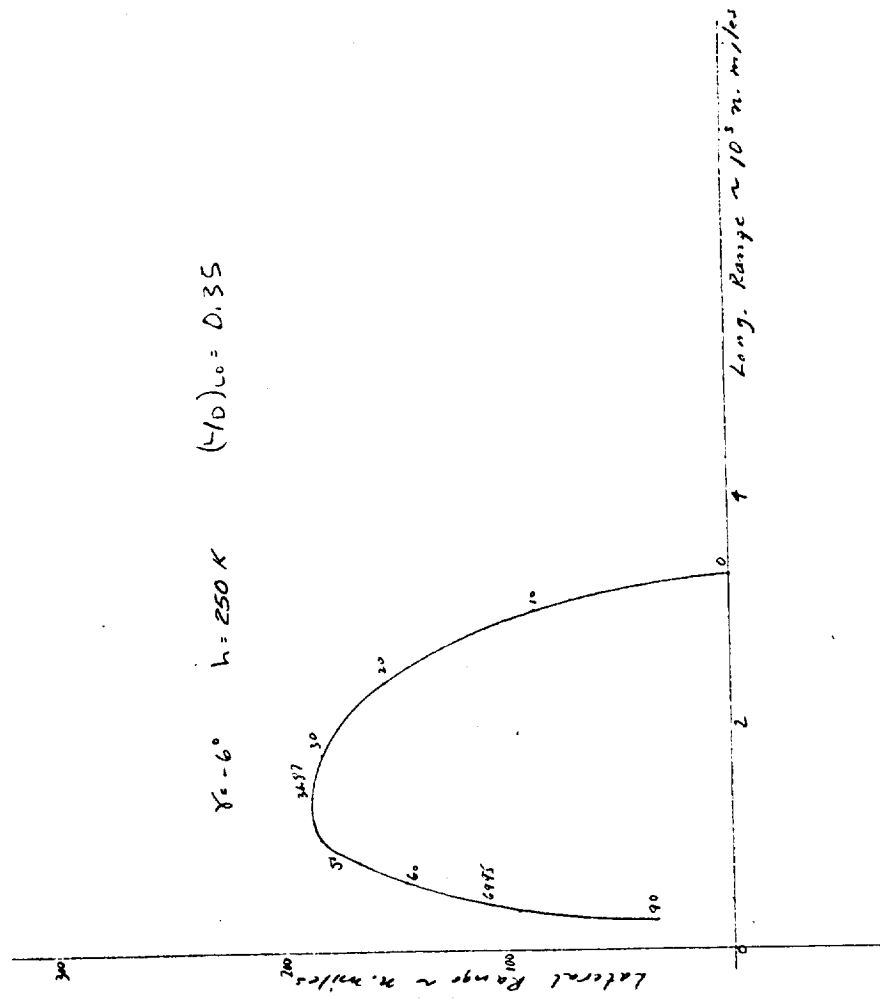
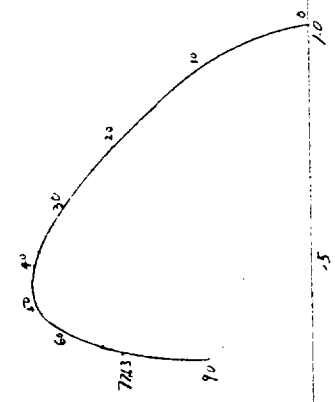


FIG 27

3970

Latitude Range = 2 miles

$\gamma = -6^\circ$     $h = 250K$     $(L/D)_{10} = 0.24$



Long Range ~ 103 n. miles

FIG 28 | 398a



$\chi_i = -7^\circ$   $h = 250 \text{ K}$   $(L/D)_{L_0} = 0.7$

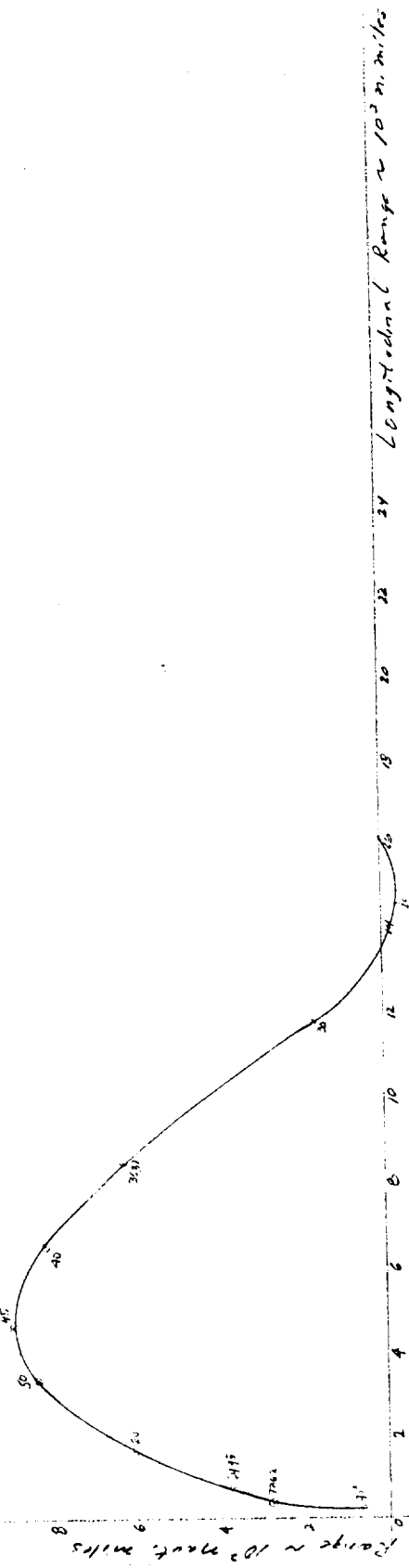


FIG 21 1399w

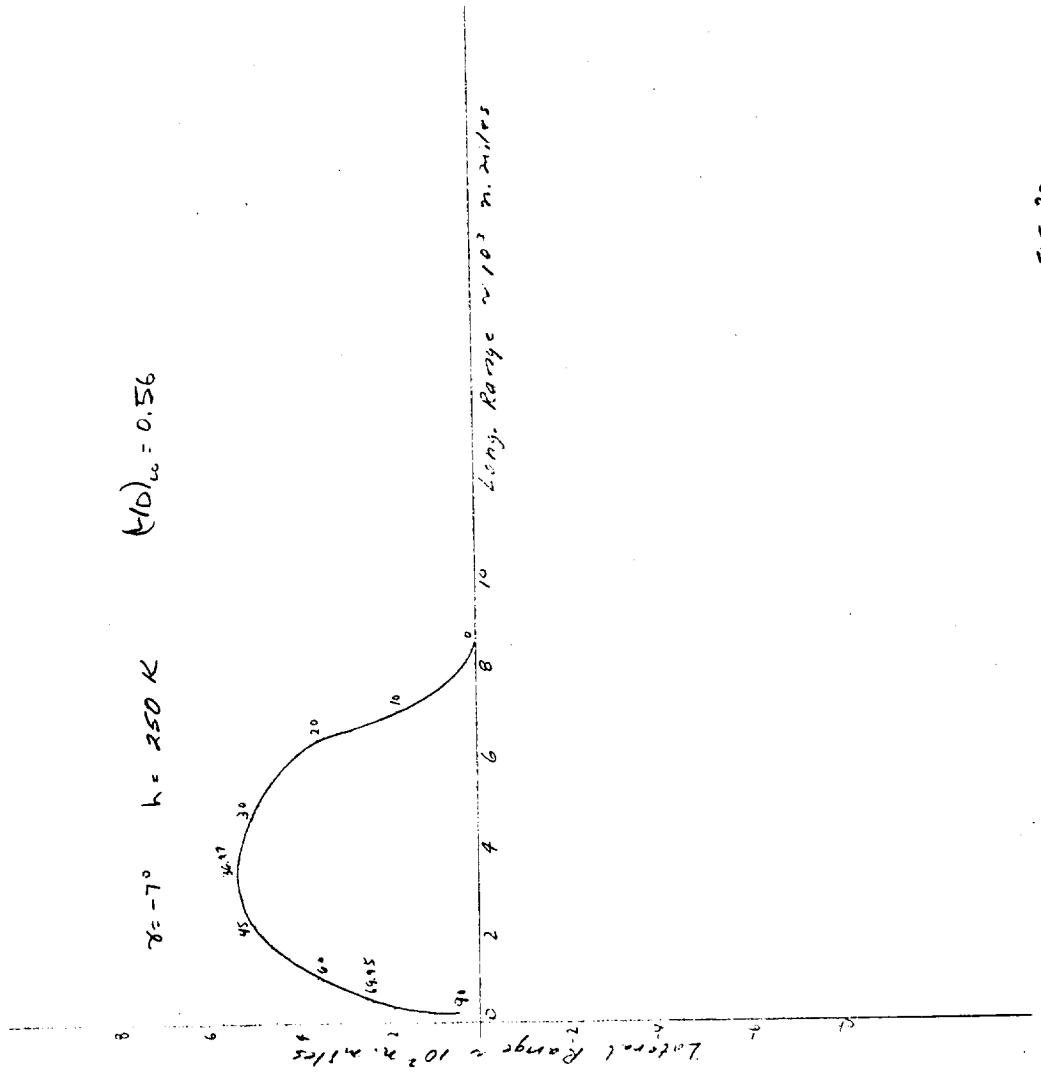


FIG 30

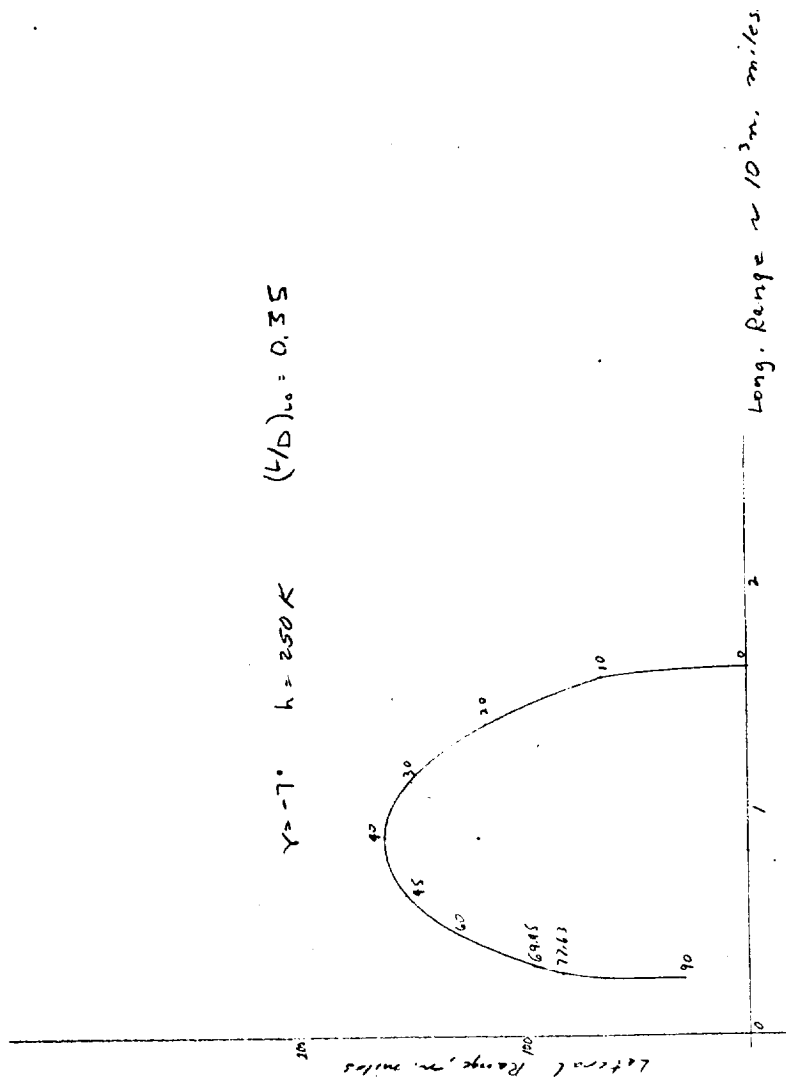
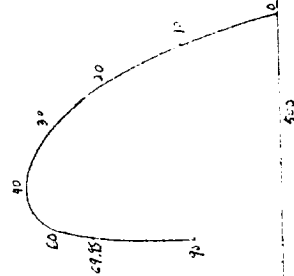


FIG 31

$$\gamma = -7^\circ \quad h = 350 \text{ K} \quad (210)_{L_0} = 0.24$$


Long Range 2 miles

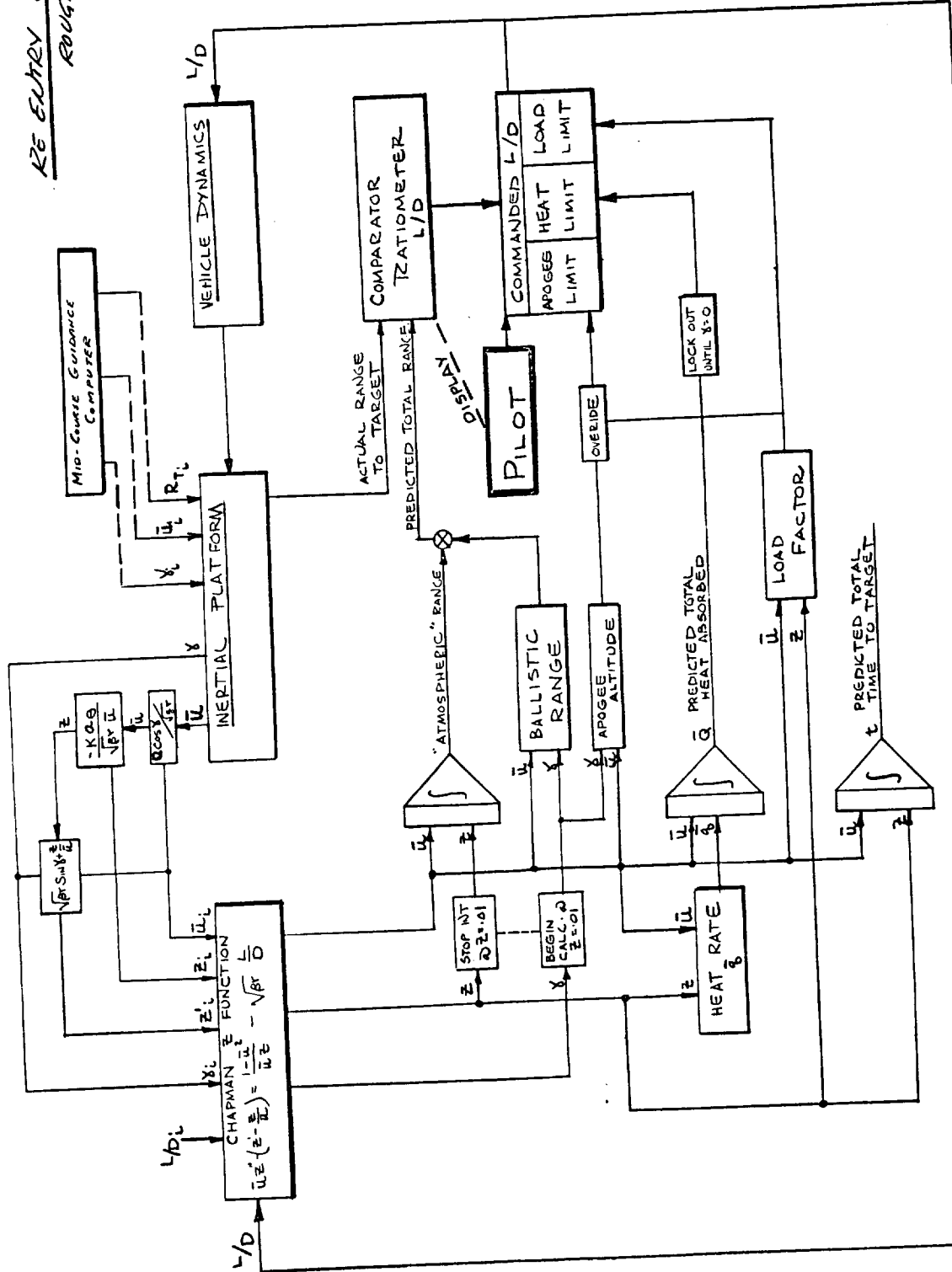
Lateral Range is 2 miles

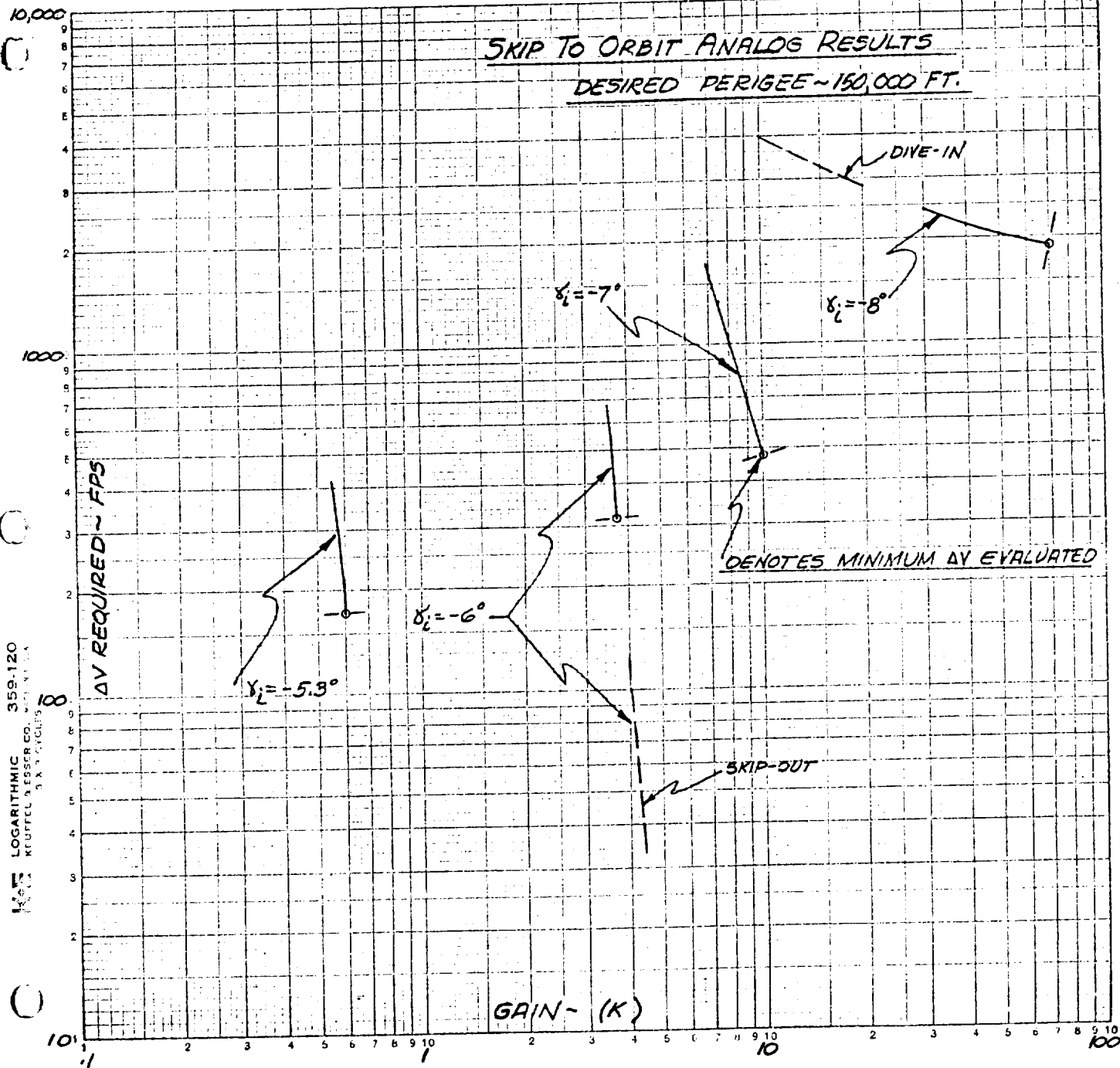
FIG 32.

402a

402  
7/11/12

RE ENTRY CONTROL LOOP  
ROUGH DRAFT!







10,000

( )

SKIP TO ORBIT ANALOG RESULTS  
DESIRED PERIGEE ~ 350,000 FT.

DENOTES MINIMUM  $\Delta V$  EVALUATED

1000

$\Delta V$  REQUIRED ~ FPS

LOGARITHMIC 359-120  
KNUFFEL DESIGN CO. VINCENNA, IN  
3 IN. CIRCLE

100

10

GAIN (K)

--- SKIPS BEYOND 400 N.M.  
— ORBITS BELOW 400 N.M.

$\delta_i = -6^\circ$

$\delta_i = -5.3^\circ$

$\delta_i = -7^\circ$

$\delta_i = -8^\circ$

406

FIG 3. TM



Reentry Corridor Definition

TM-13

CORRIDOR WIDTH ALLOCATIONS

Technical Memorandum No. 13

6 March 1961

C. Perrine

SUMMARY:

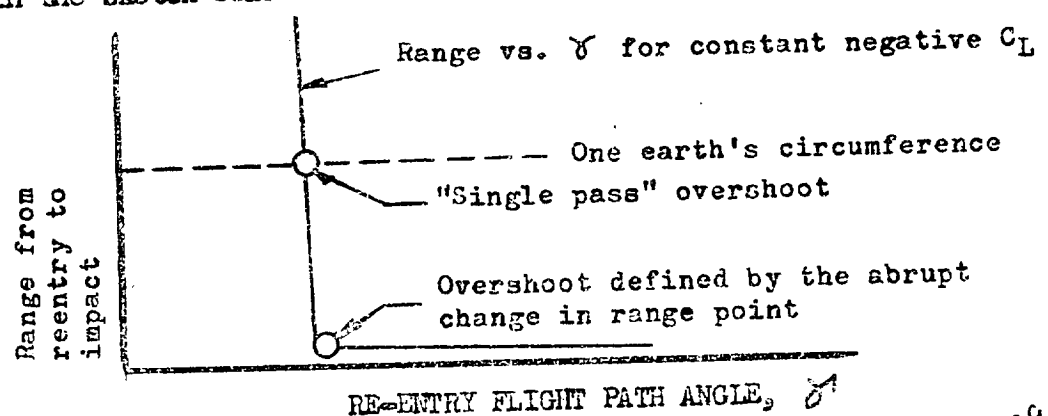
This memorandum describes the corridor width allocations for the W-1 and L-2-C vehicles. The 10 N. mi. guidance corridor, the 40 N. mi. design corridor and the modulated lift load factor limited corridors are presented and their positions relative to each other are indicated. Alternative positioning arrangements are also included to show the influence of positioning of the various corridors on maximum load factor and maximum stagnation point heating rate.

I. DEFINITION OF CORRIDORS

All corridor widths mentioned in this document refer to the vacuum perigee width as used by Chapman. The following terms are defined for use in the later discussion:

1. Negative  $CL_{max}$  Overshoot

There are a variety of definitions in use for the overshoot boundary. For example, there is the "single pass overshoot" which is defined as the maximum perigee altitude at which the vehicle can enter at maximum negative lift coefficient and reach the earth within a range of one earth's circumference from the entry point. There is also in use the definition of overshoot based on the abrupt change in range to impact described in the sketch below:



The difference in overshoot entry angle between these two definitions is about  $.05^\circ$  which is equivalent to about one half mile in corridor width.

The negative  $C_{L_{\max}}$  overshoot definition employed in this document falls somewhere between these two definitions. Here the negative  $C_{L_{\max}}$  overshoot boundary is defined as the maximum perigee altitude at which the vehicle can enter at negative  $C_{L_{\max}}$  and remain within the atmosphere. (400,000 ft.)

The primary point to be made is that the effect of the overshoot definition employed has a negligible effect on the corridor widths presented.

## 2. Positive $C_{L_{\max}}$ Overshoot

The positive  $C_{L_{\max}}$  overshoot boundary is defined arbitrarily as the maximum perigee altitude for which the vehicle can enter at positive  $C_{L_{\max}}$  to the point where  $\gamma = 0^\circ$  at which time negative  $C_{L_{\max}}$  is applied and the vehicle is able to remain within the atmosphere.

The purpose of introducing this overshoot definition is to illustrate the reduction in corridor width which would occur if it were necessary to enter the atmosphere without precise flight path angle information. For example, in emergency situations in which knowledge of the exact reentry conditions are not available, the vehicle would have to enter at positive lift until it was determined (from a load factor time history, for example) that an overshoot condition existed. Once this was determined, a roll to negative lift would be performed. The positive  $C_{L_{\max}}$  overshoot boundary is then representative of a practical boundary for this emergency condition.

This overshoot boundary is approximately 5 to 7 n.mi. below the negative  $C_{L_{max}}$  boundary.

### 3. Guidance Corridor

The guidance corridor is the  $3\sigma$  corridor width attainable for a final midcourse correction at 30,000 n.mi. from the earth. This corridor width is estimated to be 10 n.mi. or  $\pm 5$  n.mi. about the desired perigee altitude. The reason for making no midcourse corrections closer than 30,000 n.mi. is the rapid increase in propulsive velocity increments required to produce a given change in perigee altitude as the altitude decreases. The improvement in altitude measurement accuracy at the point where the radar altimeter becomes effective results in improved knowledge of the reentry conditions. It is estimated that the entry flight path angle will be known to within  $\pm 0.05^\circ$  by the time reentry is initiated. This means that the location of the vehicle within the 10 n.mi. guidance corridor will be known to within about 0.5 n.mi. This accuracy is sufficient for reentry trajectory predictions required for reentry guidance.

### 4. Design Corridor

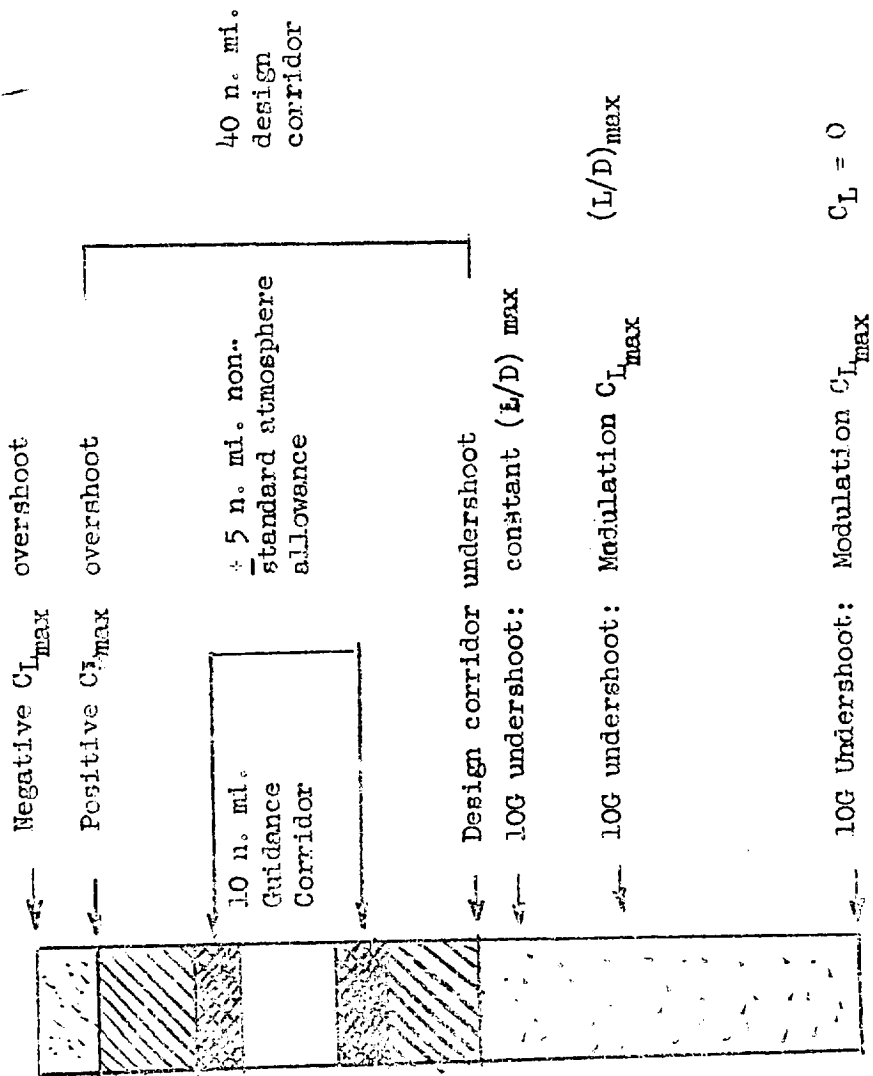
It is not considered practical to design the reentry vehicle for only the 10 n.mi. guidance corridor. However, it is not yet clear how much additional corridor width should be provided. Until such information becomes available, it will be assumed that the reentry vehicle will be designed for a 40 n.mi. corridor width. In addition, it has been assumed that this 40 n.mi. corridor is measured with respect to the positive  $C_{L_{max}}$  overshoot.

The combination of these two assumptions will result in a conservative reentry vehicle design.

#### 5. G-limited Undershoot

The minimum perigee altitude at which the vehicle can re-enter and not exceed a specified maximum load factor (G) load factor is referred to as the G-limited undershoot boundary of the corridor. In order to be able to determine this boundary for a given vehicle, two quantities must first be specified: (1) the maximum allowable load factor and (2) the technique by which the vehicle's attitude is to be controlled. Figure 1 and 2 illustrate some of the possible combinations of these two variables for the W-1 and L-2-C vehicles respectively. Also shown for later information are the corresponding maximum stagnation point convective and radiative heating rate and the time duration for which the load factor exceeds 5G. Total heat loads have not been shown because of their dependence on other parameters not considered here. The corridor widths presented in these two figures are referenced to the positive  $C_{L_{max}}$  overshoot.

# W-1 CORRIDOR ALLOCATION



## II. Corridor Width Allocations

The tentative positioning of the various corridors with respect to each other is shown in Figure 3 for the W-1 vehicle. The figure is essentially the same for the L-2-C configuration with the exception of the region below 40 n.mi. corridor. This additional corridor capability does not exist for the L-2-C due to the restriction on allowable angle of attack imposed by after-body heating considerations. This additional corridor capability may or may not be available to the W-1 depending on the detailed characteristics of the heat shield design which evolve from the 40 n.mi. design corridor.

The important characteristics to be noted from Fig. 3 are:

1. The use of the positive  $C_{L_{max}}$  overshoot in defining the design corridor.
2. The central location of the guidance corridor within the design corridor.
3. The  $\pm 5$  n.mi. corridor allocation for expected variations in atmospheric density leaving  $\pm 10$  n.mi. additional corridor margin within the design corridor.

The maximum load factors and heating rates associated with the above corridor arrangement are tabulated in Table 1. The column on the left of the table lists five possible combinations of overshoot definition, guidance corridor location, and lift control technique during the initial phase of the reentry. The possible overshoot definitions are the positive and negative  $C_{L_{max}}$  overshoot. The guidance corridor locations within the design corridor are (1) the "mid" location with the desired perigee 20 n.mi. below the  $+ C_{L_{max}}$  overshoot and (2) the upper location with the desired perigee 10 n.mi. below the  $+ C_{L_{max}}$  overshoot. The lift control techniques shown are



constant  $C_{L_{max}}$ , constant  $(L/D)_{max}$  and lift modulation from  $C_{L_{max}}$  to  $(L/D)_{max}$ .

Combination #1 in the first column is the proposed method of operating the vehicle. The resulting peak load factors of 6 to 8G in the guidance corridor are within the experimental human G tolerances. However, it may be found that the period of weightlessness prior to the reentry reduces the crew's G tolerance. In this event, it would be of interest to learn what alternatives to the present plan are available. Combinations #2 through #5 present four possible alternatives. Both the reduction in load factor and change in peak heating rates are shown. It is apparent that substantial load factor reductions may be achieved at the expense of more severe heating conditions or reduced margin between the guidance and design corridor overshoots. A very similar situation exists for the L-2-C.

CONFIDENTIAL

TABLE 1

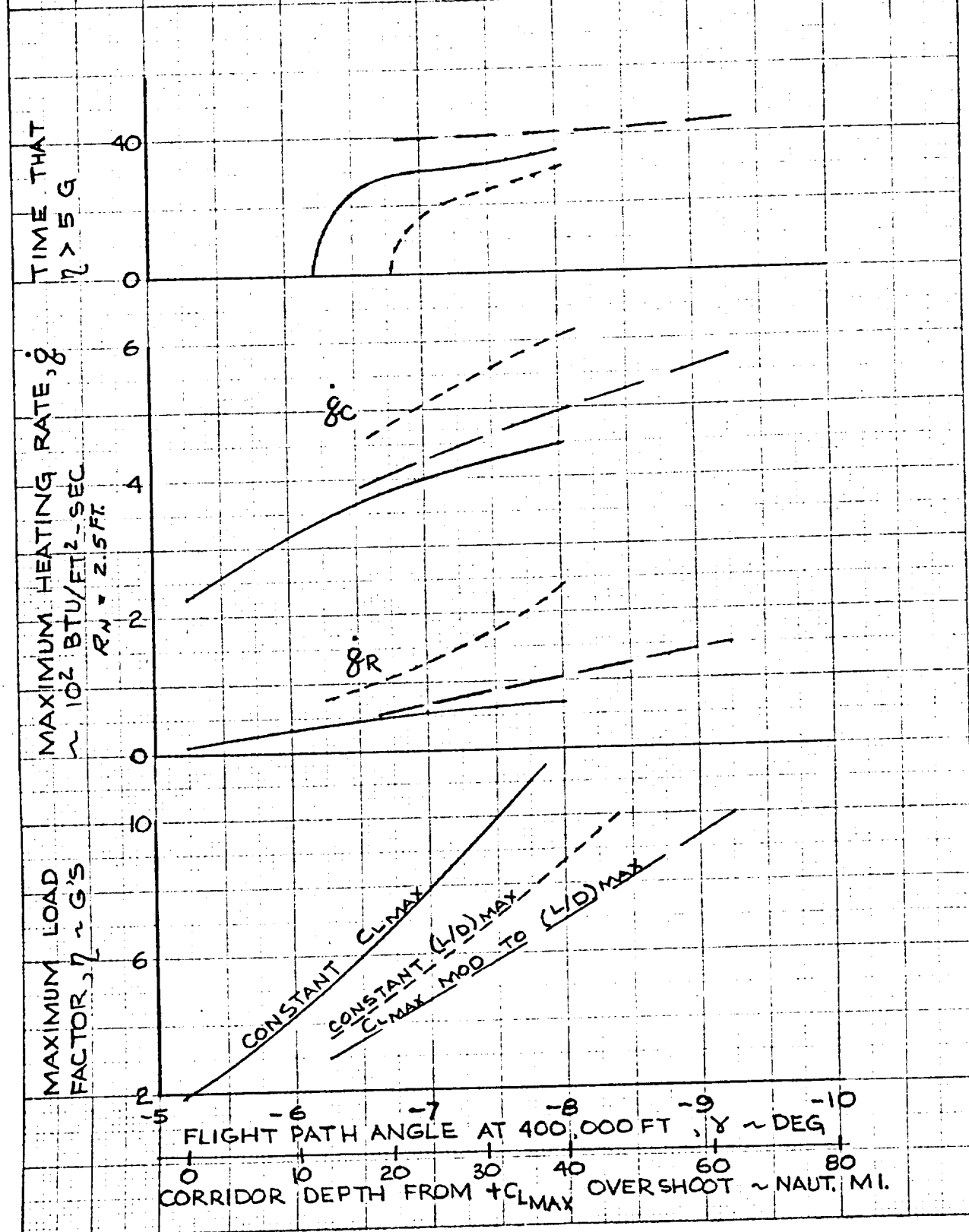
SUMMARY OF MAXIMUM LOAD FACTORS AND HEATING RATES FOR W-1

\*Numbers in brackets are radiative heating rates, without ( ) are convective.

	Maximum Load Factor (G)			*Maximum Stagnation Heat Rate		
	Guidance Corridor Overshoot	Guidance Corridor Undershoot	Design Corridor Undershoot	Guidance Corridor Overshoot	Guidance Corridor Overshoot	Design Corridor Undershoot
1. +CL <sub>max</sub> overshoot, mid location, CL <sub>max</sub> constant.	5.6	8.3	12.0	352 (40)	404 (59)	460 (75)
2. +CL <sub>max</sub> overshoot, mid location, (L/D) <sub>max</sub> constant.	3.9	5.9	8.7	468 (83)	518 (135)	605 (235)
3. -CL <sub>max</sub> overshoot, mid location, CL <sub>max</sub> constant.	4.3	6.4	10.3	315 (35)	372 (49)	439 (65)
4. +CL <sub>max</sub> overshoot, upper location, CL <sub>max</sub> constant.	3.0	5.6	12.0	270 (22)	352 (40)	460 (75)
5. +CL <sub>max</sub> overshoot, mid location, modul. CL <sub>max</sub> → (L/D) <sub>max</sub>	3.1	4.9	7.0	380 (40)	435 (71)	497 (105)

# W-1 VEHICLE REENTRY CORRIDOR SUMMARY

$V_E = 36,000$  FPS



TM-13 FIG-1

# L-2C VEHICLE REENTRY CORRIDOR SUMMARY

$V_E = 36000 \text{ FPS}$

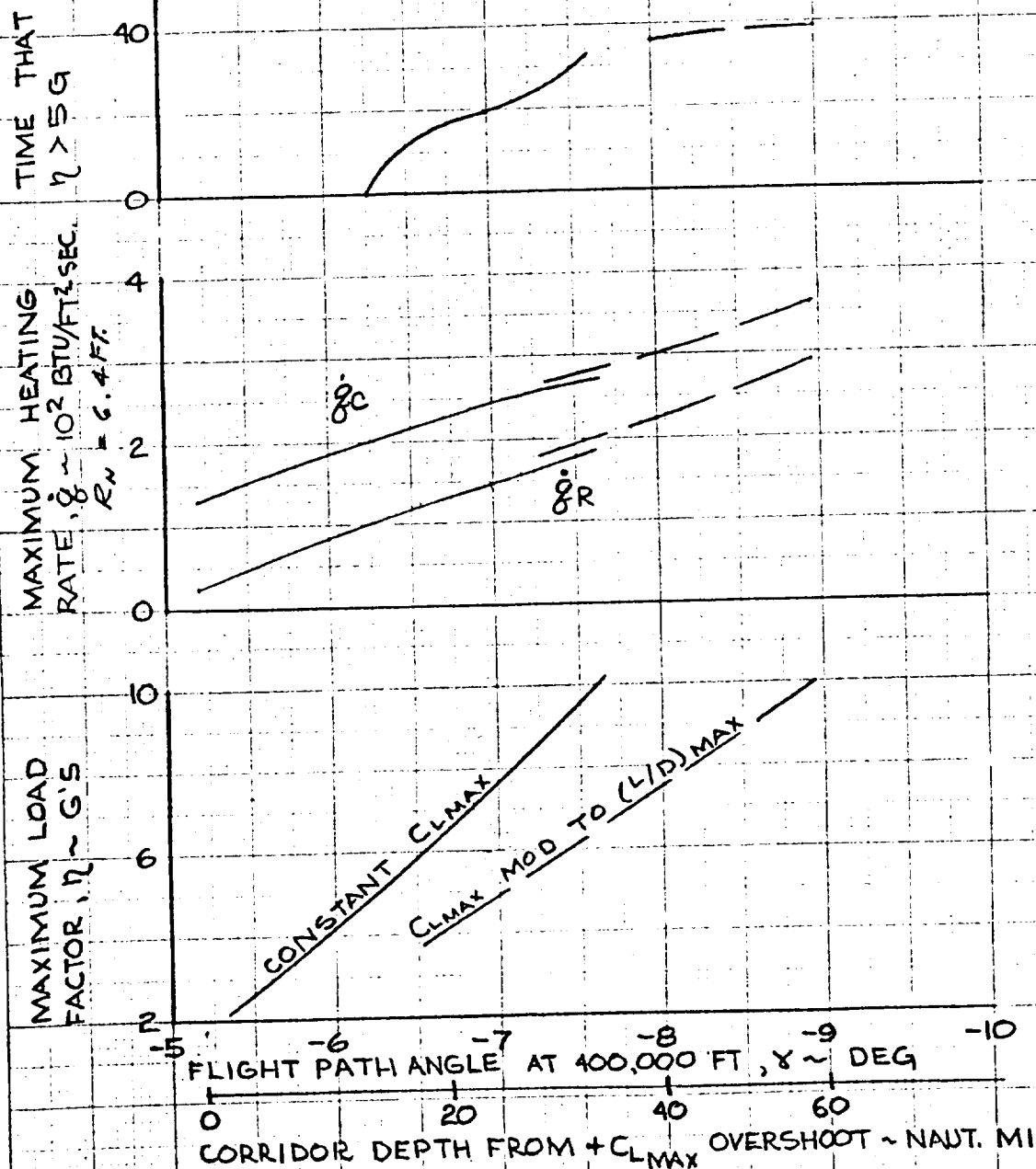
TIME THAT  
 $\eta > 5G$

MAXIMUM HEATING  
RATE,  $\dot{q} \sim 10^2 \text{ BTU/FT}^2\text{SEC.}$   
 $R_N = 6.4 \text{ FT.}$

MAXIMUM LOAD  
FACTOR,  $\eta \sim G'S$

FLIGHT PATH ANGLE AT 400,000 FT,  $\gamma \sim \text{DEG}$

CORRIDOR DEPTH FROM  $+C_{LMAX}$  OVERSHOOT  $\sim \text{NAUT. MI}$



TM-13 FIG - 2